EROSION-CORROSION MITIGATION USING CHEMICALS

by

Chun Wang

MSc (BSc)

Thesis submitted in accordance with the requirements for the degree of

Doctor of Philosophy

The University of Leeds

School of Mechanical Engineering

March 2007

ACKNOWLEDGEMENTS

I would like to express my sincerest gratitude to Professor Anne Neville for her invaluable supervision, guidance, understanding, advice, comments, patience, kindness, and dedication through the course of the PhD and preparation of this dissertation. She has encouraged me incredibly in this work and will encourage me in my work in the coming years.

I would like to thank the staff at both the Heriot-Watt University and the University of Leeds who have made my research possible and enjoyable. Thanks to all the administrators and technicians.

My great appreciation must also go to my research collaborators, S. Ramachandran, C. Gamble, and Wai Mok from Baker Petrolite USA and UK, who kindly provided useful information. The financial assistance provided by Baker Petrolite is greatly appreciated.

There are also so many individuals who gave their valuable attributions and assistance in the completion of this dissertation. It is not possible to list all. I apologise for any omissions. I would like to thank Chen, Faisal, Haque, Dao, MuZhong for interesting discussion. I also like to thank friends from University of Leeds, Ugur, Ardian, Jico, Juan, Inga, Aurilie, Elefthera, Annelise, Kuldeep, John, Rock, Ley, Zhaomiao, David and Bertram; Thanks friends from Edinburgh, James, Hugo, Hao, Jinping, Xiaodong, Hong, Taoxin, XiaoYan and MC for their friendship, kindness and emotional support. Special thanks goes to the great person for our group, Mark for his invaluable help for my son during my PhD study. I want to thank you all for the good memories and the good time.

Specially and most importantly, dedicated to my parents, ShuHong Wang and SuYing Liu, my sisters Yan and Ai for their unlimited support, patience, understanding and love. I owe them my most sincere thanks. Last but not least dedicated to my son Sitong Chen, to wish him a very bright future.

ABSTRACT

The presence of entrained sand in oil and gas production is becoming increasingly prevalent as wells age and this is leading to erosion-corrosion in CO_2-saturated conditions becoming a major mechanism of material attack. Its understanding, prediction and control are key challenges to sound facilities design.

The use of carbon steel in conjunction with corrosion inhibitors in preventing erosion-corrosion has been observed as an economically viable solution for oil and gas piping systems. In order to produce highly effective corrosion inhibitors, it is important to understand how inhibitors act on each of the components of erosion-corrosion. Although research into *corrosion* inhibition has been extensively conducted, there is less documentation of inhibitors in retarding *erosion-corrosion*. This thesis has attempted to construct a quantitative structure relationship between erosion, corrosion and their synergistic effects to investigate erosion-corrosion and inhibition mechanisms with four fully formulated CO_2 inhibitors (CGO, CRO, CRW8 and CRW9) along with some mechanistic studies involving single components from inhibitor formulations.

Two experimental set-ups were used: a rotating cylinder electrode (RCE) and a submerged impinging jet (SIJ). In both experimental methodologies, gravimetric measurement, cathodic polarisation, Linear Polarisation and AC impedance techniques were used to ascertain the extent of corrosion as a function of conditions and inhibitor dosing/type. Both RCE and SIJ test samples were studied using surface analysis techniques such as scanning electron microscope (SEM), Light microscope, Energy dispersive X-ray (EDX) and X-ray photoelectron spectroscopy (XPS).

In this thesis, through integration of electrochemical analysis and gravimetric measurements the damage has been identified as being associated with mechanical erosion, electrochemical corrosion or interactive electrochemical/mechanical processes. The role that inhibitors can play in reducing damage in addition to that caused by corrosion, namely by erosion and their synergistic action has been shown. Under both configurations, erosion-corrosion interactions play a major role in damage with

corrosion being a controlling parameter. The thesis has made substantial advances in the understanding of the extent to which corrosion inhibitors could be used to control erosion-corrosion damage and in understanding the mechanisms of how this can be achieved.

THESIS RELATED PUBLICATIONS

1) Neville, A. and Wang, C., Ramachandran, S. and Jovancicevic, V. (2003). Erosion-corrosion mitigation using chemicals, *CORROSION 2003, NACE*, paper No. 319, April, 2003, San Diego, USA.

2) Wang, C., Neville, A. and Ramachandran, S. (2004), Understanding the action of inhibitors in mitigating erosion-corrosion in impinging flows. *CORROSION/2004, NACE*, paper No. 4658, March, 2004, New Orleans, USA.

3) Wang, C., Neville, A. and Ramachandran, S. (2004), Understanding inhibitor action on components of erosion, corrosion and their interactions in CO_2-containing slurries, *Proceedings of the First International Oilfield Corrosion Symposium; SPE*, paper No. 87551, Aberdeen, UK.

4) Wang, C., Neville, A., Ramachandran, S. and Jovancicevic, V. (2005). Alleviation of erosion-corrosion damage by liquid-sand impact through use of chemicals, *Wear*, Vol. 258, no. 1-4, pp. 649-658.

5) Wang, C. and Neville, A. (2005), The action of inhibitor on corrosion, corrosion-erosion in CO_2 containing sand by RCE and impinging jet. *CD-ROM. Proceedings of the 16th International Corrosion Congress*, Beijing, China.

6) Wang, C and Neville, A. (2006), Inhibitor performance on corrosion, erosion-corrosion under turbulent flow with sand and CO_2 saturated system—AC impedance study. *Proceedings of the Third International Symposium on Oilfield Corrosion, SPE*, paper No. 100441. Aberdeen, UK.

CHAPTER 1 INTRODUCTION

1.1 Problems Caused by CO_2 Corrosion

CO_2 is an important component in oil well corrosion. Although it occurs naturally, its level can be increased as a result of enhanced oil recovery. This can be achieved through a gas drive mechanism, where the gas may be in the form of injected CO_2. Apart from aiding the recovery of oil after the primary stage, carbon dioxide, due to its high solubility in oil, is able to reduce oil viscosity and assist mobility. Due to the use of enhanced oil recovery techniques, it is apparent that CO_2 corrosion of carbon and low alloy steels, or "sweet corrosion", is by far the most prevalent form of attack in oil and gas production, from downhole to gathering transportation and processing facilities (Dugstad, 1992).

The term "sweet" is applied to environments containing carbon dioxide (CO_2) and "sour" to those containing H_2S. Corrosion-related failures constitute over 25% of failures experienced in the oil and gas industry. More than half of these failures are associated with sweet and sour producing fluids. Corrosion costs typically in any one year represent about 3% of gross domestic product (GDP) for developed countries. If this is translated directly onto a company's balance sheet as a percentage of turnover, then it represents major costs in any one year (Dugstad, 1992). Reduction of costs that are currently unavoidable or even potentially avoidable will depend on advances in technology and thus present challenges for research and development.

The wide-ranging environmental conditions in the oil and gas industry necessitate appropriate and cost-effective materials choice and corrosion-control measurements. Industry continues to lean heavily on extended use of carbon and low-alloy steels, which are able to meet many of the mechanical, structural, fabrication, and cost requirements. Corrosion of carbon low alloy steel must always be seen as a potential risk. Because of both high corrosion rates and severe localized corrosion (Dugstad *et al.*, 1994). CO_2 corrosion of carbon and low alloy steels has been reported as one of the important problems in the oil and gas industry since 1940. It has been observed over the

past four decades (e.g. Ikeda. 1984; Crolet, 1994). The problem has long been recognized to cause corrosion damage in many components, such as scrubbers and condensers, in pumps, in pipes, in storage systems and distribution lines as well as in production equipment and therefore has prompted extensive studies. Rigorous laboratory testing and practical field testing have allowed development methods to control uniform corrosion by inhibition, coatings etc. However, localized corrosion is still an unsolved problem which needs a much more systematic research effort.

Although there is some debate about the mechanism of CO_2 corrosion in terms of which dissolved species are involved in the corrosion reaction, it is generally accepted that the carbon dioxide partial pressure and temperature influence the corrosion rate. However, a recent study by Nesic *et al.* (1996) has concluded that there are several different pH-dependent anodic mechanisms for iron dissolution in CO_2 solutions. Velocity effects also are very important in the CO_2 system; turbulence is often a critical factor in pushing a sweet system into a corrosive regime. Notwithstanding, the mechanisms of carbon dioxide corrosion is a complicated process that is influenced by many factors and conditions. Existing quantitative models are unreliable in predicting the actual long-term CO_2 corrosion rate of carbon and low-alloy steels, which invariably results in over-specification of materials and impacts adversely on the cost of production of oil and gas (Kermani and Harrop, 1996). A very simple " rule of thumb" approach often cited in the industry in defining the risk of CO_2 corrosion of carbon steel and low-alloy steels is given in Table 1.1, which is based on field experience, principally in the US (Kermani and Morshed, 2003). More specific questions on service life, risk analysis, corrosion allowance, and inhibited corrosion rates require the ability to conduct a quantitative assessment. Thus the ability to predict corrosion rates for a given set of conditions is important.

Uniform corrosion rates in a CO_2 system are low, could be up to 40 mpy and less than 4-8 mpy (mils per year) due to the presence of a protective layer or corrosion inhibitor. As to localised corrosion, the penetration rate can reach very high levels (thousands of mils per year), and efforts has been made to work on better localised inhibitors. Corrosion in the presence of CO_2 can be controlled through the use of adsorption

inhibitors. The development of corrosion inhibitors for the oil industry occurred mainly in 1940s and 1950s (Harrop, 2004). In the mid-1940s, long-chain polar compounds were shown to have inhibitive properties. This discovery dramatically altered the inhibitor practices in primary production oil and gas wells. It permitted operation of wells, otherwise, entire reservoirs would have to be abandoned because of the corrosivity and volume of water produced along with the hydrocarbons. Inhibitors used in gas and oil wells include a number of nitrogen-containing compounds, such as amines, imidazolenes, amides and quaternary ammonium salts. These inhibitors adsorb on the metal surface by forming a film. Improving the effectiveness and efficiency of oil field corrosion inhibitors can undoubtedly still save industry millions of pounds per year in chemicals and lost production. An important part of corrosion inhibition is good inhibitor selection.

Conditions	**Corrosivity**
P_{CO_2} < 0.5 bar	Corrosion unlikely
0.5 bar < P_{CO_2} < 2 bar	Possible corrosion
P_{CO_2} >2 bar	Corrosion likely

Table 1.1 Rule of Thumb – CO_2 corrosion of carbon and low-alloy steels (P_{CO_2} is partial pressure of CO_2) (Kermani and Morshed, 2003)

Using organic adsorption corrosion inhibitors continues to be one of the primary methods of controlling internal corrosion. Other methods are available to control CO_2 corrosion, although it is common practice in most places to use simultaneous combination of corrosion control methods. Highly corrosion-resistant steels are rarely used because of the prohibitive cost of such materials. Using carbon steel in conjunction with chemical inhibitor treatments remains a cost-effective method of corrosion control. However, the inhibition mechanism of inhibitors remains poorly understood in the respects of the properties of inhibitor film (Zhang *et al.*, 2001; Villamizar, 2006).

Once the inhibitor is in use, good management and monitoring becomes important. Accurate predictions of corrosion in crude oil production systems are very difficult. The acid gas partial pressures, temperature, produced water composition, crude oil composition, and level of produced water combine to influence corrosion characteristics of steel in production fluids. Inability to accurately define production conditions where dangerous levels of corrosion will occur generally necessitates a very conservative approach because of the consequences of failure.

The engineer ideally wants a predictive tool that can be readily applied and is suitable for application at all stages of project development and subsequent operation. CO_2 corrosion process has the overlying effects of such factors as flow regime, film formation/deposition, hydrocarbon phase and corrosion inhibitor which cloud or complicate the picture.

1.2 Erosion-Corrosion Effect in Oil and Gas Production

In the search for new sources, oil and gas will increasingly be produced from deeper wells in more difficult-to reach regions, where multiphase transport is deployed, this has created increased challenges to the economy of project development and subsequent operations. All practical piping systems require turbulent flow. The fluid would not flow fast enough if laminar flow were maintained. Not only localised corrosion but erosion-corrosion can be attributed to multiphase fluid flow. The damage to the interior of pipe walls can be enormous, resulting in unexpected shut down of the line. In addition, as sand entries into the production line, the metal damage of fittings, valves, chokes and tubing then results from corrosion-erosion effects. Repair and maintenance work on these pipelines is extremely expensive. An example of the damage in gas condensate wells is shown in Figure 1.1.

The effect of flow on CO_2 corrosion generally remains a grey area in the predictive process. It is not only flow velocity that needs to be determined; the flow regime is of equal importance, for accelerated corrosion happens under aggressive flow regimes (Efird *et al.*, 1993). The flow parameter currently favoured for determining the effect of

velocity on corrosion rate and inhibitor film formation stability is liquid shear stress at the pipe wall. Although there is limited reported data on upper limits regarding shear stress, a figure of above 100Pa for carbon steel is considered to be disruptive to surface films. However, for specific situations it is necessary to conduct laboratory tests under simulated flow conditions.

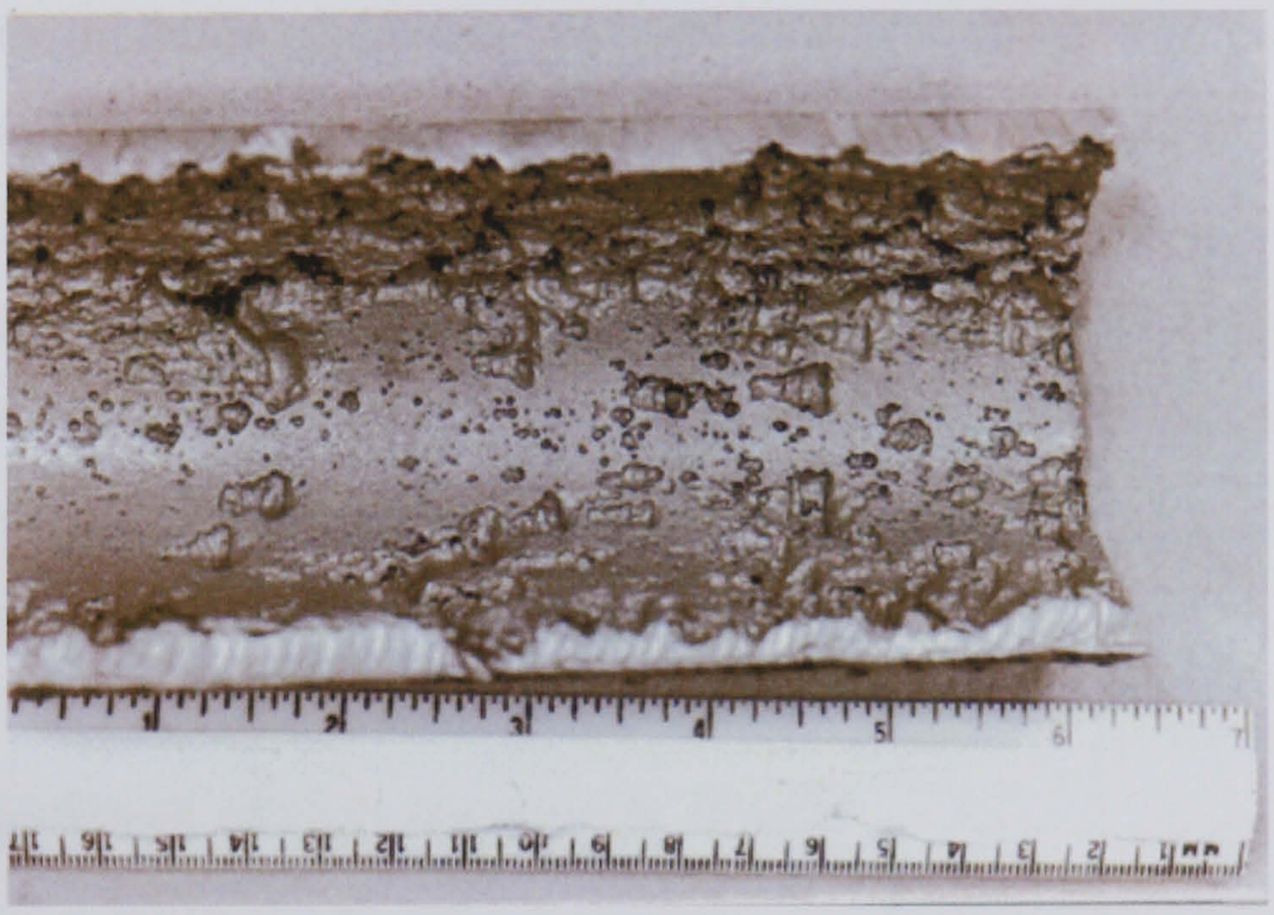

Figure 1.1 Damage due to erosion-corrosion in gas condensate system, causing deep pits with tails (Waids, 2005)

The complexity of the phenomena, the large amount of variables involved (such as temperature, pressure, flow, variable environment chemical compositions, etc.) and the broad number of different particular cases present in real life, have forced scientists to study the phenomena using many different approaches, ranging from crude experience-based criteria to sophisticated computer theoretical modelling (Dawson, 1993; Harrop, 1993). Laboratory testing becomes particularly critical when erosion is concerned to be caused by the presence of particles. There are no industry guidelines that adequately cover this situation.

When sand and particles are present, the most commonly cited equations for predicting purely erosion rates are that of Salama and Venkatesh (1983). They suggested that the fluid properties have an effect on erosion rate, but they selected the constant of the equation based on calibration with sand erosion in air. In addition, they did not account

for the sand particle size which is known to have an effect on erosion rate for particles less than 400 microns. For many situations, the mechanism is erosion-corrosion and there are very few equations to predict rates of metal loss.

Although organic corrosion inhibitors are very widely used, most inhibitor evaluations are generally only based on test results under stagnant or low flow rate (<1m/s) conditions. Those inhibitor evaluation methods may not be valid for multi-phase flow involving gas, oil, water and sand in various mixtures, which is most frequently encountered in flow lines of the oil and gas industry. Some work has been done to assess the behaviour of corrosion inhibitor films under multiphase conditions (Heeg *et al.*, 1998). Little mechanistic work under turbulent conditions has been done. The effects of flow velocity and entrained sand on inhibitor performance must be understood if the use of chemicals for erosion-corrosion can be optimised.

1.3 The Objectives of this Research Work

Up to now, corrosion inhibitor injection, especially nitrogen-based organic surfactants, such as amide amines, amido amines, imidazoline, and their salts, is still the most cost-effective method to manage and solve the corrosion problem in the oil and gas industry. Slight improvements in inhibitor performance can save the oil industry millions of pounds per annum. Research towards assessing the efficiency of carbon dioxide corrosion inhibitors is extensively conducted. However, little is done about the mechanism of carbon dioxide erosion-corrosion and its inhibition. Research under severe and extreme conditions is more and more important as companies want to increase the production rates but do not what to damage infrastructure.

In this study of erosion-corrosion prevention, it is essential to understand the mechanism of corrosion, erosion, their interactions and their inhibition. Generally, electrochemical methods (i.e., linear polarisation, anodic or cathodic polarisation, electrochemical spectroscopy or AC impedance, and electrochemical noise and Tafel measurements) are the preferred techniques for the monitoring of corrosion. Gravimetric methods are used to assess overall erosion-corrosion performance.

Cathodic protection or gravimetric measurements under N_2 with deionised water can be used to assess the pure erosion components. To obtain molecular information about the adsorbed species, such as the identity of reacting species at electrode/electrolyte interface, and the resulting interphase, a wide range of surface analysis techniques are used in the mechanistic studies of corrosion and erosion control.

Generally two qualities of corrosion inhibitors are discussed, the persistency of an inhibitor film and the efficiency of the film. The study of persistency of corrosion inhibitor films under multiphase flow regimes and its relation to the wall shear stress or mass transport is important from the fundamental aspect of understanding the mechanism of inhibition and relating inhibitor persistency to chemical structure. It is also important practically in the design of pipelines for multiphase flow and selection of suitable inhibitors. In general the efficiency and persistency of inhibitor films under multiphase flow conditions probably depend on four major factors, i.e. the type of adsorption of the inhibitor film (physisorption, chemisorption, packing order, composition and roughness of the substrate), the chemical composition of the multiphase flow, the wall shear stress/mass transport coefficient and the erosive nature of the flow.

A few studies have been carried out to investigate the mechanical persistency of corrosion inhibitors by using rotating cylinder, impingement rig, small-scale loop or even cavitation facilities (Efird *et al.*, 1993; Heeg *et al.*, 1998; Olsen *et al.*, 1995). The effects of slug flow on the inhibition performance were investigated by Ohio University a few years ago (Chen *et al.*, 2000). However, the results on inhibitor evaluations under field condition, such as high-speed single-phase flow or multiphase flow erosion-corrosion conditions, especially for liquid-solid two-phase flow are still lacking. To develop more cost-effective inhibitors, a better understanding of the mechanisms of inhibition of current inhibitors is required and one aim of the study is to progress this.

The focus of this work is to investigate the corrosion and erosion-corrosion behaviour of carbon steel with inhibitors, to characterise material loss rates and mechanisms of corrosion and erosion-corrosion in liquid-solid conditions. The effect of parameters

such as temperature, velocity, inhibitor concentration under erosion-corrosion conditions has been estimated.

The objectives of this study are:

- to assess the potential for using corrosion inhibitors to control erosion-corrosion damage in slurry flows
- to understand the controlling parameters in erosion-corrosion of carbon steel in CO_2 environments
- to study impact processes for assessing the kinetics of inhibitor film destruction and repair

The role of particles and velocity in breaking down the inhibitor film are investigated under two different configurations. One is using the rotating cylinder electrode to assess the inhibitor performance under turbulent conditions but with sand particles ploughing the material surface. Another one is to use the impinging jet to evaluate the inhibition mechanisms with sand particles impinging the metal surface at high angle. For both of these cased a series laboratory-based experiments under erosion-corrosion conditions was desired for understanding of whether inhibitor can offer an economically viable solution for carbon steel piping systems under different flow regimes. The ultimate aim is to establish a base for life prediction mainly for gas condensate systems using inhibitors. AC impedance has been used as a main tool to model the inhibitor film formed on the metal surface and its parameters can provide valuable information on the characteristics of the inhibitor film.

The liquid-solid tests have shown that the presence of the solids can bring about a sharp increase in the corrosion rate as well as accentuating mechanical damage. Inhibitors can provide protection under erosion-corrosion to an acceptable level. The components of corrosion, erosion and their interaction vary with different configurations. Under both conditions, the erosion-corrosion interaction is the main component, but corrosion is also a controlling parameter.

1.4 Outline of the Thesis

Chapter 2 presents fundamental theory of corrosion used to understand the analysis performed during electrochemical tests. Electrochemical techniques are also introduced.

Chapter 3 covers the literature review including the topics involving in this work, such as CO_2 corrosion mechanisms, erosion-corrosion and corrosion inhibitor, corrosion control and inhibition, as well as AC impedance applications.

Experimental techniques, methodology and material characterization used in this research work are presented in Chapter 4

The experimental results and discussion for carbon steel under static condition with and without inhibitors are presented in Chapter 5. It provides a detailed corrosion analysis, such as, free corrosion potential, linear polarisation and AC impedance, scanning electron microscopy, light microscopy.

Overall erosion-corrosion assessment and cathodic protection test results are presented and discussed in Chapter 6 with extensive analysis using SEM and light microscope. The corrosion *in-situ* study using RCE are presented and discussed in Chapter 7. It also provides a detailed analysis of linear polarisation and AC impedance measurements.

The experimental results using the impinging jet are presented in Chapter 8. Overall erosion-corrosion results, *in-situ* corrosion measurement analysis using linear polarisation and AC impedance, synergistic effects results, and XPS are all presented and discussed.

In Chapter 9 the main conclusions of this work are presented as well as the future work which could be carried out based on this research.

CHAPTER 2 FUNDAMENTAL THEORY

As fundamental theory, a condensed review of some of the ideas developed in the field of corrosion is presented in this chapter. The basic principles of corrosion monitoring by DC and AC methods relevant to this work have been presented and discussed.

2.1 Electrochemical Corrosion

Corrosion has been defined as 'the undesirable deterioration of a metal or alloy', namely, the metal that is to be preserved interacts with its environment causing adverse effects to its properties (Stansbury and Buchanan, 2000). The environments are most commonly air, water and soil. Depending on the environment, corrosion has been classified into low-temperature and high-temperature corrosion or wet and dry corrosion. Dry corrosion occurs in the absence of a liquid phase or above the dew point of the environment and is often associated with high temperatures. For this study, it is not relevant. Wet corrosion or aqueous corrosion occurs in the presence of liquids and usually involves aqueous solutions or electrolytes. It accounts for the greatest proportion of corrosion problems in industry.

Aqueous corrosion was defined as the degradation of a metal by an electrochemical reaction with the environment (Stansbury and Buchanan, 2000). In aqueous environment, metallic materials generally corrode by an electrochemical process. This is an interfacial phenomenon, which involves the flow of electrical charge. All metals exhibit a tendency to be oxidized. A tabulation of the relative strength of this tendency is called the galvanic series.

2.1.1 Electrochemistry Reactions of Aqueous Corrosion

Aqueous corrosion is an electrochemical process including the exchange of electrons between anodic and cathodic half reactions. Anodic reactions produce electrons and complementary cathodic reactions consume the electrons. Basic wet corrosion cells

comprise a single anode, cathode, electrolyte and connections, as shown in Figure 2.1. The removal of any one of the four components of the simple wet corrosion cell will stop the corrosion reaction.

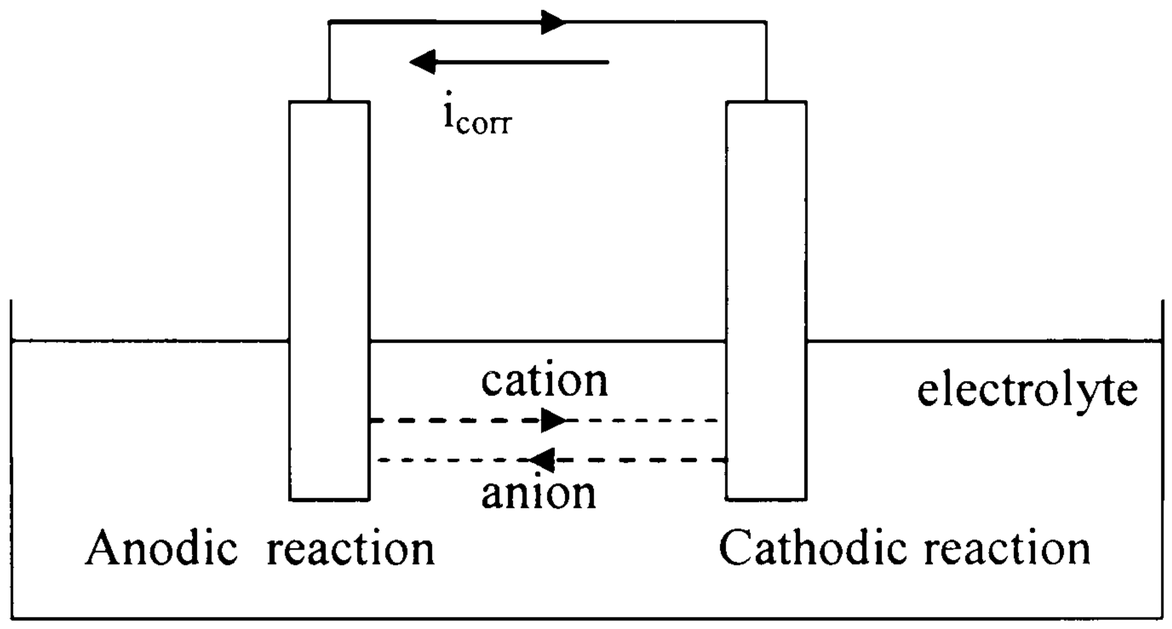

Figure 2.1 Schematic corrosion cell showing various components that are involved in a corrosion process

The types of anodic reactions oxidation can be as follows:

$$M \rightarrow M^{Z+} + ze^{-} \quad (1)$$

where z is the number of electrons released by the metal M. The process is called "oxidation". But electron produced do not flow into the solution but remain behind on the corroding metal, where they migrate to the cathode.

The types of cathodic reaction (reduction) can be as follows:

1) displacement reaction

$$M^{Z+} + ze^{-} \rightarrow M \quad (2)$$

or metal ion reduction:

$$M^{Z+} + e^{-} \rightarrow M^{(Z-1)+} \quad (3)$$

2) hydrogen gas formation:

in acid environment:

$$2H^{+} + 2e^{-} \rightarrow H_2 \quad (4)$$

in neutral or alkaline environment:

$$2H_2O + 2e \rightarrow H_2 + 2OH^{-} \quad (5)$$

3) oxygen reduction and generating hydroxyl ions:

in acid environment:

$$O_2 + 4H^+ + 4e^- \rightarrow 2H_2O \tag{6}$$

in neutral or alkaline environment:

$$2H_2O + O_2 + 4e^- \rightarrow 4OH^- \tag{7}$$

Oxygen reduction is dependent upon the level of dissolved oxygen in solution. In well-aerated solutions this is typically about 5-10ppm and is quite sufficient for this process to be important.

Electrochemical processes take place across phase boundaries. They involve effects of both mass and charge. The distribution of the anodic and cathodic areas depends upon the energetics of the various parts of the surface such as crystal lattice imperfections, strains, the distribution of surface contaminants such as adsorbed substances or insoluble metal compounds, and the environmental conditions such as the access of the corrosive medium, air or other gasses to various parts of the surface. The energies in the regions with crystal defects are higher than their adjacent crystal lattice. Therefore, the crystal defect regions are more chemically active and are potential sites for preferential attack under aggressive environment (Thomas, 1979). Macroscopic defects in the metal such as discontinuities in the metal surface, cut edges, scratches, and discontinuities in oxide films, bimetallic couples or dissimilar metals will produce the necessary conditions to form anodic or cathodic areas.

Two electrochemical half reactions combine to form a corrosion reaction; its free corrosion potential and corrosion rate are different from that for the two half reactions. After the reaction, the species are transported to and from the electrodes by diffusion, convection and migration. Figure 2.2 represents the reaction schematically for an acidic environment.

When an alloy is corroded, the different metal ions of the alloy go into the electrolyte, so there is more than one anodic reaction taking place. At the same time, there also can

be more than one cathodic reaction taking place. For example, in acid solution, the evolution of hydrogen and reduction of oxygen are possible.

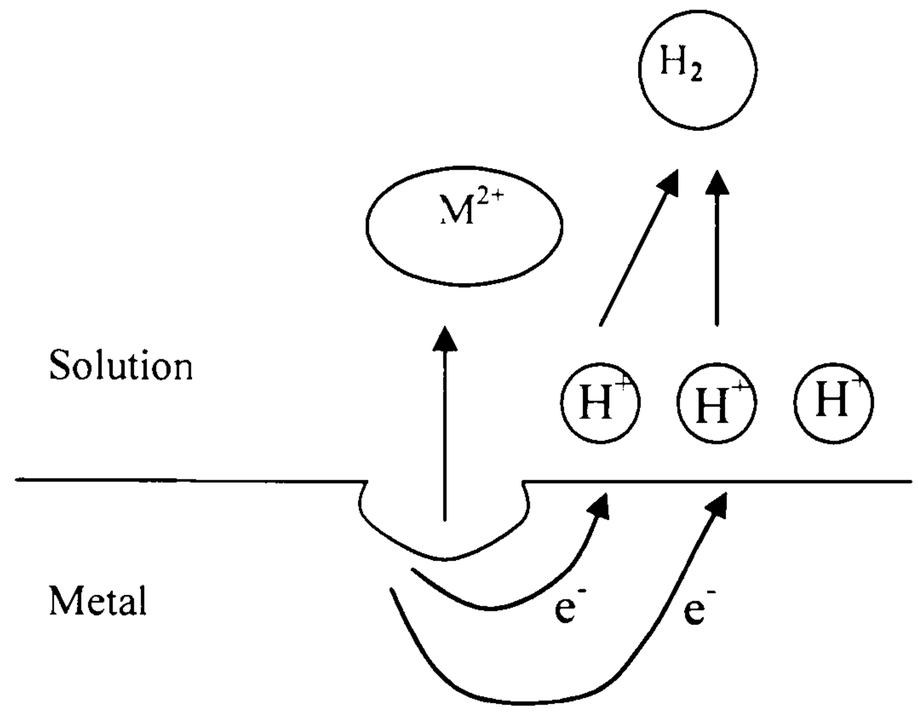

Figure 2.2 Schematic diagram of metal dissolution, liberating into solution a metal ion and into the metal electrons, which are consumed by reduction of H^+ then to H_2

2.1.2 Thermodynamics of Corrosion Reactions

Thermodynamics determines the *tendency* for a metal to react with its environment. It has been widely applied in corrosion studies for many years. It is particularly useful in defining the nature and structure of phases when equilibrium has been attained. The energy profile is of assistance in the understanding of corrosion processes. Whether a reaction is likely to proceed in any environment is dependent upon the Gibbs free energy change, ΔG, which is the driving force for a corrosion process. The higher the magnitude of this value in the negative sense, the greater the tendency for the reaction to occur. When ΔG is positive, the metal is stable and it will not react spontaneously. When ΔG is equal to zero, the system is at equilibrium.

The free energy differences (the driving force) are measurable as electrical potentials and flow of current. Thus, electrical measurements are one way of studying corrosion in more detail. Michael Faraday expressed the work done (the free energy change of the corrosion process) in terms of the potential difference and the charge transported as:

$$\Delta G = (-nF)E \tag{8}$$

where n is the number of electrons involved in the reaction. F is the Faraday's constant, which is the electrical charge carried by a mole of electrons (96,485 coulombs) and E is the driving force or potential difference for the reaction to take place. The negative sign is used for cathodic reactions and a positive sign is given to indicate anodic reactions. Under standard conditions, temperature 273.15 K and one atmosphere of pressure:

$$\Delta G^0 = (-nF)E^0 \tag{9}$$

The half cell redox potentials listed in emf (electromotive force) series are for systems under standard conditions, available at handbooks. However, all corrosion is dependent upon temperature because the free energy states of the species depend upon temperature. In addition, half cell potentials change with the concentration of the ions present in the reactions. Using the important thermodynamic equation the value of ΔG at any given temperature and at given concentration can be calculated.

$$\Delta G = \Delta G^0 + RT \ln \frac{[\text{products}]}{[\text{reactants}]} \tag{10}$$

From combining the thermodynamic equations and Faraday's Law the Nernst equation was deduced, which has great theoretical and practical significance as below:

$$E = E^0 - \frac{RT}{nF} \ln \frac{[\text{products}]}{[\text{reactants}]} \tag{11}$$

where: E is the equilibrium potential for non standard conditions. E^0 is the equilibrium potential for standard conditions, R is the molar gas constant (8.134 J K^{-1} mol^{-1}), T is the absolute temperature (K), n is the number of electrons exchanged in the reaction and [products] indicates that activities of all species on the oxidised side of the reaction are to be multiplied together, likewise, [reactants] indicates that activities of species on the reduced side are to be multiplied. For example, if the equations for anodic/cathodic reaction in an iron-hydrogen system are:

$$Fe + 2H^+ \Leftrightarrow Fe^{2+} + H_2(gas) \tag{12}$$

then the Nernst equation is:

$$E = E^0 - \frac{RT}{nF} \ln \frac{[Fe^{2+}][H_2]}{[Fe][H^+]^2} \tag{13}$$

where $[H^+]$ is activity of H^+, and $[H_2]$ is the pressure of H_2 gas.

Pourbaix diagrams (potential-pH) graphically represent the thermodynamic and electrochemical equilibrium between metal and water, indicating thermodynamically stable phases as a function of electrode potential and pH. These diagrams are constructed from calculations based on Nernst equations, thermodynamic data and solubility data for various compounds. Using this information can obtain domains of corrosion behaviour. The E-pH diagram for iron water system is shown in Figure 2.3 (Thomas, 1979).

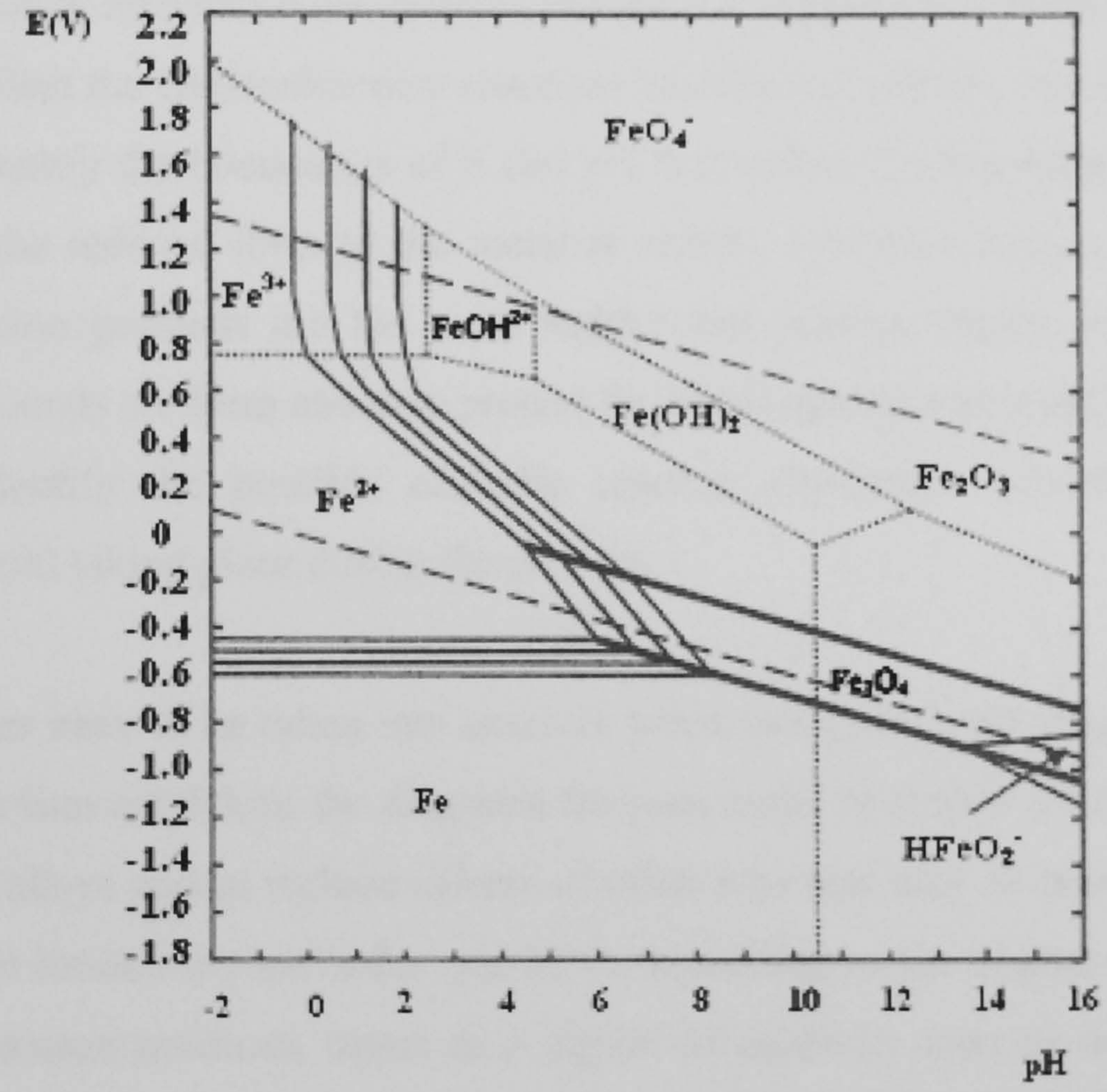

Figure 2.3 Pourbaix diagram for the Fe-H_2O system, showing the zones of stability of cations, anions and solid hydroxides (Thomas, 1979)

Pourbaix diagrams have three different types of lines. Horizontal lines are independent of pH. The equilibrium does not involve hydrogen ions (it depends only on potential), for example the boundary between the Fe^{3+} and Fe^{2+} regions. Vertical lines do not involve oxidation or reduction (the reaction depends only on pH). The boundary between the Fe^{2+} and $Fe(OH)_2$ regions shows that iron remains in the +2 valence state with no electrons exchanged, so the reaction can take place at any potential, positive or

negative. Sloping lines involve both hydrogen ions and electrons. The mathematical equations for these lines are given by Nernst equations (Equation (13)).

The major uses of these E-pH diagrams are (Thomas, 1979):

1. To predict the spontaneous direction of reactions.
2. To estimate the composition of any corrosion products that can be formed at particular potential or pH.
3. To predict environmental changes (solution composition, potential or pH) which can affect the electrochemical reactions to reduce or prevent corrosion attack.
4. To identify the boundaries of E and pH that define the immunity region (where only the reduced form of the metal is stable), corrosion region (where soluble corrosion products are the most stable) and passive region (where insoluble compounds are form and may protect the metal against corrosion).
5. To identify the possible cathodic reaction (hydrogen evolution or oxygen reaction) taking place during the process.

Considerations have to be taken into account when using the E-pH diagrams. It has to be for equilibrium condition; the diagrams for pure metal in simple solutions have to be modified for alloys and to include effects of other ions that may be present in different electrolytes; It limited to pure water and 25°C; depending on the degree of perfection of the solid corrosion products, metal in a region of passivity may or may not be well protected; The pH in the diagrams is not the pH of the bulk solution but the pH of solution in contact with the metal in pits for example. It provides no information on the rate of corrosion. Its rate is determined by kinetic mechanisms.

2.1.3 The Kinetics of Corrosion Reactions

When an irreversible potential develops on the electrode, corroding occurs. Corrosion reactions not in equilibrium cause current to flow. The current density and corrosion rate can be equated. Hence, to know the corrosion kinetics, there is a need to fully investigate the relationship between potential and current.

2.1.3.1 The Electrical Double Layer (EDL)

At the electrode/electrolyte interface, a charge separation between the metal surface and the electrolyte occurs. The spatial region corresponding to the charge separation is called the electrical double layer (EDL).

Usually the Gouy-Chapman-Stern model (GCS) is widely used to describe the EDL (Sastri, 1998). The GCS model consists two layers; Stern layer (SL) and diffuse layer (DL). SL layer is formed by specially adsorbed ions and Coulomb interactions in that a sheet of charges at the metal surface exist caused by an excess or deficiency of free electrons. It is the whole array of charged species and oriented dipoles existing at the metal-solution interface. The DL is the region next to the SL and ions in the DL can move freely in any direction. The SL has two planes; the inner Helmholtz (IHP) and outer Helmholtz plane (OHP) as shown in Figure 2.4 (where the metal attains a net positive charge balanced by local negative charge). IHP layer contains solvent molecules and sometimes other species (ions or molecules) that are specifically adsorbed. Solvated ions can only approach the electrode to a distance, which the locus of centres is called the OHP. The interaction of the solvated ions with the charged metal is caused by electrostatic forces, independent of the chemical properties of the ions (Sastri, 1998).

To easily understand the structure of the EDL, Lyklema (1991) introduced three types of ions in the solution; potential-determining, specifically-adsorbed and indifferent ions. Potentially-determining ions are adsorbed at the surface directly. Their equilibrium distribution between the surface and the solution determines the surface potential relative to potential in bulk solution. The adsorbed potential-determining ions form the surface charge density. Indifferent ions are affected by Coulomb force of the surface charge. Specifically-adsorbed ions are strongly interacted with the surface through all interactions other than purely Coulomb force. In the triple layer model, the IHP is located at the centre of specifically-adsorbed ions and the OHP is located at the centre of indifferent ions.

The potential difference between the inner and outer Helmholtz planes is about 1 V and since the separation of the double layers is about 1nm; the potential gradient is about 10^9 V/m. The Helmholtz double layer can be treated as a parallel plate capacitor, but the capacitance of the double layer (C_{dl}) is often a function of potential, instead of like real capacitors, whose capacitance is independent of the voltage across them.

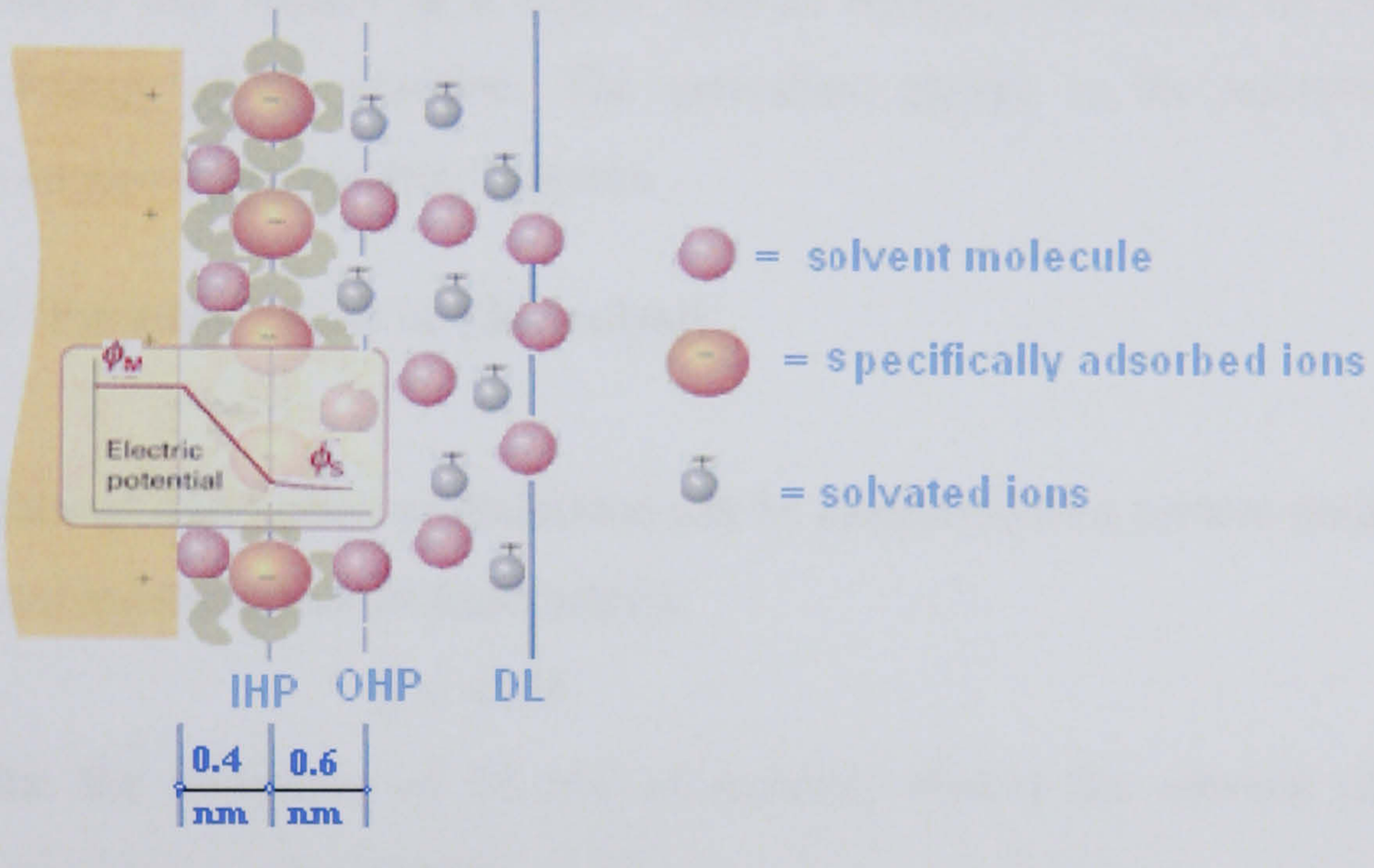

Figure 2.4 Schematic representation of the electrical double layer with metal attaining net negative charge, according to Sastri (1998)

Across the double layer region, the potential varies linearly from the electrode to the IHP and from IHP into the solution; the potential varies exponentially until a value of zero at some distance. Charge separation in an EDL also produces an electrical potential that can be measured as a difference between two metal electrodes, or a metal and reference electrode. Nernst equation mathematically relates EDL composition to electrical potential.

2.1.3.2 Arrhenius Equation

Common sense and chemical intuition suggests that the higher the temperature, the faster a given chemical reaction will proceed. The relationship between the rate a reaction precedes and its temperature is quantitatively determined by the Arrhenius equation, as shown in Equation (14).

$$k = A\exp^{(\Delta G^{*}/RT)} \tag{14}$$

where k is the rate coefficient, A is a constant, ΔG^{*} is the activation energy, R is the universal gas constant, and T is the temperature (in degrees Kelvin).

At higher temperatures, the probability that two molecules will collide is higher. This higher collision rate results in a higher kinetic energy, which has an effect on the activation energy of the reaction. The activation energy is the amount of energy required to ensure that a reaction happens.

2.1.3.3 Faraday's Law of Electrolysis

The rate of metal dissolution or deduction can be expressed as a current density (A/cm²) according to Faraday's Law of Electrolysis:

$$Q = nFM \tag{15}$$

It states that the ionisation of M mol of material creates the amount of charge Q. Differentiating with respect to time, gives:

$$i = nFJ \tag{16}$$

The flux of substance Q is another name for corrosion rate per unit area. Hence, current density is the measurement of corrosion rate, J, mol/s.

Current is in units of coulombs per second. Coulombs can be equated to the weight of the electroactive material by using Faraday's law. The current then is related directly to the corrosion rate as following:

$$\text{Rate ox} = \text{Rate red} = \frac{i_o}{nF} \tag{17}$$

At the equilibrium electrode potential, the flux of charge through the double layer is the same in both directions and is called the exchange current density i_0 mol/m².s. The potential, at which the sum of the anodic and cathodic reaction rates are equal to zero, is termed the free corrosion potential. E_{corr}, which is dependent on the metal and the nature

of the solution. The corresponding current density is called corrosion current density, i_{corr}.

The way to convert current density to weight loss is to use Faraday's Law as following:

$$m = \frac{i_{corr} MAt}{nF} \tag{18}$$

where m---mass loss (g)

i_{corr}---corrosion current density (A/cm²)

M--- Molar weight (g/mol)

A----Sample area (cm²)

t-----Time of experiment (s)

n----Number of electrons involved in the reaction

F----Faraday's constant (96485 C/mol)

2.1.4 Electrochemical Polarisation

In general terms, the change of potential caused by a flow of current is called "polarisation". When a metal is not in equilibrium with a solution of its ions, the electrode differs from the equilibrium potential by an amount known as polarisation, expressed as η. Polarisation is an important parameter from which the corrosion rate can be measured. The magnitude of polarisation η is:

$$\eta = E - E^0{}_{M^{n+}/M} \tag{19}$$

where E is the new potential obtained at the metal-solution interface when an external current is applied, $E^0{}_{M/M^{n+}}$ is the half cell electrode potential at equilibrium.

The total polarisation is the summation of three individual elements: activation polarisation, concentration polarisation and resistance polarisation. Activation polarisation is a manifestation of the relative changes in the activation energies for dissolution and deposition, when equilibrium is disturbed. Concentration polarisation is a function describing the limitations to the rate at which ions can carry charges through the solution to and from the electrode. Resistance polarisation follows Ohm's law and describes polarisation that occurs when a current passes through an electrolyte or through any other interface.

Consider the reaction of metal dissolution. at equilibrium, the half cell electrode potential $E^0{}_{M^{n+}/M}$ is established. When the overpotential is present, there exist the energy barriers, which are activation energy barriers. According to Equation (9), the activation energy difference of forward and reverse reactions will be:

$$\Delta G_f^* - \Delta G_r^* = \Delta G_{M^{n+}/M} = -nFE^0_{M^{n+}/M} \tag{20}$$

If the reaction rate constant for forward and reverse reactions is denoted by k_f and k_r respectively, the rate of forward and reverse reactions (r_f and r_r) can be expressed as a function of the respective activation energies according to the Arrhenius Equation (14):

$$r_f = k_f \exp(-\Delta G_f^* / RT) \tag{21}$$

and

$$r_r = k_r \exp(-\Delta G_r^* / RT) \tag{22}$$

At equilibrium, both reaction rates are the same, the exchange current density can be expressed as a function of the activation energies:

$$i_0 = A_0 \exp(\frac{-\Delta G^*}{RT}) \tag{23}$$

When the polarisation is the combination of an anodic polarisation on the metal and a cathodic polarisation of the environment, the anodic polarisation can be defined as $\alpha\eta$ and the cathodic polarisation as (1-$\alpha\eta$). As the polarisations can be converted into free energies by multiplication by the factor, nF, the anodic current of polarisation can be written as:

$$i_a = A_0 \exp(\frac{-\Delta G^* + \alpha\eta nF}{RT}) = i_0 \exp(\frac{\alpha\eta nF}{RT}) \tag{24}$$

The expression for the cathodic reaction is:

$$i_c = i_0 \exp(\frac{(1-\alpha)\eta nF}{RT}) \tag{25}$$

Then come to the equation for measured current density i_{meas}:

$$i_{meas} = i_0[\exp(\frac{\alpha\ \eta nF}{RT}) - \exp(\frac{(1-\alpha)\eta nF}{RT})] \quad (26)$$

It is Butler-Volmer equation. A plot is shown in Figure 2.5. It shows the measurement of current density for anodic and cathodic polarisation parts of the E-I curve. At high anodic polarisation i_c becomes small and i_{meas} becomes i_a.

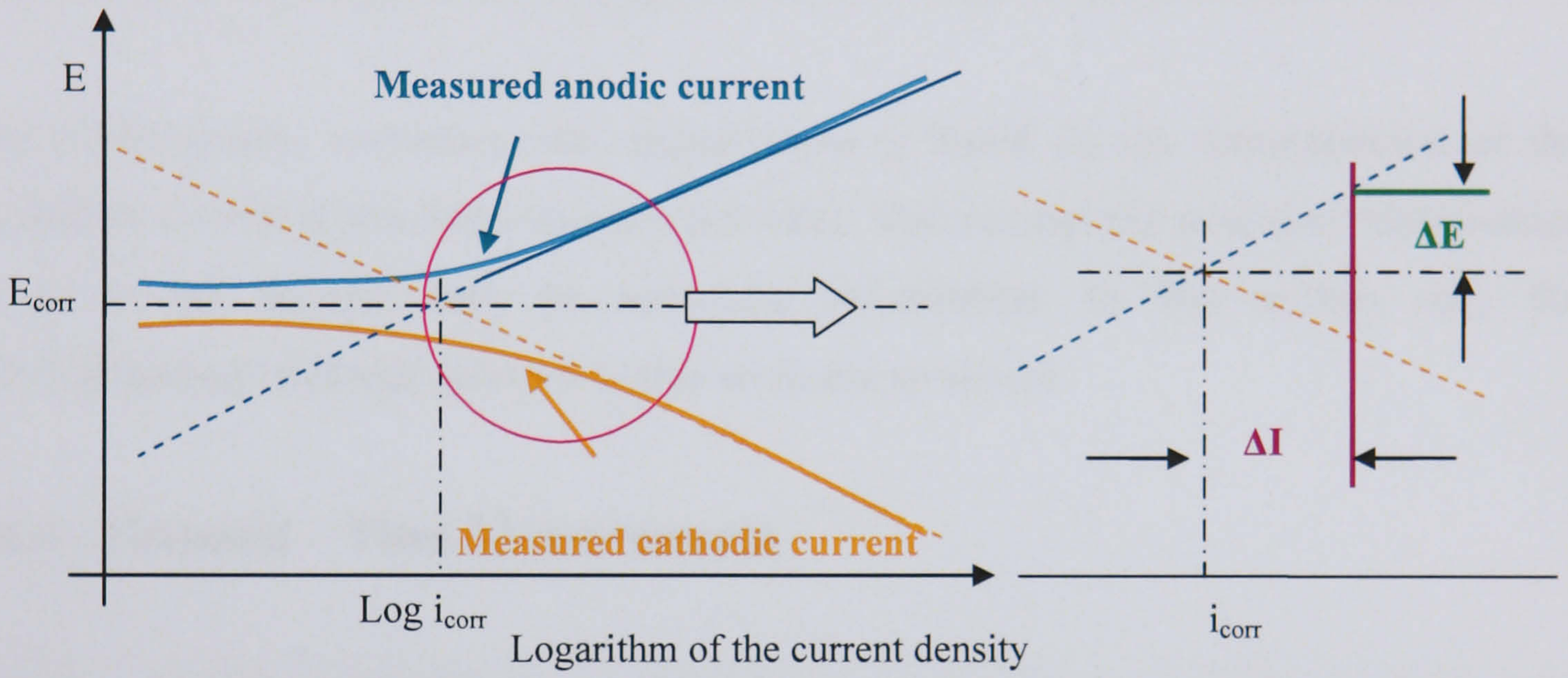

Figure 2.5 A plot of the Butler Volmer equation and its enlarged part showing the method of corrosion resistance measurement

From straight line β_a can be extrapolated as well as β_c for large cathodic polarisation. At the intersection of these lines, i_0, the exchange current density can be found. It is used to determine experimentally i_{corr} from which the corrosion rate is calculated.

The measurement may be affected by concentration polarisation and a drop in resistance, Concentration polarisation occurs when the reaction rate is so high that the electroactive species cannot reach or be removed from the electrode surface at a sufficiently rapid rate. The reaction rate becomes diffusion controlled. As η increases, the current becomes diffusion limited and the linear current range becomes smaller. Stirring the solution minimizes the effect of concentration polarisation. The drop in resistance across the solution can also cause non-linear Tafel behaviour at high currents: R_s is the uncompensated resistance of the solution or the resistance between the working electrode and the reference electrode bridge tube and this depends on the geometry of

the electrodes. As i_{meas} increases, E_{IR} also increases, causing an error in the true potential at the working electrode. The effects of concentration polarisation and resistance drop are serious when i_{corr} is large and high currents are required to verify Tafel behaviour.

2.2 Electrochemical Techniques for Corrosion Rate Measurement

Electrochemically, corrosion rate measurement is based on the determination of the oxidation current at the free corrosion potential. The current and potential relationships given so far depend only on activation polarisation. In this section only the electrochemical methods relevant to this work are reviewed.

2.2.1 Potential – Time Measurements

When a metal is immersed in solution, the metal tend to react with the electrolyte, changing its potential until the value of free corrosion potential, E_{corr}, which is a mixed potential between the anodic and cathodic potentials. To provide information on electrochemical processes, this simple measurement can be useful in the understanding of the thermodynamic stability of a metal under certain conditions such as the domain in which the electrode rests in a Pourbaix diagram, or determining galvanic relationships in a specific environment (Thomas, 1979), so that the polarisation measurement in certain electrolyte is valid.

The potential versus time measurement is a very simple non-perturbed technique. It is widely used to understand and correlate different processes, for example, the study of film formation and film breakdown, as indicated by an increase or decrease in the corrosion potential, respectively (Thomas, 1979). When the conditions are changed, the changes in free corrosion potential have been used to indicate which process is retarded or accelerated. For example, when inhibitors are added to the system, if E_{corr} moves to positive direction there is anodic control; displacement in the negative direction indicates cathodic control and small changes in corrosion potential means that both processed are retarded.

The potential measurement technique is also useful on localized corrosion. such as pitting or crevice corrosion. A potential-time record makes it possible to distinguish several stages in the crevice corrosion processes. Such as, growth of an oxide film can be detected by a rise in potential; depletion of oxygen inside the crevice can result in a retardation of the potential rise; breakdown of the film corresponds to a potential drop; activation stage indicates permanent breakdown and corrosion propagation (ASTM G 106-189, 1999).

Although the corrosion potential measurement is very useful, it is important to be complemented with other electrochemical techniques to be certain about the corrosion mechanisms.

2.2.2 DC Linear Polarisation Test Method

Current-potential relationships are commonly used as measurements of corrosion in evaluating inhibitors. They are used to determine the potential versus current for both anodic and cathodic reactions. Data are plotted on a semi-logarithmic current scale and are extrapolated backward toward the low current direction until the anodic and cathodic curves intersect, the current density at that point representing the rate of corrosion, as shown in Figure 2.5. Another way of the technique is used to measure the polarisation resistance, which is the slope of the polarisation curves at the point of corrosion, as shown in Figure 2.5 enlarged part, which is called DC linear polarisation method.

Linear polarisation resistance method can provide a sensitive and instantaneous measurement of the corrosion rate under steady state conditions. It is a DC technique and is the most widely adopted electrochemical monitoring technique in laboratory and field corrosion monitoring applications.

The basis of the technique for corrosion rate measurements was developed by Stern and Geary (1957). The method assumes that in activation controlled systems, the exponential anodic and cathodic polarisation curves are approximate to a straight line

close to the free corrosion potential. Typically, a small external DC potential signal (≤ ±10mV) is applied to the system, and the current flow in the external circuit is measured. Their ratio, "the linear polarisation resistance (R_p)", is then calculated.

$$R_p = \frac{\Delta E}{\Delta i} \tag{27}$$

where ΔE = applied voltage change with respect to the free corrosion potential

Δi = measured current density

The corrosion current density is then given by:

$$i_{corr} = \frac{B}{R_p} \tag{28}$$

where, B is the Stern Geary constant which is dependent on the corrosion system.

$$B = \frac{\beta_a \beta_c}{2.3(\beta_a + \beta_c)} \tag{29}$$

The linear polarisation technique can be applied using either a two or three electrode configuration, and is for the prediction of general corrosion rates. The use of the "polarisation resistance" for measuring corrosion rates has one particularly important advantage. The potential range investigated is close to the corrosion potential and the applied currents are generally smaller than the corrosion current. Thus, the nature of the surface is not changed significantly, and the reactions which proceed during polarisation are those which actually occur during the corrosion process. This is not necessarily the case when a corroding surface is markedly polarized, since under such conditions, the subsequent corrosion rate may be affected for some time after polarisation has been discontinued.

The following is a list of situations where it appears that the use of linear polarisation measurements can supply valuable information (Stern and Geary, 1957).

1. Studies of the effect of environment variables on corrosion rate. These include changes in composition, velocity, and temperatures.
2. Evaluation of inhibitors in controlling corrosion.

3. Comparison of the corrosion rates of various alloys of similar composition in a given environment.
4. Determination of changes in corrosion rate with time, including studies of underground structures as well as materials in aqueous solutions.
5. It also may be possible to evaluate the condition of coatings in service which cannot be inspected by visual methods.

2.2.3 Cathodic Protection Test Method

Cathodic protection is the process whereby the corrosion rate of a metal is decreased or stopped by decreasing the potential of the metal from E_{corr} to some lower value and in the limit to the thermodynamic equilibrium half-cell potential (Stansbury and Buchanan, 2000).

There are two ways to conduct cathodic protection, one is by sacrificial anodes and the other is by impressed current. The former includes the metal to be protected as part of a galvanic couple, where the working electrode receives electrons from the corroding less noble metal to which it is coupled. The latter includes the metal structure as part of the driven three-electrode electrochemical cell and the potentiostat is used to alter the potential of the working electrode. In this study, cathodic protection by impressed current is used to try to investigate pure erosion component. The circuit used to accomplish this is shown in Figure 2.6, in which the metal to be protected is carbon steel and the cathodic reaction supporting corrosion is hydrogen-ion reduction.

When an external current is not applied, steady-state corrosion occurs under the conditions E_{corr} and i_{corr}. If electrons are supplied to the metal, the potential is pushed in the negative direction from E_{corr} to E_1 and the rate of the metal dissolution is reduced from i_{corr} to i_{1a}. A current balance requires that, $i_{ex}=i_{a,M}-i_{c,H}$ (i_{ex} is exchange of current density of the corrosion cell, $i_{a,M}$ is the anodic current density of metal and $i_{c,H}$ is the cathodic current density of hydrogen). This external current density is represented in Figure 2.7 as the span between the respective polarisation curves at E_1. It is evident that for corrosion to be stopped, E must be reduced to E_{Fe} and to maintain this protection.

the external current density will be $i_{ex,complete\ protection}$. For iron in an environment of pH 5.5, according to the Pourbaix diagram, the potential of -800mV is used for cathodic protection.

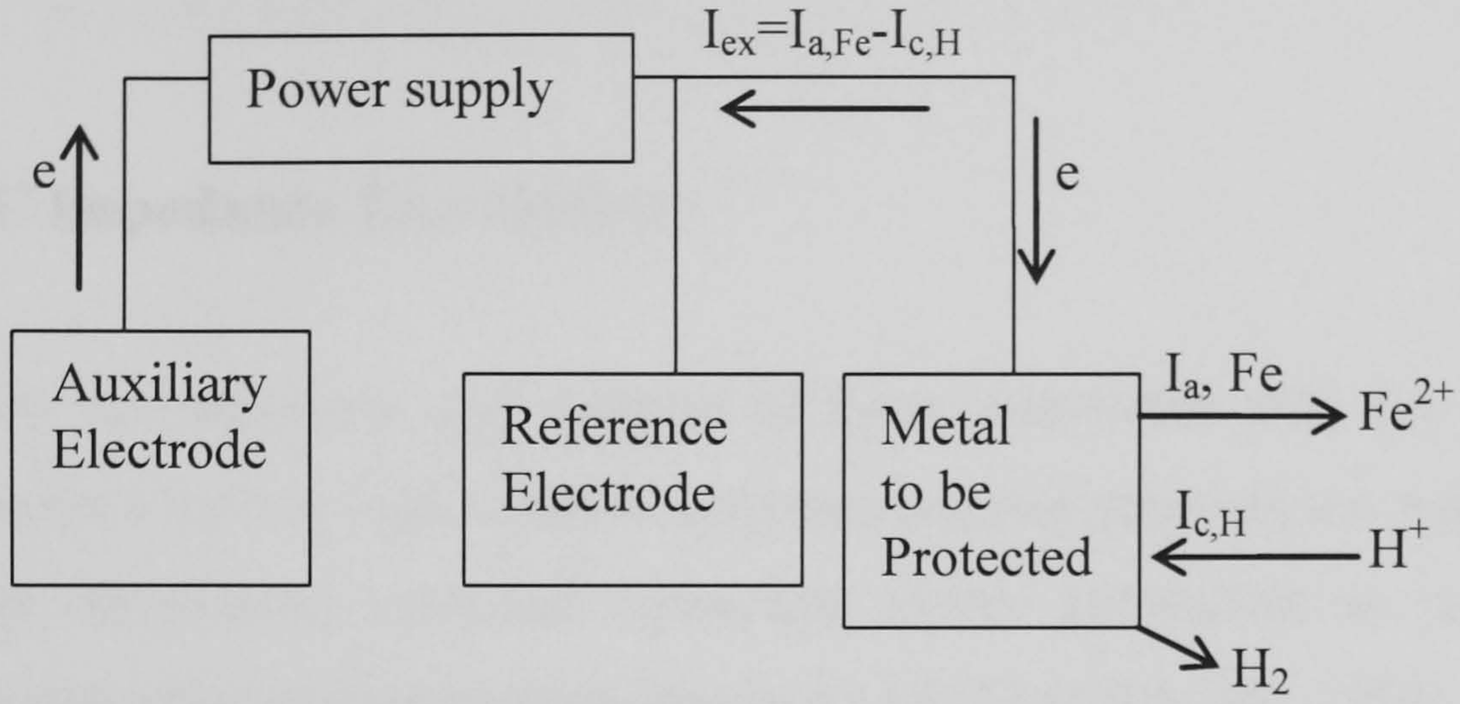

Figure 2.6 Schematic diagram showing the charge transfer processes involved in cathodic protection by an impressed external current

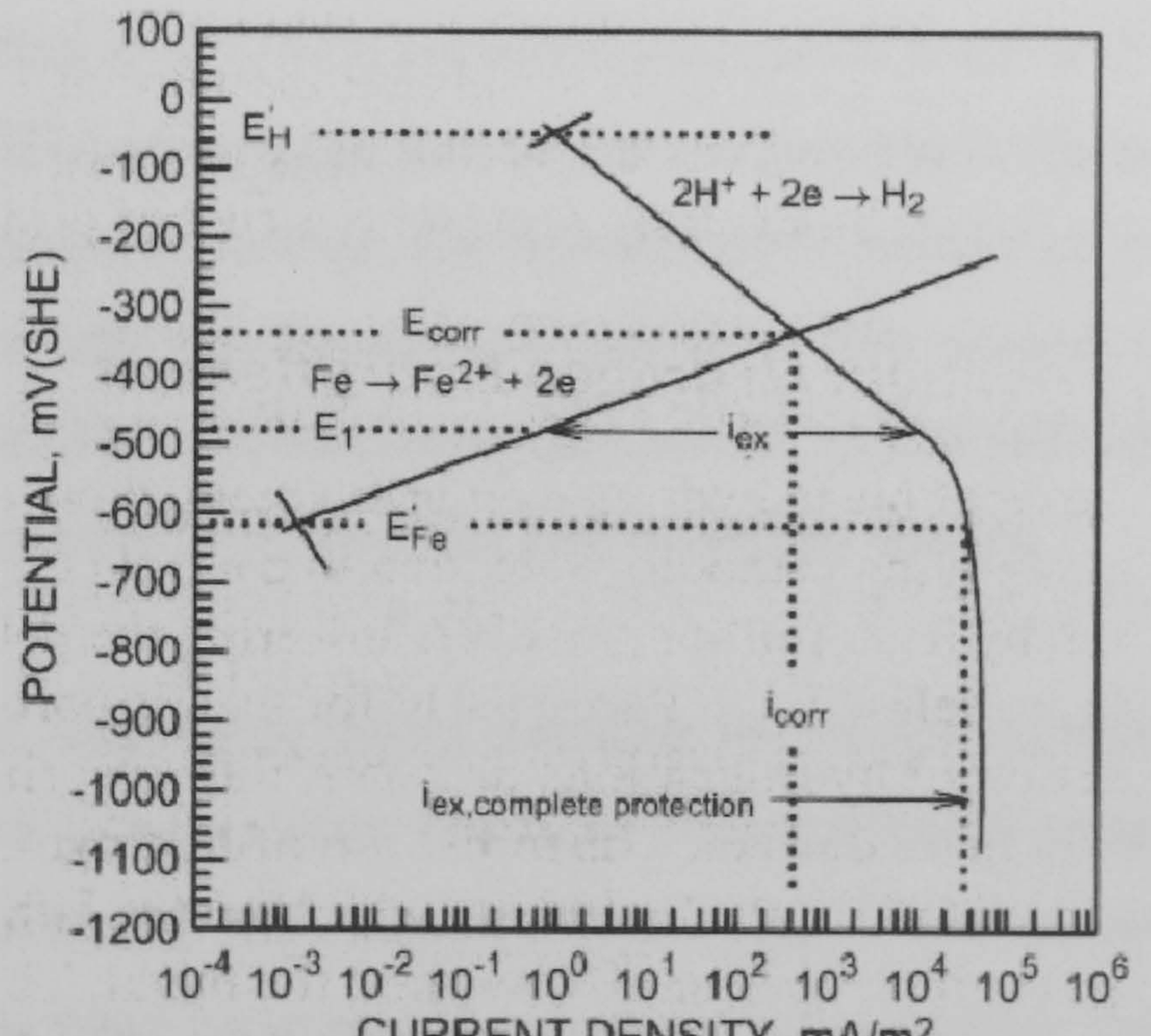

Figure 2.7 Schematic polarization curves used in the analysis of cathodic protection by an impressed external current. Cathodic reaction is under Tafel control (Stansbury and Buchanan, 2000)

If the potential is maintained below -800mV, the metal dissolution remains zero. So the total protection is achieved by supply of a cathodic current greater than i_p. A current

greater than this value can increase the rate of hydrogen evolution and can increase the susceptibility of the metal to hydrogen embrittlement. This phenomenon is associated with the presence of hydrogen gas in the lattice of the material entering by a diffusion process.

2.2.4 AC Impedance Test Method

Some of the complications and sources of error associated with the polarisation resistance method such as high solution resistance and fast scan rate are explained more readily after introducing electrical equivalent circuit parameters to represent and simulate the corroding electrochemical interface (ASTM G 106-189, 1999).

The AC impedance method, also called Electrochemical Impedance Spectroscopy (EIS), has gained increasing favour for making practical corrosion predictions of any system since Epelboin *et al.* (1972) published their earlier work on the system iron (Fe)-sulphuric acid (H_2SO_4)-propargylic acid in that it is possible to obtain information about the chemical mechanisms involved. The first area of its application is to determine wide range of corrosion rate rapidly and automatically. The second is its insights into corrosion rate-controlling mechanisms at the material surface and within the electrolyte, especially in the presence of an adsorbed film or organic coating.

Electrochemical AC impedance theory describes the electrical properties of an electric double layer with or without surface film as an electrical circuit composed of resistors, a capacitor and/or inductor, and monitors its response to an alternating voltage as a function of frequency and measures the output current magnitude and phase shift over a range of frequencies.

An electric double layer can be simulated as that shown in Figure 2.8, which is referred to as an equivalent electrical circuit model (EC). This EC allows the establishment of correlations between electrochemical system parameters and characteristic impedance elements. An EDL capacitive reactance is similar to the capacitor capacitance C_{dl}, which is determined by the type of metal and associated electrolyte composition. R_{ct} is

similar to corrosion resistance, which resists transferring its excess electrons to electrochemically active species.

The distinct advantages of AC over DC techniques are as follows:

1. It can provide full information on the corrosion process and cell performance in that potentials are applied over the frequency range of approximately 10^{-3} to 10^{4} Hz and also the amplitude of the potential wave is small, on the order of 10mV.
2. It provides data on both electrode capacitance and charge transfer kinetics. This valuable mechanistic information allows the separate determination of the components of the metal solution interface.
3. It does not involve potential scan and hence can be applied to low conductivity solutions.

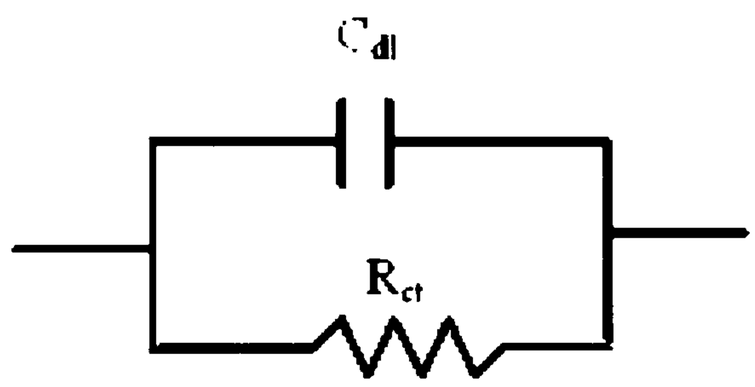

Figure 2.8 Simple electrical circuit having electrical properties similar to an EDL

Although EIS has above advantages, it does not allow determining the Tafel constants, which are required to calculate corrosion component. Therefore, this technique has to be complemented with DC techniques to establish these parameters.

2.2.4.1 AC Impedance Phase Behaviour

Similar to resistors, capacitors and inductors also resist the flow of electrons in AC circuits. This kind of resistance is called impedance. Thus, impedance is the AC analogue of DC resistance. A capacitor or inductor takes time to reach full charge (relaxation), and this charging-time produces a shift between current and voltage amplitude curves, as illustrated in Figure 2.9. A resistor does not exhibit time behaviour during polarisation and the phase angle is zero, as illustrated in Figure 2.10.

The times taken for this relaxation is called time constant (τ). The shift referred to as the phase angle and its magnitude is different for each polarizing voltage frequency. Phase angle is the difference between points on the X-axis where current and voltage curve amplitudes are zero, as shown in Figure 2.10. Although phase angle values are negative, the values are often plotted as positive quantities for EIS data.

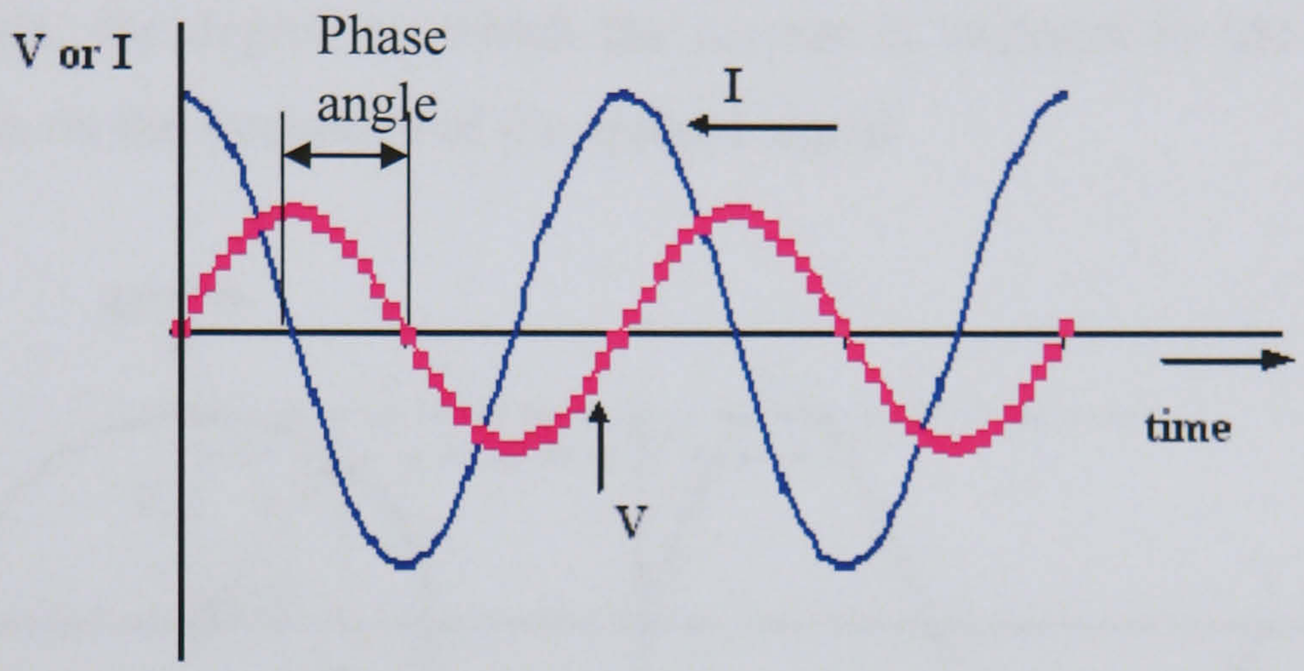

Figure 2.9 Schematic diagram of AC voltage-current phase angle in a circuit with capacitor

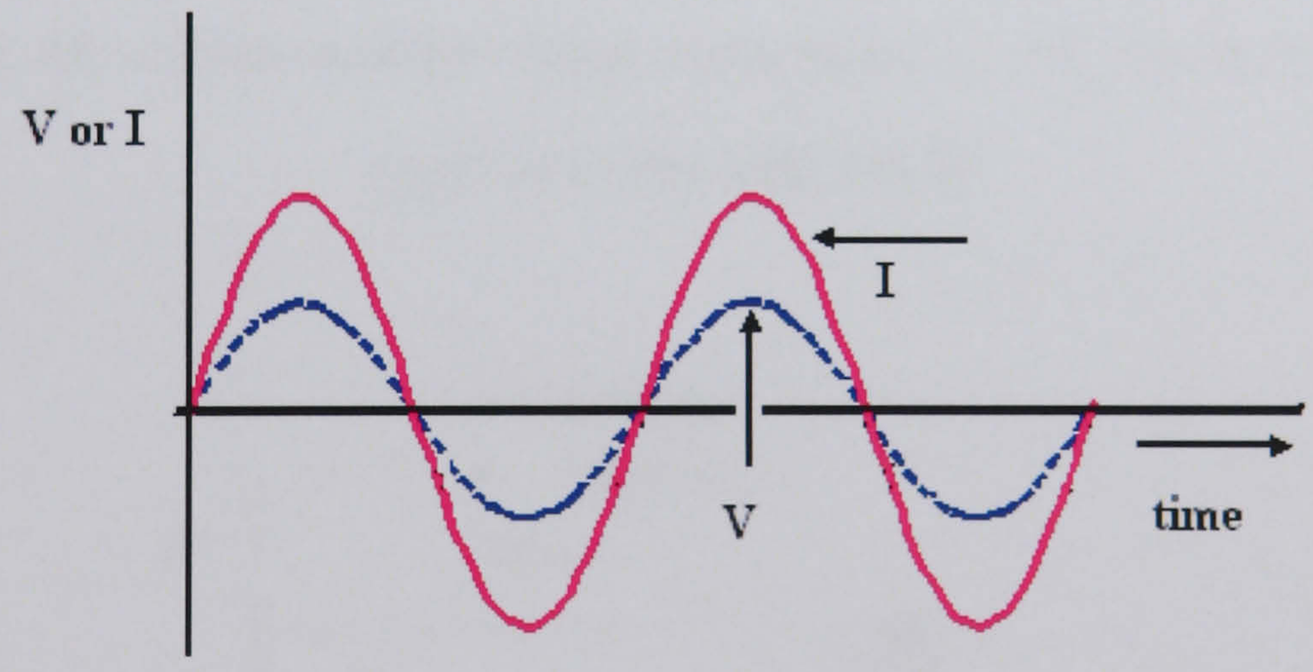

Figure 2.10 Schematic diagram of voltage and current response in a purely resistive circuit

A sinusoidal voltage can be pictured as a rotating vector, which is illustrated in Figure 2.11 (ASTM G 106-189, 1999). The voltage (V) is seen to rotate with a constant angular frequency, ω, the x component becomes the real component of the vector (V_x), while the y component represents the imaginary component of the vector (V_y). So does the current.

Consequently, impedance is also a vector because it is AC voltage divided by current according to Ohm's law. An impedance vector can be resolved into component vectors as illustrated in Figure 2.12 (ASTM G 106-189, 1999), where Z is the total resistance of the system created by all elements that impede the flow of the current, such as capacitors, resistance and inductors. This total resistance is called impedance. The total impedance Z is represented by a solid arrow, and component vectors are dashed arrows. φ is phase angle, the degree by which the current is impeded in the case of an AC voltage depends on the frequency of the applied signal.

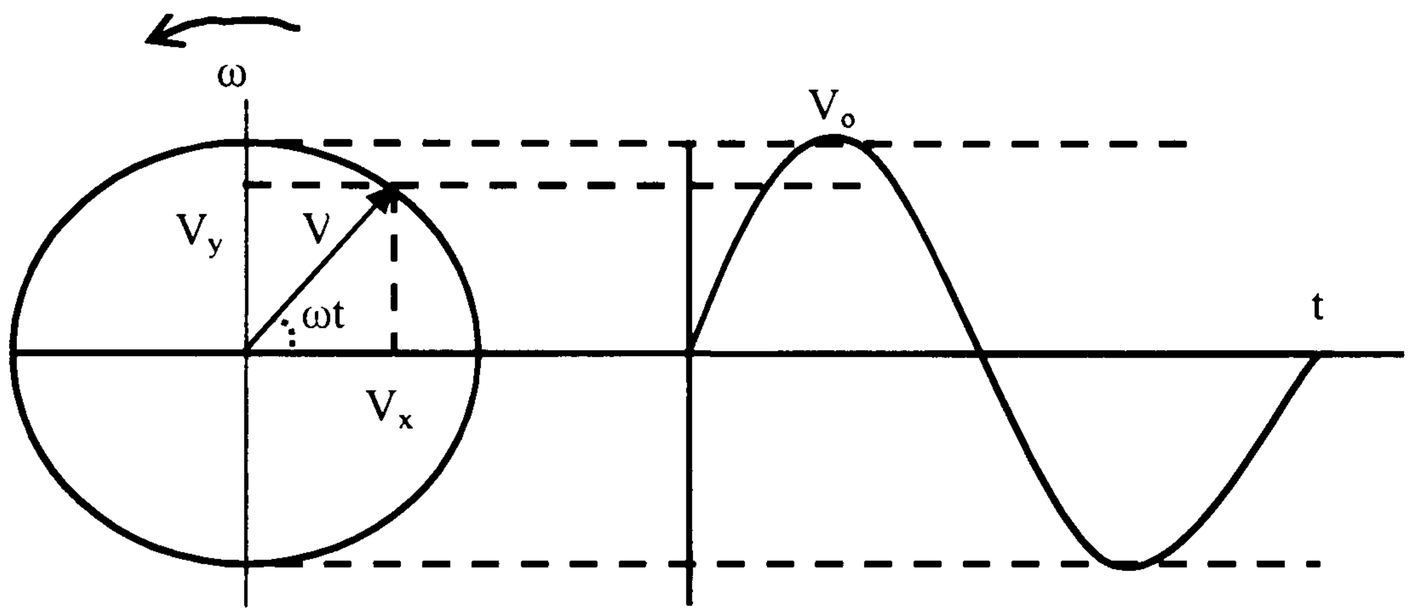

Figure 2.11 AC voltage and its vector component, $V_x = V_o \cos \omega t$; $V_y = V_o \sin \omega t$ (ASTM G 106-189, 1999)

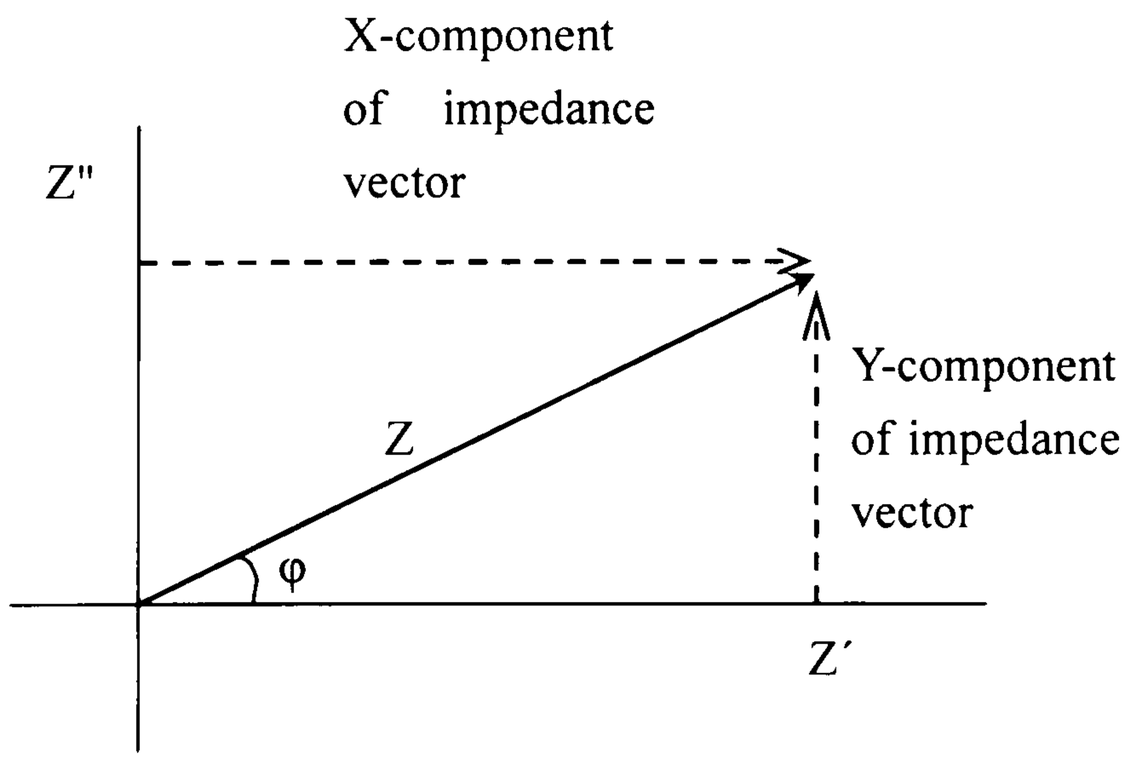

Figure 2.12 Vector nature of impedance

Therefore, the impedance $Z(\omega)$ of the electrochemical interface can be shown in Equation (30). The impedance values for the pure component of resistor, capacitor, and inductor are as shown in Table 2.1.

$$Z(\omega) = \frac{E}{I} = Z' + jZ'' \tag{30}$$

where Z' is real impedance magnitudes and Z'' is imaginary impedance magnitudes.

Table 2.1 Impedance values for the pure components commonly used in electrochemical impedance

Resistor, R	Z'=R	Z''= 0	φ=0
Capacitor, C	Z'=0	Z''= -1/ωC	φ=90°
Inductor, L	Z'=0	Z''= ωL	φ=-90°

2.2.4.2 Common Ways to Graph AC Impedance Data

AC impedance data can be graphed a number of different ways, among which the most common types are Nyquist plot, Bode magnitude and Bode phase plots.

Nyquist plot, also called Complex plane plots or Cole-Cole plot is a graph of real and imaginary impedance magnitudes for each frequency. For example, simple corrosion systems which are entirely under charge transfer control and the cases of uniform corrosion on homogeneous surfaces can be described by the simple equivalent circuit (EC) in Figure 2.13 (a). All ohmic resistances in the system under study such as the electrolyte resistance, cable resistances, etc. are contained in R_s, the solution resistance term. The impedance modulus Z(jω) for the EC can be expressed as a function of frequency ($f = \frac{\omega}{2\pi}$) as follows:

$$Z(j\omega) = R_s + \frac{R_{ct}}{1 + j\omega C_{dl} R_{ct}} \tag{31}$$

Solution resistance value of R_s equals the high frequency limit of the impedance (Equation (32)); and R_{ct} can be determined from the low frequency limits of the measured impedance spectra according to Equation (33).

$$R_s = \lim_{f \to \infty} |Z| \tag{32}$$

$$R_s + R_{ct} = \lim_{f \to 0} |Z| \tag{33}$$

Thus, the complex plane plots for equivalent circuit is a semi-circle as shown in Figure 2.13 (b). This semicircle is obtained with a radius of $R_{ct}/2$. The capacitance C_{dl} can be obtained from the frequency, f_{max}, (at the maximum of the imaginary impedance Z'') and R_{ct} as shown in Equation (34). The value can be affected by many factors, such as electrode potential, temperature, ionic concentration, types of ions, electrode roughness and impurity adsorption etc. (Gamry Instruments, 1997).

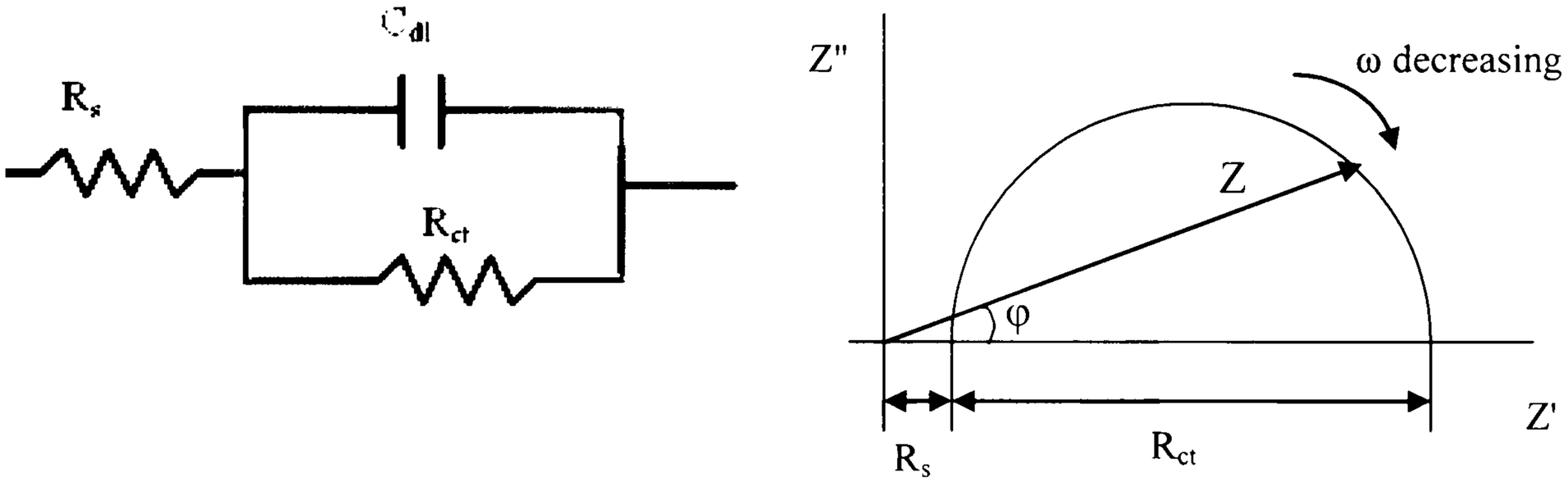

(a) **(b)**

Figure 2.13 (a) EC for a single corrosion system, (b) Nyquist plot for the simple corrosion system; In this example, there is no mass transport limitations, R_p=R_{ct}

$$C_{dl} = \frac{1}{2\pi f_{max} R_{ct}} \tag{34}$$

The representations of log |Z| (the absolute value of impedance) and phase angle φ versus frequency are called Bode magnitude and Bode phase plots respectively. For the simple corrosion interface shown in Figure 2.13 (a), the Bode plots are schematically shown in Figure 2.14. Bode plots have advantages in that the impedance and impedance phase angle are shown as explicit functions of the frequency.

From the Bode plots, a resistor has impedance that is independent of frequency, and exhibits a horizontal line in the log |Z| versus log f plot; the phase of the impedance of a resistor is zero. A capacitor has an impedance that is proportional to $1/f$, giving a straight line with a slope of -1 on the Bode plot. The phase of the impedance of a

capacitor is -90°. Comparing Bode magnitude and Bode phase diagrams. the inflection point in phase plot corresponds to the region where the Bode magnitude slope is negative.

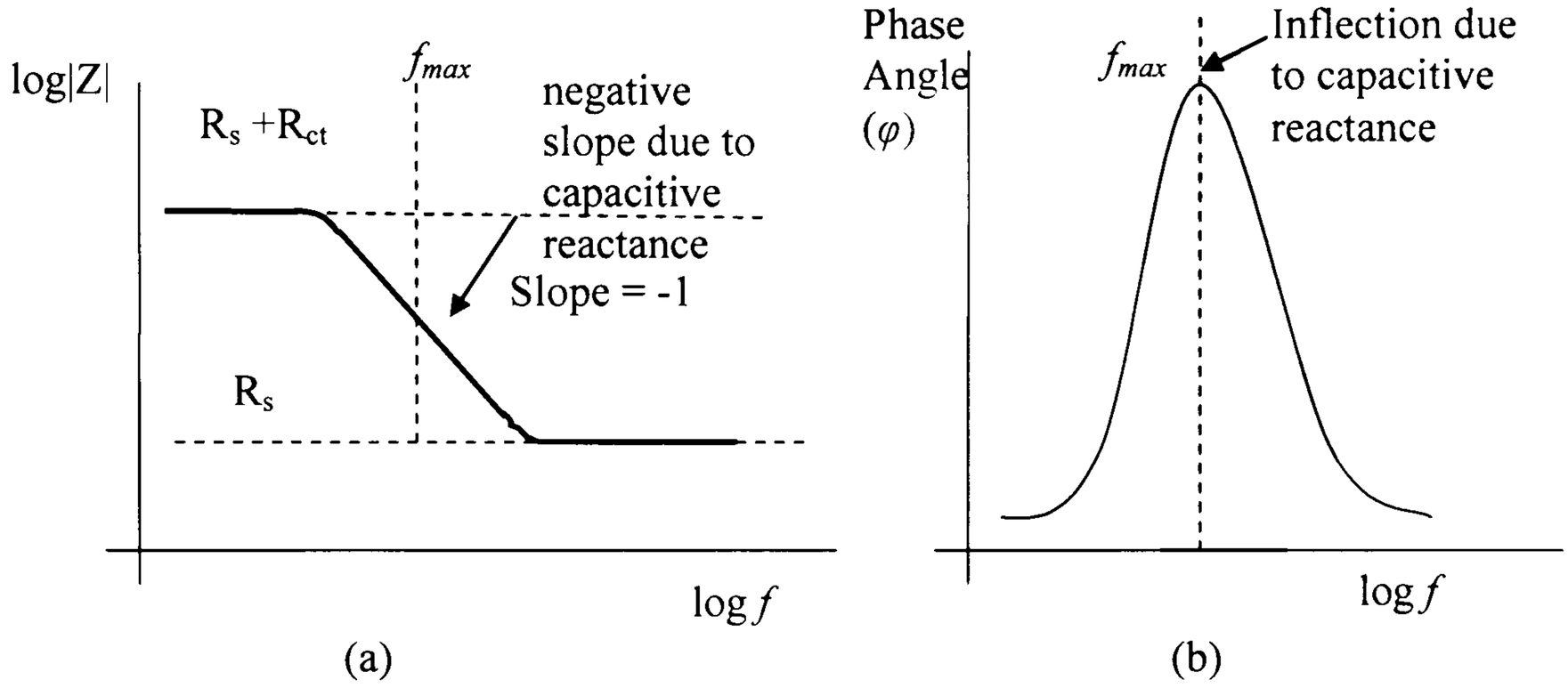

Figure 2.14 Bode plots for Simple Corrosion System, (a) Bode magnitude plot and (b) Bode phase plot

A corrosion process involving more than one time constant will produce more than one semicircle in the Nyquist plot. Sometimes, their time constants are very similar, so the semicircles will overlap making them difficult to be distinguished. However, it may possible be distinguished from Bode plot for each time constant associates with the frequency break points.

2.2.4.3 Constant Phase Element

Practically, impedance data obtained have the shape of depressed semicircles with the centre of the circle below the real axis as shown in Figure 2.15 (a) with its corresponding EC shown in Figure 2.15 (b), in which CPE represents the Constant Phase Element. It is a non-intuitive circuit element. Mansfeld *et al.* (1985) have accounted for such deviations from the ideal behaviour by introducing an exponent α which leads to Equation (31) changing to following Equation (35):

$$Z(j\omega) = R_s + \frac{R_{ct}}{1 + (j\omega C_{dl} R_{ct})^{\alpha}} \tag{35}$$

The constant phase element (CPE) in Equation (35) is expressed as an exponent affecting the imaginary component. The use of the exponent α in the equation is only a formal description of the experimental data and that the physical meaning is not clear. The relationship between a capacitor (C) and a CPE is as follows (Boukamp, 1988):

$$j\omega \mathrm{C} = (j\omega)^{\alpha}\,\mathrm{CPE} \tag{36}$$

If $\alpha = 0$ then CPE represents a resistor with resistance, R=1/ CPE, If $\alpha = 1$ then CPE represents a capacitor with a capacitance C = CPE. If $\alpha = 0.5$ then CPE represents a Warburg (purely diffusional) impedance, a 45° straight line will occur in the Nyquist diagram. The CPE with $\alpha = 0.5$ can be used to produce an infinite length Warburg element, which occurs when charge carrier diffuses through a material. When α is between 0 and 1, its value can provide information about diffusion phenomena, surface morphology, and other dissipative processes (Leibig and Halsey, 1993).

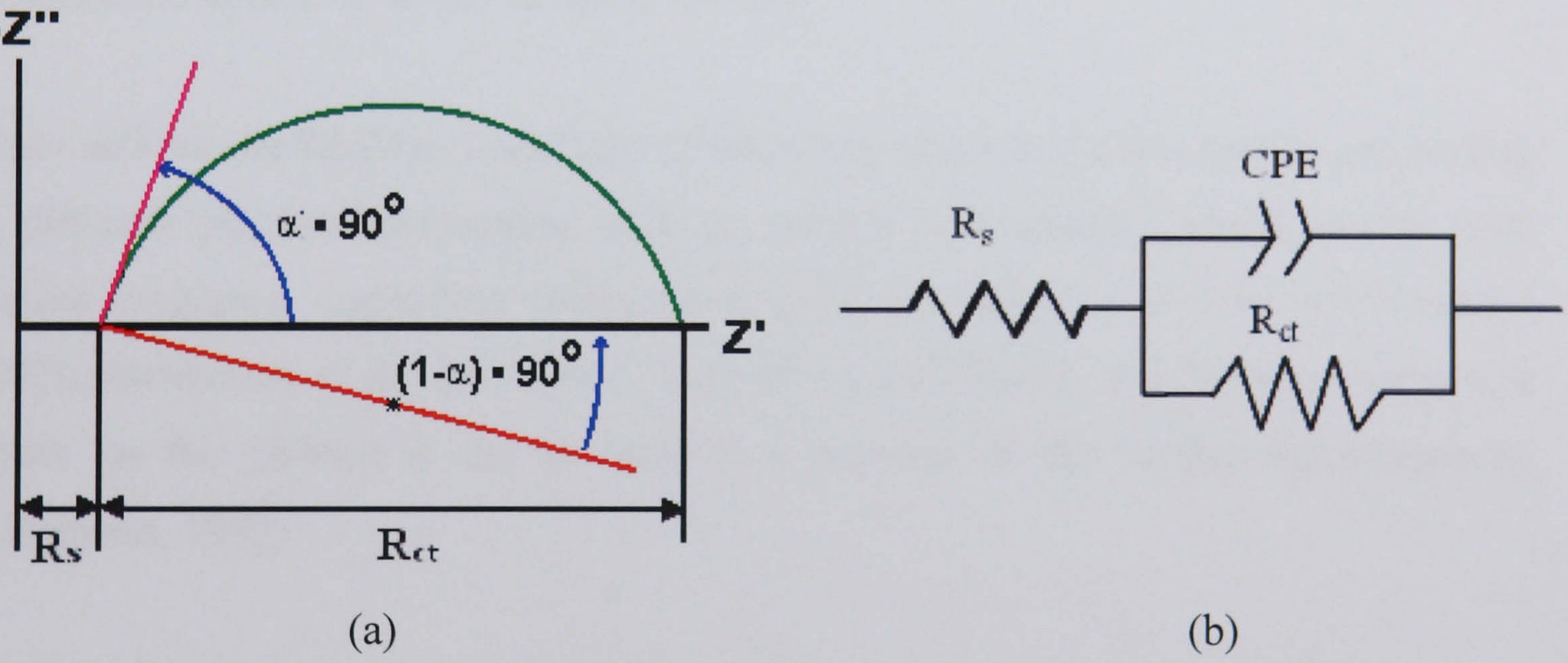

Figure 2.15 Nyquist plot of simple corrosion system consisting of CPE

The impedance of a capacitor and inductor can be expressed as Equation (37).

$$Z = \frac{1}{C(j\omega)^{\alpha}} \text{ and } Z = L(j\omega)^{\alpha} \tag{37}$$

where C = ideal capacitance (F cm^{-1})

L = ideal inductance (H cm^{-1})

α = empirical constant ($0 \le \alpha \le 1$)

Kendig and Mansfeld (1983) have found that the impedance spectra for iron and steel rotating cylinder electrodes, for which the measurements are carried out under turbulent

flow, generally were in agreement with Equation (35) corresponding to depressed semicircles in Nyquist plots. The term α lines between 0 and 1 and shows the degree of depression below the real axis.

Kim *et al.* (2003) describe the causes of CPE, or capacitance dispersion caused by surface roughness, chemical heterogeneity, or other sources of nonuniform current distribution and thus yields deviations from ideal capacitive impedance behaviour. Different crystallographic orientations also cause time constant distribution and may result in the capacitance dispersion (Kim *et al.*, 2003). Roberge and Sastri (1994) concluded that there exists a strong correlation between the extent of pitting corrosion and the CPE analyzed from AC impedance measurements. The CPE exponents calculated from AC impedance measurements correlated well with the microscopically measured pit depths observed on the electrodes.

Many authors use CPE for modelling of frequency dispersion behaviour corresponding to different physical phenomena such as surface heterogeneity which results from surface roughness, impurities, dislocations, grain boundaries (Gabrielli and Keddam, 1992), distribution of the active sites, adsorption of inhibitors, and formation of porous layers. In this context α can be used as a measure of the surface inhomogeneity (Silverman, 1989).

2.2.4.4 Multiple Time Constants

Corrosion systems with inhibitor films formed on the metal surface generally exhibit multiple time constants. The equivalent circuit shown in Figure 2.16 contains two time constants, indicating two processes taking place in the investigated frequency range including two EC elements. One time constant in the high frequency region is corresponding to the response of the surface film (film capacitance (C_f) and the film resistance (R_f)). Another time constant at low frequency range is used to model the interfacial process at the interface between pores of film areas filled with electrolyte and the metal substrate (the double layer capacitance (C_{dl}) and the charge transfer resistance (R_{ct})). R_{ct} can be used as overall resistance to corrosion.

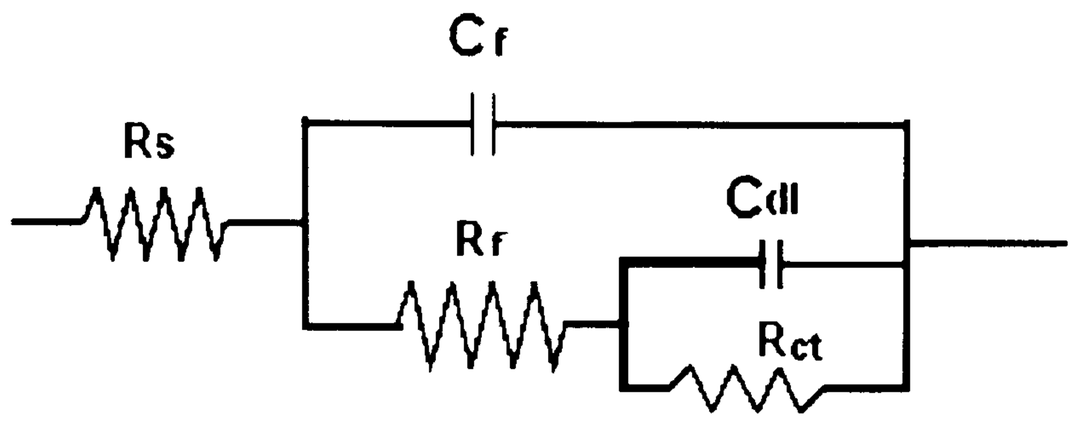

Figure 2.16 Equivalent circuit for model the interfacial process at interface between surface film and metal substrate

Induction, diffusion and parasitic pathways can produce time constants like coatings or other film formed on the metal surface (Stephen, 1994). The inductive feature of the ac impedance is often found in electrochemical measurements of electrocatalysis, electrodeposition and electro-dissolution. An example is the electrocatalytic reaction controlled by an intermediate absorbed species (Bisquert, 2006). It is suggested that an inductive feature arises in capacitive systems from relaxation of the charge in one of the phases that compose the system. Thus one or more of the individual steps in a complex reaction can be significantly slow the others and the slowest step can restrict fast electrical double layer (EDL) chemical composition changes in response to polarizing voltage magnitude and polarity changes. Restricting EDL chemical changes can produce induction. Adsorption or desorption equilibrium of surface active species, or corrosion inhibitors on a metal surface have also been reported as a possible source of induction in AC spectra (Stephen, 1994 and Murray *et al.*, 1988). Induction produces negative impedance magnitudes at high and low frequencies in Nyquist plots also produce negative impedance magnitudes in Bode magnitude plots, and positive phase angles in phase plots.

Sometimes electron exchange between a metal and an electrochemically active species is so rapid that the corrosion rate is controlled by the rate of electrochemically active species diffusion to a metal surface. Corrosion products like hydrogen gas bubbles can block access of electrochemically active species to a test electrode surface, thereby restricting hydrogen ion diffusion to the surface and thus impede the overall corrosion reaction rate. Diffusion time constant are typically observed at lower frequencies. It has a unique characteristic known as the diffusion or Warburg impedance, Z_w. Warburg

impedance is observed whenever a reaction is under partial or complete mass transport control by diffusion. Frequency dependence of this impedance is original studied by Warburg in 1899. While these mathematical formalisms accurately describe the behaviour of the electrified interphase, an intuitive physical origin of the peculiar nature of Warburg impedance has still been studied.

The Warburg impedance assumes that the diffusion process is over an infinite diffusion length such as an infinitely thick boundary layer, δ. However, in many practical cases a finite diffusion length is present due to factors such as convection in the solution, surface films or small volumes of electrolyte. In these cases the diffusion layer thickness becomes significant (Turgoose and Cottis, 1993). Warburg impedance has amplitude that is proportional to $\omega^{-1/2}$, which gives a slope of -1/2 on the log |Z|-log f plot. The phase angle tends to -45°. At low frequencies the Warburg impedance may tend to a limiting value due to the finite thickness of real diffusion boundary layers. At low frequency, if Nyquist plot appears to be a "flattened-out" semicircle, the diffusion path for electrochemically active species is considered to have a finite length (Stephen, 1994).

Multiple time constants can be also produced by surface inhomogeneity or defects. For example, polycrystalline metal and alloy surfaces are not homogeneous, and cause complex plane semicircle or phase plot inflection point distortion, rather than producing distinct symmetrical semicircles, or sharp phase inflections for each time constant (Walter, 1986). Surface roughness is also believed to produce multiple closely-spaced time constants that cause semicircle and inflection distortion (Rammelt and Reinhard, 1987).

Many corrosion problems involve situations where the environment moves. This is what this study is focused on. In most generic sense, erosion-corrosion is a form of corrosion that is caused or accelerated by the relative motion of the environment and the metal surface. Erosion-corrosion occurs partly by mechanical and partly by electrochemical or chemical mechanisms, which related to many factors in a specific condition. Its theory will be discussed in chapter 3.

CHAPTER 3 LITERATURE REVIEW

3.1 Aspects of CO_2 Corrosion

3.1.1 Carbonic Dioxide and its Corrosivity

3.1.1.1 Carbon Dioxide Hydration and Dissociation

CO_2 is extremely soluble in water and brines. At room temperature, the solubility of carbon dioxide is about 90 cm^3 of CO_2 per 100 ml of water. It is much higher than oxygen. The mechanisms of CO_2 corrosion involve either carbonic acid or the bicarbonate ion formed on dissolution of CO_2 in water. The reaction is as follows:

$$CO_{2(g)} + H_2O \rightarrow CO_{2(dissolved)} \tag{38}$$

According to Henry's law, the dissolution constant (K_d) can be defined as:

$$K_d = \frac{[CO_{2(dissolved)}]}{P_{co_2(g)}} \tag{39}$$

where, $[CO_{2(dissolved)}]$ is the molar concentration of dissolved carbon dioxide (mol/dm^3) and $P_{co_2(g)}$ is the partial pressure of the CO_2 gas (bar).

The hydration reaction is as follows:

$$CO_{2(dissolved)} + H_2O \Leftrightarrow H_2CO_3 \tag{40}$$

The hydration constant has been found at a value of K_{hyd} = 2.58 x 10^{-3} at room temperature (Palmer and van Eldik, 1983).

The carbonic acid once formed, can then dissociate as the follows:

$$H_2CO_3 \Leftrightarrow H^+ + HCO_3^- \tag{41}$$

At room temperature only less than 0.1% carbonic acid molecules dissociate (Alberty, 1983). For this first step,

$$K_{a1} = \frac{[H^+][HCO_3^-]}{[H_2CO_3]} = 1.72 \text{x} 10^{-4} \tag{42}$$

The hydration of CO_2 is not rapid and a large proportion of the gas remains unconverted in solution. In this solution, it is difficult to distinguish between H_2CO_3 and CO_2. If all CO_2 is counted as H_2CO_3, the first dissociation constant of carbonic acid is therefore becomes:

$$K'_{a1} = \frac{[H^+][HCO_3^-]}{[H_2CO_3]+[CO_2]} = \frac{[H^+][HCO_3^-]}{[H_2CO_3](1+\frac{[CO_2]}{[H_2CO_3]})} = \frac{K_{a1}}{1+K_{hyd}} = 4.426\text{x}10^{-7}\,(mol/dm^3) \quad (43)$$

The dissociation of the bicarbonate ion can proceed further producing carbonate ions as follows:

$$HCO_3^- \Leftrightarrow H^+ + CO_3^{2-} \quad (44)$$

the dissociation constant (Alberty, 1983):

$$K_{a2} = \frac{[H^+][CO_3^{2-}]}{[HCO_3^-]} = 4.70\text{x}10^{-11}\,(mol/dm^3) \quad (45)$$

Turgoose *et al*. (1992) based on historical review on the work of Kern (1984) about the hydration of carbon dioxide concluded that: at CO_2 partial pressure of 1 bar, 25° C, 1) the dissolution of CO_2 gas and the hydration reactions are pH independent; 2) at acid values of pH between 5-7 the main carbonic species in the solution is the bicarbonate ion (HCO_3^-) and as the pH increases, the presence of carbonate ions becomes important.

3.1.1.2 Cathodic Kinetics of CO_2 Corrosion

A solution of H_2CO_3 can be more corrosive compared to a solution of a strong acid at the same value of pH (Whitman *et al*., 1924). This behaviour suggests that pH alone can not be considered as a parameter to determine the corrosiveness of solutions of weak acids.

The corrosion rate in solutions containing CO_2 is said to be highly dependent on the cathodic reduction of hydrogen, since studies showed that the amount of H_2 that is evolved during the CO_2 corrosion process increases as the corrosion rate of the steel increases (Schmitt and Rothmann, 1977; Eriksrud and Sontvedt, 1983). However, the explanation of the strong corrosivity of carbonic acid has been a controversy among

researchers as to the rate-determining step in the reaction of the dissolved CO_2 with steel surface.

De Waard and Milliams (1975) describe the mechanisms of CO_2 corrosion as that the cathodic hydrogen evolution is in a 'catalytic' way by direct reduction of undissociated adsorbed carbonic acid on the metal surface. The mechanism is:

$$H_2CO_{3(ad)} + e^- \rightarrow H_{(ad)} + HCO_3^- \text{---(rate determining step)} \quad (46)$$

$$2H_{(ad)} \rightarrow H_2 \text{---(fast step)} \quad (47)$$

Once this undissociated H_2CO_3 is adsorbed on the surface of the electrode, it can be directly reduced to adsorbed atomic hydrogen and bicarbonate ion. So diffusion of H_2CO_3 is the rate determining step. On the other hand, the hydrogen ions that are diffusing from the bulk of the solution to the metal surface reacts with the bicarbonate ion produced from above equation, reforming the carbonic acid as following:

$$HCO_3^- + H^+_{(bulk)} \rightarrow H_2CO_3 \quad (48)$$

Then the overall cathodic reaction will be:

$$\mathrm{H}^+ + e^- \rightarrow \mathrm{H}\cdot \quad (49)$$

This mechanism became the basis of a series of predictive models, widely used by engineers in the industry. However it could not explain the results obtained by Schmitt and Rothman (1977) relating to the influence of flow rate on the cathodic kinetics.

The detailed process of the cathodic reduction reaction of CO_2 corrosion was studied by Schmitt and Rothmann (1977) as discussed in the following paragraphs.

The electrochemical measurement of the limiting current density ($i_{\lim,CO_2}$) is a function of the rotational rate of the disk, so it is a result of "the superimposition of processes influenced by diffusion and by reaction", which expressed as:

$$i_{lim,CO_2} = i_{lim,diff} + i_{lim,R} \quad (50)$$

where, $i_{lim,diff}$ is a limiting current density component associated with the diffusion of the reducible species (mainly H^+ and H_2CO_3) from the bulk of the solution, which is dependent on the rotation rate of the electrode, and the $i_{lim,R}$ is the limiting current

density component associated with a chemical reaction. This chemical reaction is the slow hydration of CO_2 (Equation (40)) and the reduction of carbonic acid adsorbed on the metal surface (Equation (46)).

These ideas involved the effect of flow on the observed limiting current density. Although they were limited to the rotating disk electrode which is laminar flow conditions, it provides the basis for understanding corrosion mechanisms in flow conditions containing CO_2.

Based on electrochemical measurements and taking into account the previous work by Schmitt and Rothman, Mendoza-Flores and Turgoose (1995) studied the cathodic kinetics of rotating cylindrical mild steel electrodes immersed in aqueous solutions containing CO_2. The measured current density at the natural pH of saturation of the solutions and in turbulent flow conditions (i_{lim}') can be expressed as follows:

$$i_{lim}' = i_{lim,diff}' + i_{lim,R}' \quad (51)$$

where $i_{lim,diff}$' represents a limiting current density component dependent on flow and associated to the diffusion of H^+ ions and H_2CO_3 molecules, and $i_{lim,R}$' is flow independent component. This model extended the ideas proposed by Schmitt and Rothman (1977) to the turbulent flow regime.

Ogundele and White (1986) based on a thermodynamic and kinetic analysis of cathodic polarisation curves of mild steel in deaerated aqueous solutions containing CO_2, determined that the cathodic polarisation characteristics were a result of reduction reaction of water and bicarbonate ions to produce hydrogen gas as discussed in the following paragraphs.

Firstly, the bicarbonate ion diffuses from the bulk of the solution to the metal surface and is reduced at the cathode producing adsorbed atomic hydrogen and carbonate ion.

$$HCO_3^- + e \rightarrow H_{(ad)} + CO_3^{2-} \text{ ----rate determining step} \quad (52)$$

also the reduction of reactions of water as:

$$2H_2O + 2e \rightarrow H_2 + 2OH^- \quad (53)$$

Secondly, the reduction of a second bicarbonate ion occurs at the surface of the electrode together with the combination of the $H_{(ad)}$ to form H_2 gas and carbonate ion.

$$HCO_3^- + H_{(ad)} + e \rightarrow H_2 + CO_3^{2-} \quad (54)$$

However it is only valid between pH 4.9 and 5.3. Also, it does not explain the results obtained on rotating electrodes.

Nesic *et al.* (1995) published a model considering the interaction among the reduction reactions of hydrogen, carbonic acid, oxygen and water. Based on electrochemical experiments using rotating cylinder electrode for carbon steel, it is concluded that in environments containing CO_2, in addition to the H^+ ions reduction reaction, an additional cathodic reaction is the direct reduction at the metal surface of H_2CO_3 molecules. The authors also concluded that, the reduction of H_2CO_3 molecules is dominant cathodic reaction at pH 5.

In addition, the complexity will be more if the corrosion products film on the metal surface and the impurities in the solution, etc. is taken into consideration.

3.1.1.3 Anodic Reactions in CO_2 Corrosion

The anodic reaction is mainly the oxidation or dissolution of metal in solutions containing CO_2. In general, the main anodic reaction for a carbon steel structure in CO_2-containing solution can be as follows:

$$Fe \leftrightarrow Fe^{2+} + 2e^- \quad (55)$$

According to the mechanism proposed by Bockris *et al.* (1965), the Fe is oxidized by reaction with water as Equation (56).

$$Fe + H_2O \leftrightarrow FeOH_{(ad)} + H^+ + e \quad (56)$$

then the $FeOH_{(ad)}$ is oxidised once more to Fe^{2+}, as following, which is considered as the rate determining step in the overall anodic reaction:

$$FeOH_{(ad)} \rightarrow FeOH^+ + e \quad (57)$$

Finally, the Fe^{2+} is produced as Equation (58):

$$FeOH^+ + H^+ \rightarrow Fe^{2+} + H_2O \quad (58)$$

In literature, most of the mechanistic analyses about anodic reactions of steel in CO_2-containing solutions supported the Bockris mechanism.

3.1.2 CO_2 Corrosion Products and Their Effect on Further Corrosion

The mechanistic studies presented above to help in the understanding of the anodic dissolution did not consider the corrosion products forming on the metal surface. However, the formation of surface layers and their influence on corrosion rate is an important factor in the mechanisms, kinetics and pattern of CO_2 corrosion (Videm and Dugstad, 1989; Palacios and Shadley, 1991). When a protective scale is present, mass transfer to and from the metal surface can become the corrosion rate-controlling factor, rather than cathodic hydrogen-evolution (Ikeda *et al.*, 1984). This can invalidate the de Waard-Milliams equation (De Waard *et al.*, 1991) as shown in Equation (59). The corrosion scale, with its nonuniform formation and localized destruction, is the key factor contributing to localized CO_2 corrosion (Palacios and Shadley, 1991).

$$\log(V_{cor}) = 5.8 - 1710/T + 0.67\log(pCO_2) \quad (59)$$

where, V_{cor} is corrosion rate in mm/yr, T is operating temperature in K, pCO_2 is partial pressure of CO_2 in bar.

Several studies of the corrosion of carbon steel in flowing carbon dioxide saturated solutions have identified iron carbonate as a major constituent (Schmitt *et al.*, 1996; Heuer and Stubbins, 1999). The main film detected is iron carbonate which may be due to the reaction of Fe^{2+} ions with carbonate ions or due to a direct reaction of iron with bicarbonate (Ogundele and White, 1986) and iron carbide (Fe_3C) left from the steel matrix. Film formation occurs when the solubility of iron carbonate in solution is exceeded. Iron carbonate film is coarse in nature and films up to 80 μm thick have been obtained in conditions where uninhibited corrosion rates varied from 390 to 1580 mils per year (Heuer and Stubbins, 1999). The nature of this film depends on environmental factors (i.e. temperature, CO_2 partial pressure, solution chemistry, fluid velocity, fluid

phase, and pipe geometry and solution pH) and the metallurgy of steel. For example. with a ferrite-pearlite grain structure for low carbon steel, the ferrite dissolves very fast while leaving behind pearlite platelets. It may roughen the surface of the specimen creating high local turbulence which in turn increases the corrosion rates.

In CO_2 saturated solutions, in the pH range 5-8, at the free corrosion potential, it is detected that $Fe(HCO_3)_2$ was presented up to 21 hours in existence with $FeCO_3$, and after 184 hours, only $FeCO_3$ was detected (Xia *et al.*, 1989). According to Xia *et al.* (1989), the initially intermediate metastable phase, hydrogen carbonate formation occurs as a result of the anodic and cathodic reactions as follows:

$$Fe \rightarrow Fe^{2+} + 2e^{-} \quad (60)$$

$$H_2CO_{3(ad)} + e^{-} \rightarrow H + HCO_3^{-} \quad (61)$$

$$Fe^{2+} + HCO_3^{-} \rightarrow Fe(HCO_3)_2 \quad (62)$$

The transition of $Fe(HCO_3)_2$ to $FeCO_3$ then occurs through the electrochemical reduction of $Fe(HCO_3)_2$.

$$Fe(HCO_3)_2 + 2e^{-} \rightarrow FeCO_3 + CO_3^{2+} \quad (63)$$

X-ray diffraction was then only able to show the presence of $FeCO_3$.

Ogundele and White (Ogundele and White, 1986), determined that with carbon steel, in static CO_2-containing aqueous solutions at room temperature, $FeCO_3$ layers can be formed at pH> 4.95. In short periods, 2h, the surface film was no-uniform and lacking compactness, but with time the compactness improved and after eight days $FeCO_3$ crystalline cubes appeared.

It has been reported that $FeCO_3$ precipitation is very temperature dependent (Johnson, and Tomson, 1991; Dugstad, 1992). Dugstad (1992) also indicated that the morphology of the surface films is a function of the temperature. Below 40°C, surface films present an open porous structure and are formed mainly of Fe_3C with some $FeCO_3$ and alloying elements of the steel. Nesic and Lunde (1994) found that in two phase flow at pH 4-7 and T = 20-80°C, the formation of protective film is difficult, flow could have a positive role by eroding the Fe_3C films that accelerate corrosion by galvanic action. In a CO_2

medium, the conservation of a Fe_3C layer at the surface increases the corrosion rate of the underlying steel. The explanation for this negative protectiveness is an internal acidification of the solution imprisoned within the layer, due to local depletion in HCO_3^- ions.

Supersaturation with Fe^{2+} is required for $FeCO_3$ precipitation (Dugstad, 1992), which can be 5-10 times higher than the thermodynamic calculated values of solubility. Crolet *et al.*, (1998) established that $FeCO_3$ can precipitate not only on steel, but also directly on the Fe_3C, as a result of the Fe^{2+} concentration and the additional HCO_3^- anions produced on Fe_3C by the cathodic reduction of CO_2. It is suggested that Fe_3C increases the cathodic reaction. Fe_3C forms easily even at high velocities because of the high pH generated near the surface as a result of a high corrosion rate. If a dense protective $FeCO_3$ film is formed close to the metal and it decreases the corrosion rate quickly. The importance of Fe_3C accumulation on metal surfaces and the implicit benefit in the formation of $FeCO_3$ scales is also reported by Videm *et al.* (1996). They indicated that this compound can anchor the corrosion film making it more resistant to turbulent flow. If the iron content in the test medium is high from the moment of immersion of the specimen, $FeCO_3$ can precipitate on the metal, and the layer is protective. If the iron concentration subsequently falls and a certain amount of external redissolution of $FeCO_3$ exposes an outer layer of Fe_3C, this has no effect on the overall protectiveness of the corrosion layer. If the iron content of the medium becomes high only after an initial phase of corrosion leading to the formation of a Fe_3C layer, then internal acidification prevents further precipitation of $FeCO_3$ in contact with the metal, even though the outer part of the layer becomes obstructed. The layer is then non-protective, and even enormous iron supersaturation cannot subsequently render it protective.

3.1.3 CO_2 Corrosion Models

The deWaard-Milliams equation and the corresponding nomogram (as shown in Figure 3.1) is a starting point for the prediction of corrosion rates of carbon steel in CO_2-containing environments.

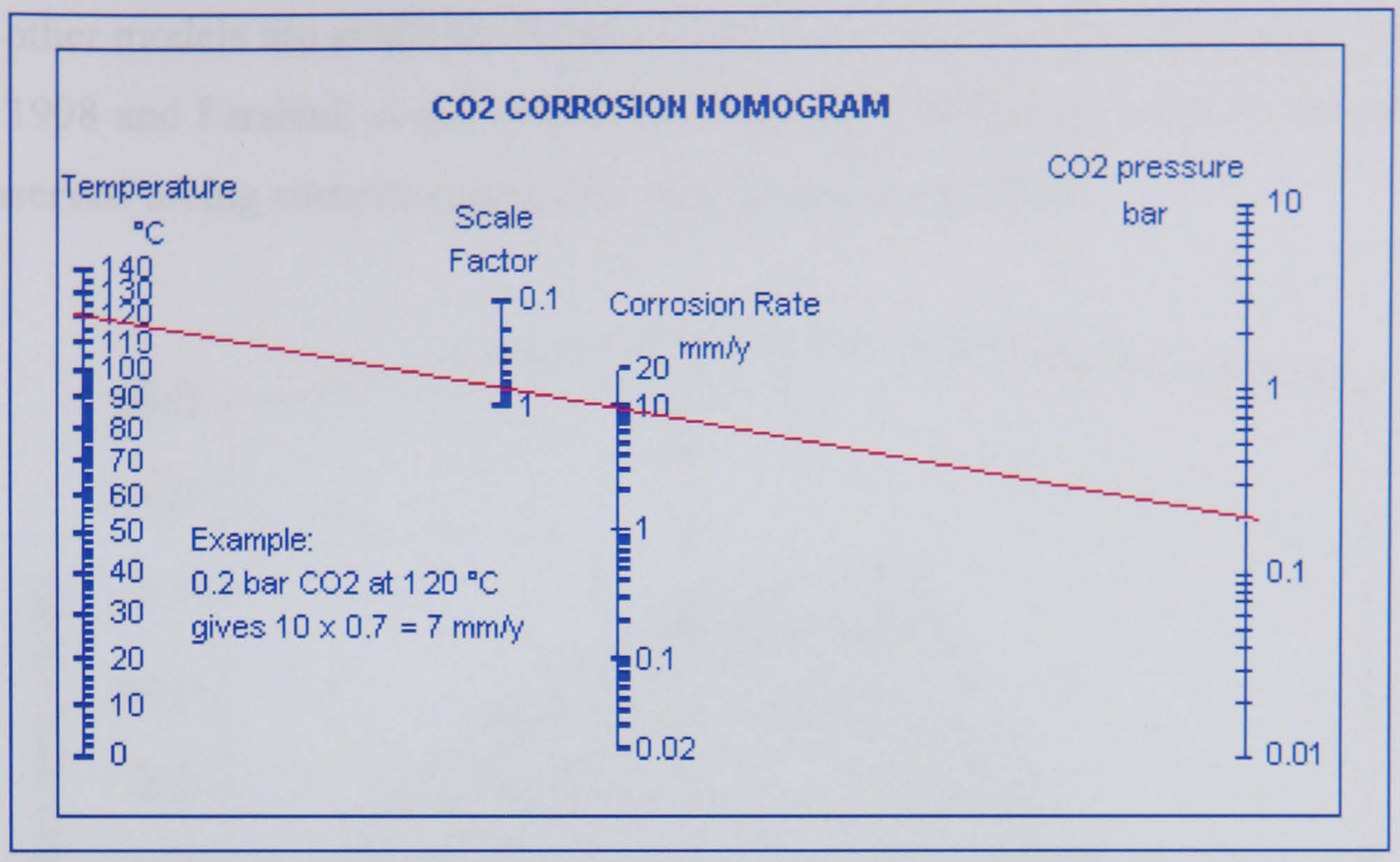

Figure 3.1 deWaard-Milliams nomogram for predicting of corrosion rates of carbon steel in CO_2-containing environment (CorCon 2004)

Although the deWaard-Milliams equation often gives surprisingly good results, there are many cases where it only reflects part of the story. For example, the influence of pH and liquid velocity on corrosion rate is interrelated in a rather complex manner, as shown in Figure 3.2.

For an activation-controlled mechanism of corrosion, which is applicable below 60°C in a CO_2-saturated solution at atmospheric pressure, a corrosion rate equation has been developed for iron alloys using the fundamental reaction rate theory as expressed in Equation (64) (Al-Hassan *et al.*, 1998).

$$Corrosion\ \ rate(mm/y) = C \text{x}\ pH^{1.33} \text{x}\ P_{CO_2}^{0.67} \text{x}\ e^{-Q/kT} \qquad (64)$$

where k is the Boltzmann constant, T is the absolute temperature, and Q is the activation energy for corrosion reaction. This equation compares very well with most of empirical relationships developed within a restricted range of T, pH, and P_{CO_2} and allows the inclusion of other variables, such as flow, impurities, inhibitors, and steel microstructure through the reaction constant (C).

Many other models are available for predicting CO_2 corrosion of carbon steel (Dayalan, *et al.*, 1998 and Farshad, *et al.*, 2000). However, the differences between the predicted and observed tubing corrosion rates can vary up to a factor of 10.

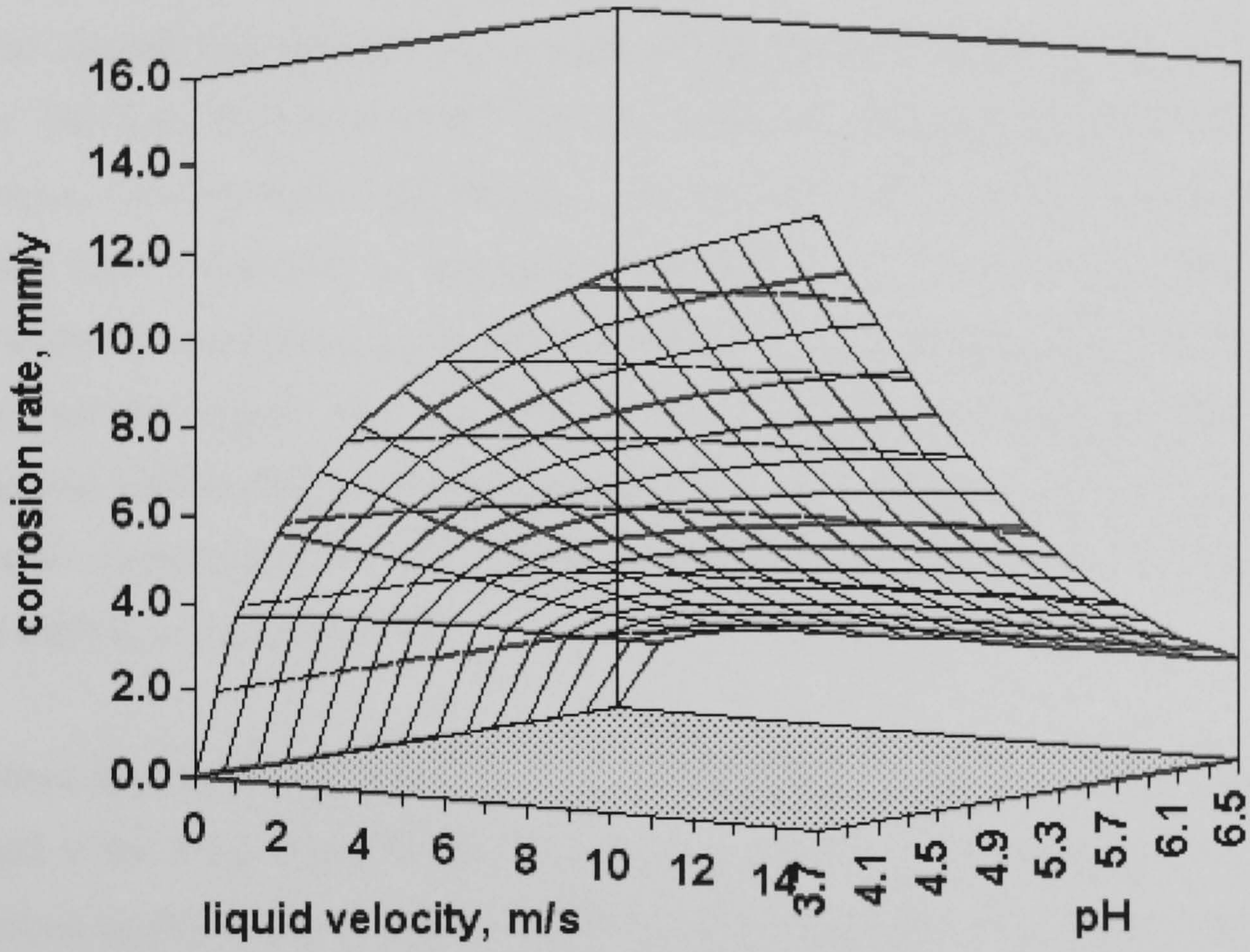

Figure 3.2 The effect of pH and liquid velocity on corrosion rate for example of CO_2 corrosion rates at 1 bar CO_2 and 40°C(CorCon, 2004)

3.1.4 Microstructural Effects on Corrosion

From the corrosion point of view, ferrite is anodic to Fe_3C, and Fe_3C has a lower overpotential for hydrogen evolution, which results in the dissolution of iron from the ferrite phase. Little is known about the effect of the shape and distribution of carbides on corrosion rate of steel that consists of ferrite/pearlite microstructure. The decrease in corrosion rate can be attributed to the decrease in the surface area of Fe_3C. The Fe_3C /ferrite interfacial area seems important in controlling corrosion rate. In ferrite/pearlite structures, a higher corrosion rate can be predicted when the distribution of pearlite in ferrite matrix is more uniform and the interfacial area between the phases is higher (as in normalized carbon steel), than in a banded structure of ferrite and pearlite (as in annealed carbon steel) (Mishra *et al*. 1997).

3.2 Aspects of Erosion and Erosion-Corrosion on Carbon Steel

3.2.1 Erosion Behaviour of Carbon Steel

When an aircraft flies through dust clouds, the gas turbine blades can be damaged by erosion. This kind of erosion occurs when the solid or liquid particles impact the surface of an object causing permanent damage. The definition of erosion by Stachowiak and Batchelor (2001) refers to *an unspecified number of wear mechanisms which occur when relatively small particles impact against mechanical components*. This definition is empirical by nature and relates more to practical consideration than to any fundamental understanding of wear. Although usually considered undesirable, erosion has useful applications in such processes as sand blasting, abrasive deburring and erosive drilling of hard materials.

The known mechanisms of erosion are illustrated in Figure 3.3. The impingement angle, the speed of the erosive particle and the size of the particle are the main factors to affect the erosion process. The erosion of ductile alloys depends markedly on the particle velocity and on the impingement angle (Levy 1981).

The impingement angle is the angle between the eroded surface and the trajectory of the particle centre immediately before impact. It can range from 0° to 90°. At zero impingement angle, the eroding particles do not impact the material surface, therefore there is negligible wear. Although even at relatively small impingement angles of about 20°, severe wear may occur if the particles are hard and the surface is soft. Wear similar to abrasive wear prevails under these conditions. If the surface is brittle, severe wear by fragmentation of the surface may occur reaching its maximum rate at impact angles close to 90°.

For simplifying the erosion analysis, Finnie (1960) first distinguish two main types of material behaviour of erosion, ductile and brittle. Wood (2006) reviewed that the failures of the ductile surfaces should be related to accumulated plastic strain or low cycle fatigue induced by cyclic plastic deformations from successive impacts. Whereas

in the brittle material, it will be removed by the intersection of cracks which radiate out from the point of impact of eroding particle.

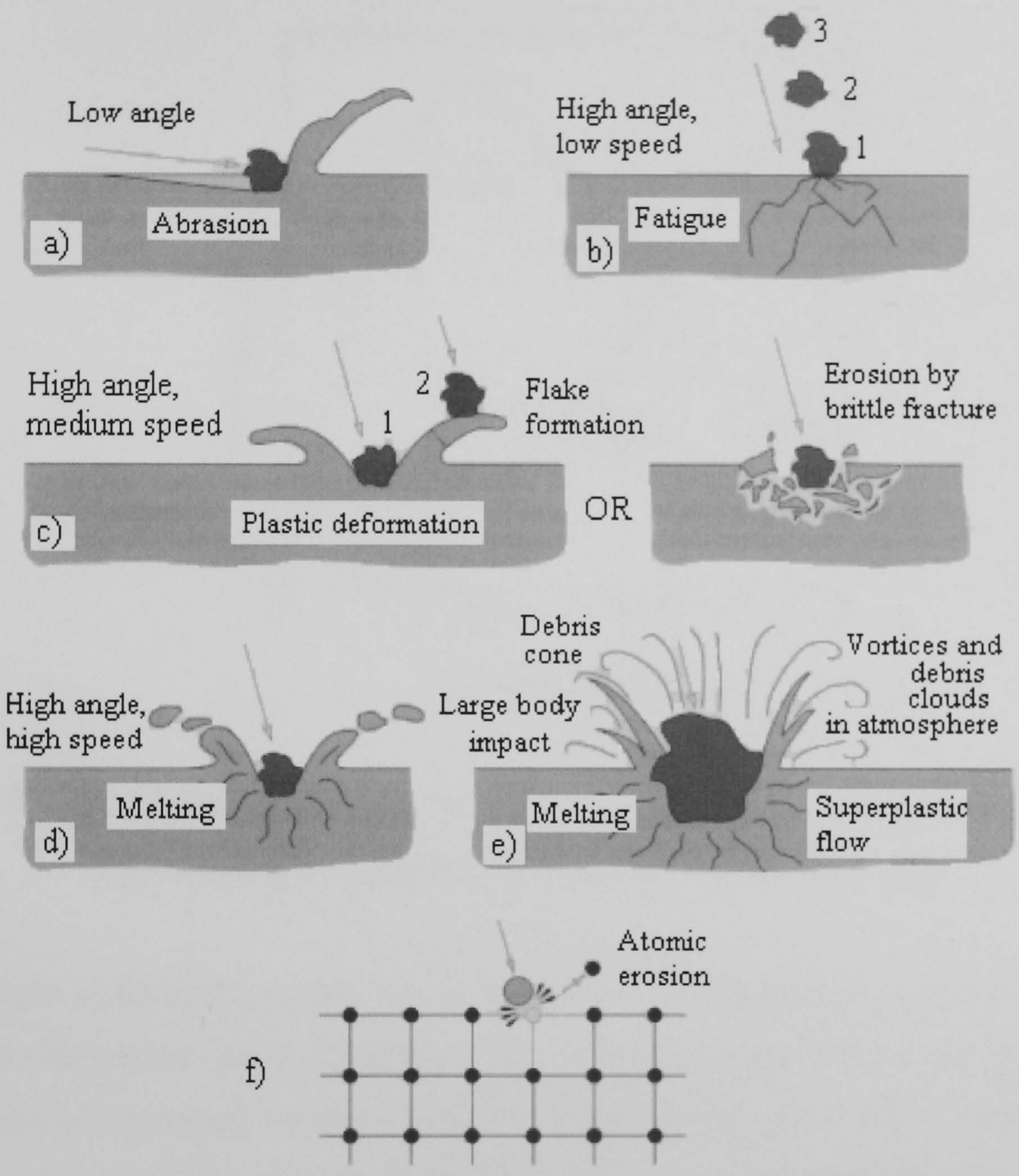

Figure 3.3 Possible mechanisms of erosion; a) abrasion at low impact angles, b) surface fatigue during low speed, high impingement angle impact, c) brittle fracture or multiple plastic deformation during medium speed, large impingement angle impact, d) surface melting at high impact speeds, e) macroscopic erosion with secondary effects, f) crystal lattice degradation from impact by atoms (Stachowiak and Batchelor, 2001)

Figure 3.4 shows the schematic diagram of erosion effect as a function of impact angle for both cases. Many engineering materials such as low carbon steel and ceramics fall into one of these two categories, while also many other materials may not be so easily categorized. At least, when erosion shows a maximum at low impact angles, the ductile

mode of erosive wear prevails. On the other hand, if the maximum erosion is at high impingement angles then the brittle mode of erosive wear is assumed.

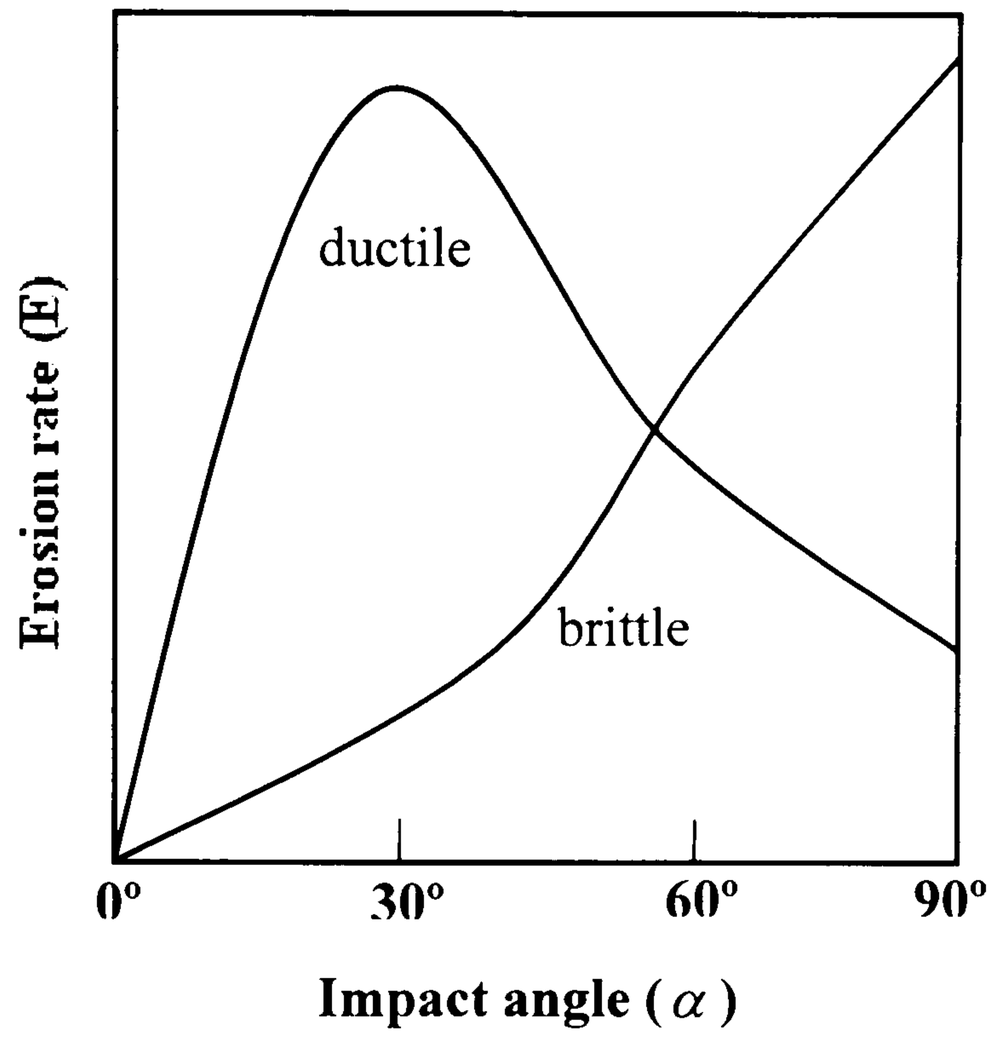

Figure 3.4 The schematic diagram showing the relationship between the erosion rate and impact angle for ductile and brittle materials

In oil and gas production, erosion results from the impingement of sand and depends on a multitude factors and good models have yet to be developed. Wood *et al*. (2004) listed the numbers of important variables related to slurry erosion as shown in Table 3.1. It is well recognized by researchers that prediction for erosion is a difficult task. The most well-known guideline in oil and gas industry is the American Petroleum Institute Recommended Practice 14E (API RP 14E, 1991). It gives a limiting production velocity (or the erosional velocity limit), V_e (ft/s) by the following equation:

$$V_e = \frac{C}{\sqrt{\rho_m}} \tag{65}$$

where ρ_m (lb/ft^3) is the fluid mixture density at flowing pressure and temperature. The API formula is very simple and easy to use, as the only variable accounted is fluid density. Also the formula does not recognize many contributing to erosion/corrosion and the use of this formula can result in unrealistically low production velocity limits for preventing pipe damage in erosion service (Shirazi *et al*., 1995)

Table 3.1 Some of the main variables which influence erosion (Wood, 2004)

Slurry variables	Component variables
Liquid: viscosity, density, surface activity, lubricity, corrosivity, temperature Particles: brittleness, size, density, relative velocity, shape, relative hardness, concentration, particle/particle interactions Flow field: angle of impingement, particle impact efficiency, boundary layer, particle rebound, degradation, particle drop-out, turbulence intensity	Bulk properties: ductility or brittleness, hardness and toughness, melting point, microstructure, shape and roughness Surface properties: work hardening, corrosion layers, surface treatments, coating type, coating bond, microstructure Service variables: contacting materials, pressure, velocity, temperature, surface finish, lubrication, corrosion, hydraulic design, intermittent slurry flows

To modify API RP 14E, Salama (1998) extended his previous model to account for multiphase flow by adding terms that account for mixture density and velocity. This model applies a geometry-dependent constant that must be obtained experimentally as shown in (66).

$$ER = \frac{1}{S_m}\frac{WV_m^2 d_p}{D^2 \rho_m} \tag{66}$$

where ER = erosion penetration rate, mm/yr; W = sand production rate, kg/day; V_m = fluid mixture velocity, m/s; dp = sand size, micron; D = pipe diameter, mm; ρ_m = fluid mixture density, kg/m^3 and S_m = geometry-dependent constant, specified by this equation.

Alternatively Shirazi *et al.* (1995) developed a mechanistic erosion prediction model for use over a broad rang of operating conditions that accounted for geometry type, size, and material; fluid properties and rate; and sand size, shape and density. This model computes the maximum penetration rate in carbon steel elbows as shown in Equation

(67). The McLaury *et al.* (1999) model is based on penetration rates in elbow geometry because it is more susceptible to erosion damage than a straight pipe section. A common procedure presented in the literature is to extrapolate a threshold flowstream velocity relation from erosion rate data for an elbow geometry based on an allowable amount of erosion, such as a penetration rate of 5 or 10 mpy. Jordan (1998) extended the McLaury and Shirazi erosion model to account for multiphase carrier fluid. It showed that Jordan's analysis agrees well with field experience.

$$h = F_M F_S F_P F_{r/D} \frac{W V_L^{1.73}}{(D/D_0)^2} \tag{67}$$

where h is penetration rate (m/s) (can be converted to mm/yr or mpy); F_M is empirical constant that accounts for material hardness; F_S is empirical sand sharpness factor; F_P is penetration factor for steel (based on 1″ pipe diameter) m/kg; $F_{r/D}$ is penetration factor for elbow radius; W is sand production rate, kg/s; V_L is the characteristic particle impact velocity, m/s; D is pipe diameter (inch); D_0 is reference of 1 inch pipe diameter.

McLaury *et al.* (1999) recognized that the erosion prediction model must be able to capture the exchange of momentum between the fluid and the particles. For elbows. much erosion occurs when the exchange of momentum between the fluid and the particles is low. This is a result of the inability of the fluid to redirect the particles as they travel through the bend; therefore, the particles travel in a relatively straight path and impinge the pipe wall. Any factor that increases the efficiency of the exchange in momentum will decrease the erosion rate in elbows. This includes decreasing the particle size or increasing the fluid density or viscosity. Therefore, the flow velocity has a tremendous effect on the erosion rate.

For multiphase flow. Ramachandran *et al.* (2002) accounts for chemical inhibition effects in erosion by adapting the expression for calculating the erosion rate h, produced by McLaury *et al.*, (1999) and Jordan (1998) and including an empirical constant F_i which accounts for chemical inhibition effects in erosion as shown in equation.

$$h = F_i F_M F_S F_P F_{r/D} \frac{W Q_F V_L^{1.73}}{D^2} \tag{68}$$

where, w is the weight fraction of sand; Q_F is the production rate of fluid; D is ratio of pipe diameter in inches to a one inch pipe.

The literature available on the effect of steel microstructure on erosion rates suggests that ductile steel is the most erosion resistant (Stachowiak and Batchelor, 2001). Hardening of steel to form martensite offers little improvement except at very low impingement angles, and the formation of massive or lamellar carbides reduces erosive resistance. For low alloy carbon steels, the ferritic phase with sufficient spheroidal carbide inclusions to induce strengthening is very effective against erosive wear (Pearlitic steels show inferior wear resistance to spheroidized steels. It was found that the erosive wear of steels shows the classical ductile erosion characteristic, such as a maximum wear rate a low impact angle from 15°-30° and with subsurface and surface cracking (Levy, 1981).

3.2.2 Aspects of Erosion-Corrosion

Fluid motion can influence the corrosion mechanism and in turn affect the corrosion rate. For example, when the corrosion rates are controlled wholly or partially by mass transfer of reactant to or product from the surface, or by direct impingement of the sand particles or occasionally the fluid itself against the surface, such influence would occur. The relative motion between the corroding metal and its environment can introduce different types of flow-induced corrosion as shown in Figure 3.5 (Heitz, 1991), which is defined as increased corrosion from increasing turbulent intensity and mass transfer as a result of the flow of a fluid over a surface (Efird *et al.*, 1993).

Erosion-corrosion occurs in areas where turbulence intensity at the metal surface is high enough to cause mechanical or electrochemical disruption of the protective film. The process is usually accelerated under slurry conditions, when abrasive solid particles, such as sand, are entrained in the fluid.

Erosion-corrosion is tribo-corrosion material loss mechanism, which presents different challenges to material selectors and designers than pure corrosion situations. The

material loss experienced in erosion-corrosion conditions includes chemical dissolution (which can be increased by mass transfer at the surface), mechanical erosion caused by fluid flow and/or impingement of particles on the pipe wall and electrochemical corrosion enhanced erosion and vice versa (Burstein and Sasaki, 2001; Oltra *et al.*, 1995). Because of the strong interactions between mechanical erosion and electrochemical corrosion the production of surface films (e.g. corrosion products) are very important in erosion-corrosion. Depending on the flow conditions, Shadley *et al.* (1998) determined the corrosion regimes to be 1) $FeCO_3$ scale formation and low metal loss rates at low velocity 2) sand abrasion and removal of the scale and high metal loss rates at high velocities and 3) partial removal of scale and localized pitting at intermediate velocities. Of course the regimes and the transition velocities will be dependent on the environment as well as the material.

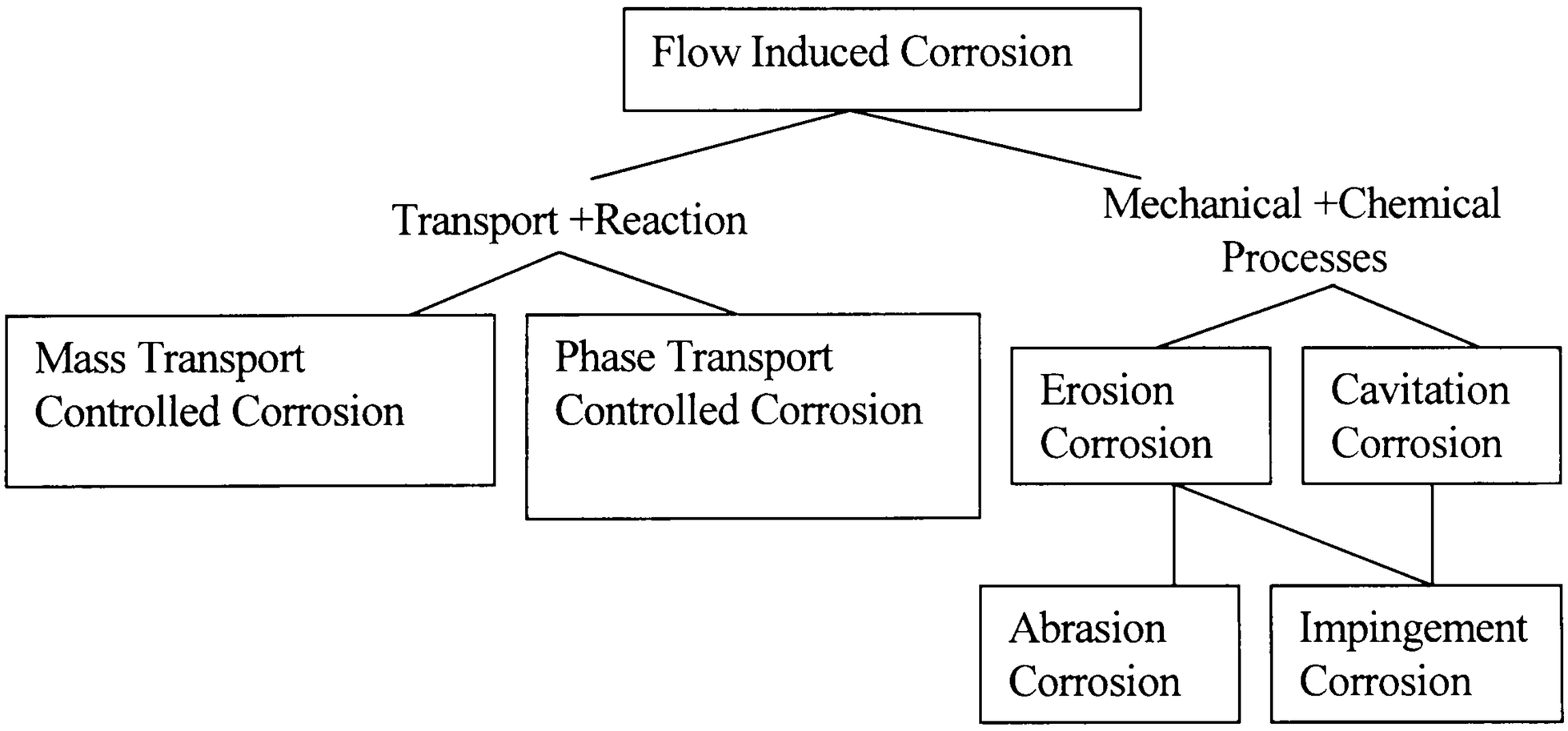

Figure 3.5 Classification of flow-induced corrosion by Heitz (1991)

An increase in fluid flow can also decrease corrosion rates by eliminating aggressive ion concentration or enhancing passivation or inhibition by transporting the protective species to the fluid/metal interface (Roberge, 2004). The morphology of surfaces affected by erosion-corrosion may be in the form of shallow round or horseshoe shaped pits or other local phenomena related to the flow direction (Roberge, 2004). Six important factors affecting erosion-corrosion were summarized by Roberge (2004) based on a review of scientific and engineering work on stress corrosion cracking (SCC) failures as following:

1. Material factor—the properties of surface film both naturally formed and formed as corrosion products are important element to understand the resistance of metallic materials to erosion-corrosion.
2. Environment factor—dissolved oxygen, salinity, pH etc.
3. Temperature—for carbon steel, sensitivity to temperature usually occurs between 100-280◦C
4. Fluid movement—hydrodynamic factors that contribute to the rate of erosion-corrosion include velocity, surface shear stress, turbulence intensity, and the mass transfer coefficient.
5. Surface roughness—surface roughening tends to increase the subsequent damage from erosion-corrosion
6. Galvanic interactions

For two-phase liquid particle flow, Lotz (1990) recognized that sand may cause severe erosion and erosion-corrosion attack in oil and gas production and suggested an erosion-corrosion rate of the form:

$$R = \text{Constant} \times V^n \tag{69}$$

where V is the flow velocity and the exponent n can be in the range of 1-3 depending upon whether corrosion (closer to 1) or erosion (closer to 3) is the rate-controlling process.

There has been a lot of emphasis in erosion-corrosion in determining the contributions to mass loss from these different components in order to understand what processes are controlling the mass loss in different situations. In recent years, the synergistic effect between erosion and corrosion has been received more and more attention to provide information for engineers designing or maintaining components subjected to both wear mechanisms. The synergy occurs when the total material loss under erosion-corrosion condition is more than the sum of material loss due to pure erosion and pure corrosion.

In literature, there are two ways in describing the meaning of synergistic effect in aqueous erosion-corrosion. Some authors (Stack *et al*. 1997; Wood, 2006) describe it as the sum of the enhancement of erosion due to corrosion and vice versa. Some (Souza

and Neville 2003; Zhang *et al.* 2004) used the term "additive effect" to refer to the corrosion enhancement due to erosion, and the synergistic effect is restricted to the erosion enhancement due to corrosion. However, both parties have agreed that there is enhanced degradation when the wear rates of the material can be significantly higher than the combined effects of erosion and corrosion acting separately. Synergy is also found to be both positive and negative and appears to be angle dependent, but is difficult to determine precisely (Wood and Speyer, 2004).

In order to determine the synergism both erosion and corrosion must be studied under controlled conditions. It is to separate the erosion-caused metal loss from the corrosion-caused metal loss to clarify the transition between the erosion-corrosion regime. This indicates whether erosion or corrosion is the dominant wastage process and provides useful information on the selection of materials and prevention of erosion-corrosion. Three types of test are required: 1) pure erosion tests to determine the erosion rate; 2) pure corrosion tests to determine the corrosion rate; 3) combined tests to determine the total erosion-corrosion rate which is under slurry flow condition. Neville *at al.* (1995) used a range of engineering alloys to evaluate the percentage damage caused by synergy using the equation:

$$S = TWL - (E + C) \tag{70}$$

where S is the synergistic wear rate, TWL is the total erosion-corrosion rate, E is the erosive rate and C is the corrosive rate. S, T, E and C can be either mass loss rates or depth-of-penetration rates.

To characterize the predominant mechanisms of material degradation under erosion-corrosion condition, it is crucial to understand hydrodynamic characteristics of the flow.

3.3 Basic Hydrodynamics of Multiphase Flow Regime

The basic hydrodynamic characteristics is important to be determined for simulation of field conditions, because, firstly, hydrodynamic relationships can be used to correlate inhibitor performance in the laboratory and in the field (Papavinasam *et al.*, 2003); secondly, CO_2 corrosion can be impeded by the formation of protective films and in

cases of film offering protection, the hydrodynamics of the system can become an important factor (Dawson *et al.*, 1991); thirdly, it is important to understand the solid-liquid multiphase flow so that to characterize the predominant mechanisms of material degradation under erosion-corrosion conditions. The fundamental assumption above is that, when the hydrodynamic parameters of the different geometries are the same, the corrosion mechanism will be the same. Under these conditions, the corrosion rates and the efficiencies of inhibitors in the laboratory and in the pipe are similar.

To describe the flow conditions, parameters such as heat transfer, mass transfer and momentum transfer must be well defined. Therefore the understanding velocity profile of the flow is essential. Turbulence occurs when laminar flow is disrupted. In turbulent flow conditions the velocity and pressure at a fixed point in space do not remain constant with time. This variation with time is very irregular and of high frequency. Due to the random nature of the turbulent flow, direct methods for calculating velocity profiles are not available. The continuity and motion equations commonly used in the analysis of laminar flow conditions also apply for turbulent flow (Bird *et al.*, 1976). However, the solution of these equations in turbulent conditions is an extremely complex process and beyond the scope of this thesis.

Fluid mechanics offers several parameters, such as mass-transfer coefficient, wall shear stress, Sherwood number, Reynolds number, which could be used to define conditions so that velocity-sensitive corrosion mechanisms in the field are duplicated in the laboratory, especially the mass-transfer coefficient and fluid shear stress seem to offer the best connection.

For the study of erosion-corrosion under turbulent condition, shear stress (τ) is the predominant parameter to describe the hydrodynamic fluid condition. Shear stress is a frictional force associated with the velocity gradient across this boundary. It has been suggested that this may control the mechanical stability of surface films. Reynolds number is used to define the turbulent characteristics of the flow. The following sections describe the empirical relationship used in the study of turbulent flow in the rotating cylinder electrode and submerged impinging jet systems.

3.3.1 Hydrodynamic Characteristics of RCE

There are a number of systems that have been proposed as laboratory devices, for example, the stirrer housing coupons, the stirrer moving fluid relative to stationary coupons, rotating electrodes of various geometries, impinging jets, and flow loops with cylindrical spool pieces in variety of configurations. Rotating cylinder electrode is one of the simplest devices to construct. The rotating cylinder electrode (RCE) test system is compact, relatively inexpensive and easily controlled. The apparatus operates under known and controlled hydrodynamic conditions, which often are turbulent. The experiments require small amounts of fluid, and gravimetric and electrochemical measurements can be made simultaneously. These have led to many at temptation to use the results from rotating cylinder electrode to predict the effect of fluid flow and particle impact on corrosion in real life geometrical configuration.

A criterion for fully developed turbulent flow to occur when wider gaps exist (r_{outer}-r_{inner} $> 0.5(r_{inner}+r_{outer})$) between the inner and outer electrode is for the Reynolds number to be greater than about 200 (Gabe and Walsh, 1983). If low rotation rates are to be examined, they should be checked to determine the hydrodynamic conditions under which the rotating cylinder is operating so that it is operating in the turbulent regime, which is of most interest to erosion-corrosion studies.

Reynolds number defines a relative flow velocity in terms of a characteristic length "*l*" and can be used to take account of such effects and allows the prediction of either laminar or turbulent. The Reynolds number is defined as:

$$\mathrm{Re}=\frac{ul}{\nu} \tag{71}$$

where, u (m/s) is the mean velocity of the fluid and ν (m^2/s) is the kinematic viscosity of the fluid. The kinematic viscosity is given by:

$$\nu=\frac{\mu}{\rho} \tag{72}$$

where μ (Pa.s) and ρ (kg/m^3) are the viscosity and density of the fluid respectively.

Gabe and Walsh (1983) expressed relationship between the hydrodynamic system of RCE and Reynolds number as following:

$$\tau_w = 0.0791 \mathrm{Re}^{-0.3} \rho r^2 \omega^2 \quad (73)$$

where τ_w is the wall shear stress for RCE, ρ is the density of the fluid. r is the radius of the rotating electrode, ω is the rotational speed of RCE.

3.3.2 Hydrodynamic Characteristics of SIJ

Submerged impingement jet (SIJ) is commonly used to study flow-accelerated corrosion and erosion-corrosion. The test can simulate high-turbulence conditions in multiphase systems reliably and repeatedly. This geometry is attractive because of a high mass transfer rate, but its use for evaluating performance of corrosion inhibitors is relatively new (Dawson *et al.* 1987). The flow field established for a circular jet impinging on a flat plate with the jet central axis normal to the plate is shown in Figure 3.6 (Efird, 1993). When a submerged jet collides perpendicularly with a flat plate in a stationary electrolyte, there form three flow regimes. Region A is the stagnation zone. The flow is laminar near the plate, and the principal velocity component is changing from axis to radial, with a stagnation point at the centre. Region B is a region of rapidly increasing turbulence with the primary flow vector is parallel to the solid surface. The flow pattern is characterized by high turbulence, a large velocity gradient at the wall, and high wall shear stress. Thus this region is most interest for studying fluid flow effects on corrosion in high-turbulence areas. In this region, the equation for wall shear stress is (Efird, 1993):

$$\tau_w = 0.179 \rho U_0^2 \mathrm{Re}^{-0.182} \left(\frac{r}{r_0}\right)^{-2.0} \quad (74)$$

In region C in Figure 3.6. the bulk flow rate and turbulence decay rapidly as the thickness of the wall jet increase. momentum is transferred away from the plate and the surrounding fluid is entrained in the jet.

This empirical approach and the use in laboratory of well characterised flow systems such as rotating electrodes. submerged impinging jets. have been very successful in

providing useful numerical correlations used in the understanding of the corrosion phenomena in turbulent flow conditions (Dawson *et al*., 1991).

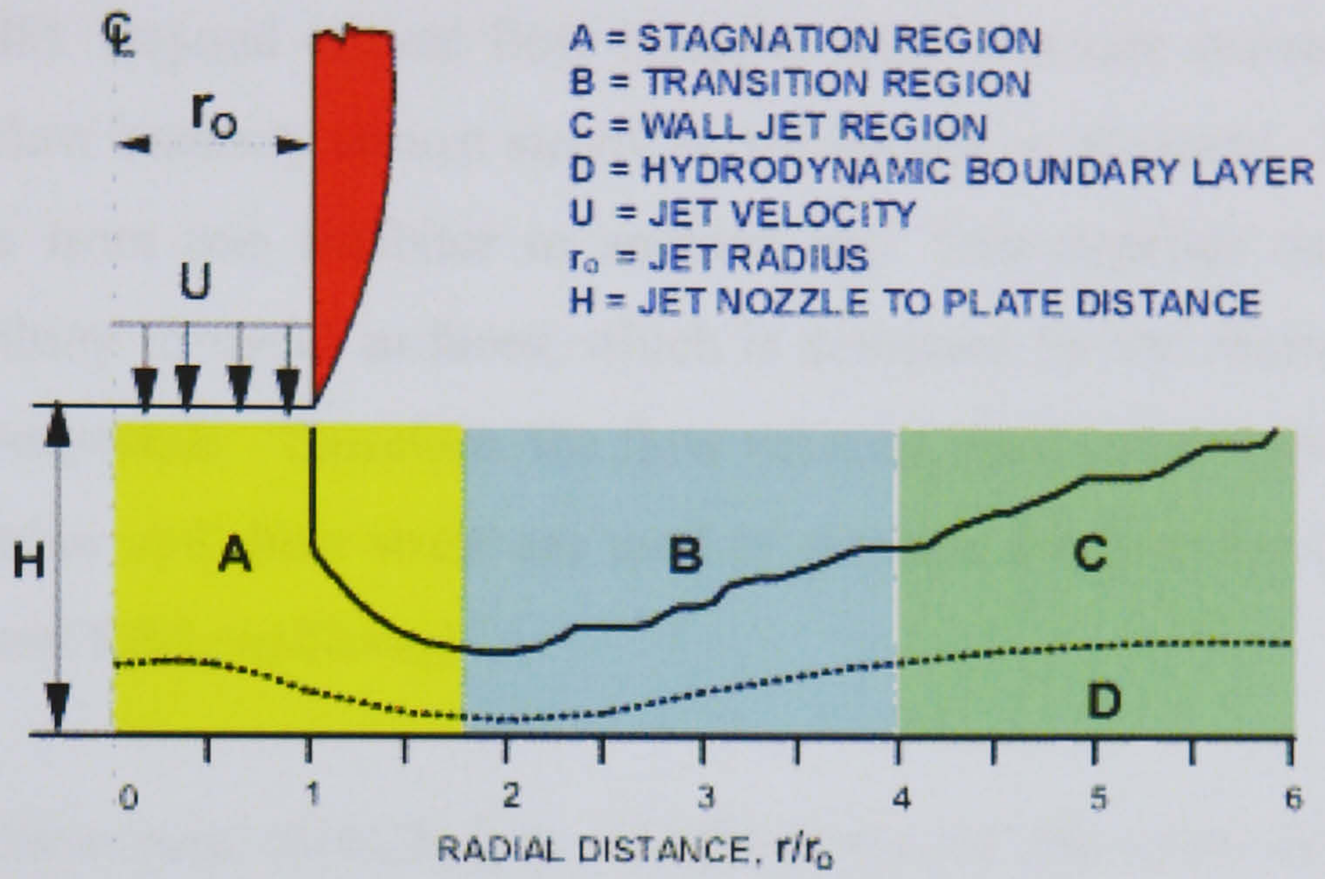

Figure 3.6 Hydrodynamic characteristics of jet impingement on a flat sample showing the three characteristic flow regions (Efird, 1993)

When two systems are at the same value of wall shear stress, at the same flow regime and without slip at the wall, then both systems should have the same flow velocities near the surface and the same mass transfer conditions (Silverman, 2004). However, the above hydrodynamic parameters are defined under the conditions without sand. In this thesis, which is erosion-corrosion with sand impact, the wall shear stress (τ_w) calculation has been mainly used as approximate data to describe the condition for the results obtained in different hydrodynamic systems, i.e. rotating cylinder electrode and submerged impingement. The laboratory method should be rapid and should simulate the worst case, such as pitting corrosion.

Hausler and Stegmann (1988) argue that corrosion rate in flowing media containing inhibitor depends on flow intensity. The flow intensity refers to the combined effects of flow velocity and pattern, sand content and particle size, as well as many other flow-influenced parameters. As velocity is increased in which mass transport dominate, the largest increase in corrosion rate occurs at certain speed. Beyond this range, the corrosion rate becomes constant activation control. This is so called critical velocity

beyond which the corrosion rate becomes independent of flow (Ikeda *et al.*, 1984). The corrosion rate can also be increased through the presence of solids in the flowing environment, leading to impingement and more rapid film degradation (Lotz and Sydberger, 1988). Beyond critical flow intensity corrosion rate increases sharply and below critical flow intensity almost steady corrosion rate is observed. The critical flow intensity varies from one inhibitor to another one. This depends on the adsorption strength of inhibitor to metal surfaces, which is dominant by the chemical structure of the inhibitor compounds. Therefore, the flow velocity, sand content and size as well as the Ronald number and shear stress are used to describe the flow comparison between the laboratory and field conditions.

RCE and SIJ have been identified as suitable tools for the study of slurry erosion-corrosion occurring in turbulent flow conditions and the determination of the constituent components and controlling mechanisms (He *et al.*, 2005; Stack *et al.*, 2004). It is also acknowledged that estimating the actual impact velocity and the impact angle of solid particles is difficult in the design. This is the limitation of these systems. but they can give a comparitive performance of the different materials with or without inhibitors. Studies of the slurry erosion-corrosion of Cr containing steel in RCE system showed that increases the flow velocity resulted in higher current densities for the anodic reaction (Stack *et al.*, 2004). For stainless steel, the pure corrosion or the corrosion component in erosion-corrosion was smaller than the pure erosion and the erosion component in synergistic interaction. The more susceptive to corrosive the steel is, the smaller of the ratios of erosion to corrosion and also at high velocities. the removal of material mainly came from mechanical damage (He *et al.*, 2005).

3.4 Corrosion and Erosion-Corrosion Inhibition

Corrosion prevention concepts consist of i) use of carbon steel in combination with corrosion inhibitors, ii) use of corrosion resistant alloys (CRA) without adding corrosion inhibitors, iii) mixed completion: upper part carbon steel (+ inhibitor), lower part CRA.

At the first sight the second alternative seems to be the right choice for deep hot wells. However, at high temperatures, high salinity formation waters, high H_2S partial pressures and in presence of elemental sulphur CRA may suffer severely from corrosion attack (shallow and deep pitting, stress corrosion cracking).

Once localized attack is generated, the site of localized attack, e.g. a pit, can be enlarged by fluid flow due to local microturbulences, even if no solid particles are present. At sites of high energy microturbulences fluid dynamic forces can also destroy passive layers on CRAs, thus producing FILC on CRAs. In addition, the inhibition of CRAs is much more difficult to achieve than of carbon steels. For some corrosion systems, so far no effective inhibitors are available at all. In addition, highly corrosion-resistant steels are rarely used for the cost of such materials is high. They are only used in downhole and offshore applications where corrosion inhibitor treatments may be less effective. Using carbon steel in conjunction with chemical inhibitor treatments remains a cost effective way to reduce corrosion attack.

It should be appreciated in gas/condensate production tubing or flow lines that local velocities can be much higher than the bulk velocity. Flow disturbances can lead to erosion of protective films. In practice, velocities exceeding 17-20m/s may affect inhibitor performance.

Corrosion inhibitors have been observed to allow producers to produce at higher velocities in situations that contained sand (Shadley *et al.*, 1998). Earlier work about oilfield chemicals to retard erosion-corrosion in gas systems containing sand has been conducted for both carbon steel and corrosion resistant alloys (Evans *et al.*, 2004). Substantial work needs to be done to investigate the inhibitor effect on erosion-corrosion or erosion only.

3.4.1 The Importance of Corrosion Inhibitors

A corrosion inhibitor can be added to a system of interest at a very low concentration. If the chemicals are successful, they can substantially suppress the rate of metal

dissolution. There is a strong reliance on corrosion inhibitor deployment in controlling corrosion associated with oil and gas production and transportation. such as drilling and stimulation fluids, producing wells water injection systems. transportation and refining systems. This is because carbon and low alloy steels are extensively used for many applications but they exhibit poor CO_2 corrosion resistance.

In deep hot wells, even a small increase of surface roughness due to deposition of scales or corrosion attack will increase the pressure drop in the production tubing significantly. thus reducing the production rate. Corrosion inhibitors can be added to the system which functions as drag reducers. i.e. they reduce the wall shear stress between the flowing produced liquids and the tubing wall. An example of the flow improving property of CO_2 corrosion inhibitor has shown that the inverse linear relationship between the active inhibitor concentration and change of pressure drop (Schmitt. 2003). It also reported that the wall shear stress could be reduced by a factor of 5 by addition of CO_2 corrosion inhibitor, thus reducing the risk of flow induced localized corrosion (Schmitt, 2003).

An inhibitor can be defined as: "a chemical substance or combination of substances that, when present in the proper concentration and forms in the environment, prevents or reduces corrosion without significantly changing the concentration of any other corrosive agent." (Sastri, 1998; Xia *et al*., 1989).

The protective nature of inhibitors depends on many factors: interaction between inhibitor and environment, incorporation of the inhibitor in the surface layer. chemical reactions, electrode potential, concentration of inhibitor. pH. oxygen content, temperature, presence of other ions, etc.

3.4.2 General Aspects of Inhibition by Inhibitors

Inhibitors often work by adsorbing themselves on the metallic surface, either by blocking active cathodic or anodic reaction sites on the metal itself, or by incorporating

in the corrosion product and preventing further access of the corrosive fluid. Inhibitors slow corrosion processes by either:

1. Increasing the anodic or cathodic polarisation behaviour (Tafel slopes);
2. Reducing the movement or diffusion of ions to the metallic surface;
3. Increasing the electrical resistance of the metallic surface.

Organic inhibitors are mainly used where the main cathodic reduction reaction is hydrogen evolution. Both anodic and cathodic effects are sometimes observed in the presence of organic inhibitors but, as a general rule, organic inhibitors affect the entire surface of a corroding metal when present in sufficient concentration. Organic inhibitors usually designated as 'film-forming', protect the metal by forming a hydrophobic film on the metal surface.

The effectiveness of these inhibitors depends on the chemical composition, their molecular structure, and their affinities for the metal surface. Because film formation is an adsorption process, the temperature and pressure in the system are important factors. Organic inhibitors will be adsorbed according to the ionic charge of the inhibitor and the charge on the surface. Cationic inhibitors, such as amines, or anionic inhibitors, such as sulphonates, will be adsorbed preferentially depending on whether the metal is charged negatively or positively. The strength of the adsorption bond is the dominant factor for soluble organic inhibitors. Organic inhibitors is mainly used in CO_2 environments, and also called adsorption inhibitors.

As corrosion results from electron transfer reactions at metal surfaces, a primary mechanism for an efficient inhibitor is to adsorb onto the metal surface to form a barrier lowering the corrosion rate. When a corrosion inhibitor is added to a system, adsorption of the inhibitor molecule at the metal-solution interface occurs almost as a first stage (Sastri, 1998), and this is accompanied by a change in potential difference between the metal electrode and the solution due to the non-uniform distribution of electric charges at the interface. The metal-electrolyte interface is characterized by an electrical double

layer. The role of the electrical double layer in corrosion inhibition processes has been dealt with extensively in the literature (Yariv and Cross, 1979).

The introduction of an inhibitor into the electric double layer changes its composition and structure. Hence, measurement of the capacitance of the double layer before and after the addition of the inhibitor can be used to monitor the adsorption of the inhibitor.

In the inhibitor adsorption processes, the dielectric properties of solvent water are affected. In bulk solutions, the water molecules are disoriented and the dielectric constant is about 80 at 25°C. In the electric double layer, the dipoles of water molecules are oriented and this decreases the dielectric number, which is the 6 and 40 in the IHP and OHP respectively, and no longer a constant. The dielectric properties of water molecules in the EDL changes when ions or molecules with high dipole moment adsorbed at the metal surface (Sastri, 1998).

When surface active substances with amphiphatic structure, for example RNH_3^+, or $RCOO^-$ and hydrophobic groups such as hydrocarbon chains, achieve the inhibition. hydrophobic effect occurs. The hydrophobic group of the surface active substances dissolved in water and affect the structure of hydrogen bonding in water. The polar functional groups adsorbs on the metal with a hydrophobic tail. The hydrophobic groups of the free inhibitor molecules in solution interact with the hydrophobic groups of the adsorbed molecule at the interface and results in aggregation known as hemimicelle formation (Sastri, 1998). Formation of micelles takes place, when the inhibitor concentration is increased. The concentration above this micelles form is called critical micellar concentration. The temperature above which micelles are formed is the Kraft point.

3.4.3 Adsorption of Inhibitors

Four primary modes of adsorption are associated with organic compounds at metal surfaces: (i) electrostatic adsorption. (ii) π-back bonding. (iii) chemisorption and (iv)

oranometallic complex formation (Riggs, 1981). The two main types of adsorption of an organic inhibitor on a metal surface are physical or electrostatic and chemisorption.

Physical adsorption is due to the electrostatic attraction between the inhibiting ions or diploes and the electrically charged surface of the metal. It is influenced by the nature and the surface charge of the metal, the type of aggressive electrolyte and its molecular interaction with the surface-active agent, the chemical structure of the organic compound and the reaction and interaction between adsorbed inhibitor species. The inhibiting species whose action is due to electrostatic adsorption interact rapidly with the electrode surface. The forces in electrostatic adsorption are generally weak. The process has low activation energy and it proves to be relatively independent of the temperature. The surface charge on the metal is defined by the position of the free corrosion potential, E_{corr}, of the metal with respect to its potential of zero charge, (PZC). At PZC the net charge on the electrode is zero, (PZC = E_q = 0). At potentials more positive than PZC, the electrode is positively charged and at potentials more negative than PZC the electrode is negatively charged. When $\varphi = E_{corr} - E_q$ is negative, cations are adsorbed and when φ is positive, anions are adsorbed. This occurs in the case of inorganic or organic ions as well as dipoles. At equal values of φ for different metals such as iron and mercury, similar behaviour of a given inhibitor is expected in the same environment. Therefore, at the same potential φ, electrostatic interaction should be independent of the metal nature and this has been used as a basis for researchers to compare adsorption of inhibitors on different metals (Sastri, 1998).

In some case, the degree of inhibition in the presence of both absorbable anions (e.g. Chloride ions) and inhibitor cations is higher than the sum of the individual effects (Sastri, 1998). For example, chloride ions are adsorbed on the metal surface and dipoles oriented to the metal surface are created. Thus PZC shifts to more negative values than the free corrosion potential, then, adsorption of inhibitor cations will occur easier than that with no chlorides. However, co-operative and competitive adsorption has to be distinguished. In co-operative adsorption, the organic compound is adsorbed on the halide, pre-adsorbed on the metal surface, while in competitive adsorption, it displaces adsorbed water molecules and competes with halide ions in the adsorption onto the

metal so that the hydrocarbon chains or rings of the inhibitor protects the surface from attack by halide ions (Sastri, 1998).

Chemisorption is probably the most important type of interaction between the metal surfaces and an inhibitor molecule. In this type of adsorption, the adsorbed species actually is in contact with the metal surface by electron transfer from inhibitor to the metal to form a co-ordinate type of bond (Sastri, 1998). The chemisorption process takes place with higher activation energy. The influence of organic inhibitor structure on their adsorption in aqueous solution has not been studied systematically and the results are sometimes contradictory. A coordinate type of bond involving electron transfer from inhibitor to the metal is assumed to take place in the process. The bonding occurring with electron transfer depends on the nature of the metal and the nature of the organic inhibitor. Electron transfer is facilitated when the inhibitor molecules has an unshared lone pair of electrons on the donor atom of the functional group. Availability of π electrons due to the presence of multiple bonds or aromatics rings in the inhibitor molecule would facilitate electron transfer from the inhibitor to the metal. An opposing view, that there is necessarily no chemical bond between the metal and the adsorbed species, is held by Bockris (1974).

Wang *et al.* (1999) provided information on electron configuration of several imidazoline inhibitors and concluded that the N-C-N bond in imidazoline molecule is of p-π configuration property. Introduction of electron releasing substituent or conjugation system on the C atom will remarkably strengthen the chemical adsorption of the N atom on the metal surface. Campbell and Jovancicevic (1999) confirmed that nitrogen is clearly shown from the imidazoline-inhibited surface, which provides a marker for the presence of the chemical inhibitors on the metal surface or corrosion products.

Most organic inhibitors are substances with at least one functional group considered as the reaction centre for the chemisorption process, and the strength of the adsorption bond is related to the electron density and to the functional group plarizability.

The chemisorption process is slower than electrostatic sorption and has higher activation energy. The temperature dependency shows higher inhibition efficiencies at higher temperatures.

3.4.4 Inhibitor Action in Acid Solutions

Inhibitor action in acid solution is generally assumed due to the adsorption of the inhibitor on to the metal-solution interface. The adsorbed substance could be ion or neutral polar molecule. A number of organic compounds represent this type of inhibition, such as those containing elements of nitrogen, phosphorous, arsenic, sulphur, oxygen and selenium. The interaction of ions or neutral polar molecules at the electrical double-layer changes its properties and structure. The water molecules pre-adsorbed at the metal surface are involved in the successive adsorption processed. The displacement reaction between the water and inhibitor at the metal-solution interface can be expressed as following (Bockris and Drazic, 1972):

$$Inh_{(sol)} + mH_2O_{(ads)} = Inh_{(ads)} + mH_2O_{(sol)} \quad (75)$$

where, m is the number of water molecules removed from the metal surface for each molecule of inhibitor adsorbed and m is assumed to be independent of coverage or charge of the electrode (Bockris and Drazic, 1972). The value of m is associated with the cross section area of organic molecule and water molecule.

Adsorbed inhibitors in acid solution function due to retarding either the cathodic hydrogen reaction or anodic dissolution process of the metal, or both. This effect can be due to the change of the electric double layer, the reduction of the metal reactivity, participation of the inhibitor in partial electrode and the formation of a physical barrier.

Reducing the metal activity means that the adsorbed inhibitor may not cover the entire metal surface, but adsorbs on active sites by which reducing the extent of anodic or cathodic reaction or both. Although the corrosion mechanism is not changed, the reaction rates will be decreased in proportion to the extent to which the active sites are blocked by the inhibitor molecules. The current density changes to lower but the Tafel slopes are not changed (Sastri, 1998).

It is generally assumed that the reaction of metal dissolution proceeds by steps with the formation of adsorbed intermediates on the metal surface. The adsorbed active may participate in the intermediate formation, reducing or stimulating the reaction, depending on nature (e.g. the stability) of the adsorbed surface complex. For iron in acid environment, FeOH is assumed as adsorbed intermediate, and when the addition of organic inhibitor, the complex of [(FeHO)Inhn] is assumed adsorbed on the iron surface (Sastri, 1998). This complex can change the reaction mechanism, increasing or reducing the anodic Tafel slope.

Some inhibitors are able to form multimolecular layers on the metal surface. The film layers formed may involve chemisorption bonds, π electron interactions and attractive lateral interactions. The barrier film prevents diffusion of ions to or from the metal surface. Prevention of mass transport results in inhibition of corrosion can be manifested by concentration polarisation and resistance polarisation of the cathodic branches (Trabanelli, 1989).

General corrosion and hydrogen entry into the metal are probably occur in acid solutions. Using suitable concentration of inhibitors above the critical concentration can prevents general corrosion to occur. But it might be accelerate the hydrogen entry into the metal. Quaternary ammonium compounds, amines, aldehydes and sulphoxides are capable of inhibiting both general corrosion and hydrogen entry into the metal (Sastri, 1998).

3.4.5 CO_2 Corrosion Inhibitors

Organic adsorption-type corrosion inhibitors historically used in the oil and gas industry containing CO_2 generally have structures similar to those of surfactant molecules (ASTM handbook, 1987). These corrosion inhibitors can be broadly classified into amides/imidazolines, salts of nitrogenous molecules with carbonxylic acids, quaternaries, polyoxyalklated amines/amide/imadazolines, nitrogen heterocyclics and other non-nitrogenius compounds containing phosphorus/sulphur/oxygen atoms, etc. Typically, the chemistry of a commercial corrosion inhibitors is a blend of one or a

combination of the above compounds together with the incorporation of other components, e.g. surfactants, solvents and demulsifier, etc. (Bregman, 1963; Kelley and Bowman, 1984). They are either polar or ionized salts with the charge centred on the nitrogen, oxygen or phosphorus group. For example, a charged polar "head" joined to a long, generally straight chain alkyl group. Inhibitor works by attaching the polar head group to the anodic and cathodic sites on the corroding steel surface. The hydrophobic tail extends into the solution, lending itself to the co-adsorption of oil and producing a protective hydrophobic film barrier that can further retard steel corrosion (Schaschl, 1981). Many inhibitors described in literature (Pospelov and Fokin, 1993; Lahodny-sarc, 1994) are all film forming. That a corrosion inhibitor prevents attack by formation of a film on the metal surface is illustrated in Figure 3.7. The inhibitor may interfere with either the anodic or cathodic reaction. The integrity of the barrier and the amount of additive necessary to form the barrier is interesting information for evaluation of the inhibitor effectiveness.

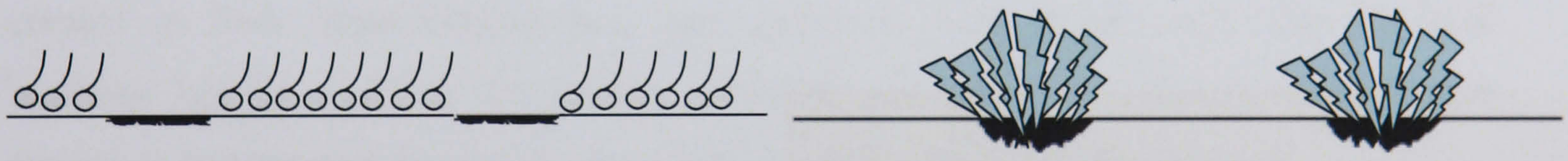

Inhibitor film formed at cathodic site of the metal surface

Inhibitor film formed at anodic site of the metal surface

Figure 3.7 Corrosion inhibitor preventing attack by formation of a barrier on the metal surface

A more simplistic view of the mechanism of corrosion inhibitors can be described as controlled precipitation of the inhibitor from its environment (water and hydrocarbons) onto metal surfaces. As a metal surface in an aqueous environment will have a surface charge and the inhibitor will rapidly be adsorbed onto the metal surface. This process is rapid and reversible, which means that the concentration of adsorbed inhibitor will rapidly decrease if the local environment is depleted.

A later view of the mechanism of oil and gas field corrosion inhibitors invokes the incorporation of the inhibitor into a thin corrosion-product film. Mansfield *et al*. (1985) point out that interface inhibition presumes a strong interaction between the corroding substrate and the inhibitor. This film then becomes more resistant to the flow of ions and electrons, so the corrosion reaction is slowed. Ramachandran *et al*. 's (2001) model (Figure 3.8) indicates that inhibitor bilayer film formation on $FeCO_3$ can increase the stability of the $FeCO_3$ film and reduce its porosity, thereby blocking access to the reacting surface. Schmitt *et al*. (1995) found that inhibitor molecules adsorbed upon the surfaces of clean metal or corrosion products through polar groups shielding the metal from hydrophobic interaction of nonpolar. The morphology and degree of crystallinity of the scale and its porosity will be influenced by adsorbed molecules. The presence of effective inhibitors thus decreases the intrinsic stresses and increases the critical strains for cracking and spalling of the scale (Schmitt *et al*., 1996). Incorporation of inhibitors in the surface scale and adsorption of inhibitors on it can also lead to drag reducing effects, for example, to a reduction of wall shear stresses and local flow intensities created at flow imperfections (e.g. pits, grooves, weld beads etc.). The Physical inhibitor barrier modifies the surface potential and limits the adsorption-desorption processes and reaction steps that occur in both anodic and cathodic reactions.

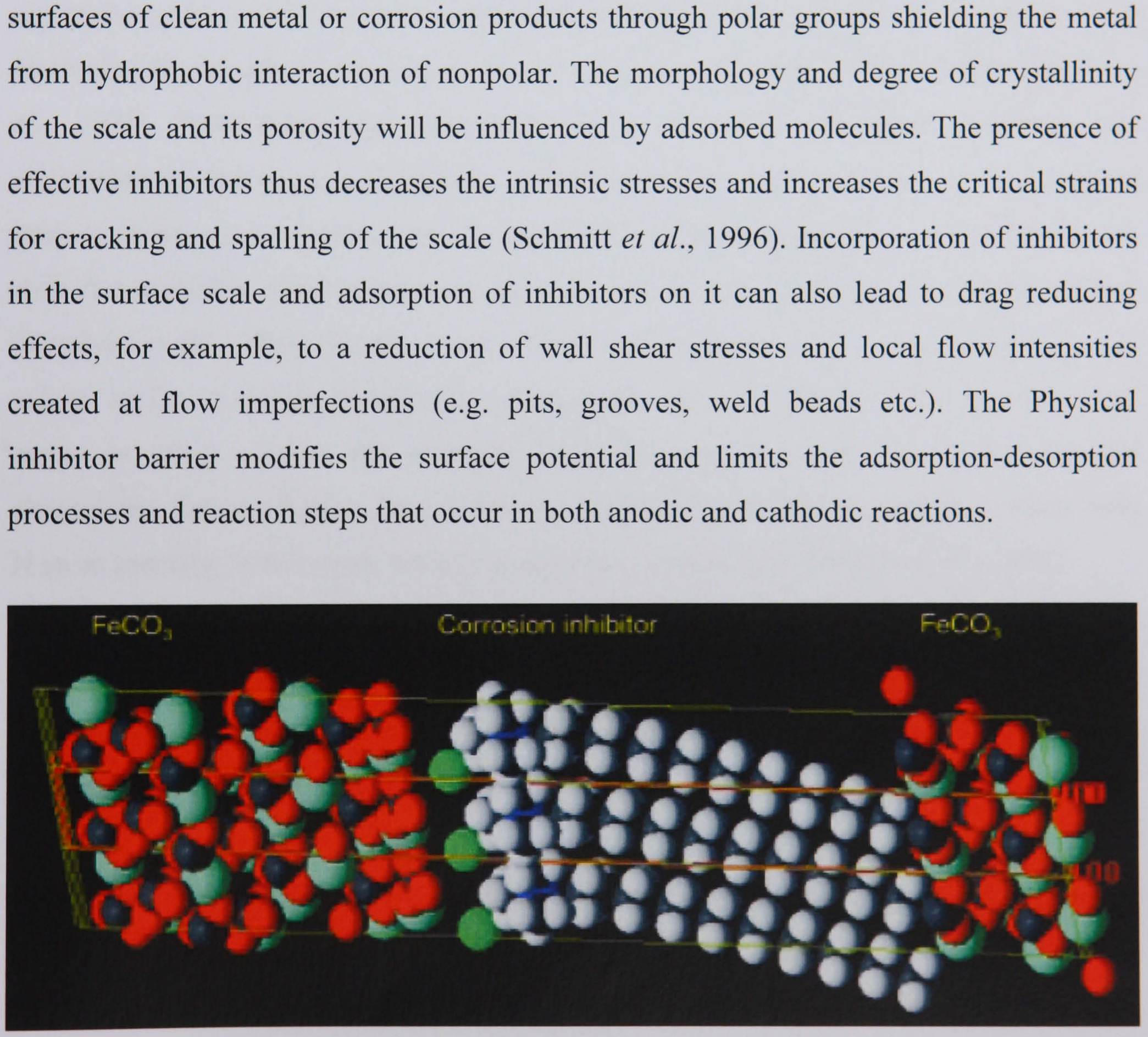

Figure 3.8 Simulation cell that includes trimetrhl n-octadecyl ammonium bromide in a pore of crystalline $FeCO_3$ (Ramachandran *et al*., 2001)

Chokshi *et al*. (2005) observed that the protective effects of the corrosion inhibitor and the scale were complementary and no antagonism was observed. However, some

interference was seen: the presence of inhibitors hampered the growth of iron carbonate scale. This was initially attributed to the scale inhibition properties of corrosion inhibitor.

It is generally believed that hydrocarbons in crude oil interact with inhibitor films by co-adsorbing onto the inhibitor film, enhancing the hydrophobicity of the film and providing a more effective barrier against corrosion. It is also found that the presence of heteroatom with unsaturated bounds in an organic compound causes inhibiting effect and reduces the metal dissolution. Protecting efficiency was found to be improved with increasing the length of alkyl chain and the organic compound concentration (Srhiri *et al.*, 1996). Concerning the adsorption and/or corrosion inhibition processes. the orientation of the adsorbed organic molecules at the metal surfaces is of a special interest. It has been reported that the adsorption of the heterocyclic compounds occurs with the aromatic rings sometimes parallel but mostly normal to the metal surface (Granese *et al.*, 1992; Plieth, 1992). Those orientations could be dependent on pH values and/or electrode potentials. For example, the adsorption of the nicotinic acid anion on silver surface the anion is in a flat orientation on the surface in acid electrolytes, but in alkaline electrolytes the molecule goes into an upright position with N atom pointing to the metal surface in alkaline electrolytes (Granese *et al.*, 1992).

The whole process is critically dependent on the environment--- pH, temperature and liquid shear stresses, the state of the metal surface---roughness, scales, corrosion products, surface damage, and competition from other surface active species.

The most important issue affecting the adsorption and concomitant efficacy of an inhibitor is the mechanism by which it affixes itself to the metal surface. Three type of adsorption could be possible with organic inhibitors: π -bond orbital adsorption, electrostatic adsorption, and chemisorption. If the inhibitor is chemisorbed, the process of chemisorption leads to the formation of a stable inhibitor film on the surface.

Other important factors that affect an inhibitor's performance include the thickness of the inhibitor film and the uniformity of surface coverage, and both factors are controlled primarily by the inhibitor structure.

Commercial corrosion inhibitors contain active ingredients such as fatty acids, amines, fatty amines/diamines, imidazolines, oxyalkylated amines, quaternary amines, and other compounds containing sulphur or oxygen. The application of these compounds is very common in oil and gas production (Pospelov and Fokin, 1993). A large number of such inhibitors are amines with long aliphatic chain in molecules. They are often used under anaerobic conditions in oil and gas wells, primarily recommended for applications in sour wells. In sweet wells, better results are attainable with more complex organic inhibitors containing not only nitrogen but phosphorus or sulphur and phosphorus, too. Effort has been made to synthesize fairly simply containing nitrogen without phosphorus and sulphur effectively in fluids under anaerobic conditions simulating the situation in sweet wells (Esih *et al.*, 1995).

Inorganic inhibitors, such as sodium arsenite (Na_2HAsO_3) and sodium ferrocyanide were used in early days to inhibit carbon dioxide corrosion in oil wells, but the treatment frequency and effectiveness were not satisfactory. This led to the development of many organic chemical formulations that frequently incorporated film forming amines and their salts.

CO_2 corrosion inhibitors also allowed the injection and production of high volumes of corrosive water resulting from the secondary-recovery concept of water flooding. Tertiary-recovery floods, such as CO_2, steam, polymer, and in-situ combustion floods, would usually be uneconomical without the application of corrosion inhibitors (Martin and Braga, 1987).

Over the years, many improvements in inhibitor formulation and application have been made. The methods of evaluating the performance during their use have also advanced considerably. Highly corrosive wells, such as those found at the Talco Field (Texas) required daily batch treatments with those proprietary organic inhibitors.

The inhibitors currently in used are generally more complex mixtures of reaction products and have been formulated to meet the demands of a very competitive industry.

CO_2 corrosion inhibitors used in hydrocarbon transmission lines are long chain compounds. Many available inhibitors are produced from only a few types of starting molecules. Fatty acids and some form of basic nitrogen-containing precursor are the principle active-ingredient sources. Historically, the first proprietary organic inhibitors were fatty imidazolines made from by-product fatty acids and polyethylene amines. The reaction is a condensation reaction that produces the following structure:

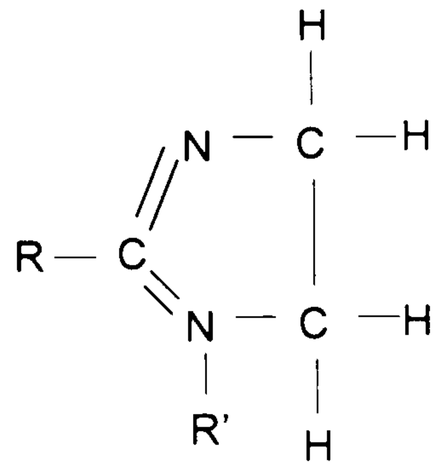

In which R is a chain of carbon molecules (average: C18), and R' is a hydrogen atom or C_2H_4N group.

The molecules produced from these products were dissolved in hydrocarbon solvent or water-alcohol-based solvent, depending on whether they are further reacted. Typical further reactions were salting with acetic acid (CH_3COOH) or quaternizing with a short-chain alkyl chloride.

The cationic molecular structures are found in many commercial inhibitors. These amines or cationic molecules are often neutralized with an organic acid or quaternized to achieve a final basic product. In many inhibitor formulations, the choice of the acid or anionic molecule is critical to the performance of the final product. Also, a mixture of acids is sometimes used to obtain a desired property.

3.4.6 Inhibitor Effects under Flow Conditions

The efficiency of corrosion inhibitors in flowing media depends on local flow intensities, which can be quantified in terms of wall shear stress. Figure 3.9 (a) shows that above critical flow intensities inhibitor loose their efficiency. Under these conditions the materials surface is subject to flow induced localized corrosion. Figure 3.9 (b) shows critical flow intensities initiation can also depend on the inhibitor concentration, which depends on the chemical structure of inhibitor compounds and formulation of inhibitor packages (Schmitt, 2001).

Schmitt (2001) emphasised that inhibitor substance can mitigate the corrosion attack of scale-covered metal surfaces in flow systems by drag reducing phenomenon. It is mainly the reduction of the transmittance of hydrodynamic forces onto the scale by drag reducing effects of the inhibitors. Interaction of inhibitor molecule aggregates with near-wall turbulence elements causing reduction of vortex energy and frequency, increase of the momentum exchange surface area of the votex, and hence, reducing of scale fatiguing intensity of near-wall turbulence elements. Therefore, to be effective in water these inhibitors must be water soluble and exhibit a predominantly linear structure.

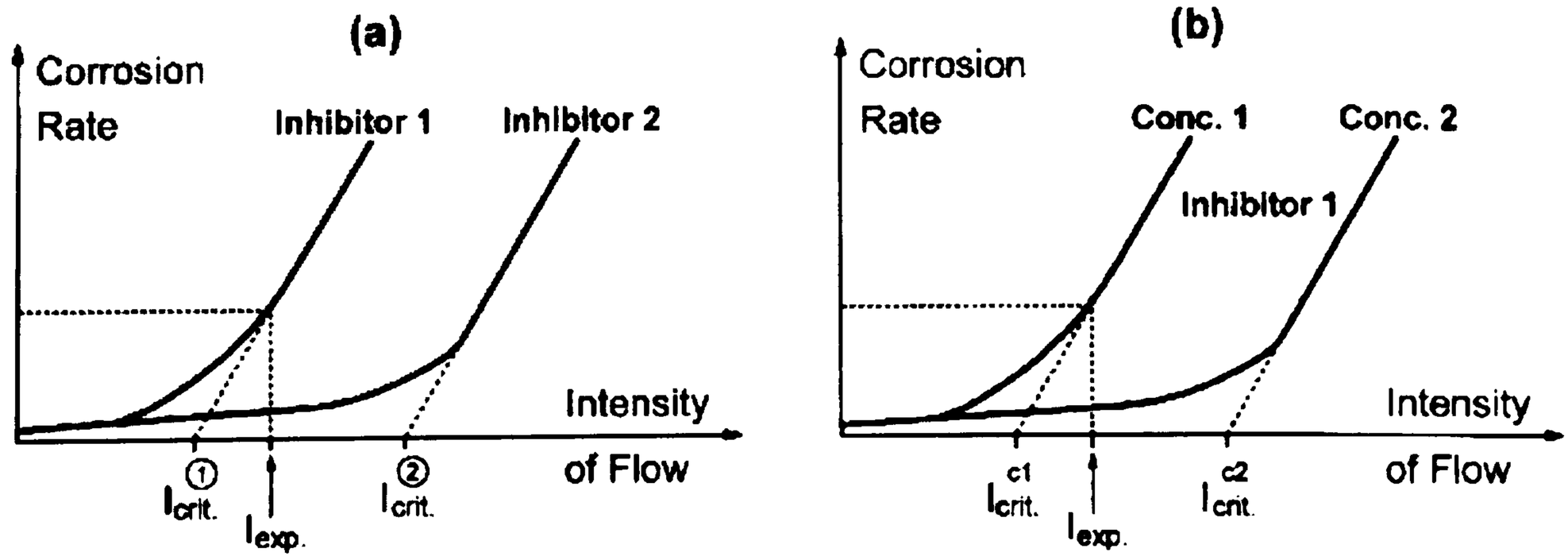

Figure 3.9 Effect of flow intensity on corrosion inhibitor performance (Schmitt, 2001)

It is found that drag reduction can only occur when the solution contains rod-like micelles of surfactants (Hoffmann *et al.*, 1986). These rod-like micelles are formed

above a critical concentration, after surfactance molecules have aggregated to lamellar or spheroidal micelles at a concentration lower than critical micelle concentration as shown in Figure 3.10. In turbulent pipeflow the rod-like micelles are initially oriented in the bulk flow direction with more pronounced orientation in the near-wall region compared to the core regions of the pipe as shown in Figure 3.11 (Schmitt, 2001). Eventually a destruction of the initially rod-like micelles takes place leading to a rearrangement of the surfactant molecules into smaller aggregates part of which, in turn, build up lose but lasting superstructures (Lindner *et al.*, 1990). This effect is a reduction of the friction factor, i.e. a drag reduction (Schmitt, 2001).

This has been clearly shown by Schmitt (2001) that the third generation CO_2 corrosion inhibitors reduce the corrosion rate to 0.1 mm/y and prevent flow induced localized corrosion (FILC) at wall shear stresses in the order of 550 Pa with increasing the inhibitor concentration. This concentration effect can not be explained simply by considering adsorption and surface filming phenomena, because the inhibitor concentration needed for complete surface coverage lies for below 500ppm of the active inhibitor compounds. In sweet corrosion system fracture stresses of iron carbonate scales were measured to range between 49 and 100 MPa in the absence of inhibitor and between 375 and 1080 MPa in the presence of the inhibitor (Schmitt, 2001).

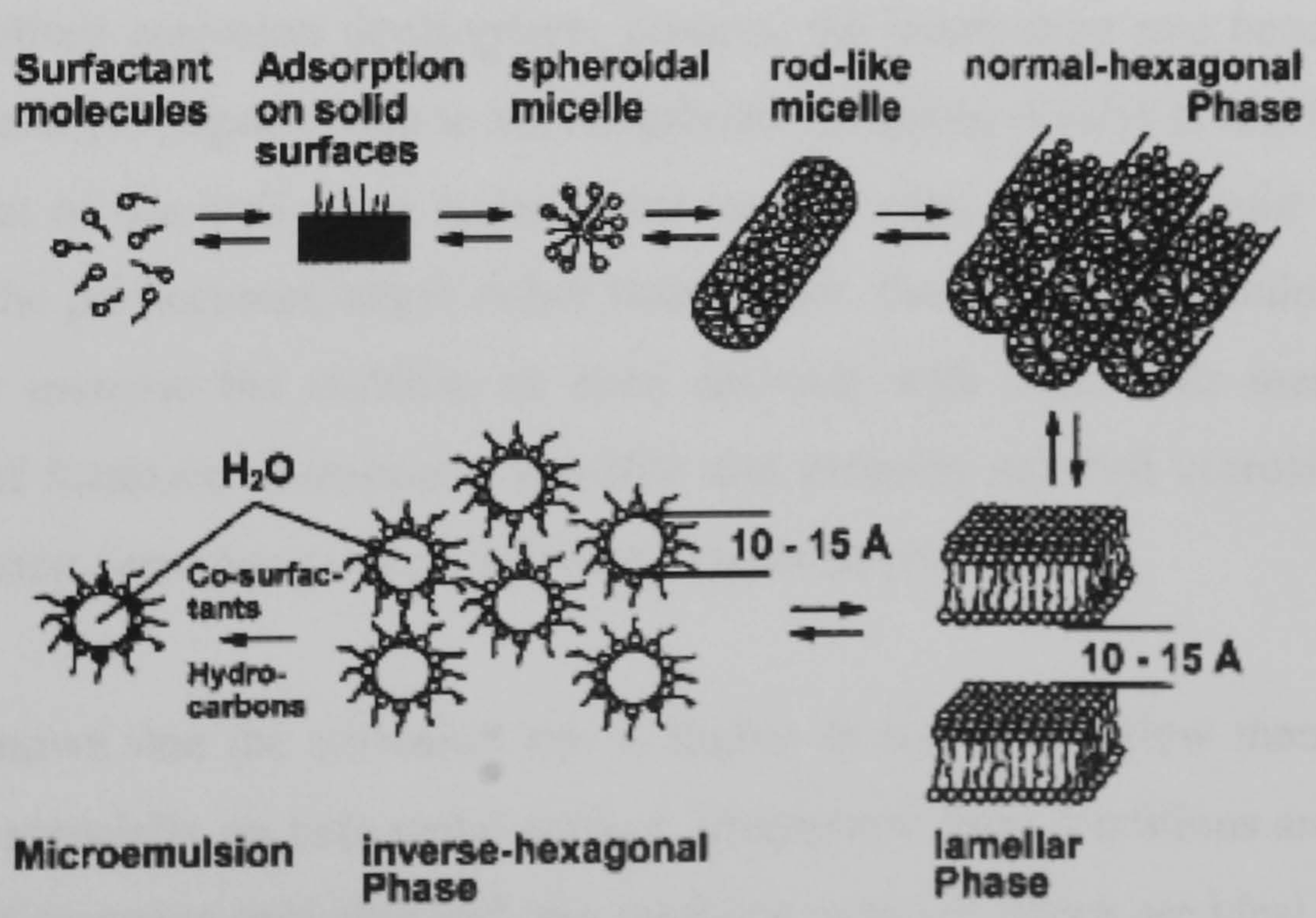

Figure 3.10 Aggregation of amphipathic substances in aqueous solution (Schmitt, 2001)

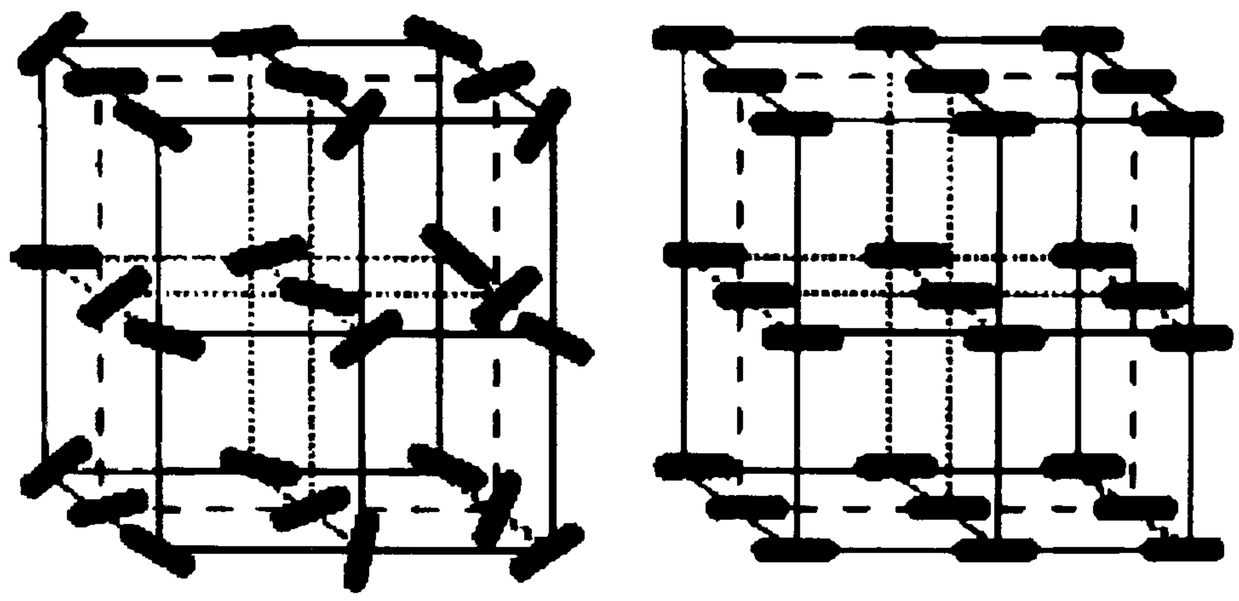

Figure 3.11 Effect of flow on SAC: Orientation of rod-like micelles under the influence of shear (Schmitt, 2001)

Organic corrosion inhibitors exhibit an amphipathic structure like surfactants, therefore can also interfere with near-wall turbulence elements and exhibit drag reducing effects.

Schmitt (2001) also verified that the roughness pattern of a metal surface under FILC should correspond to the sizes of the turbulence elements (eddies, vortices) in the near-wall flow region. From a roughness measurement with and without corrosion inhibitors under jet impingement, the inhibitor reduces the amplitudes of the roughness indicating the effect of the corrosion inhibitor on transfer of hydrodynamic forces.

During localised corrosion development process, the penetration rate becomes slower than the lateral propagation due to lateral galvanic coupling (Crolet *et al.*, 1998) and/or enhancement of the wall shear stress at the leading edge of pit (Schmitt and Gudde, 1995). As the pit becomes larger rather than deeper, the degree of turbulence will not continue to increase but stabilise or even decrease with time. This means that the inhibition of localised corrosion is possible and properly selected corrosion inhibitor can almost stop corrosion even on a severely corroded pipe surface.

It is well known that the corrosion rate is higher in multiphase flow than in stagnant conditions, especially on bare metal surface. Multiphase flow conditions are favourable for localised corrosion initiation and also inhibitor removal, which are ideal for inhibitor selection. However there is very limited information about the mechanism of CO_2

corrosion inhibitors under multiphase flow conditions. Little is known about the inhibitor film formation and the porosity and thickness of the inhibitor film. Tan *et al.* (1996) adopted the methods for evaluating coating film system (Walter, 1991) to study the inhibitor film.

In general the efficiency and persistency of inhibitor films under multiphase flow conditions probably depend on 4 major factors, e.g. the type of adsorption of the inhibitor film (physisorption, chemisorption, packing order, composition and the roughness of the substrate), the chemical composition of the multiphase flow, the wall shear stress/mass transport coefficient and the erosive nature of the flow.

3.5 Analyzing and Interpreting AC Impedance Spectra

Since Epelboin and co-workers first introduced AC impedance techniques in 1960s (Epelboin and Keddam, 1972), It has been developed and applied in many areas of electrochemical corrosion research. Mansfeld *et al.* used the AC impedance technique to evaluate the corrosion mechanisms of organic and inorganic compounds, corrosion inhibitor (Mansfeld, 1977 and 1981). Tan *et al.* (1996) explored the possibility of using AC impedance as a method for evaluating inhibitor film persistency and for studying inhibitor mechanisms (Tan *et al.*, 1996). AC impedance has been also extensively used to study carbon dioxide corrosion products scales (Kinsella *et al.*, 1998).

In this work, AC impedance technique has been used to investigate the corrosion behaviour of inhibitor film formed on the carbon steel substrate so as to study the relationship between the corrosion behaviour and film properties under turbulent conditions. A review of the application and interpretation for inhibitor film presented.

Complexity of the AC impedance data analysis results in developing user friendly software to analysis the data. Most of software can be used bases on equivalent electrical circuit models to obtain parameters from AC impedance spectra to obtain useful information about corrosion process and mechanisms by performing curve fit.

Two of several statistical tests are used to assess goodness of model fit to experimental data, Chi square statistic, and sum of residuals. Actual Chi square statistic less than 1 and sum of residuals nearly zero are considered sufficient to indicate a good fit of a model to experimental data. No matter how good the fit, it must be based on the physical and chemical properties of the system under study.

3.5.1 Application of AC Impedance to Study Corrosion Inhibitor Films

The use of AC impedance analysis to examine inhibitors is well-documented, especially in acidic solutions (Gabrielli, 1980).

To study the inhibitor film formation and destruction mechanisms of CO_2 corrosion, Tan *et al.* (1996) proposed an equivalent circuit for an electrode filmed with a non-conducting imidazoline inhibitor film as shown in Figure 3.12 (a). This model was derived from the one proposed by Mansfeld *et al.* (1985) for degradation of organic coating system as shown in Figure 3.12 (b) which has been applied in a large number of publications to simulate the impedance characteristics of an electrode filmed with a nonconducting inhibitor film (Mansfeld, 1991). The EC in Figure 3.12 (a) was also reduced to three layer film for a system with inhibitor under CO_2 saturated condition by De Marco *et al*. (Marco *et al*., 2002). The electrochemical reaction at the film/substrate interface is controlled by the activation process. The EC consists of the solution resistance (R_{ohm}), the inhibitor film resistance (R_{pore}), the film capacitance (C_{film}), the charge transfer resistance (R_{ct}) and the double layer capacitance (C_{dl}). The parameter R_t (=R_{ct}), and C_{dl} provides an insight into the properties of inhibitor film and the electrochemical double layer. The semicircle at higher frequency range would be due to the inhibitor film because a surface dielectric film normally has a small time constant (Tan *et al.*, 1996). The resistance values (R_1-R_4) of inhibitor layers are reflection of the penetration of the inhibitor layer by electrolyte so is related to the inhibitor molecular density in the layer. The physical model can be suggested as shown in Figure 3.12 (c).

De Marco *et al.* (2002) used the equivalent circuit with the addition of an inductance term (Mansfeld. 1981) for simulating corroding steel electrode for blank test as shown

in Figure 3.13. The charge-transfer reaction rate is inversely proportional to R_{ct} for a transient period until the adsorbed intermediate coverage was formed. Once the coverage is formed creating an interphase that slows the reaction, the overall reaction rate is given by $R_p = R_{ct} + R_{film}$ at the DC limit.

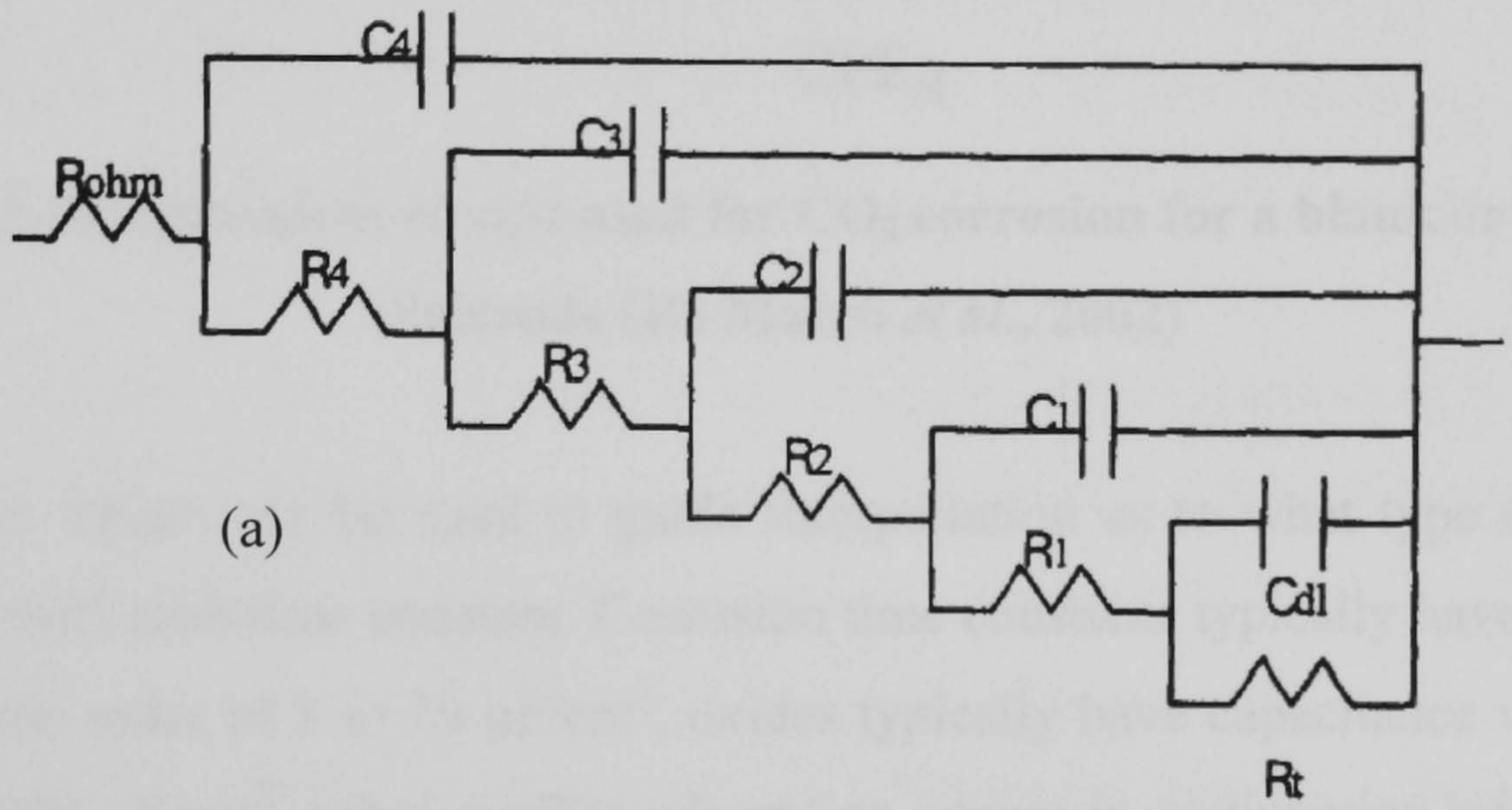

Figure 3.12 (a) Equivalent circuit used for fitting the impedance spectra for an electrode filmed with a non-conducting inhibitor film (Tan *et al.* (1996); (b) Equivalent circuit proposed by Mansfeld for two time constants defect coating system; (c) A physical layer for an electrode filmed with a four-layer, non conducting inhibitor film

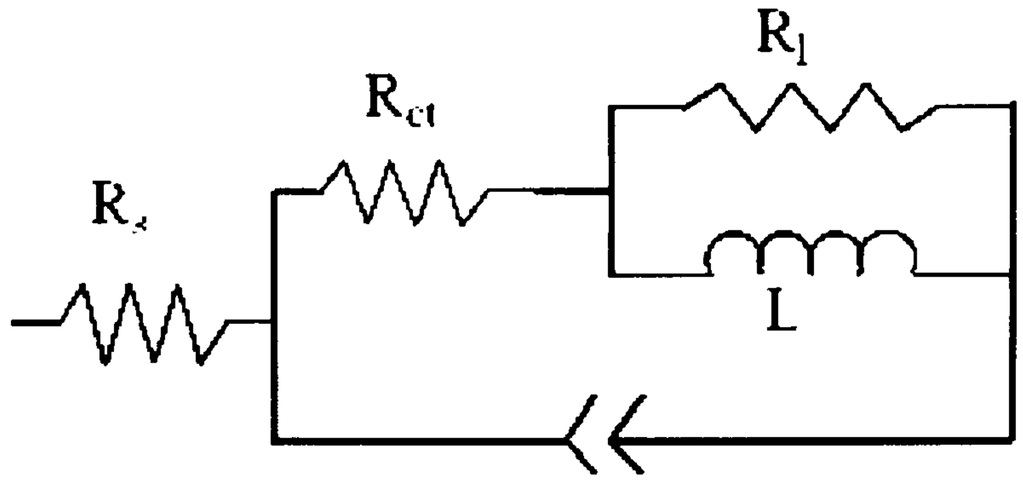

Figure 3.13 Equivalent circuit used for CO_2 corrosion for a blank or unfilmed electrode (De Marco *et al.*, 2002)

Capacitance values can be used to guide interpretation as to what type of process is associated with each time constant. Corrosion time constants typically have capacitance values on the order of 1 to 20 $\mu F/cm^2$, oxides typically have capacitance values on the order of 1000 $\mu F/cm^2$, when surface adsorption occurs in conjunction with corrosion, capacitance values on the order of $\geq$ 100 $\mu F/cm^2$ (Murray *et al.*, 1988). The low frequency time constants can be used to illustrate how capacitance magnitudes are used to determine what type of process is associated wit a given time constant. For example, capacitance for low frequency time constant is on the order of $\mu F/cm^2$ may due to corrosion, while $0.01 F/cm^2$ may due to corrosion, but is probably due to another process like diffusion (Stephen, 1994).

For a depressed semicircle, if the high-frequency part which contains the influence of the transport phenomena is different from the low-frequency part. It should be pointed out that for these complicated spectra, determination of the capacitance C from the frequency f_{max} of the maximum of the imaginary part of the impedance and the diameter R_p of the semicircle as $C = 1/2_{\pi}f_{max}$. R_p is impossible. The model parameters such as Juettner model can only be obtained by a fit of the experimental data to the model. Because of the large number of fit parameters, Juettner, *et al.* (1988) found it necessary to make certain assumptions concerning the values of some parameters and fit the others.

3.6 Summary of Literature Review

In the oil and gas industry, erosion-corrosion was rated in the top five most prevalent forms of damage. Cost reduction considerations favour replacing expensive solid alloy components with a solution where carbon steel can be used in the presence of inhibitor. Corrosion inhibitors allow producers to produce at higher velocities in situations containing sand. This implies that the inhibitor may not only provide inhibition to corrosion but also has effect on erosion-corrosion or erosion only. The erosion-corrosion data and models published in the literature provide information on material selection in many conditions. However, little is known about the inhibitor performance on erosion-corrosion as has been demonstrated in the literature review.

To understand the inhibition mechanisms of inhibitor in erosion-corrosion conditions containing CO_2, this chapter has developed a review of several studies concerning the use of inhibitor to inhibit CO_2 corrosion, erosion-corrosion mechanisms of carbon steel, the use of AC impedance techniques for inhibitor film integrity assessment and the few pieces of earlier work on oil field chemicals to retard erosion-corrosion. Although those studies are different from the conditions with multiphase flow and high velocity containing CO_2, their discussion is very helpful for analysing the current results.

CHAPTER 4 EXPERIMENTAL PROCEDURES

The experimental procedures carried out in this work fall into three main sections:

1. Erosion-corrosion tests carried out in a rotating cylinder electrode (RCE)
2. Erosion-corrosion tests carried out in a submerged impinging jet (SIJ) rig
3. Post and pre-test examination carried out using surface analysis

The electrochemical techniques used in this work to assess the corrosion characteristics are listed as follows:

1. DC potentiodynamic and potentiostatic measurements
2. AC impedance measurements

In addition the following techniques were used for surface analysis:

1. Optical Microscopy
2. Scanning Electron Microscopy (SEM)
3. X-ray photoelectron spectroscopy (XPS)
4. X-ray Diffraction (XRD)

4.1 Composition of the Test Solution

4.1.1 Blank Solution

All the experiments were carried out in the aqueous solutions saturated with CO_2, whose composition is shown in Table 4.1. The tests were carried out using simulated produced water corresponding to the gas condensate system. The gas condensate system is part of the distillation process and the fluid comprises the same composition as shown in Figure 4.1. The most commonly used types of condenser are horizontal shell-side and vertical tube-side (Coulson and Richardson, 1999). The solutions were prepared with

AR grade chemicals and distilled water. All tests were carried out using freshly prepared test solutions.

Table 4.1 Blank solution composition used in experiments described in this work

Salt	mg/l
$CaCl_2 \bullet 2H_2O$	50
Na HCO_3	170
NaCl	1800

In this study, all experiments were carried out at 1 atm CO_2 pressure and it was saturated by bubbling with 99.998%-pure CO_2 gas from a gas cylinder into the test solution. Impurities in the gas were $O_2 < 2 \times 10^{-4}$ %, $N_2 < 8 \times 10^{-4}$ %, $H_2O < 3 \times 10^{-4}$ %, CO $<1 \times 10^{-4}$ %, and hydrocarbon gases $<1 \times 10^{-4}$ %. Before each experiment, the CO_2 gas was bubbled through the solution for at least 8 hours. This was done in order to ensure that all the dissolved oxygen was removed and to reach CO_2 saturated condition for the test solution. However, during the experiment, this was performed at a very slow rate to prevent solution flow effects. Saturation was found to reduce the bulk pH of the solution to a constant value of 4.9-5.0 for solution made up with distilled water and 5.5 for solution made up with tap water. Only a small change of about + 0.2 in the pH was observed at the end of the tests. A maximum oxygen concentration of 40ppb-50ppb was left in solution when measurements started and this oxygen concentration was almost constant until the end of the experiments.

4.1.2 Inhibitors

Four different CO_2 corrosion inhibitors were studied in the experiments. Their formulation names are CGO, CRO, CRW8 and CRW9. The chemical packages are based on the combinations of proprietary complex blends of phosphorus, nitrogen and carboxylic acid containing corrosion inhibitors, film forming inhibitors and other organic constituents. The example of the generic forms of these is listed in Figure 4.1. CGO and CRO are oil soluble inhibitors and CRW8 and CRW9 are water soluble inhibitors. Eleven single and various combinations of single components were also

studied. Their formulation names are SA, SB… SK. The test matrix for single components or various combinations of single components is shown in Figure 4.2.

Light aromatic naphtha	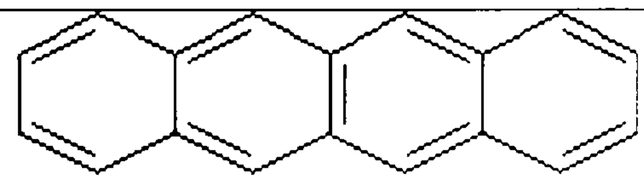
Diethylbenzene	**$C_{10}H_{14}$**
1,2,4,-Trimethylbenzene	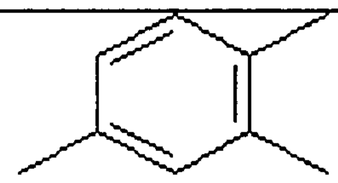
Dimethayl benzene	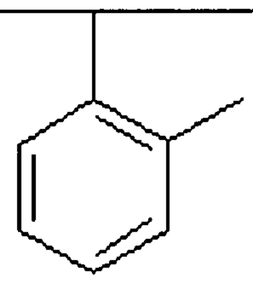
Isopropanol benzene	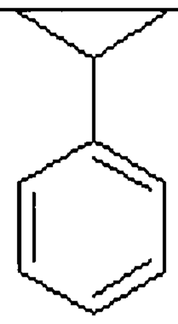
Isopropanol	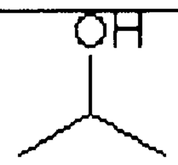
Carboxylate acides	$C_nH_{2n+1}COOH$
Amine derivative	
Phosphates	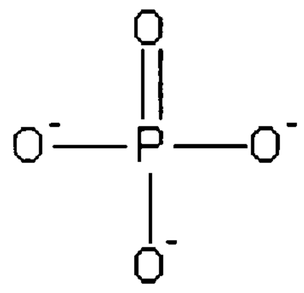
Quaternary ammonium chloride	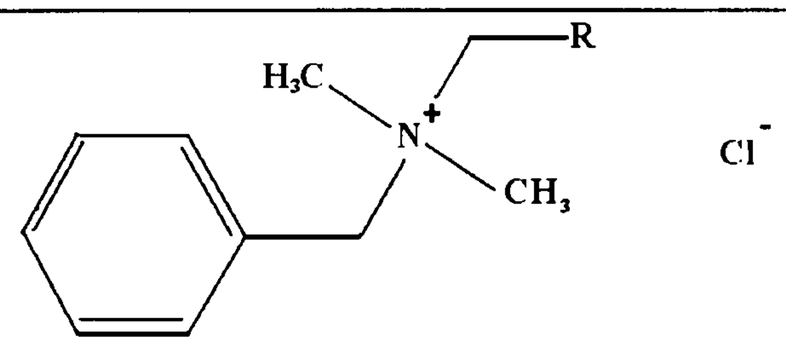
Methanol	**CH_3OH**
Ethoxylated imidazoline	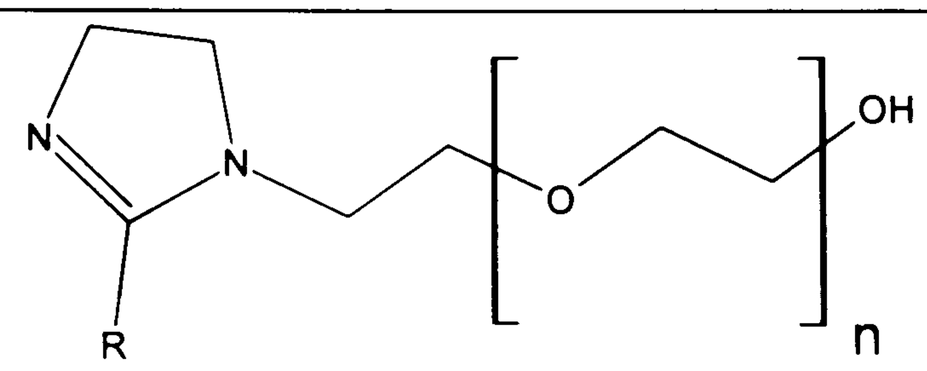

Sulphur compound	**R-S**
Polycarboxylic acid	**R-COOH**
Heavy aromatic naphtha	

Figure 4.1 Organic structure of the inhibitor constituents of CGO, CRO, CRW8 and CRW9

	Ethoxylated Imidazoline	Anhydride/ polyamine reaction product	Quaternary Ammonium	Compound Thioalcohol
SA				√
SB	√			
SC		√		
SD			√	
SE	√	√		
SF	√		√	
SG		√	√	
SH	√			√
SI		√		√
SJ			√	√
SK	√	√	√	

Figure 4.2 Organic structure of the constituents from the single components test matrix

Unless otherwise stated the dose of inhibitors and single components is 100ppm. Inhibitor in required volumes was taken by means of a micropipette. The injection of the inhibitor into the electrochemical cell or erosion-corrosion apparatus was usually less than 30 minutes before the specimen immersion to help the distribution of the inhibitor on the test environment.

4.1.3 Sand

The sand shape and size distribution is given in Figure 4.3 (a) and (b) respectively. In most tests 1% sand and 0.1% silica sand was added to the system of RCE and impinging jet respectively to simulate high speed solid loading.

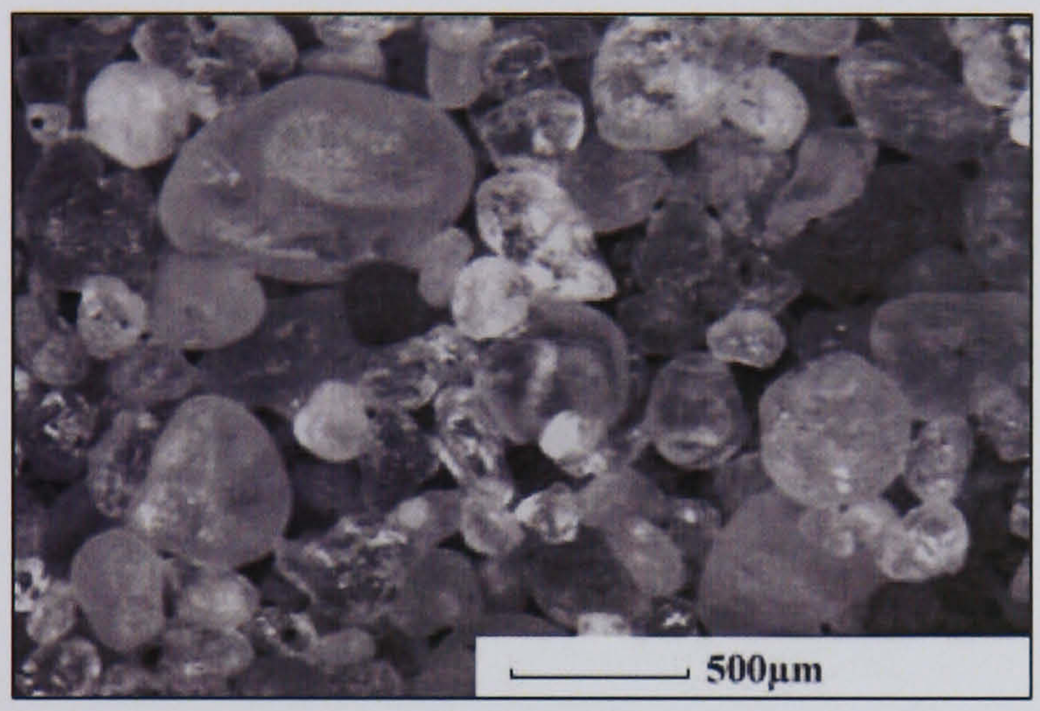

(a) **(b)**

Figure 4.3 Sand (a) shape and (b) size distribution (De Souza and Neville, 2003)

4.2 Erosion-corrosion Tests – RCE Versus SIJ

Both RCE and SIJ methodologies have well-established flow patterns that are well-characterized hydrodynamically. RCE produces a flow with sand particles ploughing the metal surface with low angle, or random impingements due to the fluctuating velocity component. The submerged impingement jet can produce much higher turbulent intensity as well as sand particle impacts the material at a maximum 90 degree. The sample experiences a significant amount of erosion due to direct impingement. Although the linear rotation speed is limited in RCE, it is necessary to assess inhibitor with different flow patterns.

4.2.1 Erosion-Corrosion Tests RCE Apparatus

These experiments were carried out in a small glass cell of 1 litre capacity at atmospheric pressure. In all experiments the CO_2 gas mixture was continuously bubbled through the test solution for at least 8 hours before the experiment, and for the duration

of the experiment. This ensured complete deareation of the solution; saturation with CO_2. The experiments were conducted in a brine representative of a typical gas condensate system as described in Table 4.1.

The aim of the experiments was to consider the performance of chemical corrosion inhibitors in retarding degradation by erosion-corrosion and to relate the rotating speed (flow velocity) and temperature. At the same condition, also study the performance of the chemicals in retarding erosion using cathodic protection methods or corrosion using linear polarisation resistance measurements (LPR) and EIS and compare these results with data from the blank solution.

The RCE used for the tests was a Princeton Applied Research (formerly EG&G) instrument, Model 636 Ring-Disk-Electrode system. Figure 4.4 is a top view diagram of the standard glass cell (1 litre volume). It comprised a polypropylene lid containing one inlets used for CO_2 gas entry, working electrode immersion, salt bridge or reference electrode, counter electrode, pH probe and thermometer. All entries were sealed with glass stoppers, except for the working electrode, which was used as gas outlet. A metallic cylindrical sample was used as working electrode (WE), which was rotated at a controlled rate. A platinum-rod Redox electrode was used as the auxiliary electrode (AE) and a KCl saturated Silver chloride electrode (Ag/AgCl) acted as reference electrode (RE). The rotation rate of the Model 636 rotator of the Ring-Disk-Electrode system and the potential of the reference Ag/AgCl electrode were checked regularly to make sure a correct control of the specimen rotation rate and the correct recording of potentials. A magnetic thermostat stirrer hot plate was used in the experiments to control the temperature at 20°C ± 2°C or 50°C± 2°C.

Figure 4.5 shows the experimental set-up used in the electrochemical experiments. The current passing between the working electrode and the auxiliary electrode was recorded. while the potential of the sample was polarized.

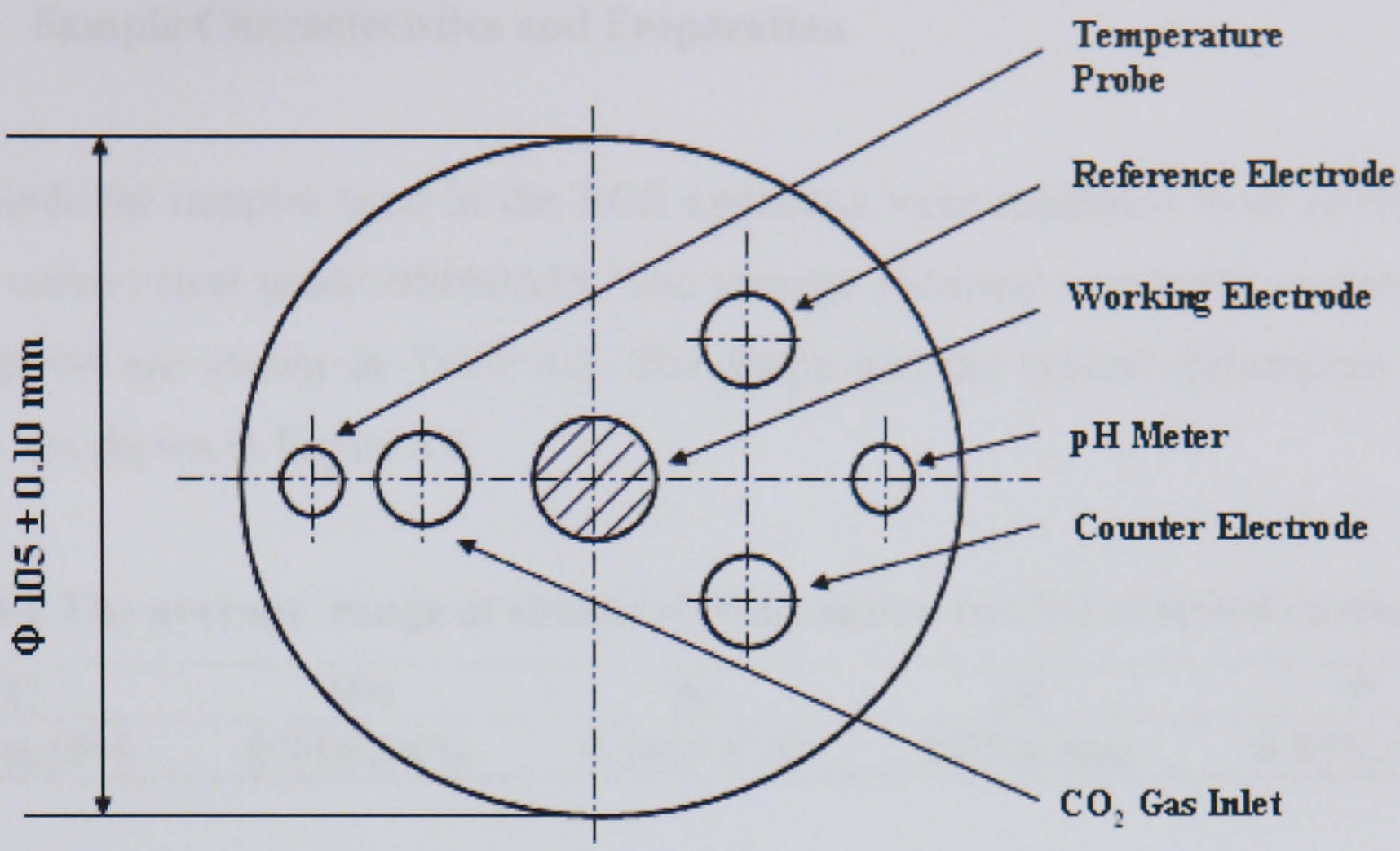

Figure 4.4 Top view of the glass cell set up in RCE experiments

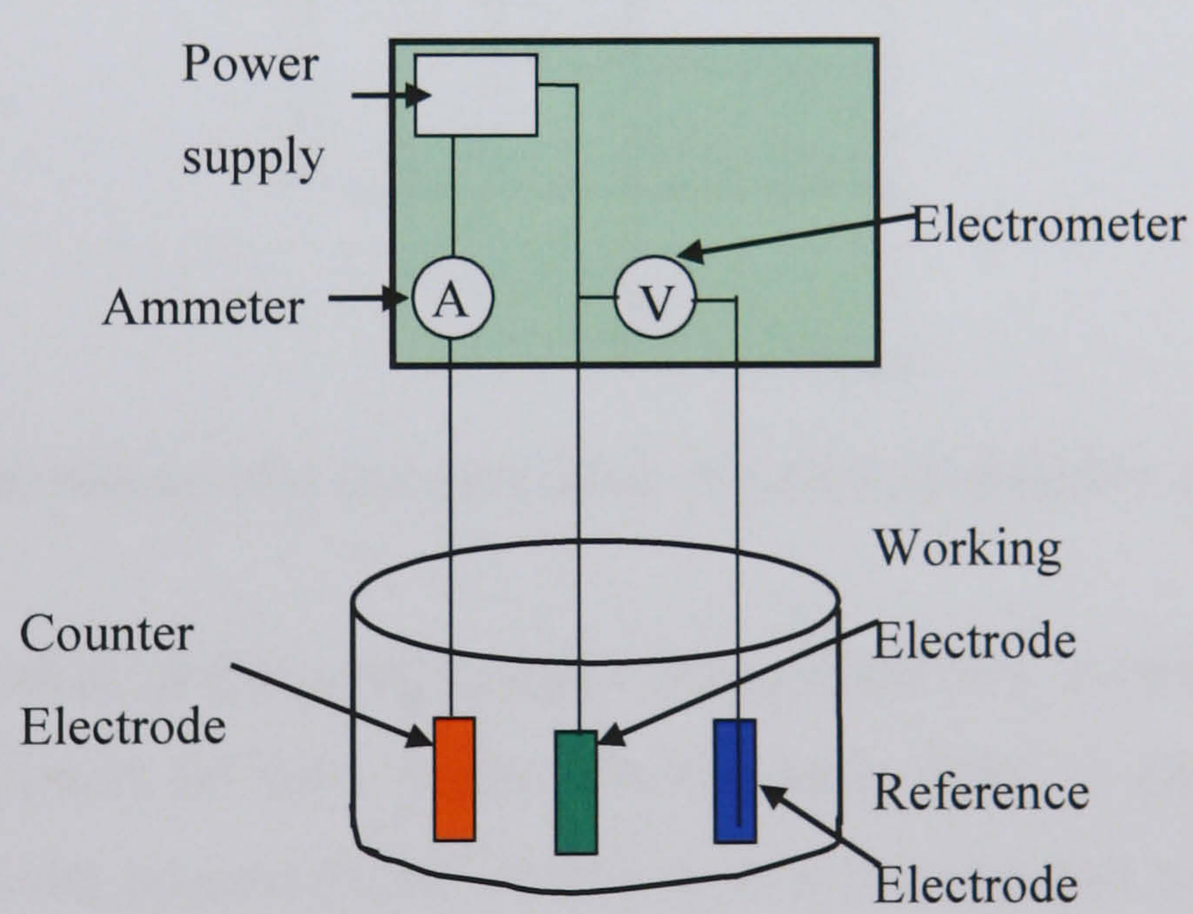

Figure 4.5 Electrochemical experimental set-up

The electrochemical measuring units employed were:

1. One Solartron Model 1280 impedance gain-phase analyzer, controlled by personal computer. In this system the Corrware electrochemical software was employed.
2. One EG&G potentiostat, which was computer-controlled and was supported by the 352 SOFT-CORR III software

4.2.1.1 Sample Characteristics and Preparation

The cylindrical samples used in the RCE apparatus were machined from commercial rods of carbon steel grade BS080A15. The average chemical compositions quoted for this material are shown in Table 4.2. The shape and the typical dimensions of the samples are shown in Figure 4.6.

Table 4.2 The average range of chemical composition (wt.%) of tested carbon steel

C	Mn	Si	S	P
0.13-0.18%	0.70-0.90%	0.10%-0.40	0.05%max	0.05%max

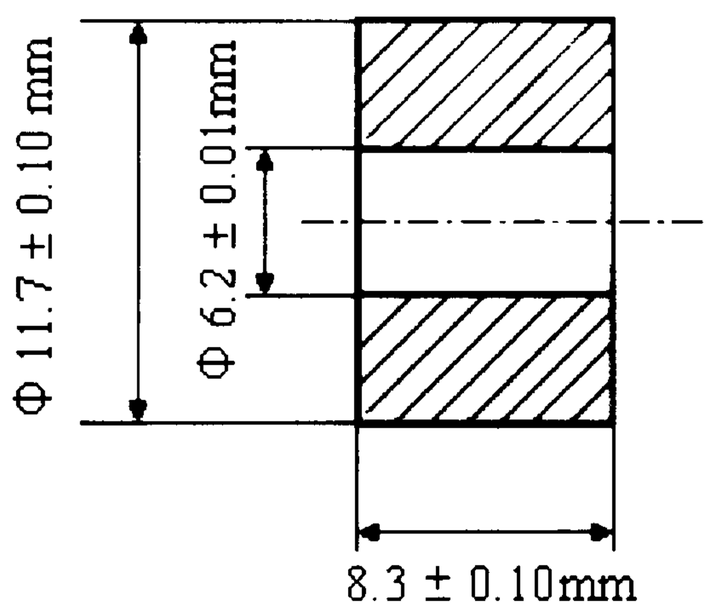

Figure 4.6 Dimensions of a test specimen of rotating cylinder electrode (RCE)

The cylindrical surface of the tested samples were ground to a roughness of R_a = 0.2 μm and they were stored in oil prior to use. Before being fitted on the rotator apparatus, they were rinsed with acetone (CH_3COCH_3) in an ultrasonic bath then deionised water three times and finally dried with compressed air. Samples were then mounted onto the rotating cylinder by sandwiching the steel cylinder between polytetrafluoroethylene washers. Each experiment was carried out on a freshly prepared new sample.

After the experiments, the specimen was rinsed with water to get rid of sand and then washed with Clarke's solution and rinsed with deionised water again and kept into desiccators over silica gel, for later surface examination.

4.2.1.2 Experimental Procedure

Both potentiodynamic and potentiostatic methods were used for the electrochemical experiments. DC linear polarisation and AC impedance are measured for most tests. Four types of tests were carried out as described in the following paragraphs.

Test 1 The RCE was rotated at a constant speed of (either 1000rpm or 6000rpm for 1 hour); AC impedance tests (EIS) and DC linear polarisation (LP) tests were carried out at 0, 0.5 and 1 h exposure time. The free corrosion potential (E_{corr}) was also monitored at the start of each LP test.

Test 2 The RCE was rotated at a fixed speed for 8 hours. At the end of the test the sample was cleaned with Clarke's solution and the mass loss was determined.

Test 3 Tests were conducted with applied cathodic protection (CP) by the impressed current method at a potential of –0.8V (Ag/AgCl), in order to avoid corrosion of the working electrodes while they were immersed in the test solution. These tests were performed to assess the effect of reducing corrosion by electrochemical means and also to assess whether CP and inhibitor would complement each other in reducing material loss. The current as a function of time was monitored. The sample was weighed at the end of the test. The tests were conducted at 50°C and 6000rpm with 1% sand for 8 hours.

Test 4 Tests were conducted in which the sand was pre-soaked in a 100ppm inhibitor solution stirred at 1250rpm using a 2.5cm magnetic stirrer for 2 hours. The test was then conducted in the same solution for 8 hours. The mass loss from the metal was compared with the mass loss in the test where no sand pre-soaking was performed.

After 8 hours CO_2 gas bubbling, the gas flow was decreased and kept constant for the rest of the experiments. Once the desired temperature was reached, the following experimental procedure was followed:

1. Inhibitor was put into the solution (only for inhibitor tests)
2. Sand was added into the solution.
3. The pH was measured.
4. A freshly prepared cylindrical sample was weighted and fitted on the RCE apparatus and all the electrical connections were made.
5. The sample was introduced into the glass cell and a fixed rotation rate set.
6. After allowing the corrosion potential of the sample to stabilise for a period of 5 minutes, electrochemical measurement was carried out.
7. After 8 hours, the samples were taken out of the solution.
8. The sample was washed with Clark's solution (Neville, 1995) and rinsed with distilled water then dried and weighed.
9. The pH was measured again.
10. The test solution was discarded.

For linear polarisation tests, the sample potential was scanned from 20mV more negative than the free corrosion potential (E_{corr}) to 20mV more positive than the free corrosion potential at a rate of 0.25mV/s; For AC measurements, tests were performed with a sinusoidal signal of +10 mV (r.m.s.) amplitude over a frequency range from 0.1 Hertz to 20 kilohertz. AC measurements were done at the free corrosion potential; For cathodic protection test, the potential was set at 0.8V versus reference.

4.2.1.3 Hydrodynamic Analysis of RCE

The follows are several hydrodynamic parameters calculated and used to describe the intensity of the flow under liquid erosion-corrosion flow conditions. It is a guide only for erosion-corrosion condition with sand. These parameters include the Reynolds number (Re) and wall shear stress (τ_w).

Reynolds number:

$$\mathrm{Re} = \frac{Vd}{\gamma} \tag{76}$$

According to equation (71), the Reynold number values under experimental conditions used in RCE are shown in Figure 4.7, where, $u\ (m/s)$ = ω r, ω = $\frac{rot.speed(rpm)\times 2\times\pi}{60}$, r is the samples outer radius for RCE = 0.00585m, l (the characteristic dimension), for RCE, is the samples outer diameter = 0.0117m, v (the kinematic viscosity of water) at $20\,^{o}C = 1.004\times10^{-6}\ m^2/s$; at $50\,^{o}C = 5.53\times10^{-5}\ m^2/s$. They all lie in the range of turbulent flow.

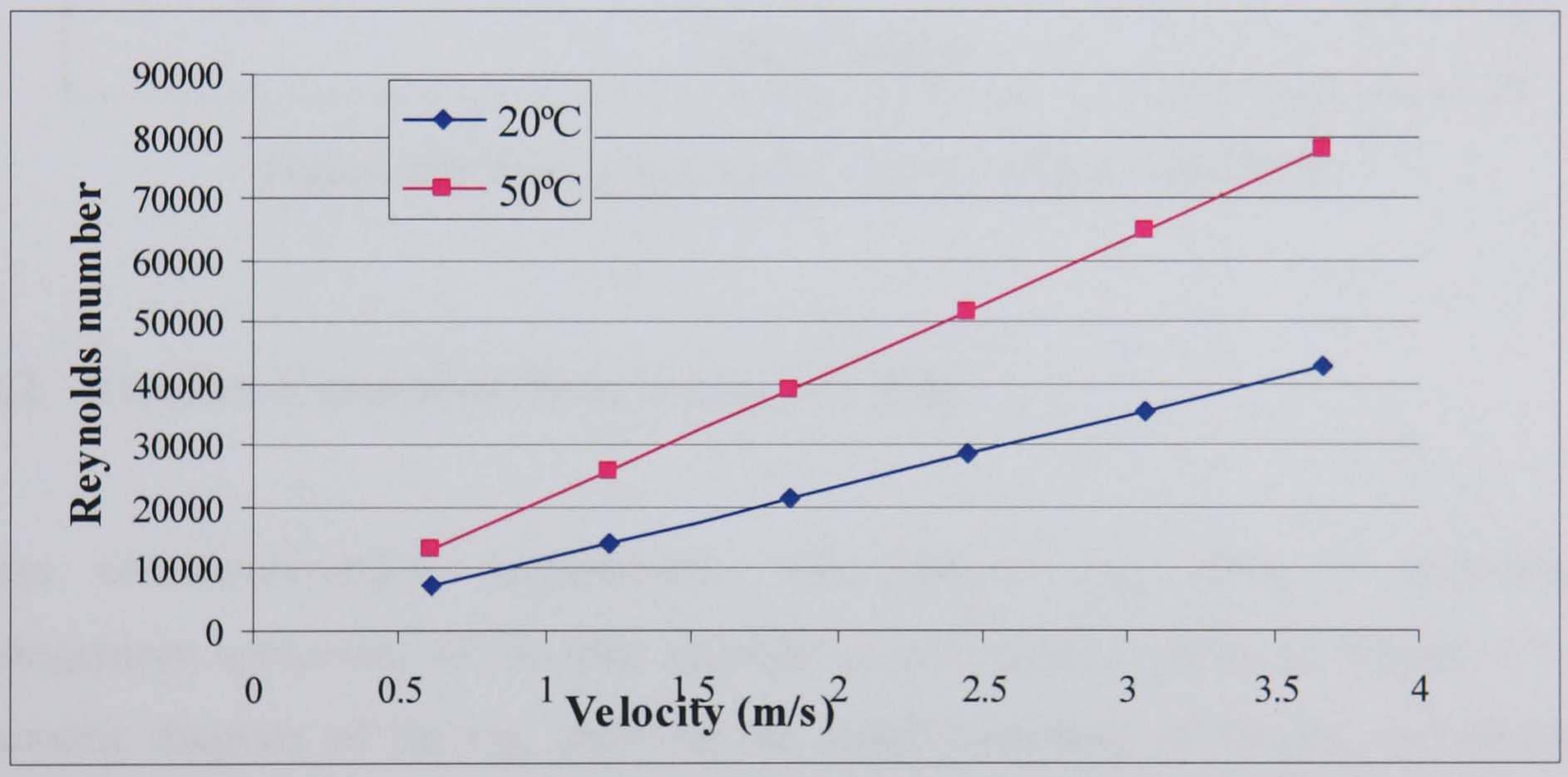

Figure 4.7 Reynolds number versus velocity at 20°C and 50°C for RCE tests

Wall shear stress:

The equation for calculating wall shear stress (τ_w) for rotating cylinder in turbulent flow was shown in equation (**73)** as (for $r_{outer} - r_{inner} > 0.5\ (r_{inner}+r_{outer})$), where ρ is the density of water at $50\,^{o}C = 988.063\ kg/m^3$, at $20\,^{o}C = 998.203\ \ kg/m^3$

This empirical equation was based on liquid and gas flow. Therefore it is only a guide to describe the wall shear stress under the multiphase flow condition with sand. Figure 4.8 shows the shear stress values versus flow rate under experimental conditions.

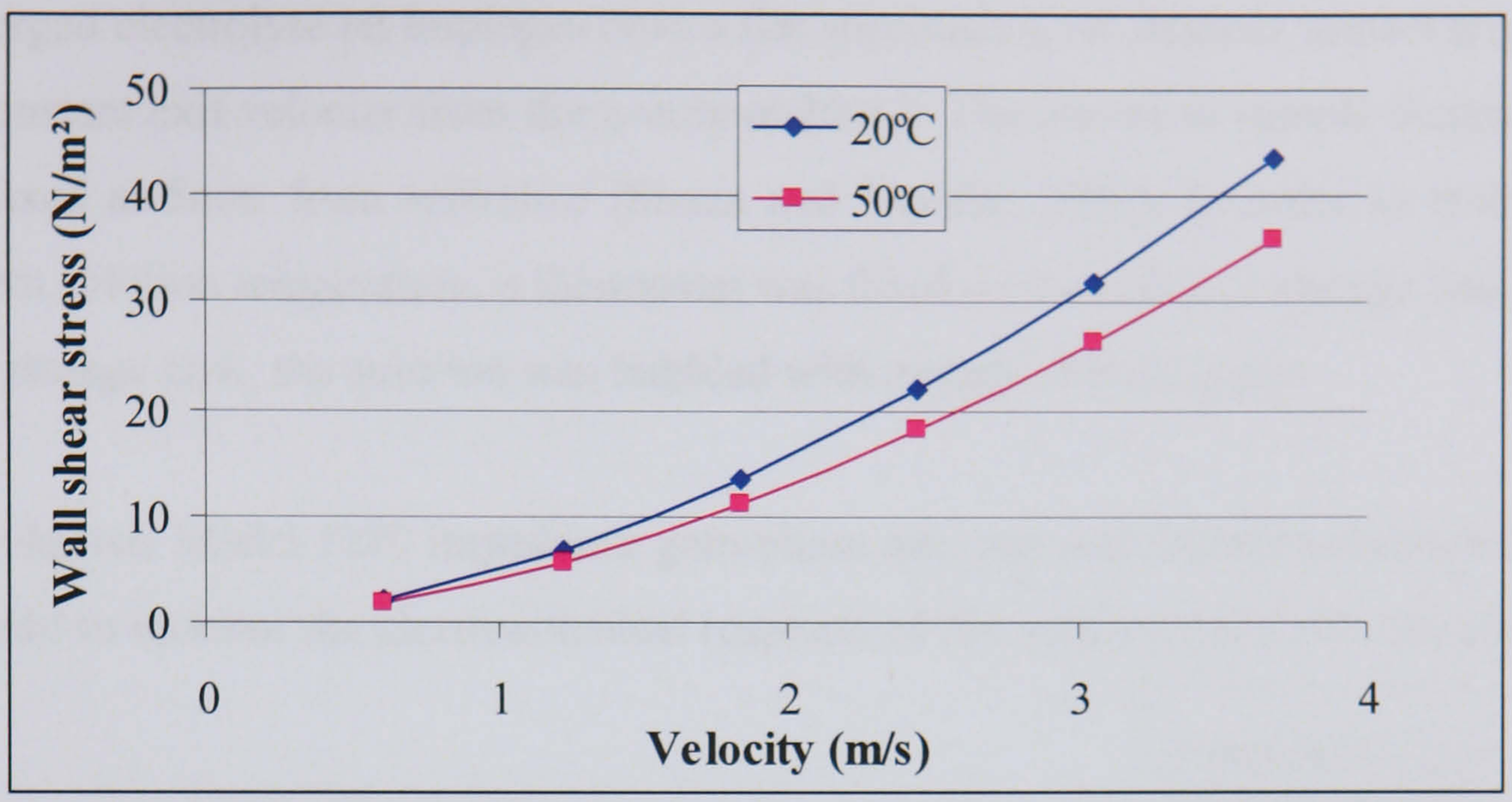

Figure 4.8 Wall shear stress versus velocity for RCE

4.2.2 Erosion-Corrosion Tests Using SIJ Rig

These erosion-corrosion experiments were carried out using a recirculating impingement apparatus, of 70 litre capacity at atmospheric pressure. Figure 4.9 is a schematic diagram of the rig, showing the relative position of the jet, the reference, working and counter electrodes. Before commencing the test the solution was sparged with CO_2 for at least 12 hours to remove dissolved oxygen. This was done in order to ensure that all the dissolved oxygen was removed and to reach CO_2 saturated condition for the test solution. However, during the experiment, this was performed at a very slow rate to prevent solution flow effects. Saturation was found to reduce the bulk pH of the solution to a constant value of 5.5. Only a small change in the pH was observed at the end of the tests, the end result being 5.6-5.8. The residual oxygen level was maintained at lower than 50 ppb and this oxygen concentration was almost constant up to the end of all experiments. The experiments were conducted in brine representative of a typical gas condensate system Temperature was controlled at 50ºC.

All the pipework and the joints in the rig were constructed using PVC and tank was made of PP. A centrifugal pump was used to maintain the flow of test solution through the nozzles of the rig and the arrows in Figure 4.9 represent the direction of flow. A

submerged electrolyte jet impinges onto a flat specimen at 90 degrees impact angle and at a constant exit velocity from the nozzle at 20m/s. The nozzle to sample distance was kept fixed at 5mm from reference (Souza and Neville, 2003). In order to maintain a constant solution temperature, a thermostat was fitted on the solution storage tank. Also, in the storage tank, the solution was bubbled with oxygen-free CO_2 gas.

The Solartron Model 1280 impedance gain-phase analyzer and EG&G potentiostat were also used to monitor the electrochemical response of the working electrode samples.

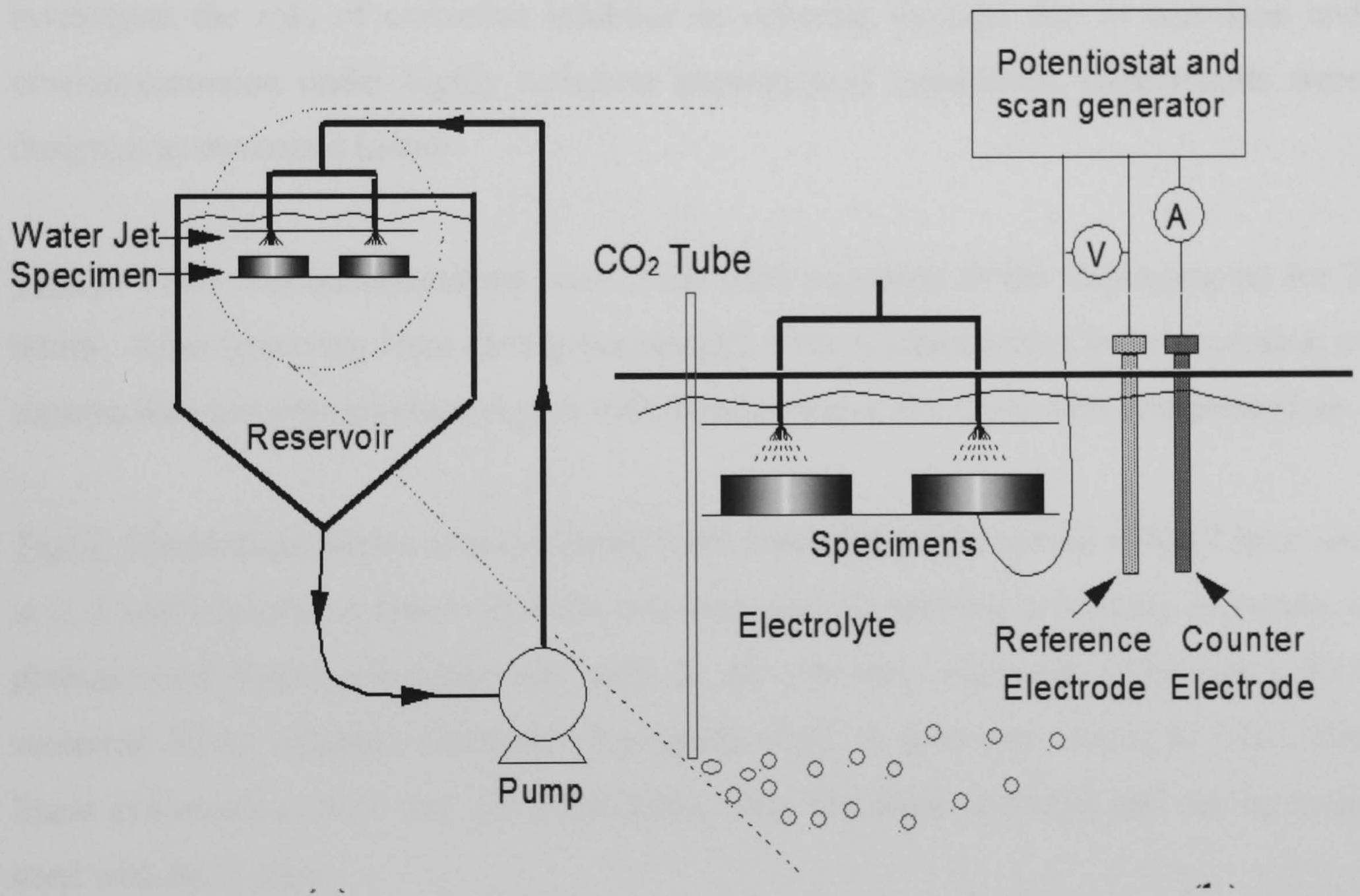

Figure 4.9 Recirculating submerge impingement rig

4.2.2.1 Sample Preparation

All the samples used as working electrodes in the impingement rig were machined from commercial carbon steel rod of grade BS080A15. A cylindrical rod of 25mm diameter and 3 metre length was obtained from C&S steels. This rod was machined into about 60-specimens 5mm thickness each, which were used as working electrode. Before they were set in place, the working electrodes were polished with silicon carbide papers of

varying grit sizes up to 1200 grit silicon carbide paper, degreased with acetone, and cleaned in an ultrasonic bath. They were then rinsed with distilled water again, dried and weighed.

4.2.2.2 Experimental Procedure

The main objective of the experiments carried out using the impingement rig was to investigate the role of corrosion inhibitor in reducing damage due to corrosion and erosion-corrosion under highly turbulent impingement conditions. Experiments were designed as described below.

Test 1 Mass loss measurements were made after exposure to the impinging jet for 2 hours. After removing from the rig the samples were washed with Clarke's solution to remove the corrosion product, rinsed with distilled water and dried with compressed air.

Test 2 Linear polarisation measurements were made during the period of the 2 hour test at 0, 1 and 2 hours. A three electrode cell was used comprising a working electrode, a platinum-rod Redox electrode was used as the auxiliary electrode (AE) and a KCl saturated Silver chloride electrode (Ag/AgCl) acted as reference electrode (RE). For linear polarisation tests and AC impedance tests, the same methods and set up were used with RCE tests.

The experimental procedure used can be summarized by the following sequence:

1. Before the test, the solution was allowed to circulate through the rig, the working electrodes, the reference electrode and the counter electrode were connected to the corresponding potentiostats.
2. For CP tests only, a potential of -0.8 V (Ag/AgCl) was set on the samples, then the test solution was allowed to circulate through the rig.
3. The pump was switched on, the flow rate was adjusted to the desired value in the system.

4. After 5 min waiting time to let the potential stabilise, electrochemical tests were carried out.

4.2.2.3 Hydrodynamic Analysis of the Impinging Jet

Jet impingement testing is employed to study inhibitor effects on erosion-corrosion under high turbulent flow with sand. From literature the wall shear stress range obtainable is from 20 to 1000 Pa (Efird, 1998).

The surface can be subdivided into four zones, as shown schematically in Figure 4.10. Some reference can be made to detailed studies of the impinging jet such as that by Chin and Tsang (1978), but it is an important distinction that in the current study there are solids present in the impinging jet. Some work has been conducted by Benchaite *et al.* (1983) to track the particles and their trajectories at the surface, but still there are uncertainties about the exact nature of the flow regimes in a solid-containing impinging jet. In Figure 4.10, the approximate sizes of the different zones are given in relation to the nozzle diameter. Zone (I) is located directly under the jet. In this zone, most frequent and highest angle solid impacts occur. Hence the material suffers severe erosion-corrosion and the surface is heavily plastically deformed by the impinging particles which are impacting at angles near to normal incidence. The diameter of this zone is about 6-8 mm. The regions out from zone (I), defined as zone (II), is zone with lower frequency impact, which has previously been referred to as the "halo" by Wood (1986). The diameter for zone (II) is about 8-12 mm. There is low angle impacting at zone (II). According to the surface profile, two zones with small difference on pitting number are defined as zone (III) with diameter from 12 to 20mm and zone (IV) with the diameter of 20 to 25 mm at the edge.

The wall jet region is of primary interest for studying fluid flow effects on corrosion in high-turbulence areas. Using equation (74), wall shear stress in the wall jet region is 508.6 Pa at 50°C, where U_0 is the fluid velocity at the jet, r_0 is the radial of the nozzle, r is radial distance of interesting. The jet Reynolds number is defined as:

$$\mathrm{Re} = \frac{2r_0 U_0}{\nu} = 144665 \tag{77}$$

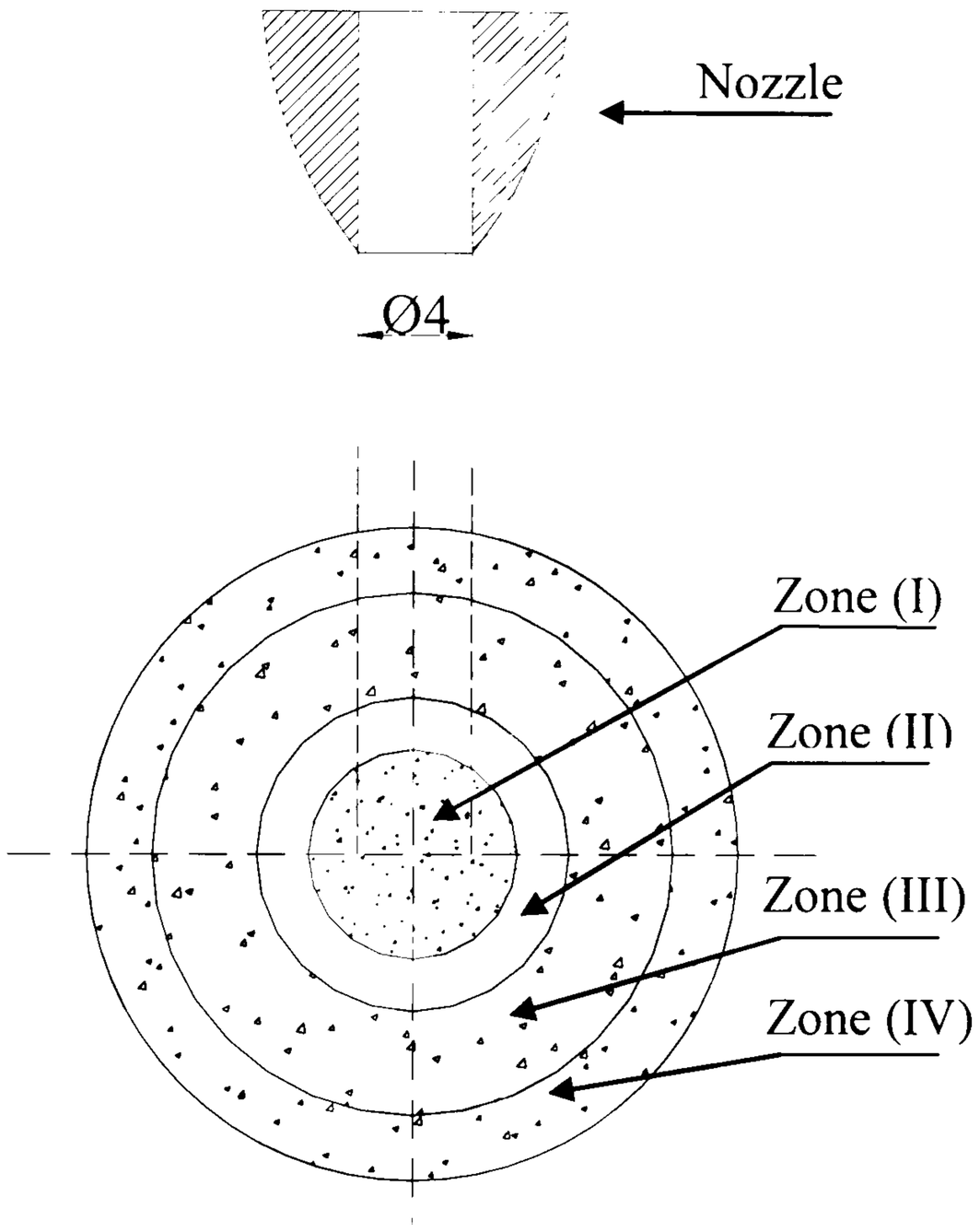

Figure 4.10 Schematic diagram showing different impacted regions of the sample surface. Approximate diameters of each zone are: Zone (I) 6.3-8.3 mm, Zone (II) 12 mm, Zone (III) 20mm, Zone (IV) 25mm.

4.3 Surface Analytical Techniques

After each test, an important aspect of the study was the post-test analysis of the damage mechanisms. From analysis of the extent and nature of mechanical (e.g. ploughing, cutting) and electrochemical damage (e.g. pitting) in the absence and presence of inhibitors some assessment of the performance of the inhibitors could be made. In order to analyze corrosion products and inhibitor molecules formed on the metal surface, optical microscope, X-ray diffraction, scanning electron microscope (SEM) and X-ray photoelectron Spectroscopy were used in this study.

4.3.1 Optical Microscope

An optical microscope (NIKON) was used to study the corrosion behaviour with and without inhibitors and the information related to the corrosion mechanisms and degradation of materials due to corrosion, erosion and synergistic effects in erosion-corrosion. Images of the surface were also used to compare the damage to the materials under different test conditions.

The optical microscope used in this study is a NIKON standard binocular metallurgical microscope. The objective lenses used were calibrated using a graticule and the individual magnification bar and is shown in each microscope image. A mounted camera on the microscope enabled the observations to be recorded.

4.3.2 X-ray Photoelectron Spectroscopy

Surface analysis by X-ray Photoelectron Spectroscopy (XPS) was performed in a Scienta ESCA 300 at the National Centre for Electron Spectroscopy and Surface Analysis (NCESS). This powerful technique is used in this study mainly for the purpose of identifying chemical single component compound on the metal surface.

The equipment involves a solid in vacuo with monoenergetic soft x-rays and analyzing the emitted electrons by energy. The spectrum is obtained as a plot of the number of detected electrons per energy interval versus their kinetic energy. Each element has a unique spectrum. The spectrum from a mixture of elements is approximately the sum of the peaks of the individual constituents. Because the mean free path of electrons in solids is very small, the detected electronsoriginate from only the top few atomic layers (about 5nm), making XPS a unique surface-sensitive technique for chemical analysis.

The technique involves detecting photo-electrons emitted by the absorption of X-rays incident on the sample. An incident X-ray transfers all its energy (hv) to an inner shell electron such that kinetic energy of emitted photoelectron is equal to that of the x-ray minus the binding energy of the electron. Small shifts in the measured kinetic energy of

the photoelectron of 1-10 Ev indicate changes in the binding energy and hence the local chemical state. All elements can be detected by XPS with the exception of hydrogen and helium due to their extremely low photoelectron generation cross sections.

Quantitative data can be obtained from peak heights or peak areas, and identification of chemical states often can be made from exact measurement of peak positions and separations, as well as from certain spectral features. The base pressure in the experimental chamber was lower than $5x10^{-8}$ mbar. The spectra were collected using Al Kα (hν=1486.7) radiation and the overall energy resolution was about 0.3 eV.

Samples of 1.2 cm^2 were used. Analyses were conducted on the wear scar in the case of sample after erosion-corrosion test. The binding energies were calibrated to the common C 1s peak at 284.6 eV for charge correction whenever possible. A survey scan is obtained first in order to identify elements present, and then the long scans of the selected peaks are obtained to determine a more comprehensive image of the chemical information. Acquisition conditions for the survey spectra were recorded at 150 eV pass energy, 0.8 mm slit size and 1.0 eV step interval. For the regions of interest: C 1s, O1s, Fe 2p, N, and P, the higher resolutions scans of 0.05 eV steps were used. All the spectra were acquired in transmission mode.

4.3.3 X-ray Diffraction (XRD)

Characterisation of the corrosion products on the metal surface after the tests is an important factor for the study of corrosion and erosion-corrosion mechanisms. Corrosion products formed on the metal surface were identified using X-ray diffraction (XRD) technique. The equipment used was a Siemens D500 diffractometer. The copper Kα X-rays (1.5418 Angstrom) were diffracted by the crystalline phases in the specimen based on the Bragg's law ($\lambda = 2d \sin\theta$, where λ is the wavelength of the x-rays, d is the spacing between atomic planes in the crystalline phase, and 2θ is the angle between the incident and diffracted X-rays). The intensity of the diffracted X-rays was then measured as a function of the diffraction angle and the sample orientation. The resulting

diffraction pattern was collected into the diffraction-AT peak identification software to identify the corrosion products on the metal surface after the blank tests.

Figure 4.11 shows the XRD pattern of carbon steel after blank test at 50°C. After two hours tests, a very thin black and brownish layer was found on the surface of the specimen. Analysis of the pattern shows that the composition of the film is the combination of $FeCO_3$ and Fe_3C. Possible phases can be detected by XRD and identified by various databases and possible phases are summarized in Table 4.3.

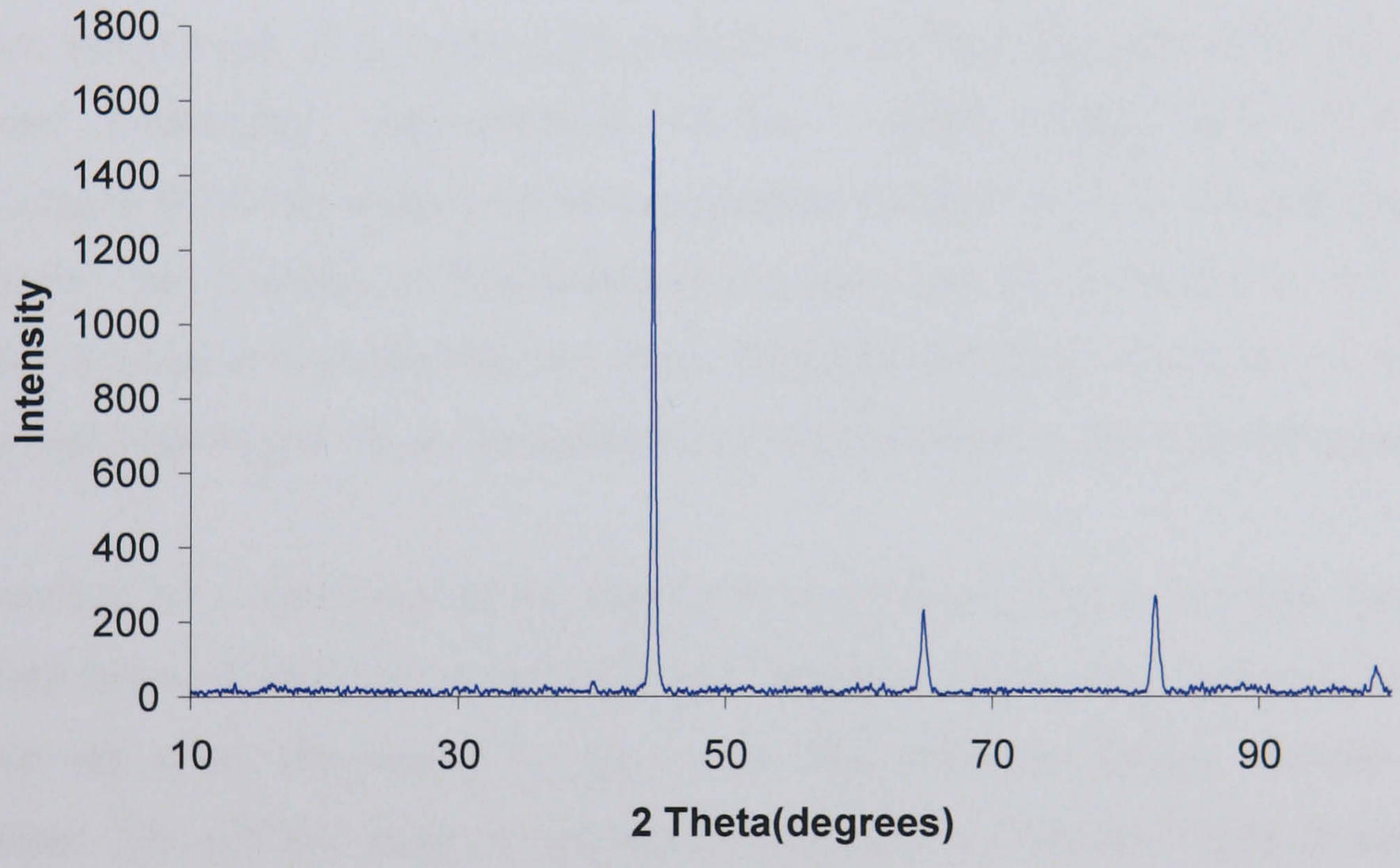

Figure 4.11 XRD pattern of carbon steel after blank test

Table 4.3 Possible phases for carbon steel after blank tests under 50°C and 0.1% sand loading detected by XRD (PaulingFile, 2004)

2 Theta (θ)	D(A)	Possible Phases Present
44.684	2.0264	Fe_3C
64.921	1.4352	$FeCO_3$
82.303	1.1706	$FeCO_3$

When carbon steel corrodes, the corrosion product $FeCO_3$ and the iron carbide Fe_3C left on the steel surface may form a mixture on the metal surface. This has been verified by Crolet *et al.*, (1998). The main effect of cementite is to form additional cathodic sites.

The results confirm the intensity of the corrosion product $FeCO_3$ to be very low. One reason is that it can be dissolved in the CO_2 saturated solution with HCO_3^- content (Videm *et al.*, 1996); the other reason is due to high turbulent multiphase flow which makes it difficult to form a protective corrosion product layer on the metal surface.

4.3.4 Scanning Electron Microscopy (SEM)

The Philips XL30 Environmental Scanning Electron Microscope (ESEM) was used for electron microscopy. It provides high resolution secondary electrons (SE) and primary electron bombarding back-scattered electrons (BSE) image and offers good performance for X-ray analysis at all accelerating voltages on conventionally prepared specimen. The intensity of backscattered electrons can be correlated to the atomic number of the element within the sampling volume by which some qualitative elemental information can be got. X-ray analysis gives more quantitative elemental information.

The surface of a specimen to be examined is scanned with an electron beam; the reflected beam of electrons is collected and displayed at the same scanning rate on a cathode ray tube. The image on the screen represents the surface features of the specimen. The surface must be electrically conductive. The technique is extremely useful in determine the mode of mechanical fracture and the mechanisms of material degradation in detail.

4.4 Material Microstructure and Characterization

The microstructure of the carbon steel used in the experiments BS080A15 is shown in Figure 4.12. It reveals a typical hypoeutectoid steel, with less than 0.8% carbon content. It can be seen that carbon steel microstructure contains a mixture of α -ferrite (the lighter areas) and pearlite (darker areas). pearlite consisting of alternating plates of α -ferrite and cementite, Fe_3C. This photomicrograph presented here can be used to compare the one from corrosion tests to study the corrosion mechanism of the carbon steel under static condition.

SEM-EDX analyses were also performed to characterise the microstructure of carbon steel. The microstructure from SEM (in Figure 4.13) shows a clear grain boundary from which the lighter areas are pearlite and darker areas are α -ferrite. Their colour is opposite with that obtained from light microscope. It is more clearly seen in SEM image that pearlite appears as a lamellae eutectoid structure, which consists of α -ferrite and Fe_3C. The elemental compositions measured from EDX analysis for the whole material, the α -ferrite region and the pearlite region are shown in Table 4.4. The obvious difference is that the Mn percentage is higher in the α -ferrite site.

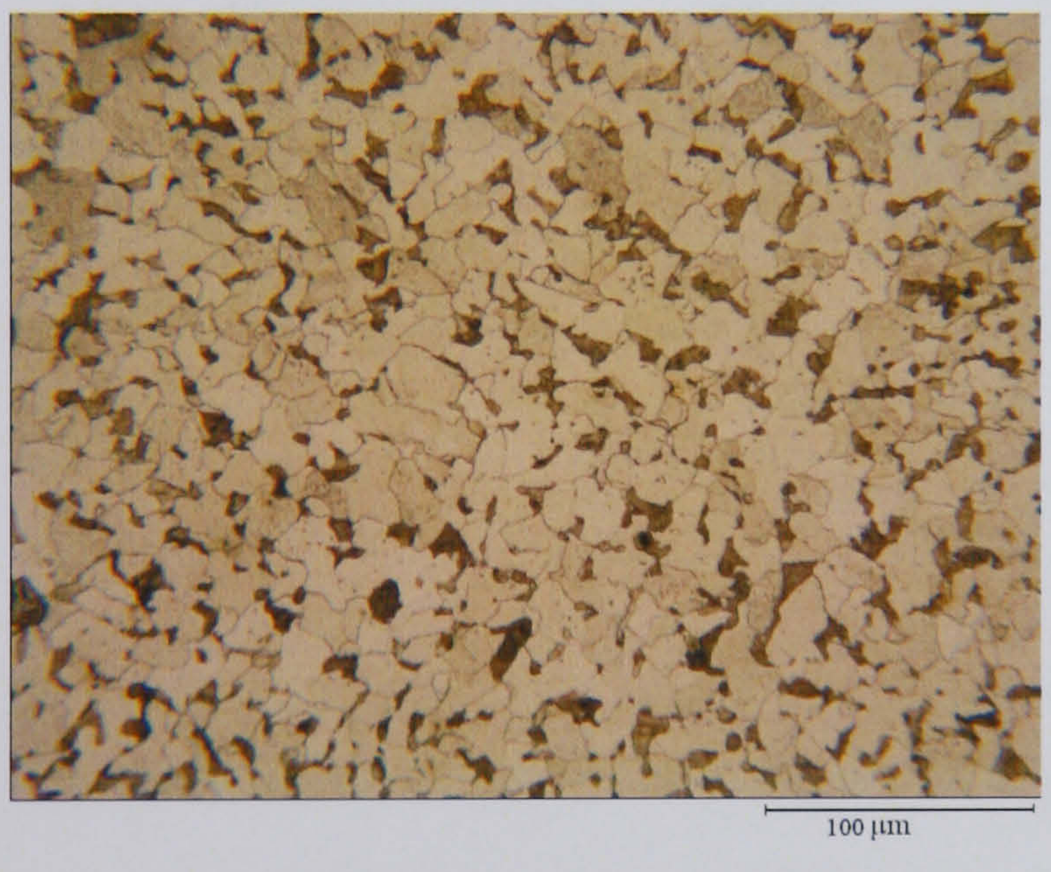

Figure 4.12 Microscope image of as polished sample after etched at 2ml HNO_3 nital solution (ASTM, 1993) for 10 seconds

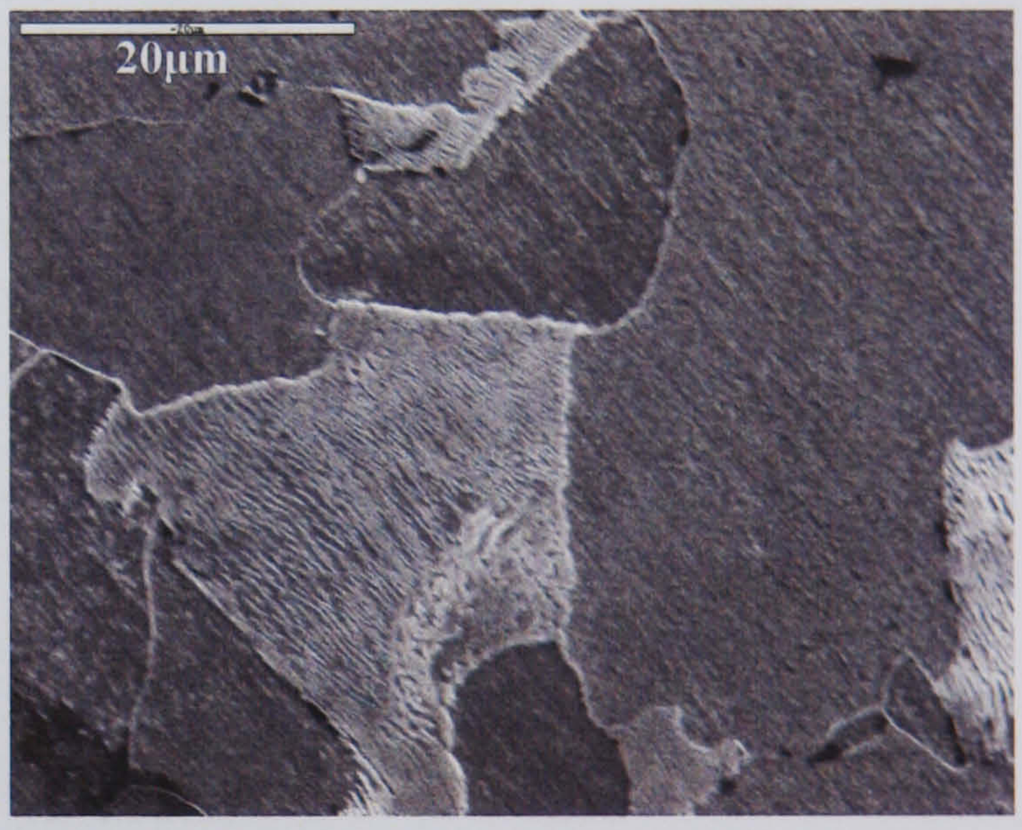

Figure 4.13 SEM image of the microstructure of as polished sample after etching at 2ml HNO_3 nital solution (ASTM, 1993) for 10 seconds

From calculations using the Fe-Fe_3C phase diagram and using average carbon composition 0.15% by weight, the amount of pearlite is only 18.75%. Therefore it can be specified that the amount of carbon in pearlite is only 18.75% x 0.15% =0.028%.

According to EDX point analysis, the main and addition element are distributed evenly on the microstructure, as additional element percentage in pearlite and ferrite regions are quite similar. It is important to know that carbon analysis is excluded as this element is too light of atomic weight to be traced by EDX.

Element	**Element percentage (%) from whole material**	**Element percentage (%) from α -ferrite region (1μm)**	**Element percentage (%) from pearlite region (1μm)**
Si	0.34	0.26	0.27
P	0.06	0.04	0.07
S	0.05	0.12	0.03
Mn	0.89	0.94	0.71
Fe	98.71	98.65	98.91

Table 4.4 Chemical compositions from EDX analysis

CHAPTER 5 RESULTS AND DISCUSSION OF STATIC CORROSION

Up to now, corrosion inhibitor injection, especially nitrogen-based organic surfactants, such as amines, imidazolines and their salts, is still the most cost-effective method to solve the problems of CO_2 corrosion of carbon steel pipelines. Although this study focuses on the mechanism of inhibitor action in flowing conditions (and specifically erosion-corrosion), it is necessary to compare with the characteristics of the inhibitors under static conditions to illustrate the effect of flow velocity and entrained sand on the inhibition efficiency and mechanisms. Understanding the static inhibition mechanisms is important from the point of view of having reference data where the best performance of the inhibitor can be achieved.

This chapter explains the inhibition mechanism in static CO_2-saturated conditions without flow or sand, and the focus is on the adsorption and the inhibition of corrosion of carbon steel by the inhibitors CRW8 and CRW9 as two water soluble inhibitors. The inhibitors CGO and CRO were also studied to compare the inhibition performance between oil-soluble (partially soluble in water) and water-soluble inhibitors. Free corrosion potential, DC linear polarisation and AC impedance measurements were performed to obtain the corrosion inhibition efficiencies and to determine the inhibitor film formation and repair mechanisms under static conditions in a simulated gas condensate solution. The inhibition mechanism analysis was supported by post-test analysis using CRW8 as an example. AC impedance data were used to calculate corrosion-related electrochemical parameters. Blank tests were studied by DC and AC electrochemical techniques to obtain corrosion mechanisms in static conditions.

The main focus of the thesis is to study the inhibitor effects on erosion-corrosion under turbulent slurry conditions. Tests under static conditions were only conducted at 20°C, as there is no significant $FeCO_3$ corrosion product layer formed under this condition. These results provide information on how inhibitors interact with and adsorb directly onto the carbon steel surface. According to Hawkins (1995), there is a non protective corrosion product layer formed on the metal surface up to temperatures of 85°C under

the same CO_2 partial pressure as in this study. It is reasonable to assume that the corrosion mechanisms will be the same at both 20°C and 50°C, although the corrosion rates will be increased with increasing temperature as explained by Arrhenius equation (Equation (14)). There are corrosion product molecules ($FeCO_3$) accumulated on the metal surface at 50°C as was shown by the small $FeCO_3$ peak in Figure 4.11. They should be more than that at 20°C. How inhibitors react with these non protective corrosion products on the metal surface under 50°C will be studied under low flow rate conditions in the following Chapters.

A map to describe the experiments conducted for this part of study is presented in Figure 5.1.

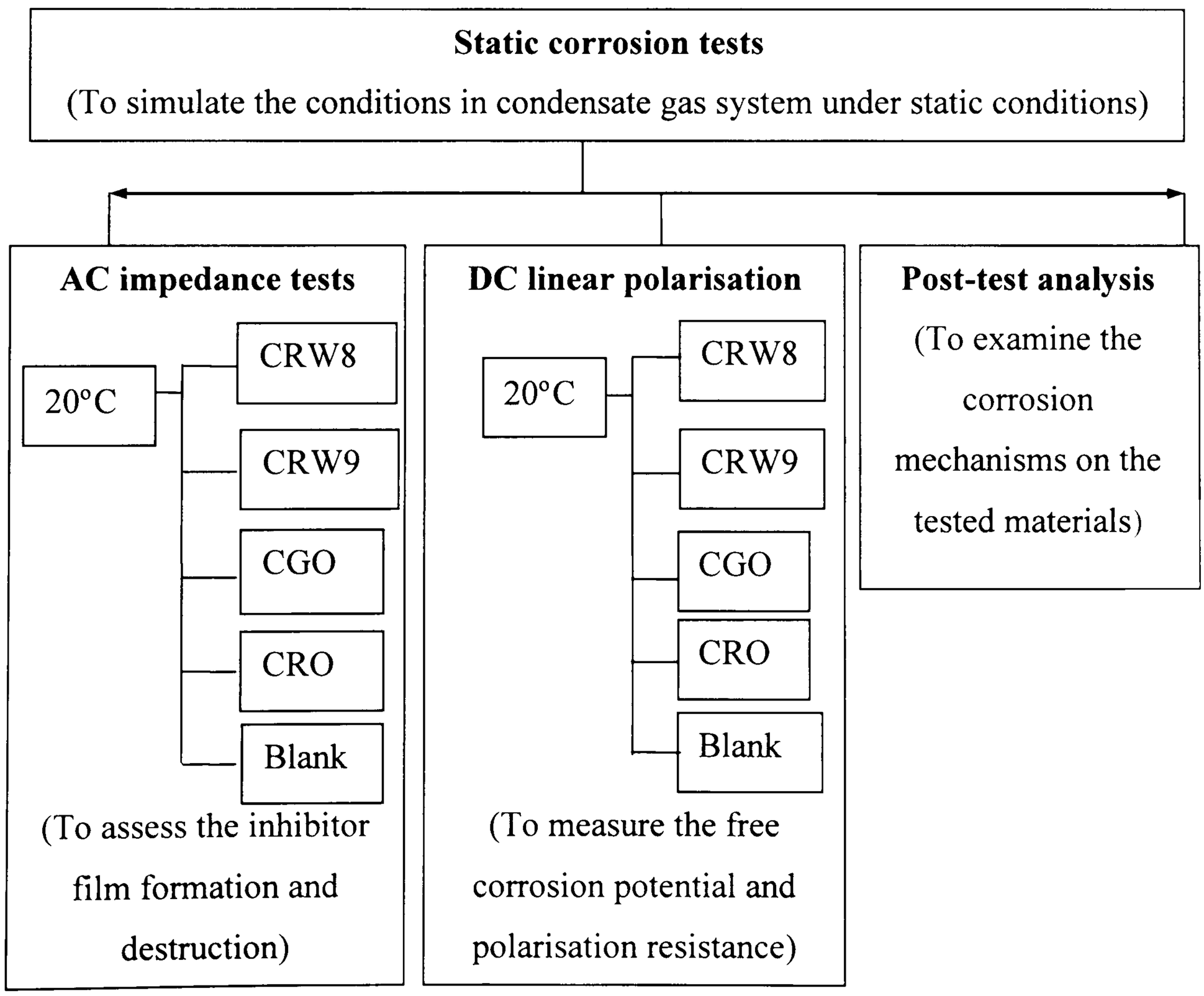

Figure 5.1 The map of experimental work presented in Chapter 5

5.1 Free Corrosion Potential Measurements

Free corrosion potential values change depending on how electric double layer (EDL) chemistry adjusts to accommodate electrolyte chemistry. For example, if a passive film forms on the metal surface that protects the metal from further corrosion due to hindering the active site reactions, an increasing free corrosion potential will normally be observed. With inhibitor tests, the mechanism of inhibitor adsorption on the metal surface will change the potential accordingly.

The corrosion potential versus immersion time was measured with respect to the Ag/AgCl electrode and the results are presented in Figure 5.2 for blank tests, inhibitors CRW8 and CRW9 tests at 20°C. The tests were continuously monitored until up to the time that there was an obvious change of the corrosion resistance as reported in the next section. At 20°C for the blank test, the potential was stable around -703 mV at the experimental duration. The addition of inhibitor CRW8 or CRW9 shifts the free corrosion potential in the noble direction. The fluctuation of potential with inhibitor tests is observed. It may relate to the inhibitor adsorption and desorption processes which are discussed later. It is not the case for blank tests. It was observed that some gel-like inhibitor film covered the metal surface.

The free corrosion potential at 0, 0.5 and 1 hour immersion time was also measured for inhibitors CGO and CRO. The comparison of free corrosion potential of these two oil soluble inhibitors and blank solution is shown in Figure 5.3. There is a small shift of the free corrosion potential in the anodic direction with addition of the two inhibitors as well.

The free corrosion potential is representative of the surface electrochemistry under the condition where the anodic and cathodic reactions are in equilibrium. Under static conditions, for CO_2 corrosion, coverage of $FeCO_3$ produced is mainly occurring at anodic sites through the following reactions (Ogundele and White, 1986)

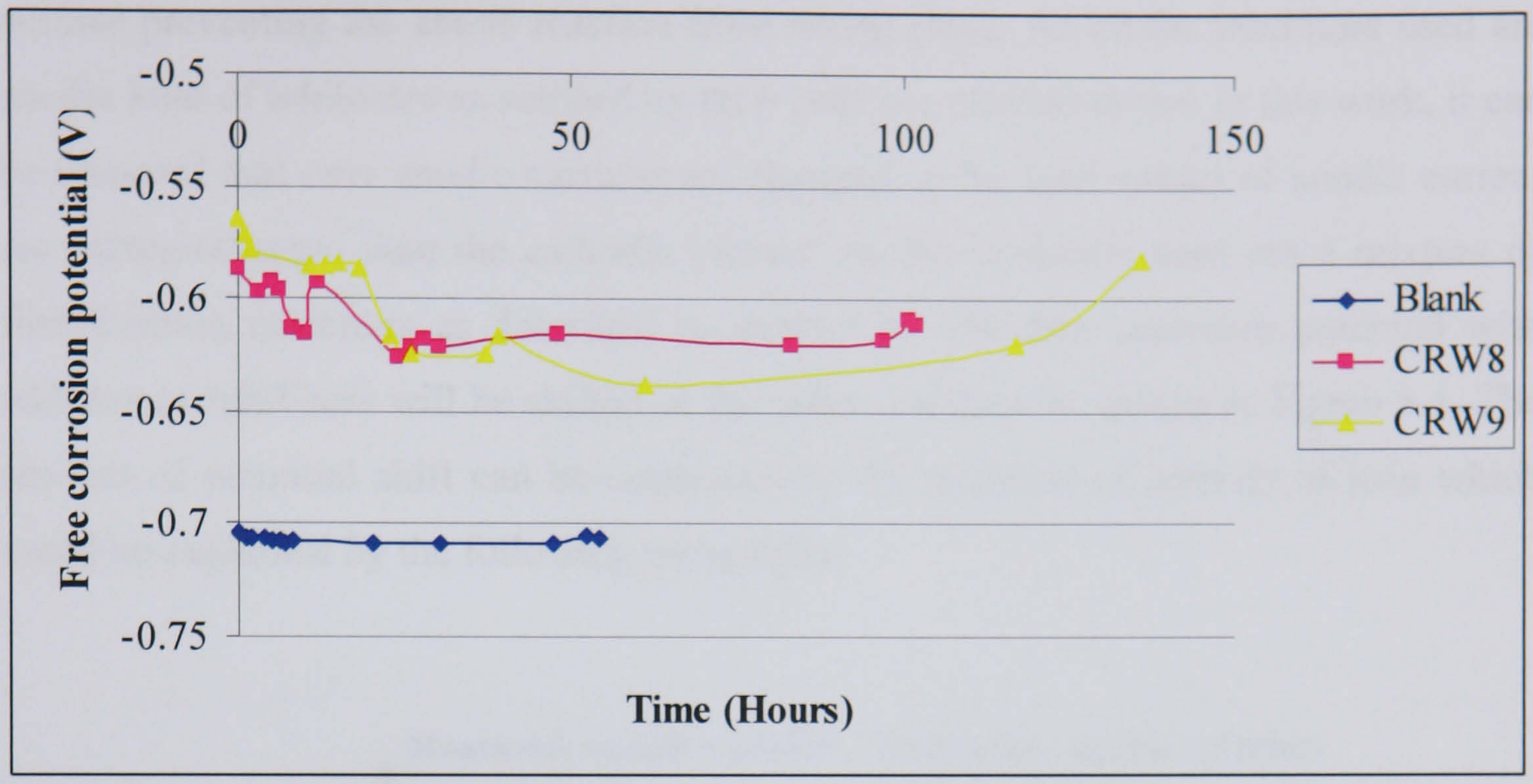

Figure 5.2 Free corrosion potential versus time for blank, CRW8 and CRW9 tests at 20°C

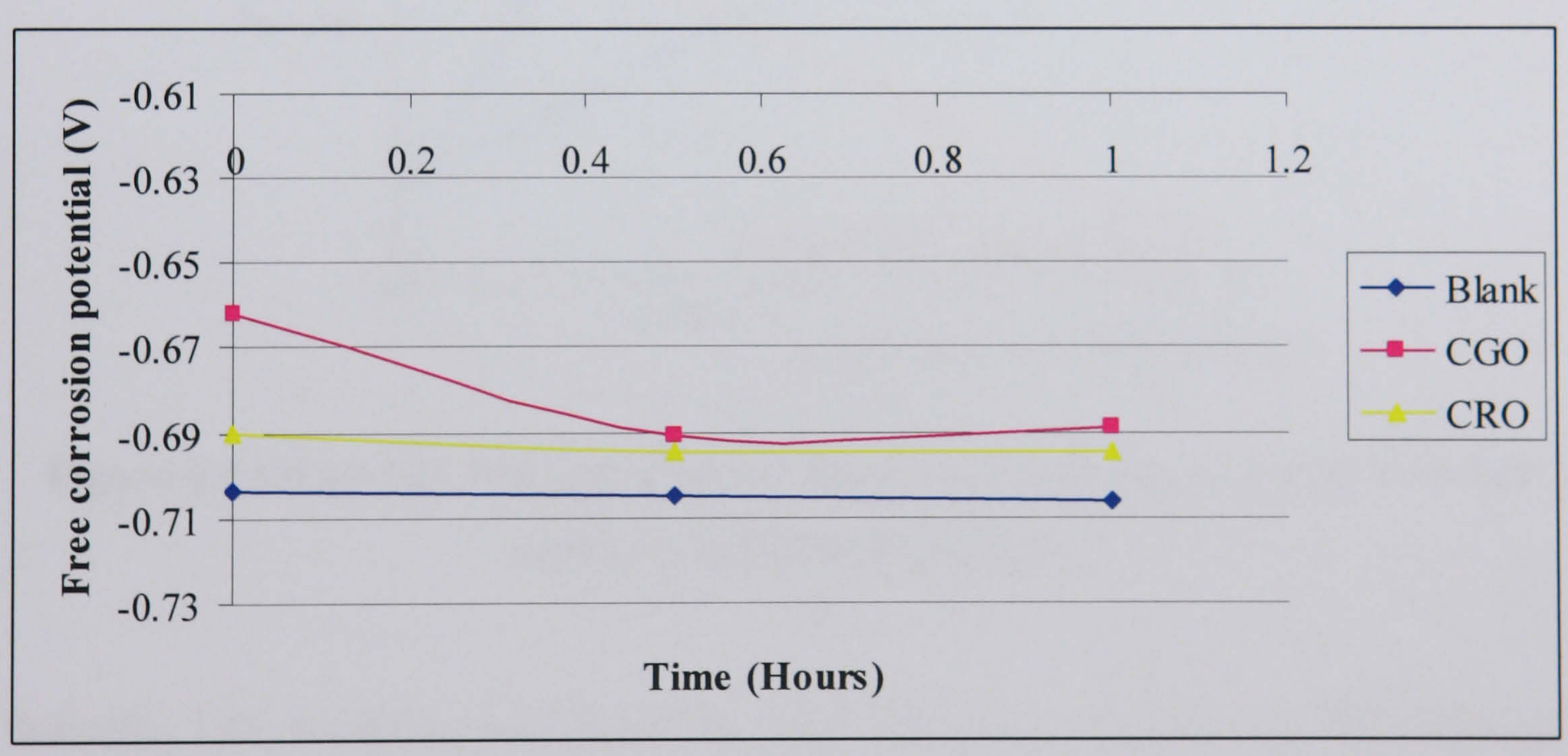

Figure 5.3 Comparison of free corrosion potential versus time for blank, CGO and CRO tests at 20°C under static conditions

$$Fe + H_2CO_3 = FeCO_3 + 2H^+ + 2e \quad (78)$$

$$Fe + HCO_3^- = FeCO_3 + H^+ + 2e \quad (79)$$

With addition of inhibitors, the free corrosion potential shifts in the noble direction. This indicates that the inhibitors are adsorbed mainly on the anodic sites of the metal

surface preventing the above reaction from taking place. As all the inhibitors used are anodic kind of inhibitors as verified by their shift in potential shown in this work, it can be assumed that only anodic currents are changed or the total values of anodic current are increased more than the cathodic current (as the inhibitors used are a mixture of film-forming inhibitors as described in chapter 4). The free corrosion potential with addition of inhibitors will be shifted in the noble direction as shown in Figure 5.4. The amount of potential shift can be expressed by the decrease of activity of iron which could be explained by the following paragraphs.

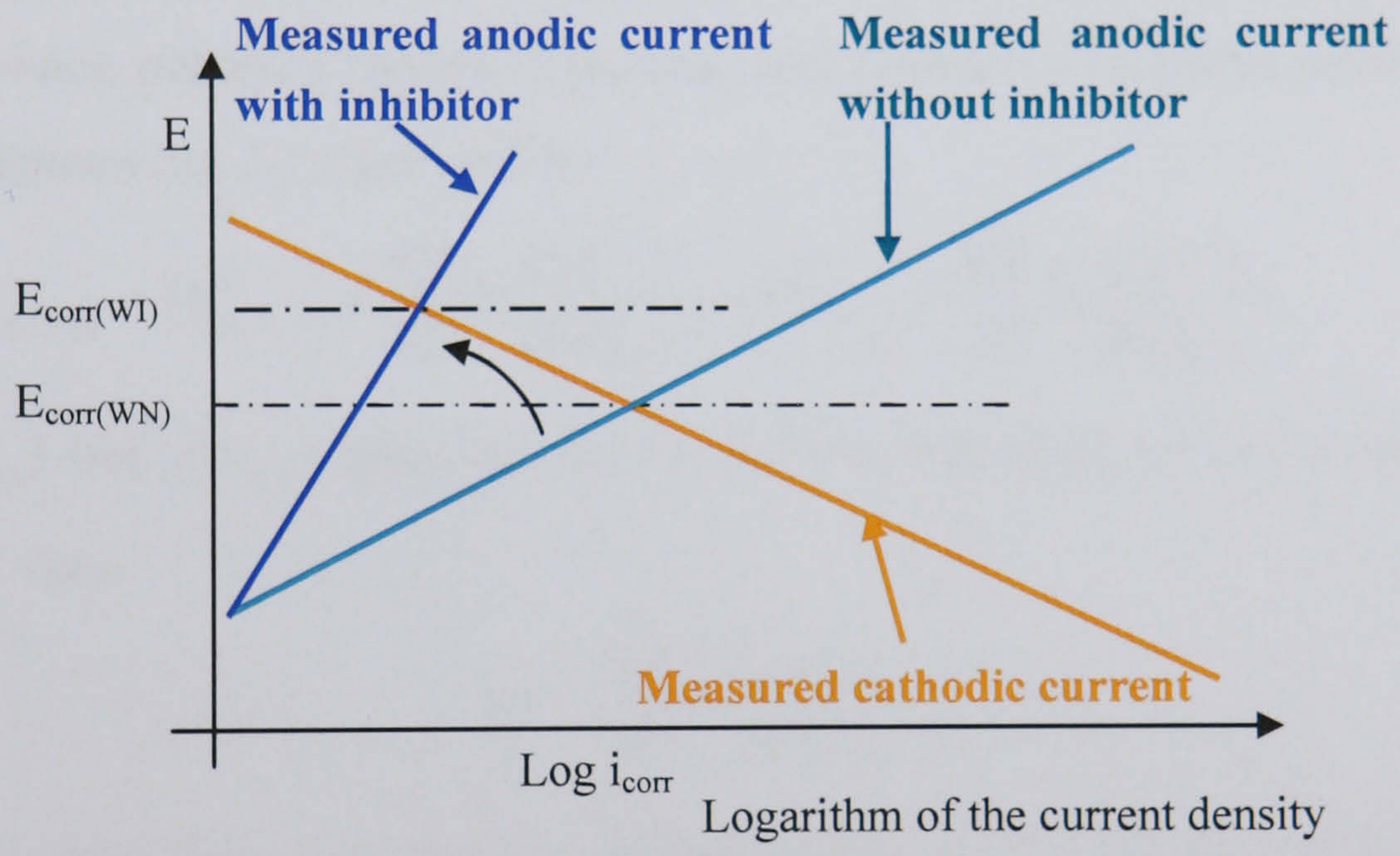

Figure 5.4 Schematic diagram of changing of free corrosion potential with and with out addition of inhibitor

Basically, CO_2 corrosion is a process in which iron loses electrons and hydrogen ions obtain electrons. If all the potential changes are due to change of half cell potential, the change of the potential after adding inhibitor into the solution ΔE can be expressed as:

$$\Delta E = E_{corr}\,(WI) - E_{corr}\,(WN) = \Delta E_{Fe^{2+}/Fe} \tag{80}$$

where, E_{corr} (WI) and E_{corr} (WN) represent free corrosion potential in inhibitor solution and blank solution respectively, $\Delta E_{Fe^{2+}/Fe}$ is the potential change of the anodic half cell.

From the iron ion concentration[Fe^{2+}], after adding the inhibitor, if the inhibitor can react with iron to form a complex, then [Fe^{2+}] on the metal surface will be reduced. Thus, there will be more Fe^{2+} formed, resulting in acceleration of the corrosion rate. If [Fe^{2+}] increased, then the inhibitor did not provide protection to the metal. Therefore, it is deduced that [Fe^{2+}] will not be changed due to addition of the inhibitor to the solution. From the following explanation, it is the change of Fe activity that results in the change of the E_{corr}.

According to the Nernst equation (Equation (13)), for half cell reaction of the electrode, the free corrosion potential change of carbon steel between with blank solution and with inhibitor solutions can be expressed as:

$$\Delta E_{Fe^{2+}/Fe} = (E^0_{Fe^{2+}/Fe} + \frac{RT}{nF}\ln\frac{[Fe^{2+}]}{[Fe]_{WI}}) - (E^0_{Fe^{2+}/Fe} + \frac{RT}{nF}\ln\frac{[Fe^{2+}]}{[Fe]_{WN}}) \quad (81)$$

where, $[Fe_{WI}]$ and $[Fe_{WN}]$ represent the Fe activity with inhibitor and without inhibitor respectively. then:

$$\Delta E = \frac{RT}{nF}\ln\frac{[Fe]_{WN}}{[Fe]_{WI}} \quad (82)$$

If $[Fe_{WN}] = 1$ then, $[Fe_{WI}]$ values for inhibitor CGO, CRO, CRW8 and CRW9 can be calculated and are shown in Table 5.1. It can be seen the iron activity reduced by 2 x 10^3 for the inhibitor with best performance. This is in agreement with the polarisation resistance from linear polarisation tests. Therefore, it can be used as a kind of criteria to evaluate the performance of inhibitors under static conditions.

Table 5.1 The iron activity in inhibited metal surface in the electrolyte, [Fe_{WI}]

	CGO	CRO	CRW8	CRW9
$[Fe_{WI}]$	0.0501	0.3441	0.0005	0.0002

When the bulk electrolyte composition is altered in such a way that it causes the EDL composition to change, the free corrosion potential for a metal will change. The electrical double layer is characterized by two layers of opposite charge facing each

other. In the case of the blank tests, if the EDL can be schematically shown as in Figure 5.5 (a), then with inhibitor, the reduction of the iron activity can be illustrated by Figure 5.5 (b).

With inhibitor in the solution, it is clear (Figure 5.2) that the free corrosion potential is more positive than with blank solution. Shifting the free corrosion potential of the steel in the positive (noble) direction is an indication of the nature of the electron acceptor. As the inhibitors are a mixture of corrosion inhibitors, there may be some constituents which are electron acceptors or some that are proton acceptors, but overall the inhibitor behaves like an electron acceptor. They are attracted to anodic sites, slowing the anodic reaction. It also can be seen that with inhibitor tests, although the potential is about steady, they are not as stable as blank test, indicating the dynamic process of inhibitor film form action on the metal surface and the self-repairing ability.

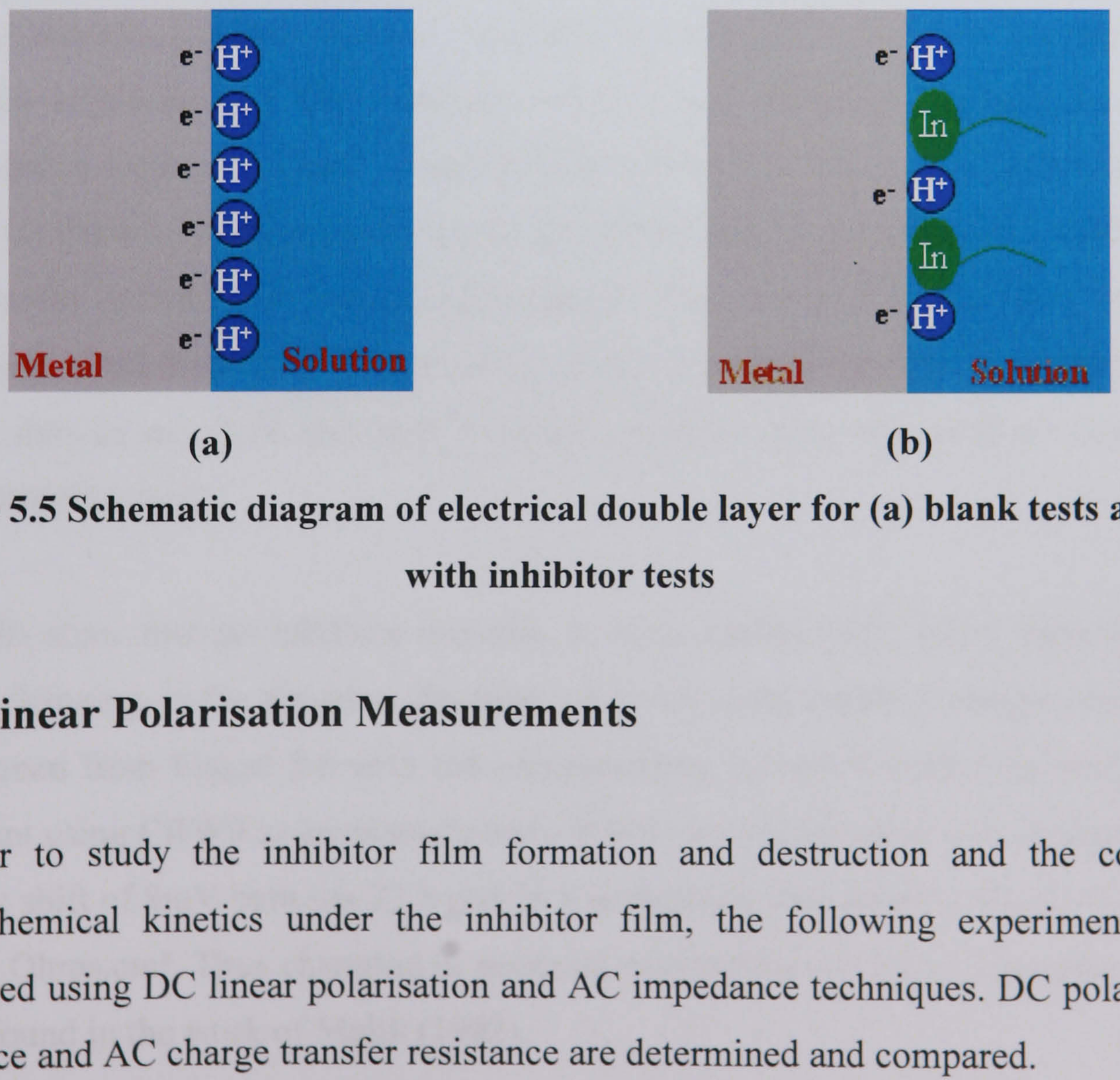

Figure 5.5 Schematic diagram of electrical double layer for (a) blank tests and (b) with inhibitor tests

5.2 Linear Polarisation Measurements

In order to study the inhibitor film formation and destruction and the corrosion electrochemical kinetics under the inhibitor film, the following experiments were performed using DC linear polarisation and AC impedance techniques. DC polarisation resistance and AC charge transfer resistance are determined and compared.

From the linear polarisation tests, the results of the R_p values versus immersion time are shown in Figure 5.6 for blank and inhibitor CRW8 and CRW9 tests. Each experiment was stopped when the R_p values starts to drop obviously. It can be seen that the R_p for blank tests is relatively constant with less fluctuation over the first 50 hours and then a trend to drop afterwards. It indicates that the corrosion process actually occurs after 50 hours. Malik (1992) studied the corrosion performance of carbon steel in CO_2-saturated 5% NaCl at pH 5.2 showing the same trend of the R_p measurements. It is in the same level of the corrosivity (R_p around 372 Ohms.cm^2) with this work which is at pH 5.0 (R_p around 420 Ohms.cm^2).

The R_p value as a function of time for inhibitor CRW8 and CRW9 at 20°C (Figure 5.6) shows that the R_p values increase to maximum values of 40,000 Ohms.cm^2 and 100,000 Ohms.cm^2 for CRW8 and CRW9 respectively then decreases afterwards. The process of increasing R_p values indicates that inhibitor adsorbed on the metal surface continuously with self repairing abilities. It can be assumed that the film becomes thicker and denser. From the appearance of the electrode, a transparent white gel-like film covers the shining metal surface. In Malik's work (1992), at pH 5.2, the R_p values versus time with 20ppm inhibitor E (designated E) shows the same trend as the result of CRW9 in this work and the maximum R_p value reaches 60000 Ohms.cm^2 and this started to drop after 100 hours immersion time. Examination of the corrosion product on a precorroded surface showed no voids and least corrosion products with that inhibitor among the other inhibitors used.

R_p results show that the inhibitor was able to work rapidly from initial immersion and E_{corr} is changing in the negative direction while the polarisation resistance rises. This can be seen from Figure 5.6 with the corresponding corrosion potentials next to each data point using CRW9 as an example and CRW8 has similar behaviour. It shows that a cathodic shift of 8mV between 23 h and 26 h immersion time allowed the R_p to increase to 7400 Ohms.cm^2. Thus changing in potential may reflect its rate of adsorption, which is also found in the work of Malik (1992).

The R_p values for inhibitors CGO and CRO are compared with blank tests at 0, 0.5 and 1 hour immersion time as shown in Figure 5.7. As can be seen values of R_p obtained in inhibitor solution both with CGO and CRO are higher than that in blank solution, however they are less than 1000 Ohms.cm^2. They are not as efficient as the CRW inhibitors, therefore only 1 hour tests were done for them to compare with their behaviour under erosion-corrosion conditions.

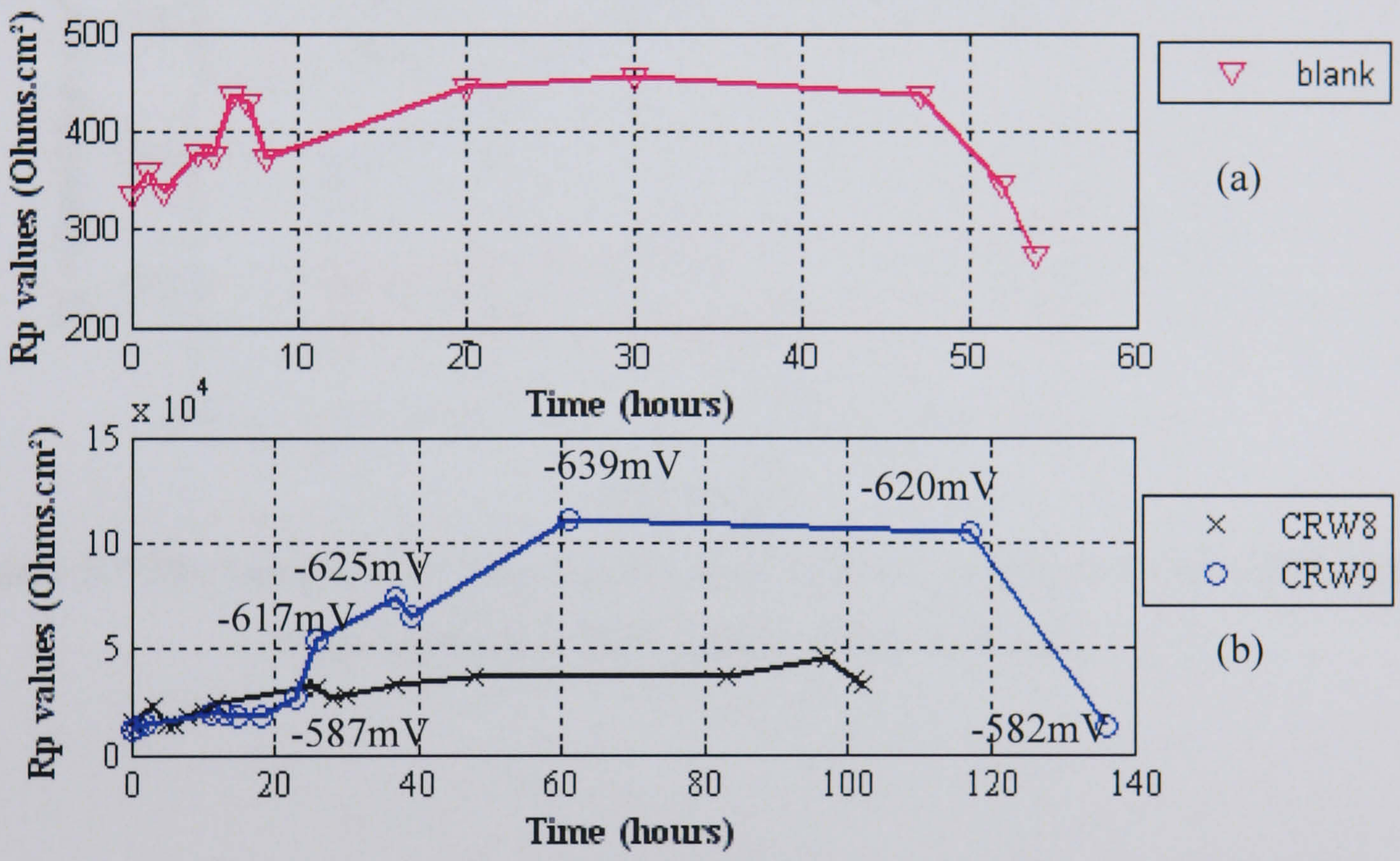

Figure 5.6 R_p values versus time for (a) blank tests and (b) inhibitor CRW8 and CRW9 at 20°C in static conditions

Figure 5.8 show the linear polarisation plots for inhibitor tests at 1 hour immersion time. It is obvious that the CRW inhibitors show smaller current density than CGO and CRO.

Figure 5.9 shows examples of the linear polarisation plots for inhibitor CRW9. The E_{corr} shifts slowly in the negative direction with time, which relates to the inhibitor adsorption processes. It indicates that the inhibitor was adsorbed on the anodic site as an electron acceptor; and then more inhibitor absorbed on the surface with time having a blockage effect. When the whole surface is covered, the potential will be shift accordingly. With inhibitor tests (Figure 5.9) the plots oscillate more as time progress and this is thought to be due to a thicker inhibitor film being built up. This oscillation is very similar to chemical oscillation, which is related to the Belousov-Zhabotinsky (BZ)

reaction (Peterson, 2006; Scott, 1994). According to the BZ reaction, the concentrations of the inhibitor species are given to stochastic fluctuations in small regions. The change of the concentration of the chemical species in the EDL due to BZ reaction results in the change of the free corrosion potential with time.

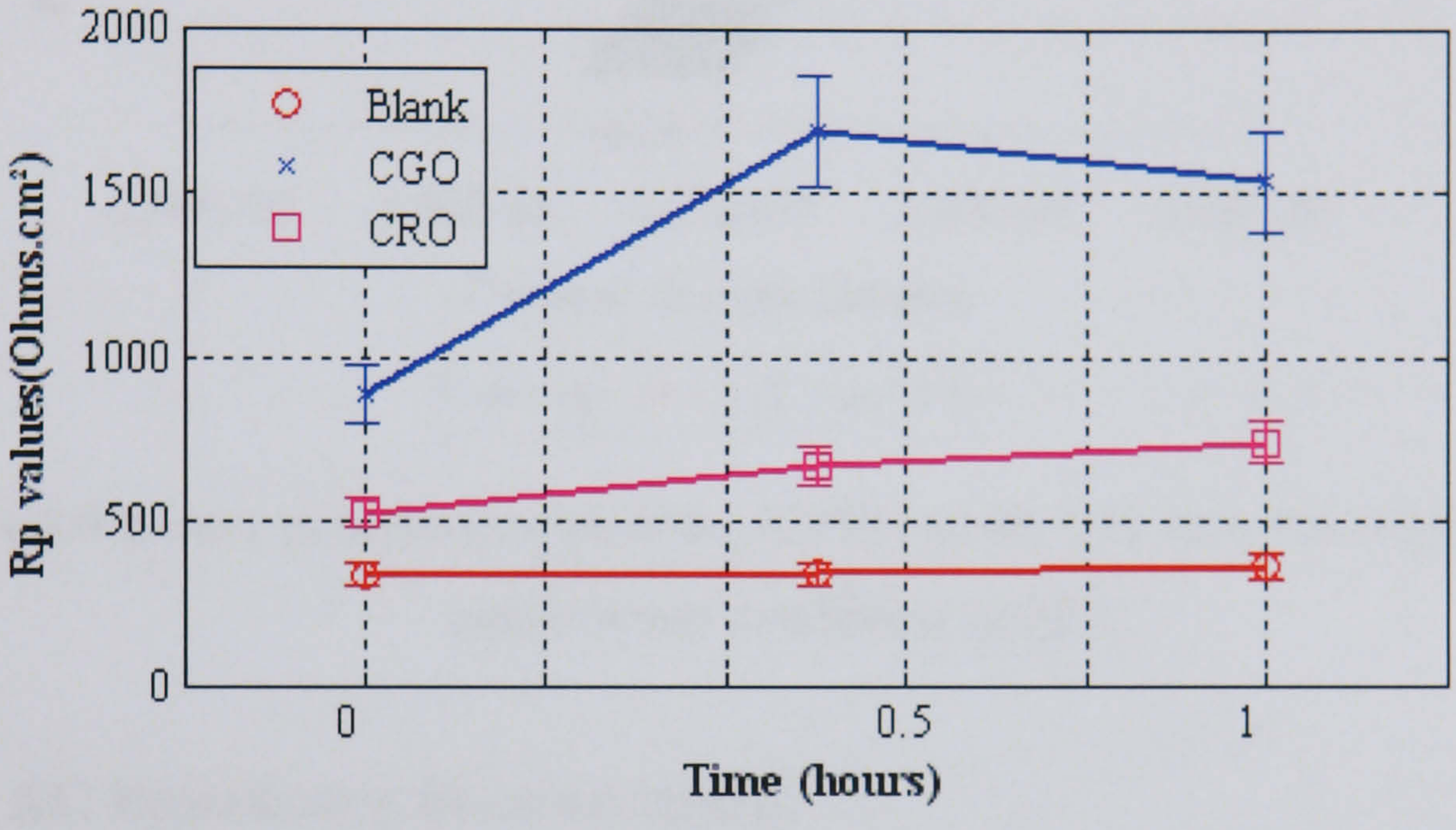

Figure 5.7 The comparison of R_p values versus time for inhibitor CGO, CRO and blank solution at 20°C under static conditions

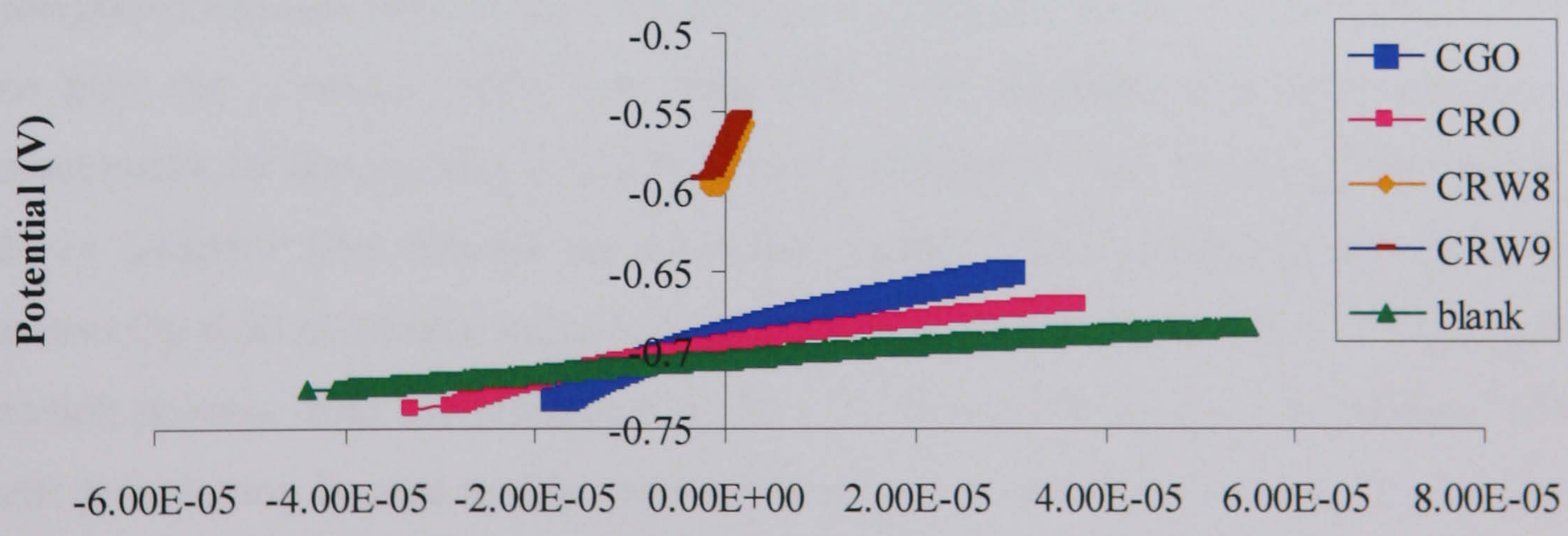

Figure 5.8 The linear polarisation plots for inhibitors after 1 hour immersion time under static condition and 20°C

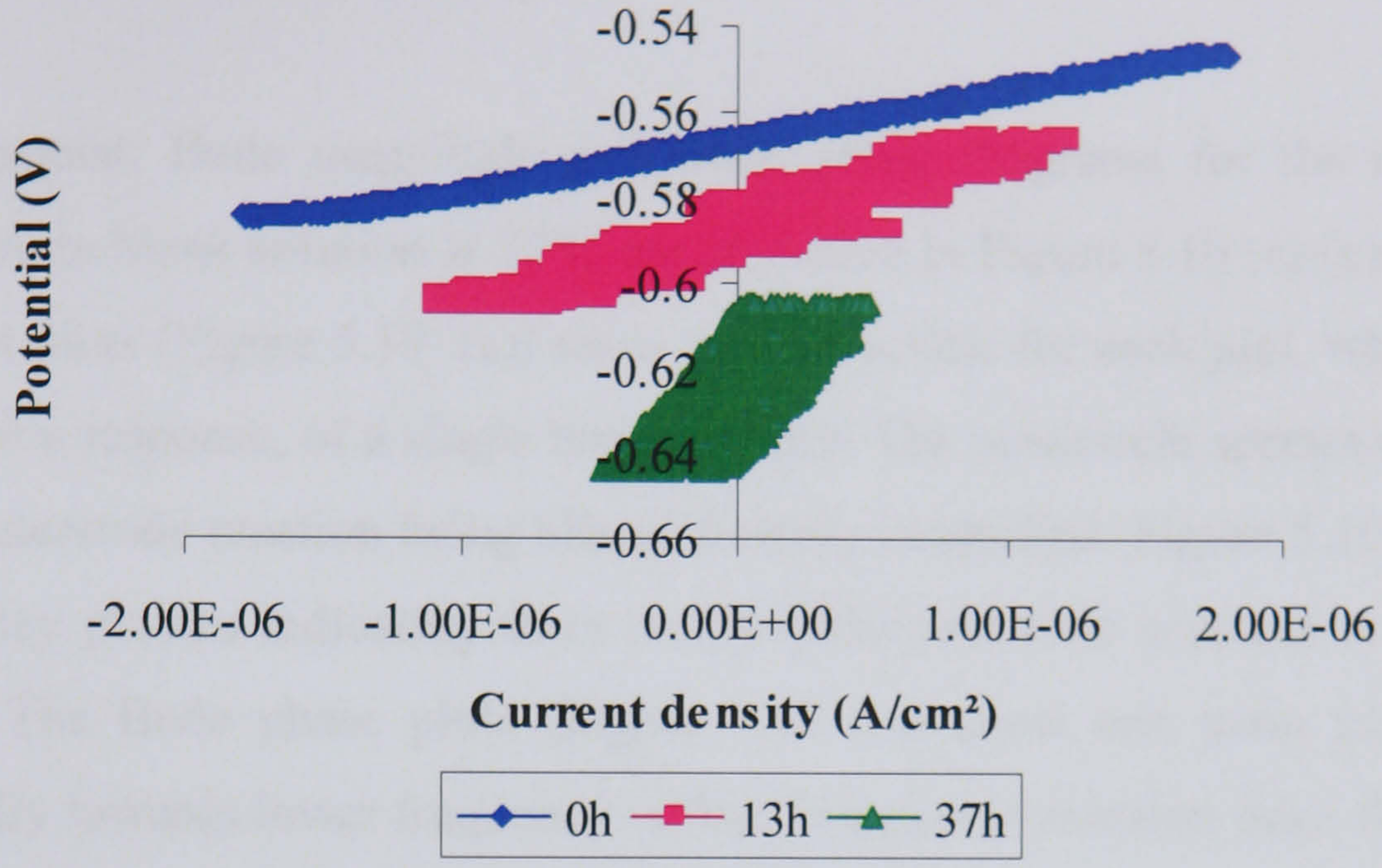

Figure 5.9 Linear polarisation plots for CRW9 at 0h, 13h and 37h immersion time under static conditions at 20°C

5.3 AC Impedance Measurements

AC impedance is used to investigate corrosion behaviour of the carbon steel with and without inhibitor film formed on the metal surface under static conditions. It is also used to understand the inhibitor film characteristics. Mass loss measurements give only an integrated measurement of the total damage occurring over the test period but do not show how the corrosion rates vary with time. The accuracy of linear polarisation measurements in determining corrosion rates is reduced if there is a corrosion product scale or inhibitor film formed on the metal surface. This is because the technique measures the total resistance and does not separate the resistance of the electrochemical corrosion process from the resistance of the corrosion products scale or inhibitor film. Linear polarisation is used in this work and can give a semi-quantitative idea and good indication of correct equivalent circuit (EC) selection for analysis of AC impedance data. Even much different corrosion resistance value can fit the same electric circuit well. Fitting results with charge transfer resistance similar to R_p values can lead to correct AC impedance data.

5.3.1 Blank Solution Tests

The Nyquist, Bode magnitude and Bode phase diagrams for the carbon steel after exposure to blank solution at 20°C are presented in Figure 5.10 (a)-(c) respectively. The Nyquist plots (Figure 5.10 (a)) show one semicircle for each plot, which is typical of a capacitive response, of a single time constant. The semicircle spectra can be interpreted as the electrode reaction being charge transfer controlled. Figure 5.10 (b) shows a high frequency plateau indicating there are no additional time constant at higher frequency range. The Bode phase plots (Figure 5.10 (c)) show one main peak and it shifted gradually towards lower frequency within 31 hours immersion time, then it stays at low frequency of 1 Hz, but the peak value of the angle decreased with time, indicating that corrosion rate increased with time.

After the experiment data were obtained, Zview program was used to fit the experimental data with electrical equivalent circuits (EC). The EC presented in Figure 5.11 is used to characterize the corrosion behaviour of the carbon steel immersed in the blank solution. The equivalent circuit has been used in several research works to model the single time constant system in blank solution tests, which there is no protective film formed on the metal substrate (Mansfeld *et al.*, 1993). Charge transfer resistance (R_{ct}) and double layer capacitance (CPE_{dl}), were obtained. It is to note that the CPE is used to take into account the inhomogeneity of the electrode due to the variation of the roughness along with the time which resulted from corrosion reaction. The constant phase element, CPE, contains two parameters, CPE and α. α is a general diffusion related element which has no physical interpretation. CPE is used in the following studies to obtain approximate values for the capacitance of the systems. α expresses the extent of the depressed semicircle.

The variation of the charge transfer resistance R_{ct} and capacitance represented by CPE_{dl} obtained from curve fitting is plotted against time in Figure 5.12. It can be seen that R_{ct} and CPE_{dl} are relatively stable until 47 hours that the R_{ct} dropped while the CPE_{dl} increased. The rapid drop of the R_{ct} indicates pitting initiation on the metal surface. This was confirmed by microscopy as will be discussed later.

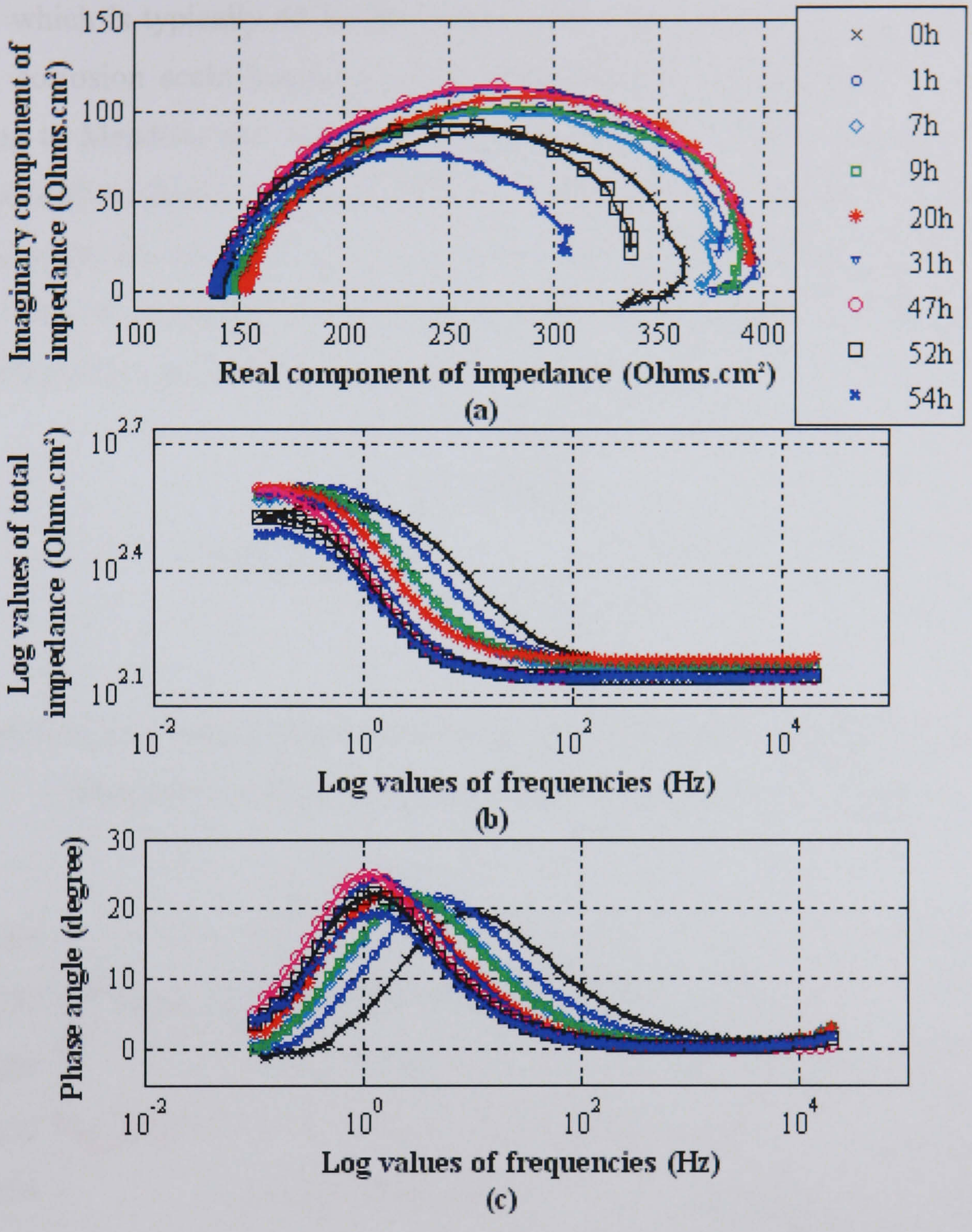

Figure 5.10 Impedance spectra for blank tests at 20°C (a) Nyquist, (b) Bode magnitude and (c) Bode phase plots at 0, 1, 7, 9, 20, 31, 47, 52 and 54 hours immersion time

The increase of the CPE_{dl} values is associated with the change of the double layer characteristics. It is due to the dissolution of the surrounding ferrite (α-Fe) from pearlite leave a lamellar structure of non-oxidized Fe_3C, which is not removed from the metal surface. Thus the surface area increases resulting in increase of capacitance (Lopez *et al.*, 2003). The capacitance value is very sensitive and can be used to detect very low corrosion process. The C_{dl} is larger than the C_{dl} of iron in normal oxygen corrosion

systems, which is typically 40 to 100 microF/cm². This could have been caused from the CO_2 corrosion scale having a much larger surface area (Kinsella *et al.*, 1998). According to Mendoza and Turgoose (2002), the increase in the capacitance value is associated with an increase in the surface area available for the cathodic reaction, which is related to the electrochemical activity of the non-oxidized cementite (Fe_3C) residue exposed after the corrosion process. At the same time, it leads to a decrease in the values of R_{ct} with time which is in agreement with this work.

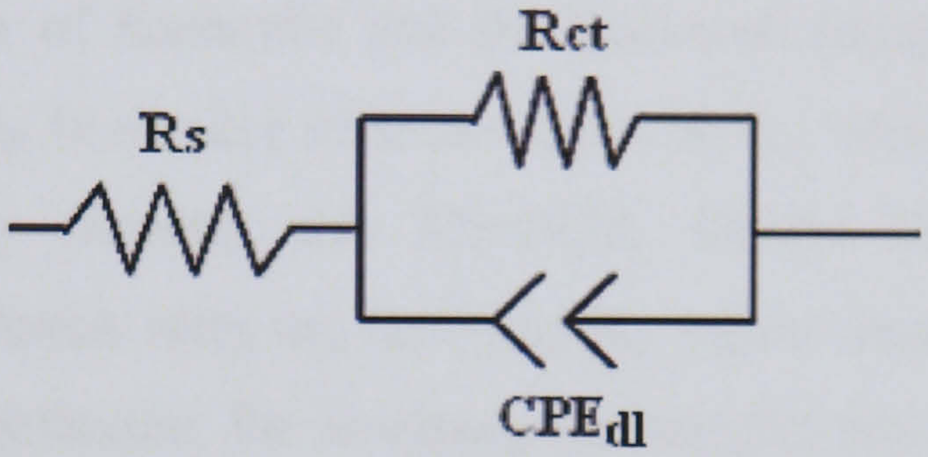

Figure 5.11 Equivalent circuit used to fit the impedances obtained in the CO_2 saturated solution with no inhibitor (Mansfeld *et al.*, 1993)

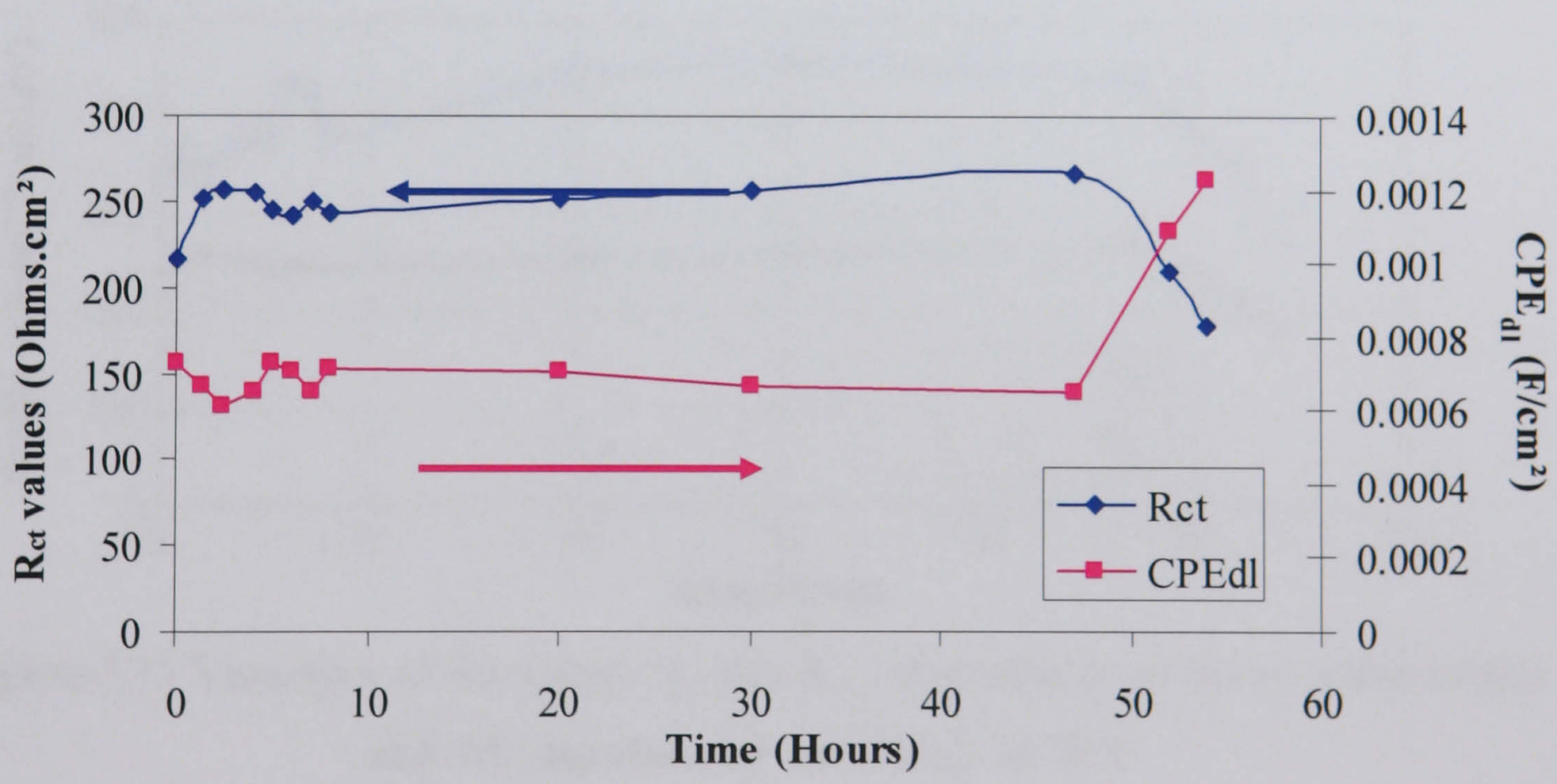

Figure 5.12 Variation in the values of R_{ct} and CPE_{dl} obtained from curve fitting for blank tests at 20°C under static conditions

Figure 5.13 presents the comparison of R_p values and R_{ct} values for blank tests at 20°C. It can be seen that there is differences between them, from 80-200 Ohms.cm² with average of 143 Ohm.cm². Although both values followed the same trend, however the R_p values show more fluctuation than R_{ct}. As the accuracy of the linear polarisation

technique is fundamentally limited by the fact that it is a DC measurement that assumes a steady state is achieved during the measurement. However a corrosion cell is complex impedance compromising both resistive and capacitive components (Silverman, 1990). It must also be noted that the experimental value R_p contains contributions from Ohmic resistances, such as the electrolyte layer between Luggin capillary and test electrode, surface layers, electrical leads, etc. The question, whether R_{ct} or R_p have to be determined for calculation of corrosion rates, had been a goal of a joint programme between the University of Karlsruhe and the Rockwell International Science Centre. They suggested that R_{ct} is smaller than the value of R_p, which is as the same as the results for this study (Lorenz and Mansfeld, 1981). Therefore, the following calculations of the corrosion rates are based on R_{ct} values instead of R_p. But R_p values can still be used as a reference for obtaining meaningful equivalent circuit models in analyzing the AC impedance data.

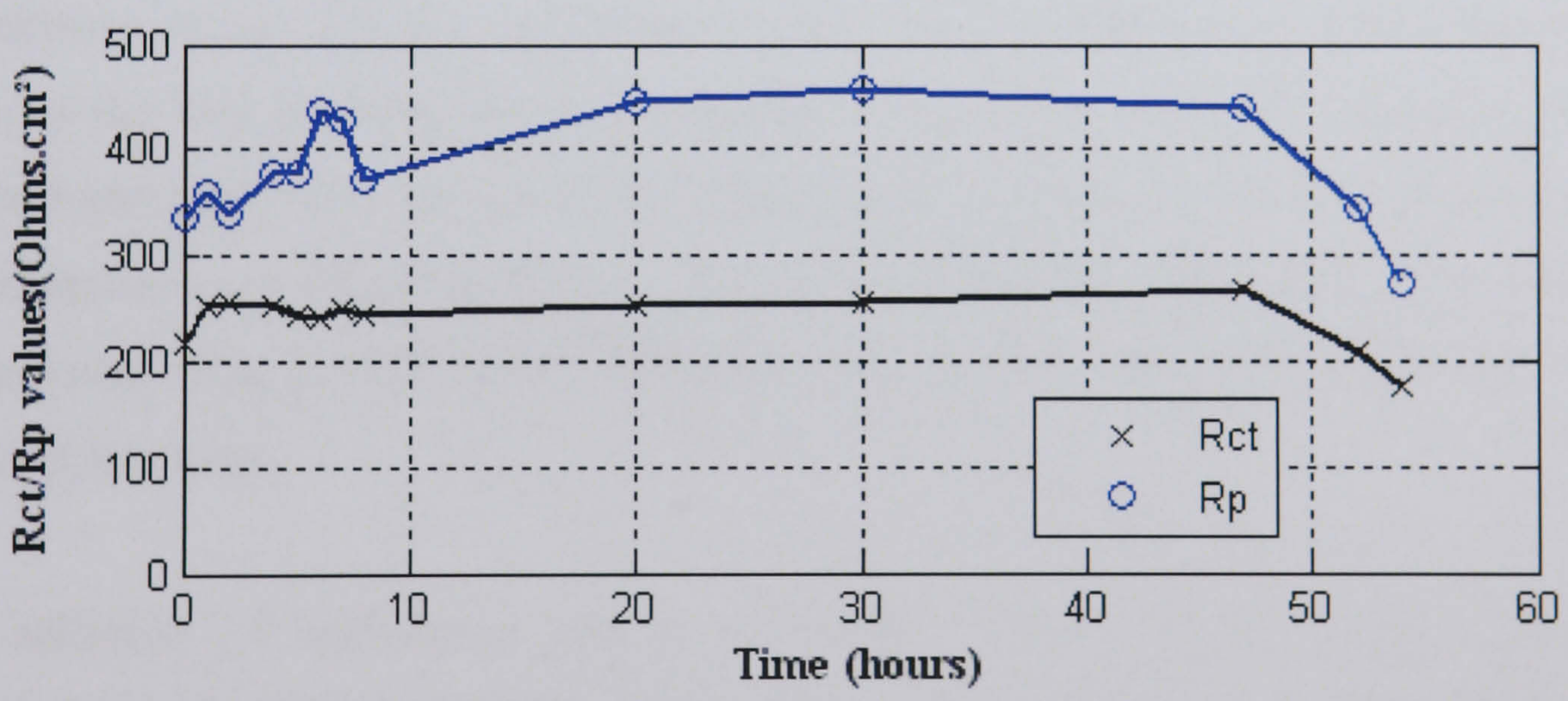

Figure 5.13 Variation of the values R_p and R_{ct} calculated from linear polarisation and AC impedance respectively at 20°C

From the impedance data analysis, it can be summarized by the following features, which can be used as a guideline reference for analysis of the AC impedance data at erosion-corrosion conditions:

1. Nyquist plots show solution resistance decreases with the immersion time. indicating that the dissolution of iron to form iron ions into the solution. R_{ct} decreases with the time
2. Bode magnitude plots show a decrease of the negative slope with time and the decrease of the impedance magnitude with time
3. Bode phase plots show a decrease of the phase angle with time and a shift of the peak phase to the lower frequency direction

5.3.2 With CRW8 Inhibitor

The following experiments were performed under static conditions at 20°C to see how and what protection the inhibitor can provide. Although inhibitor testing should be performed under experimental conditions simulating those in the field, a clear understanding of mechanism and kinetics of the corrosion inhibition processes makes it necessary to provide the information under static conditions at which the inhibitor shows the best performance as a reference. Two inhibitors, CRW8 and CRW9, were monitored until the corrosion resistance starts to drop. In order to compare the performance of CRW inhibitors, tests with inhibitors CGO and CRO also were conducted. Due to their lower efficiency, they are only tested for 0, 0.5 and 1 hour's immersion time.

A selection of impedance spectra according to the increase of the diameter of semicircles for inhibitor CRW8 tests under static conditions are presented in Figure 5.14 (a)-(c) for Nyquist, Bode magnitude and Bode phase plots respectively.

Nyquist plots (Figure 5.14 (a)) show unfinished semi-circular curves, which increased in diameter for up to 97 hours immersion. The diameter of the curves then reduced after 101 and 102 hours immersion time. However from 48 to 83 hours there was no change of the impedance data. This indicates that during this period the inhibitor film is stable and one possibility is that the formation and destruction reach equilibrium. The continuous increase in the diameter of Nyquist semi-circles during the 97h of filming process suggests that the presence of inhibitor greatly but gradually changed the

corrosion kinetics on the electrode surface. The constant increase of arc diameter is generally significant for inhibition and the appearance of unfinished arcs is the consequence of slow diffusion through the film containing adsorption inhibitors on the metal surface (Esih *et al.*, 1995). This proves the existence of two rate-determining steps for the corrosion process with different time constants (Esih *et al.*, 1995). However, the number of time constants is difficult to determine from the Nyquist diagram. More information can be obtained from the Bode phase diagram presented in Figure 5.14 (c).

The Bode phase plots (Figure 5.14 (c)) show broad peaks indicating two time constants overlapping to each other. At 0 hour immersion time, the phase angle of the first time constant at high frequency appeared at 10^2 Hz, which is associated with the porous layer of the inhibitor film; another phase angle of second time constant at lower frequency, which is attributed to a response of electrochemical processes at the inhibitor film/metal substrate interface. After 1 hour, the two time constants overlapped at 10^0-10^1 Hz due to the close time constant values. At this initial immersion time the phase angles show lower protection due to the pores of the inhibitor film. The peak values increase with time until 97 hours immersion time; it indicates that the inhibitor film becomes denser and compact with time. The inhibitor film showed strong self-repairing ability and good persistency under the testing conditions.

The electrical equivalent circuit used to analyse the impedance responses of tests with inhibitor CRW8 under static conditions at the initial exposure and 101, 102 hours, is presented by the equivalent circuit in Figure 5.15 (a). It has been suggested that the AC impedance spectra for the metal covered by organic inhibitor films are very similar to failed coatings (Mansfeld, 1990). This is a general equivalent circuit model proposed to ascribe two sub-electrochemical interfaces and is used commonly to simulate an electrode surface with a low conducting surface film present. The nested circuits are used to indicate that pores in the film that can cause corrosion by providing areas where the electrolyte has direct access to the metal surface as illustrated by the interface model shown at the right part of Figure 5.15 (a). When there are pores within the inhibitor film, the active species of the electrolyte can pass through the pores to approach the

metal surface. Therefore the electrochemical processes with inhibitor include both electrochemical kinetic and diffusion processes (Esih *et al*., 1995).

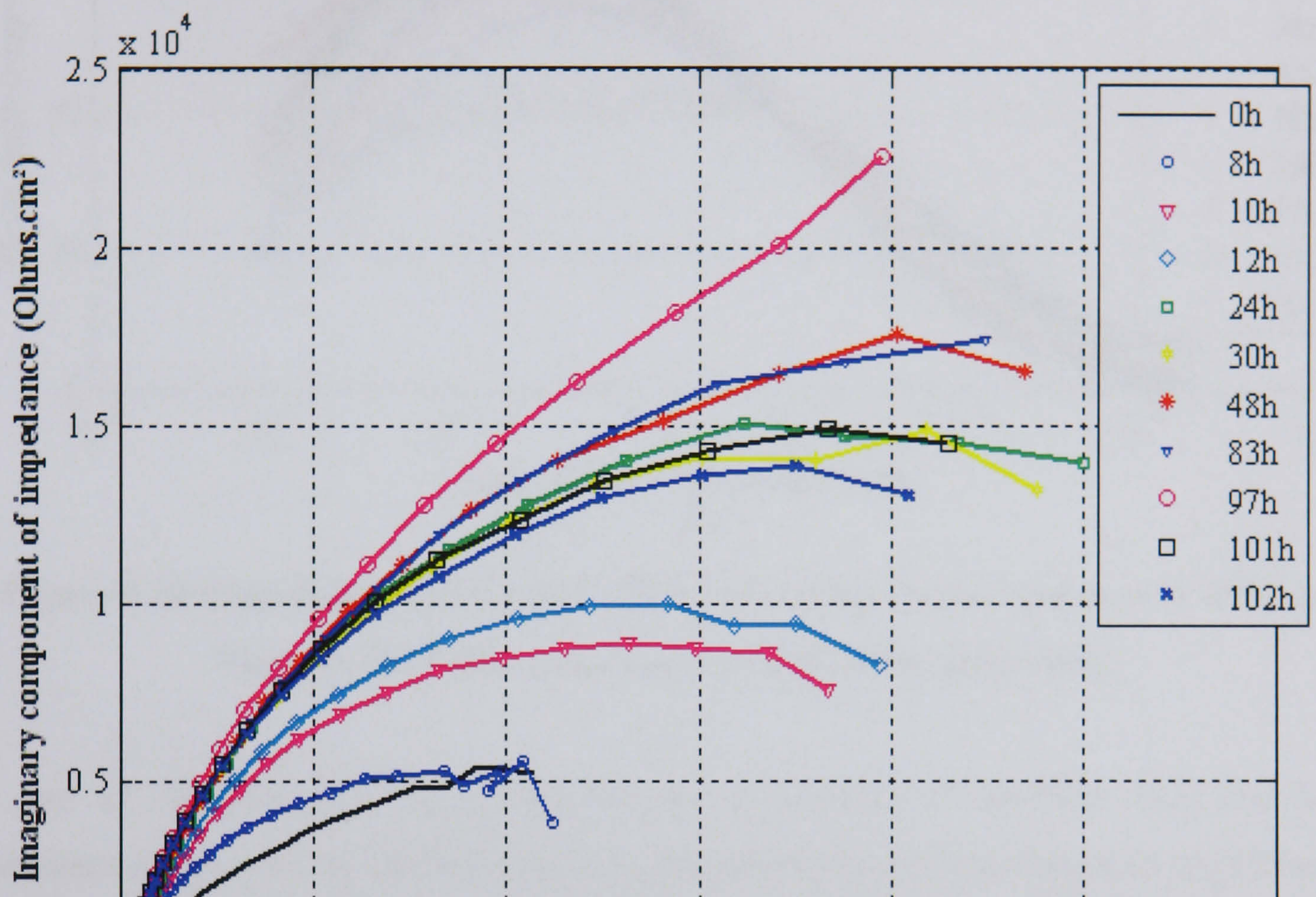

(a)

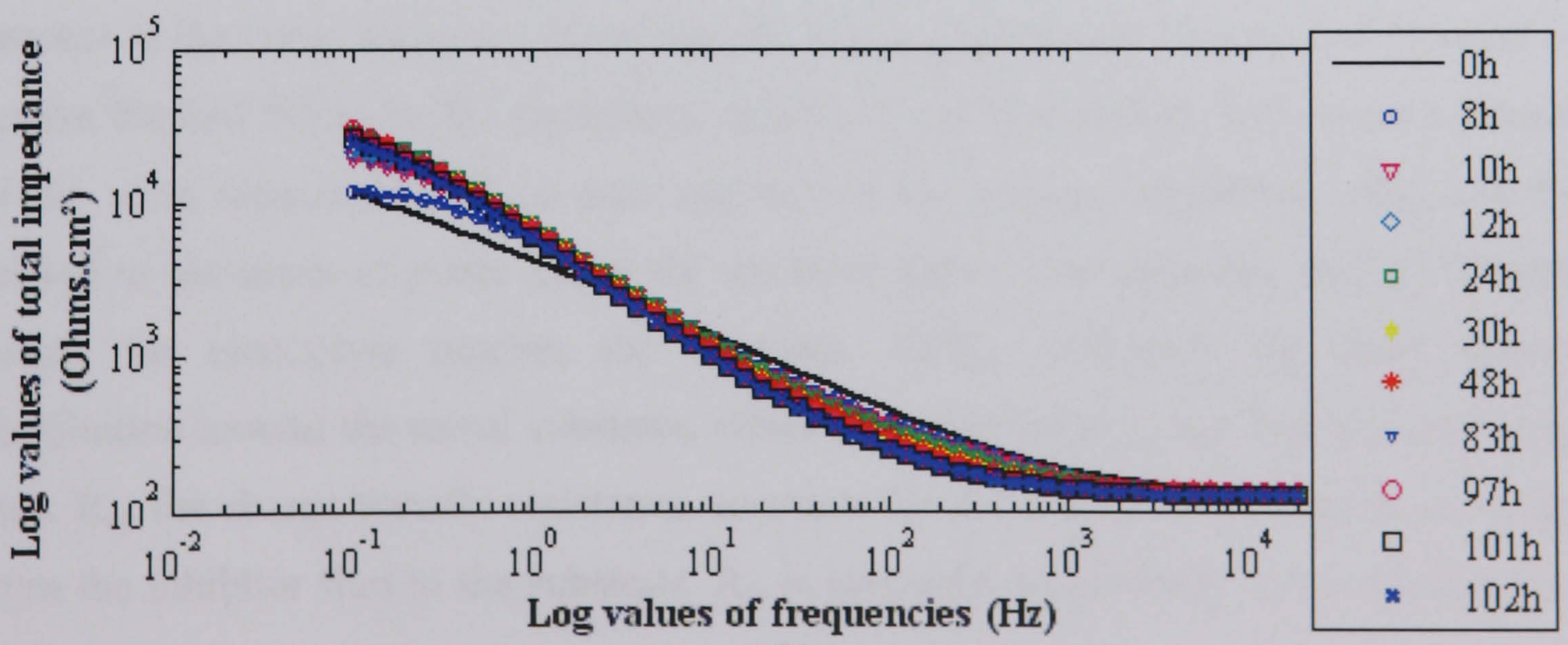

(b)

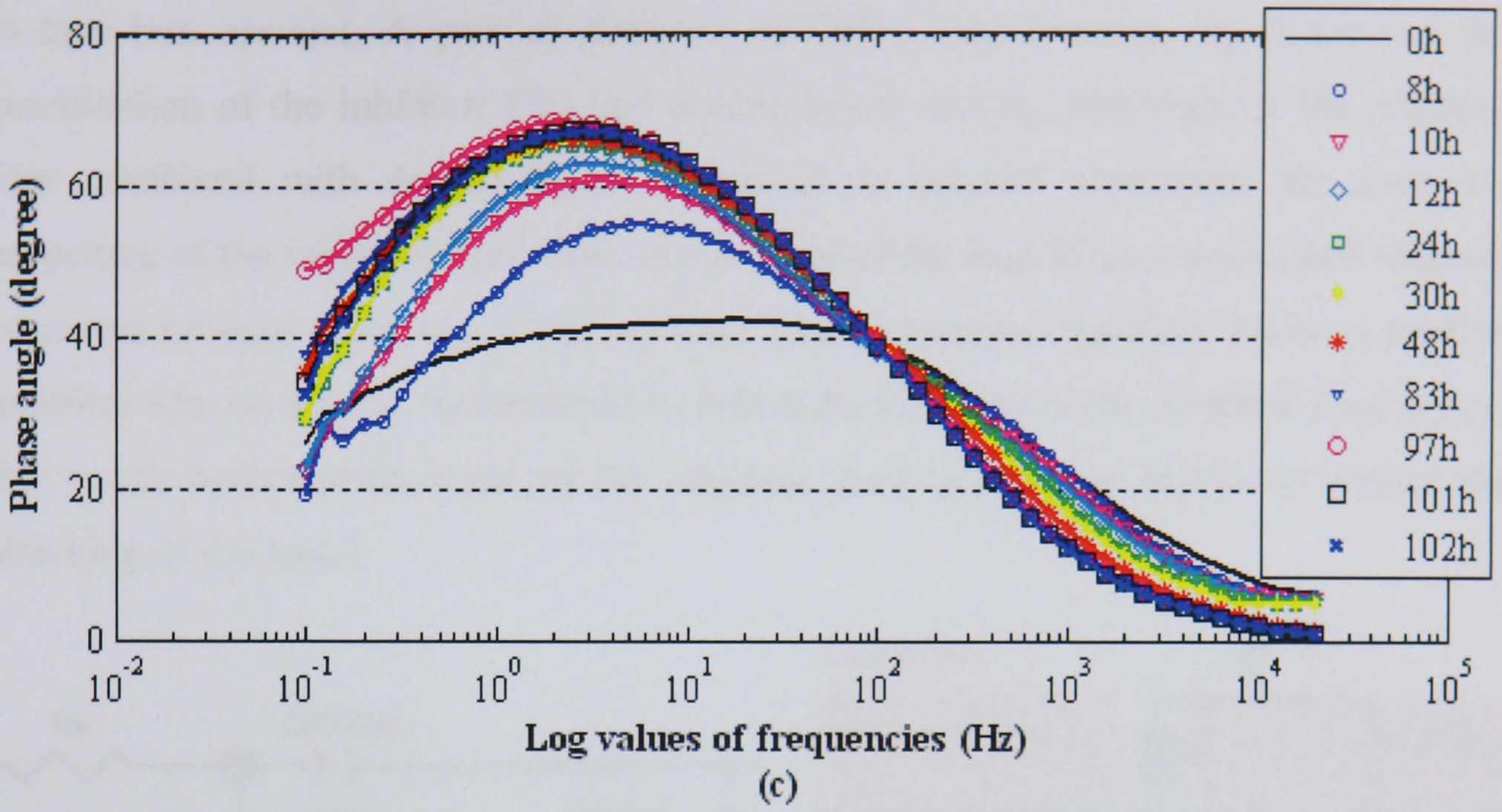

(c)

Figure 5.14 Impedance spectra of CRW8 tests under static condition at 20°C (a) Nyquist, (b) Bode magnitude, and (c) Bode phase plots

A pair of elements of CPE_{film} (representing capacitance of inhibitor film) and R_{film} (resistant of pores of the inhibitor film) in parallel represents the dielectric properties of the inhibitor film. Another pair of CPE_{dl} (representing capacitance of the electrical double layer on the metal substrate) and R_{ct} (resistance of the metal substrate, namely charge transfer resistance) in parallel was adopted to describe the charge transfer process at the metal substrate. However, the general model can be modified in order to realize the best fitting to AC impedance data from inhibitor system. CPE is used instead of the ideal capacitance (C) to take account of the surface irregularity. R_{film} can be related to the areas of pores inside the inhibitor film to the substrate surface through which the electrolyte reaches the interface. CPE_{dl} represents the ionic charge distribution around the metal substrate, which is proportional to the exposed corroding area. R_{ct}, the charge transfer resistance, accounts for the resistance to transfer of charge from the inhibitor film to the substrate. R_{ct} is inversely proportional to the surface area under corrosion.

The equivalent circuit shown in Figure 5.15 (b) is used to simulate the behaviour of the inhibitor at 1-97 hour exposure time. At this duration, the inhibitor film has been built up to a very denser film covering the entire carbon steel surface. The pores are too small

to take into account. A pair of elements of CPE_{fdl} (representing capacitance of the combination of the inhibitor film and double layer) and R_{fct} (resistant of the inhibitor film combined with double layer resistance) in parallel represents the dielectric properties of the inhibitor film. The combination of the $R_{fct}CPE_{fdl}$ is associated with the corrosion process occurring at the inhibitor film/electrolyte interface. There is another inhibitor film on the top, which could be called the top layer of the inhibitor film. It may due to the hydrocarbon chain of the inhibitor forming another barrier to protect the attacking of the metal.

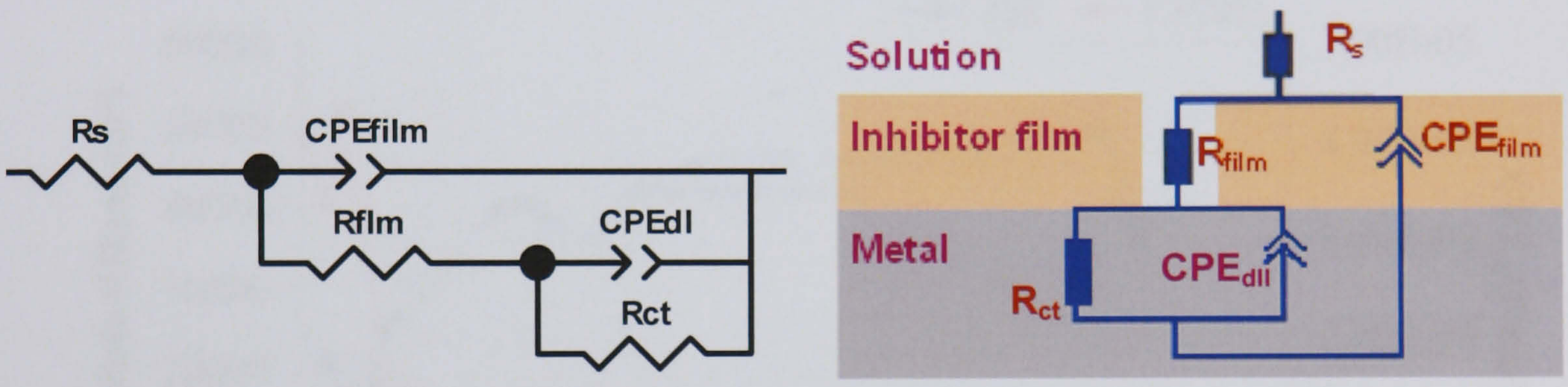

(a)

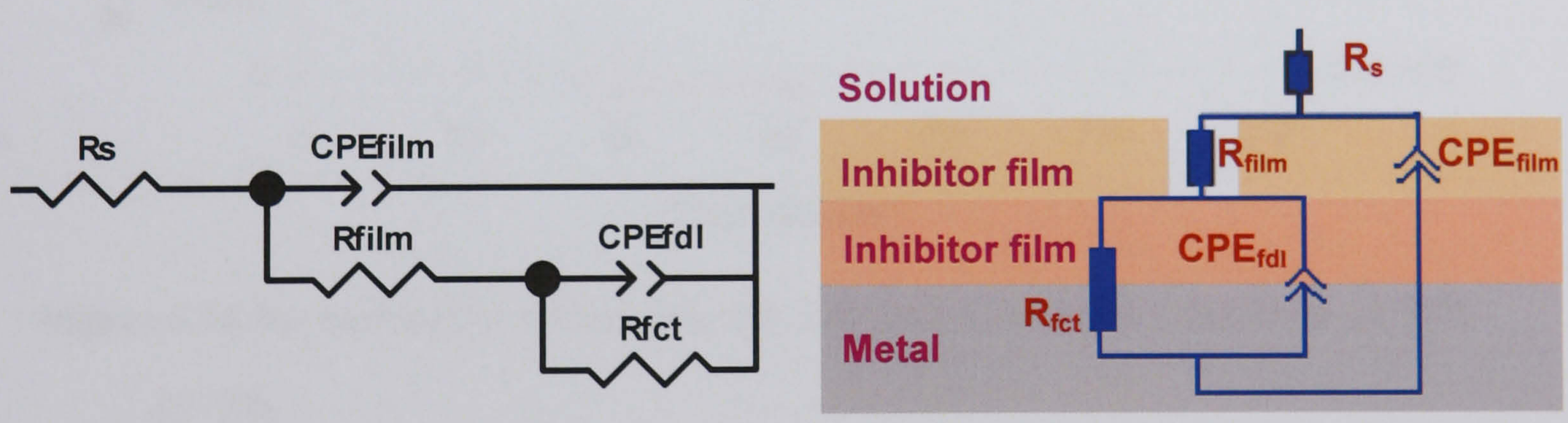

(b)

Figure 5.15 The equivalent circuits for tests with inhibitor CRW8 under static conditions at 20°C: (a) 0, 101 and 102 hours (b) 1 -97 hours

The R_{ct} and C_{dl} (represented by CPE_{dl}) values derived from AC impedance versus immersion time are shown in Figure 5.16. Upon immersion the value of R_{ct} increased from an initial value of 14744 Ohms.cm² to a maximum value of 61542 Ohm.cm² after 97 hours, and then it started to drop to 35739 Ohms.cm². The average value of R_{ct} is used to calculate the penetration rate and the efficiency of the inhibitor at this condition. The inhibitor efficiency and the penetration rate are shown at end of this section with

those for other inhibitors in Table 5.2. The CPE_{dl} values are much smaller than those recorded for the blank solution. The reduction factor ψ = 94.2% for C_{dl}, indicates the effect of inhibition basically depending upon C_{dl} and only small part depending upon other components of the equivalent circuit which might be diffusion.

The resistance of the inhibitor film is about 2000 Ohms.cm² at initial time, and the top layer resistance has an average value of 140 Ohms.cm² as shown in Figure 5.17.

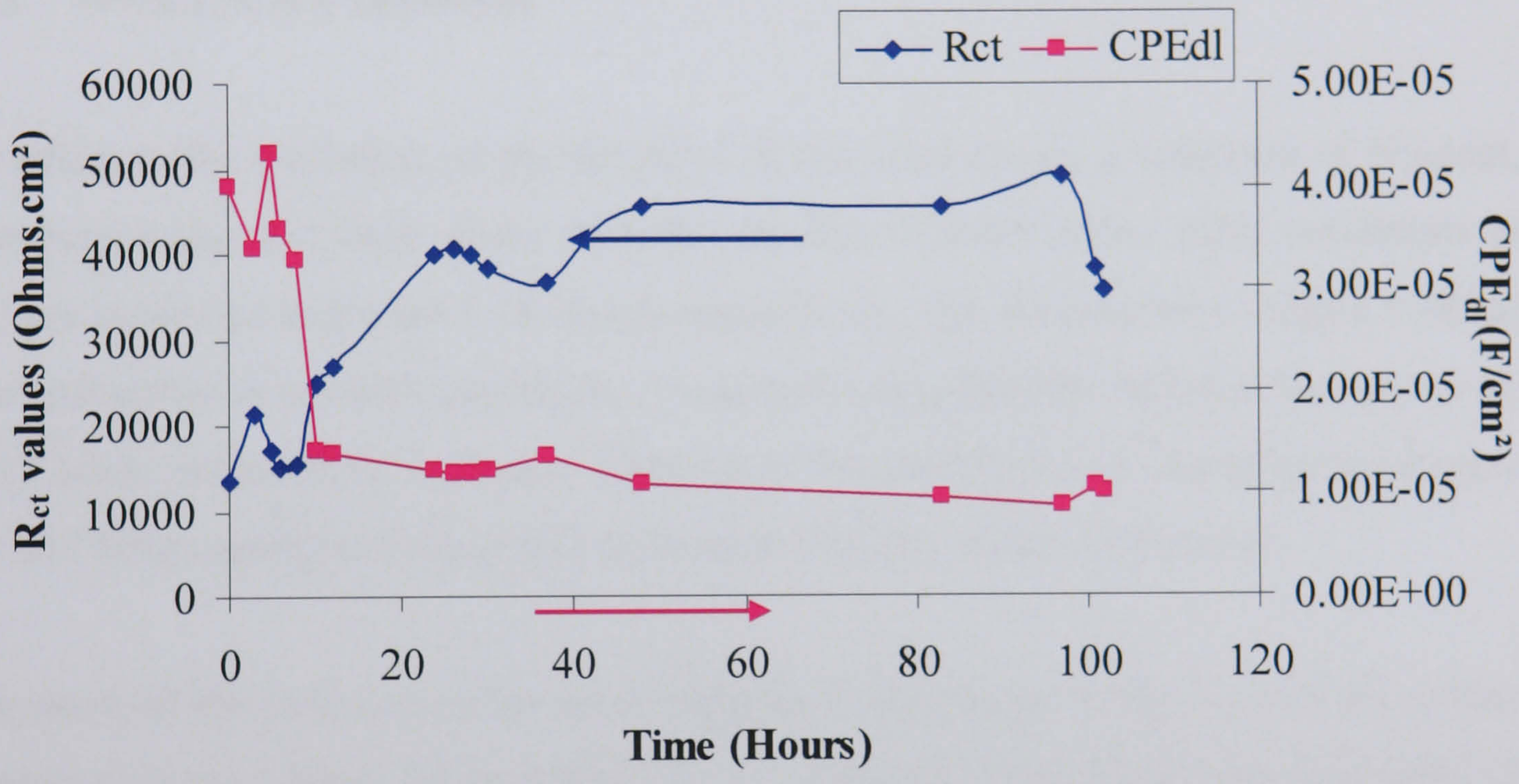

Figure 5.16 R_{ct} and CPE_{dl} versus time for CRW8 under static conditions at 20°C

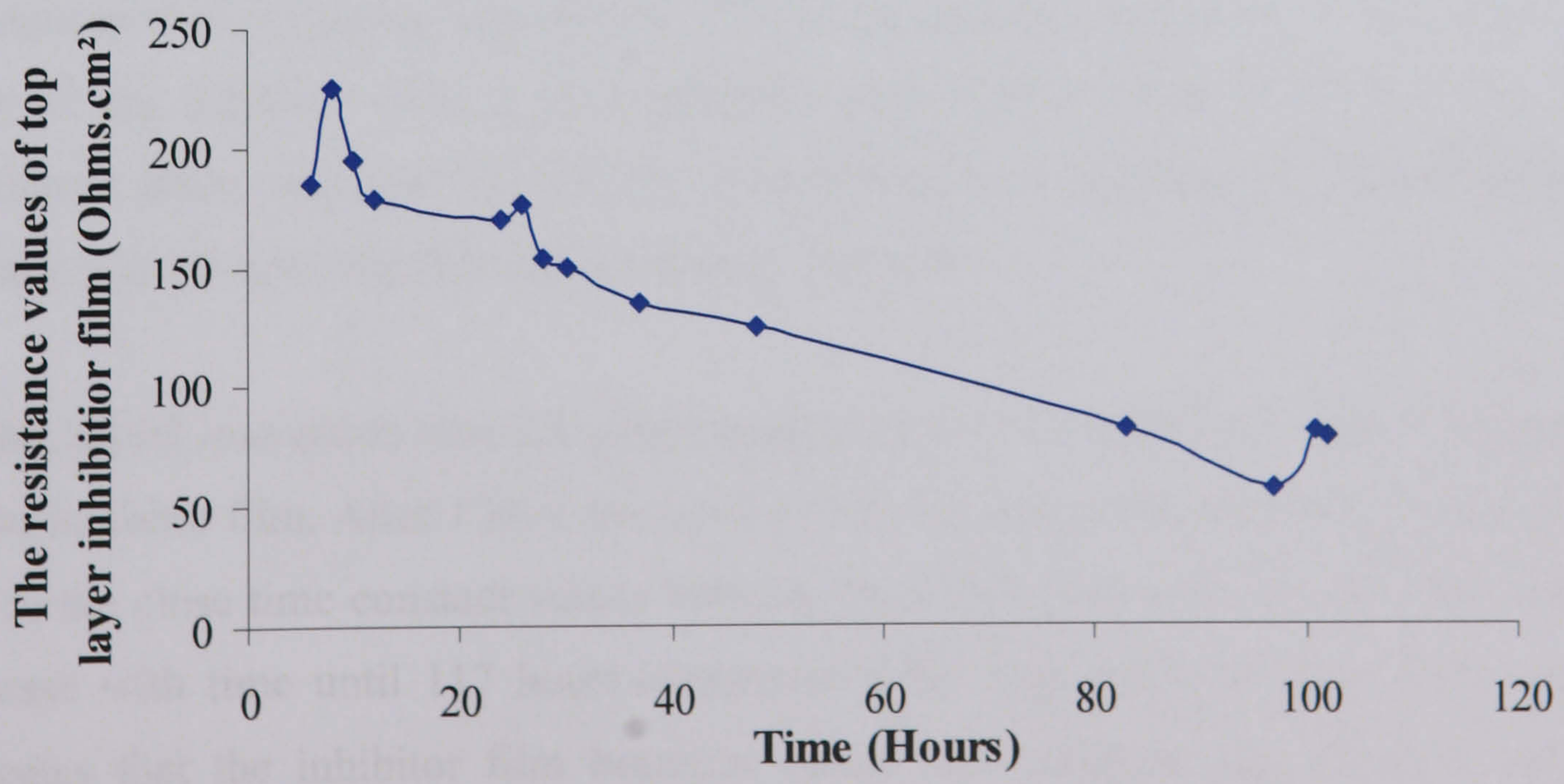

Figure 5.17 The film resistance values versus time for inhibitor CRW8 under static conditions at 20°C

The continuous formation of inhibitor film may result in both an increase of the film thickness and a decrease of the porosity. The increase of inhibitor film thickness could prevent the transportation of electrochemical active species from bulk solution on the metal surface and change the anodic or cathodic energy barriers (Cao, 1996). The decrease in R_{ct} was also accompanied by a corresponding increase in the C_{dl} values, suggesting an increase in the exposure area to the electrolyte.

5.3.3 With CRW9 Inhibitor

According to the evolution of the diameter of the semicircles, a selection of Nyquist, Bode magnitude and Bode phase plots for inhibitor CRW9 under static conditions at 20°C are presented in Figure 5.18 (a)-(c) respectively. The Nyquist plots Figure 5.18 (a) show unfinished depressed semicircles. It can been seen that the inhibitor film grows up to 117 hours indicated by increased diameter of the semicircles, followed by a decrease after 117 hours immersion time with decreased diameter of the semicircles.

Bode plots of the modulus of the total impedance, |Z| shown in Figure 5.18 (b) reflect the change in R_{ct} values. From 0 hour to 117 hours, |Z| increases almost half order of magnitude. From Figure 5.18 (c), at 0 hour immersion time, the phase angle of first time constant at high frequency appeared at 10^2-10^3 Hz, which is associated with the porous layer of the inhibitor film. It is overlapped with another peak at 10^0-10^1 Hz. The maximum phase angle at 10^0-10^1 Hz is attributed to a response of electrochemical processes at the inhibitor film/metal substrate interface.

At this initial immersion time the phase angles show lower protection due to the pores of the inhibitor film. After 1 hour immersion time, the two peaks are hard to distinguish due to the close time constant values between these two processes. As the peak values increase with time until 117 hours immersion time, high value of peak phase angle indicates that the inhibitor film becomes denser and compact with time. It can be assumed that from 1-117 hour immersion time, the inhibitor fully adsorbed on the metal surface resulting in negligible pores of the inhibitor film. The phase angle for 136 hour

immersion time exhibits two time constants. It indicates that part of inhibitor film desorbed resulting in pore beginning to appear.

The impedance spectra are very similar for inhibitors CRW8 and CRW9. Therefore, at the initial exposure and 136 hours, the EC used to analyse the impedance responses of tests with inhibitor CRW9 under static conditions, is presented by the equivalent circuit in Figure 5.15 (a), with interface model shown at the right part of it. At 1-117 hours, the EC is the same as is shown in Figure 5.15 (b).

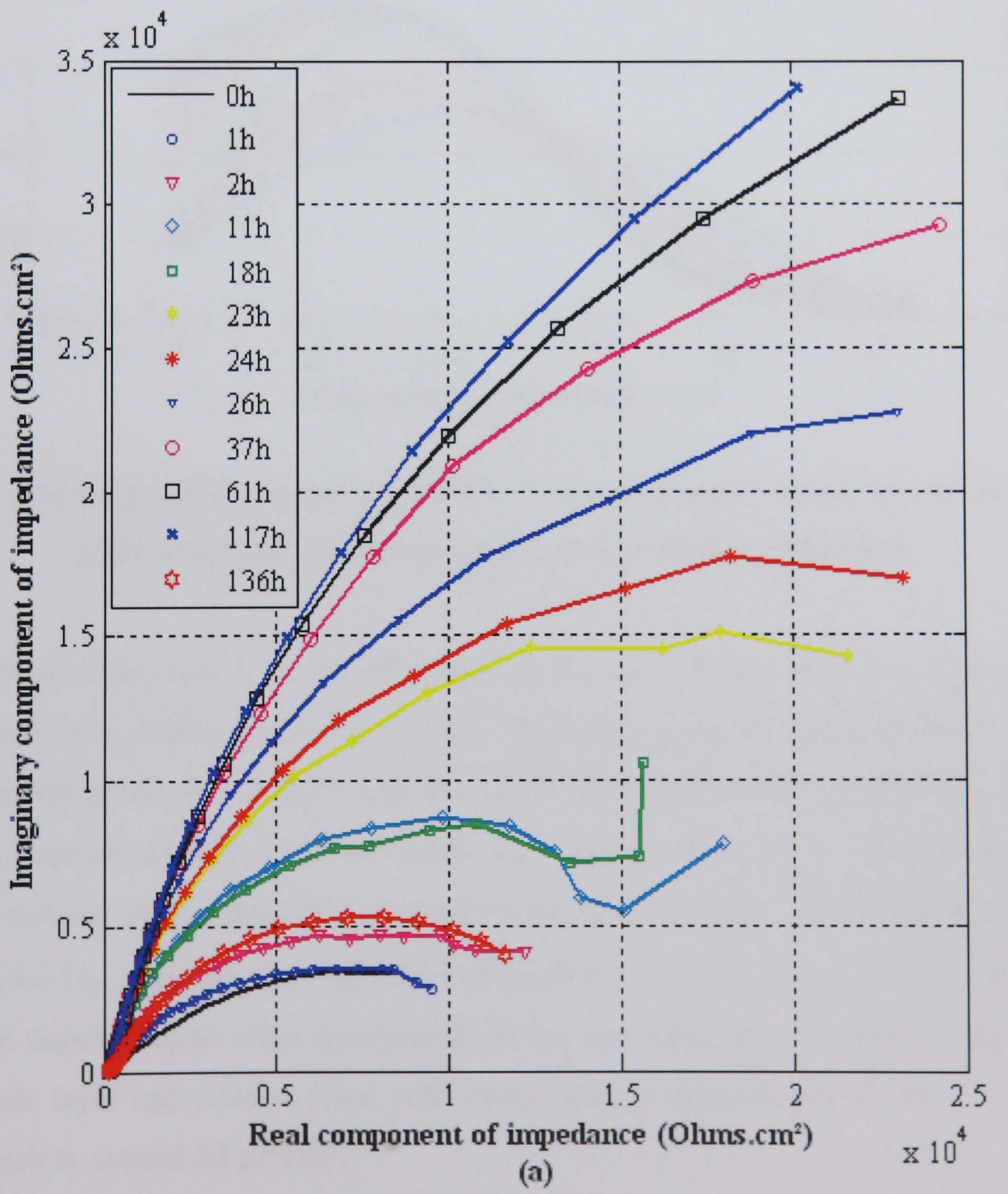

(a)

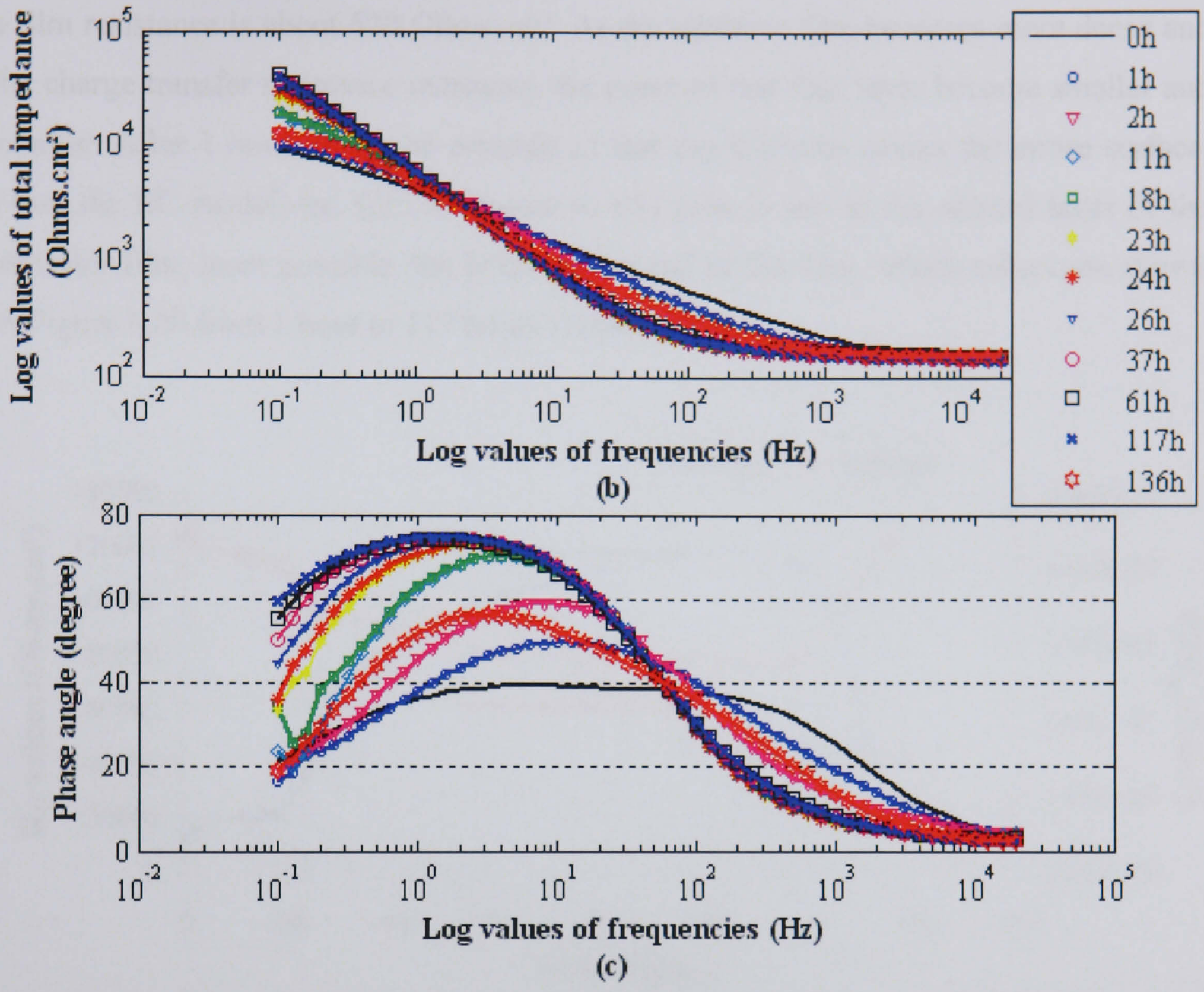

Figure 5.18 Impedance spectra of CRW9 tests under static condition (a) Nyquist plots, (b) Bode magnitude plots, and (c) Bode phase plots

The effect of immersion time on the values of R_{ct} and CPE_{dl} is shown in Figure 5.19. The maximum R_{ct} value reaches to 116000 Ohms.cm². It can be seen that the R_{ct} values are in general agreement to R_p values for both CRW8 and CRW9. It confirms that the equivalent circuits used to fit the AC impedance data are acceptable. The addition of the inhibitor reduces the average value to approximately 35 μF/cm². The reduction factor ψ = 94.2% for C_{dl}, indicates that the effect of inhibitor basically depends on C_{dl} and only small part depends upon other components of the equivalent circuit, might be diffusion. The double layer capacitance value with inhibitor is in agreement with Malik's (1992) study which is around 30 μF/cm².

To summarise the results from these inhibitors, the inhibition process can be explained. At initial immersion, the inhibitor forms a barrier on the top of the metal substrate with

a film resistance is about 520 Ohms.cm². As the inhibitor film becomes more dense and the charge transfer resistance increases, the pores of that first layer become smaller and smaller. After 1 hour, it can be considered that the inhibitor covers the entire surface. From the EC model, the film resistance in this case is due to the second layer of the inhibitor film, most possible, the hydrocarbon tail of the film, which values are shown in Figure 5.20 from 1 hour to 117 hours immersion time.

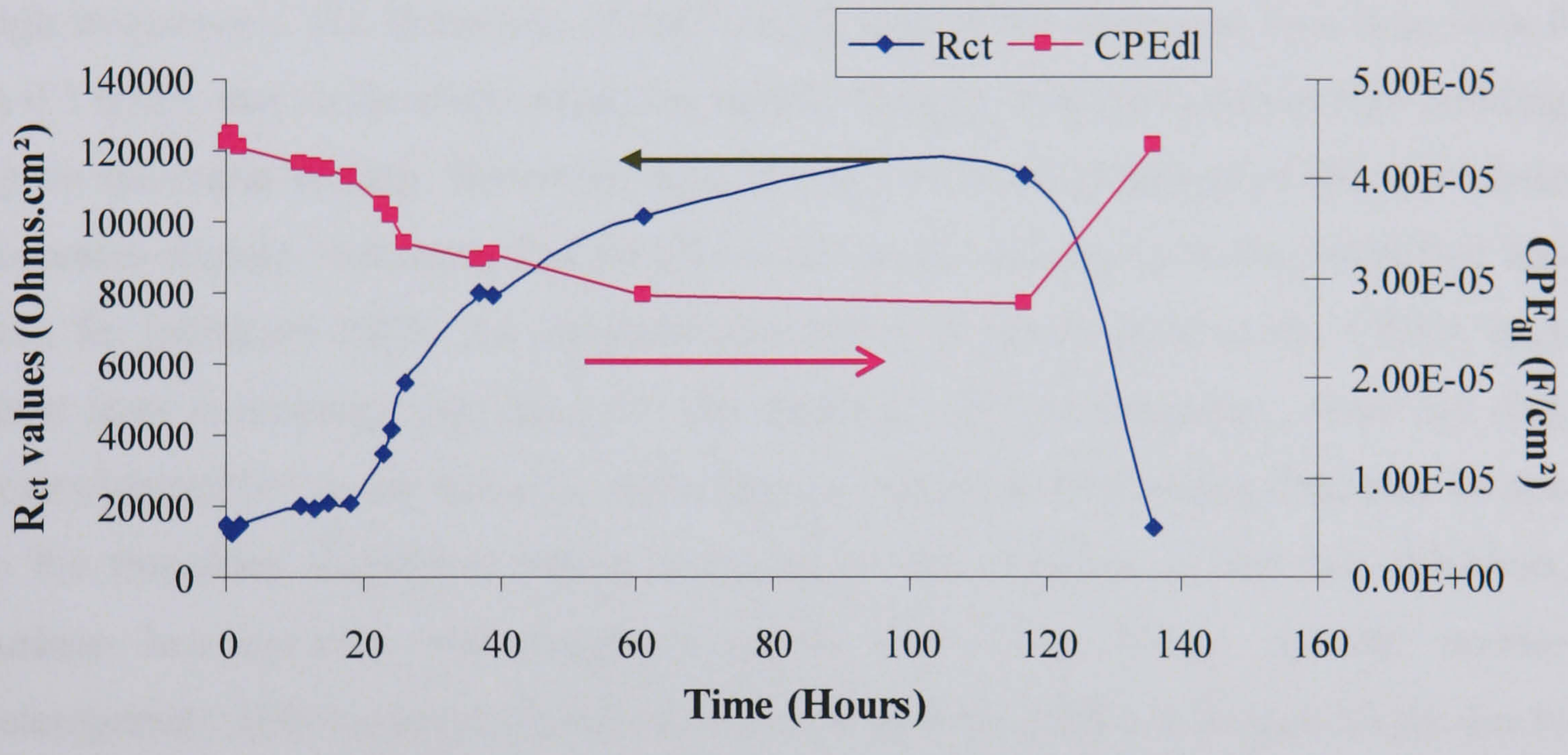

Figure 5.19 Variation in the value of R_{ct} and CPE_{dl} with time at 20°C for CRW9

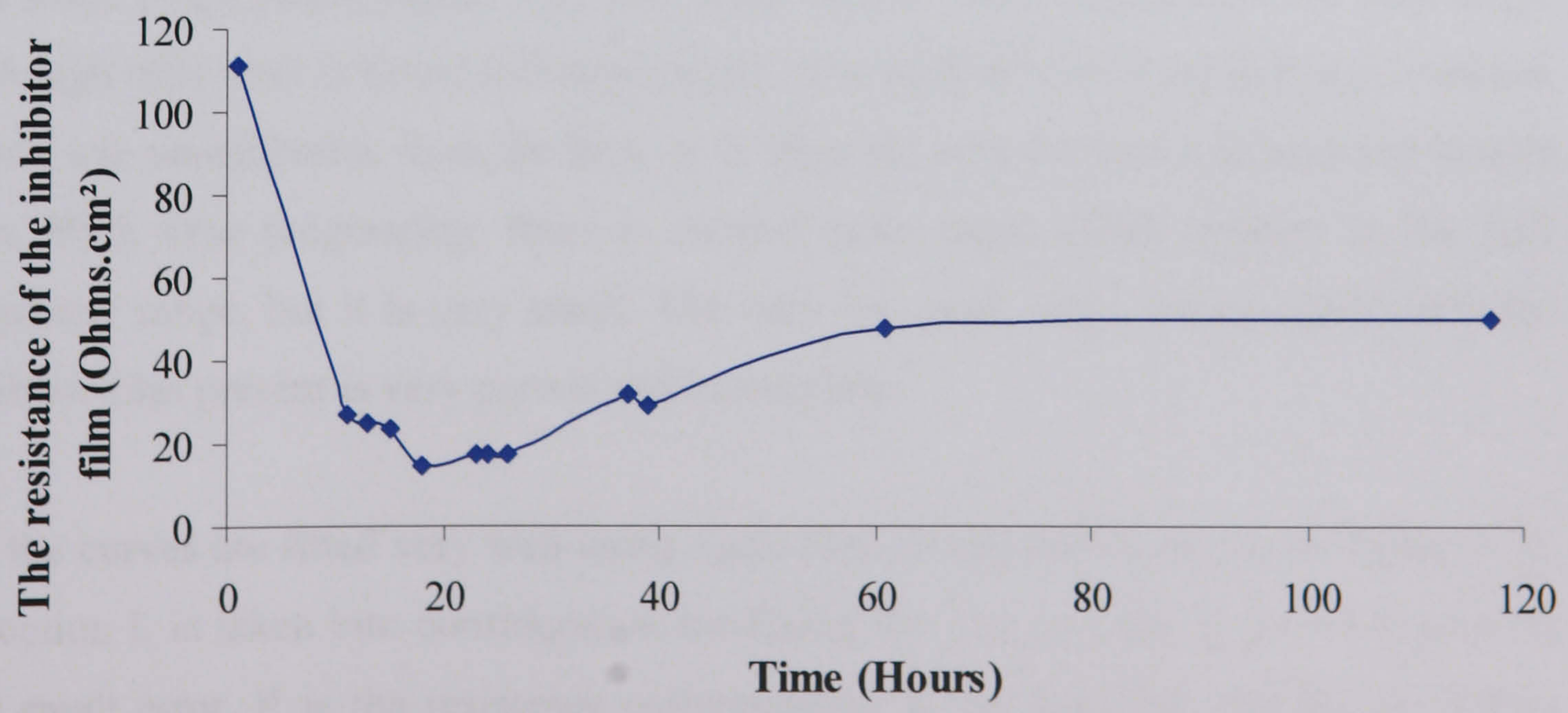

Figure 5.20 The resistance values of the pores from the top layer of the inhibitor film R_{film} versus immersion time for CRW9 at 20°C static conditions

5.3.4 With CGO Inhibitor

AC impedance spectra for inhibitor CGO are shown in Figure 5.21 (a) and (b) for Nyquist and Bode phase plots respectively. Nyquist plots (Figure 5.21 (a)) exhibit a combined semicircle, which is part from small arc from high frequency and part from a semicircle from lower frequency. This is indication of two time constants. The surface films normally have small time constants, which often result in a phase angle peak at high frequencies. The diameters of the Nyquist semicircles increased with time from 0 to 0.5 hours, due to the electrochemical kinetic changes with the inhibitor film building up on the metal surface. However, from 0.5 to 1 hour the diameter of the semicircle decreases slightly, indicating that the film is not likely building up to the extent that was seen for inhibitors CRW. As the protection ability is not as good as the CRWs, only short term monitoring was done for this inhibitor. At low frequency, there are data points located below the real axis, indicating the induction phenomena. This may be due to the frequency dispersion which is caused by the variation in the film thickness, surface heterogeneity and roughness (Cole and Cole, 1941). As the surface heterogeneity and roughness should be the same as with CRWs. It is most likely due to the film thickness difference on the metal surface for oil soluble inhibitor.

The Bode phase plots (Figure 5.21 (b)), show that at initial immersion, the peak angle (although only one) is broad and asymmetric. It is indicative of a second time constant, which was unresolvable from the first, as is often the case for an ill-defined and porous film. With time progressing, there is another peak angle which appears in the high frequency range, but it is very small. The very low peak angle values signify that the inhibitor film present is very porous and incomplete.

All the curves are fitted very well using equivalent circuit model shown in Figure 5.22. Induction L is taken into consideration for fitting the data in order to get very good fit and small error. R is the resistance corresponding to the inductor. The R_{ct} and CPE_{dl} calculated from the curve fitting are shown in Figure 5.23. The average value of inhibitor film resistance is about 72 Ohms.cm^2.

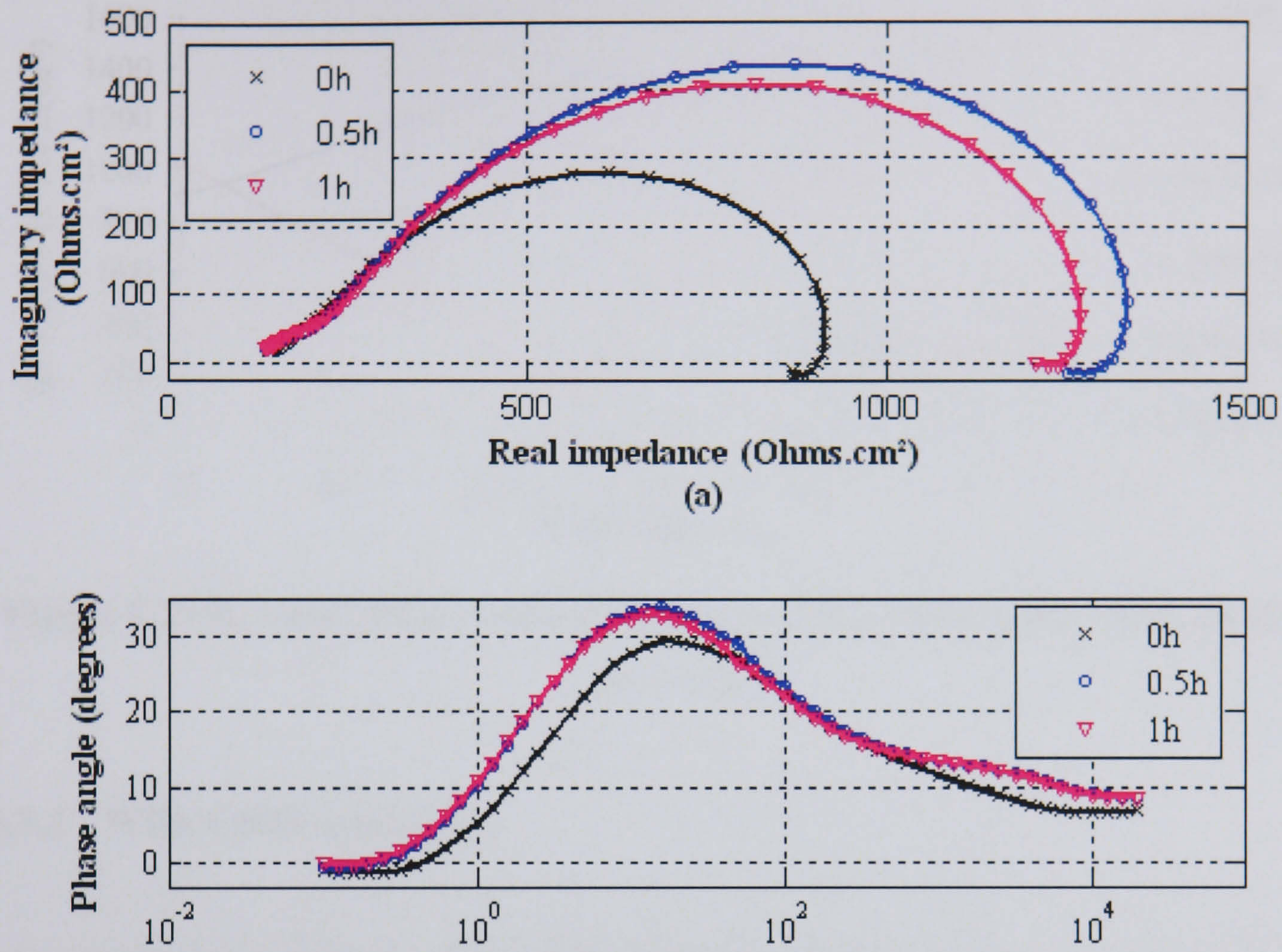

Figure 5.21 Impedance spectra of CGO tests under static condition at 20°C (a) Nyquist plots and (b) Bode phase plots

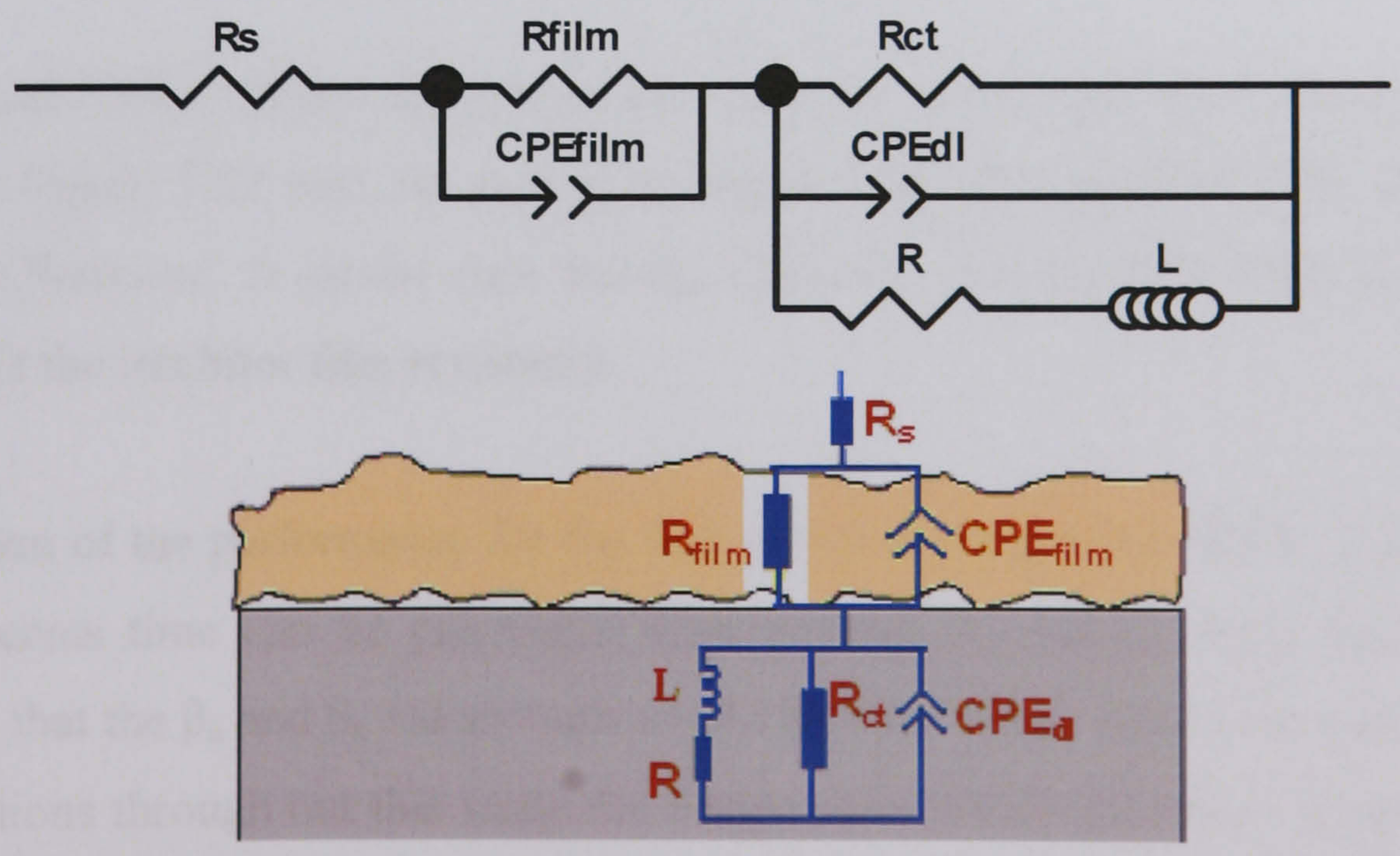

Figure 5.22 The equivalent circuits for tests with inhibitor CGO under static conditions at 20°C

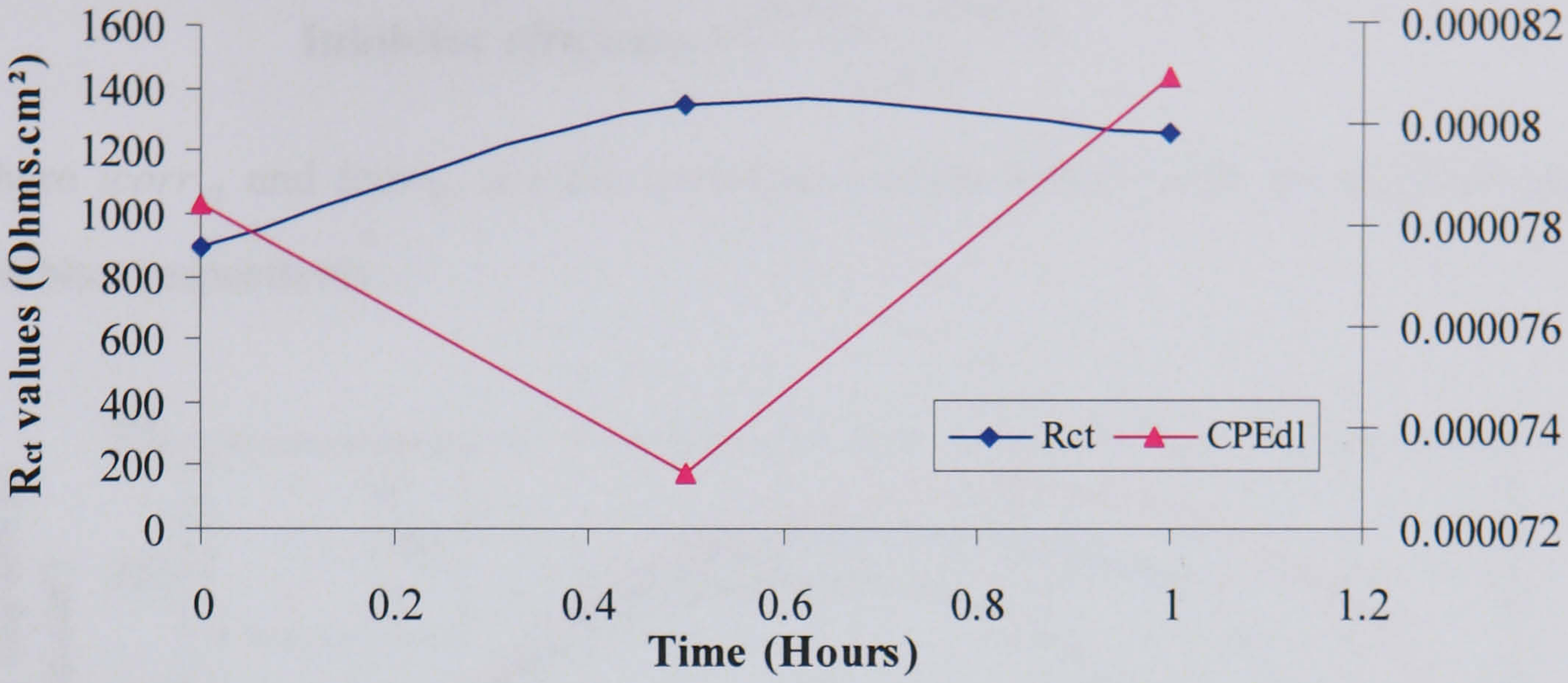

Figure 5.23 R_{ct} and CPE_{dl} values with time for CGO tests under static conditions and at 20°C

5.3.5 With CRO Inhibitor

AC impedance spectra for CRO under static conditions at 20°C are shown in Figure 5.24 (a) and (b) for Nyquist, Bode magnitude and Bode phase plots respectively. The plots are very similar to those for CGO; however the film is still growing within the experimental period. The film performance is not as good as for the CRWs, therefore only short times are considered.

The R_{ct} and CPE_{dl} values are calculated using the same equivalent circuit model as shown in Figure 5.22 and are shown in Figure 5.25. The inhibitor film resistance is about 18 Ohms.cm². It can be seen that the corrosion resistance for CRO is lower than CGO, as is the inhibitor film resistance.

Comparison of the performance for the four inhibitors is given in Table 5.2. Corrosion current versus time can be calculated from average R_{ct} values using Equation (28), assuming that the β_a and β_c values both are 0.12V/dec. These values are assumed for all the conditions through out this study for comparison, which the same values were used by Palacios and Shadley (1993). Using the average values of i_{corr}, corrosion rates are calculated in mpy. The inhibitor efficiencies for the four inhibitors can be calculated from following equation (83) :

$$\textbf{Inhibitor efficiency} = \frac{icorr_{NI} - icorr_{WI}}{icorr_{NI}} \tag{83}$$

where $icorr_{NI}$ and $icorr_{WI}$ are the corrosion current density with no inhibitor and with inhibitor respectively.

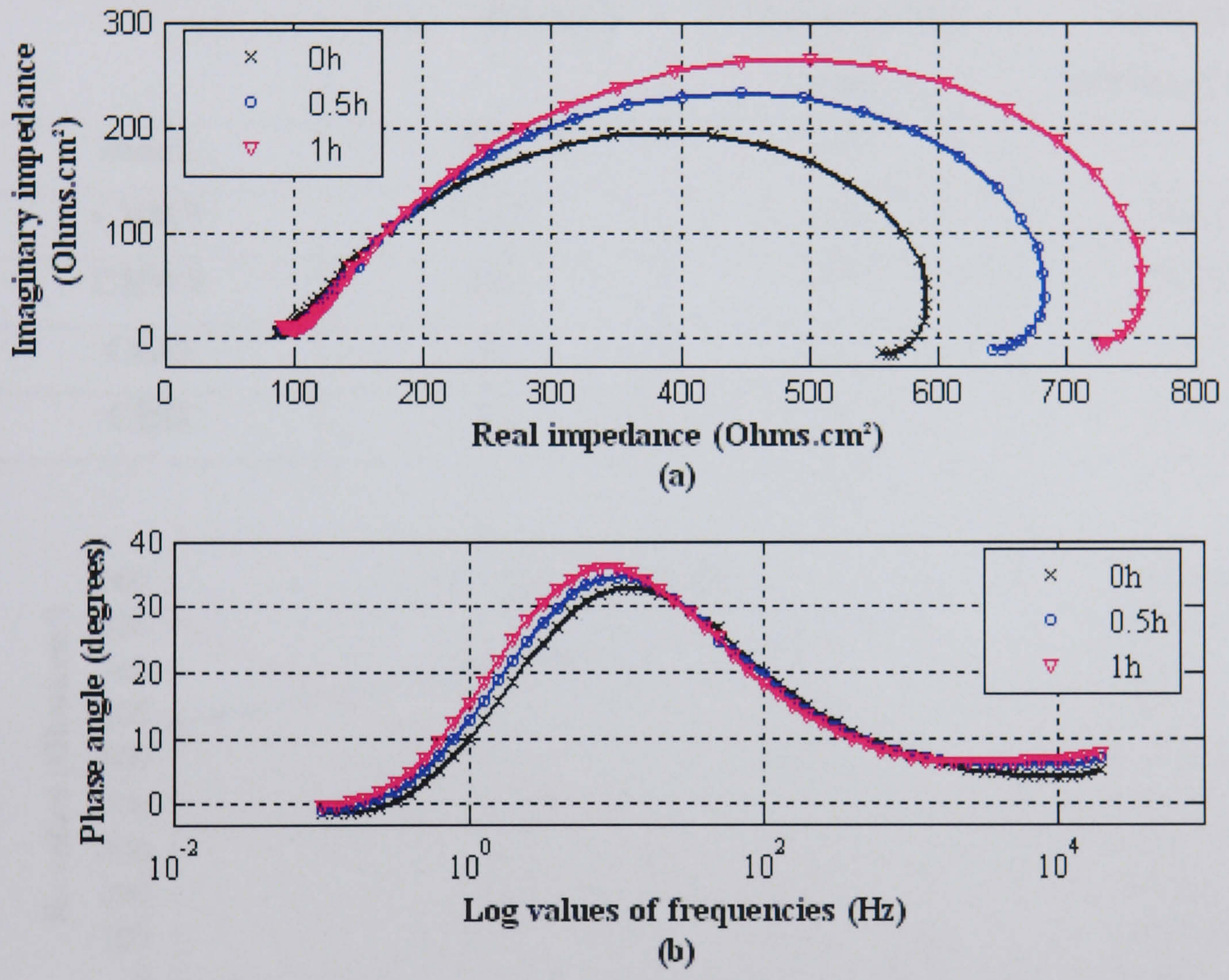

Figure 5.24 Impedance spectra of CRO tests under static condition at 20°C (a) Nyquist and (b) Bode phase plots

Oil-soluble corrosion inhibitors provide inhibition effects basically by two mechanisms. One is attributed to the protective effect of the inhibitor to shielding of the surface with either an inclined position or flat position of the hydrogen radicals. The other is through micellization (Fokin, *et al.*,1986). Water soluble organic inhibitor inhibits the corrosion of steel by twofold mechanisms that involve the formation of a protective film on the metal surface and a reduction in the susceptibility of corrosive species (Nmai, 2004). From the AC impedance analysis that the surface film of oil-soluble inhibitor is not as

even thickness as the water soluble inhibitor. This might be due to the mechanisms of micellization for oil-soluble inhibitors.

Table 5.2 Comparison of inhibitor performance for CGO, CRO, CRW9 and CRW8 under static condition at 20°C

	i_{corr} ($\mu A/cm^2$)	Penetration rate (mpy)	Inhibitor efficiency (%)
Blank	109	50	
CRW9	0.61	0.28	99.43
CRW8	0.81	0.37	99.25
CGO	23	10	79
CRO	37	17	66.1

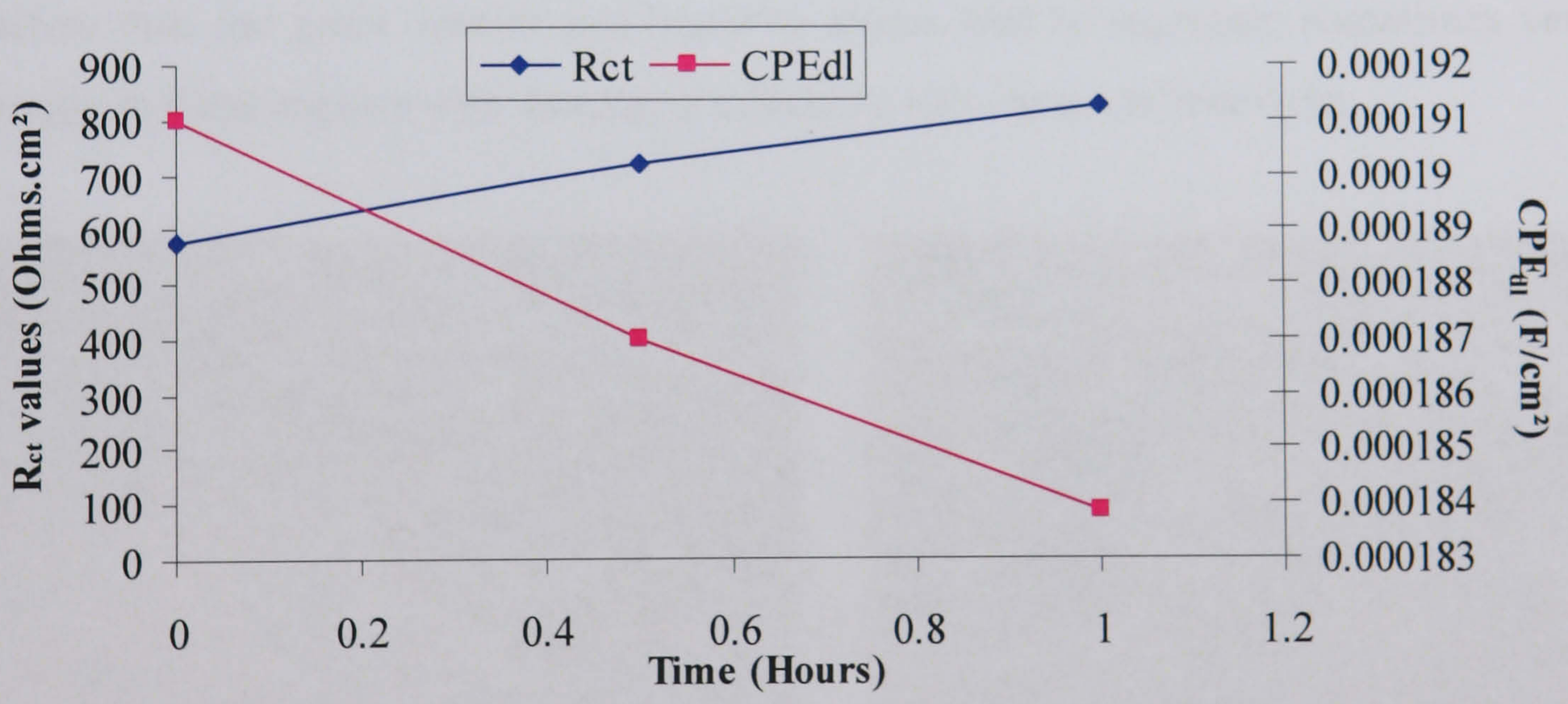

Figure 5.25 R_{ct} and CPE_{dl} values with time for CRO tests under static condition and 20°C

The inhibitor performance for CRW8 and CRW9 are in agreement with the inhibitor F and G used by Mok *et al.* (2003) in the evaluation work for static conditions. The corrosion rate for blank tests is in agreement with that depicted by Shell according to basic Shell equation (Kermani and Morshed, 2003). The very low current density values for inhibitor CRW9 compared with the blank test (180 times low) indicates that the inhibitor provides protection effectively under these conditions. It may be due to the

presence of a protective film-inhibitor film, on the metal substrate which can be proved by post test analysis.

The corrosion mechanisms of the carbon steel are revealed during post-test examination. The microscope images were taken as shown in Figure 5.26 and Figure 5.27 after blank tests and inhibitor tests respectively. At 20°C for the blank test (Figure 5.26 and the red circle enlarged image), it can be seen that general corrosion attack takes place over the whole sample surface, and pitting corrosion (black dots shown with arrows) started from the grain boundary between pearlite and α -ferrite sites and extended to the pearlite site of the surface shown in the enlarged image. The microscope images for blank tests have similar surfaces to that of Figure 4.12 in Chapter 4, taken for etched new sample, except that no pitting corrosion appeared on etched samples. These grain boundaries have special properties of their own and are usually more reactive than the grain interior and impurity atoms tend to segregate sometimes very strongly in these regions with damaging effects on the corrosion behaviour.

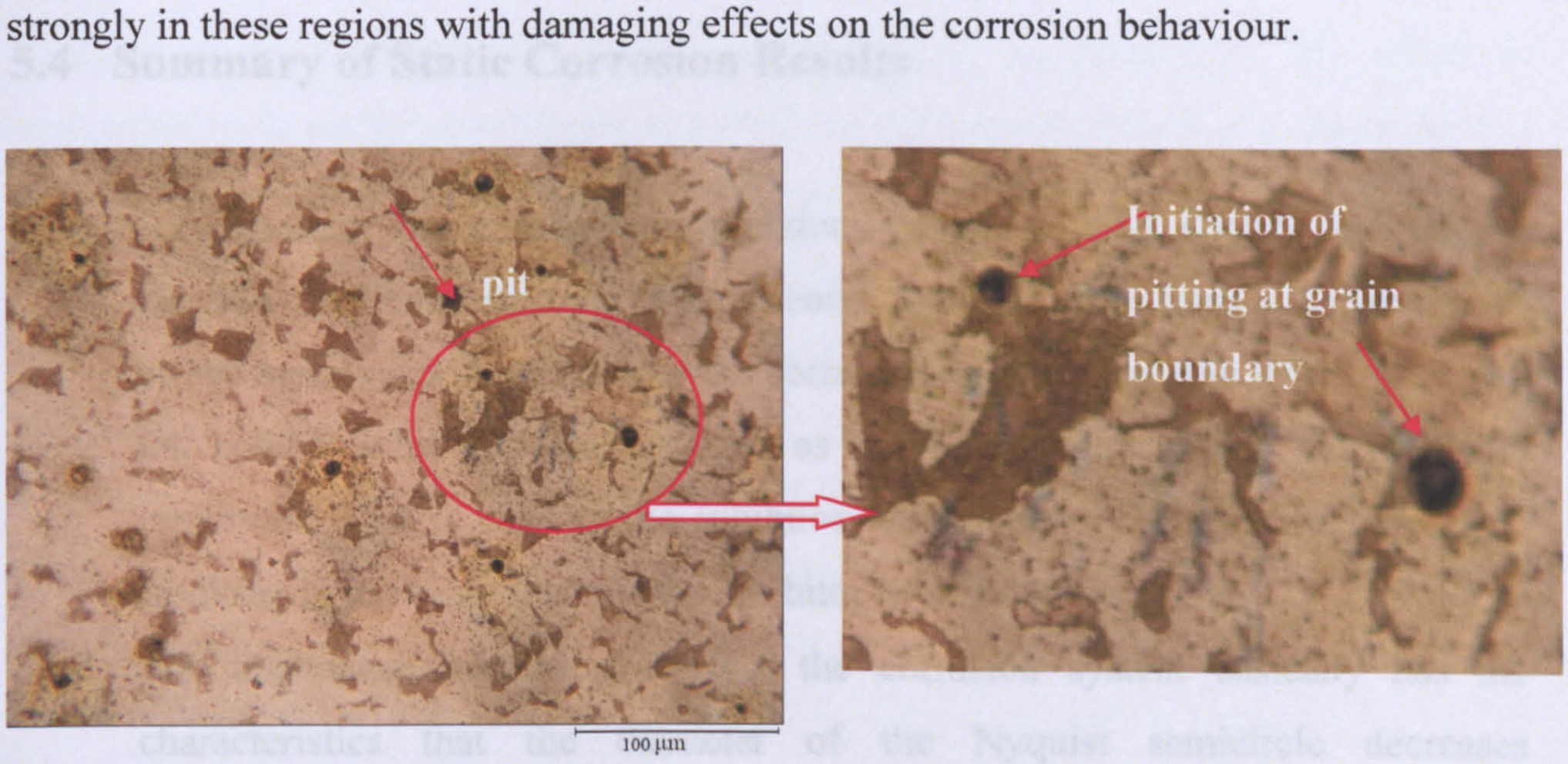

Figure 5.26 Microscope photos for samples after anodic polarisation under static condition for blank tests at 20°C showing initiation of pitting from pearlite sites

With inhibitor CRW8 tests, the microscope images after the anodic polarisation are shown in Figure 5.27. It can be seen that the inhibitor film formed on the metal surface. Thus it prevented surface from general corrosion. There is no pitting occurred but there were film removal on the site of metal surface as shown with arrow. The overall surface

is untouched, apart from general corrosion appear on the break down area of the inhibitor film. It indicates that the inhibitor film has pores and its performance depending on the conditions such as the surface roughness.

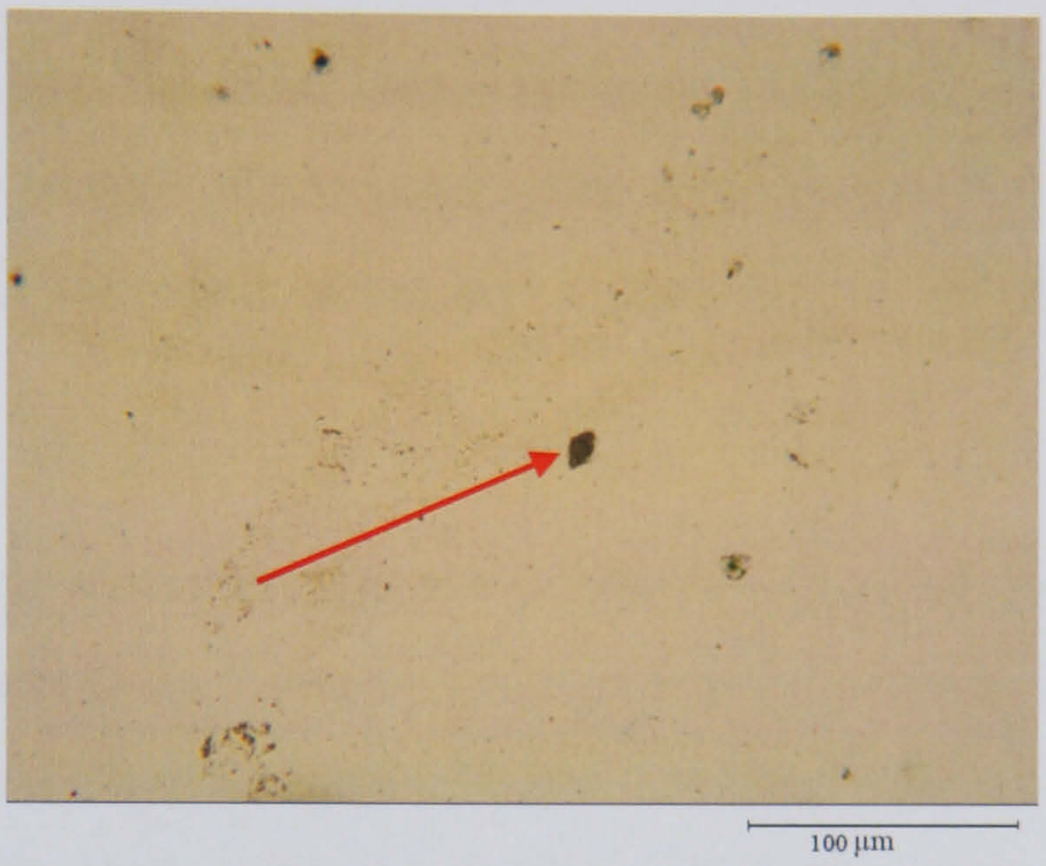

Figure 5.27 Microscope photos for samples after anodic polarisation under static condition for 100ppm CRW8 at 20°C

5.4 Summary of Static Corrosion Results

1. As expected, the commercial inhibitors (water soluble) CRW9 and CRW8 provide excellent resistance to static conditions. Both can form a denser barrier on the metal surface, and reduce the corrosion rate by more than 99%.
2. Oil soluble inhibitors did not give as good efficiency as the water soluble inhibitors. This is due to the inhibitor having poor hydrophobic properties, resulting in unevenly layer of the inhibitor film and more pores.
3. The impedance spectra show that the corrosion system basically has the characteristics that the diameter of the Nyquist semicircle decreases continuously, the peak angle shifting continuously to the lower frequency range.
4. The inhibitor changes the activity of iron by adsorption. The iron activity can be reduced by the factor of $5x\ 10^3$ for the inhibitor with best performance. Therefore, it can be used as a kind of criteria to evaluation the performance of inhibitors.
5. Pitting if initiated will start from the grain boundary and extend into pearlite phase.

CHAPTER 6 RESULTS AND DISCUSSION OF EROSION-CORROSION USING RCE

A corrosion inhibitor that functions under stagnant conditions or at a low flow rate (<1m/s) may not offer control of corrosion under more severe flow conditions, such as in multi-phase flow, in high shear stress and in the presence of sand, namely erosion-corrosion.

In order to investigate if *corrosion* inhibitors can effectively reduce *erosion-corrosion*, in this chapter the results of an assessment of erosion-corrosion performance of carbon steel with and without inhibitors under different conditions are presented. The erosion properties of the carbon steel with and without inhibitor are also studied. Figure 6.1 shows a map of experiments for the work presented in this chapter to help the reader understand the scope of the experiments conducted. The four inhibitors used are referred to as CGO, CRO, CRW8 and CRW9 as in chapter 5. The effect of concentration is studied at 6000rpm and 20°C for CRW8 and CRW9 as in this condition corrosion product hardly exist on the metal surface and the results reflect the interaction of the inhibitor with the metal surface. The effect of concentration on the interaction of inhibitor with corrosion products on the metal surface is studied in the next chapter using the impinging jet. For RCE tests, the main test conditions are 20°C/50°C and 1000rpm/6000rpm rotational speed. Post test analysis using light microscope or SEM, were followed in each test condition to investigate the inhibition mechanisms under erosion-corrosion as well as under pure erosion conditions.

6.1 Overall Erosion-Corrosion Measurement-Total Mass Loss

The total mass loss of materials when exposed to liquid-solid flow in RCE represents the overall erosion-corrosion degradation of the material. These mass loss results are presented in three main sections: the first section deals with those experiments carried out at 20°C at different rotational speeds; the second section at 50°C and the third section deals with various inhibitor concentrations at 20°C and 6000rpm conditions.

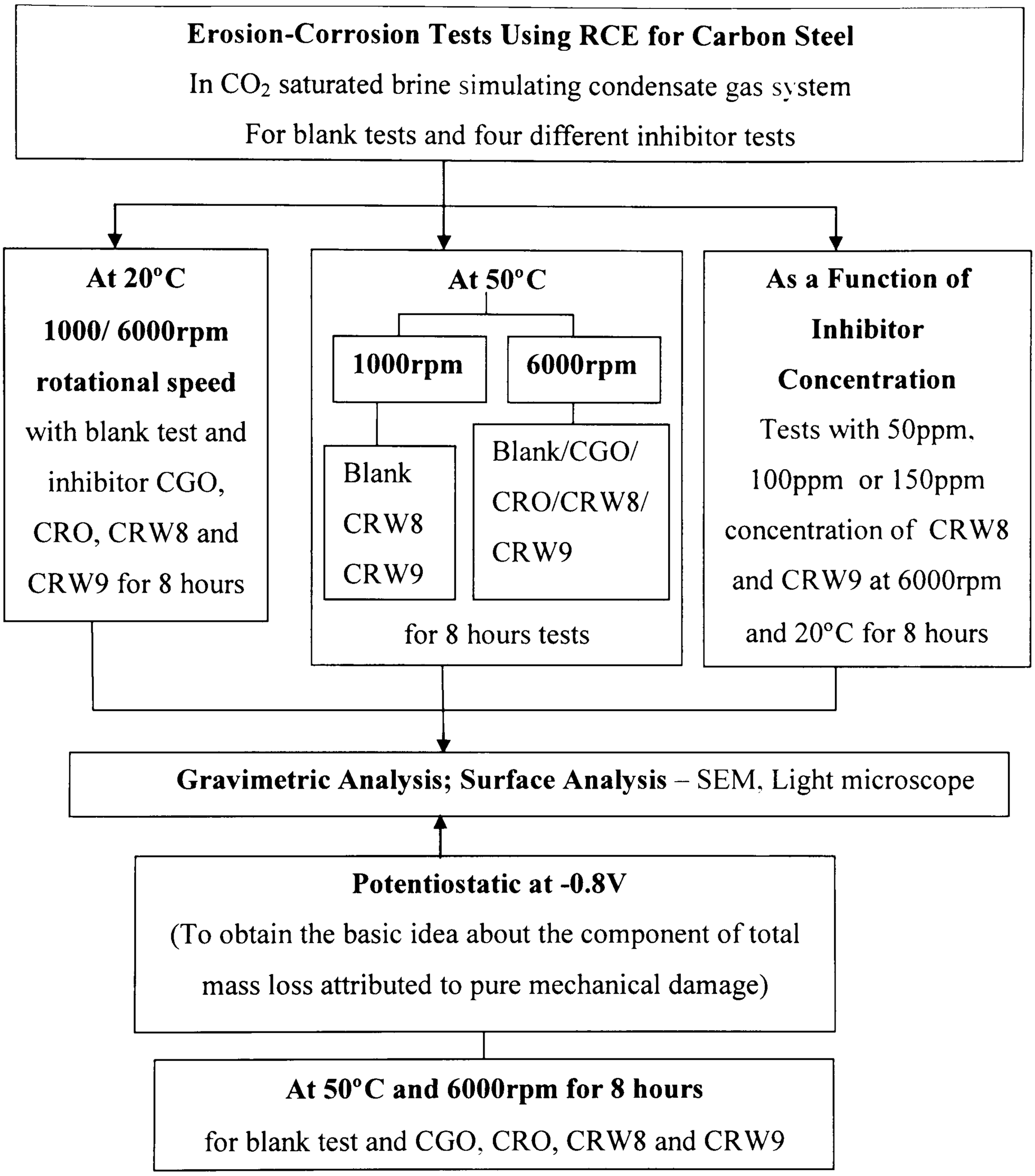

Figure 6.1 The map of experimental work presented in Chapter 6

6.1.1 Total Mass Loss at 20°C

In order to assess the inhibitor performance at 20°C in a CO_2-saturated solution, inhibitors CGO, CRO, CRW8 and CRW9 were compared with the blank solution to obtain mass loss results on carbon steel cylindrical samples at 1000rpm or 6000rpm rotational speed for 8 hours. Comparison of the mass loss results are shown in Figure

6.2 as well as in mpy which is the equivalent penetration rates to mass loss. The inhibitor efficiency is defined as Equation (84):

$$\frac{ML_{NI} - ML_{WI}}{ML_{NI}} \tag{84}$$

where ML_{NI} and ML_{WI} are the mass loss with no inhibitor (blank) and with inhibitor respectively. The efficiencies of these inhibitors were calculated using Equation (84) and shown in Table 6.1. From Figure 6.2, there are a number of interesting observations such as:

- ❖ At 20°C and 1000rpm, all the inhibitors offer a degree of protection when compared with the uninhibited case.
- ❖ CRW8 has the best performance with the inhibitor efficiency of nearly 100% at 20°C and 1000rpm, and CGO also provides reasonably good efficiency.
- ❖ At 6000rpm CGO and CRO offer no reduction in mass loss compared to blank solution. CRO even has negative effect.
- ❖ At higher roational rate of 6000rpm, CRW9 offers the most reduction in mass loss.

It is postulated that the CRW8 and CRW9 have stronger adherence (film persistency) to the surface and can also reform the film when the sand impacts peel off the film. In general terms, as the rotation rate of the electrode increases the shear stress is increased, the inhibitor film is likely to be removed by the shear stress and sand impacts. However, as rotational speed increased, CRW9 was showed to be least affected, implying that the inhibitor has the potential to be used as an inhibitor under erosion-corrosion conditions. CRW8 film persistency decreases with time faster than CRW9 at higher rotational speed which is apparent on analysis of the corrosion results measured *in-situ* presented in the corrosion results in the next chapter. This implies that reduction in corrosion rate has a significant effect in reducing the overall material loss under erosion-corrosion conditions. CRW9 under conditions of high shear stress with sand can achieve the reduction of the mass loss of about 60%.

From the mpy values, it is apparent that these are high compared to expected static corrosion rates in CO_2 environments (Kermani and Morshed, 2003). This is also

expected when the high shear rate is considered. The thickness loss of 150mpy would be above the threshold value for pitting corrosion as defined by Shadley *et al.* (1998), and would mean that the uniform corrosion is likely. The penetration rate for erosion-corrosion tests under CO_2 saturated condition with sand at 2% by weight and 34°C was reported to be 180 mpy for protruding parts of the pipe flow (Malka *et al.*, 2006). The Re number in those conditions is comparable to the Re for the current tests (about 43000) at the 6000rpm and 20°C using RCE, under which the penetration rate is about 150 mpy for blank tests. As Poulson (1993) recommended that the intensity of turbulence could be used as a design parameter in both solid-liquid and single phase flows, the pipe flow results can be related to the RCE work by the same turbulence intensity as calculated in chapter 4.

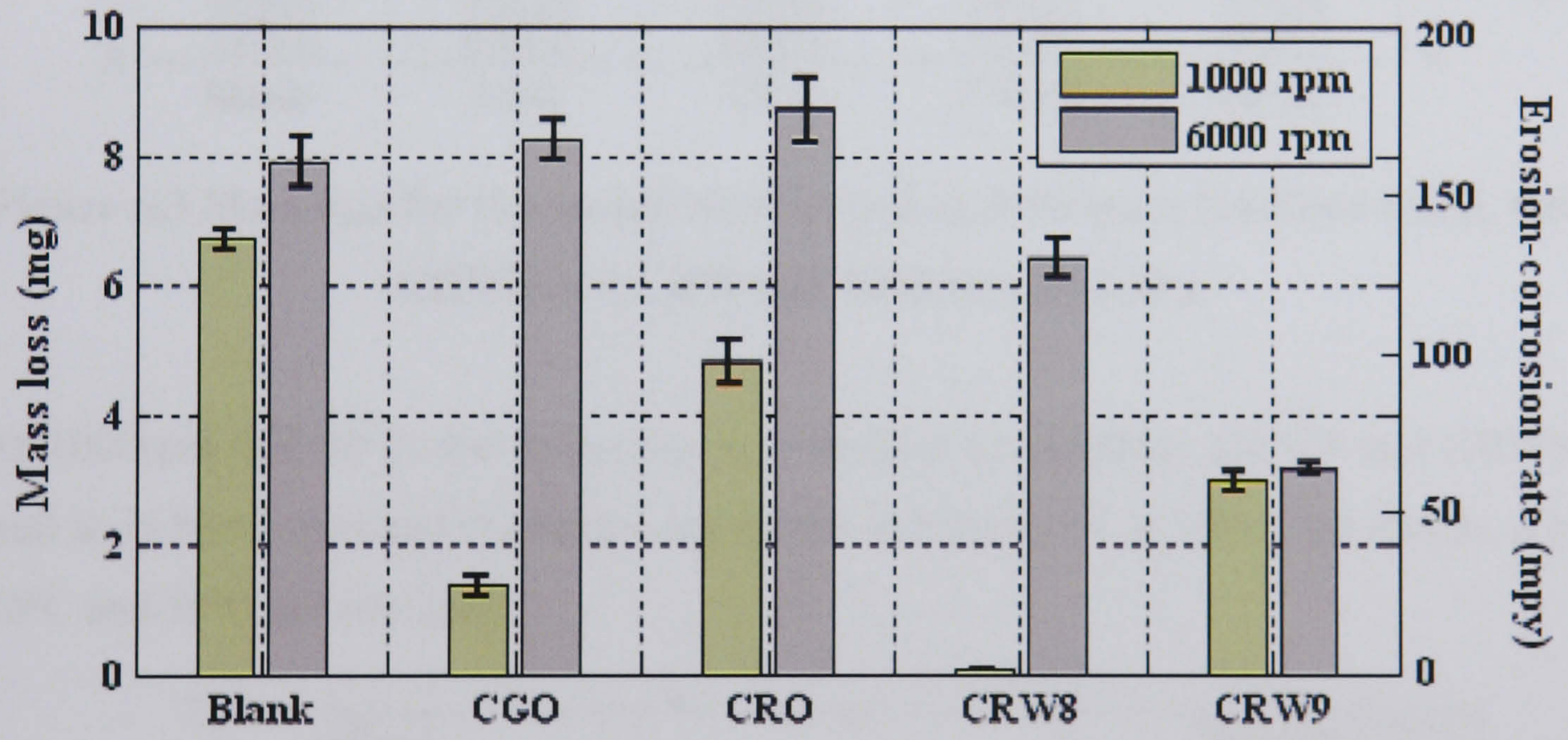

Figure 6.2 Erosion-corrosion rates in mg or in mpy for the uninhibited system and 100ppm inhibitor CGO, CRO, CRW8 and CRW9 at 1000/6000rpm and 20°C

6.1.2 Total Mass Loss at 50°C

Figure 6.3 shows the comparison results for total mass loss (in mg and in mpy) for RCE tests at 6000rpm rotational speed and 50°C. It is clear that the mass loss is significantly larger compared to 20°C. At 50°C and 6000rpm rotational speed, all the inhibitors have some inhibition effect, among which CRO and CRW8 have the best performance. The efficiencies of these inhibitors calculated using Equation (84) under 50°C, 6000rpm are also shown in Table 6.1. The results show the combination of rotational speed and

temperature is the most important factor to affect the inhibitor efficiency. CRW9 has the best performance at higher rotational speed but lower temperature, while CRW8 provides better efficiency compared with others at higher temperature.

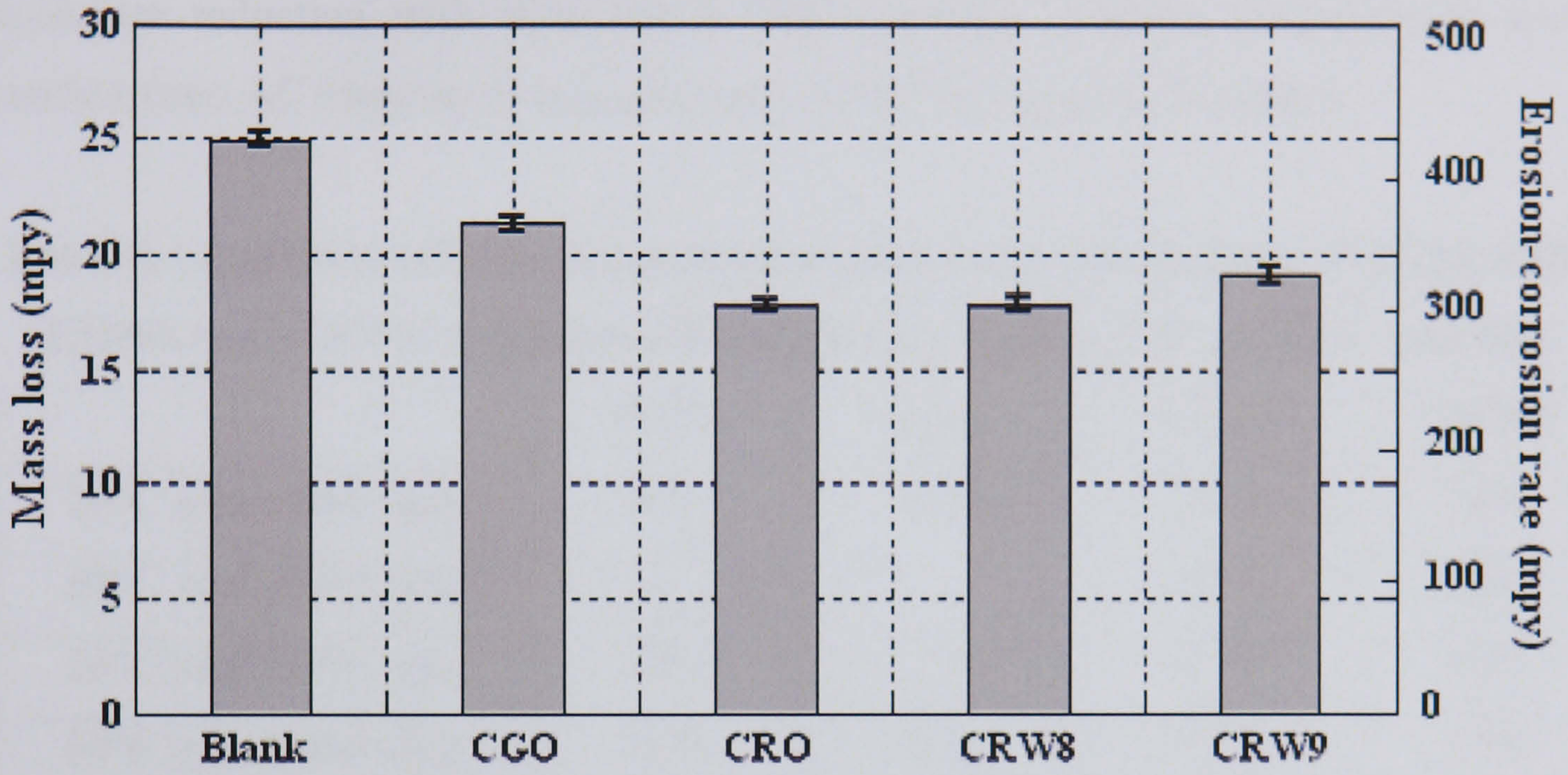

Figure 6.3 Mass loss for the uninhibited system and 100ppm inhibitor CGO, CRO, CRW9 and CRW8 at 6000rpm and 50°C

At 1000rpm and 50°C, the mass loss was studied for inhibitor CRW8 and CRW9 as well as in blank tests and the results are shown in Figure 6.4, in which the results at both 20°C and 50°C are compared.

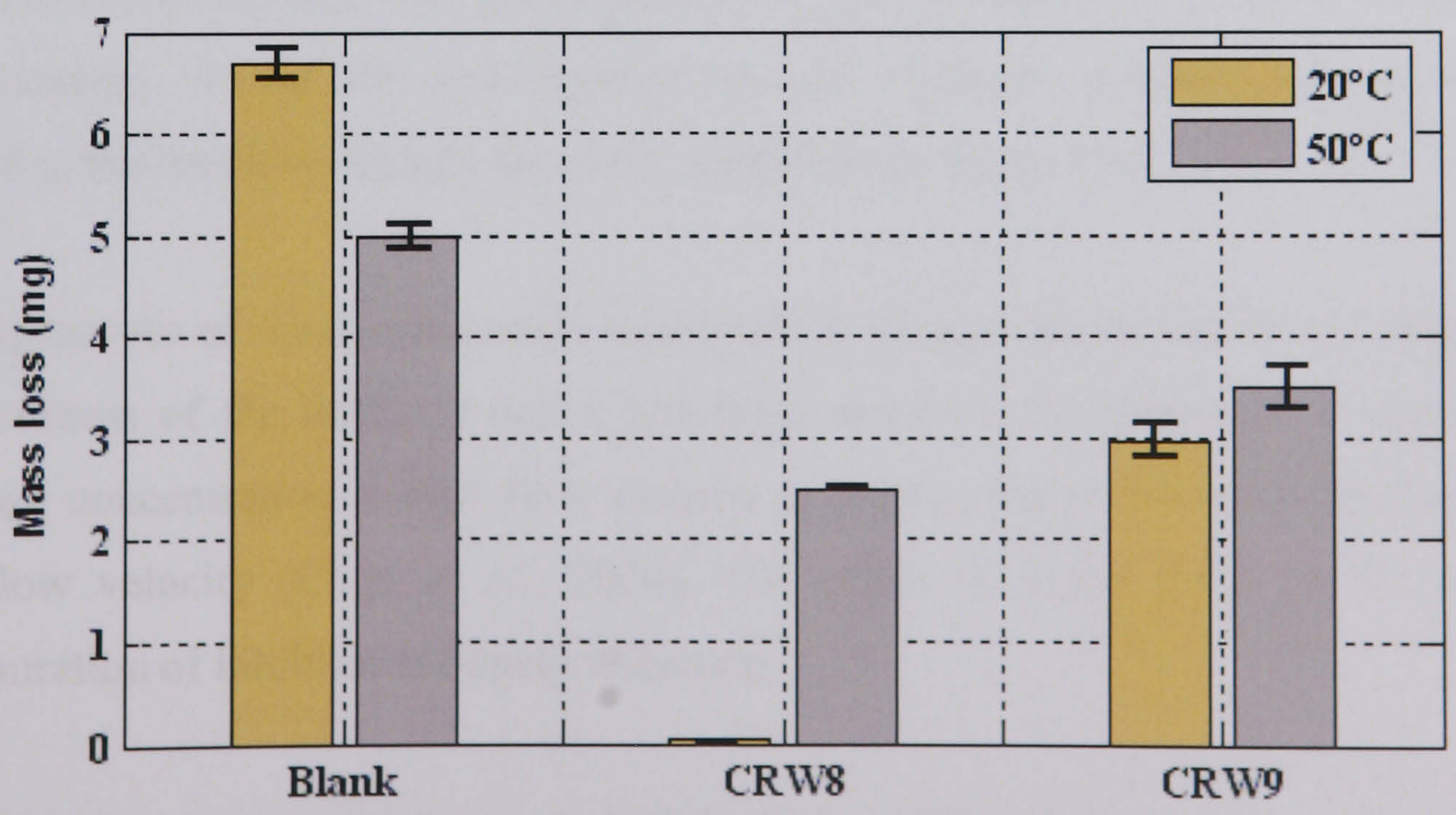

Figure 6.4 Mass loss for the uninhibited system and 100ppm inhibitor CRW8 and CRW9 at 1000rpm and 20°C/ 50°C

It is interesting that at 50°C for blank tests the mass loss is lower than that at 20°C. This is likely to be caused by the corrosion products accumulated on the metal surface protecting the carbon steel from erosion-corrosion. In these conditions, the corrosion resistance reduction with time due to the corrosion products accumulation is also verified from AC impedance measurements as will be reported in chapter 7.

Table 6.1 Inhibitor efficiencies on total erosion-corrosion damage of CGO, CRO, CRW8 and CRW9 at 1000rpm/6000rpm rotational speed and 20°C and 50°C

	CGO	CRO	CRW8	CRW9
20°C and 1000 rpm	80%	28%	99%	56%
50°C and 1000 rpm	--	--	50%	30%
20°C and 6000 rpm	-4%	-14%	20%	60%
50°C and 6000 rpm	15%	29%	29%	23%

6.1.3 Effect of Inhibitor Concentration

Usually inhibition efficiency increases with the increase of inhibitor concentration until a steady state is reached. However some inhibitors may exhibit the peak-value-phenomenon of inhibitor concentration (Singh, 1993). The concentration, where the peak-value-phenomenon (the lowest corrosion rate) is exhibited, is called the optimum concentration. So far the investigations on the optimum concentration of inhibitor existed in the literature mainly for static conditions or liquid flow.

The higher rate of shear stress could significantly enhance the corrosion and degrade the effectiveness of the inhibitor and it has been shown to be necessary to increase the inhibitor concentration at high flow velocity to get the same inhibition efficiency as at low flow velocity (Chen *et al.*, 2000). The effect of slurry flow on the optimum concentration of inhibitor is largely unknown.

The effect of concentration of inhibitor on performance was studied over a concentration range of values of 50ppm, 100ppm and 150ppm at 20°C and 6000rpm as shown in Figure 6.5 for both CRW8 and CRW9. It can be seen that for both inhibitors

at the lowest concentration of 50ppm there is a small increase in the mass loss compared to the uninhibited test, the inhibitor is therefore not effective at reducing metal loss. As the inhibitor concentration increases to 100ppm and 150ppm the efficiency was improved substantially. The inhibitor efficiency values are also shown in Table 6.2. The hydrodynamic factor had two opposite effects on inhibitor performance. It made the inhibitor reach the metal surface easily and also slurry flow causes the inhibitor to desorb from the metal surface. Inhibitor efficiency increase with inhibitor concentration can be due to the inhibitor adsorption to the sand surface.

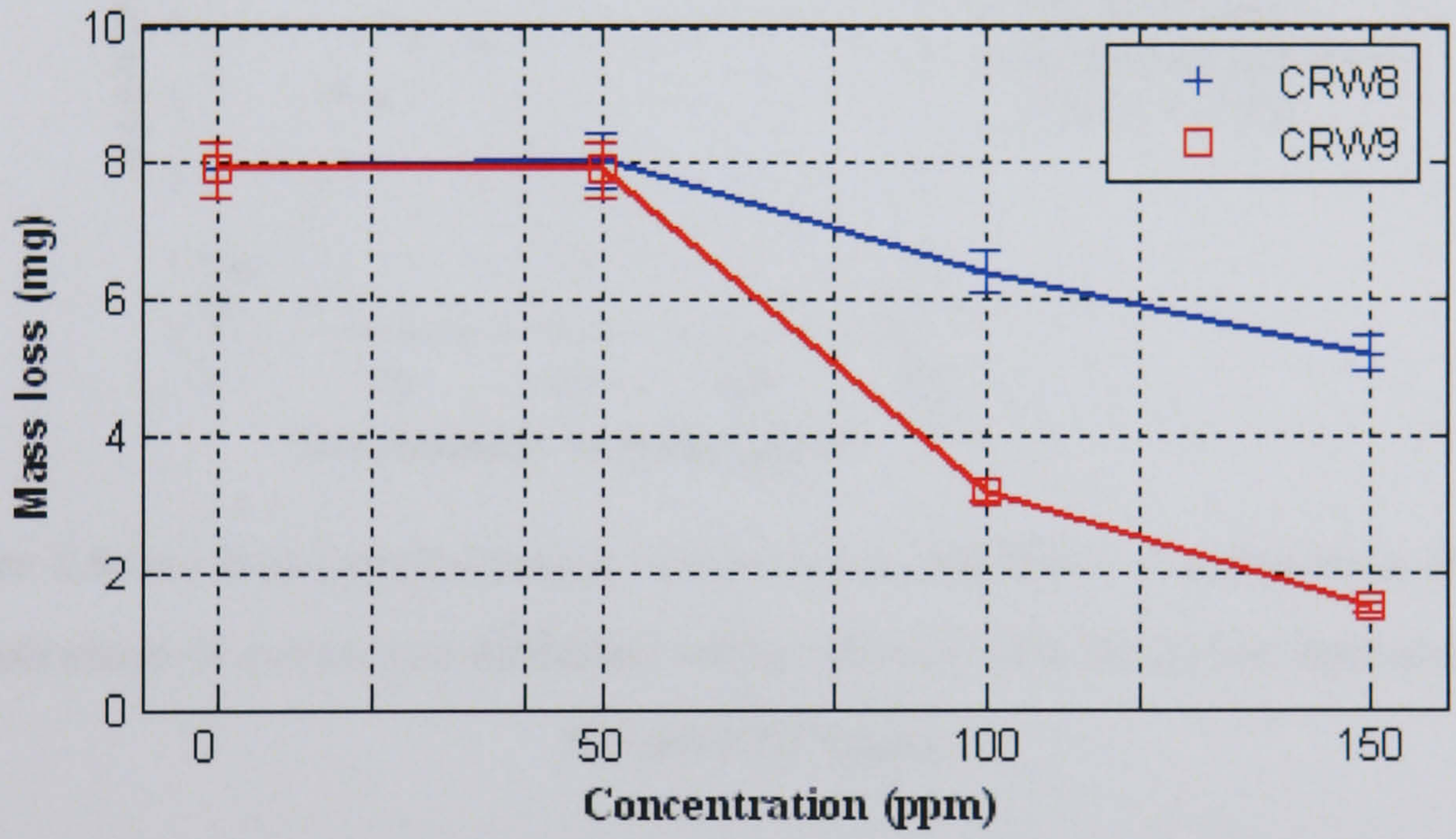

Figure 6.5 Mass loss for the inhibitors CRW8 and CRW9 with various concentrations at 6000rpm and 20°C

Table 6.2 Inhibitor efficiencies of CRW8 and CRW9 at 6000rpm rotational speed and 20°C for different concentrations

	50ppm	100ppm	150ppm
CRW8	-2%	20%	34%
CRW9	0%	60%	81%

Adsorption characteristics of sand with CRW9 have been measured by Ramachandran *et al*. (2005). The surface concentration of the inhibitor on sand as a function of liquid concentration of the inhibitor after a stirred test for 24 hours is shown in Figure 6.6. It can be seen that with the increase of the liquid concentration of inhibitor, the amount of inhibitor molecules on sand is increased. Therefore the inhibitor can reduce pitting

corrosion substantially at 150ppm inhibitor concentration as well as reduce general corrosion for all the concentrations. However, the speed at which inhibitor prevents corrosion in corrosion tests is faster than the rate of adsorption with sand (Samachandran *et al*., 2005).

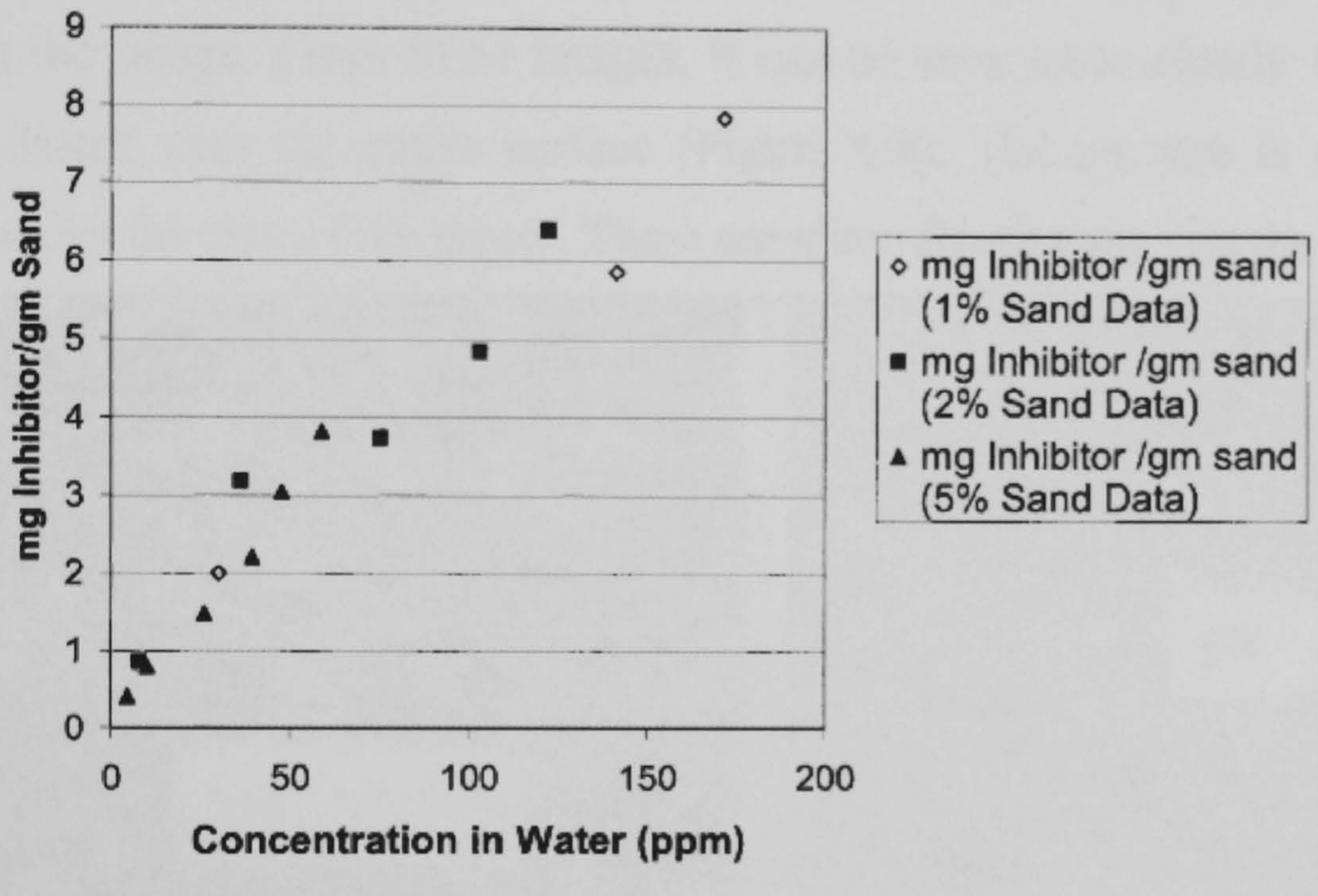

Figure 6.6 Surface concentration of corrosion inhibitor as a function of liquid concentration of corrosion inhibitor when stirred with different amount of sand for over 24 hours

6.2 Surface degradation Analysis after Erosion-Corrosion Tests

Do the sand particles hit the metal surface and damage it mechanically? How was the surface degradation affected by the flow velocity and temperature? Light microscope images or SEM images of the surface morphology of samples after tests enable surface degradation mechanism to be determined and answer the questions.

6.2.1 Surface Analysis after Erosion-Corrosion Tests at 20˚C

The characteristics of the surface after erosion-corrosion tests at 20°C and 1000 rpm are shown in Table 6.3. From the results it can be seen that with blank tests, pitting corrosion occurred on the surface combined with general corrosion. With addition of inhibitors pitting is eliminated on the surface.

Table 6.3 Surface characteristics after tests at 20°C and 1000rpm

<table>
<tr><th colspan="2">20°C and 1000rpm rotational speed</th></tr>
<tr><td>Blank</td><td>The sand impacts are shown by light microscope images in Figure 6.7 where metal material was stripped off pointed by the arrow. Pitting is also can be seen from the image. From SEM images, it can be seen more clearly that pitting is distributed over the entire surface (Figure 6.8). The pit size is about 45 μm shown by the size of the arrow. There are about 80 pits/mm² on the surface.
 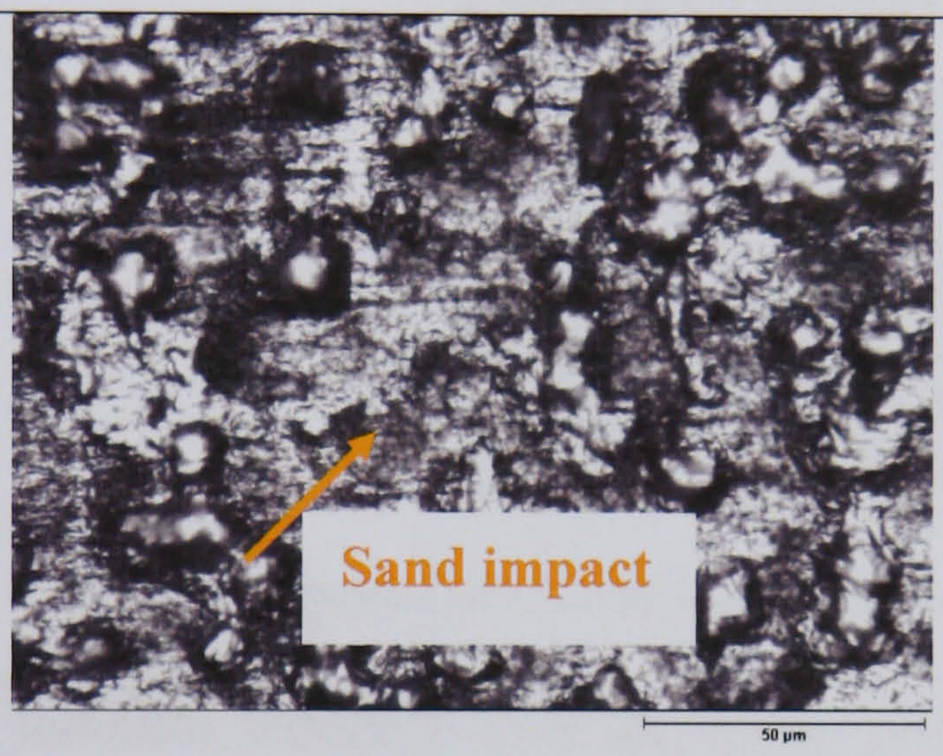

Figure 6.7 Microscope images for blank tests under 20°C and 1000rpm
 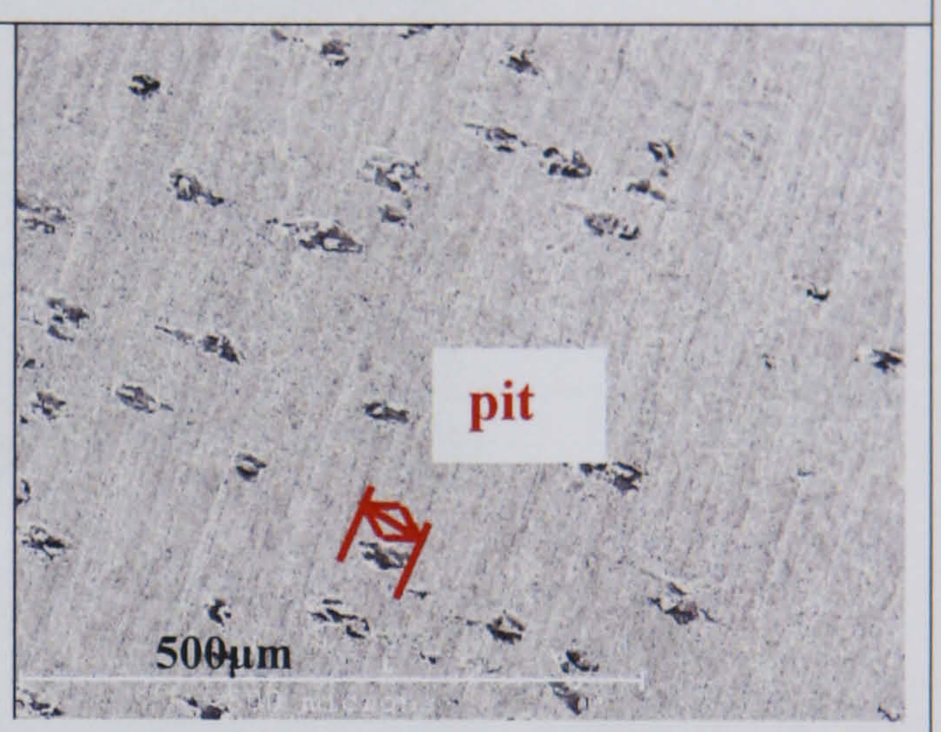

Figure 6.8 SEM for blank tests under 20°C and 1000rpm</td></tr>
<tr><td>CGO</td><td>Pitting is eliminated with addition of CGO inhibitor. The surface where the inhibitor film was removed by flow or sand, is rougher than other areas as shown by the arrow in Figure 6.9. This can be due to sand impact or due to combination of sand impact and general corrosion. The surface area covered with inhibitor film is smooth and unattacked as shown by the circle.
 

Figure 6.9 SEM for CGO tests under 20°C and 1000rpm</td></tr>
</table>

CRO	From SEM image (Figure 6.10), surface is very rough. This can be due to pitting and general corrosion as well as sand impact. With addition of inhibitor CRO, there seems no inhibitor film formed properly on the surface due to the tenacity of the film not being sufficient. This supports AC impedance results presented in next chapter.
	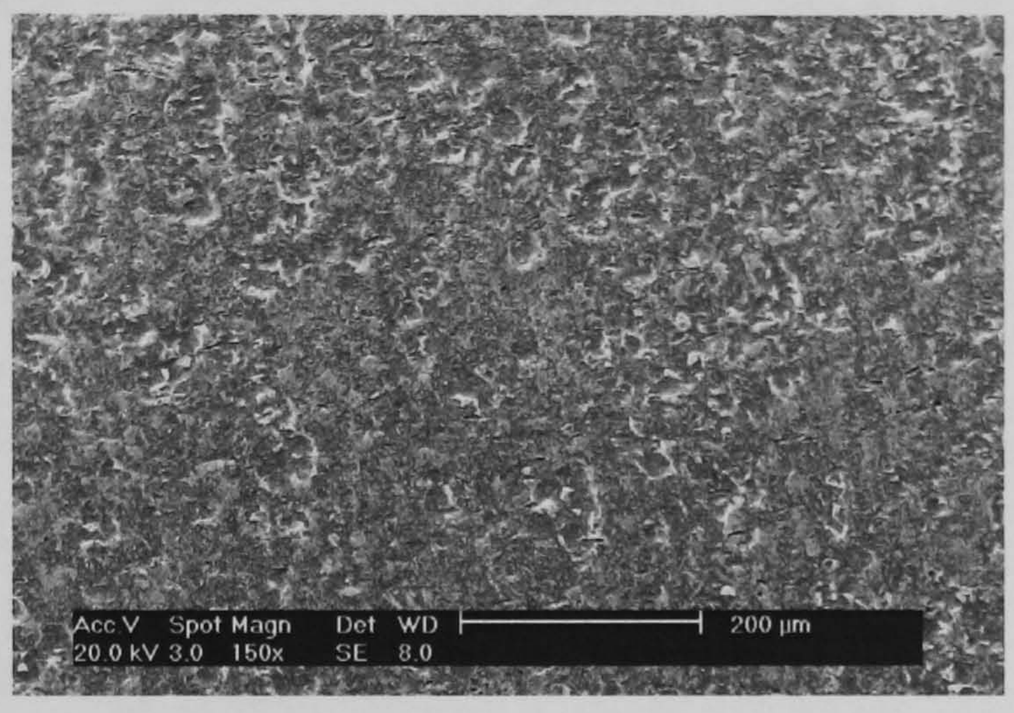

Figure 6.10 SEM for CRO tests under 20°C and 1000rpm

CRW8	Inhibitor adsorbed onto the whole surface, and isolated the surface from the corrosive medium as shown on the left image in Figure 6.11. It is comparable to the new sample prior to test (right). This is in agreement with mass loss results which show inhibitor efficiency for erosion-corrosion of nearly 100%.
	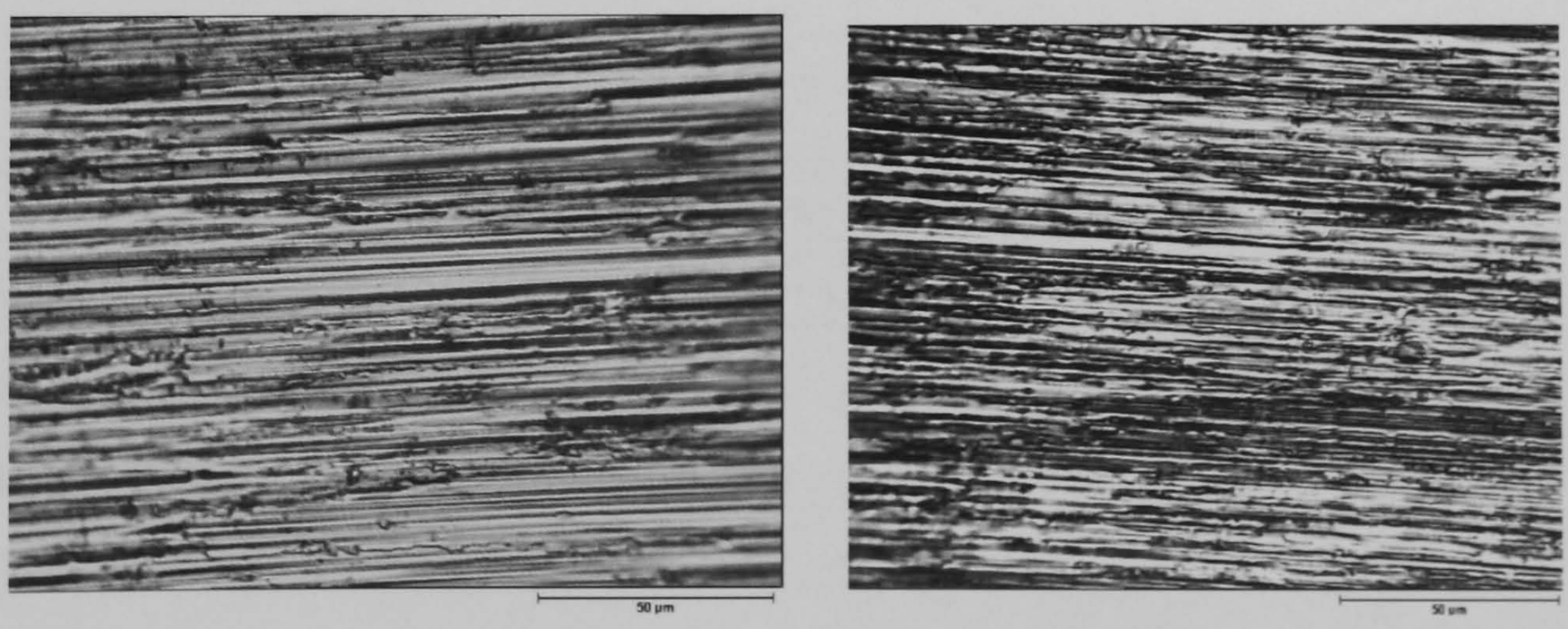

Figure 6.11 Microscope image (left) with inhibitor CRW8 test at 20°C and 1000rpm (right) new sample prior to test

CRW9	General corrosion can be seen on the surface as shown by the arrow in Figure 6.12 due to the inhibitor film being removed by sand impact. The area with good inhibitor film formed was unattacked and showing lighter in colour. Sand impact also can be seen shown by the circle.

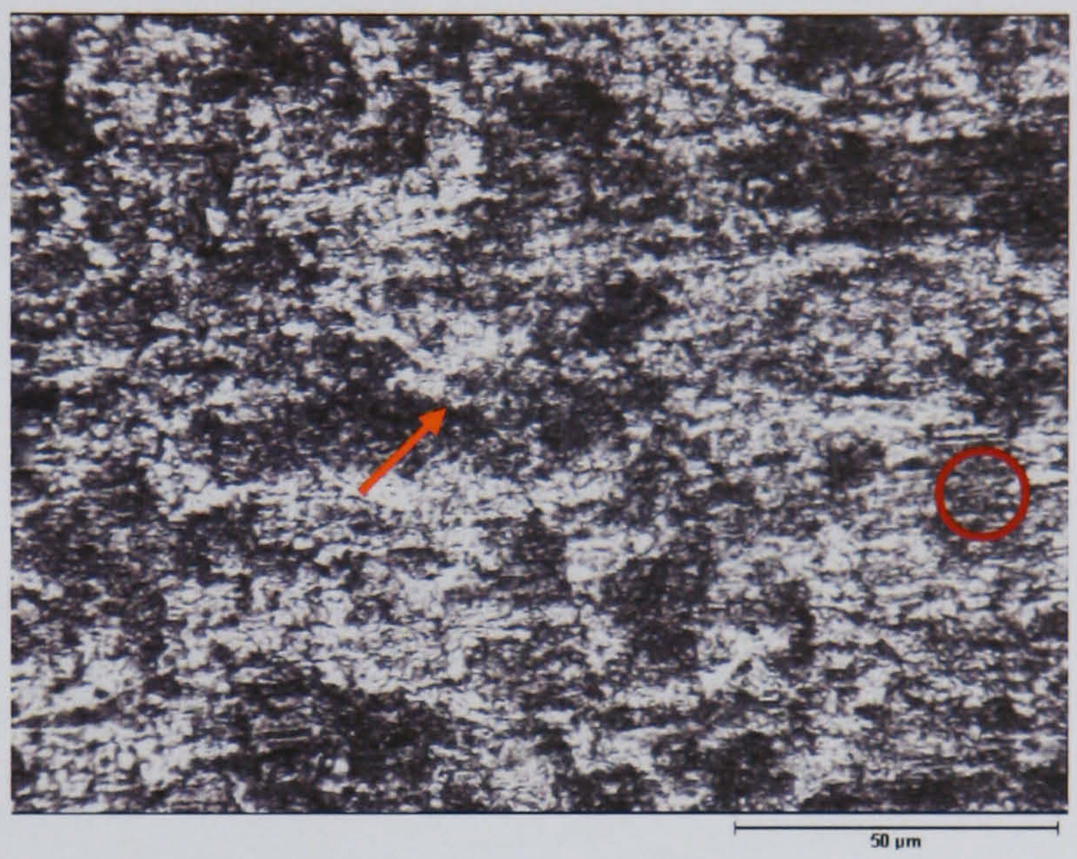

Figure 6.12 Light microscope image with 100ppm inhibitor CRW9 at 1000rpm and 20°C

Table 6.4 shows the surface characteristics after erosion-corrosion tests at 20°C and 6000rpm.

Table 6.4 Surface characteristics of sample after tests at 20°C and 6000rpm

20°C and 6000rpm rotational speed	
Blank	Pitting size increased with increase of rotational speed from 45 µm under 1000rpm to 145 µm under 6000rpm as shown by the distance of the arrow in Figure 6.13. The density of the pits per mm^2 reduced from 80 to 35. The pits are more like raindrop shape and with the tails connect with pits. The sand impacts can be seen from the microscope images as shown by the arrow in Figure 6.14. The larger size of pits indicates that erosion (mass transfer and impact) enhances the corrosion process.

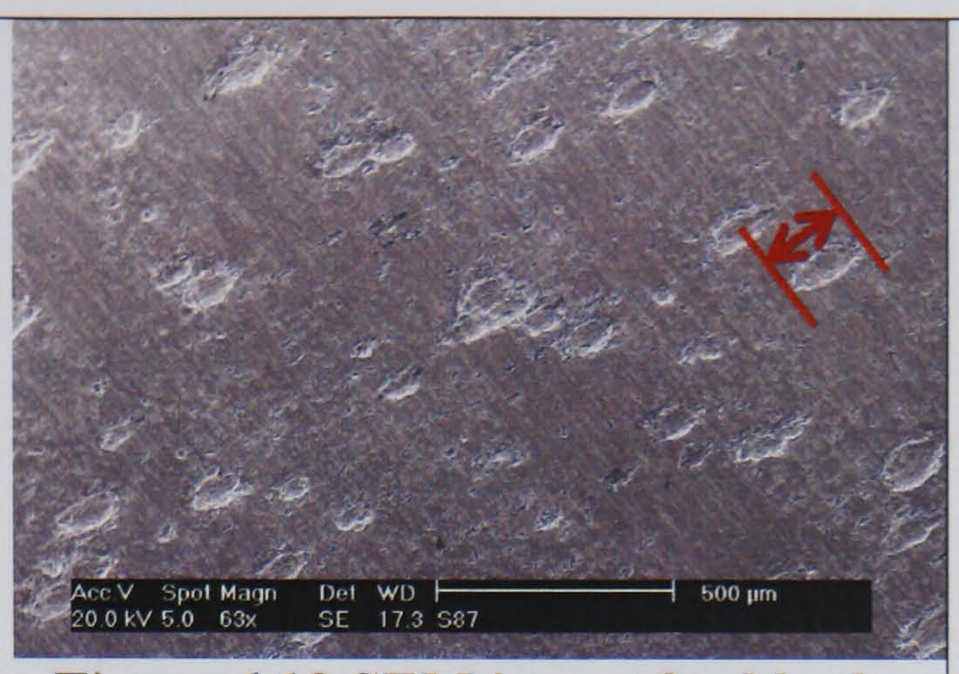

Figure 6.13 SEM image for blank tests under 20°C and 6000rpm

Figure 6.14 Light microscope images for blank tests under 20°C and 6000rpm

CGO

With addition of CGO under this condition, there is a material disboundment and pitting taking place on the surface shown in Figure 6.15. The inhibitor film is removed more easily by the flow or sand impact than at lower rotational speed. Pitting size is about 160 µm measured from Figure 6.16. It can be postulated that with higher shear stress, the inhibitor was removed and at the same time it can be removed off with $FeCO_3$ formed during the corrosion process and in turn promotes the corrosion rate of the metal.

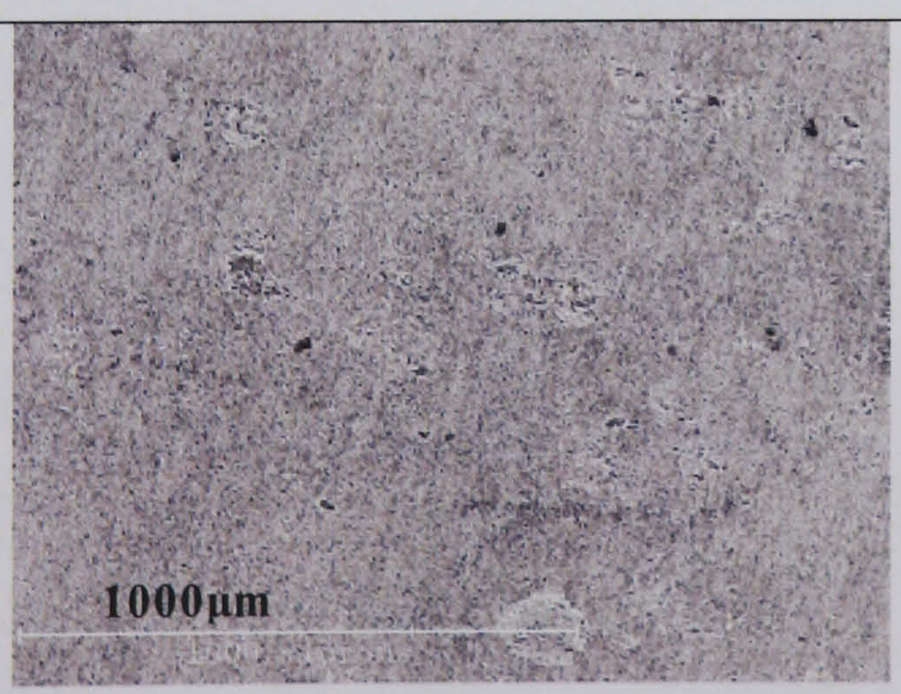

Figure 6.15 SEM image with CGO under 20°C and 6000 rpm

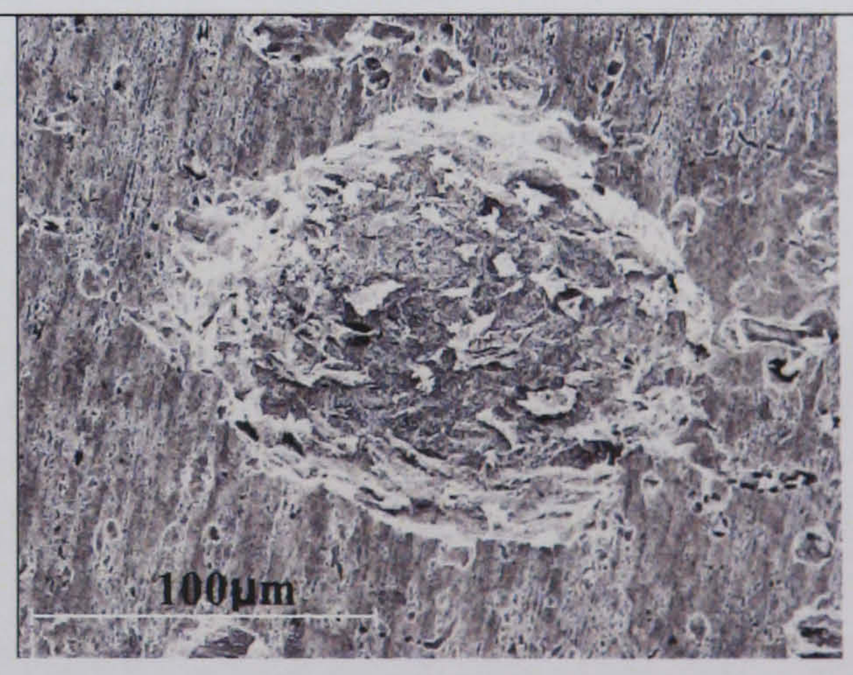

Figure 6.16 SEM image with CGO under 20°C and 6000 rpm

CRO	From Figure 6.17, the surface is smoother than that with CGO tests, but the pitting size (200μm) is larger due to the round shape instead of rain drop shape with blank tests. General corrosion is combined with pitting corrosion in which the inhibitor and $FeCO_3$ molecules disbound together or the inhibitor makes $FeCO_3$ disbound easier than with no inhibitor. The surface after disbounding becomes rough and reactivation taking place. Sand impact also enhances the corrosion rate of the metal	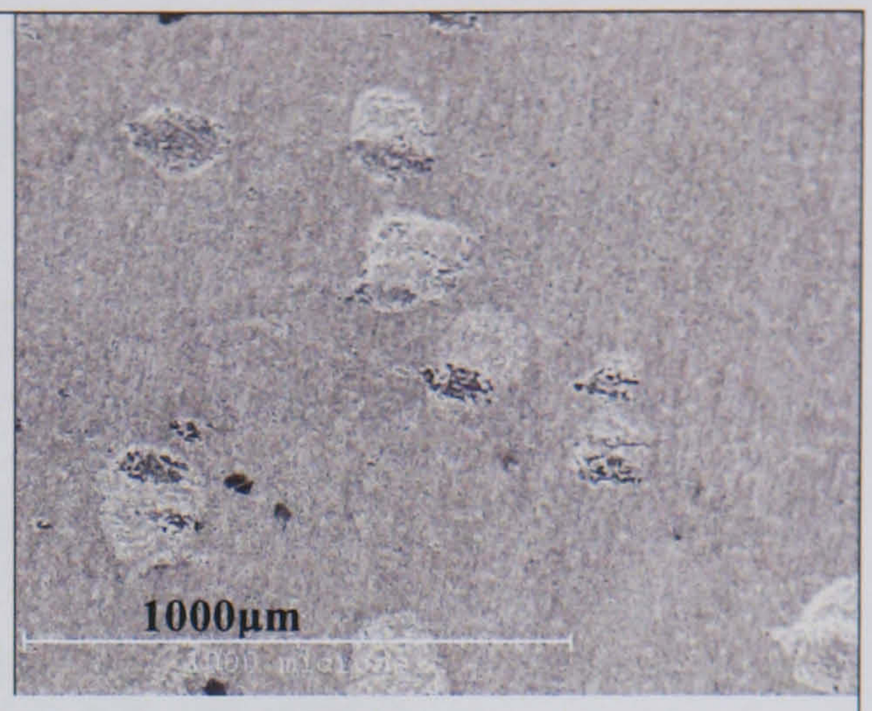 **Figure 6.17 SEM image with CRO under 20°C and 6000 rpm**
CRW8	Where the inhibitor film breaks down, the pitting corrosion occurred and the surface became rougher than at 1000rpm, and solid particle impacts the surface can be seen at the arrow in Figure 6.18. The pitting is more isolated than that of CGO, CRO and blank tests and both pitting number (12 pits per mm^2) and size (110 μm) for CRW8 are smaller than that of CGO, CRO and blank as shown in Figure 6.19.	
	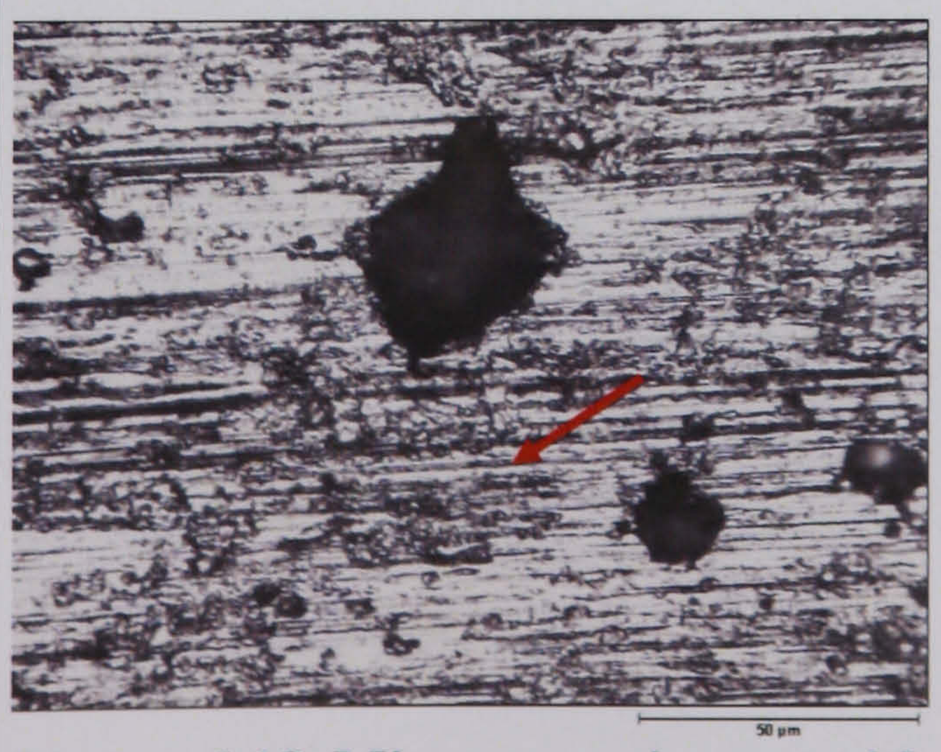 **Figure 6.18 Microscope image with CRW8 tests under 20°C/6000rpm**	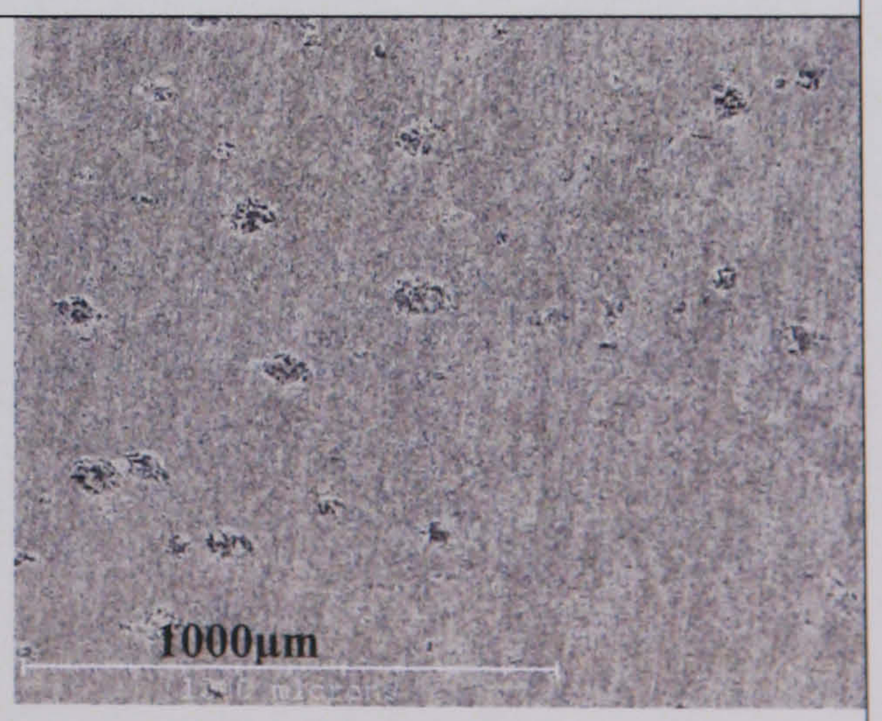 **Figure 6.19 SEM image with CRW8 tests under 20°C/6000rpm**

CRW9	From Figure 6.20, it can be seen clearly that pitting is less (9 pits per mm^2) and smaller (100 μm) with CRW9, with relatively round shape compared with blank tests.

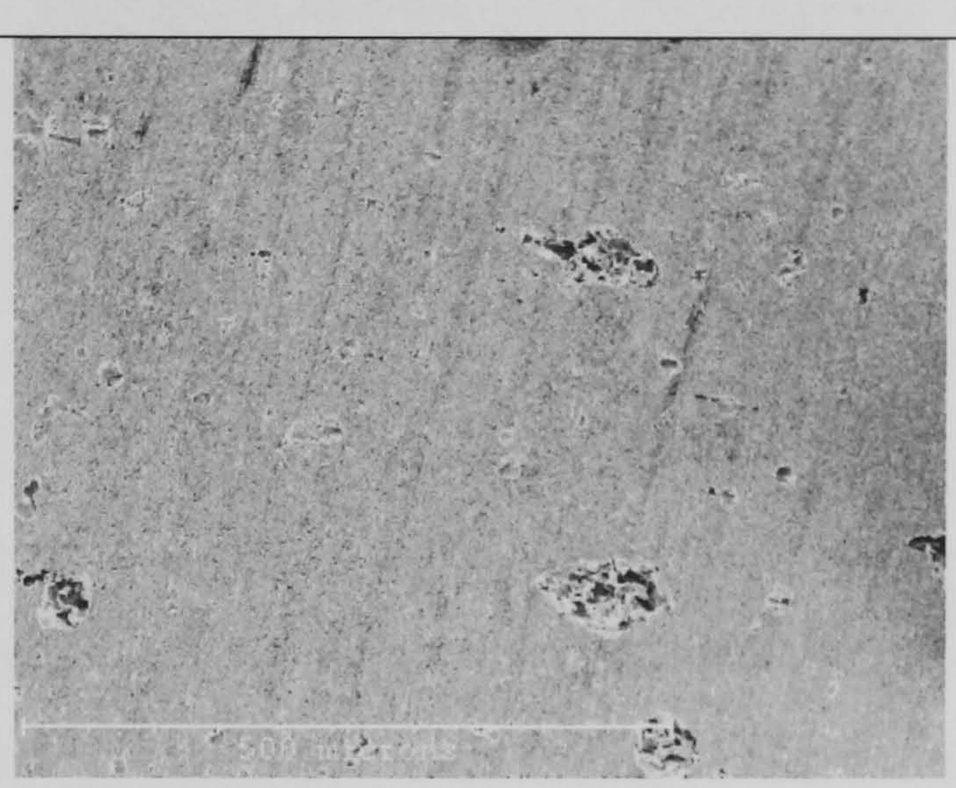

Figure 6.20 SEM image with CRW9 tests under 20°C/6000rpm

6.2.2 Surface Analysis after Erosion-Corrosion Tests at 50°C

Surface characteristics after erosion-corrosion tests at 50°C and 1000rpm are listed in Table 6.5.

Table 6.5 Surface characteristics after tests at 50°C and 1000rpm

50°C and 1000rpm rotational speed	
Blank	From Figure 6.21, corrosion is more uniform and less pitting occurs at 50°C than at 20°C. The uniform corrosion covered the entire surface. It indicates that corrosion products provide slight protection due to loose structure of the $FeCO_3$ film resulting in pitting or general corrosion. Cementite acts as a template onto which $FeCO_3$ can precipitate.

Figure 6.21 SEM image for blank tests at 1000rpm and 50°C

CRW8

Corrosion products still form, at the same time inhibitor film forms in a competitive way. This causes the products formation area smaller, producing very small pits on the surface, as shown in Figure 6.22. It also shows that inhibitor CRW8 can reduce the pit size and it means the inhibitor can make the corrosion products finer.

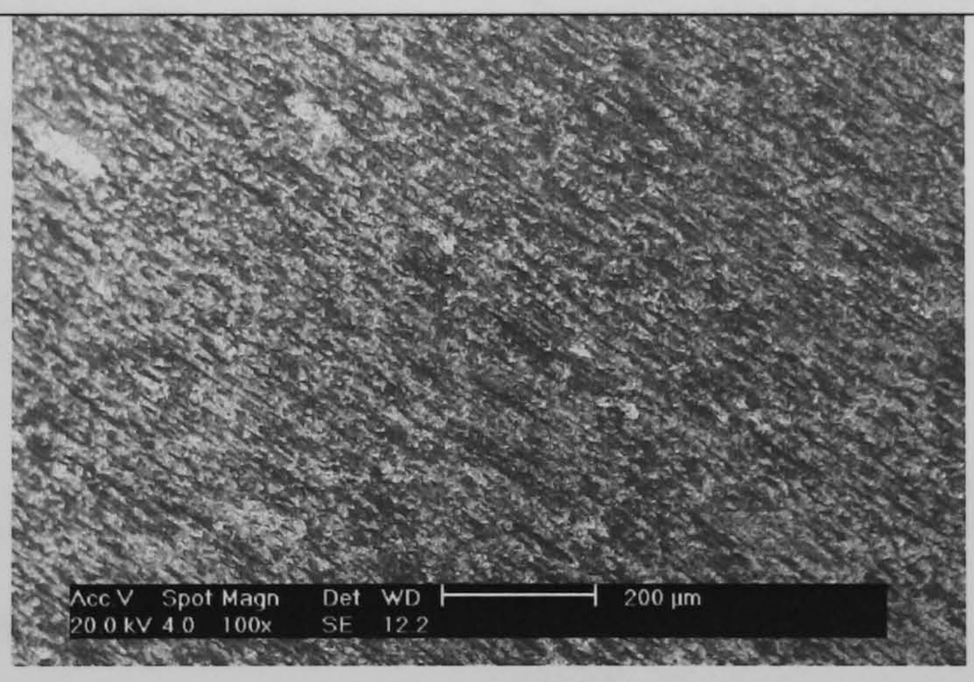

Figure 6.22 SEM image for CRW8 at 1000rpm and 50°C

CRW9

From Figure 6.23, pit size is smaller than blank tests but bigger than with CRW8 tests.

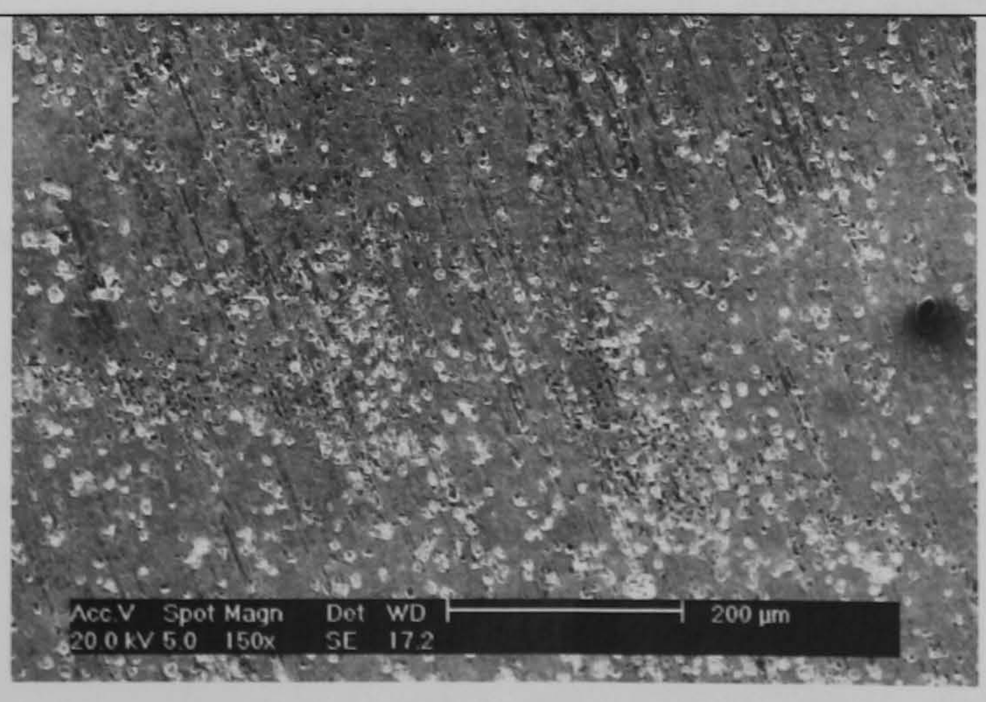

Figure 6.23 SEM image for CRW9 at 1000rpm and 50°C

Table 6.6 listed the surface characteristics after erosion-corrosion tests at 50°C and 6000rpm.

Table 6.6 Surface characteristics after tests at 50°C and 6000rpm

50°C and 6000rpm rotational speed		
Blank	From Figure 6.24, the number of pits increased with increase of speed. The pitting size is about 90 μm. Surface shows signs of spallation. Due to the iron dissolution, cementite from the pearlite is left on the surface, making the surface rough. Due to high shear stress, the cementite layer also appears to be spalled off by the flowing fluid with sand. Corrosion products can not be formed.	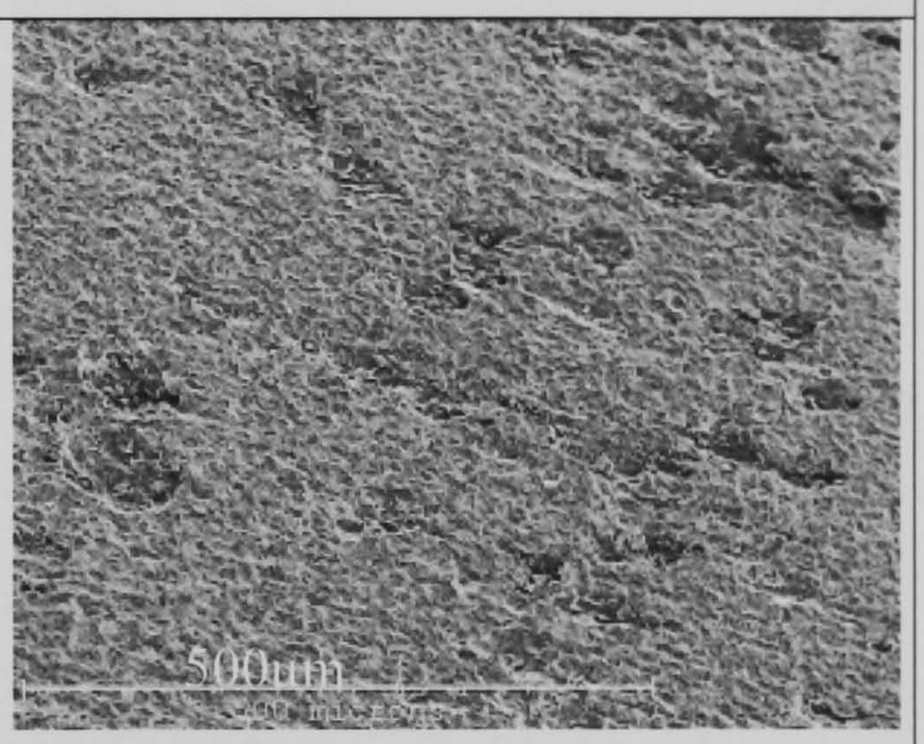 **Figure 6.24 SEM image with blank tests under 50°C and 6000rpm**
CGO	It can be seen that pitting is distributed most extensively with CGO (Figure 6.25) among the four inhibitors, and pitting size is smaller than with CRWs but it distributed over the whole surface indicates that inhibitor film is hard to formed on the metal surface. The inhibitor has no effect on reducing erosion-corrosion.	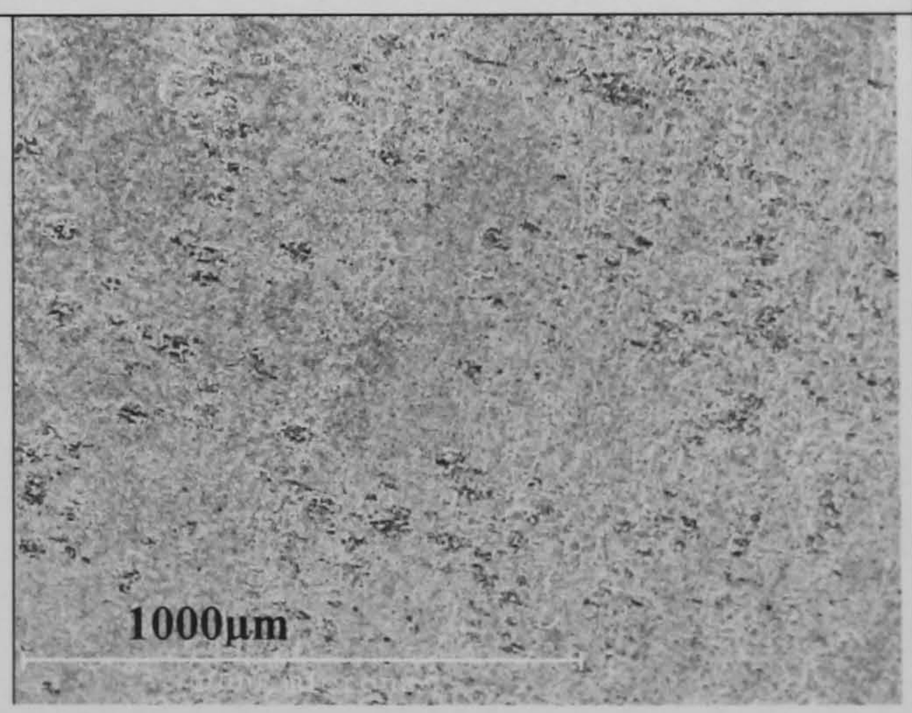 **Figure 6.25 SEM image with CGO tests under 50°C and 6000rpm**

CRO	Pitting size is small compared to the other inhibitor tests. It indicated that CRO can work with corrosion products to provide some protection for sand impact resulting in less pitting but still severe general corrosion as shown in Figure 6.26.	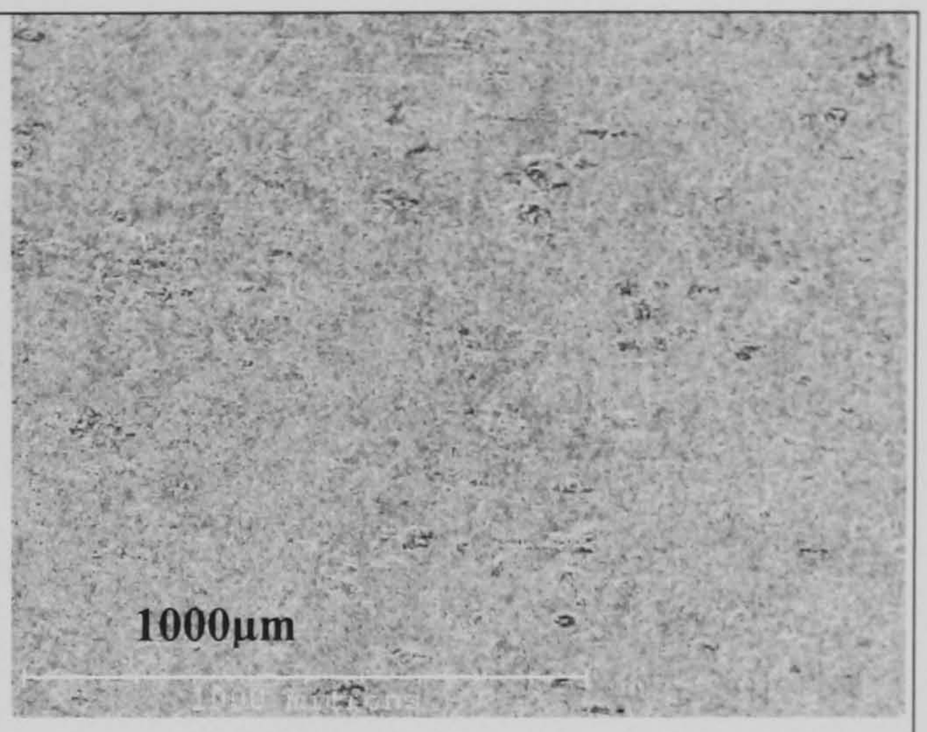 **Figure 6.26 SEM image with CRO tests under 50°C and 6000rpm**
CRW8	From Figure 6.27, general corrosion is more severe than at lower temperature, although is the least one among all the tests. It indicates that CRW8 can cooperate more with corrosion products but can be peeled off by higher shear stress, where pitting developed and larger than for CGO and CRO.	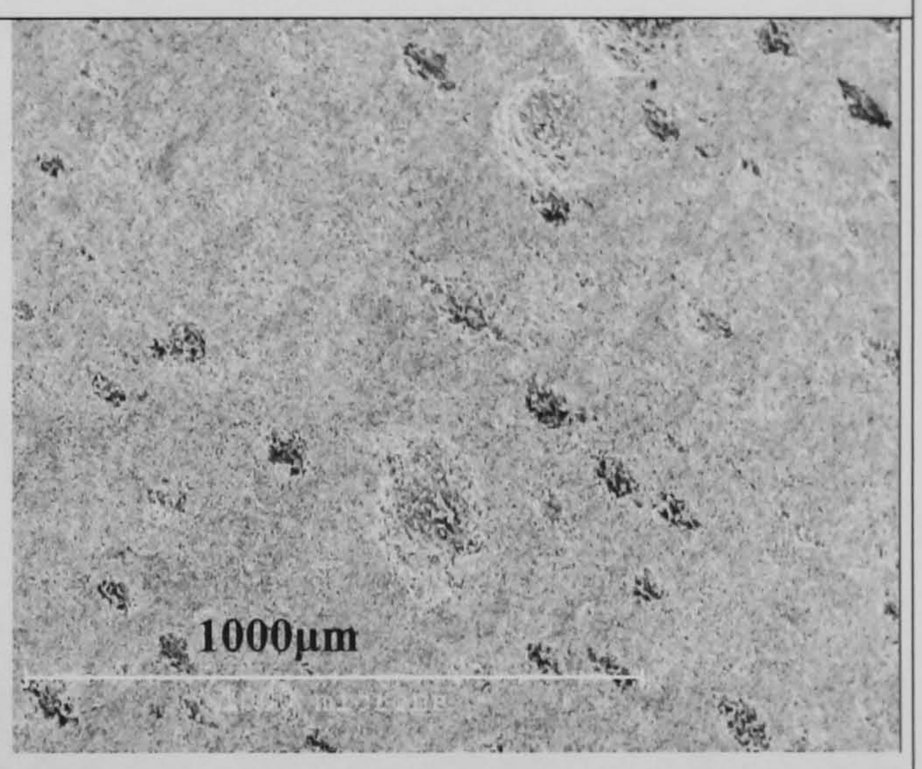 **Figure 6.27 SEM image with CRW8 tests under 50°C and 6000rpm**
CRW9	The inhibitor CRW9 is very likely removed under higher temperature resulting pitting corrosion as shown in Figure 6.28. The general corrosion makes the surface rough. Compared to blank tests, CRW9 provides low protection for both general corrosion and pitting corrosion.	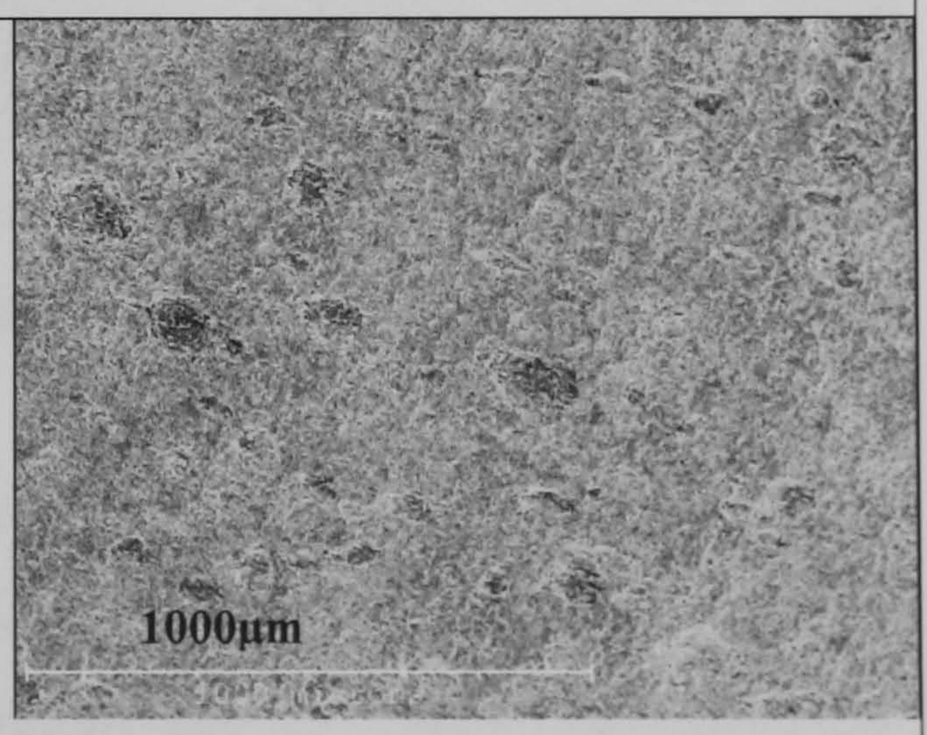 **Figure 6.28 SEM image with CRW9 tests under 50°C and 6000rpm**

6.2.3 Effect of Inhibitor Concentration

The SEM images for inhibitor CRW8 tests at 6000 rpm and 20°C for 50ppm, 100ppm and 150ppm are shown in Figure 6.29 (a), (b) and (c) respectively. The three figures demonstrate that with increase of inhibitor concentration from 50-100ppm, the number of pits is substantially reduced with 23 pits/mm², 12 pits/mm² and 2 pits/mm² for 50ppm, 100ppm and 150ppm respectively. In addition, the pitting size is reduced.

It can be postulated that at 50ppm due to insufficient inhibitor molecules accumulated on the metal surface on the area with no inhibitor pitting corrosion takes place. With increase of the inhibitor concentration, the increase of inhibitor efficiency can be attributed to two factors. One is that sufficient molecules are available to provide sufficient coverage of the inhibitor film on the metal surface; the other is that inhibitor can also be adsorbed onto the sand surface and can affect a reduction in sand velocity-impact energy.

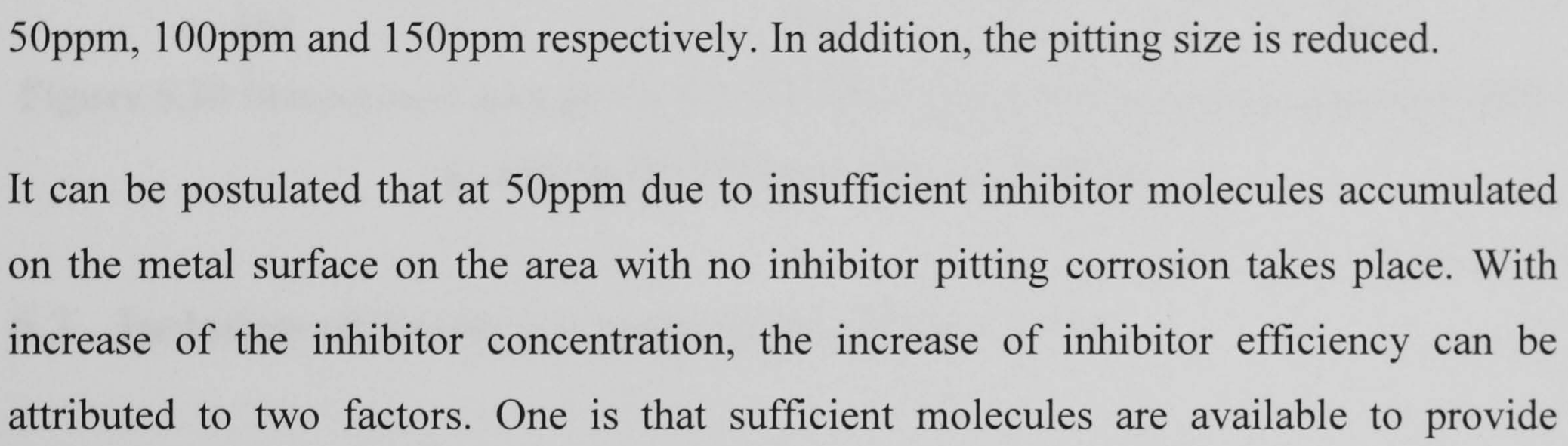

Figure 6.29 SEM images for CRW8 after 8 hours test at 6000 rpm and 20°C(a) 50ppm, (b) 100ppm and (c) 150ppm

The light microscope images for inhibitor CRW9 at 6000 rpm and 20°C for 50ppm, 100ppm and 150ppm are shown in Figure 6.30 (a), (b) and (c) respectively. Again they demonstrate that increase of the inhibitor concentration from 50-150ppm can effectively reduce pitting corrosion and general corrosion.

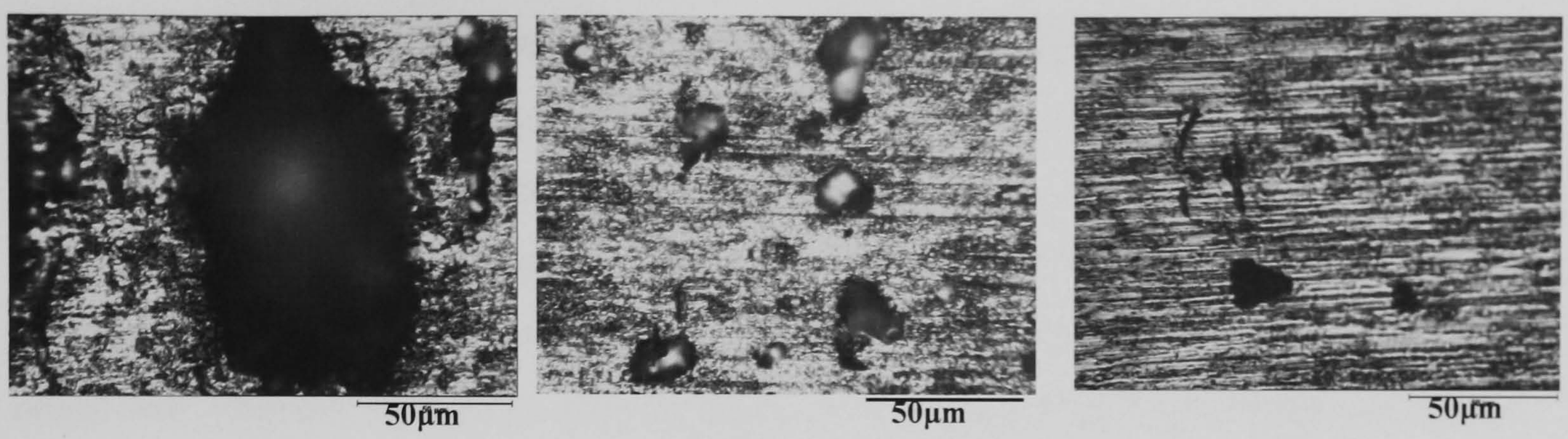

(a) (b) (c)

Figure 6.30 Microscope images for CRW9 after 8 hours test at 6000 rpm and 20°C (a) 50ppm (b) 100ppm and (c) 150ppm

6.3 Isolation of Erosion Component of Mass Loss

The total mass loss is composed of mass loss due to corrosion, erosion and any synergistic effects by the interaction of these two processes. In the previous section, the total damage of the material has been described. This section presents the mass loss due to mechanical erosion, namely pure erosion using cathodic protection to eliminate the electrochemical corrosion processes.

Impressed current from an external DC power source is provided to the metal sample to stifle anodic reactions. In this case metal corrosion can be eliminated in an attempt to measure the mass loss attributed to pure mechanical damage.

The potential applied to the samples was -0.8V for tests under 6000rpm and 50°C for 8 hours for all the four inhibitors. Two important issues for the application of potential need to be taken into account. Firstly, the over potential has to be sufficiently negative to significantly reduce corrosion, but too high an over-potential could cause hydrogen embrittlement. The second issue is charge applied to the sample with inhibitor film will change the charge of the inhibitor film and in turn change its properties. Figure 6.31 shows the 3 D chemical structure of $FeCO_3$. It shows that both C and Fe are surrounded by the bonds with O. $FeCO_3$ formation on the surface will favour the adsorption of the inhibitor onto the metal surface, because the surrounding O bond has partial negative charge. The partial positive elements from the inhibitor molecules will likely chemi-

adsorb onto the O bond on the metal surface. Without applying CP, the surface with inhibitor tests can be described schematically as shown in Figure 6.32 (a) where the partial positive charged elements from inhibitor molecules bond with the negative charged $O^{\partial(-)}$. When applying CP, there are electrons accumulated on the surface preventing the metal from corrosion. The electronegativity will favour the formation of bonds with inhibitor molecules onto the metal surface. Therefore the process will allow more inhibitor molecules to be adsorped onto the metal surface as schematically shown in Figure 6.32 (b). Therefore, with applying CP, the mechanical interface between metal and solution will potentially change as more inhibitor molecules can be adsorbed on the metal surface. Although it is appreciated that application of CP can potentially change the interface, it is assumed that the impact characteristics of the sand are such that these effects are minimal and therefore application of CP can be used as a reasonable estimate of the erosin damage.

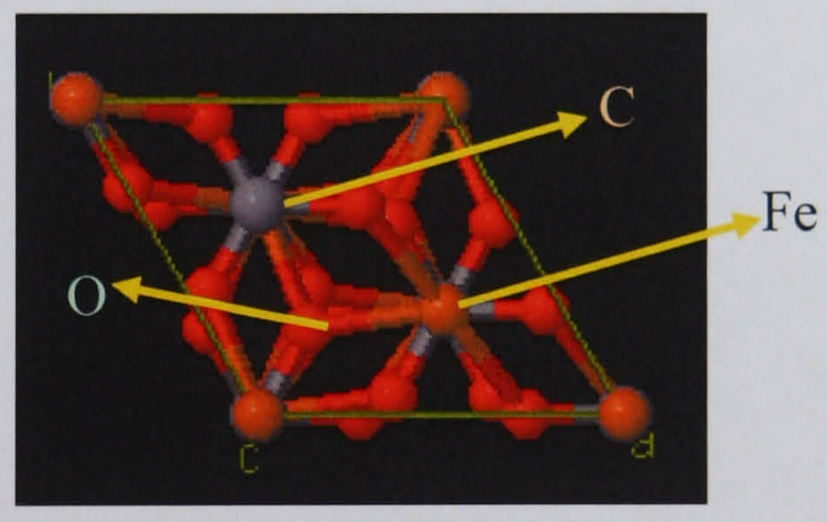

Figure 6.31 3D Chemical structure of $FeCO_3$

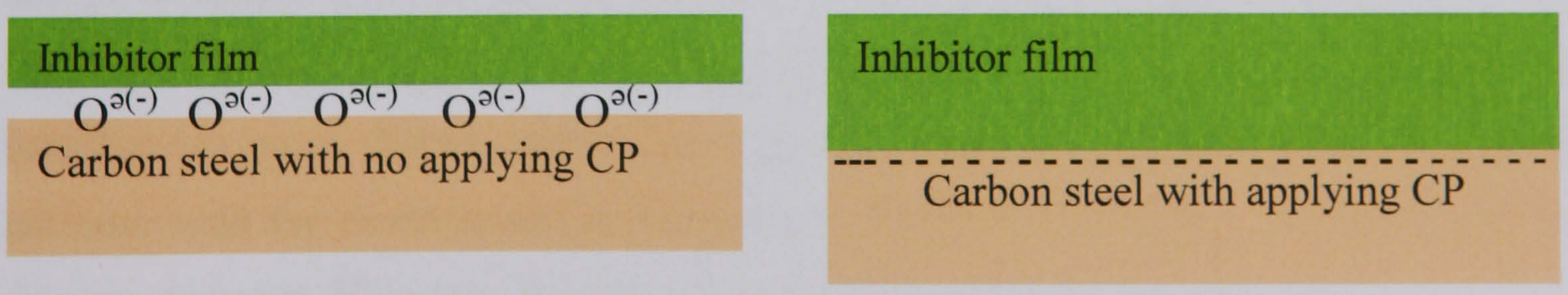

Figure 6.32 Schematic diagram for metal surface with inhibitor film form (a) when without applying CP and (b) when applying CP

PAGE

MISSING

IN

ORIGINAL

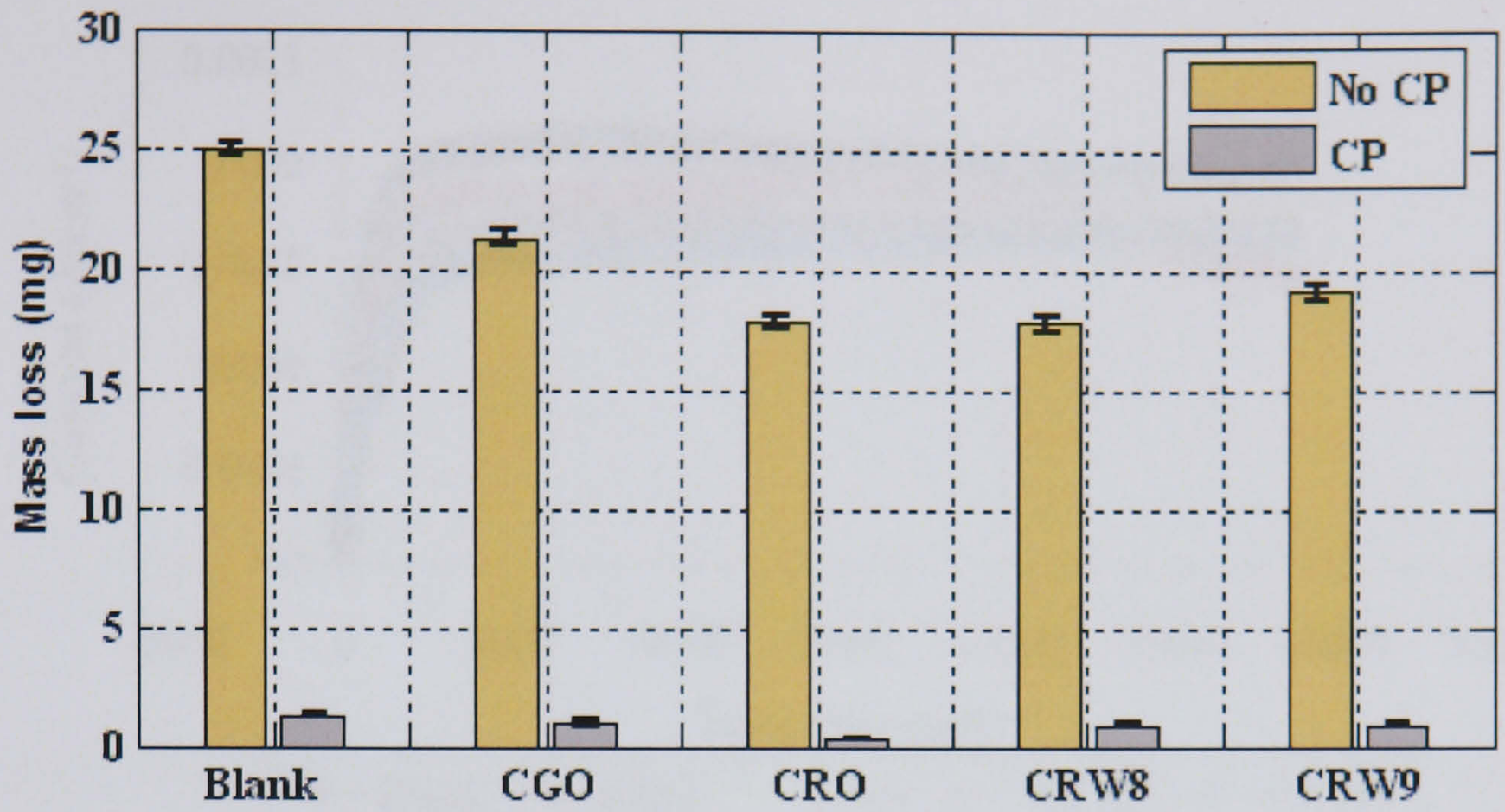

Figure 6.33 Mass loss for blank system and the inhibitor CGO, CRO, CRW8 and CRW9 for 8 hours with CP or without CP at 6000rpm and 50°C

The second important point from Figure 6.33 is the apparent reduction in mass loss with CP together with inhibitor. For all the four inhibitors, the mass loss is in the range from 0.3 to 1.0 mg. This demonstrates the reduction of the mechanical damage by the flow and the particle impact. Most likely the inhibitor film reduces the impact energy of the particles on the metal surface and facilitates the adsorption of the inhibitors on sand. The film formation is confirmed if the current versus time traces are analysed in Figure 6.34. It is clear that the application of CP in the presence of inhibitor reduces the magnitude of the cathodic current and the likely mechanism is by forming a physical barrier to charge transfer across the metal/solution interface. The current values with inhibitors are very similar to each other, which can prove the CP does not change the interface too much. These currents are related to if the CP can result in the reaction of inhibitor with the environment or dissolution of inhibitor molecules causing giving or gaining electrons. However, it could not be included in this research work.

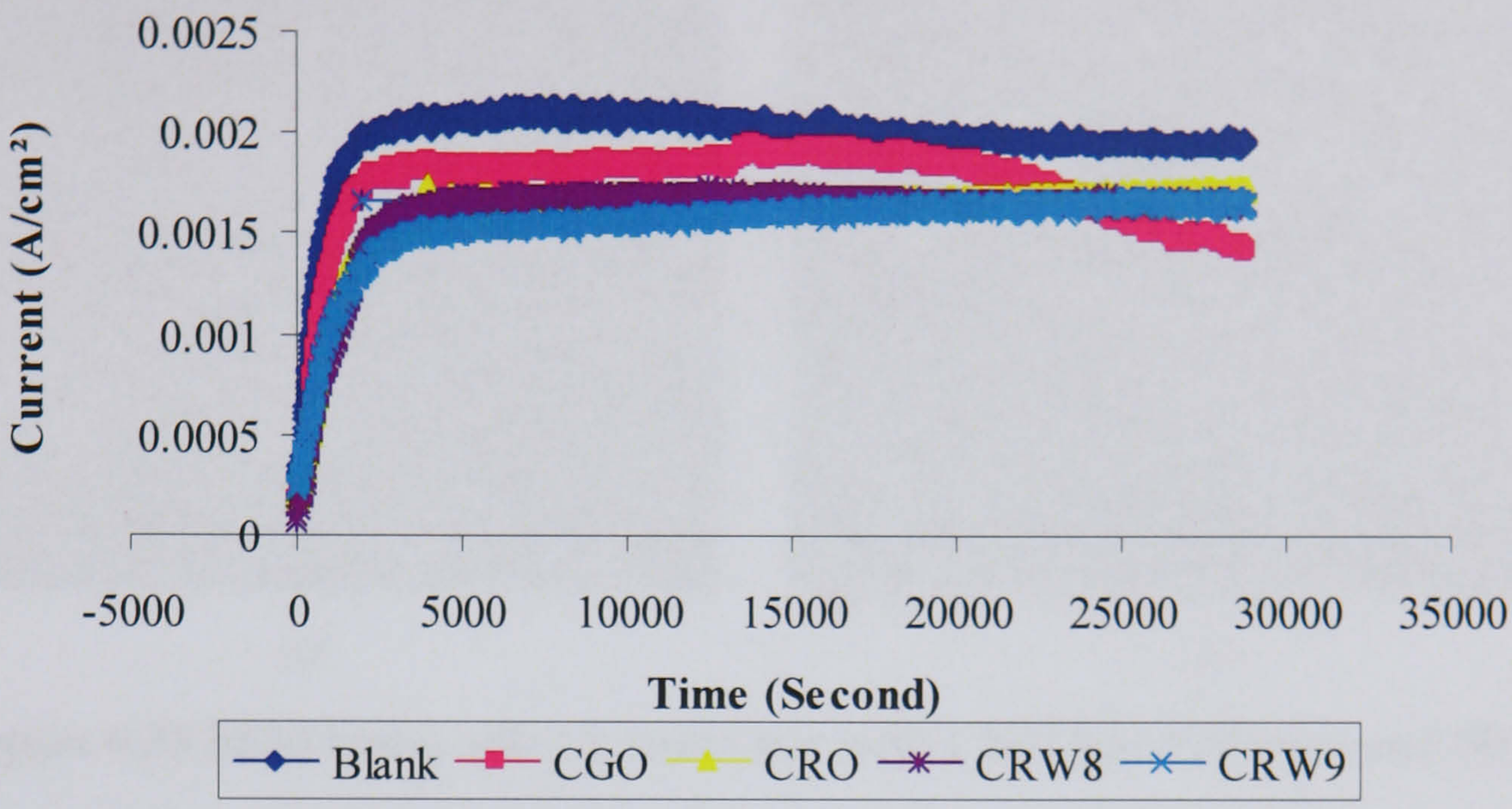

Figure 6.34 Comparison of current values for CP tests with and without inhibitor under 6000rpm and 50°C

As expected, when CP is applied, pitting is eliminated as shown in Figure 6.35 (a) for CRW9 and with its enlarged image shown at Figure 6.35 (b). It is clear that the damage by corrosion is no longer evident but there is still clear mechanical impact damage, shown by the arrows in Figure 6.35 (a), indicating low angle impact of sand on the surface. The comparison of the images after CP tests under this condition for CRW9 and blank tests shows that, CRW9 reduces the sand particle impact due to forming an inhibitor film on the metal surface.

For CP tests with inhibitor CGO, the SEM images are shown in Figure 6.37 (a) and enlarged image in (b). It can be seen from both pictures that surface is rougher compared with the CP tests with CRW9 (Figure 6.35 (a) and (b)). With small pitting size distributed all over the surface, indicating that the corrosion is not totally eliminated in this condition. For CP tests with inhibitor CRO, the SEM images after the tests are shown in Figure 6.38 (a) and (b). There are only several pits on the entire surface, which can be also due to the sand impacting the surface shown in Figure 6.38 (b).

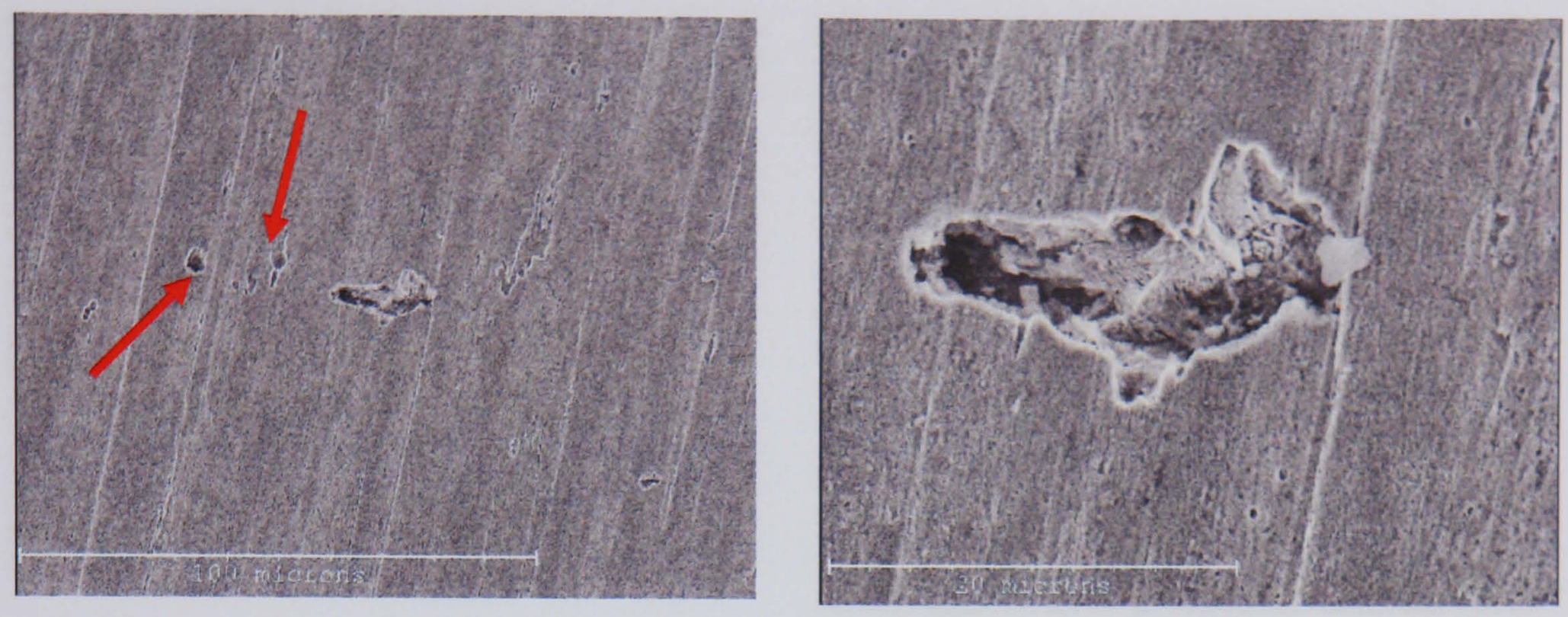

(a) (b)

Figure 6.35 SEM image after 8 hours test with CRW9 at 6000rpm and 50°C

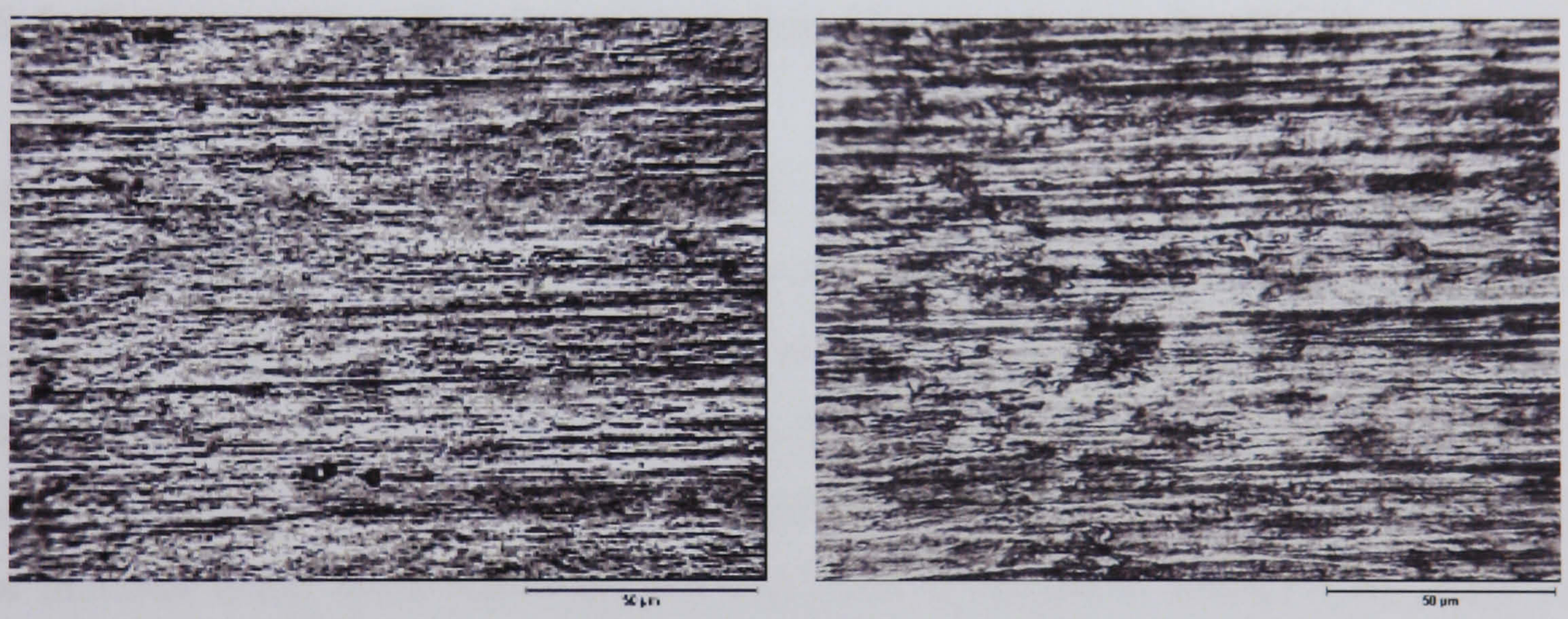

(a) **(b)**

Figure 6.36 Microscope images after 8 hours test with (a) CRW9 and (b) Blank

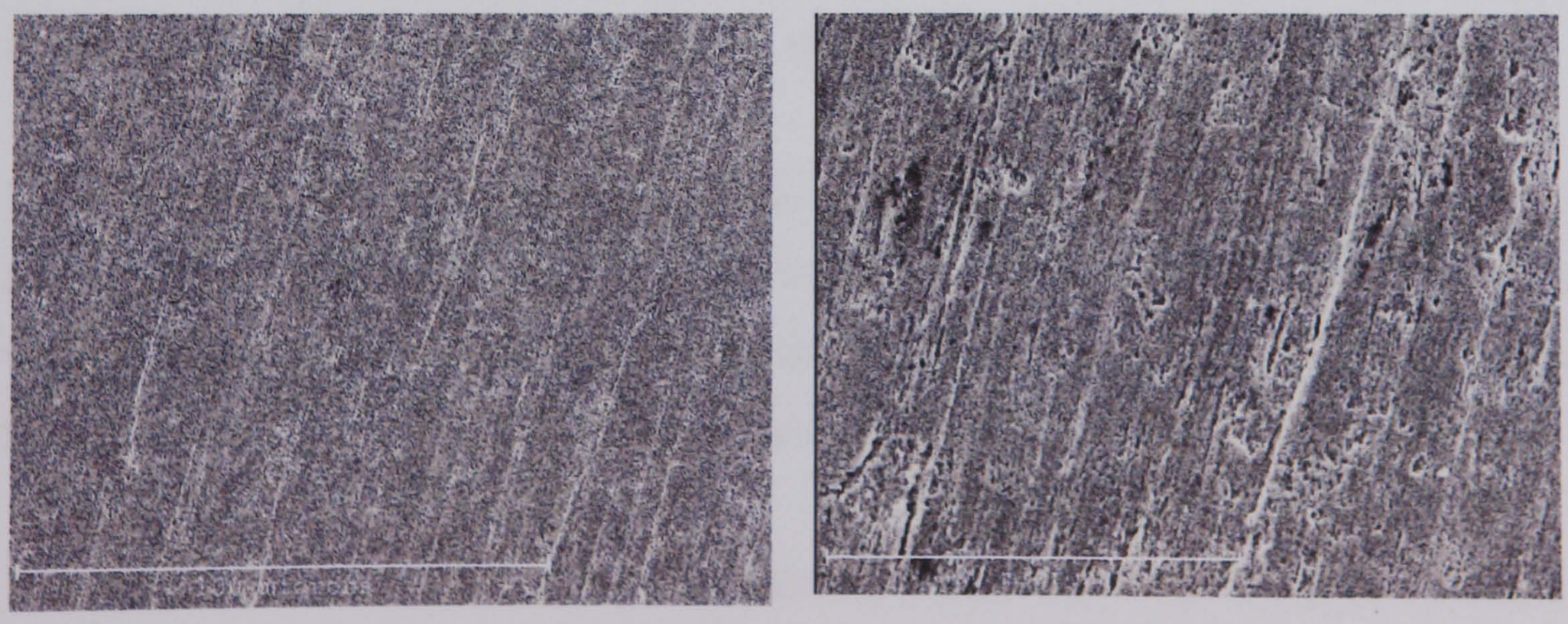

(a) (b)

Figure 6.37 SEM image after 8 hours test with CGO at 6000rpm and 50°C

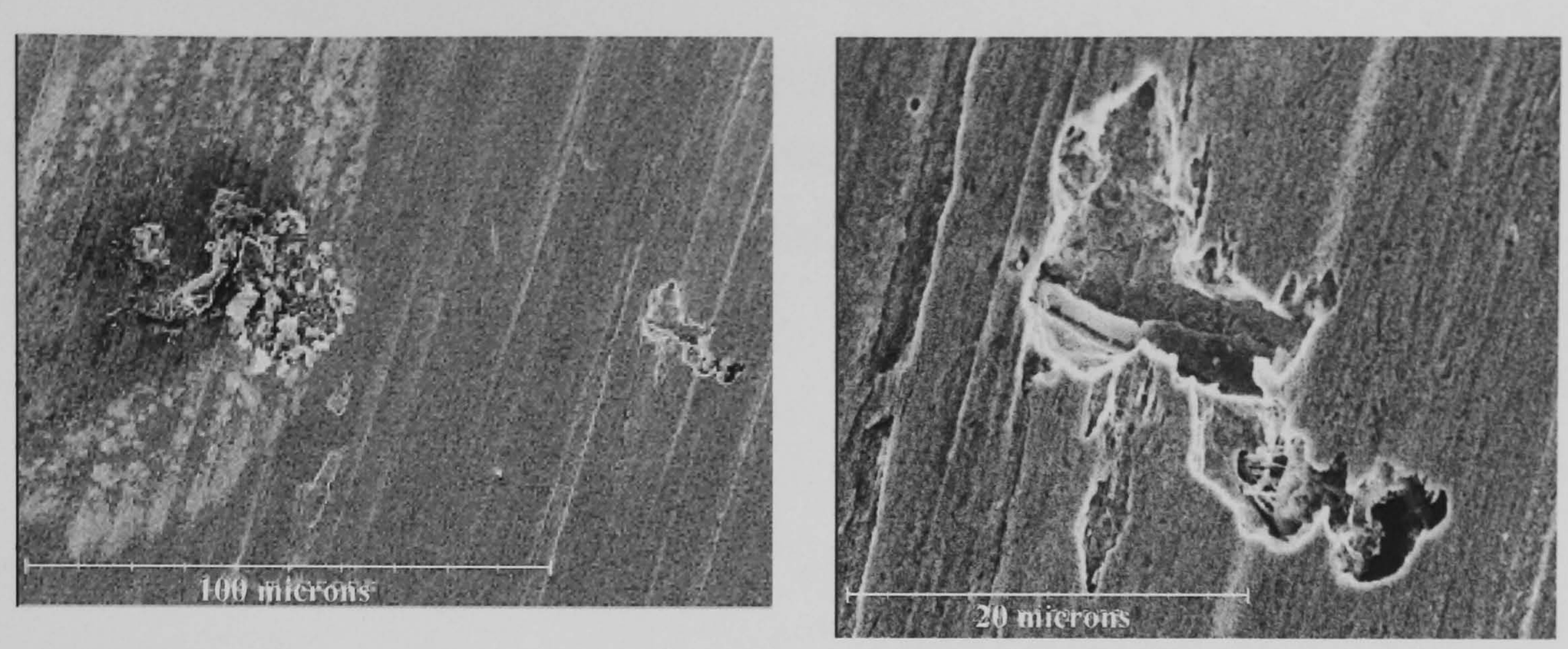

(a) (b)

Figure 6.38 SEM image after 8 hours test with CRO at 6000rpm and 50°C

6.4 Summarising Erosion-Corrosion Results Using the RCE

With blank tests under all the conditions, pitting corrosion combined with general corrosion happened on the metal surface. With increase of rotational speed, the erosion-corrosion rate is increased. At higher temperature, the corrosion products formed more than lower temperature. Thus under lower rotational speed the mass loss with higher temperature is lower than with lower temperature. Pitting can be eliminated by addition of inhibitor under lower rotational rate and lower temperature. Inhibitor has effect on erosion-corrosion. The most important aspect is that inhibitor can reduce erosion by forming a film on the metal surface or by adsorption on sand as a result reducing sand impact energy. Material degradation due to sand impacts is identified.

With CGO tests, under lower temperature and lower speed, the inhibitor can form a firm film on the metal surface through bonding interaction with iron carbonates. However, it will be peeled off from the surface with the iron carbonate products with increasing flow rate. Therefore it has no effect in reducing erosion-corrosion rate.

With CRO as an inhibitor, it only performed better than other inhibitor at higher temperature. At lower temperature and lower speed, it works as a corrosion promoter resulting from more iron carbonate products being stripped off by the flow and sand than with blank tests. Therefore, pitting size is larger than blank tests.

With CRW8 tests, it exhibits 100% efficiency under lower temperature and lower rotational speed. It performs better than other inhibitor at higher temperature. CRW9 has the best performance under higher rotational speed and lower temperature.

CHAPTER 7 RESULTS AND DISCUSSION OF CORROSION *IN-SITU* MEASUREMENTS USING RCE

This chapter presents corrosion results relating to assessment of inhibitor action using a RCE and is directly linked to the erosion-corrosion results in chapter 6. Therefore test conditions are the same as chapter 6. DC linear polarisation and AC impedance electrochemical techniques were used in this study to assess the corrosion rate *in-situ* and the corrosion inhibition mechanisms. The main parameters from AC impedance studies are discussed under different rotational speeds and temperatures. A map to describe the experiments conducted for this part of the study is presented in Figure 7.1. At the end of this chapter, the effects of flow velocity and entrained sand on inhibitor performance are studied in terms of the ability of the inhibitor to reduce corrosion, erosion and the synergistic interactions of corrosion and erosion.

7.1 Free Corrosion Potential Measurements

In electrochemical corrosion measurements, the free corrosion potential (E_{corr}) is often measured to determine if the working electrode has reached the steady state. It is also often measured to assess the changes in accordance with the step changes in the corrosion environment or corrosion regime, to qualitatively assess the change of the electric double layer (EDL) properties. The direction of potential change is determined by how the EDL chemistry adjusts to accommodate electrolyte chemistry. It is often a useful parameter to ascertain whether anodic or cathodic processes are controlling. It does not quantitatively give the corrosion rate of the material since even if potentials are similar between two corrosion regimes, the corrosion current (i_{corr}) can be very different.

Free corrosion potential measurements were carried out at 0, 0.5 and 1 hour exposure times. Figure 7.2 (a) and (b) show the free corrosion potential (E_{corr}) values at 1000rpm rotational speed at 20°C and 50°C respectively; Figure 7.3 (a) and (b) shows E_{corr} under 6000rpm rotational speed at 20°C and 50°C respectively.

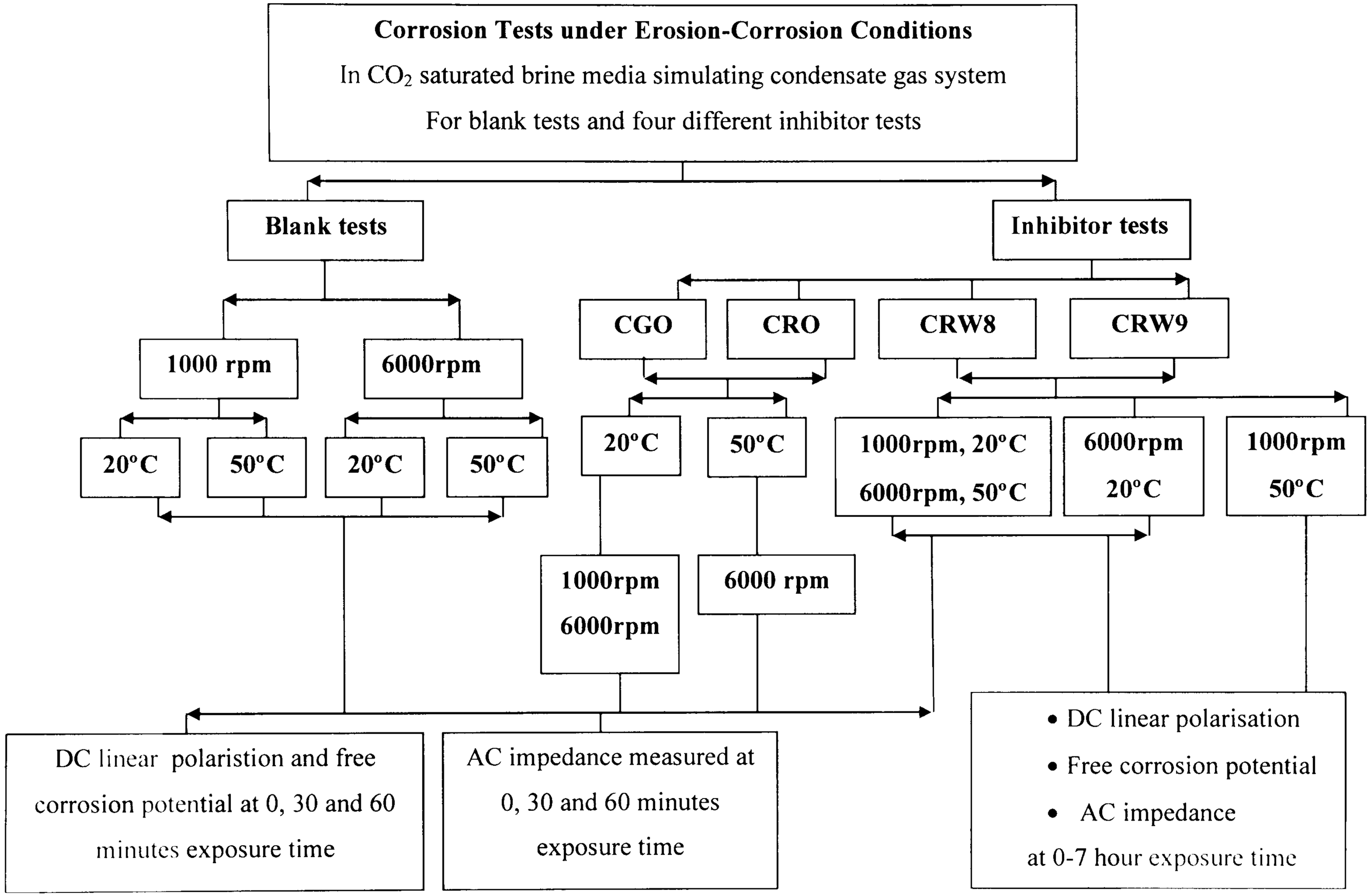

Figure 7.1 The map of experimental work presented in Chapter 7

As far as the measured values of corrosion potential (E_{corr}) are concerned, the effect of rotational speed is dominant. In flowing conditions, the temperature effect on E_{corr} is not as obvious as the effect due to flow speed. The variation of measured corrosion potential, E_{corr}, of the four tested inhibitors at different rotation rates, shows a clear tendency to be more anodic as the rotation rate increases. This shift to more positive potential has been explained by the effect of flow on the cathodic diffusion current (Silva *et al.*, 2004).

As free corrosion potential measurements can provide information about the mode of the adsorption of the inhibitor, at 1000rpm rotational speed, it can be seen that the addition of inhibitor CGO, CRO, CRW8 and CRW9 shifts the E_{corr} in the noble direction. This is an indication that the inhibitors are all anodic kinds of inhibitor. This has also been seen for static conditions. However, at 6000 rpm the potential agitation exists due to concentration change of the different species, such as CO_2. From an electrochemical point of view, by increasing the rotational speed, the concentration of Fe^{2+} ions (at the surface) should reduced resulting in potential shifting to negative direction. On the other hand, more CO_2 moving to the metal surface, after hydration the H^+ concentration increases, causes the potential to shift in the noble direction. With addition of inhibitor, the H^+ concentration is less than with blank solution. This is why the potential for blank tests is more noble than with inhibitor tests at higher rotational speed as shown in Figure 7.3 (a). Thus the results of free corrosion potential with inhibitor tests do not follow the behaviour under static conditions. Therefore to test whether the inhibitor is anodic or cathodic type, static conditions are necessary to avoid the potential agitation due to high speed. Under 1000rpm and 20°C, the presence of inhibitors CGO and CRO shift the free corrosion potential in the positive direction by a smaller amount, about 50mV compared to the 100 mV by the CRWs as shown in Figure 7.2 (a). It might be related to the coverage of the anodic sites by inhibitor and is in agreement with the results of the charge transfer resistance measurements from AC impedance tests presented later in this Chapter.

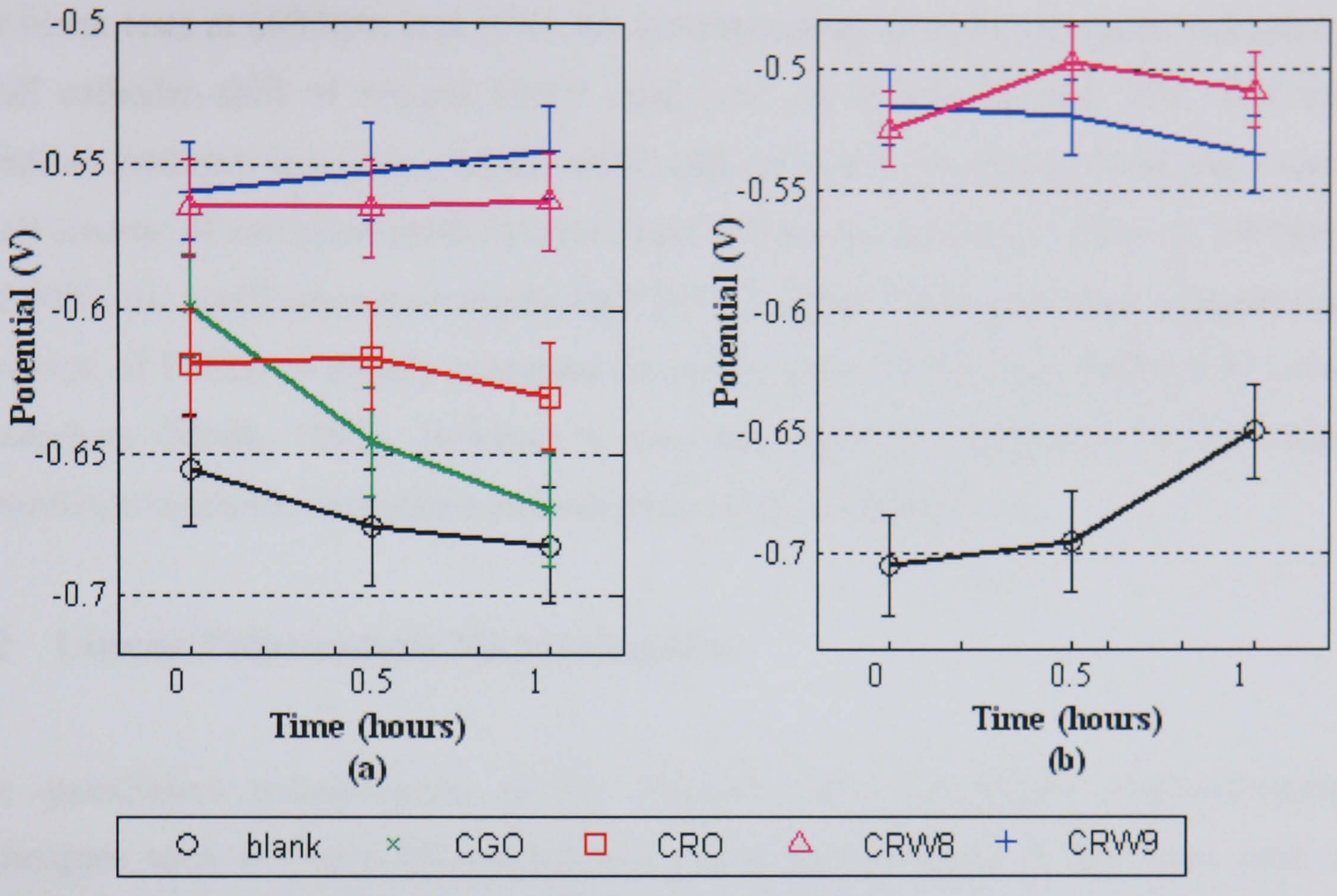

Figure 7.2 Free corrosion potential at 0, 0.5 and 1 hour exposure time at 1000rpm rotating speed and (a) 20°C or (b) 50°C

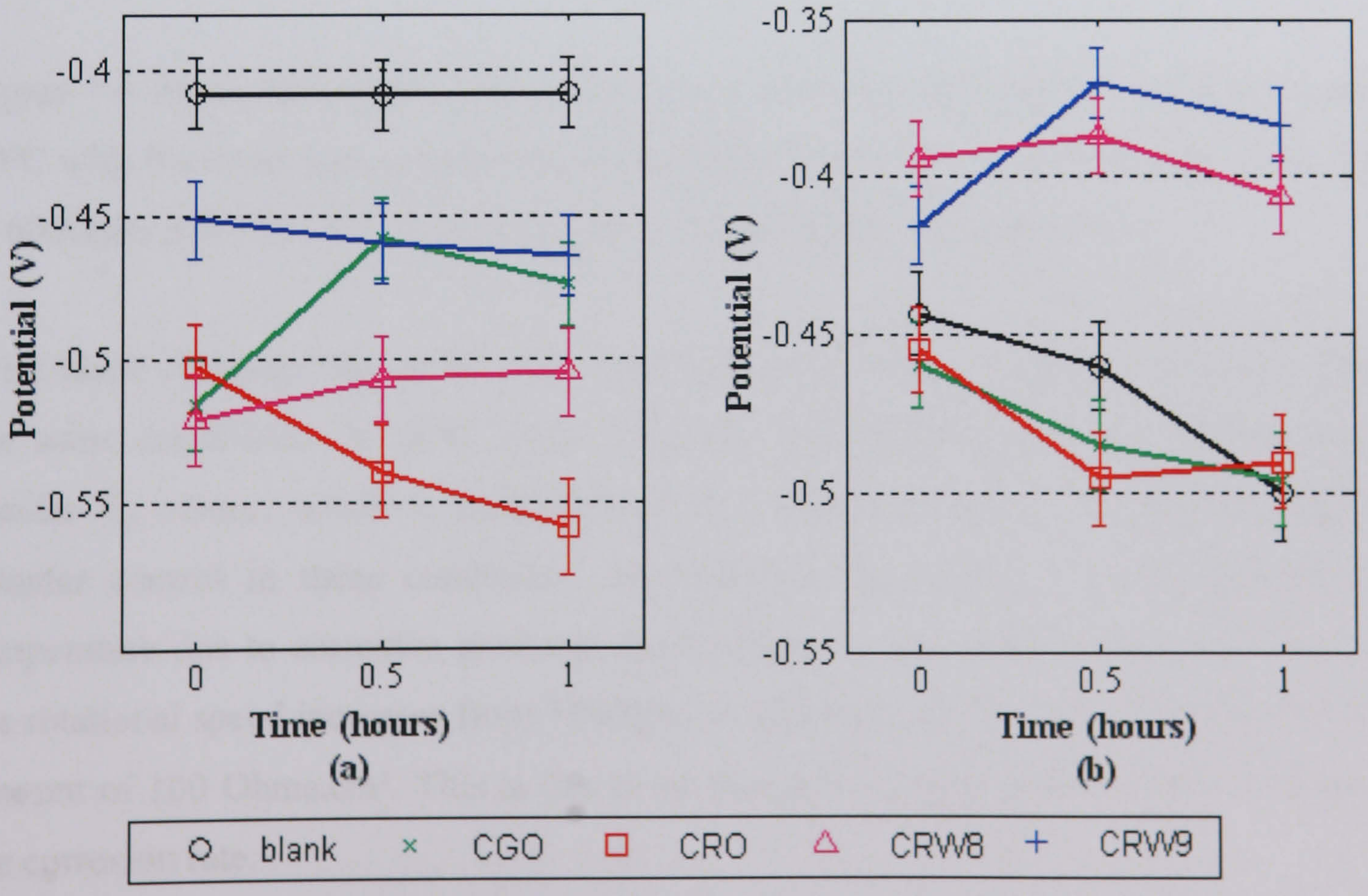

Figure 7.3 Free corrosion potential at 0, 0.5 and 1 hour exposure time at 6000rpm rotating speed and (a) 20°C or (b) 50°C

For blank tests at 6000rpm and 50°C. the corresponding corrosion potential indicates a small cathodic shift of around 50mV over time. At 1000 rpm and 50°C. the free corrosion potential indicates a small anodic shift of 30mV. It indicated that there were small amount of corrosion products layer start to form on the metal surface at 1000rpm and 50°C, the small amount of anodic shift in E_{corr}, about 50mV with time suggests that coverage of $FeCO_3$ is mainly occurring at anodic sites, which was observed by other researchers (Malik, 1992). However it does not offer any protection in this study according to corrosion resistance measurements (presented later).

7.2 Linear Polarisation Measurements

For quantitative determination of the corrosion rate, accelerated electrochemical techniques such as linear polarisation are useful. In this study, it has been used in conjunction with analysis of AC impedance data. As stated in Chapter 3, AC impedance is more accurate in terms of assessing corrosion rates in conditions where inhibitor film characteristics are important.

Figure 7.4 shows the results of the polarisation resistance (R_p) attained at 1000rpm and 20°C with the lower part is enlarged on the right. The results at 6000rpm and 20°C and at 6000rpm and 50°C are shown in Figure 7.5 and Figure 7.6 respectively.

With blank solutions, the values of R_p recorded at 0 to 1 hour are relatively stable under the same conditions. At 20°C, both, 1000rpm and 6000rpm rotational speeds have similar R_p values, which is indicative of the corrosion process being under charge transfer control in these conditions. At 1000rpm, R_p decreases with increasing of temperature due to corrosion products accumulating on the metal surface. At 50°C, as the rotational speed increases from 1000rpm to 6000rpm, the R_p value decreases by the amount of 100 Ohms.cm^2. This is due to an increase of mass transfer which increases the corrosion rate.

In all inhibitor tests, R_p values drop as exposure time progresses. This is an indication that an inhibitor film is formed on the metal surface and the coverage can be reduced by

flow and sand impact. Increasing the rotating speed, accelerates the desorption process due to the increased shear stress. Under certain experimental conditions, especially at 1000rpm rotational speed and 50°C, iron carbonate is produced even may not offer much protection but is ready to adsorb corrosion inhibitor molecules. With different conditions, carbonate layers growing in the presence of inhibitor may exhibit different performances with respect to their protection. Both the iron carbonate layer and the inhibitor film are strongly affected by flow velocity and temperature. When sand particles hit the metal surface, local stresses can be higher than calculated one in Equation (74) of Chapter 3. This is because the inhibitor molecules were stripped away from the metal surface.

Figure 7.4 Comparison of R_p values from linear polarisation at 1000 rpm rotating speed and 20°C

With CGO tests at 1000rpm, R_p has higher values than CRW9 and CRO. CRO provides little corrosion protection under any of the conditions. With CRW8, it shows that at the lower rotational speed and at 20°C the R_p values were extremely large, indicative of the inhibitor forming a film which imparts a large resistance to charge transfer on the metal

surface. Also the film appeared to remain intact and no significant lowering of R_p over time occurred. Under these conditions the inhibitor CRW8 showed approaching 100% efficiency in erosion-corrosion as shown in chapter 6. This implies that corrosion is a controlling parameter in erosion-corrosion. The linear polarisation plots in Figure 7.7 also show relatively stable free corrosion potential and polarisation resistance during the experimental time.

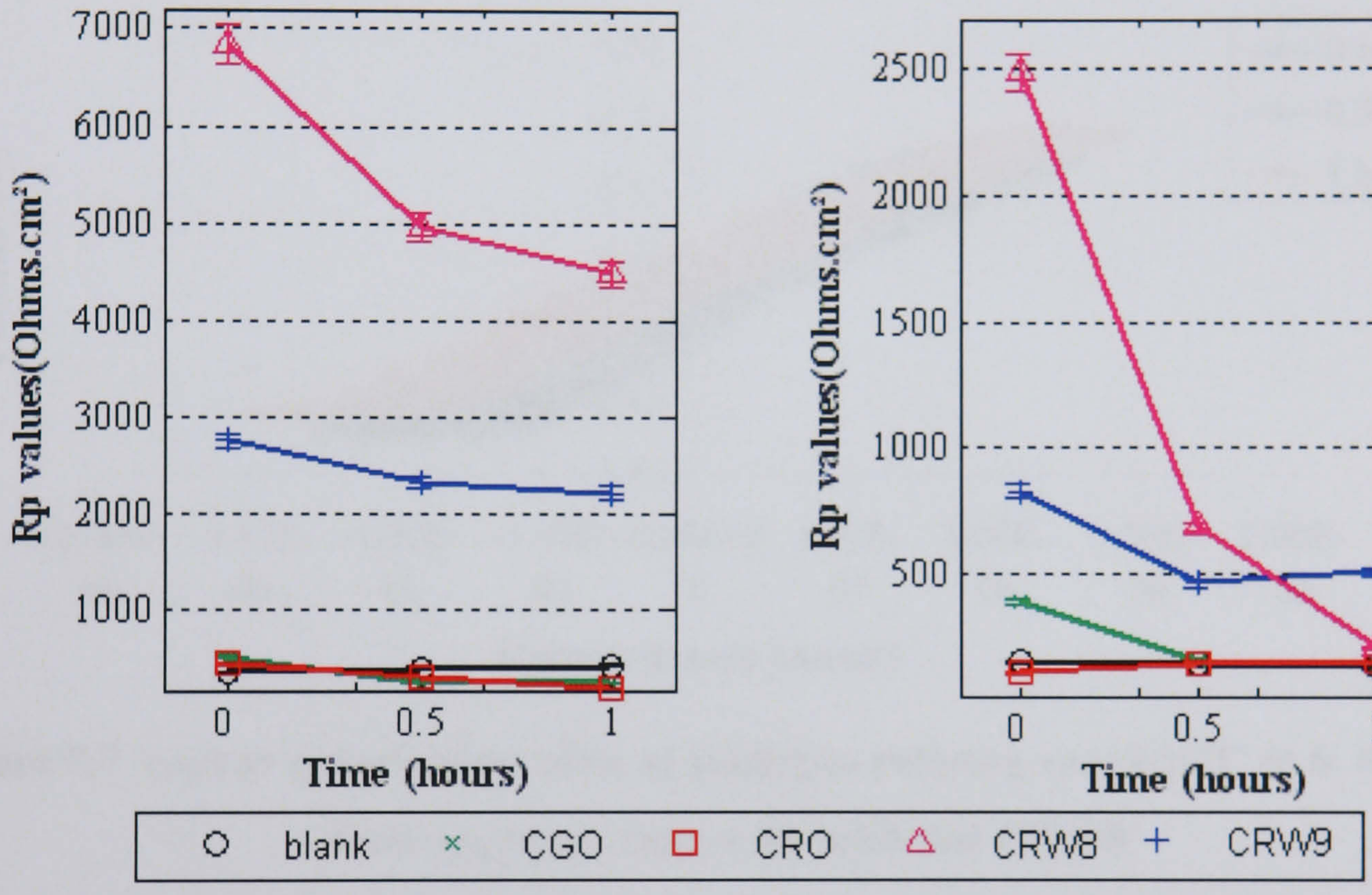

Figure 7.5 Comparison of R_p values from linear polarisation at 6000 rpm rotating speed and 20°C

Figure 7.6 Comparison of R_p values from linear polarisation at 6000 rpm rotating speed and 50°C

As at 6000rpm and 20C, CGO and CRO has no effect to erosion-corrosion, more tests at 1000rpm and 50°C were only conducted with CRWs and blank solution. R_p versus time results under these conditions are shown in Figure 7.8 for blank test, with CRW8 and CRW9 inhibitors.

The values of R_p decrease with time for tests in the presence of inhibitors. It is indicative that some inhibitor molecules impacted by the sand or flow were easily stripped away from the metal surface although they might adsorb back again onto the surface after the impacted stress was removed locally. Thus, the steel surfaces during the time that were not covered by inhibitor molecules would corrode at a quite high rate.

As a result, pitting corrosion happens. The R_p values for blank tests are relatively constant with time or as matter of fact they are increased slightly. It shows that the corrosion products accumulate on the metal surface due to the loose and coarse structure under these conditions. This is why the mass loss at 50°C is slightly lower than at 20°C at 1000rpm shown in chapter 6.

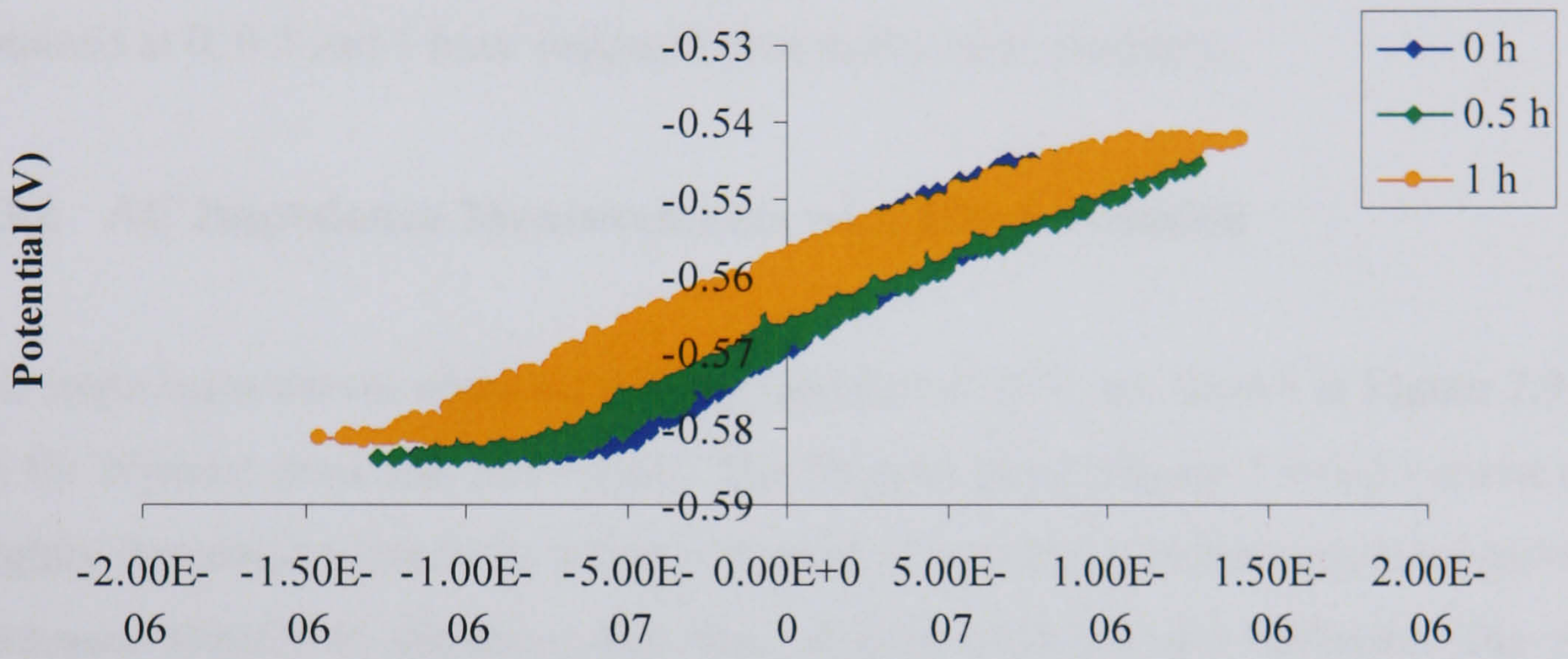

Figure 7.7 Linear polarisation plots at 1000rpm rotating speed 20°C at 0, 0.5 and 1 hour exposure time with inhibitor CRW8

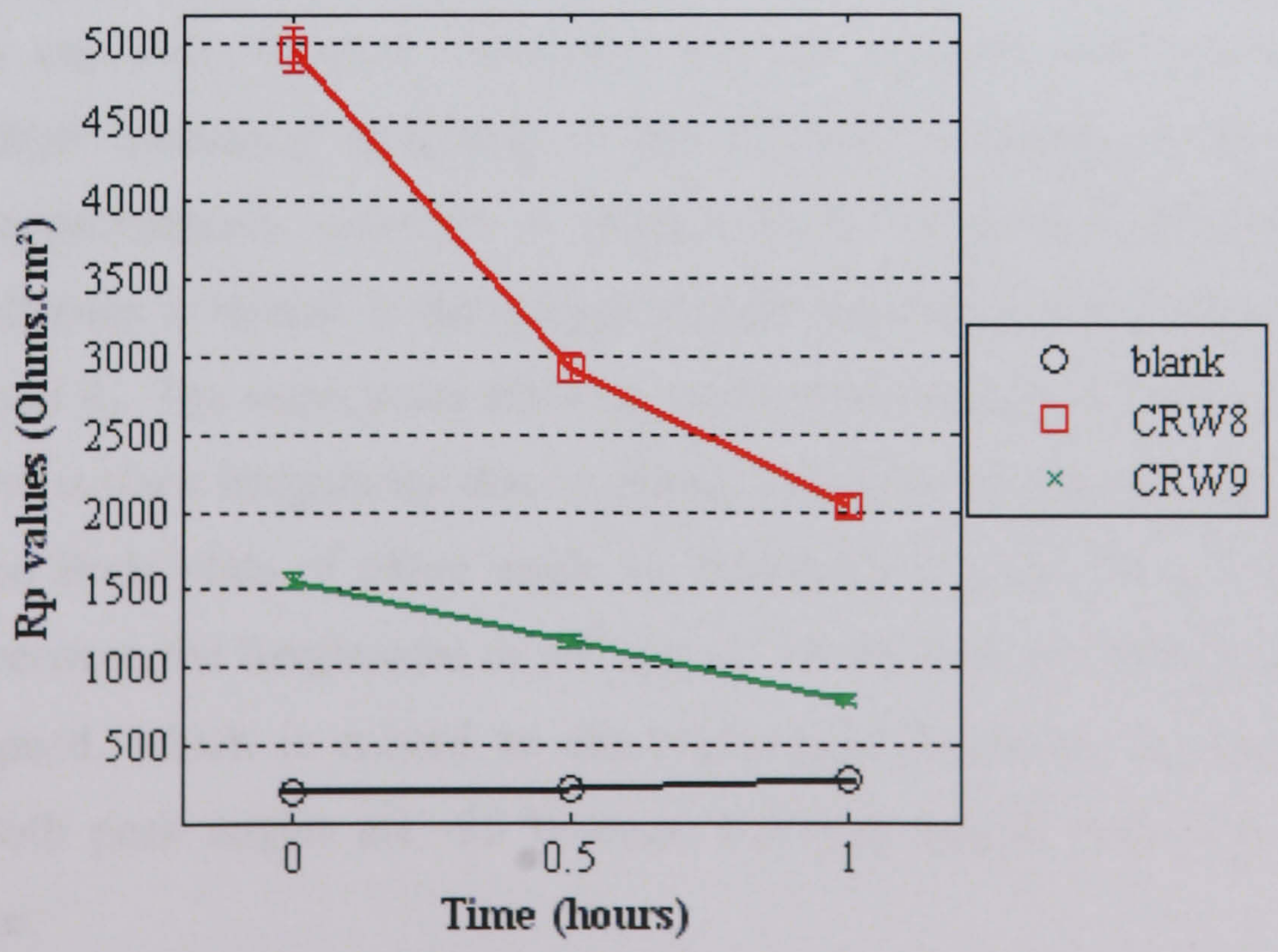

Figure 7.8 R_p values versus time for 100ppm CRW8, CRW9 and blank at 1000rpm and 50°C

7.3 AC Impedance Measurements

From linear polarisation results, it is known that the inhibitor film forms on the metal surface even at high shear stress multiphase flow conditions with sand. To obtain more detailed information about the kinetics and adsorption mechanisms of the inhibitor during the corrosion process, AC impedance was used. The impedance spectra were obtained at 0, 0.5 and 1 hour exposure time under each condition.

7.3.1 AC Impedance Measurements with Blank Solution

The impedance curves obtained without inhibitor at 20°C are shown in Figure 7.9 (a) to (c) for Nyquist plots and Bode plots. The Nyquist plots (Figure 7.9 (a)) consist of one slightly depressed semicircle, which is typical of a charge transfer controlled process. It decreases slightly in diameter with time at both 1000rpm and 6000rpm. The similar diameters of Nyquist plots indicate that corrosion rate is similar for both speeds at this temperature.

The Bode magnitude plots (Figure 7.9 (b)) at both 1000rpm and 6000rpm rotational speed show one time constant associated with the Nyquist plots accordingly. The plateau at high frequency is related to the solution resistance of the system, R_s, remaining approximately constant at around 81-91 Ohms.cm^2 at 20°C. The low frequency plateaus is related to the charge transfer resistance of the system, and is the sum of R_{ct} and R_s. The semicircles showing unfinished features at low frequency could be due to the surface irregularity due to pitting corrosion as can be seen from Figure 7.11 (a). The Bode plots of phase angle vs. frequency (Figure 7.9 (c)) indicated one main peak between the frequencies of 10^0 and 10^1 Hz for both at 1000rpm and 6000rpm rotational speed, which is related to electrochemical processes on metal/electrolyte interface. Both peak angles are -35 degrees, showing similar corrosion rates on the metal surface.

The equivalent circuit to explain the electrochemical processes for the electrode reactions is the same as the blank tests under static conditions shown in Figure 5.11. By

taking into account these impedance results and fitting them in the equivalent circuit program Zview, the parameters, such as charge transfer resistance R_{ct}, double layer capacitance C_{dl}, can be deduced as shown in Figure 7.12 and Figure 7.34 (a). As stated previously the semicircles obtained were slightly depressed so a constant phase element, CPE, was inserted instead of capacitance C. The CPE is defined by two values, CPE-T, represented by CPE (which is associated with the capacitance) and CPE-P, represented by α (related to surface irregularity and roughness).

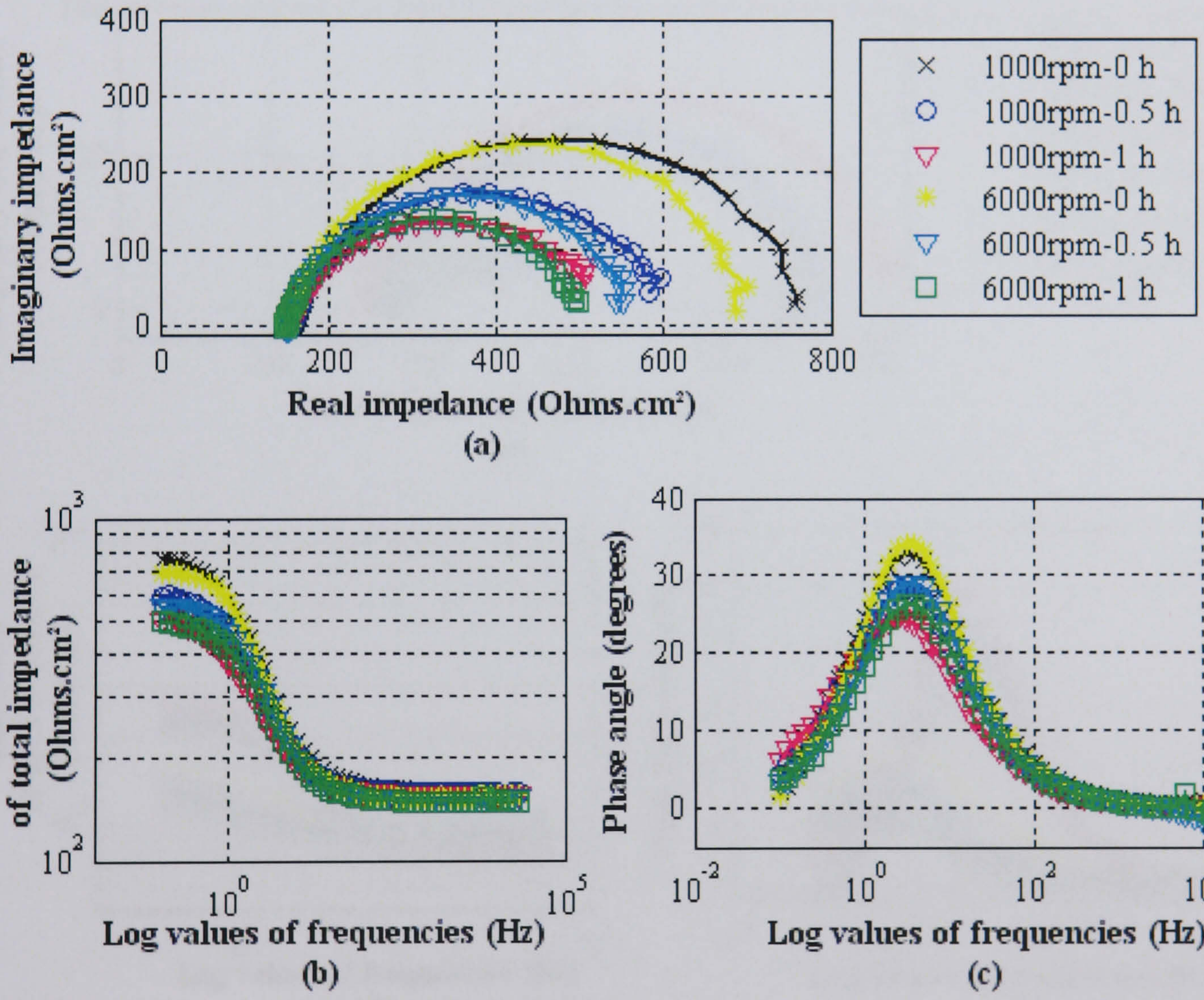

Figure 7.9 AC impedance spectra with blank tests at 20°C and 1000rpm or 6000rpm rotational speed (a) Nyquist, (b) Bode magnitude and (c) Bode phase plots

The impedance curves obtained without inhibitor at 50°C are shown in Figure 7.10 (a) to (c) for Nyquist plots and Bode plots. The Nyquist plots (Figure 7.10 (a)) consist of one depressed semicircle, which increased slightly in diameter with time at 1000rpm, indicating that corrosion products might form on the surface with time and these may lessen the corrosion rate of the system. However, the corrosion products which are

coarse in structure under this temperature and pressure, also can be removed by the flowing fluid or sand particle impacts; therefore not providing protection towards corrosion and erosion-corrosion as shown from erosion-corrosion mass loss result from chapter 6. At 6000rpm Nyquist plots appear as unfinished semicircles and decrease in diameter with time were observed, which can result from surface roughness, chemical heterogeneity or localized corrosion.

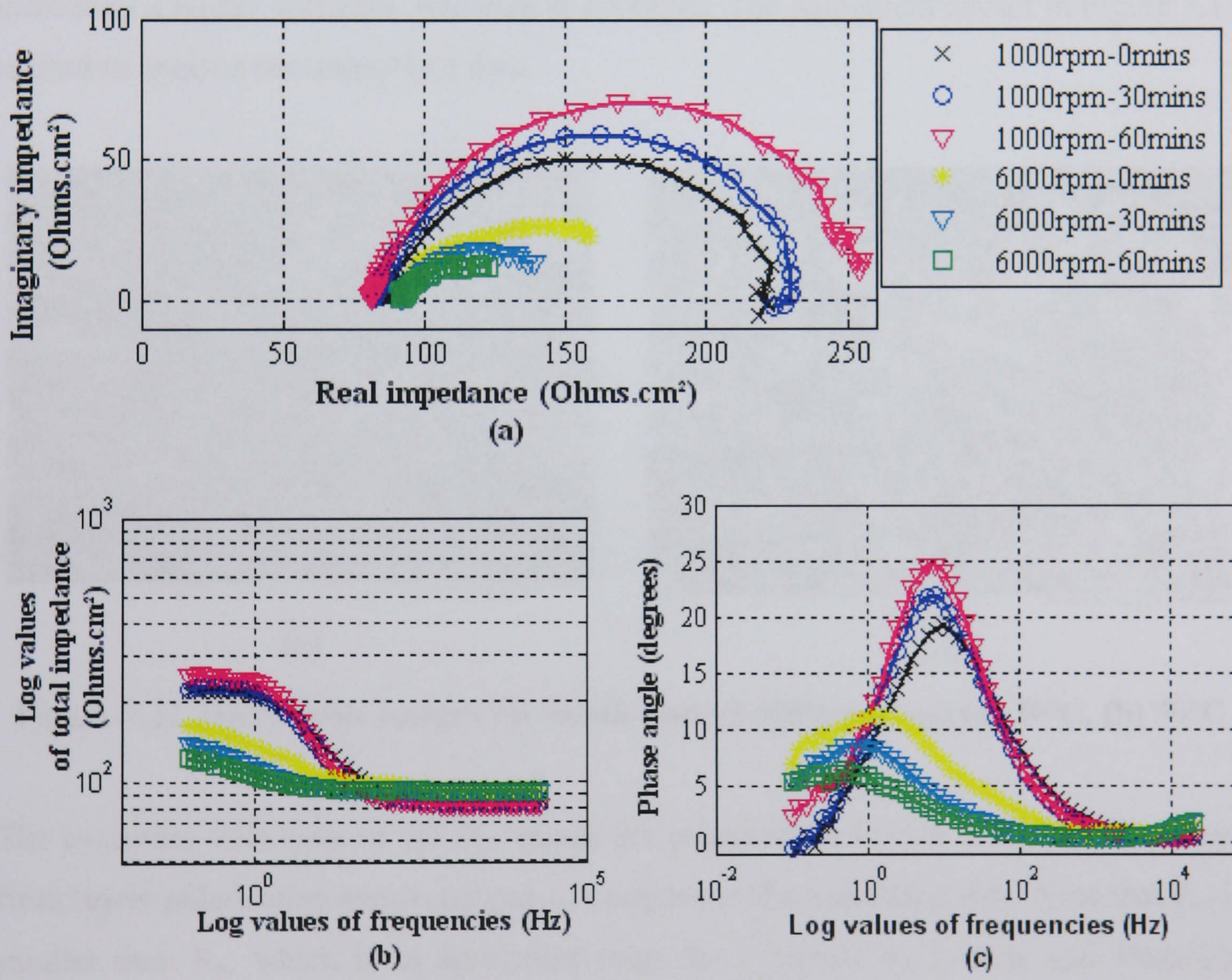

Figure 7.10 AC impedance spectra with blank tests at 50°C and 1000rpm or 6000rpm rotational speed (a) Nyquist, (b) Bode magnitude and (c) Bode phase plots

The Bode magnitude plots (Figure 7.10 (b)) show one negative slope associated with the one semicircle in the Nyquist plot. The negative slope at 6000rpm is lower than that at 1000rpm, which is associated with an even more depressed semicircle curve in Nyquist plots at 6000rpm. At low frequency the spectra does not reach the plateau (at

0.1 Hz frequency). This might be due to the very rough surface and pitting corrosion as shown in Figure 7.11 (b). The surface shows more severe general corrosion and pitting than at 20°C (Figure 7.11 (a)). The Bode phase plots (Figure 7.10 (c)) show one main peak for both rotational speeds. At 1000rpm, the peak phase angle is about -20 degrees and increased slightly with time, which is an indication that corrosion products formed on the surface. At 6000rpm, the frequency for maximum phase angle shifts slightly towards a lower frequency, and the peak phase angle (-12 degrees) decreases with time, indicating a higher corrosion rate than at 1000rpm. The equivalent circuit in Figure 5.11 is used to analyse the impedance data.

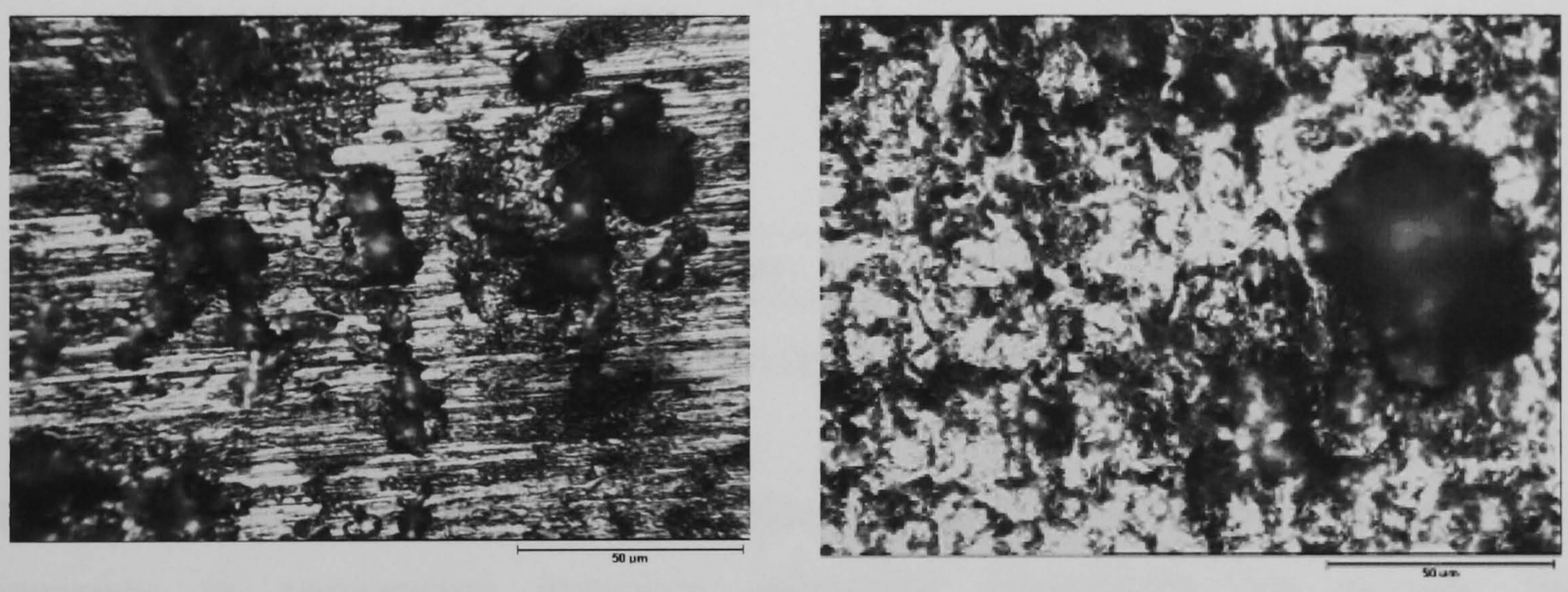

(a) (b)

Figure 7.11 Microscope images for blank tests at 6000rpm and (a) 20°C, (b) 50°C

The evolution with time of the R_{ct} values are presented in Figure 7.12 with R_p values from linear polarisation measurements to compare at the right hand side. Note that R_{ct} is smaller than R_p, which is in agreement with the literature by Lorenz and Mansfeld (1981). As stated in Chapter 5 R_{ct} is more accurate than R_p, because R_p value includes the resistance of any film formed on the metal surface and of the metal substrate, while R_{ct} only represents the resistance of the metal/electrolyte or metal/film interface. The following calculations of the corrosion rates are based on R_{ct}. R_p values can still be used as a reference for obtaining meaningful fitting results of impedance parameters for certain equivalent circuit models in that R_{ct} values can be set at a similar value as the corresponding R_p value.

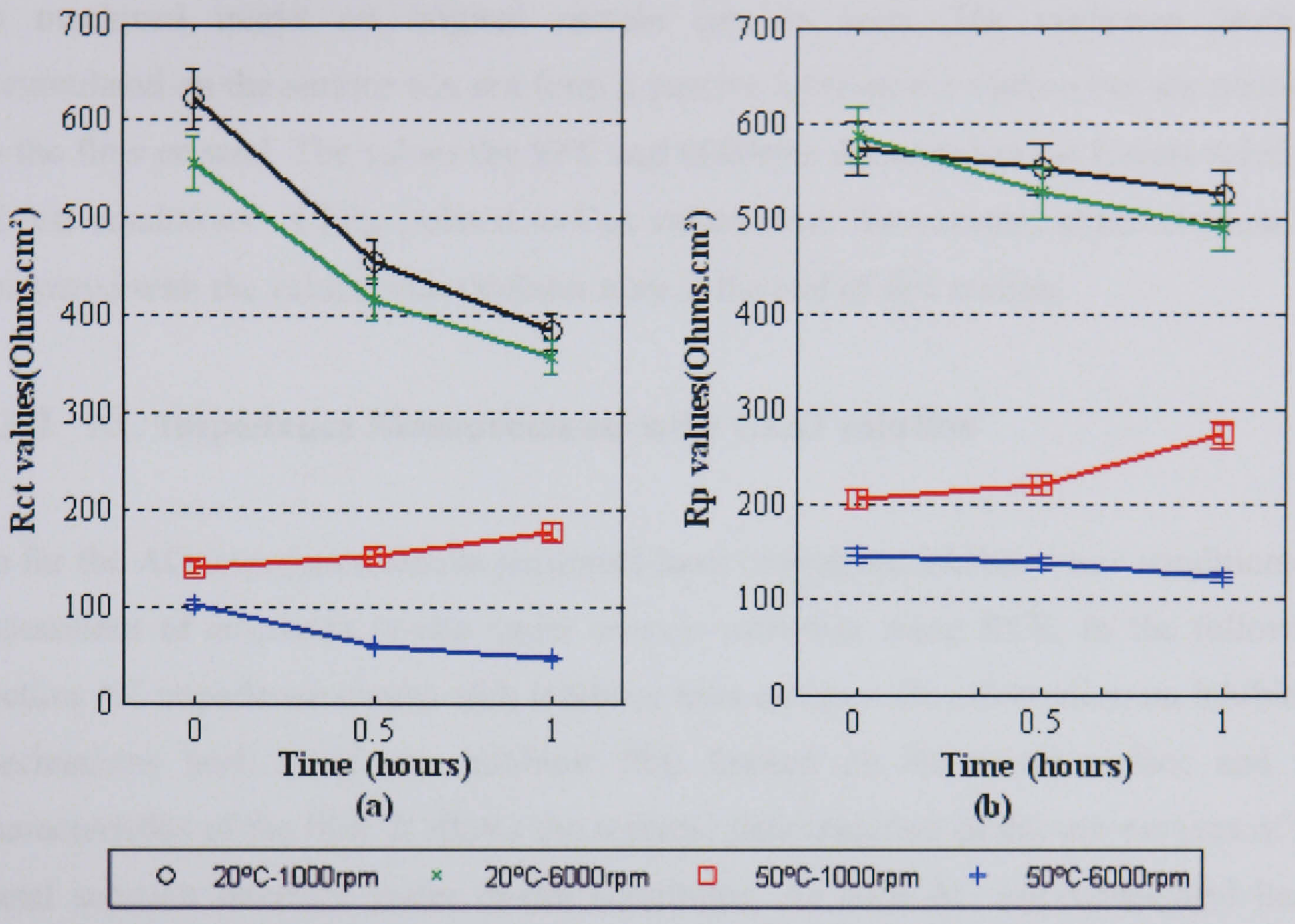

Figure 7.12 Comparison of (a) R_{ct} and (b) R_p values versus time for blank tests

It can be seen from the charge transfer data (Figure 7.12 (a)), that the corrosion rate increases as temperature increases. Increasing temperature can increase the electrochemical reaction rate, increase the rate of diffusion and affect the corrosion potential. The corrosion rate also increases with rotational speed although this is not as significant as the dependence on temperature. The corrosion process is therefore mainly charge transfer-controlled. At 1000rpm and 50°C, the charge transfer resistance increases but by a very small amount which is an indication that there is $FeCO_3$ corrosion product layer formed on the surface with a coarse structure blocking of active sites at the carbon steel surface. The very small change of the R_p value indicates that there is no protective corrosion products formed on the metal surface. Lopez *et al.* (2003) have demonstrated that at 50°C the iron carbonate is porous and inhomogeneous allowing the access of the electrolyte to the surface. It implies that it may provide a small amount of protection to the metal by restricting the mass transfer of reactants between the bulk solution and metal surface. However it will be peeled off by the flowing fluid and sand impact. At 6000rpm and 50°C, the charge transfer resistance is very small (Figure 7.12) and the surface is rougher than at 1000rpm (Figure 7.11 (b)),

no machined marks on original sample can be seen. The corrosion products accumulated on the surface can not form a passive layer on the surface but are removed by the flow or sand. The values for 50°C and 6000rpm decreased to the lowest values of all test conditions. CPE_{dl} (related to C_{dl}) values from the constant phase element are compared with the values with inhibitor tests at the end of this section.

7.3.2 AC Impedance Measurements with CGO solution

So far the AC impedance results presented have considered inhibitor-free conditions as assessment of corrosion *in-situ* under erosion-corrosion using RCE. In the following section AC impedance results with inhibitor tests can provide information on inhibition mechanisms such as if any inhibitor film formed on the metal surface and the characteristics of the film. It allows the separate determination of the components of the metal solution interface under *in-situ* conditions. As both AC impedance and linear polarisation measurement can evaluate the inhibitor performance such as resistance, linear polarisation data can still be used as a reference data for fitting the AC impedance results.

The impedance curves obtained with CGO at 20°C and 1000rpm are shown in Figure 7.13 (a) to (c) for Nyquist and Bode plots. These results are very similar to those in static conditions as shown in Figure 5.21. It can be seen that at this rotational speed, in the initial exposure time, rotation actually helps the inhibitor to reach the metal surface as shown by the larger diameter of the semicircle in initial exposure at 1000rpm than in static conditions. During the 1 hour exposure time, the total resistance values did not change significantly, indicating a relatively stable film formed under these conditions. It is an indication that the inhibitor film can offer good protection, which is confirmed by comparing the AC semicircles with blank tests as shown in Figure 7.9. Two negative slopes of the spectra in Bode magnitude plots (Figure 7.13 (b)) are associated with the semicircles shown in the Nyquist plot (Figure 7.13 (a)) and the two-peak phase angle in the Bode phase plots (Figure 7.13 (c)) also indicates that two time constants are present.

The equivalent circuit for this electrochemical reaction is given as the same as for static conditions (shown Figure 5.22) due to the same spectra of the impedance curve.

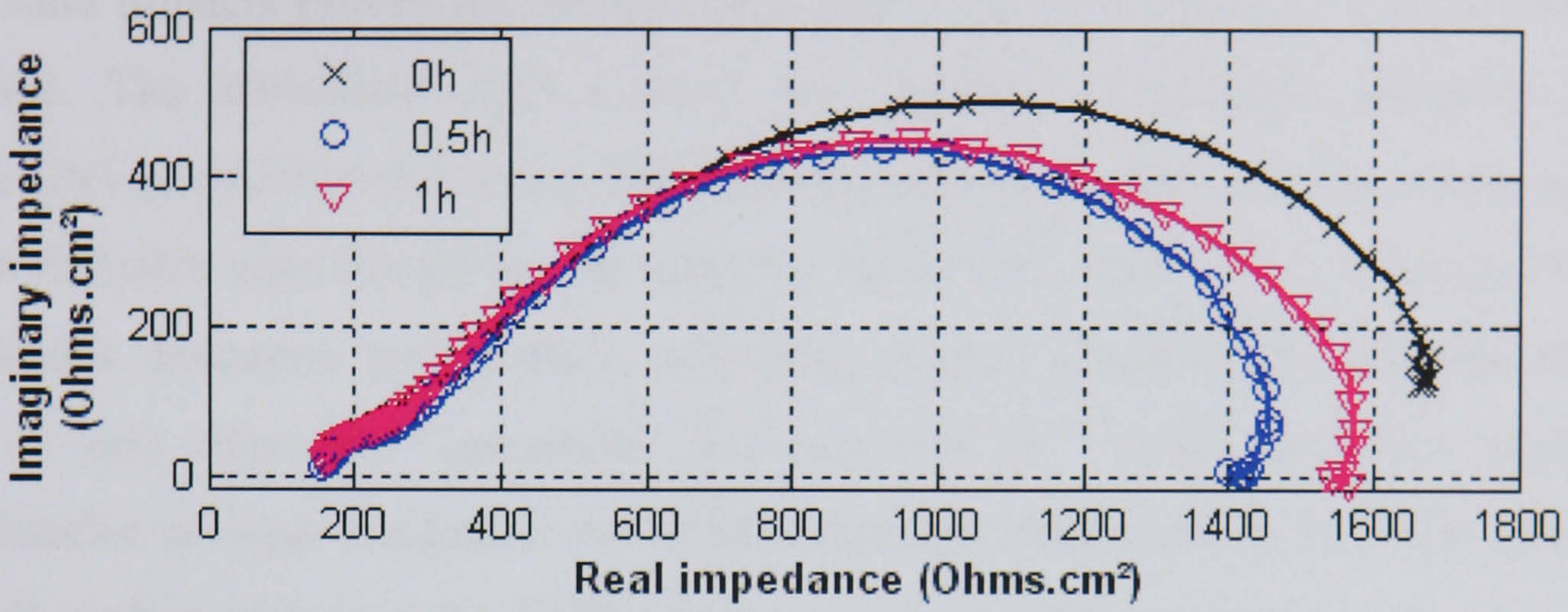

(a)

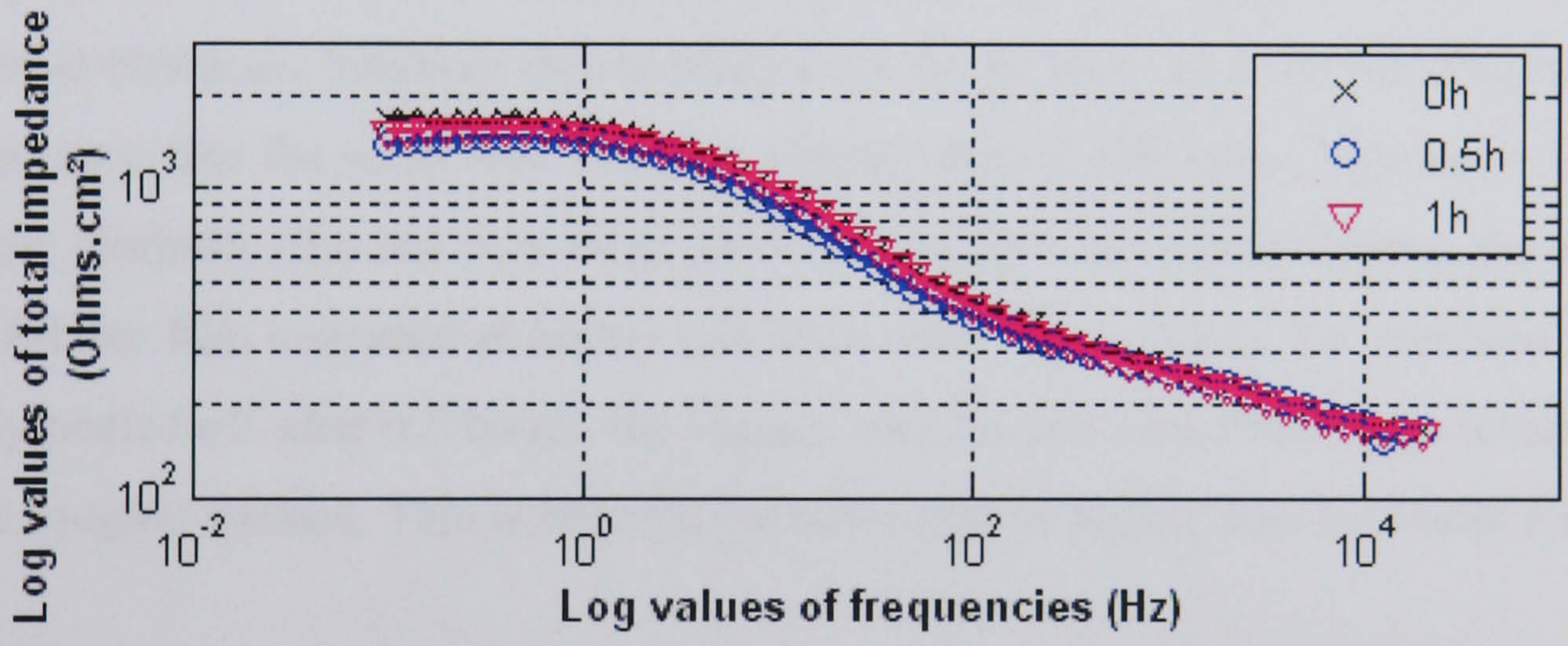

(b)

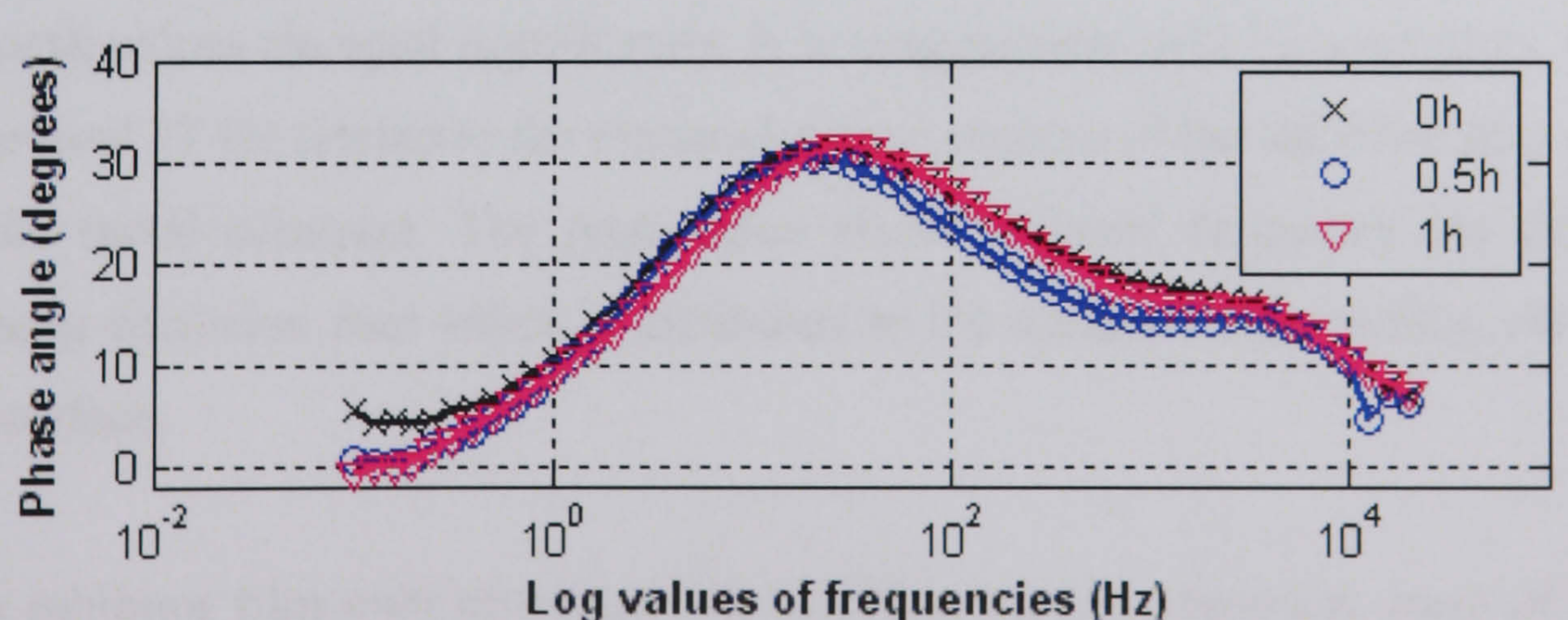

(c)

Figure 7.13 AC impedance spectra with CGO tests at 20°C and 1000rpm (a) Nyquist plots, (b) Bode magnitude plots and (c) Bode phase plots

The impedance curves obtained with CGO at 20°C and 6000rpm are shown in Figure 7.14 (a) and (b) for Nyquist plots and Bode plots. The Nyquist plots (Figure 7.14 (a))

show that in initial exposure time only one semicircle appears which is different to results in static and low rotational speed conditions. This is due to the high shear stress and sand impacts preventing the inhibitor from forming a complete film on the metal surface. The semicircle with a small tail indicates that either corrosion product molecules or inhibitor molecules diffuse away from the surface. At this temperature, the most probable case should be the inhibitor molecules. From 0.5 h exposure time, the semicircle decreases significantly, indicating an increasingly high corrosion rate. The arc of very depressed semicircles indicates that the surface becomes rough. The semicircles at these conditions are smaller than for blank tests in the same conditions. The R_p values at 1 hour for CGO are also smaller than blank tests as shown in Figure 7.5. It seems that CGO acts as a corrosion promoter under high shear stress conditions. At initial exposure, inhibitor film is formed on the surface but from the Nyquist plots it can be seen that the semicircle is much smaller than at 1000rpm. This is an indication that the inhibitor film has very large pores due to flow and sand impacts, the area with no inhibitor film corroded at higher rate than other areas. When the inhibitor film was totally peeled off after 0.5 hours, the surface was rougher and corrosion accelerated due to the rougher surface. This is why the corrosion rate is higher than for blank tests.

The corresponding Bode phase plots (Figure 7.14 (b)) show that during the 1 h exposure time, peak values changed significantly. It is in agreement with Nyquist plots. One main peak around 37 Hz related to the electrochemical process of the inhibitor film combined with the metal substrate. The peak value shifts to lower frequency are evidence of increasing corrosion rate which is attributed to the inhibitor film peeling off from the metal surface.

As the inhibitor film only provides little inhibition to the corrosion, most of the metal surface is not covered by inhibitor at the high shear stress conditions. Without a proper film formed to be counted as a layer to produce second time constant, the equivalent circuit model used is proposed by simulating the widely open pores in a coating system (Zeng *et al.*, 2002), as shown in Figure 7.15. The calculated parameter from AC impedance results can be compared with those for blank tests to get the information about inhibitor film characteristics.

The impedance curves obtained at 6000rpm and 50°C are presented in Figure 7.16 (a) to (c) for Nyquist and Bode plots. The inhibition mechanism of the inhibitor CGO in this condition is very similar to the condition of 6000rpm and 20°C. It can be concluded that CGO can only be used at low shear stress and in static conditions to offer corrosion inhibition. The equivalent circuit used to calculate the main parameters is the same as shown in Figure 7.15.

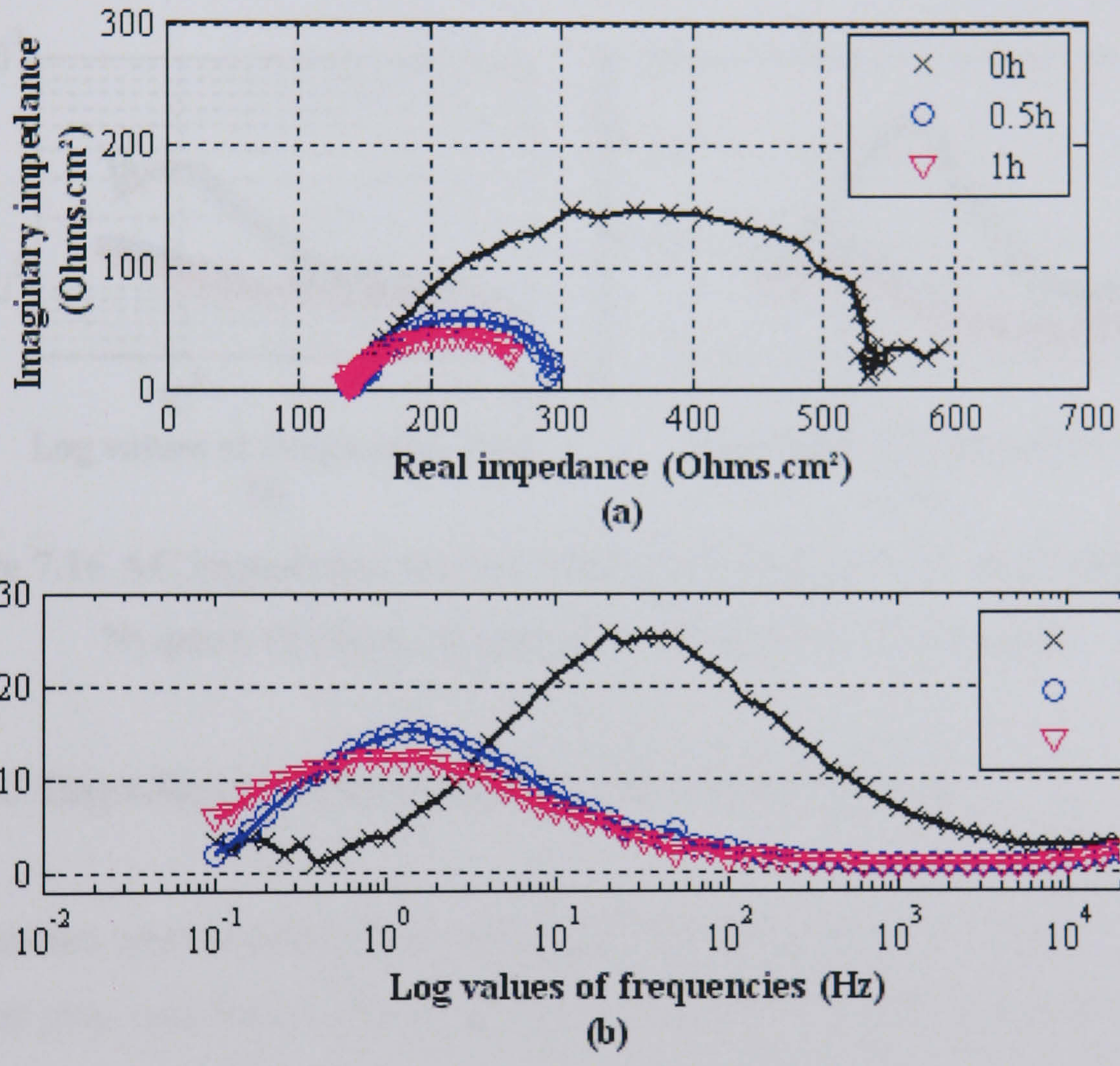

Figure 7.14 AC impedance spectra with CGO tests at 20°C and 6000rpm (a) Nyquist plots and (b) Bode phase plots

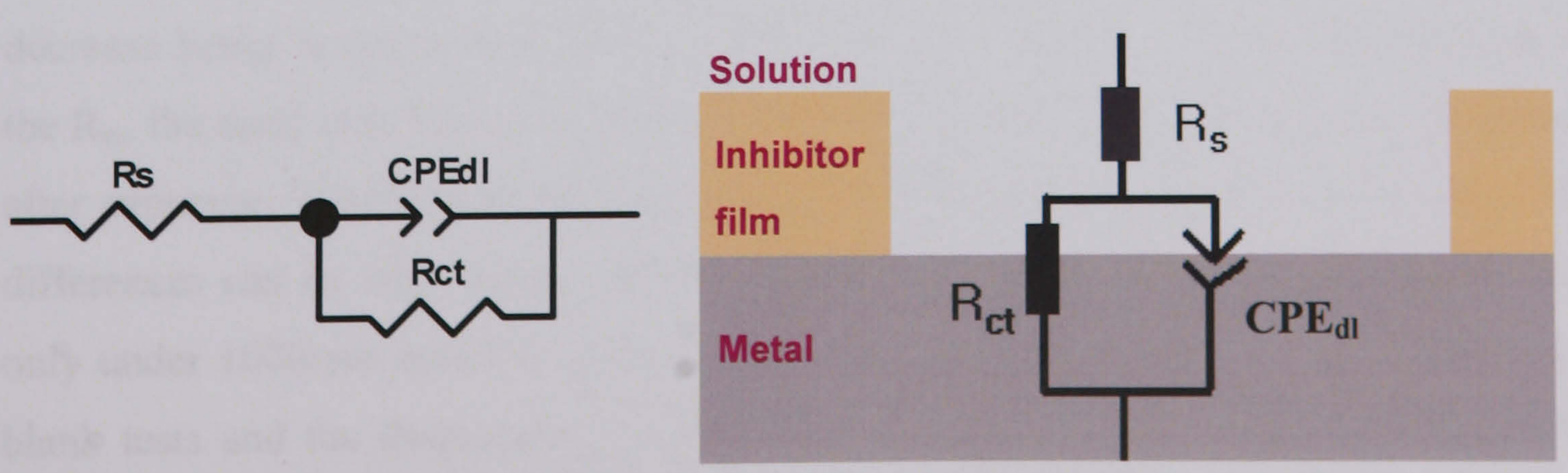

Figure 7.15 Equivalent circuit simulating the electrochemical process for inhibitor CGO at 6000 rpm and 20°C

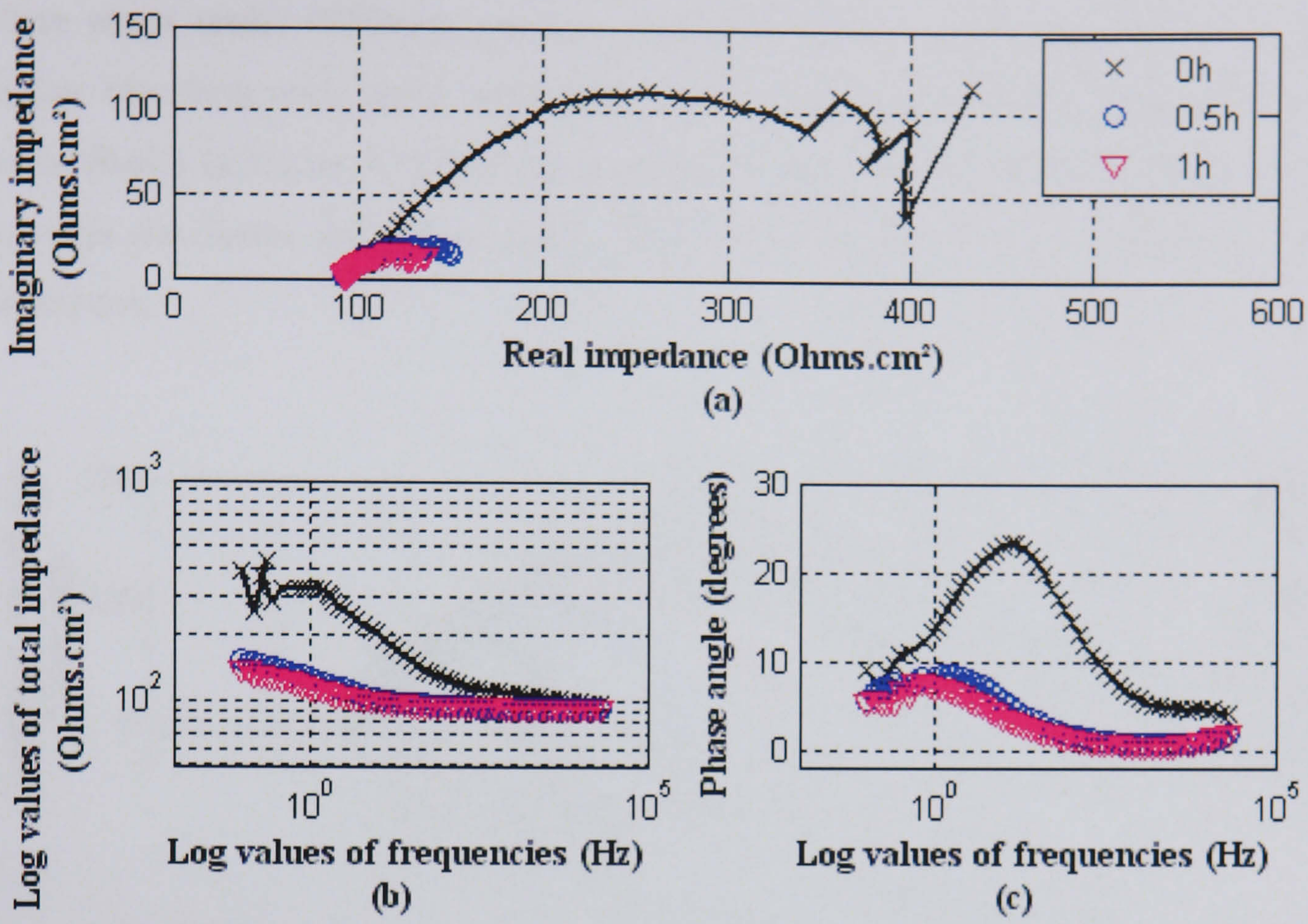

Figure 7.16 AC impedance spectra with CGO tests at 50°C and 6000rpm (a) Nyquist, (b) Bode magnitude and (c) Bode phase plots

7.3.3 AC Impedance Measurements with CRO Solution

The impedance spectra obtained for tests with CRO are shown in Figure 7.17 (a) to (b) for Nyquist plots and Bode plots at 20°C and in Figure 7.18 (a) to (b) at 50°C.

The Nyquist plots (Figure 7.17 (a) and Figure 7.18 (a)) consist of one depressed semicircle decreased in diameter with time for all the conditions, with the fastest decrease being under the condition of 50°C and 6000 rpm. Due to the fast decrease of the R_{ct}, the semicircle becomes distorted as shown in Figure 7.18 (a) at lower frequency after exposure. The shape of the semicircles is similar to the shape for blank tests. The differences can be seen clearly from the Bode plots. The Bode phase plots show that only under 1000rpm and 20°C (Figure 7.17 (b)), the phase angles are larger than with blank tests and the frequencies at peak phase angles are higher with CRO than with blank in Figure 7.9. This is due to the inhibitor film formed on the surface. At 6000rpm, the inhibitor film formed at initial exposure time, but is completely removed by higher

shear stress under 6000rpm rotation. The area without inhibitor corrodes at an even higher rate than with blank tests. This can be confirmed by the Bode plots of phase angle shown in Figure 7.18 (b). The maximum phase angle decreases rapidly and moves towards the lower frequency range after 0.5 h exposure time, indicating a loss of protection.

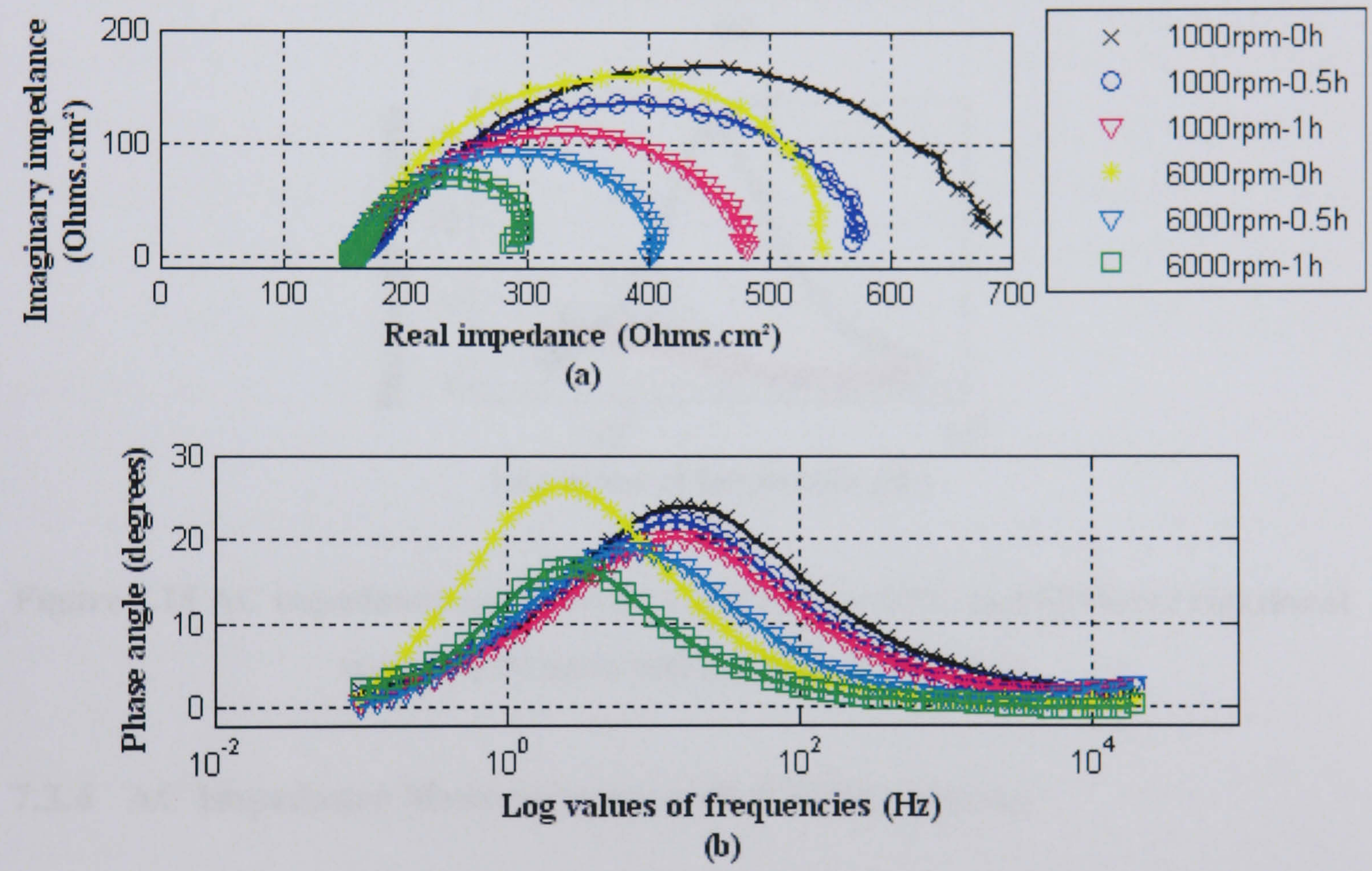

Figure 7.17 AC impedance spectra with CRO tests at 20°C and 1000 or 6000rpm rotational speed (a) Nyquist, (b) Bode magnitude and (c) Bode phase plots

As the curves obtained with CRO were very similar to those obtained without inhibitor both for the diameters of the semicircle and shape of the curve, the same equivalent circuit was used as shown in Figure 7.15.

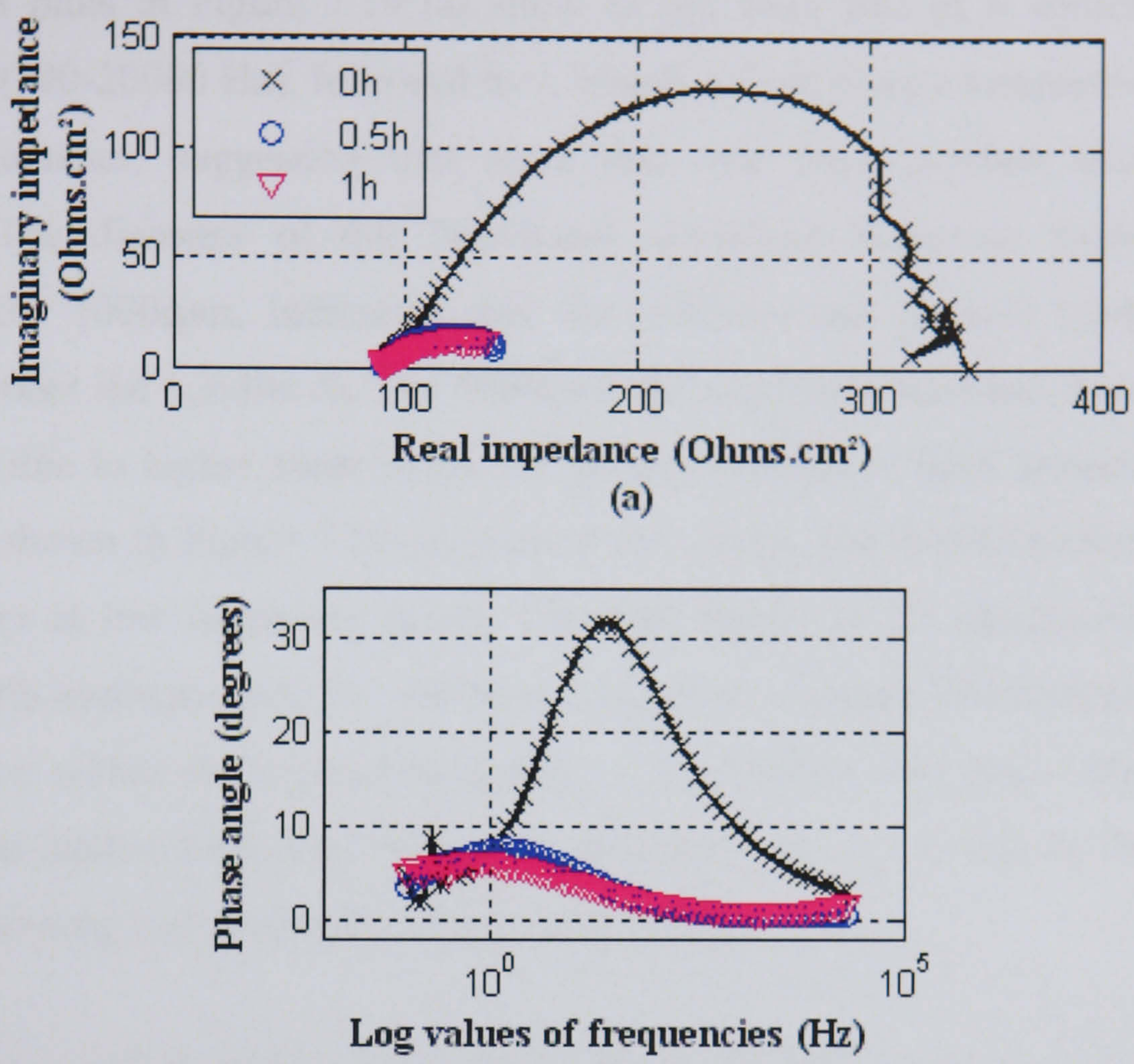

Figure 7.18 AC impedance spectra with CRO tests at 50°C and 6000rpm rotational speed (a) Nyquist and (b) Bode phase plots

7.3.4 AC Impedance Measurements with CRW8 Solution

From the tests so far, it is clear that all the inhibitors have high efficiency under static conditions, with water soluble ones having highest efficiency. The two oil soluble inhibitors CGO and CRO lose their protection under higher shear stress conditions. The following tests are conducted with water soluble inhibitor CRW8 under erosion-corrosion conditions which are in the same conditions as with CGO and CRO. In addition tests also conducted at 1000rpm and 50°C to compare the impedance response with blank tests to see if the corrosion products can positively react with inhibitor and accumulate onto the metal surface and form a layer under erosion-corrosion conditions.

AC impedance spectra for tests with CRW8 at 1000 rpm or 6000rpm and 20°C are shown in Figure 7.19 (a) to (c) for Nyquist plots and Bode plots.

The Nyquist plots in Figure 7.19 (a) show an arc from part of a semicircle at high frequencies (300-20000 Hz), followed by a broadened arc from a semicircle for the rest of the frequencies, suggesting that more than one time constant exists at these interfaces. The diameter of this broadened semicircle decreases slightly as time progresses for 1000rpm, indicating that the inhibitor can provide relatively stable protection under the conditions. For 6000rpm, the diameter decreases more with time, as expected due to higher shear stress and greater number of sand impacts. The Bode phase plots shown in Figure 7.19 (c) present two peaks, one at intermediate frequency and the other at low frequency range. The peak height of the intermediate response increases with exposure time for 1000rpm, indicating a denser film building up on the metal surface within the experimental time. For 6000rpm, the peak values of phase angle both at higher frequency and lower frequency are not as big as the values for 1000rpm, showing less protection of the inhibitor film.

The equivalent circuit model used to analyze the impedance response with inhibitor CRW8 under 1000rpm and 20°C is presented in Figure 7.20. The additional element is the diffusion element (W_s) to account for the denser structure of the inhibitor film. The position of the diffusion element indicates that the film significantly bounds the diffusion inward to the metal substrate (Li *et al.*, 1997), resulting in very low corrosion rate. It is hypothesized that the presence of inhibitor under this condition does not isolate the corrosion reaction by forming a very firm film, but rather lengthens the diffusion path of the corrosion species to lower the corrosion rate at the metal/inhibitor interface. It can be postulated that the inhibitor forms a film on the metal surface with the advantage of providing an *in-situ* repair facility.

The impedance structure at 6000rpm rotational speed and 20°C shows much less diffusion behaviour, no negative slope at lowest end of the impedance (Figure 7.19 (b)). As it has two time constants which can be seen from Bode phase plots in Figure 7.19 (c), the equivalent circuit used to analyse AC impedance data is shown in Figure 7.21.

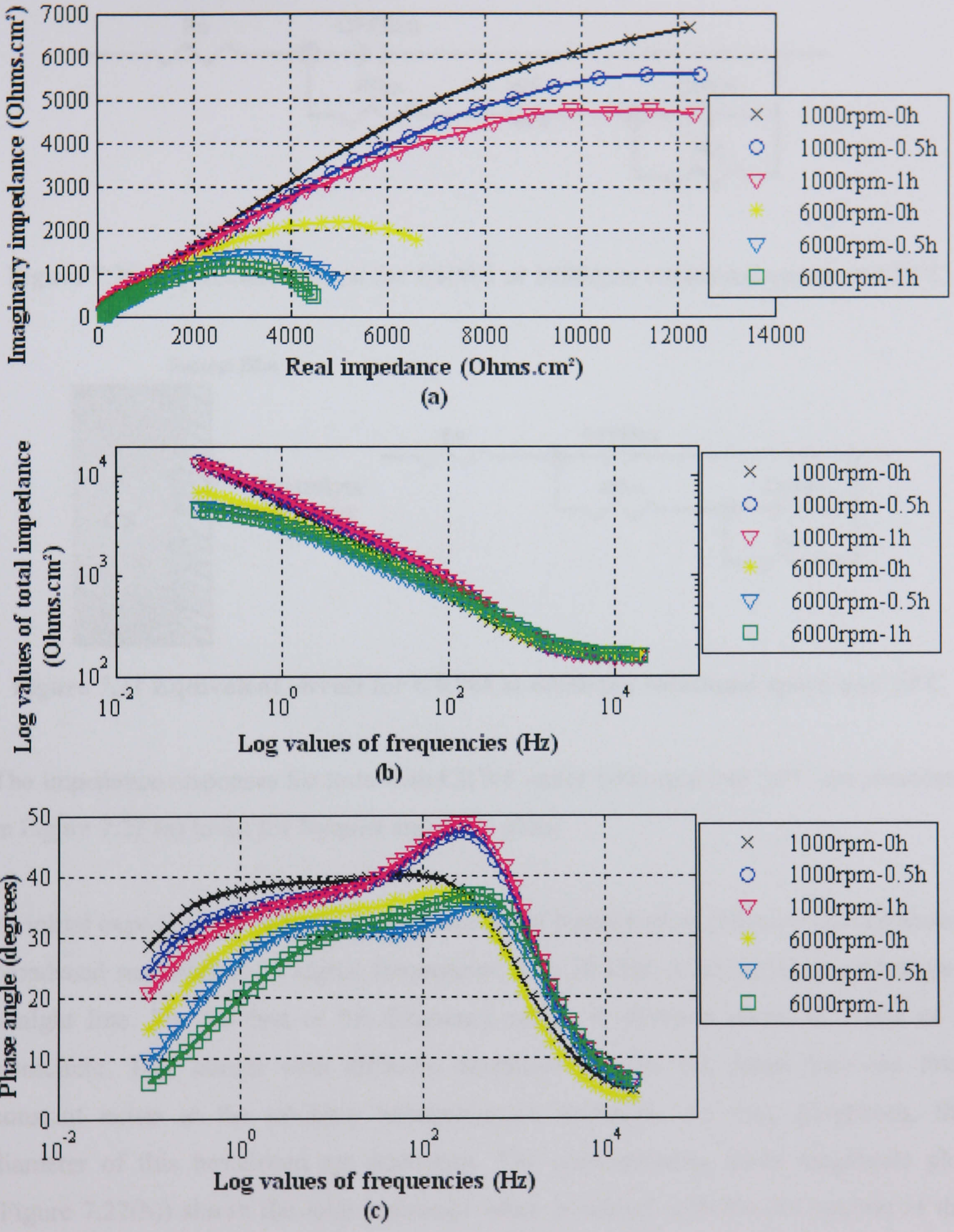

Figure 7.19 AC impedance spectra of tests with CRW8 as inhibitor at 1000rpm or 6000rpm and 20°C (a) Nyquist (b) Bode magnitude and (c) Bode phase plots

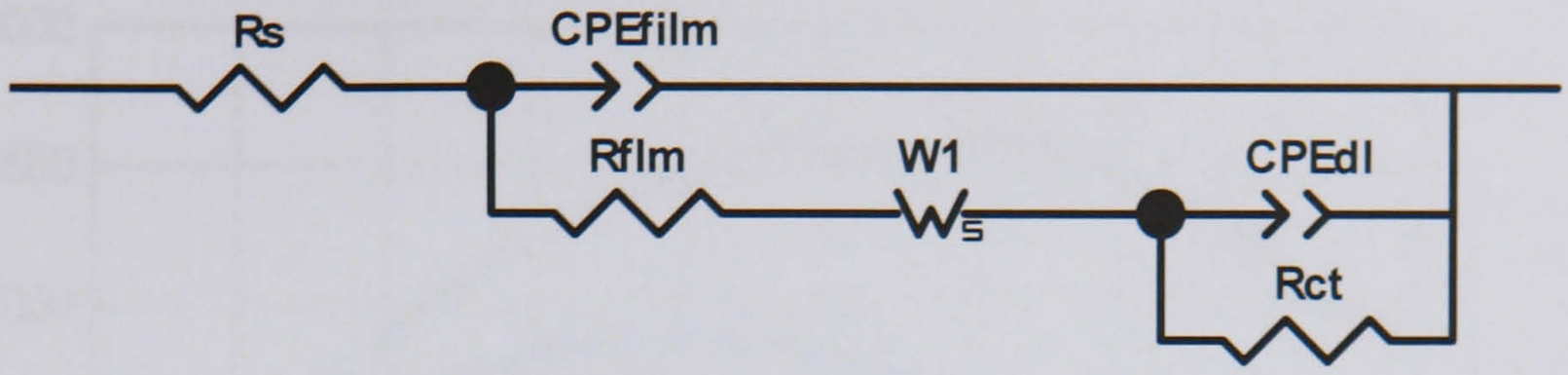

Figure 7.20 Equivalent circuit for CRW8 at 1000rpm rotational speed and 20°C

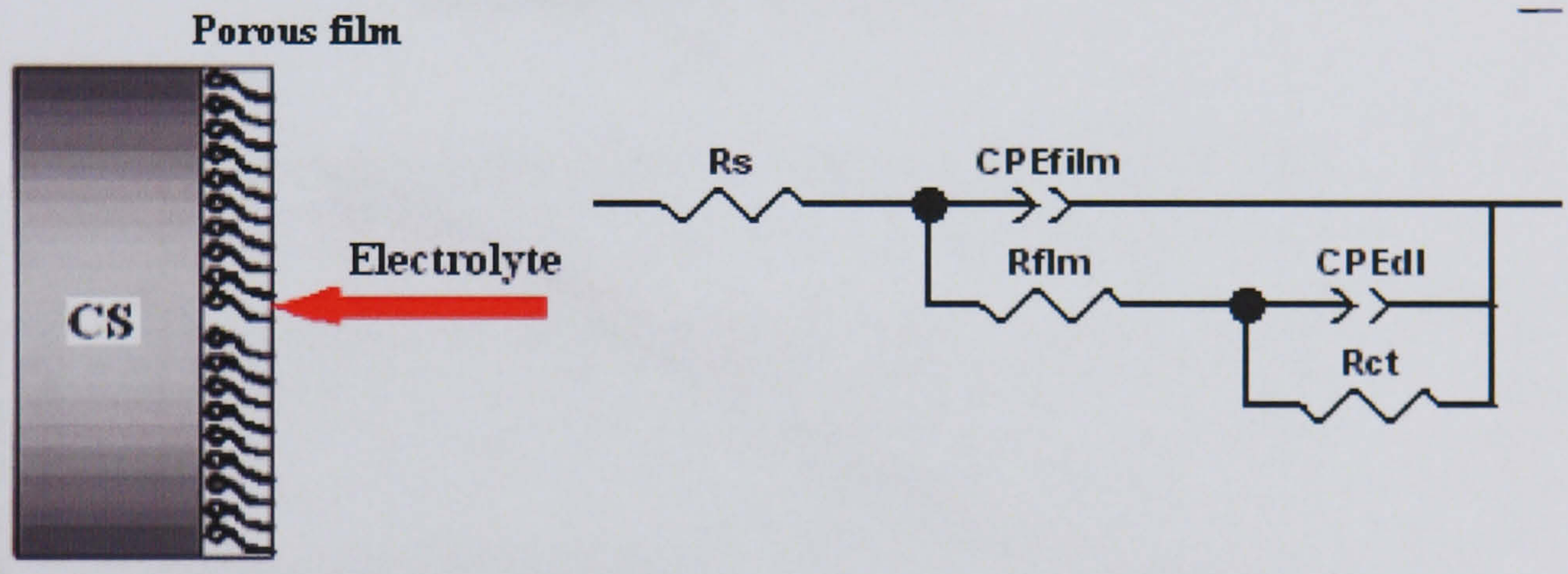

Figure 7.21 Equivalent circuit for CRW8 at 6000rpm rotational speed and 20°C

The impedance responses for tests with CRW8 under 1000 rpm and 50°C are presented in Figure 7.22 (a) to (c) for Nyquist and Bode plots.

At initial exposure, the impedance response in the Nyquist plots (Figure 7.22 (a)) shows broadened semicircles. At higher frequencies, 1 to 10 kHz, it is similar to a 45 degree straight line. For the rest of the frequency range, it shows a curve as a part of a semicircle. Two curves with different diameters suggest that more than one time constant exists at the inhibitor solution/metal interfaces. As time progresses, the diameter of this broadened arc decreases. The corresponding Bode magnitude plot (Figure 7.22(b)) shows the total resistance value is related with the intersection of the impedance response with axis at the lowest frequency. There is obviously more than one negative slope along the spectra, indicating more than one time constant.

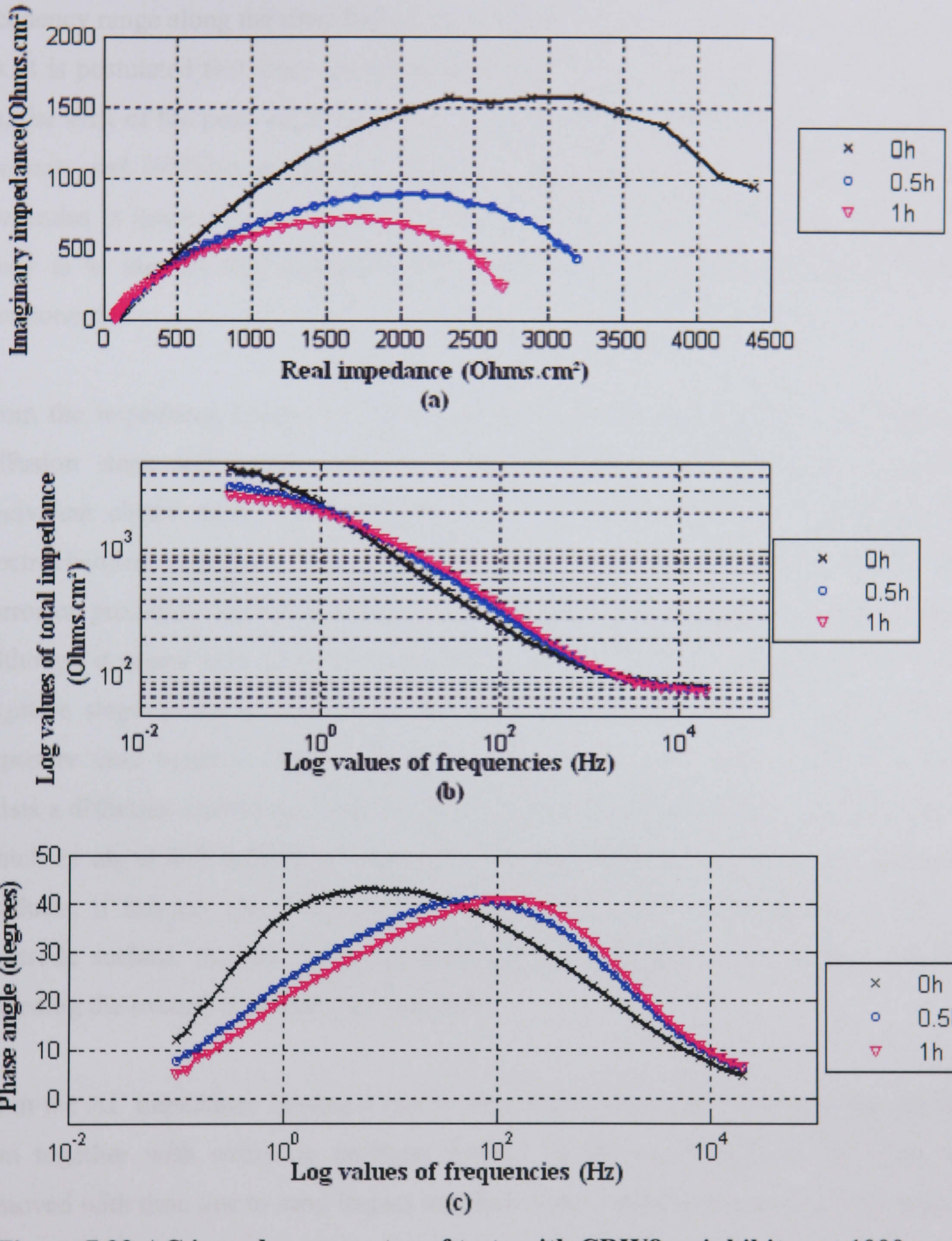

Figure 7.22 AC impedance spectra of tests with CRW8 as inhibitor at 1000rpm and 50°C (a) Nyquist, (b) Bode magnitude and (c) Bode phase plots

The very interesting observation is that in the Bode phase plots (Figure 7.22(c)), at the initial exposure, there is a broad peak which appeared around 10^1 Hz frequency. The broad shape is most probably due to the peaks for inhibitor film and the substrate are poorly separated in the intermediate frequency range. This peak shifted toward higher

frequency range along the time during test duration, indicating that inhibitor film is built up. It is postulated that since the phase angle did not increase as the surface film built up, the shift of the peak angle could be due to the combination of the coarse corrosion products and inhibitor molecules. How the corrosion products work with inhibitor molecules is interesting and should be investigated in future work. The scope of this study is to identify that inhibitor effects on erosion-corrosion and their interaction components.

From the impedance spectra, it can be seen that the corrosion process includes both diffusion steps and kinetic steps. For the impedance data simulation, a general equivalent circuit model as shown in Figure 7.21 was proposed to ascribe the two electrochemical interfaces. One is related to the response of the inhibitor film (or with corrosion products); another is related to the electric double layer of the metal substrate. Although it seems that diffusion exists, presented by the Bode magnitude plot with a negative slope at the lowest end of the response, the impedance spectra for all the exposure time could be fitted very well with the equivalent circuit. However, there exists a diffusion manifested from α values of the CPE obtained from the curve fitting, which is about 0.5 related to Warburg diffusion. Inhibitor molecules or corrosion products, if formed, can block access of electrochemically active species to the test electrode surface, thereby restricting hydrogen ion diffusion to the surface and thus impeding the overall corrosion reaction rate.

From the AC impedance spectra it can be seen that at the initial exposure, the inhibitor film together with corrosion products formed on the metal surface. The film was removed with time due to sand impact and flow shear stress, and as a result the porosity of the film becomes larger. If the corrosion products are moved away from the metal surface, inhibitor can be adsorbed again to the metal surface or adsorbed on the top of the corrosion products. Pitting can occur when the corrosion products move away from the metal surface. From the SEM image after the tests, it can be confirmed that the pitting corrosion distributed on the area that corrosion products form and move away as shown in Figure 7.23. The impedance parameters calculated using a two time constant equivalent circuit model stated above are presented in the next section.

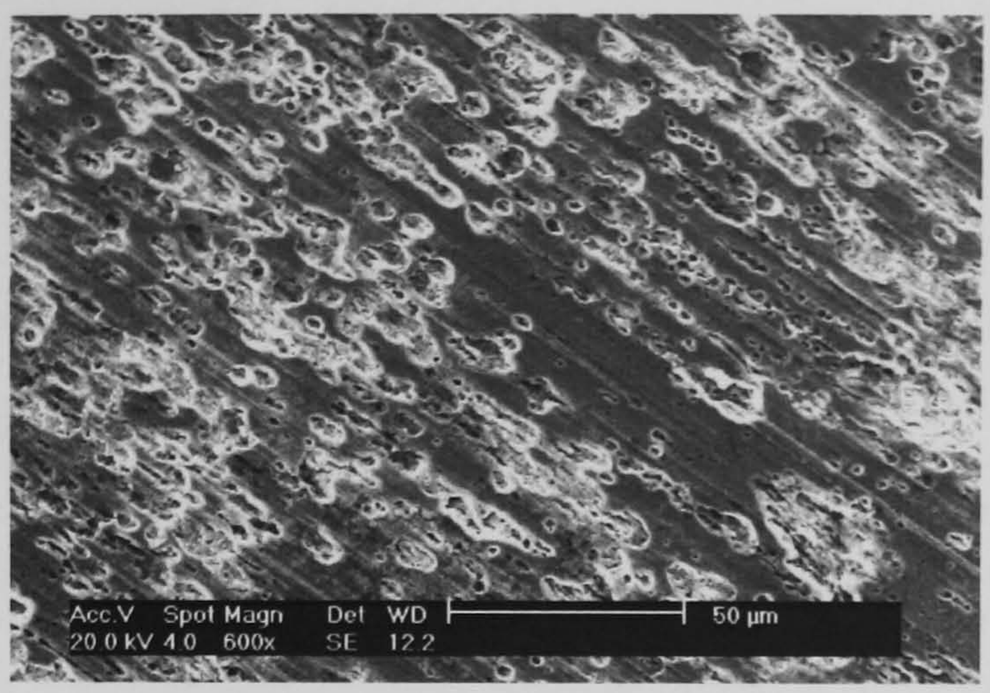

Figure 7.23 SEM image for CRW8 under 1000rpm and 50°C

The impedance curves obtained at 6000rpm and 50°C are shown in Figure 7.24 (a) - (b) for Nyquist and Bode phase plots. At initial exposure, the Nyquist plot (Figure 7.24 (a)) showed two semicircles poorly separated, indicating mixed time constants. The impedance response after 0.5 to 1 h test exhibits inductance behaviour at lower frequency. At this condition, there is no such behaviour for blank tests and CGO, CRO tests, mainly due to the fact there the inhibitor film could not form on the metal surface. At 1000rpm and 50°C for blank tests, there also is no inductance behaviour where corrosion products can be accumulated on the metal surface. Therefore, it is can be postulated that at 6000rpm and 50°C with CRW8, the inductance behaviour results from the combined effects of corrosion products and inhibitor molecules on the metal surface as well as removed off from the metal surface.

The impedance spectra at initial exposure in the Bode phase diagram (Figure 7.24 (b)) present two peaks; one very small peak at high frequency represents the dielectric characteristic of the inhibitor film on the metal surface, the other corresponds to the electrochemical processes at EDL, or mixed time constant of inhibitor film and metal substrate. After 0.5 h, the spectra showed only one peak. The decrease of peak height with exposure time indicates that the response becomes less capacitive as the inhibitor film was peeled off or the pores are getting bigger, so that water and ions penetrate more and more through the film to the metal substrate.

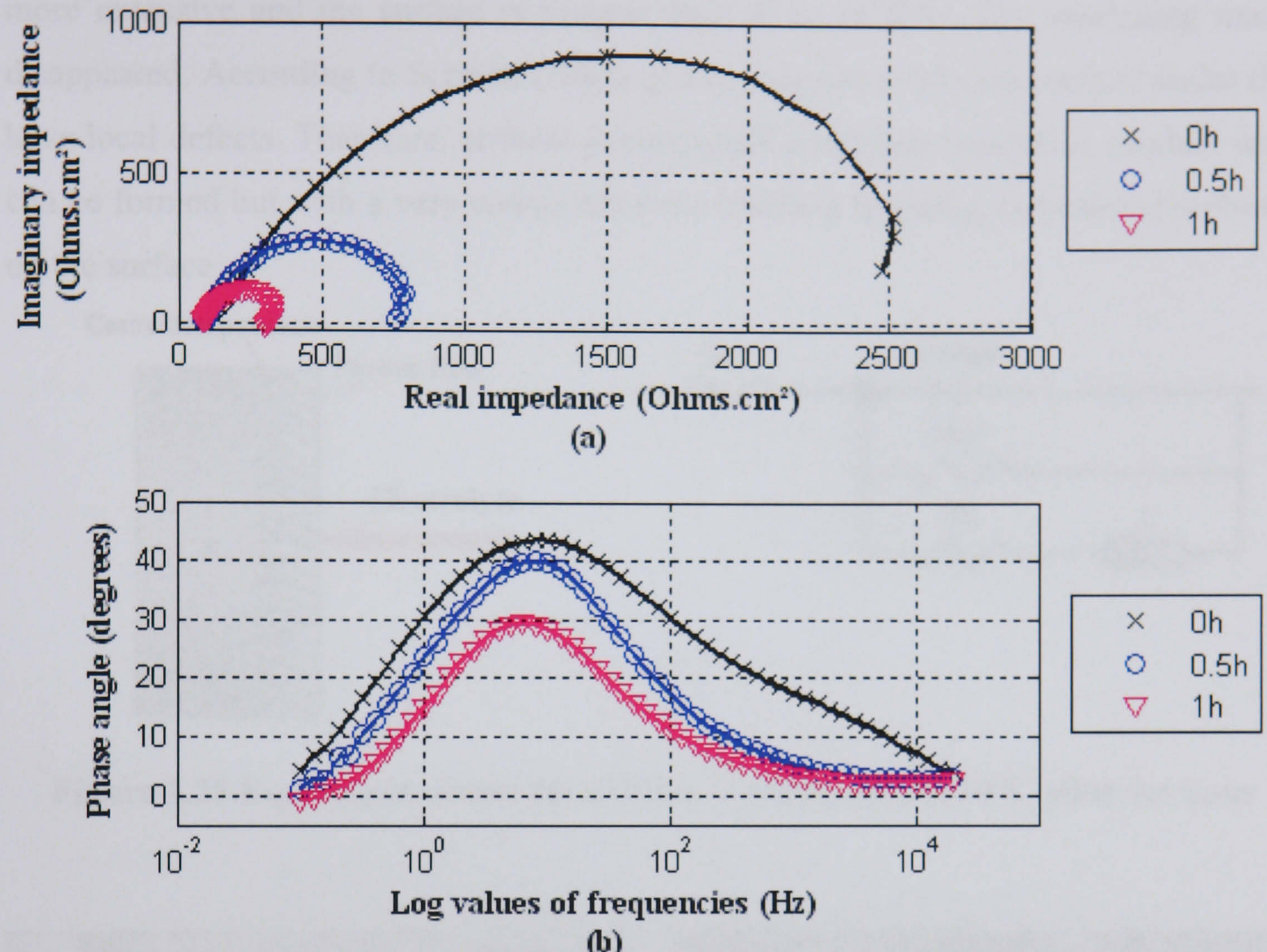

Figure 7.24 AC impedance spectra of tests with CRW8 as inhibitor at 6000rpm and 50°C (a) Nyquist, (b) Bode magnitude and (c) Bode phase plots

In the analysis of the impedance spectra at different experimental times, the electrical circuit shown in Figure 7.21 can be used to satisfactorily fit the impedance response at initial immersion time. For 0.5 and 1 hour exposure time, the circuit shown in Figure 7.25 gave the best fit for the spectra. It has been used by Jiang *et al*. (2005) to study the effect of flow velocity and entrained sand of inhibitors for CO_2 corrosion to model the behaviour of inhibitor, which was represented by one capacitive and one inductive semicircular spectrum. This indicates that the system could be described by two-time constant model, $R_{ct}CPE_{dl}$ and R_f/ L. R_f was adsorption resistance and L was adsorption inductance.

The light microscope images in Figure 7.26 (a) and (b) show the surface after 6000rpm and 20°C and 50°C respectively. It can be seen that at 6000rpm and 50˚C pitting are

more extensive and the surface is rougher than those at 20°C. The machining marks disappeared. According to Schmitt (1983), pitting requires corrosion product scales that have local defects. Therefore, at these experimental conditions, corrosion product scale can be formed but with a very coarse structure resulting in pitting corrosion distributed on the surface.

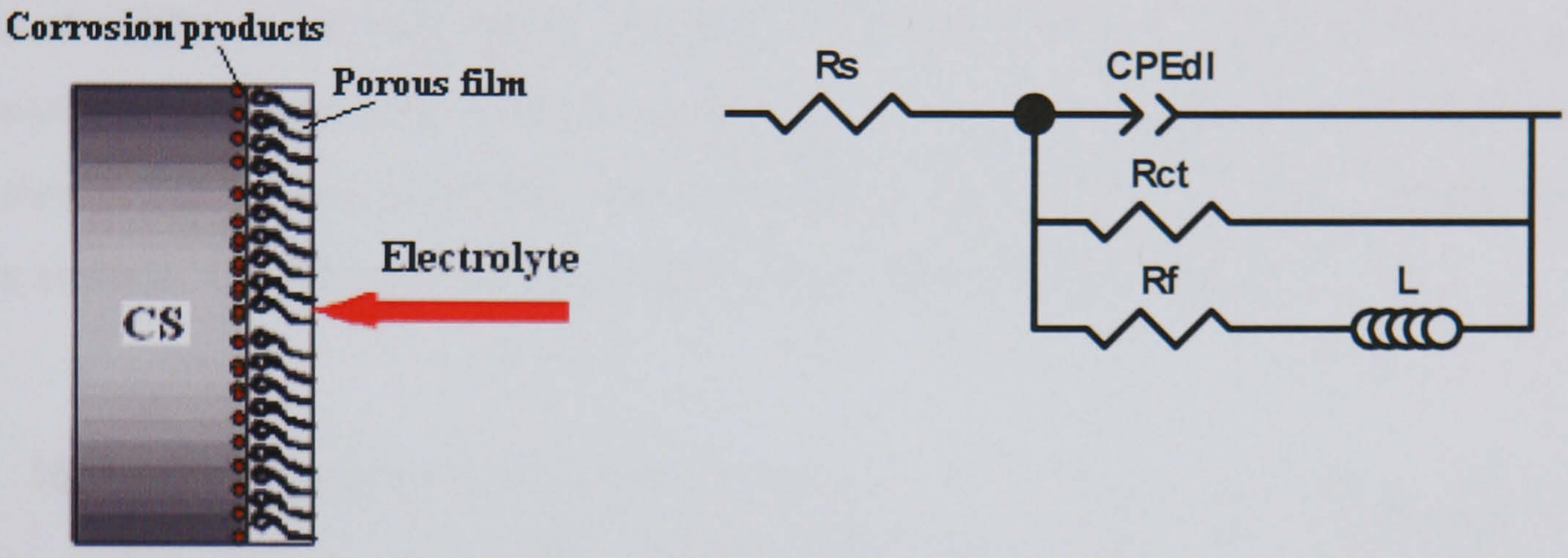

Figure 7.25 Equivalent circuit for CRW8 at 6000rpm and 50°C after 0.5 hour

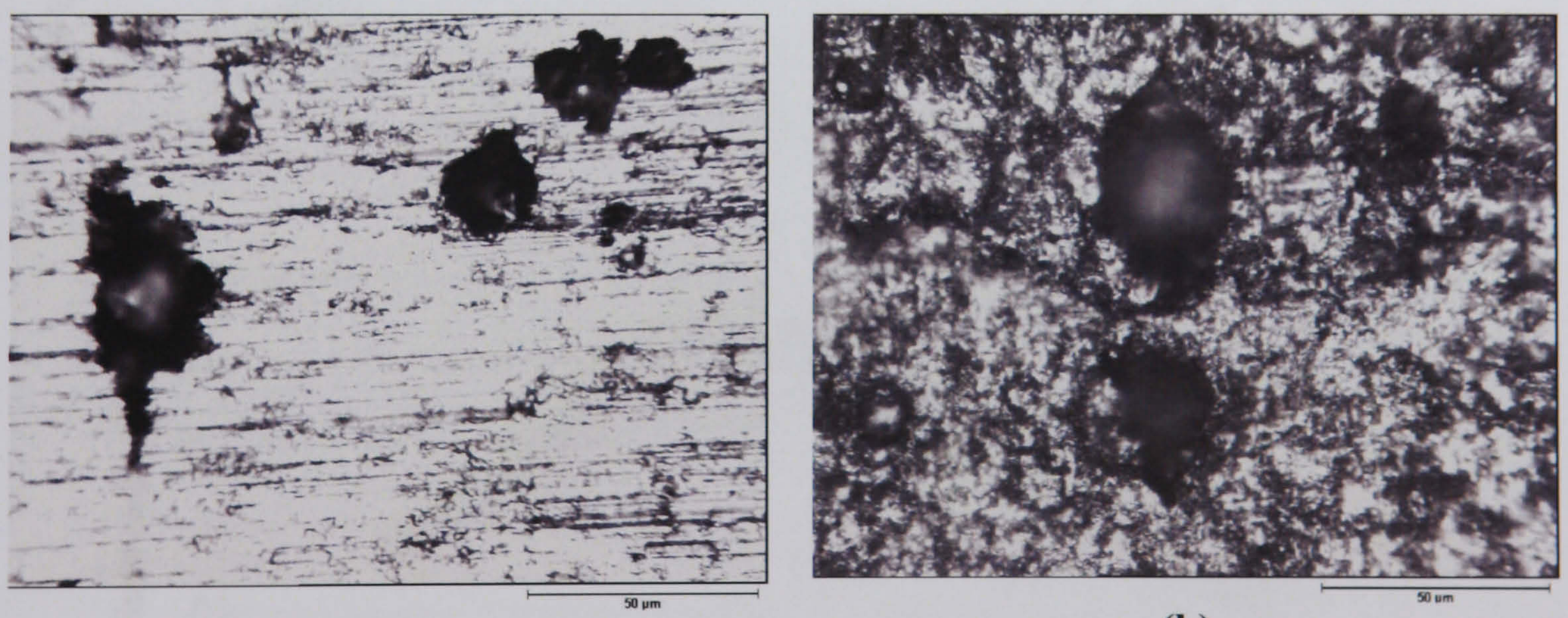

(a) **(b)**

Figure 7.26 Light microscope for CRW8 at 6000 rpm rotational speed (a) at 20°C and (b) at 50°C

7.3.5 AC Impedance Measurements with CRW9 Solution

The main difference between them is that CRW8 contains compound thioalcohol while CRW9 contains heavy aromatic naphtha. *In-situ* corrosion studies were mainly conducted at 1000rpm and 6000rpm and at 20°C or 50°C.

The impedance curves obtained for tests with CRW9 as inhibitor under 20°C and 1000 or 6000rpm are shown in Figure 7.27 (a) and (b) for Nyquist, Bode magnitude and Bode phase plots. From the Nyquist plots (Figure 7.27 (a)), semicircles show combination of two curves with different diameters. The curves show the depressed semicircles and decreasing in diameter with time. The Bode phase plots (Figure 7.27 (c)) show two peak angles at 1000rpm but only one is obvious at 6000rpm; however from the broad peak and asymmetric shape, two time constants exist. The peak values of phase angles are very similar for the two rotational speeds, indicating that CRW9 can form inhibitor film on the surface. The film can be quite stable even under high shear stress.

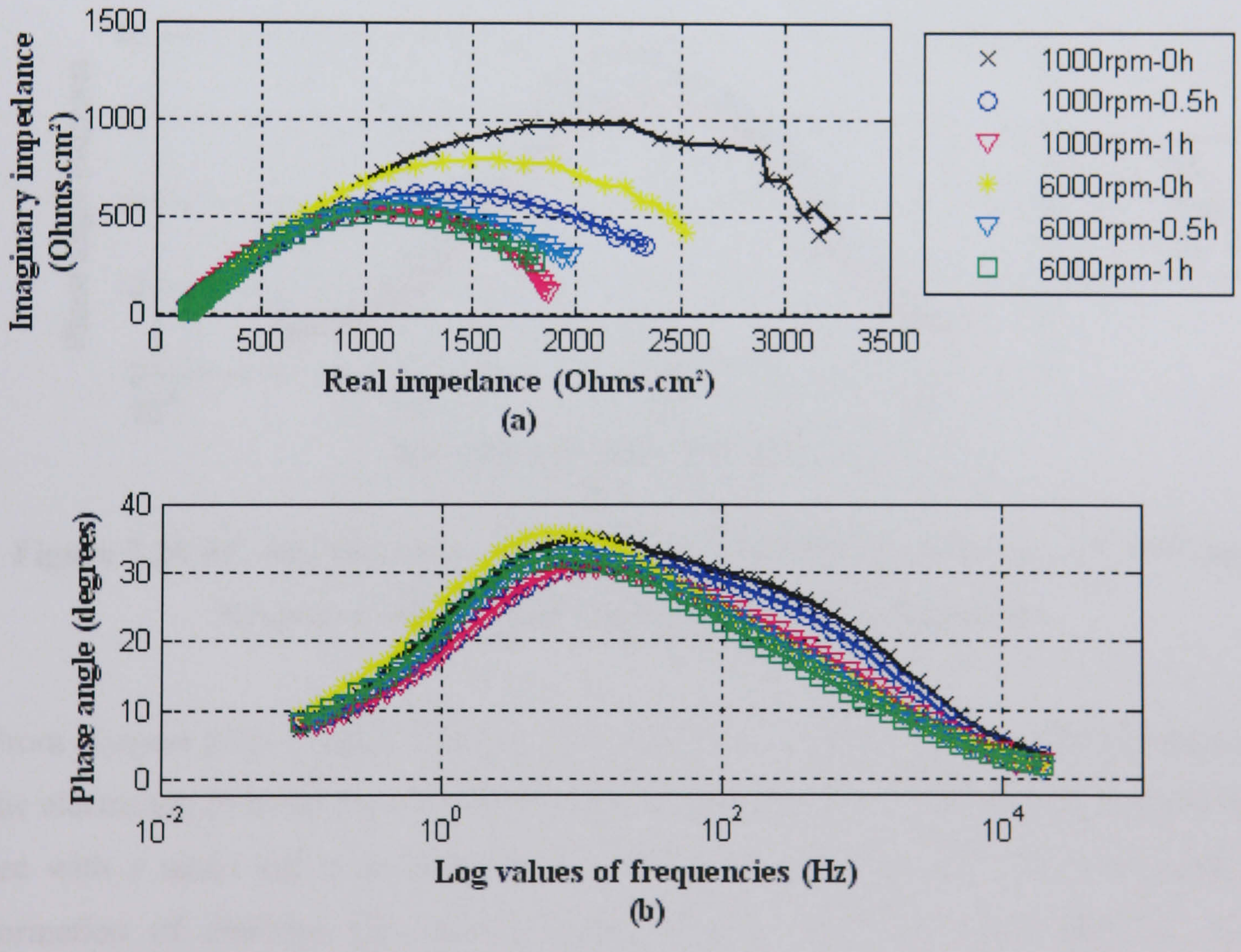

Figure 7.27 AC impedance spectra of tests with CRW9 as inhibitor at 1000rpm or 6000 rpm and 20°C (a) Nyquist, (b) Bode magnitude and (c) Bode phase plots

The equivalent circuit for these impedance curves obtained under 20°C are the same as the general equivalent circuit as shown in Figure 7.21.

The corrosion behaviour with CRW9 at 50°C and 1000rpm are presented in the Nyquist and Bode phase plots in Figure 7.28 (a) and (b) respectively.

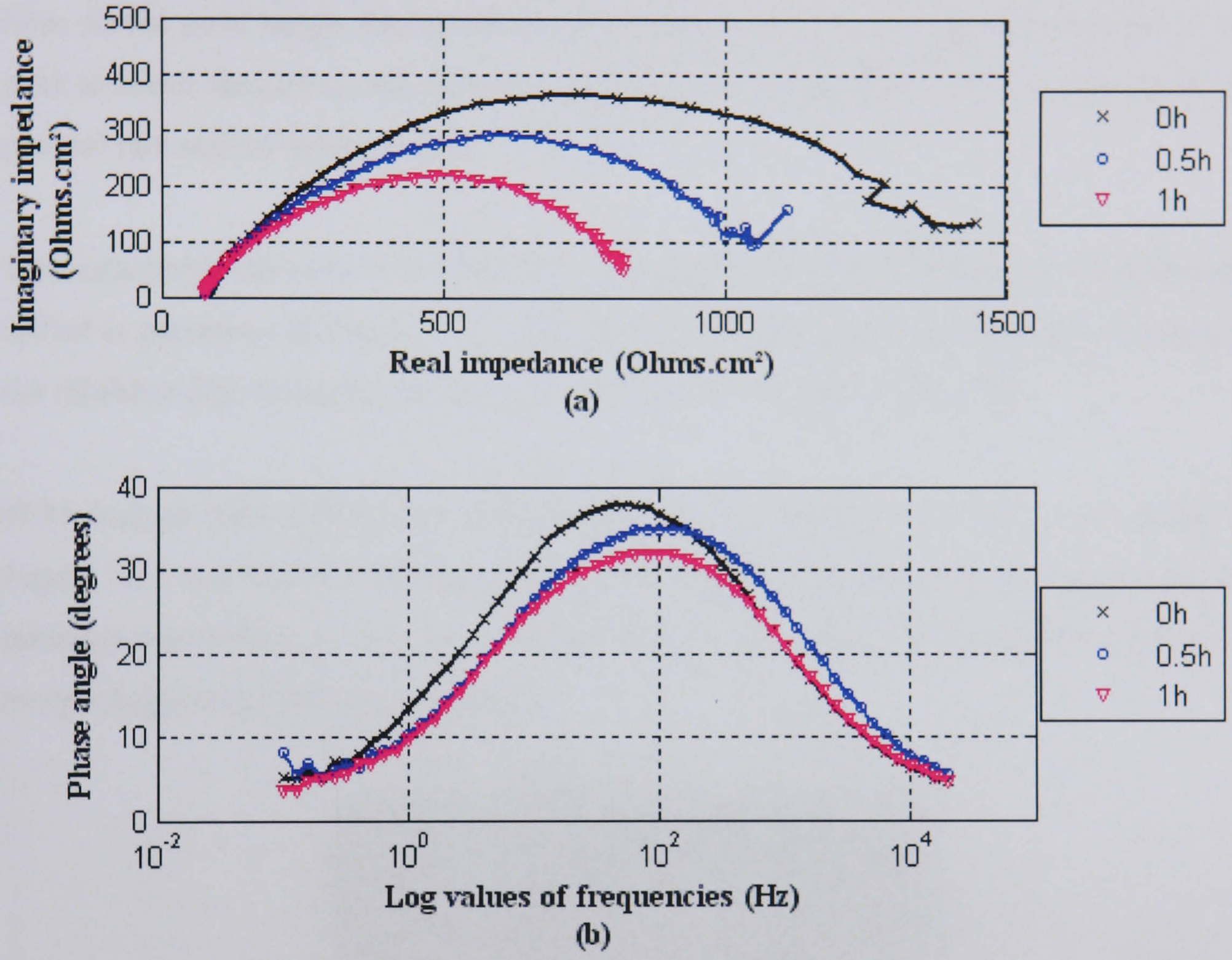

Figure 7.28 AC impedance spectra of tests with CRW9 at 1000rpm and 50°C (a) Nyquist, (b) Bode magnitude and (c) Bode phase plots

From Nyquist plots (Figure 7.28 (a)), the impedance response at the initial exposure to the electrolyte (0 h) shows a depressed semicircle followed by another poorly separated arc with a small tail at lower frequencies. The high frequency response indicates a formation of inhibitor film on the metal surface, because surface dielectric film normally has small time constants, which often results in a curve at higher frequencies. The part of the curve at lower frequencies most likely resulted from the electrochemical corrosion process. The arc with a tail formed at lower frequency can be correlated to diffusion of ions through the inhibitor film. The diameters of the semicircles both at higher and lower frequency decrease as time increases, suggesting the inhibitor film formation and removed along the time.

The response from the Bode phase diagram in Figure 7.28 (c) shows a decrease of the peak height and a shift towards higher frequency as time increases from 0 to 0.5 hour, which is possibly due to the change of the composition or the thickness of the inhibitor film. As the peak height decreased with time after 0.5h to 1h, along with the shift of the peak to lower frequency, this behaviour suggests an increasing corrosion rate due to the gradual removal of inhibitor film.

To characterise the corrosion behaviour of CRW9 at 50°C and 1000rpm, the equivalent circuit is presented in Figure 7.21. The physical model is shown at the left. It is due to the inhibitor film formed onto the metal surface with a porous structure.

SEM images after CRW8 and CRW9 tests under 1000rpm and 50 °C are shown in Figure 7.23 and Figure 7.29 respectively. The vision evidence tends to suggest that the inhibitor may behave in two ways, by adsorbing on the metal surface and by altering the morphology of the corrosion products.

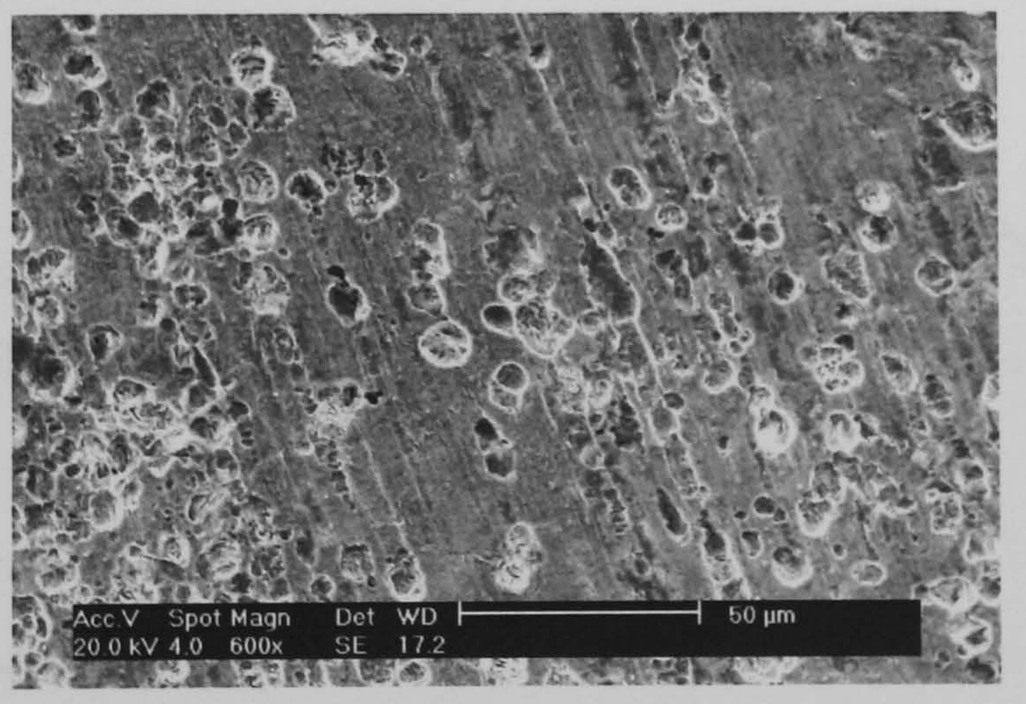

Figure 7.29 SEM image for CRW9 under 1000rpm and 50°C

At 6000rpm and 50°C, the impedance curves obtained are shown in Figure 7.30 (a) and (b) for Nyquist and Bode plots. The Nyquist plots (Figure 7.30 (a)) show a deviation of the semicircle below the real axis, which means that induction process occurred. There is more deviation at lower frequencies at initial exposure time, indicating inhibitor film forming on the metal surface, but not stable. Then at 0.5 h, the Nyquist plot showed only one depressed semicircle but increased in diameter comparing with the initial time.

It may be due to the incorporation of the inhibitor and corrosion products. At 1 h, the diameter of the semicircle decreases, indicating that the film is partially peeled off.

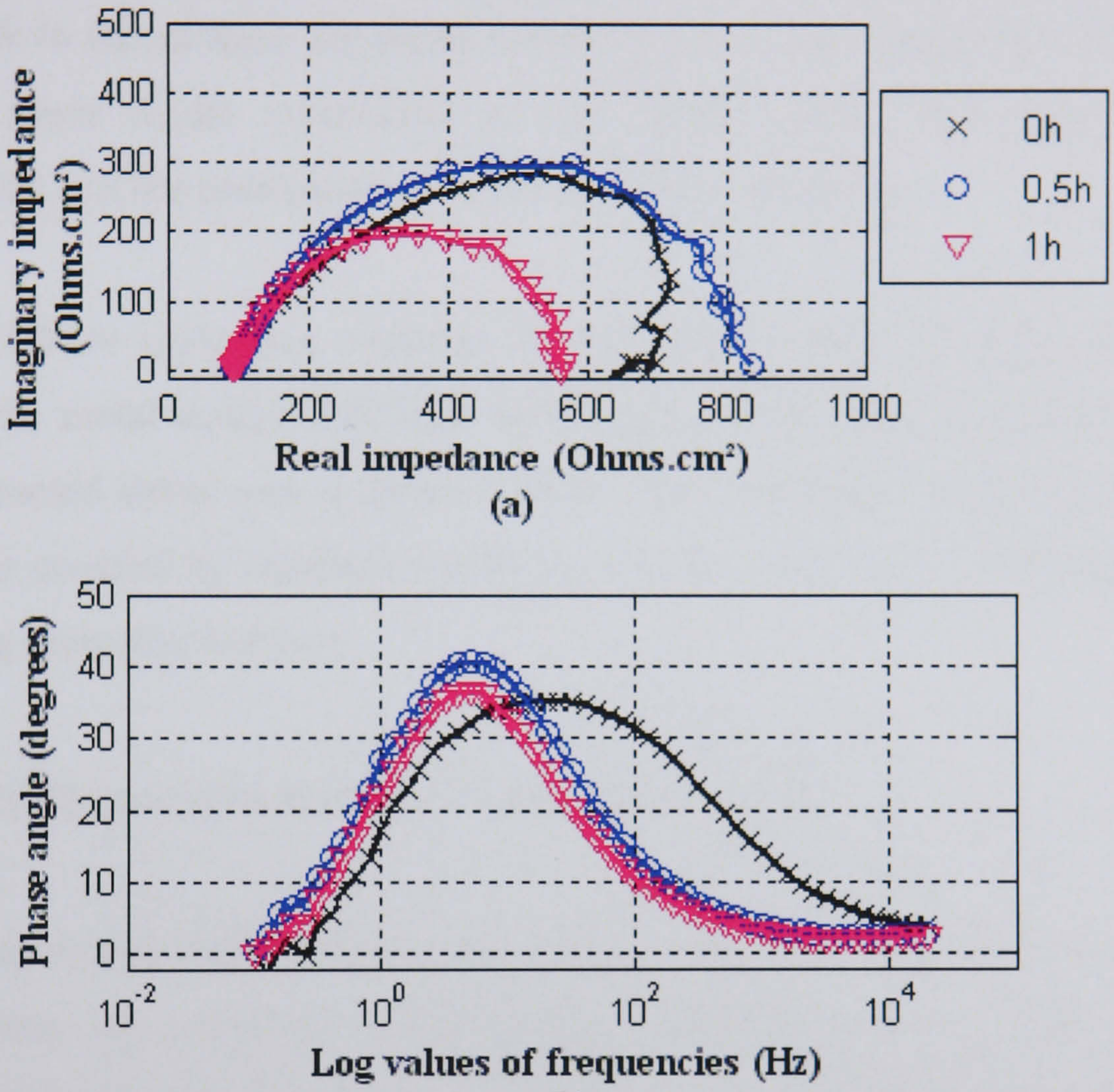

Figure 7.30 AC impedance spectra of tests with CRW9 as inhibitor at 6000rpm or and 50°C (a) Nyquist plots and (b) Bode phase plots

The Bode phases plots (Figure 7.30 (b)) presented one broad peaks at initial time, which is due to two peaks merged with each other. And then only one peak left for the 0.5h and 1h exposure time.

As the curve at initial immersion time showed inductance behaviour, the same equivalent circuit previously proposed (shown in Figure 7.25) is used to fit the impedance spectra under the condition of 50°C and 6000rpm.

From AC impedance analysis, it can be postulated that under all the conditions, the corrosion products can not form a layer on the metal surface when inhibitor effectively reduces the corrosion. The reason is that, in the presence of the inhibitors, the corrosion

rate of the metal decreases and the diffusion of Fe^{2+} from the bulk solution remains the only source of ion for precipitation at the metal surface if it is possible. Since, the precipitation of the iron carbonate is much faster than the rate of transportation of Fe^{2+} from the bulk to the surface; the precipitation becomes diffusion-controlled. This leads to slightly more acidic conditions at the metal surface and consequently the supersaturation and the precipitation of iron carbonate decreases.

As stated inhibitor molecules impacted by the sand or flowing were easily stripped away from the metal surface although they might adsorb back again onto the surface after the impacted stress was removed locally. Thus, the steel surfaces during the time that were not covered by inhibitor molecules would corrode at a quite high rate. As a result, pitting corrosion happens.

7.3.6 Main Parameters from AC Impedance Tests

The main parameters such as R_{ct} and C_{dl} obtained for all the impedances taken during the experiments are presented in this section. Together with the surface equivalent circuit, R_{ct} and C_{dl} can provide the information on corrosion kinetic and inhibition ability of the surface film.

The charge transfer resistance R_{ct} values account for the resistance of charge from the inhibitor film to the metal substrates, which are inversely proportional to the surface area under corrosion. For both blank tests and with different inhibitor tests, R_{ct} decreases with increase of temperature and/or rotational speed. Figure 7.32 (a) and (b) present the R_{ct} values for CGO and CRO and Figure 7.33 (a) and (b) for CRW8 and CRW9 respectively.

The double layer capacitance C_{dl}, consists of one metallic plate and one conducting surface of electrolyte. Capacitance is directly proportional to surface area and inversely proportional to the thickness of dielectric as shown in Equation (85). In this study, the dielectric properties between the metallic surface and electrolyte can be the same for the same brine as shown in Figure 7.31, where inhibitor film partically formed on the metal

surface and electrolyte contacts with the metal at pores of the film. Hence, C_{dl} mainly relates to the corroding surface area of the metal surface. Corrosion results in anodic site of Fe dissolution and cathodic site Fe_3C left behind. C_{dl} can be changed with change of surface area contacting to the electrolyte due to corrosion.

$$C_{\mathrm{dl}} = \frac{\varepsilon_0 \varepsilon_r A}{d} \tag{85}$$

where ε_0 = electrical permittivity of free space (8.854×10^{-14} F cm^{-1})

ε_r = relative electrical permittivity of the charges on the metal surface

A = exposed test area to the electrolyte

d = thickness of the charges on the metal surface

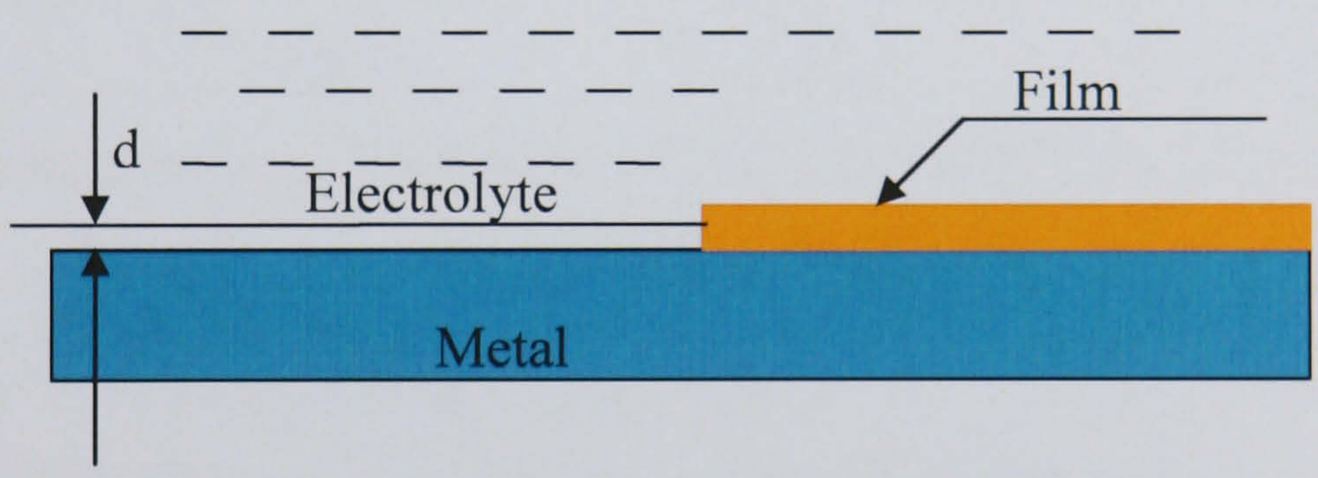

Figure 7.31 Schematic diagram of the metal/ electrolyte interface with inhibitor film formed on the surface containing pores

Among all the conditions, CRW8 has the highest R_{ct} values at initial exposure time. They are several times higher than with CRW9, which has the second highest values.

At 1000rpm and 20°C, for CRW8 tests, the R_{ct} values are slightly increased from 0 to 1 hour, so are for CRW9 tests at 6000rpm and 20°C. Both cases have high inhibition efficiency under erosion-corrosion conditions. It is postulated that the high and constantly corrosion resistance plays an important role in reducing erosion-corrosion and providing high inhibition efficiency.

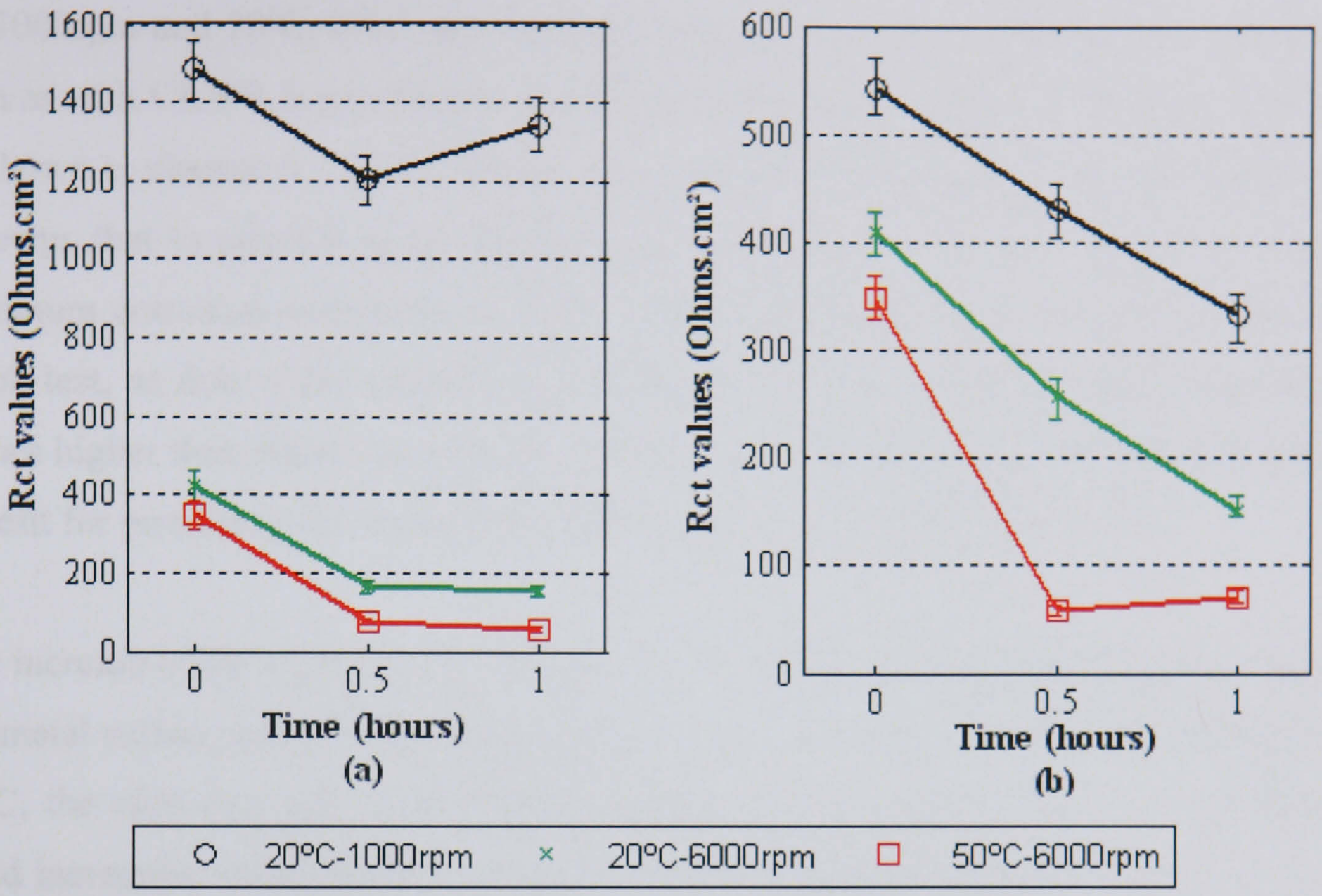

Figure 7.32 R_{ct} values for tests with (a) CGO and (b) CRO under 1000 or 6000 rpm and 20°C or 50°C

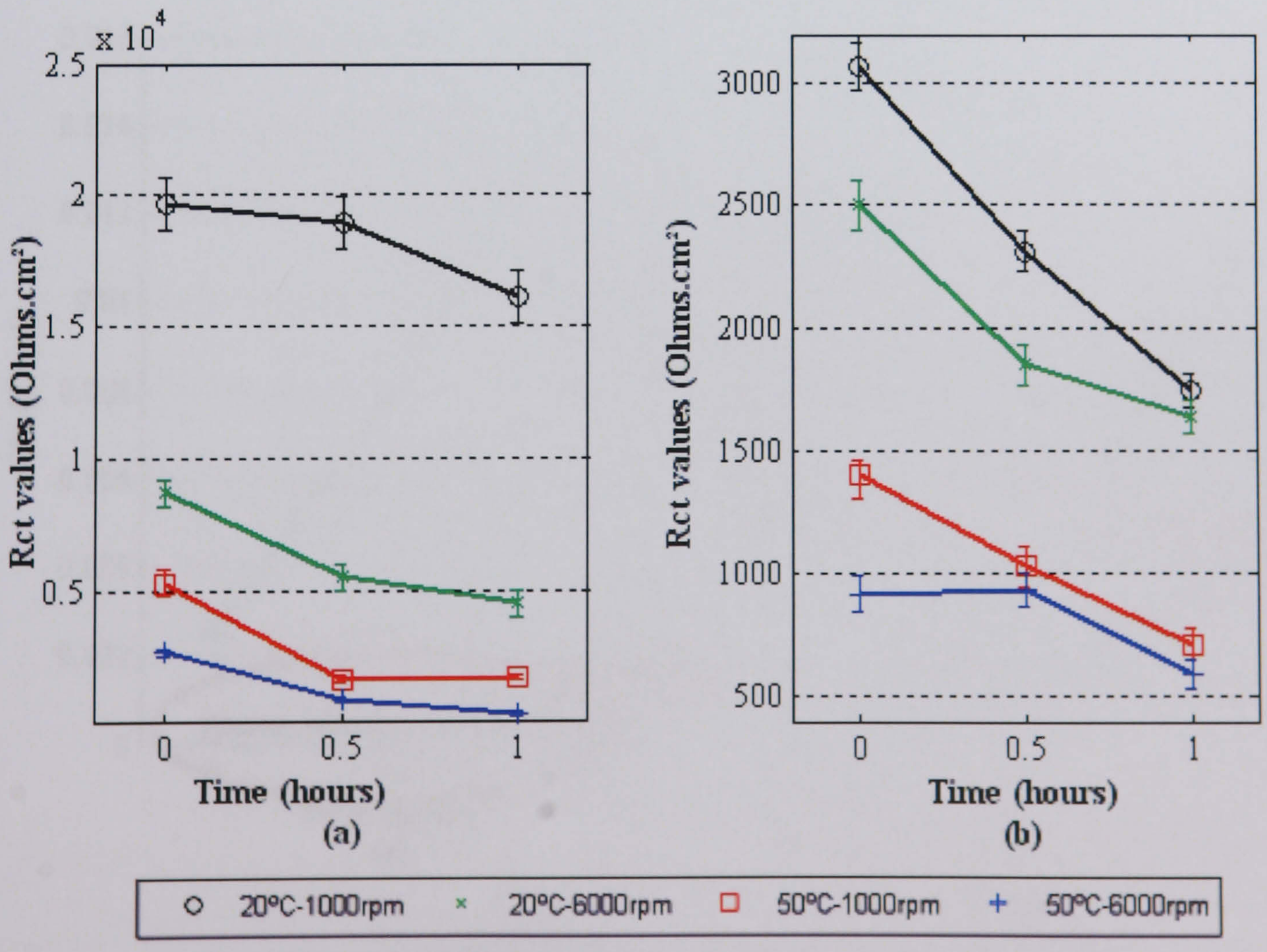

Figure 7.33 R_{ct} value for tests with (a) CRW8 and (b) CRW9 under 1000 or 6000 rpm and 20°C or 50°C

At 1000rpm and 20°C, CGO also showed constant R_{ct} values, although they are not as high as with CRW9, it provided better efficiency than with CRW9 for erosion-corrosion as shown in chapter 6. As R_{ct} values with CGO are 3 times as high as with blank tests, it seems that to provide good inhibition for erosion-corrosion it is necessary to get a minimum corrosion resistance. At 20°C, CRO has the R_{ct} values even lower than with blank test, so does CGO at 20°C and 6000rpm. At 50°C, all the inhibitor showed R_{ct} values higher than blank tests and decreasing with time. However, they are still provide benefit for protecting the carbon steel from corrosion and erosion-corrosion.

The increase of the value CPE_{dl} with time is due to the corrosion process taking place at the metal surface and corrosion rate increase with time. For blank tests, at 6000rpm and 50°C, the corrosion rate is the highest among all the condition. This is supported by rapid increasing value of CPE_{dl}, indicating that significant increase of Fe_3C left on the metal surface due to dissolution of Fe. At 1000rpm and 50°C, the value decreased with exposure time. This is due to small amount of corrosion products formed on the metal surface resulting in corrosion rate decrease, although the change is very small.

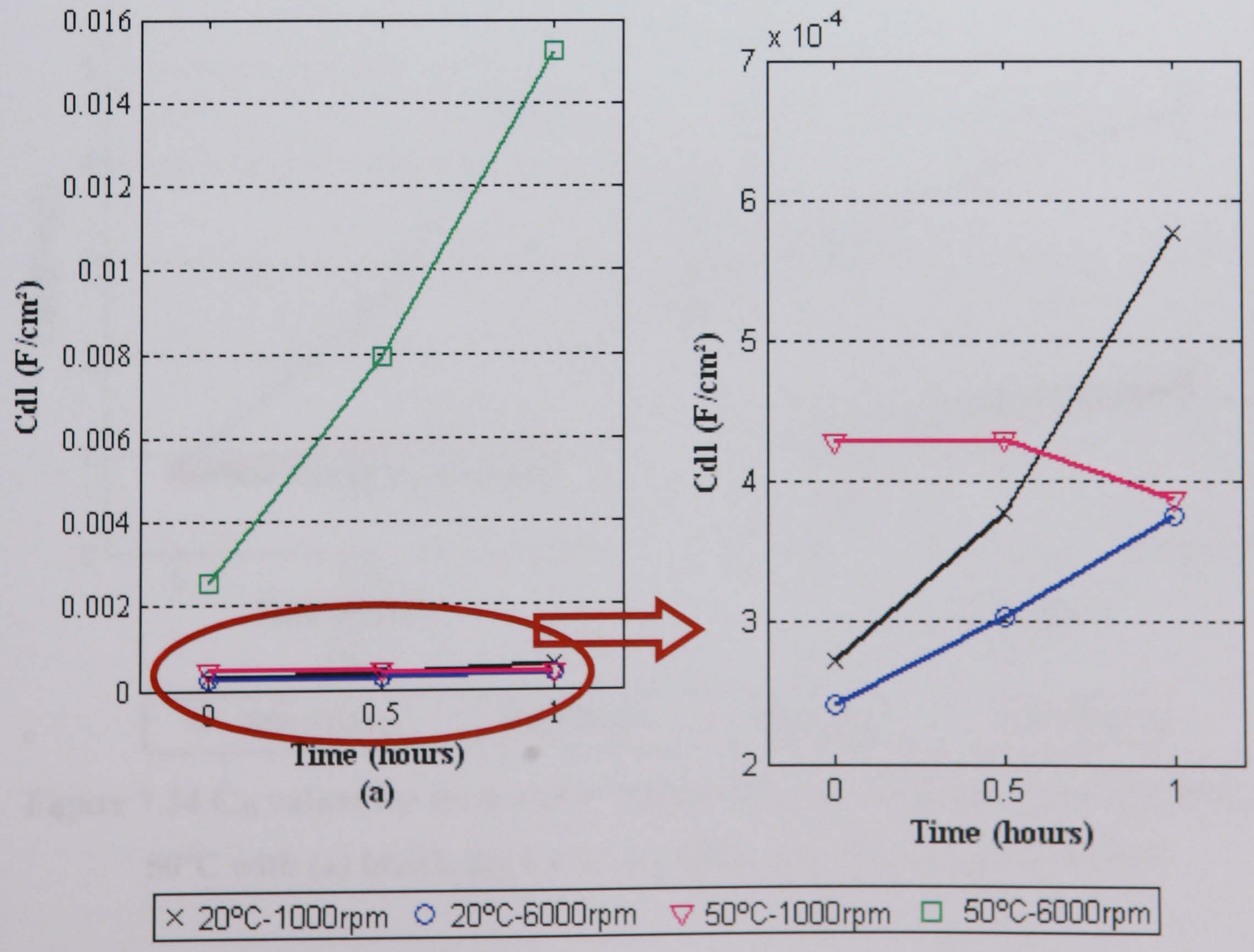

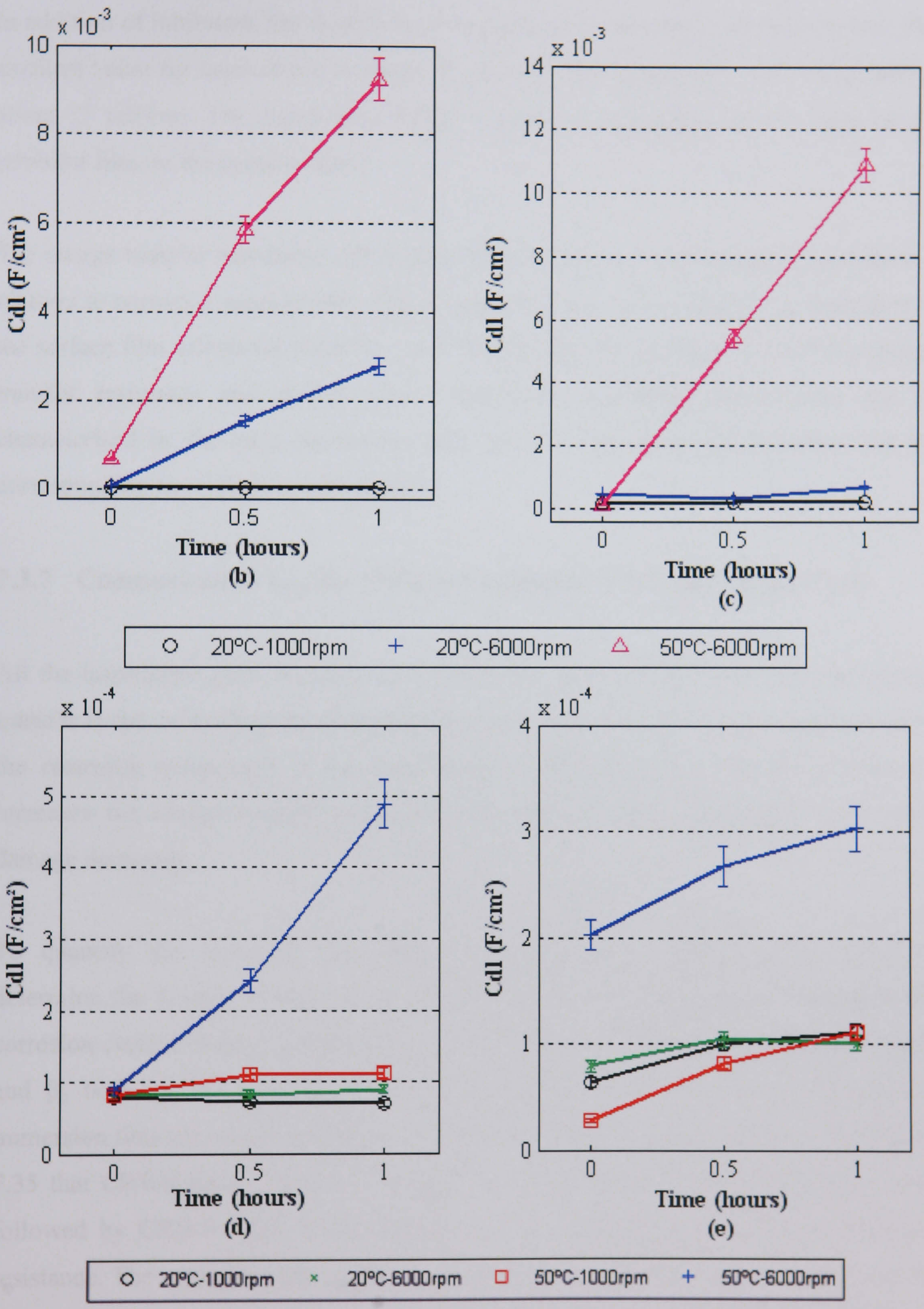

Figure 7.34 C_{dl} values for tests under 1000/6000 rpm rotational speed and 20°C or 50°C with (a) blank, (b) CGO, (c) CRO, (d) CRW8 and (e) CRW9

In addition of inhibitors, the double layer capacitance is decreased as stated above. The smallest value for capacitance is about 40 μF/cm². The biggest one with blank tests is about 15 mF/cm². The capacitance value is useful to investigate the coverage of the inhibitor film on the metal surface.

The charge transfer resistance and double layer capacitance are the main parameters in relation to corrosion mechanisms. The resistance of the surface film and capacitance of the surface film calculated from the curve fitting followed the same trend of the charge transfer resistance and double layer capacitance. Inhibition mechanisms can be characterised by the main parameters from the AC impedance measurement and the corresponding equivalent circuit model.

7.3.7 Comparison of i_{corr} for Different Inhibitor Tests and Blank Tests

All the impedance plots obtained were essentially semicircular, indicating that charge transfer is the controlling dissolution mechanism. The value of $1/R_{ct}$ is proportional to the corrosion component of the total damage. The addition of inhibitors generally increases the charge transfer resistance, then the corrosion component of the total damage decreases.

To quantify the corrosion rate under erosion-corrosion conditions and therefore determine the $C+dC_E$ component of the mass loss, it is important to determine the corrosion current density. According to the Stern-Geary equation, assuming that the β_a and β_c both are 0.12V/decade, the i_{corr} values calculated from R_{ct} at 60 minutes immersion time are shown in Figure 7.35. It can be generally concluded from the Figure 7.35 that CRW8 shows the best corrosion resistance under all the conditions, closed followed by CRW9. CRO in all conditions consistently shows the lowest corrosion resistance. The reason for this can be explained by the surface model and change of the surface area. The highest i_{corr} value for corresponds to corrosion rate of 256 mpy. If assuming the β_a and β_c both are 0.03 V/decade, it will reduce to 64 mpy. Using R_p values instead of R_{ct} to calculate i_{corr} will get corrosion rate of 130 mpy. Therefore, the high corrosion density can result from the way to calculate it. However, no matter what

values to use to calculate, i_{corr} is still high. It can be due to the enhancement of corrosion by erosion.

For inhibitor CRW8, under static conditions, the film formed on the surface has dense and even-thickness structure; the porous of the film is so small that it can be best fit with equivalent circuit model shown in Figure 5.15 (b). It then prevents corrosion by isolation up to 100 h immersion time. At such case, although the top layer surface resistance is very small, about 100 to 200 Ohms.cm² shown in Figure 5.17, the inhibition efficiency is very high. Under 1000rpm rotational speed and 20°C, the shear stress due to rotation decreases the film coverage. Porous obviously exists; the reason for very high corrosion resistance is not only because they prevent corrosion by isolation but by extending the diffusion path of corrosion species, therefore decreases the corrosion rate at the inhibitor/substrate interface. At more aggressive conditions, it still can cover the metal surface and provide inhibition. The surface area covered by inhibitor can be expressed by capacitance value C_{dl} of the double layer, represented by CPE_{dl}. The results indicate a decrease in the capacitance with addition of effective inhibitor. This decrease in the capacitance could also be accounted for by thickening of a surface film, but this seems unlikely in this turbulent flowing fluid with sand. Therefore the total corrosion can be directly related to the apparent decrease in corroding surface area.

For example, under 20°C and 6000rpm rotational speed, the double layer capacitance C_{dl} calculated from blank tests equals to 375 μF/cm² at 1 h exposure time. The addition of the inhibitor CRW8 reduces the value to approximately 88 μF/cm², whereby only a slight influence of concentration has been established. The reduction factors ψ for C_{dl} are lower than inhibitor efficiencies, indicating the effect of inhibition not only upon C_{dl} but also on other components of the equivalent circuit. Then it should be due to diffusion which is confirmed by the small difference in α values from constant phase element (CPE).

The poorest performance inhibitor CRO hardly forms a film on the metal surface under turbulent conditions. From the R_{ct} values, it can be seen that at initial exposure time, the inhibitor film partially formed on the surface, after 0.5 h, the film was completely stripped off and at the same time roughen the metal surface resulting in increase of the corrosion current density. The addition of CRO at 1 hour exposure time under 20°C and 6000rpm rotational speed increase the values of Cdl to about 681 μF/cm². It is why that the corrosion current density is even higher than with blank tests.

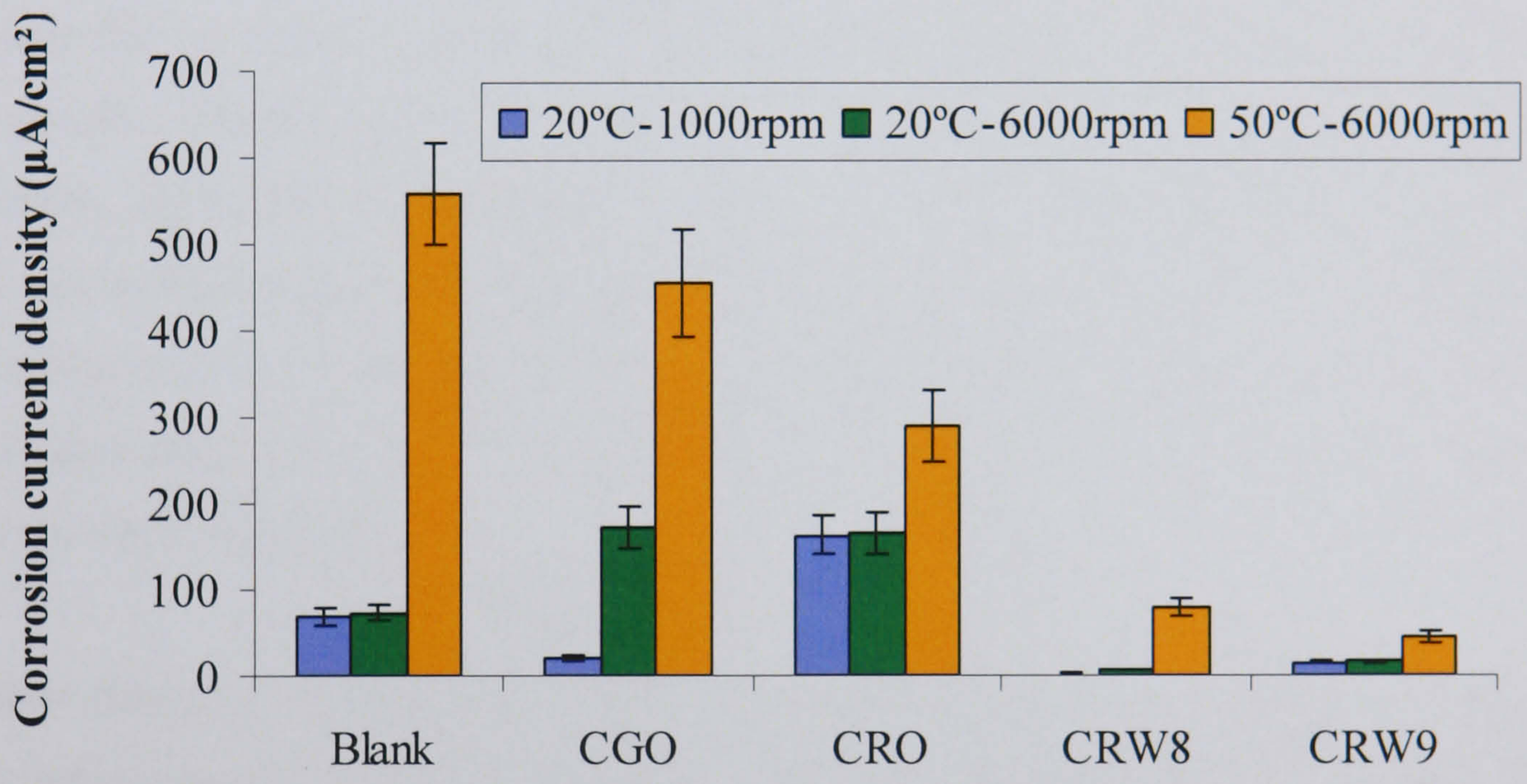

(a)

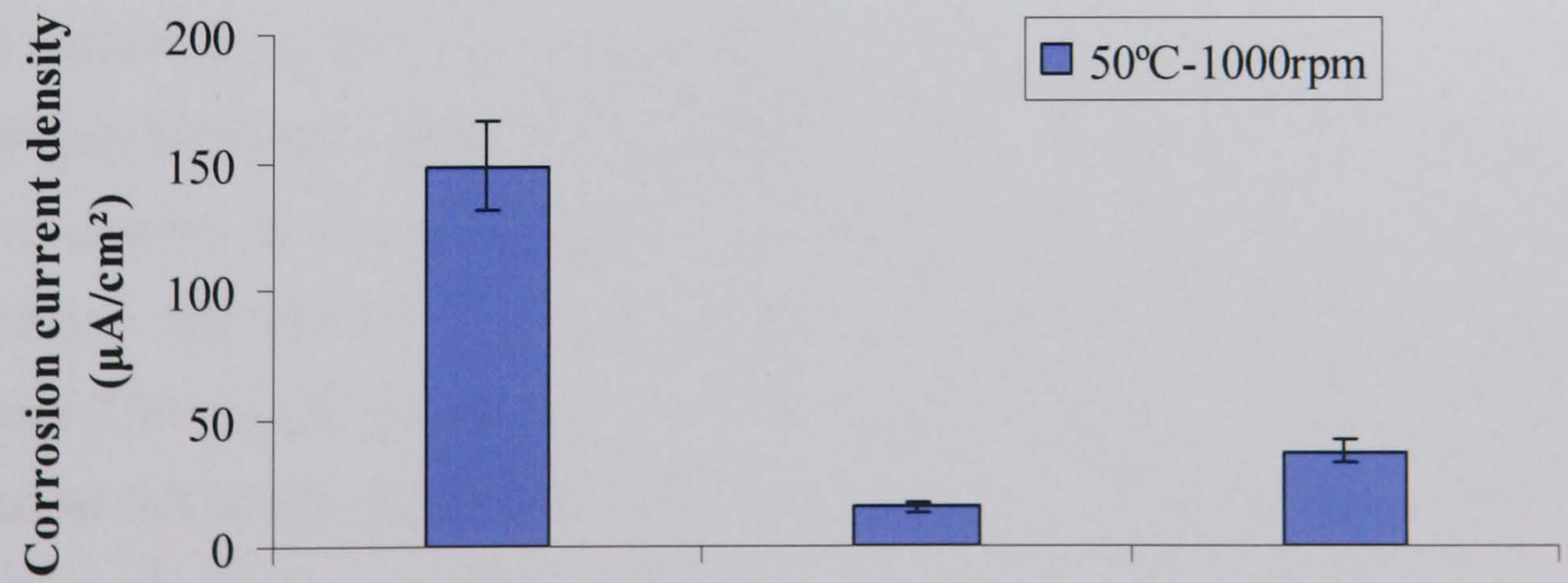

(b)

Figure 7.35 The effect of the temperature and rotational speed on corrosion *in-situ* conditions for blank tests and inhibitor tests, (a) at 20°C or 50°C and 6000rpm and 20°C and 1000rpm, (b) at 50°C and 1000rpm

7.3.8 Stability of inhibitor film

The film formation (adsorption) of surfactants onto a metal surface can be described by the same mechanism that causes the formation of micelles in aqueous solution. For water soluble inhibitors, the films have hydrophilic effects. For oil soluble inhibitor, it may be hydrophobic effects (Jovancicevic *et al.*, 1999).

From the surface models of the inhibitor/substrate, it can be seen that the stability of the inhibitor film is better under hydrophilic effects (shown in Figure 5.15) than under hydrophobic effects (shown in Figure 5.22). Especially under higher shear stress conditions, the porous of the surface inhibitor film for oil soluble inhibitor CGO and CRO are too big to present two time constants as shown in Figure 7.15). The films have been easier to strip off. While water soluble inhibitors still presents two time constants. Porous area are smaller, there is a resistance of the pores to prevent the corrosive media reach the metal substrate.

Inhibitor functions by forming a film on the metal surface. As stated on Chapter 5, under static conditions, the film is thicker and more stable in the absence of shear stress and less aggressive environment, such as lower diffusion of CO_2. However, stability and uniformity of the inhibitor films are dependent on hydrodynamic conditions. Under 6000rpm rotational speed, the film breaks down where the pits developed. To exam more closely, from the enlarged SEM images for the pits, the inhibitor effects on corrosion still can be seen. The comparison of the surface inside pits are shown in Figure 7.36 (a)–(d) for blank, CGO, CRO and CRW8 tests. It can be seen that the only material left inside pits for CGO and CRO are pearlite sites, which consist of α-Fe and Fe_3C as shown by arrows in the Figure 7.36 (a)-(d). The structure is the same as the image of material microstructure of carbon steel obtained from static tests shown in Figure 5.26. The fact that Fe_3C left on the metal surface for carbon steel due to iron dissolution is in agreement with the work from other researchers (Hawkins 1995). From the comparison, it can be seen that there are more debris intact with the substrate for CRW8 (Figure 7.36 (d)) than any that for blank, CGO, or CRO, in addition, there are more subsurface exposed for CGO and CRO, as shown by the circles.

The mechanism of corrosion under high shear condition is still the same with that under static conditions. Under high rotational speed, the diffusion of the inhibitor has a less pronounced effect than the shear stress and flow pattern effects on the inhibitor film formation. The results show that the hydrophilic head group plays important role in the formation of inhibitor film under both static and high flow conditions, which is in agreement with the work by Jovancicevic *et al.* (1999). Jovancicevic *et al.* (1999) found that at 60°C and 6000rpm rotational speed, the corrosion rate for lauric imidazoline is 40mpy. At 6000rpm and 50°C, the mass loss components from the total mass loss, calculated from i_{corr} (shown in Figure 7.35) for inhibitor CRW8 and CRW9 are about 35mpy and 20mpy.

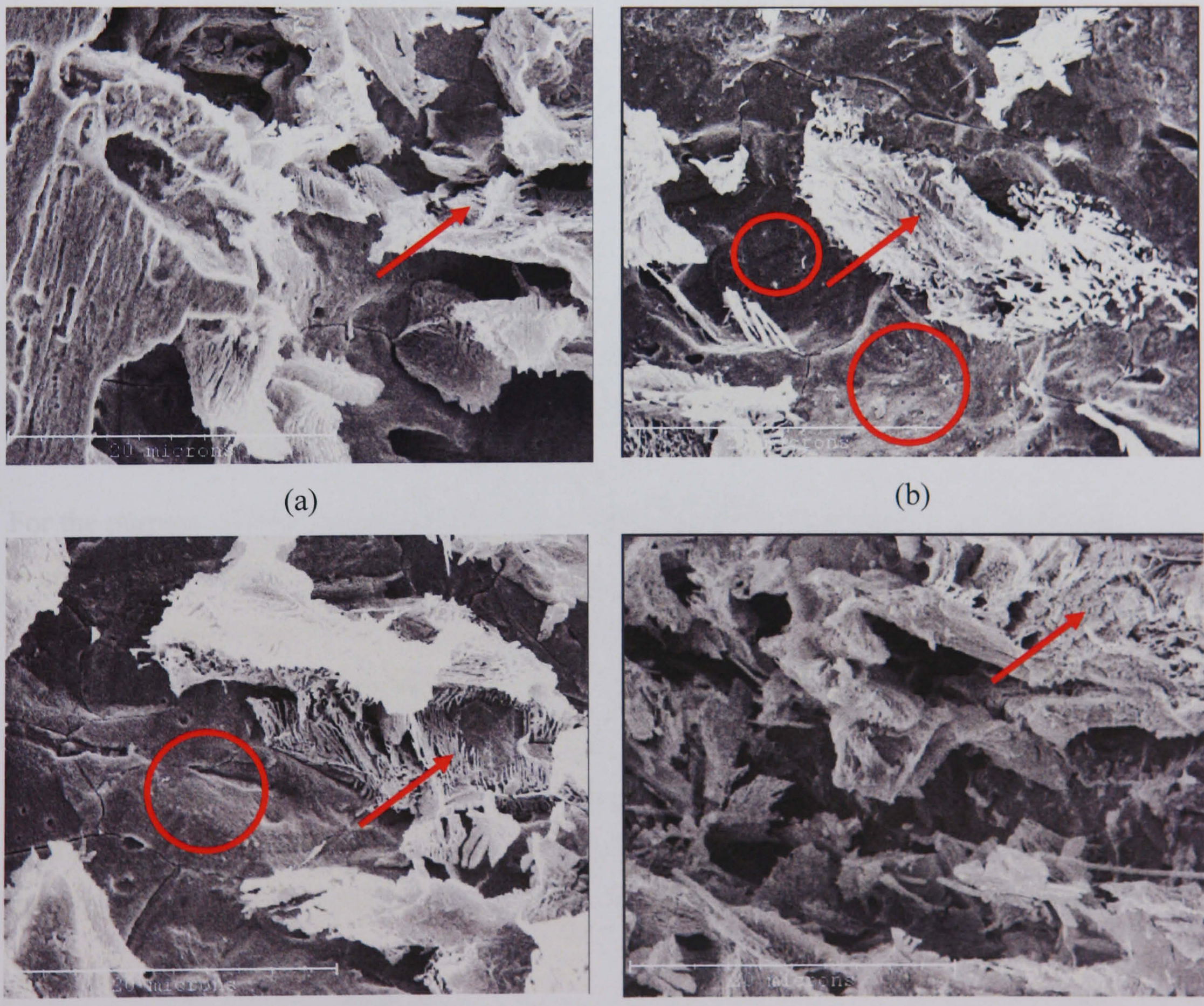

Figure 7.36 SEM images for (a) Blank, inhibitor (b) CGO (c) CRO and (d) CRW8 at 20°C and 6000rpm

7.4 Erosion, Corrosion and Synergy Calculation

It has previously been stated (Schmitt, 1995) that at production velocities of > 0.3 m/s material loss processes are not entirely controlled by mass transfer and that also charge controlled processes are important. From previous images it is clear that mechanical damage is due to sand and flowing impacts. From Figure 7.37 (a), there is no linear relationship between the mass loss results and R_p values obtained from corrosion measurement *in-sit*. Enlarge the circled data (Figure 7.37 (b)) shows that there is not linear relationship between the mass loss results and linear polarisation resistance. However, the trend exists that larger LPR resistance generally correlates with lower mass loss results. From Figure 7.38, it is very clear that mass loss calculated from R_{ct} values is only a small portion of the actual mass loss measured during the RCE tests. This is evidence that in fact there are further non-electrochemical processed which are affecting the material loss rates. This is also confirmed by Malka *et al*. (2006). In terms of assessing inhibitor action in reducing corrosion and erosion-corrosion processes, total mass loss reduced by inhibitor is larger than the corrosion component calculated from R_{ct} values. In fact the inhibitor partially reduced corrosion process and this in turn reduced total mass loss by reducing some damage due to synergistic processes.

For the purpose of improving the design of inhibitors for erosion-corrosion protection, it is crucial to understand the mechanical and electrochemical effects over the total metal degradation under erosion-corrosion conditions with or without inhibitors. One of the key objectives in this programme of work as a whole is to determine how inhibitors affect corrosion, erosion and interactive processes involved in erosion-corrosion mass loss which can increase the degradation. Under the erosion-corrosion conditions, the total mass loss can be determined by analysing the components of material loss using the simple Equation (86) (Souza and Neville, 2003; Zhang *et al*., 2004):

$$\mathbf{TML = E + C + dE_c + dC_e} \tag{86}$$

where TML is total mass loss. E is pure erosion rate in the absence of corrosion determined by measuring the mass loss rate under cathodic protection. C is corrosion

rate measured in the absence of erosion which can be determined under static condition. dC_e is the effect of erosion on the corrosion which is often called the additive effect and dE_c is the effect of the corrosion on the erosion which is often called the synergistic effect.

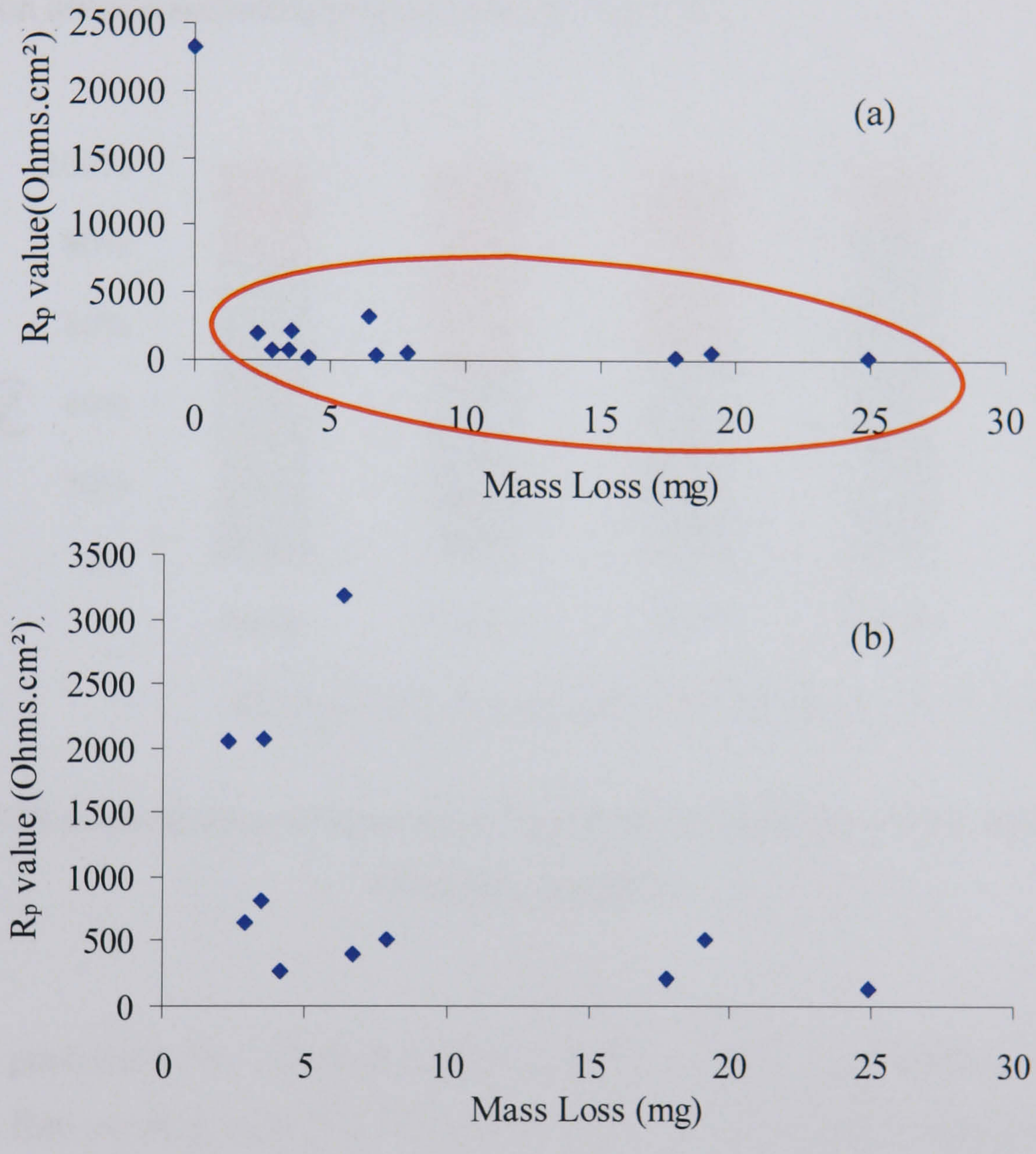

Figure 7.37 Mass loss as a function of R_p values in RCE tests, (a) total data and (b) data within the circle from (a)

The component of $(C+dC_e)$ is called corrosion *in-situ* when the material was being subjected to liquid-solid erosion-corrosion conditions. Analysis of R_{ct} from AC impedance results, corrosion current densities have been determined shown in Figure 7.35. The mass loss rate due to corrosion under erosion-corrosion conditions can be determined by calculating the i_{corr} data via Faraday's law (Equation (18)). There is no doubt that there is a significant increase in the corrosion rate due to erosion comparing with the pure corrosion rate just from the difference of value between the static

condition and erosion-corrosion conditions. Ramakrishna *et al.* (2006) investigated the erosion-corrosion rate distribution for carbon steel under CO_2 saturated condition with sand and concluded that the average increment in corrosion rate due to erosion was up to twice that of the pure corrosion rate. The interesting point is to know if inhibitor has the effect on erosion including pure erosion and synergy.

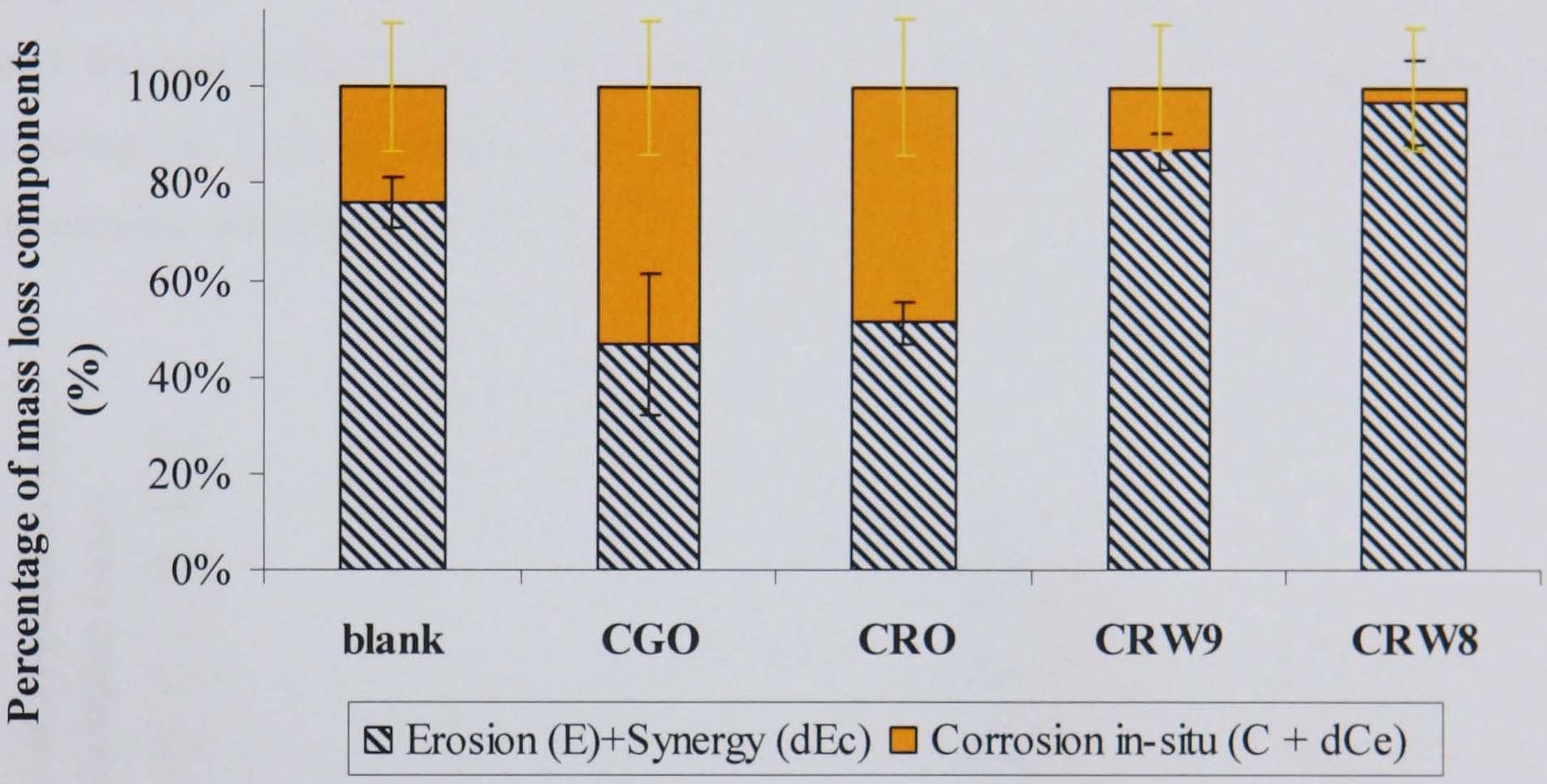

Figure 7.38 Contribution of total mass loss from its components for RCE tests at 6000rpm and 20°C

As stated previously the inhibitor has the effect to reduce pure erosion damage by forming a film or drag reduction (Schmitt, 2001). Thus, by eliminating corrosion the subsequent effects of surface roughening and local flow instabilities are also being reduced. Rmakrishna *et al*. (2006) found that, the erosion rate due to corrosion is found to be on average 3 to 4 times the pure erosion rate, which is basically in agreement with this work with blank tests. It is apparent from this study that the inhibitor acts to cut down the corrosion processes and reduce the extent (size and number) of pits. This will in turn have an effect on reducing synergistic erosion processes (dE_c). If the inhibitor could produce an effect of completely eliminating corrosion (such as it does for inhibitor CRW8 at 1000rpm and 20°C, where R_{ct} is extremely high and i_{corr} is very low) then the mass loss is completely eliminated. However, the accurate amount of the mass loss due to pure erosion with inhibitor is hardly can be determined. Therefore, the

erosion rate presented in this section is the total erosion component including the pure erosion and synergy.

The effect of inhibitors CGO and CRO on the corrosion component comparing with blank tests is shown in Figure 7.39. Figure 7.40 shows the erosion component accordingly. It can be seen that the inhibitor has effect to corrosion under 1000rpm and 20°C and through reducing the corrosion rate and reducing the surface roughness, in turn reducing the local turbulent and shear stress as a result both CGO and CRO have effect to erosion component of the total material damage.

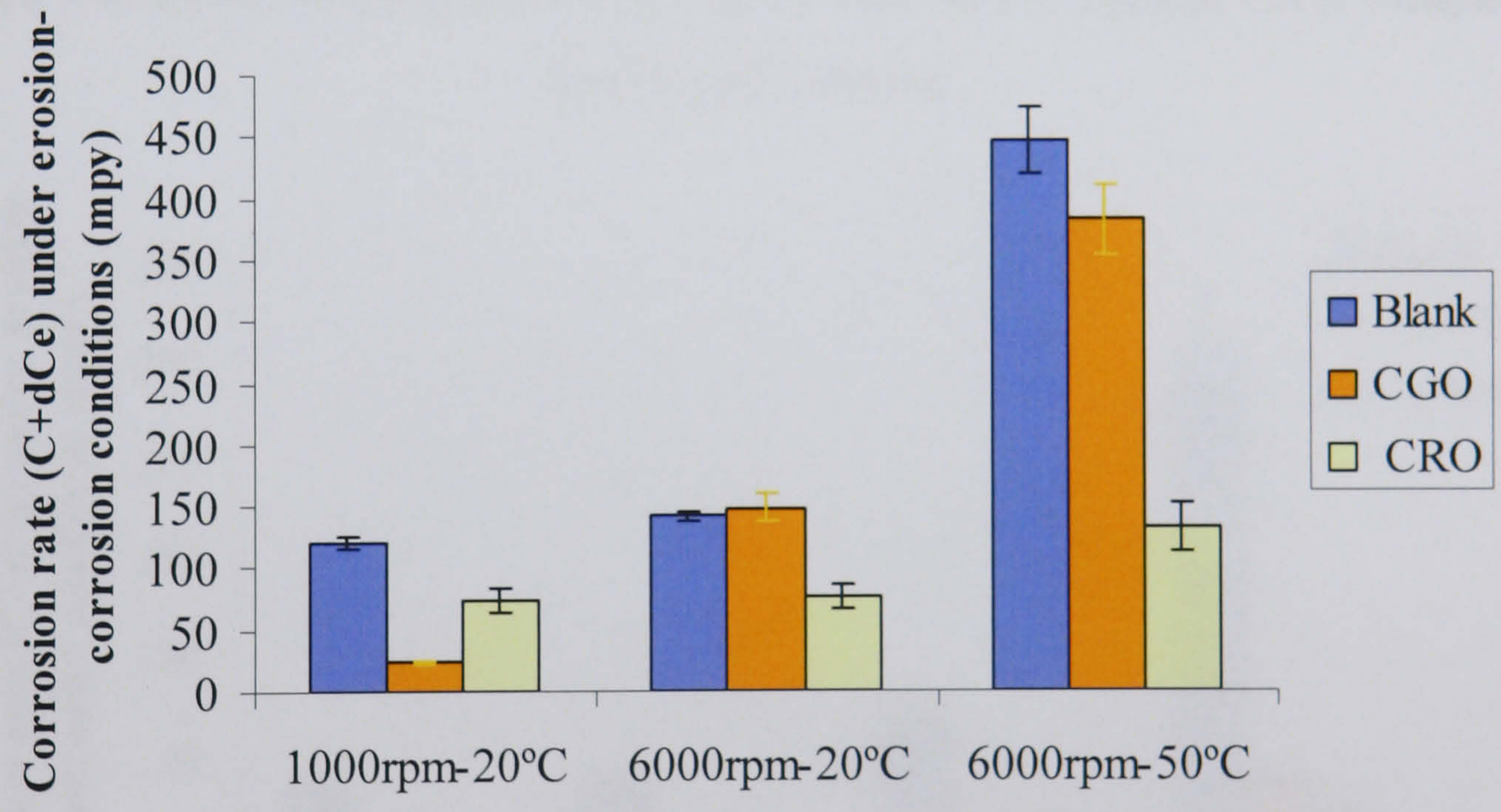

Figure 7.39 Effect of corrosion with oil soluble inhibitor CGO and CRO comparing with blank solution

The effects of inhibitor CRW8 and CRW9 on corrosion and erosion are shown in Figure 7.41 and Figure 7.42 respectively for different conditions. It can be seen that under 1000rpm and 20°C, CRW8 eliminates the corrosion and in turn eliminate erosion as well; CRW9 is not as effective as CRW8.

However, under 6000rpm and 20°C, due to the high shear stress, the corrosion resistance decrease more faster for CRW8 than CRW9, as a results CRW9 shows more resistance to erosion than CRW8.

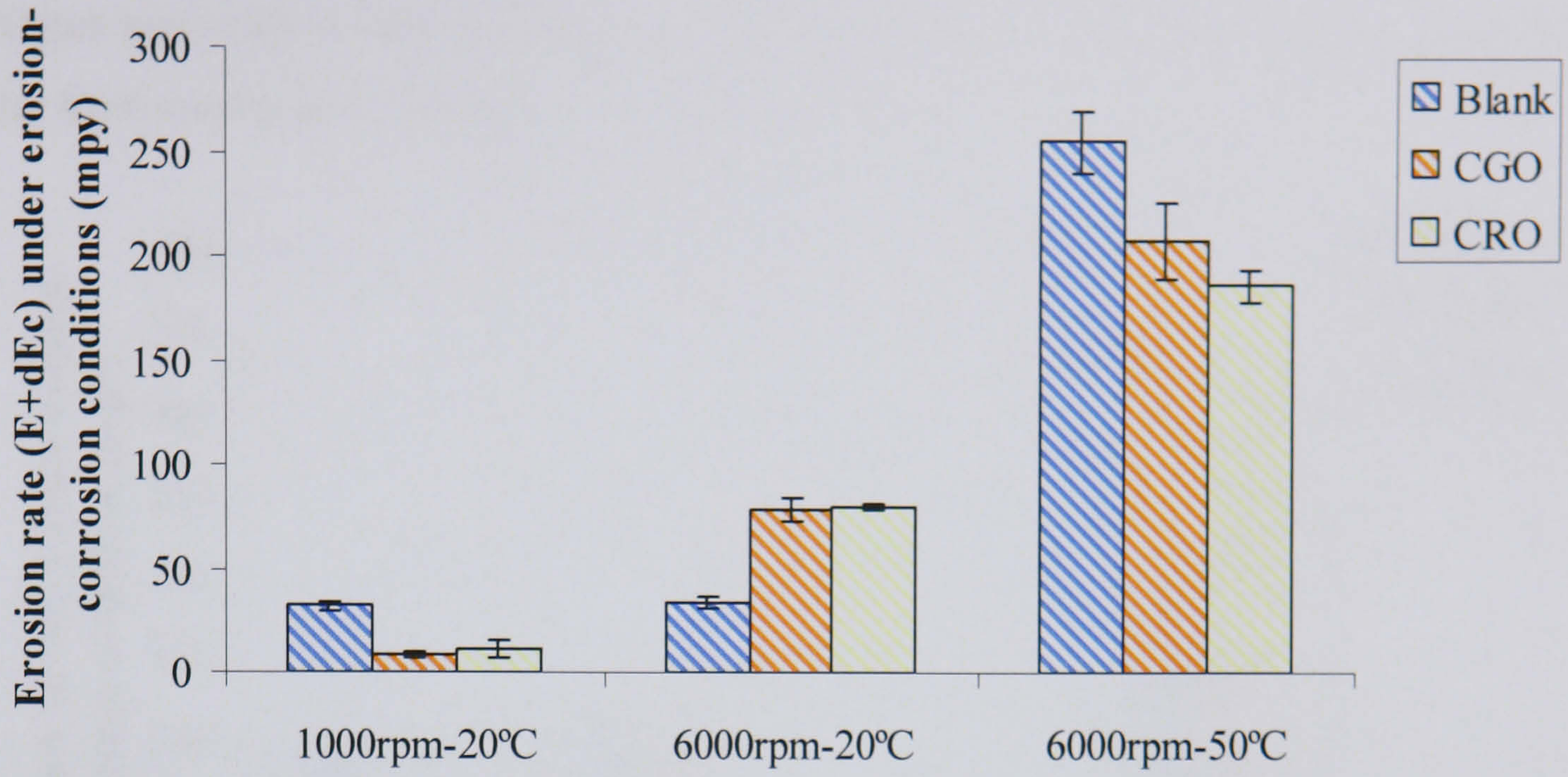

Figure 7.40 Effect of erosion with oil soluble inhibitor CGO and CRO comparing with blank solution

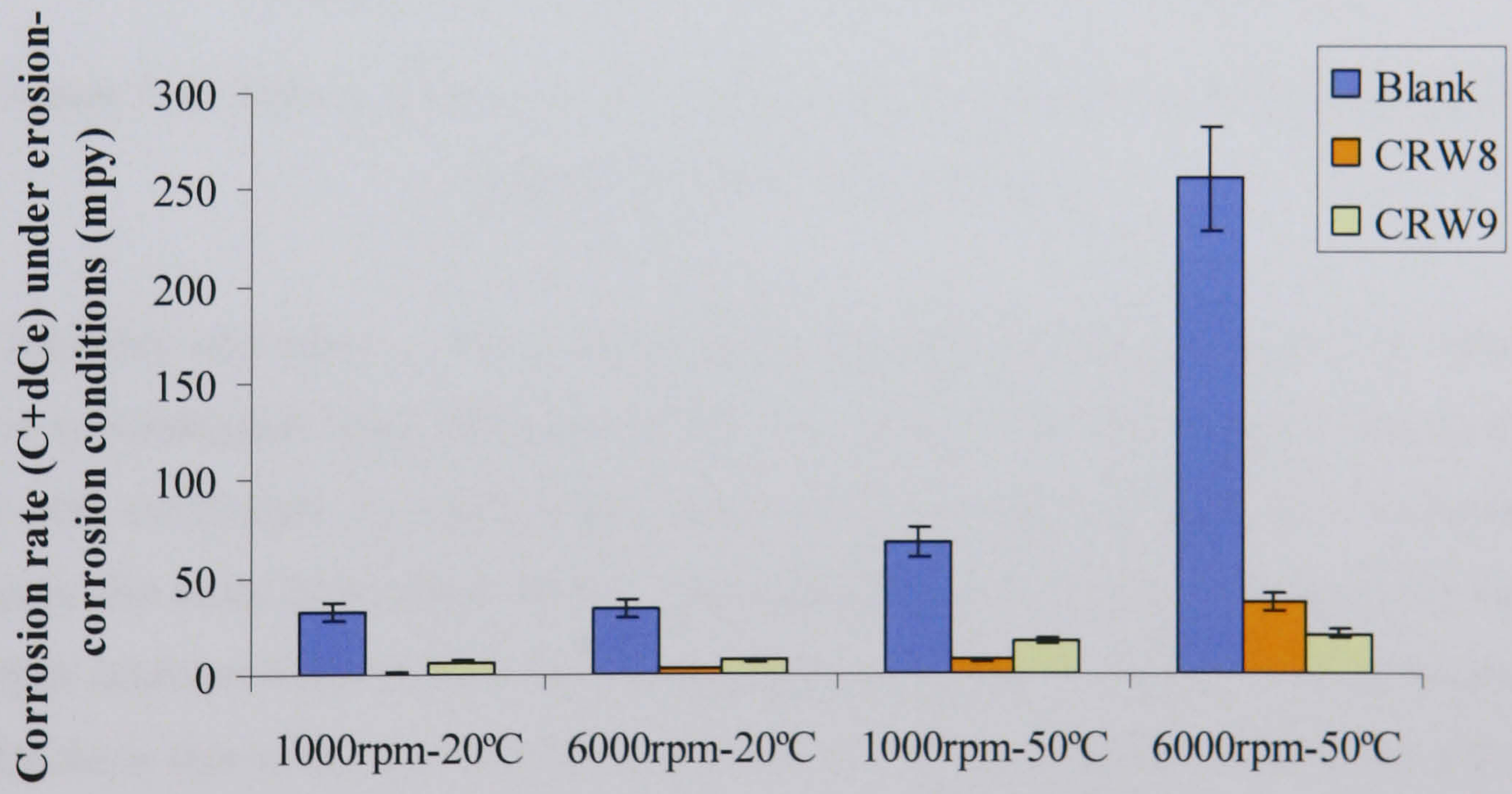

Figure 7.41 Effect of corrosion with water soluble inhibitor CRW8 and CRW9 comparing with blank solution

At higher temperature, both CRW8 and CRW9 reduce corrosion but could not reduce erosion under 1000rpm, even increase erosion under 6000rpm. The main reason should be that CRW8 and CRW9 has higher corrosion resistance resulting in difficult for corrosion product forming on the metal surface. As stated previously that with no inhibitor that extensive uniform corrosion at 50ºC and 1000rpm takes place. As corrosion products are solid having more resistance for solid and liquid erosion than pure inhibitor films. Therefore, it is important for corrosion products cooperating with

inhibitor molecule so that forming fine and dense corrosion products layer protecting metal from mechanical damage.

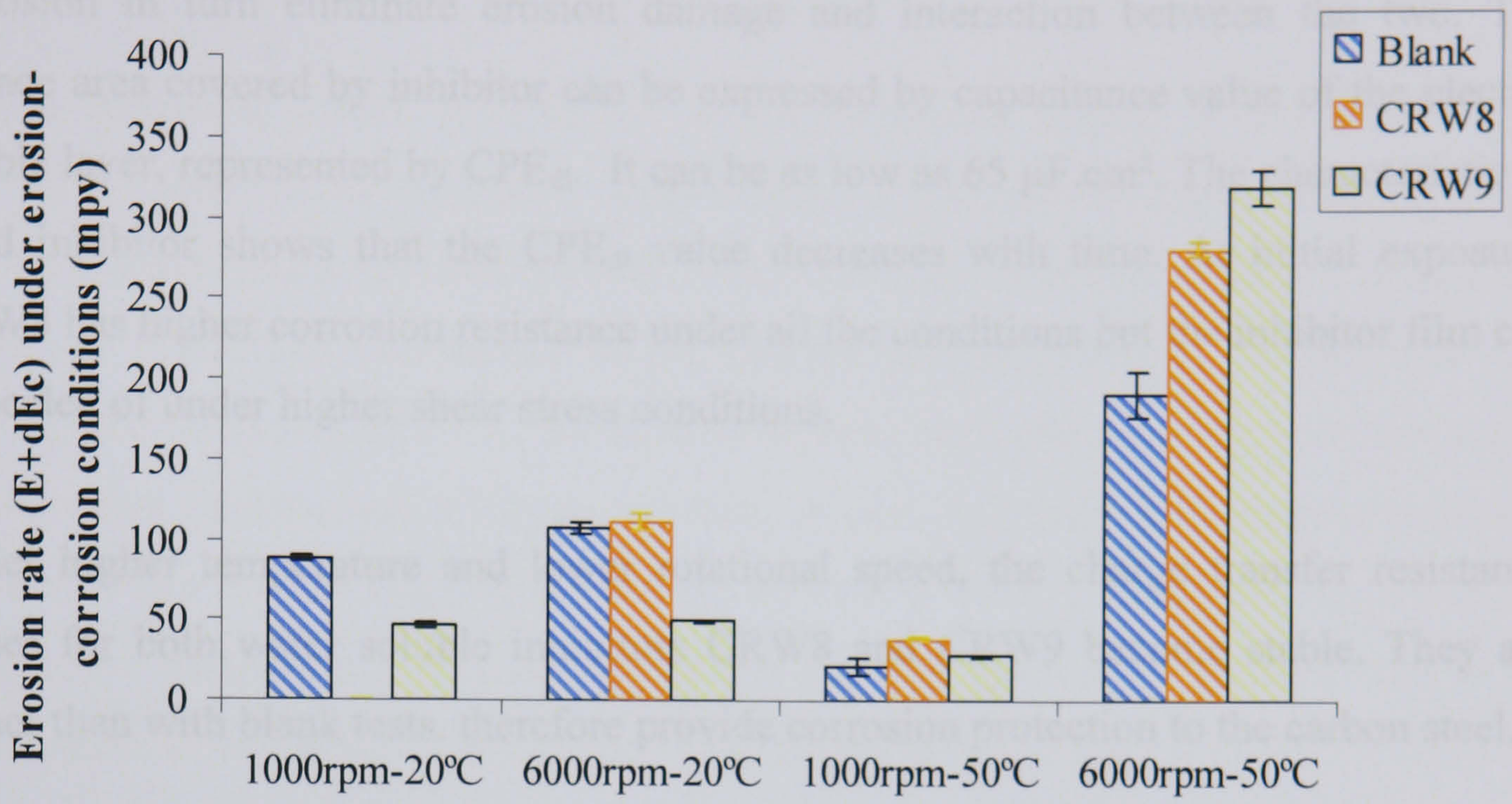

Figure 7.42 Effect of erosion with water soluble inhibitor CRW8 and CRW9 comparing with blank solution

The inhibitor also plays a role in reducing the mechanical damage caused by sand and this is an additional effect often not realised in inhibited systems. This is shown by CP tests and confirmed by pre-soaking tests. The pre-soaking tests are conducted to compare the mass loss results without pre-soaking and with pre-soaking of the sand at 100ppm inhibitor CRW9 for 2 hours, then tests at 6000rpm and 20°C for 8 hours. The results show that without pre-soaking sand, with 100ppm inhibitor CRW9, the mass loss is about 3.2mg, with pre-soaking sand, with same condition, the mass loss is about 1.1mg. There is a 66% reduction of sand impact to the metal damage from the results.

7.5 Summarising Corrosion *in-Situ* Results for RCE

With increase of rotational speed, the free corrosion potential shifts to noble direction for all the conditions. With blank tests, the charge transfer resistance is relatively stable with time compared with addition of inhibitors.

Water soluble inhibitors perform better than oil soluble ones. Under lower rotational speed and lower temperature, CRW8 forms a very firm inhibitor film and eliminate corrosion in turn eliminate erosion damage and interaction between the two. The surface area covered by inhibitor can be expressed by capacitance value of the electric double layer, represented by CPE_{dl}. It can be as low as 65 $\mu F.cm^2$. The characteristic of good inhibitor shows that the CPE_{dl} value decreases with time. At initial exposure. CRW8 has higher corrosion resistance under all the conditions but the inhibitor film can be peeled of under higher shear stress conditions.

Under higher temperature and lower rotational speed, the charge transfer resistance values for both water soluble inhibitors CRW8 and CRW9 become stable. They are higher than with blank tests, therefore provide corrosion protection to the carbon steel.

CRW9 has higher corrosion resistance under higher rotational speed. It forms a more stable film than other inhibitors. The reduce rate of charge transfer resistance with time is lower than other inhibitors.

Both oil soluble inhibitors exhibits higher capacitance value of the electric double layer than with blank tests under higher rotational speed. Inhibitor film is hardly formed on the metal surface under this condition due to the inhibitors act as corrosion promoter by moving away iron carbonate molecules from the metal surface. The capacitance value can be as high as 30 $mF.cm^2$.

Under lower temperature corrosion component is only small portion of the total damage and the corrosion enhanced erosion is dominant. Under higher temperature corrosion component increase due to charge transfer increased.

Inhibitor can reduce corrosion rate as well as reduced synergistic effects between corrosion and erosion. Corrosion component is bigger part of the total damage with CGO under higher temperature or higher rotational speed.

CHAPTER 8 RESULTS AND DISCUSSION OF CORROSION AND EROSION-CORROSION USING SIJ

Erosion-corrosion, often referred to as impingement attack is associated with mechanical removal of protective surface films, enhanced electrochemical corrosion and synergistic effects between the two. Fluid movement with sand presence is the most important factor that contributes to the rate of erosion-corrosion. In previous two chapters the focus was on RCE, where sand impacts the surface mainly with low angle. It shows that inhibitor has effect on reducing erosion-corrosion. This chapter considers SIJ where sand impact angle changes from normal to oblique incidence. Regardless of the erosion mechanism, the most vulnerable parts of production systems tend to be components in which the flow direction changes suddenly or high flow velocities occur caused by high volumetric flow rates (Barton, 2003). It relates not only velocity shear stress, turbulent intensity and mass transfer coefficient but also the impingement force and direction of sand particle`s attack on the metal surface. Components and pipe work upstream of the primary separators in gas condensate systems carry multiphase mixtures of gas, liquid and particulates and are consequently more likely to suffer from particulate erosion and erosion-corrosion. The submerged impinging jet with jet velocity 20m/s can produce much higher turbulent intensity than RCE. In SIJ in this study 0.1% sand was added to the system, the sample experiences a significant amount of erosion due to direct impingement.

A detailed mechanistic understanding of inhibitor action with different concentrations is of value in understanding inhibitor performance and enabling them to be used at optimum efficiency. This chapter presents the results relating to *in-situ* corrosion measurement under erosion-corrosion conditions and gravimetric erosion-corrosion results using an impinging jet rig. Inhibitors CRW8 and CRW9 with different concentrations were used to investigate the inhibitor efficiencies. Single components from which the CRW8 and CRW9 are formulated are also evaluated to understand the role of the individual constituents and their potential interactions. The experimental work conducted using SIJ are shown in Figure 8.1 (a) and (b) for erosion-corrosion tests and electrochemical *in-situ* tests respectively.

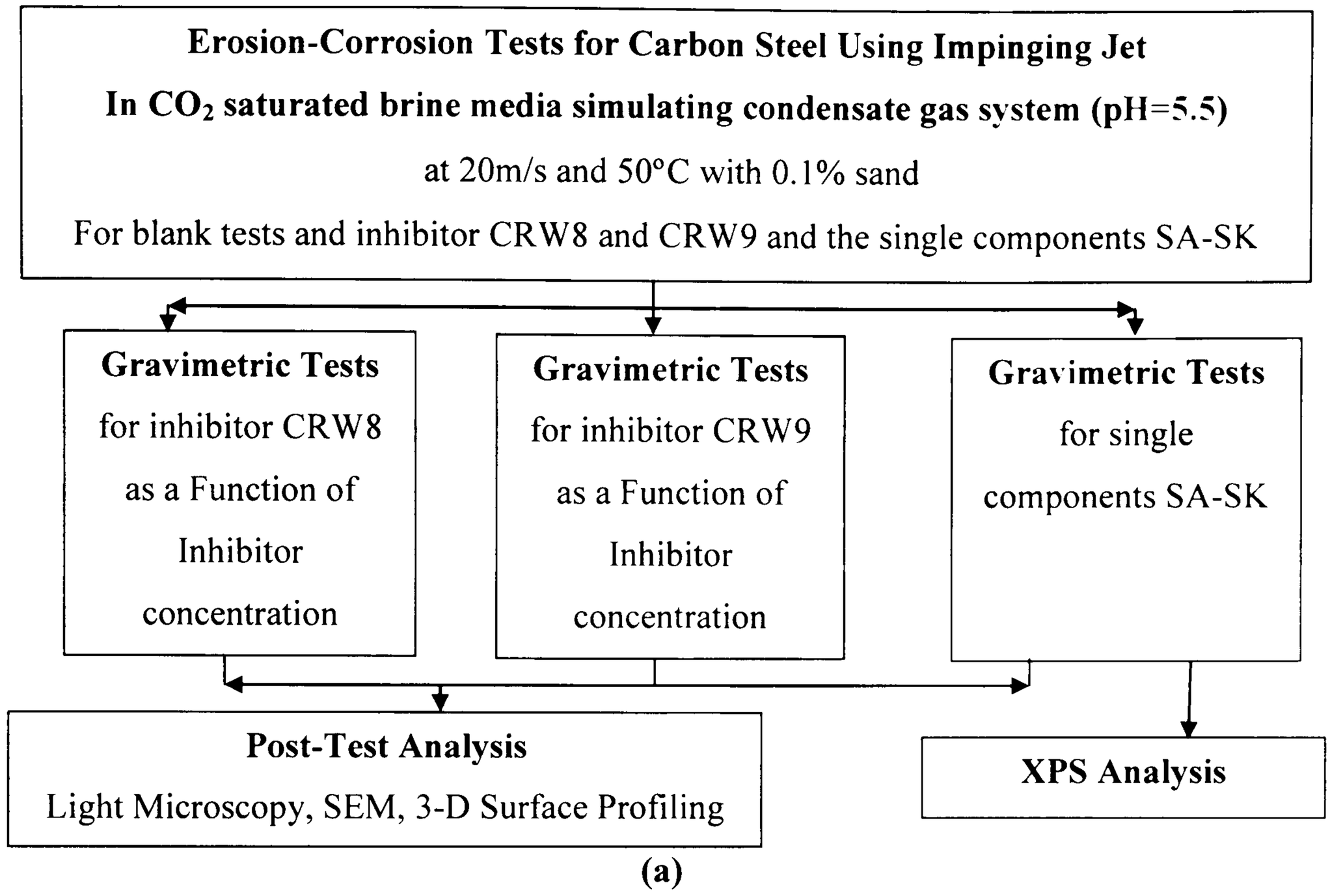

Figure 8.1 The map of experimental work presented in Chapter 8 with (a) erosion-corrosion gravimetric tests and (b) electrochemical tests under erosion-corrosion

8.1 Erosion-Corrosion Results Using Impinging Jet

8.1.1 Results of Total Mass Loss

In order to assess the mass loss as a function of the inhibitor concentration, experiments were conducted for blank (no inhibitor) tests and tests with inhibitors CRW8 and CRW9 at concentrations of 25ppm, 50ppm, 100ppm and 150ppm. Tests with UNS S31603 stainless steel were also included as a reference. One of the major questions in the oil and gas sector in terms of material selection is whether carbon steel with inhibitor is more economically favourable than stainless steel. Figure 8.2 shows the mass loss results with CRW8 at concentrations of 0ppm, 25ppm, 50ppm, 100ppm and 150ppm compared with the blank results from stainless steel. Figure 8.3 shows the mass loss results of the same conditions with inhibitor CRW9.

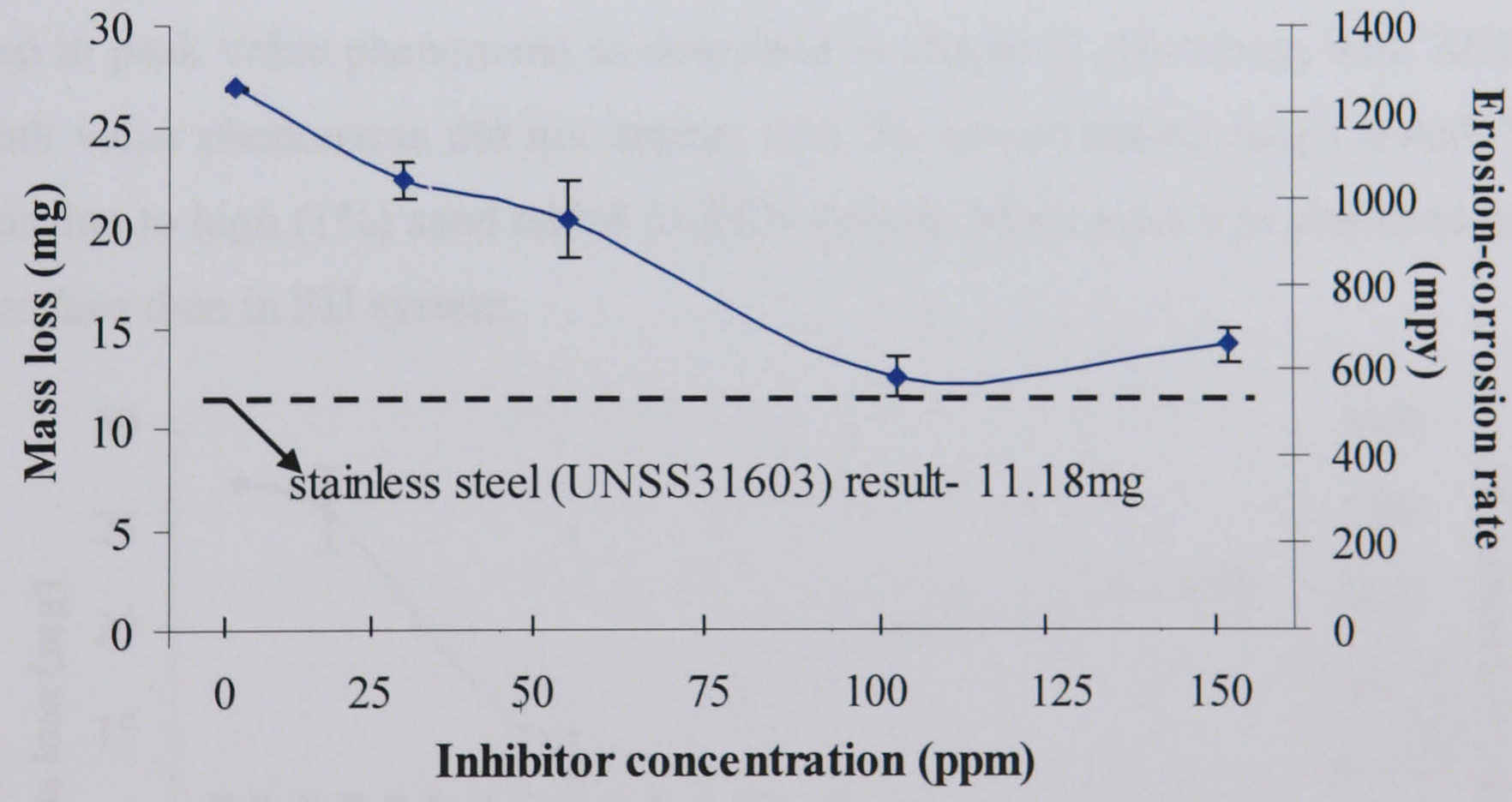

Figure 8.2 Mass loss results for inhibitor CRW8 after impinging tests

It is clear that at all concentrations the inhibitors are effective in reducing mass loss over the 2-hour test duration. Under these severe impingement conditions with solid particles it is perhaps surprising to record such large reductions in mass loss and also note that the mass loss for carbon steel with inhibitor approaches the mass loss on stainless steel UNS S31603. Percentage inhibition efficiencies, obtained by overall mass loss, at different inhibitor concentrations are shown in Table 8.1. The efficiency is

defined by Equation (84). In terms of penetration rate in mpy, a mass loss of 10mg in 2 hours corresponds to a thickness loss of 450mpy. According to Shadley (1998), this is in a severe erosion-corrosion regime. It is shown that inhibitor CRW8 showed its maximum efficiency at 100ppm, whilst inhibitor CRW9 at 50ppm. It is observed that the mass loss increased with increasing inhibitor concentration once a certain optimum concentration for both inhibitors was reached.

Usually, the inhibition efficiency increases with the increase of the inhibitor concentration until a steady state is achieved beyond some higher inhibitor concentration. However, the inhibition efficiency increases with increasing inhibitor concentration at low concentration, e.g., 25 ppm for CRW9, 25-50ppm for CRW8, but decreases with continuous increasing inhibitor concentration when inhibitor concentration is beyond critical values, e.g. 50ppm for CRW9 and 100ppm for CRW8. The same phenomena were observed by Singh (1993) and Ateya *et al*. (1984). This is referred to peak value phenomena as described in chapter 3. However, with RCE tests, the peak value phenomena did not appear with the concentration range tested. This is perhaps due to high (1%) sand added to RCE system. More sand was absorbed onto the sand surface then in SIJ system.

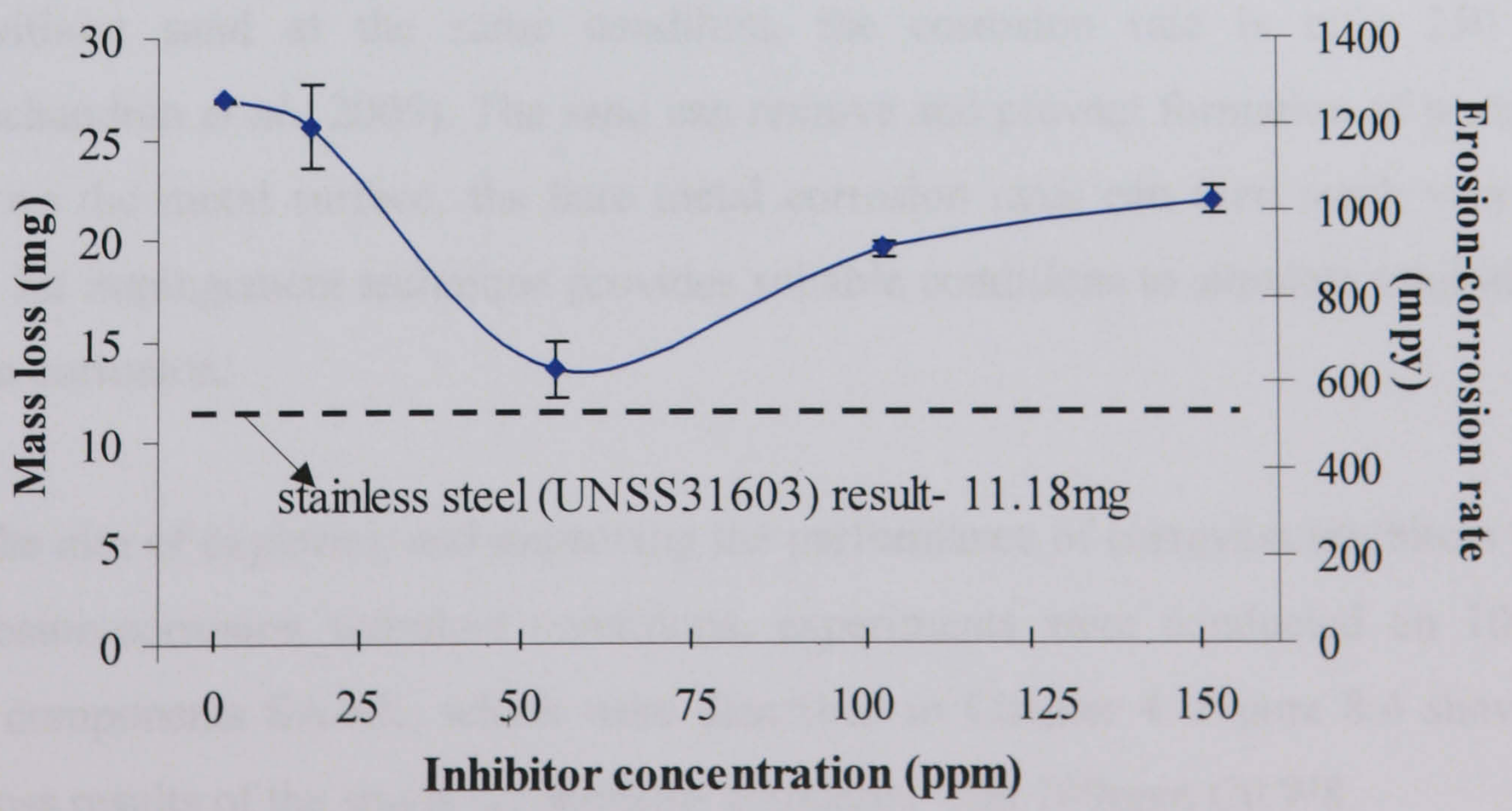

Figure 8.3 Mass loss results for inhibitor CRW9 after impinging tests

Under static conditions, Durnie *et al.* (1999) studied inhibitors containing amines and ammonium compounds and suggested that the peak-value phenomenon is attributed to the adsorption mode of the inhibitor. When the inhibitor concentration is lower than a critical value, adsorbed inhibitor molecules paralleled to the metal surface. The higher the inhibitor concentration was, the more inhibitor molecules adsorbed on the metal surface and more the active corrosion sites were blocked. Organic inhibitors are basically long chain molecules, with increase of inhibitor concentration: inhibitor molecules repelled each other more greatly. When the concentration is beyond certain critical value, the molecules tended to perpendicularly adsorb onto the metal surface, which results in the increase of corrosion rate.

Table 8.1 Percentage inhibitor efficiency under erosion-corrosion

	25ppm	**50ppm**	**100ppm**	**150ppm**
CRW8	17.1%	24.3%	56%	47.5%
CRW9	4.8%	49.8%	27.6%	18.6%

With temperature increased to 121°C and CO_2 partial pressure to 6 bars, Ramachandran *et al.* (2005) showed that the carbon steel penetration rates can be as high as 1600 mpy. But without sand at the same condition, the corrosion rate is only 250 mpy (Ramachandran *et al.*, 2005). The sand can remove and prevent formation of protective scales on the metal surface; the bare metal corrosion rates can then reach very high levels. Jet impingement technique provides suitable conditions to simulate inhibition of erosion-corrosion.

With the aim of exploring and improving the performance of corrosion inhibitors under the erosion-corrosion turbulent conditions, experiments were conducted on 100ppm single components SA-SK, which were described in Chapter 4. Figure 8.4 shows the mass loss results of the single components compared with 100ppm CRW8.

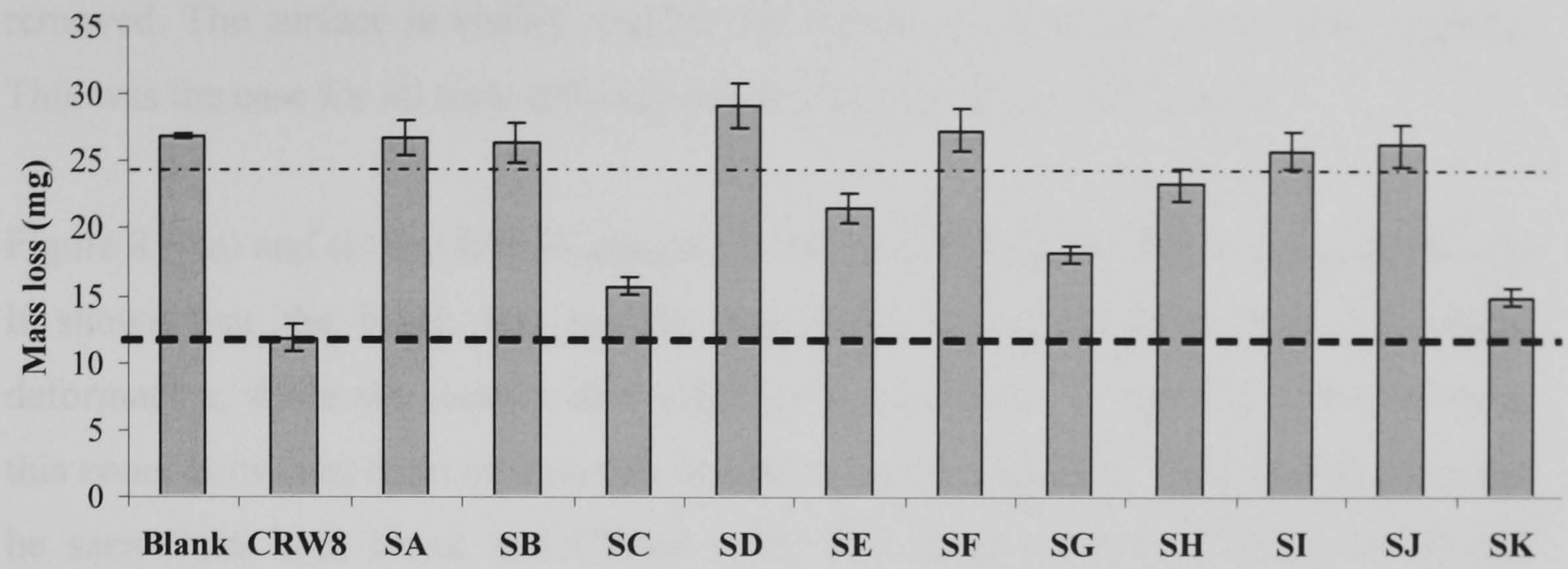

Figure 8.4 Mass loss results comparison of blank solution, inhibitor CRW8 and the single components at 100ppm concentration

From the mass loss results, the single components split into three categories: 1) ones that offer just as good protection as fully formulated inhibitor, such as SK and SC; 2) ones that offer some protection, such as SE, SG and SH; 3) ones that offer no protection or even increase the mass loss, such as SA, SB, SI and SJ provide no protection and SD and SF have even opposite effects. The most possible way is that the inhibitor reacts with the carbon steel through the factor of $FeCO_3$ resulting in that the mixture of inhibitor has better efficiency than the single inhibitor alone.

8.1.2 Steel Degradation Mechanisms

Surface degradation mechanisms investigation is carried out for fully formulated inhibitors only. In future work it would be useful to exam the material loss mechanism by single components but in this study time was not available.

The surface of the specimen can be subdivided into four zones defined by the fluid dynamic influence, as shown schematically in Figure 4.10. Figure 8.5 (a) and (b) show the SEM image at the boundary of Zone (I) near Zone (II) for blank test and 100ppm CRW8 test respectively. It is shown that sand impinges the surface and causes plastic deformation. The wear patterns are similar for the two samples. Both of them show the pearlite phase protruding from the surface because most of the α-ferrite phase has been

removed. The surface is visibly rougher for the blank test sample than with inhibitor. This was the case for all tests although the depth of the wear scar differed.

Figure 8.6 (a) and (b) are BSEM images for blank and 100ppm CRW8 test respectively. It shows that the blank test sample has pitting corrosion apart from the plastic deformation, while the sample after inhibitor test exhibits only plastic deformation in this zone. However, from microscope images shown in Figure 8.7, pitting corrosion can be seen from both blank and CRW8 tests. The observation from both BSEM and microscope indicates that pitting exists but with CRW8, not only pitting size is smaller, but also the pitting depth is less than with blank.

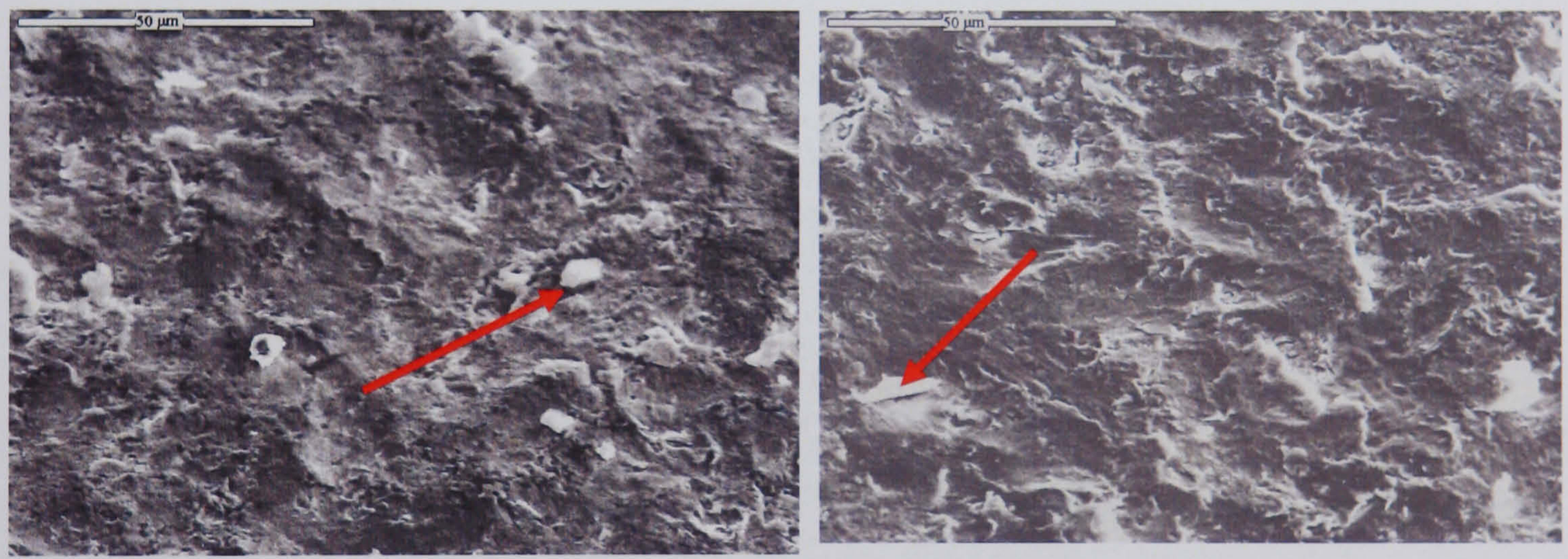

(a) (b)

Figure 8.5 SEM images at Zone (I) for (a) blank (b) 100ppm CRW8 tests

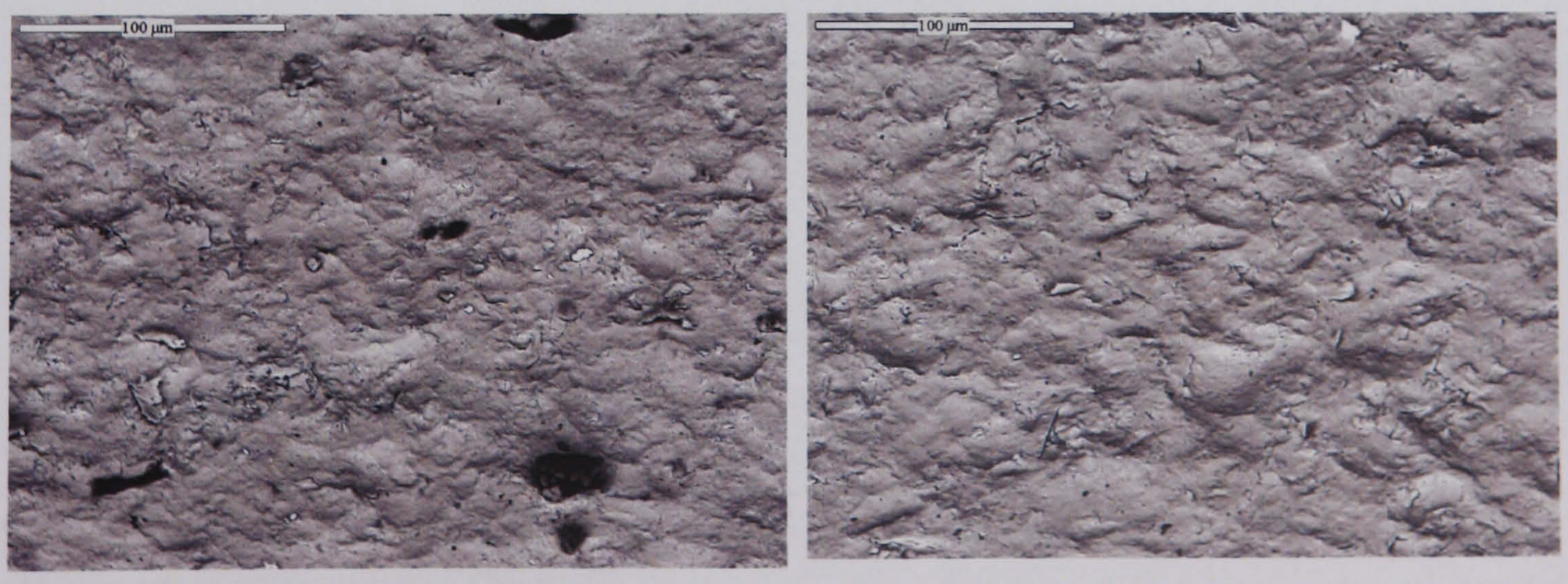

(a) (b)

Figure 8.6 BSEM image at Zone (I) for (a)blank (b) 100ppm CRW8 tests

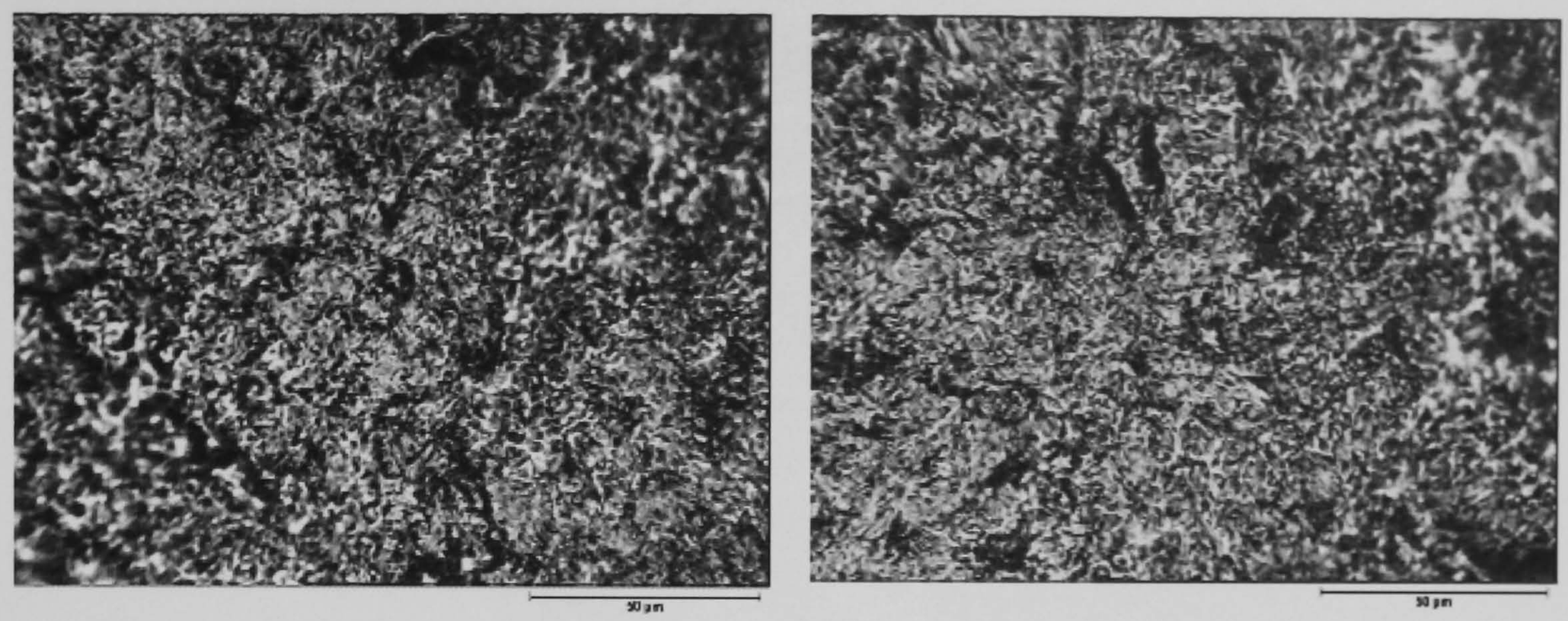

(a) (b)

Figure 8.7 Microscope images at Zone (I) for (a) blank (b) 100ppm CRW8 tests

It can be postulated that inhibitor was adsorbed onto the sand surface and then reduced the sand impact energy to the metal surface, in turn reduce the surface roughness comparing without inhibitor. This is why inhibitor has effects on erosion. On reducing erosion, the synergistic effect of erosion to corrosion can be reduced. In addition, inhibitor also was adsorbed onto the metal surface and prevents it from pitting corrosion in this zone. Reducing corrosion can also decrease the surface roughness in turn reducing corrosion enhanced erosion.

A three-dimensional profiling image is presented in Figure 8.9 after erosion-corrosion tests with blank solution. The wear scar around Zone (I) (defined in chapter 4), showed the cross section profile is of a bowl shape. At the very centre of the sample, there is a stagnation point. Within the area from the centre until about the same diameter as the nozzle, the sand impinges the surface from high angle to oblique angles causing flake formation due to the ductile material of the sample as shown in Figure 3.3 (c). The debris shown by arrows in Figure 8.5 can result from the flake formation. It seems that the wear scar should be of 'W' shape like the case for stainless steel, but for carbon steel is softer than stainless steel, the middle 'W' shape can be stripped away by both indentation due to the impingement and cutting mode of the slurry flow as a result removed all the material inside the 'bowl' as shown in Figure 8.8 of red bottom of the bowl.

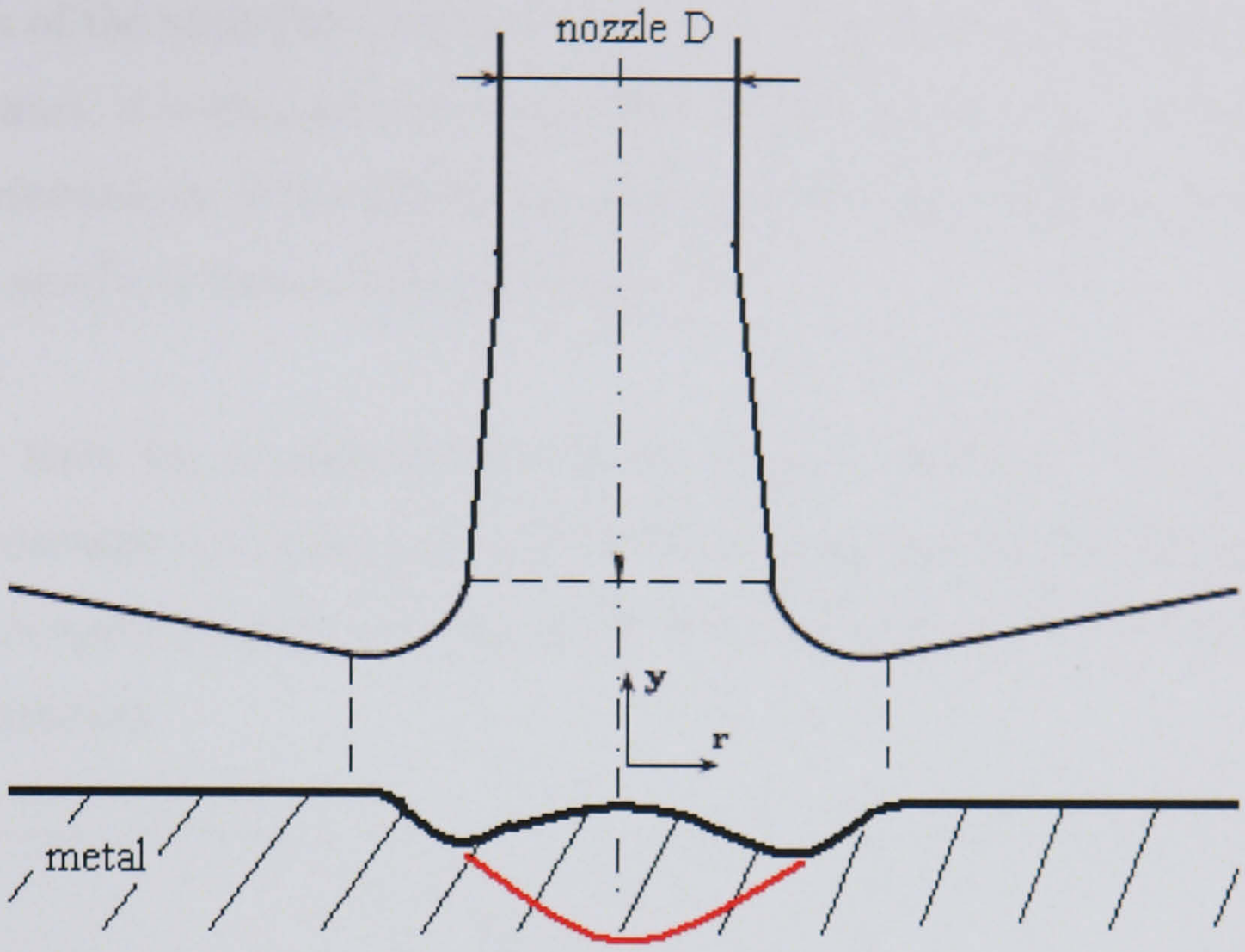

Figure 8.8 Schematic diagram showing formation of the wear scar in cross section for carbon steel under the flow region of the SIJ

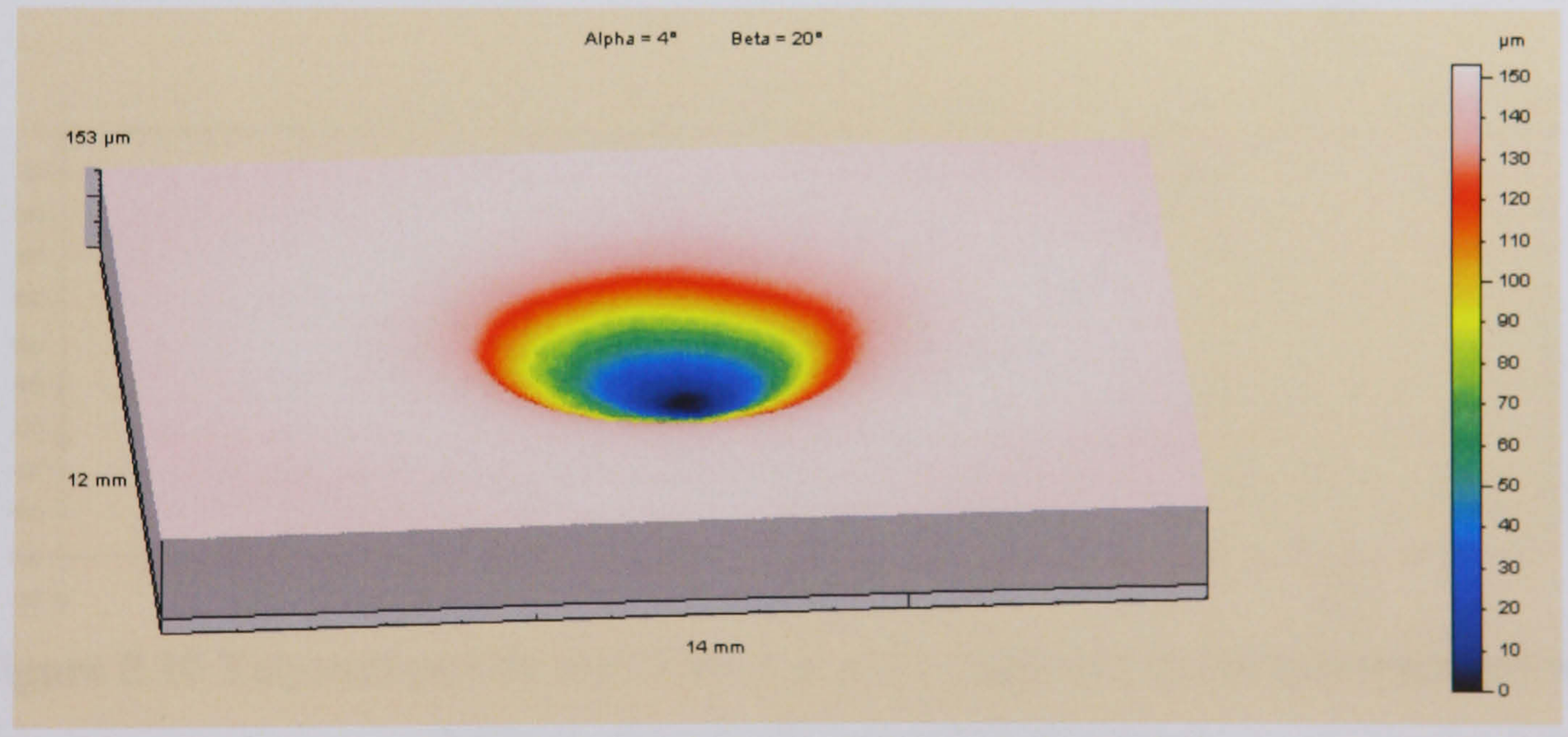

Figure 8.9 Talysurf profile for blank test after exposure to the impingement

The cross section profile with blank tests had the deepest depth about 150 micrometers as shown in Figure 8.10 (a). Although the whole experiments have been done by adding 0.1% sand by weight to the system, a few tests were done by adding 0.2% sand to see how the sand effect the material loss as shown in Figure 8.10 (b). When add 0.2% sand to the system. The central Zone (I) is more heavily plastically deformed than that with 0.1% sand and the wear depth are doubled. This is due to the increase of the

concentration of the sand, the kinetic energy of the fluid with sand impinging the metal surface increases. It is indication that sand is one of the most important factors causing the plastic deformation. When adding no sand to the system, under liquid condition, the cross section profile is shown in Figure 8.12.

In solid-free tests the damage level was substantially reduced. In tests free from inhibitor the damage was reduced by nearly 50% comparing with blank tests with sand. Therefore, it is again an indication that the sand concentration is an important parameter in erosion-corrosion.

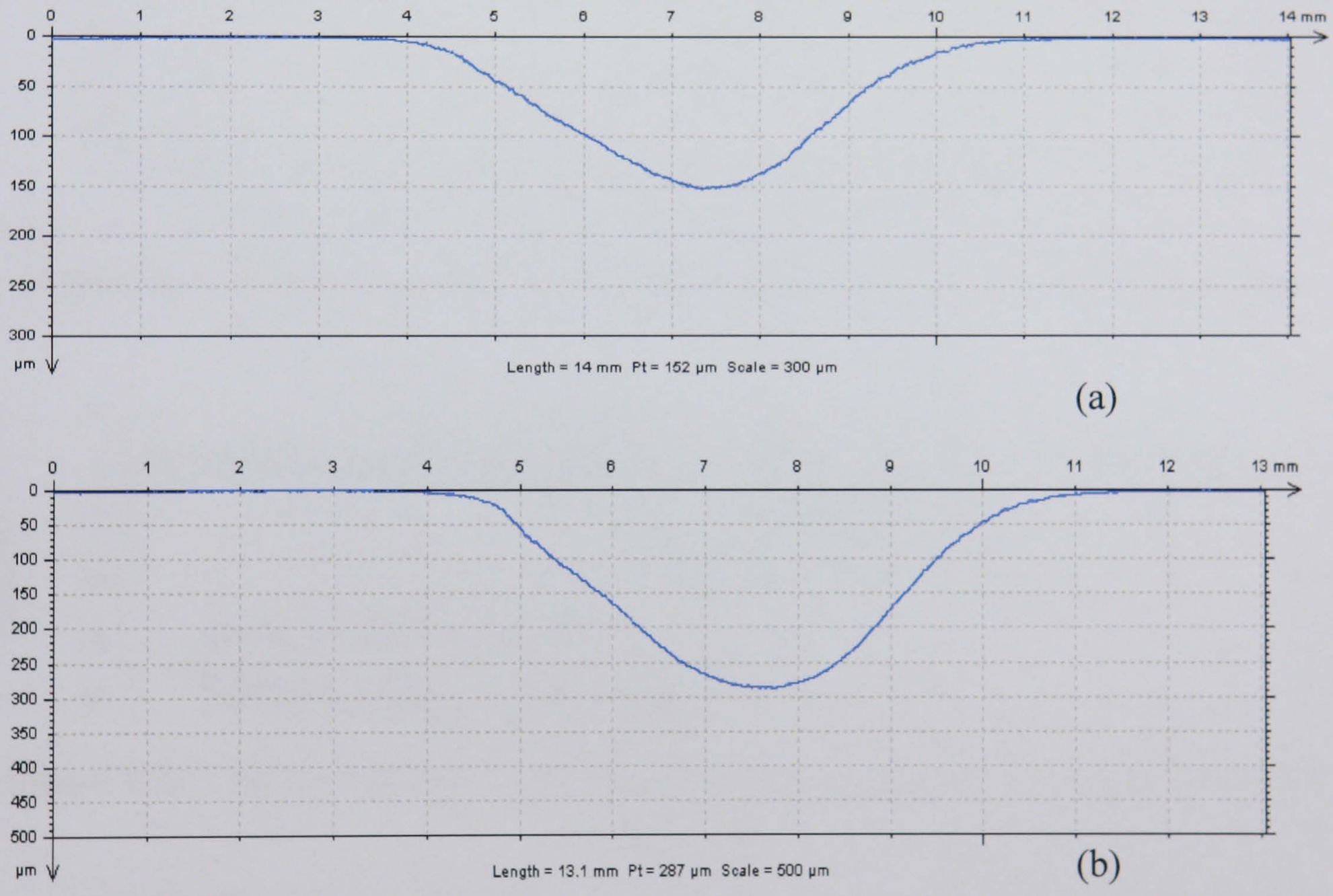

Figure 8.10 Talysurf profile for blank test after exposure to the impingement with addition of (a) 0.1% and (b) 0.2% sand

When 100ppm inhibitor CRW8 is added to the system, after the test, the cross section profile is shown in Figure 8.11. The depth of the wear scar reduced by about 70% comparing with blank tests. This is again due to two reasons; one is that the inhibitor has effect to erosion-corrosion through forming an inhibitor film which forms a barrier for reducing sand impact energy to the metal surface; the other is that the inhibitor adsorbed on to the sand surface. In solid-free tests with 100ppm inhibitor CRW8 the

damage level was substantially reduced. The inhibitor shows 97.5% efficiency. This is indicative of not only the sand being an efficient abrasive but also that the inhibitor effectiveness is substantially reduced when sand impacts can breach any protective surface films. The cross section profiles for inhibitor CRW8 test without sand are shown in Figure 8.13.

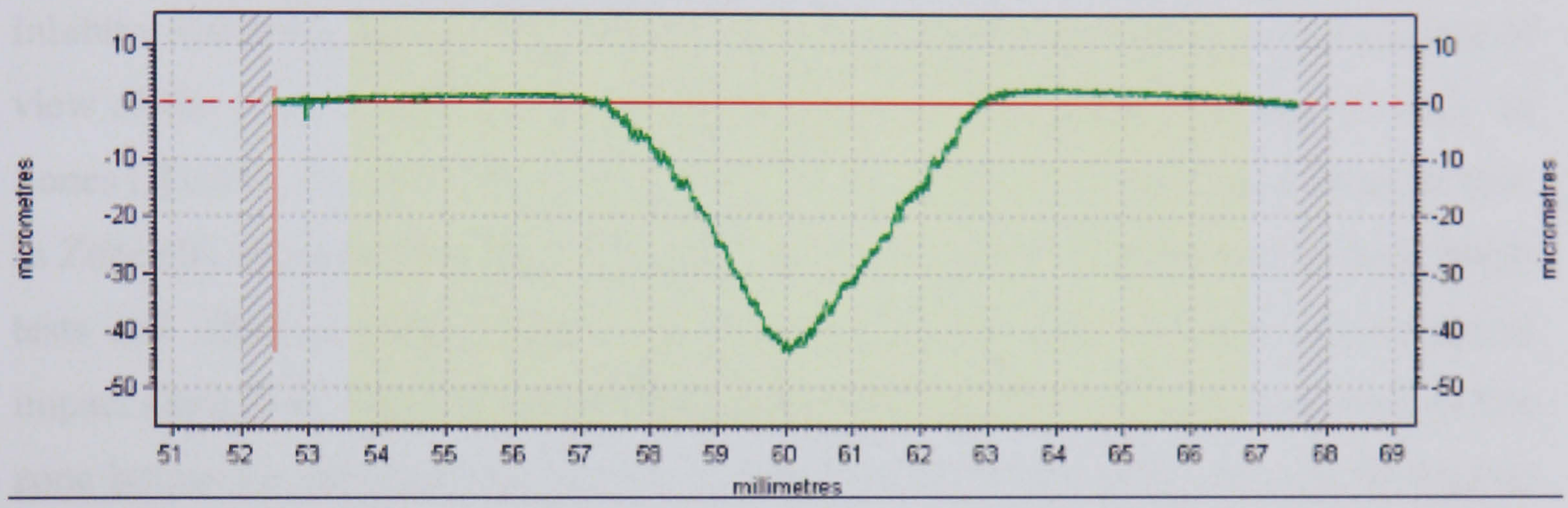

Figure 8.11 Talysurf profile for CRW8 test after exposure to the impingement

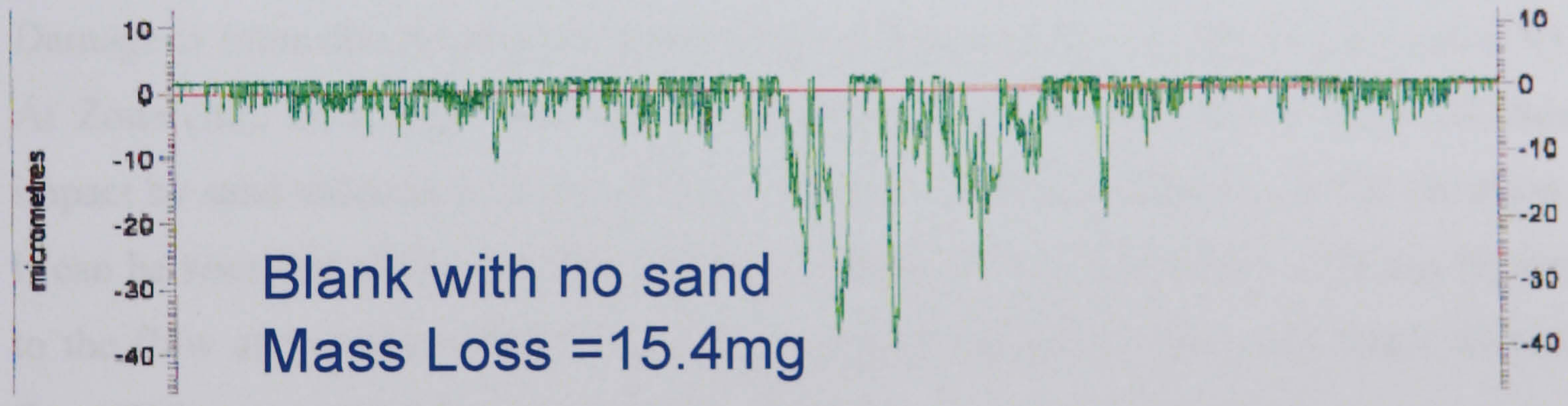

Figure 8.12 Talysurf profile for blank test but with no sand after exposure to the impingement

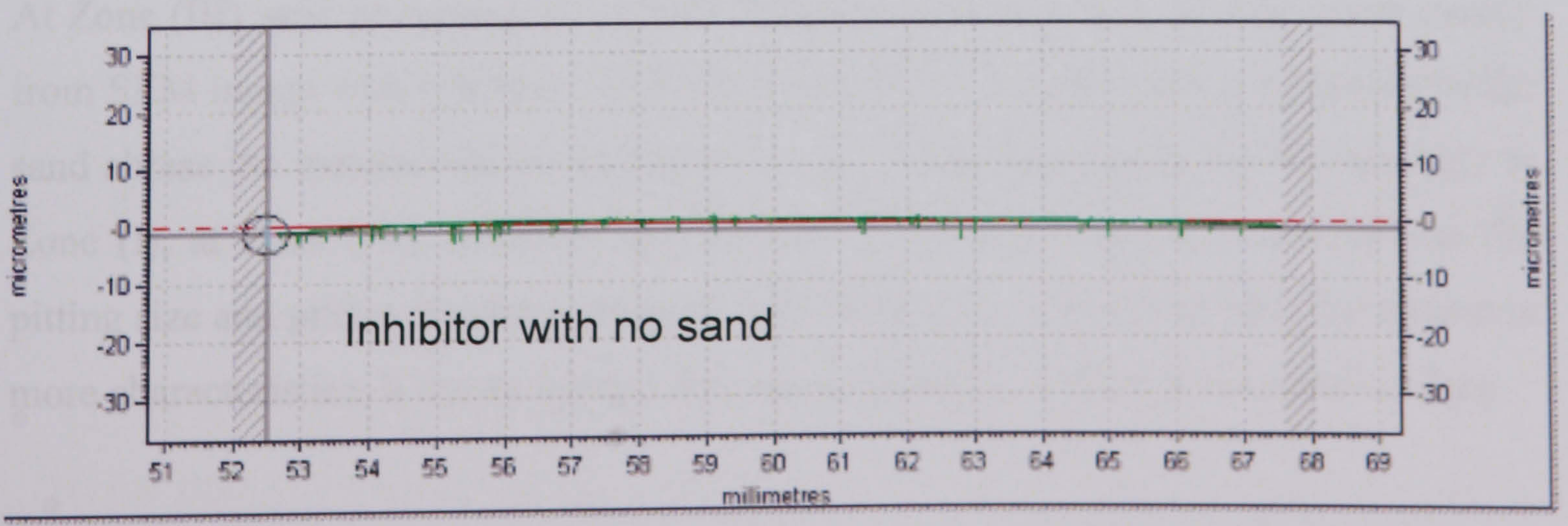

Figure 8.13 Talysurf profile for CRW8 test with no sand after exposure to the impingement

From above talysurf profile, it can be seen that the sand impact damage is evident from the mechanical deformation on the surface in zone (I). The damage also can be seen in zones (II)-(IV).

Figure 8.14 a) and b), c) and d), and e) and f) show the comparison of the microscope images for Zone (II) to Zone (IV) for blank tests and inhibitor CRW8 tests respectively. Inhibitor CRW8 is used as the example but inhibitor CRW9 is similar from the point of view of the type of damage. The effect of inhibitor in different zones can be seen. In Zones (II)-(IV), the main effect is to eliminate the extent of pitting visible after the test. In Zone (II), the sand impinged the surface at lower angle like ploughing for both blank tests and inhibitor tests. There is no apparent difference in the type of mechanical impact damage by visual examination. Pitting corrosion is obvious for blank tests in this zone but no for inhibitor tests. This is a confirmation that inhibitor film can be formed on the surface and reduces pitting corrosion.

Damage is more characteristic at lower angle of impingement in Zones (III), and (IV). At Zone (III), flow with sand impact the surface at low angle, and at Zone IV, this impact by sand reduced as kinetic energy of the flow reduces along the radius direction. It can be seen that pitting number is more at Zone (IV) than Zone (III). This can be due to the flow and sand moving the corrosion species H_2CO_3 at Zone (III) faster than at Zone (IV) as a result reduces the pitting corrosion.

At Zone (III) sand ploughing the sample surface at low angle can be seen more clearly from SEM image with inhibitor CRW8 in Figure 8.15. It is the same mechanism as the sand abrase the material shown in Figure 3.3 (a). As the same effect of the inhibitor to Zone (I). at Zone (III). inhibitor also reduces the surface roughness and reduces the pitting size and pitting number compared with blank tests. As in Zone (III) the surface is more characteristics, it can be used to analyse the inhibitor effects to the metal surface.

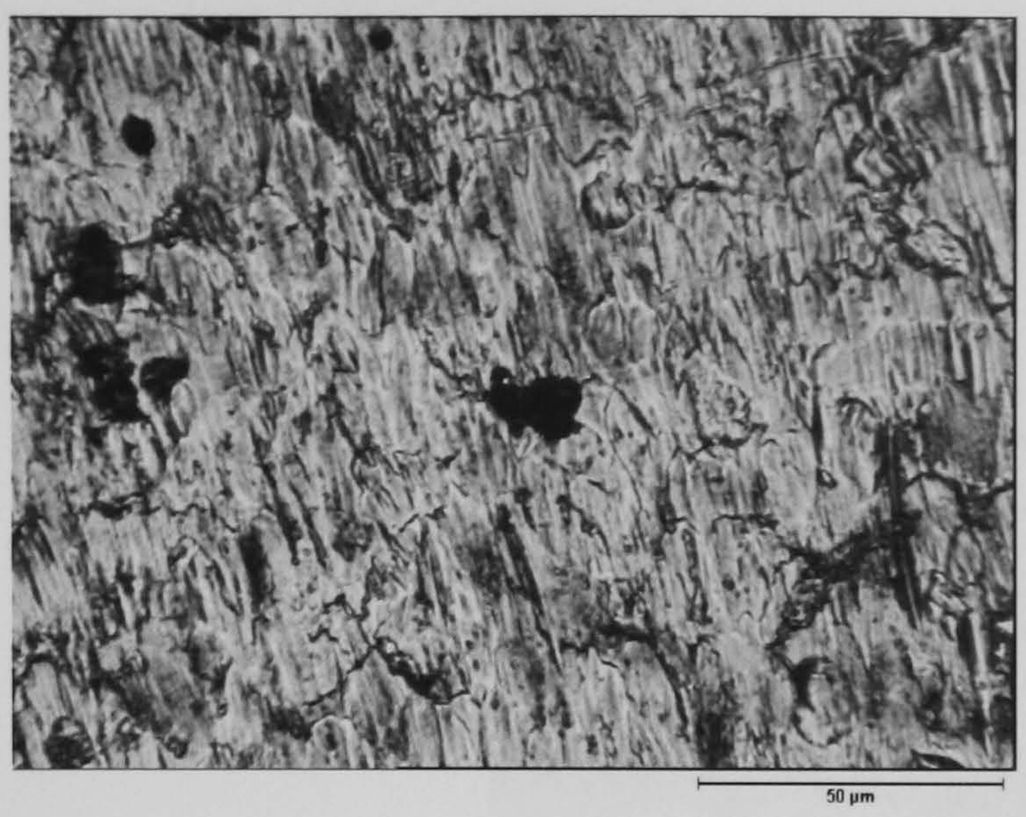

(a)

(b)

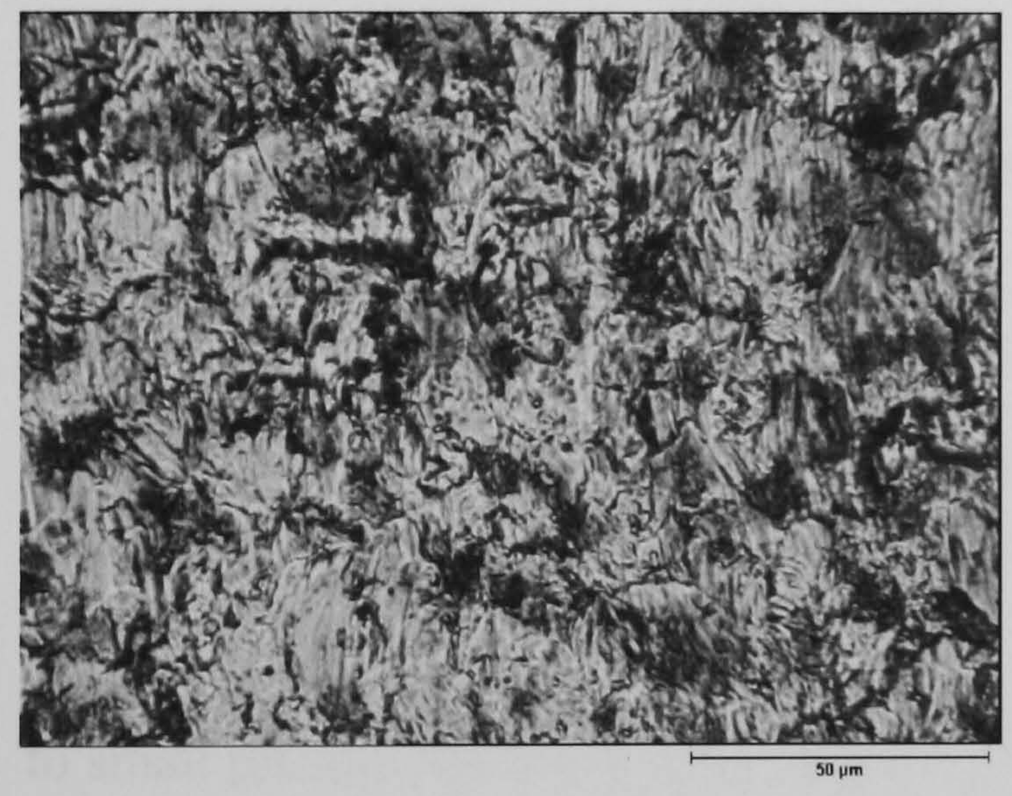

(c)

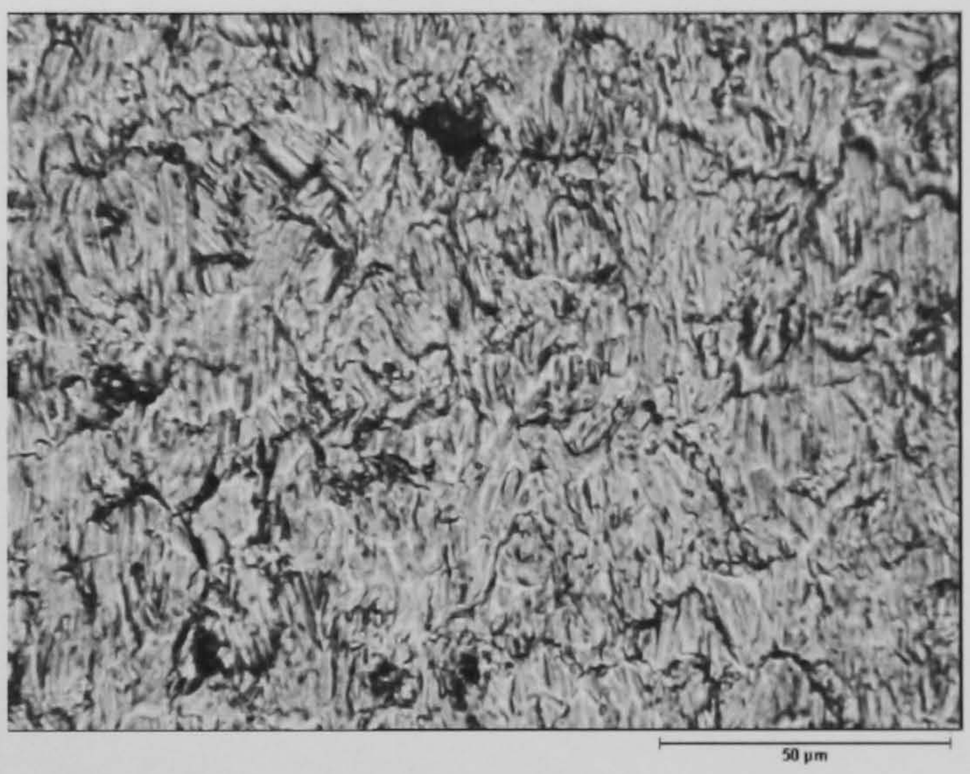

(d)

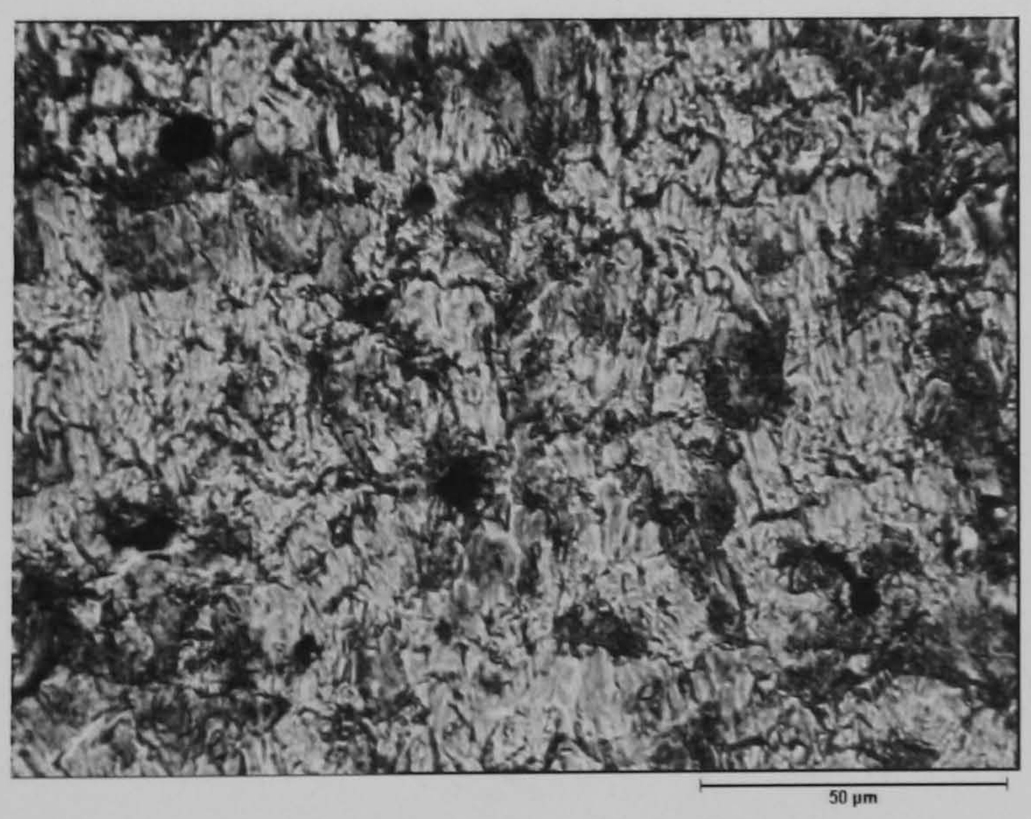

(e)

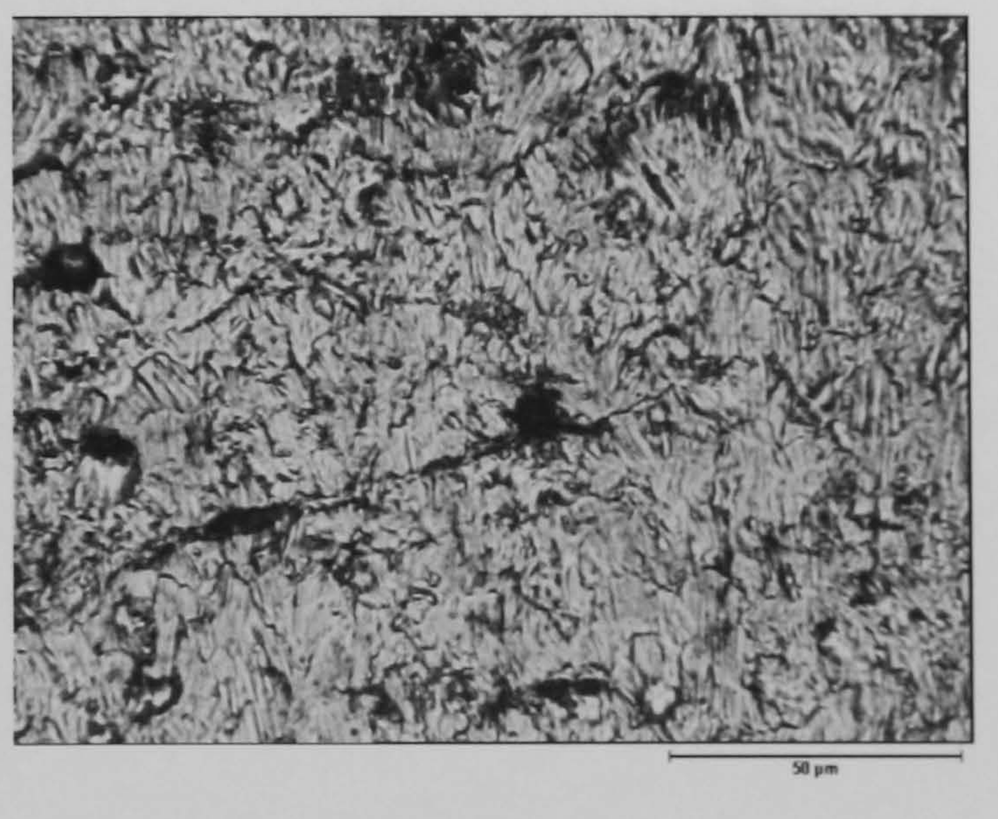

(f)

Figure 8.14 Microscope images of each region of samples after testing a) Zone (II) for Blank , b) Zone (II) for 100ppm CRW8, c) Zone (III) for blank, d) Zone (III) for 100ppm CRW8, e) Zone (IV) for Blank, f) Zone (IV) 100ppm CRW8 tests

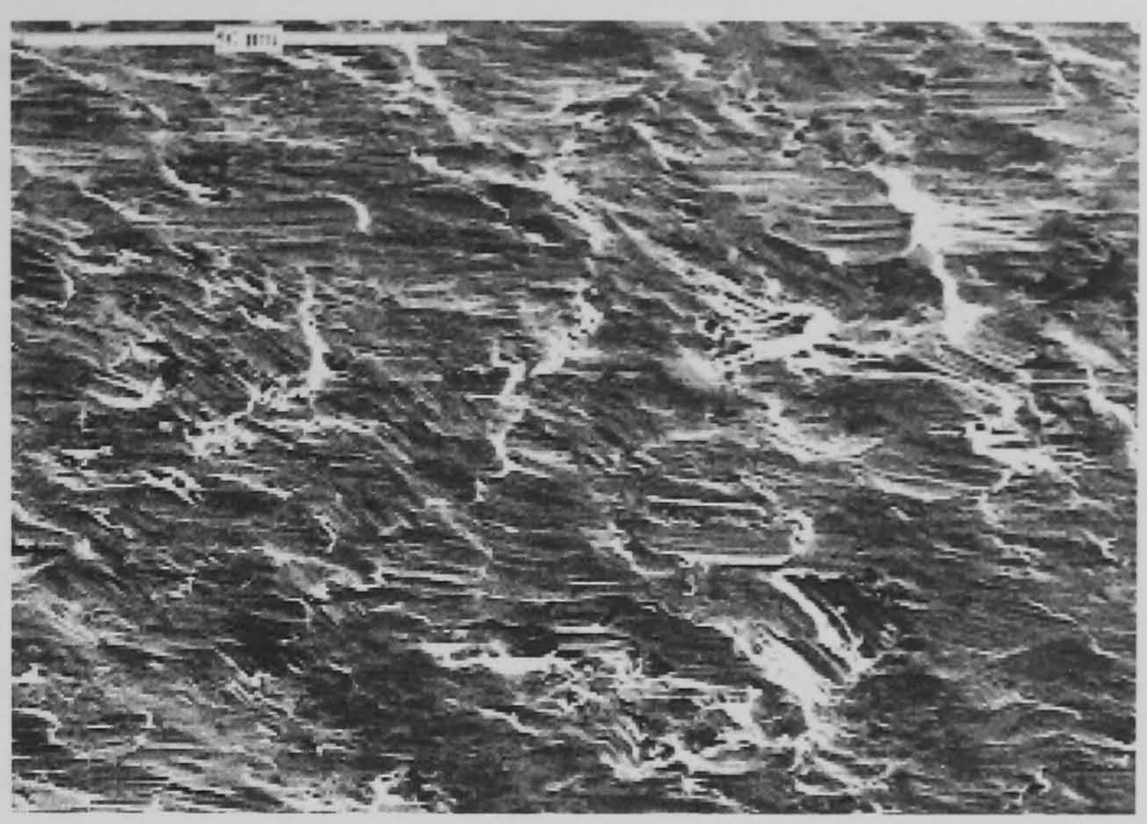

Figure 8.15 SEM image at Zone (III) for sample after 100ppm CRW8 test

Figure 8.16 (a) and (b) show BSEM images for blank and 100ppm CRW8 at Zone (III) respectively. It is confirmed again that inhibitor film formed on the surface and preventing it from severe pitting corrosion, while with no inhibitor, pitting corrosion distributed on the entire zone. Pitting taking place is due to the corrosion products formed on the surface were removed by the slurry flow. From microscope image (Figure 8.14 (d)), pitting still exists, it could not be seen from the BSEM images is due to small pit size and depth with addition of inhibitor.

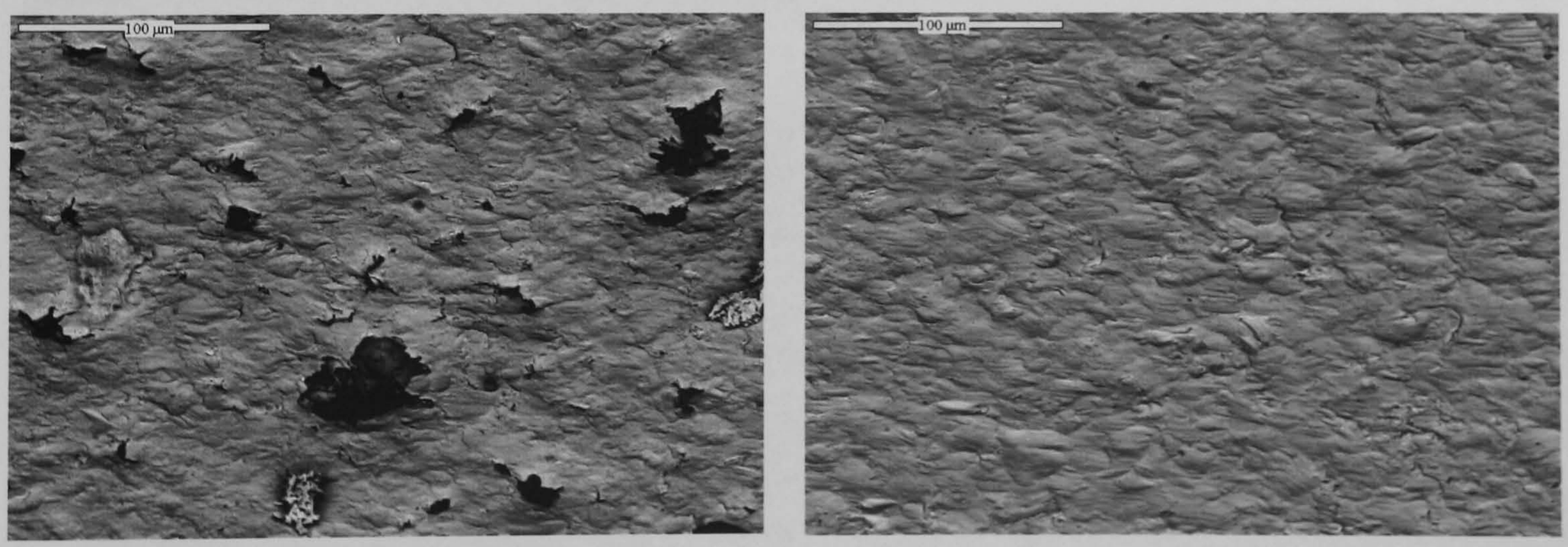

(a) (b)

Figure 8.16 BSEM images of Zone (III) after test for (a) blank test and (b) 100ppm CRW8 test

Figure 8.17 shows the SEM images for Zone (I) with inhibitor CRW9 tests at various concentrations. It also shows that in Zone (I) the pattern of wear scars is the same for

different concentrations. However, it can not be seen the different roughness with different inhibitor concentrations.

Inhibitor effects with different concentrations can be distinguished from Zone (II) as shown in Figure 8.18 for inhibitor CRW9 with various concentrations. The direction of the flow at various concentrations is shown by arrows. Among Figure 8.18 (a)-(d), 50ppm (Figure 8.18 (b)) shows the smoothest surface and least pitting. It confirms the mass loss results that the optimum concentration with CRW9 under this impingement conditions is 50ppm. This is due to the inhibitor film can be formed best at 50ppm on the metal surface.

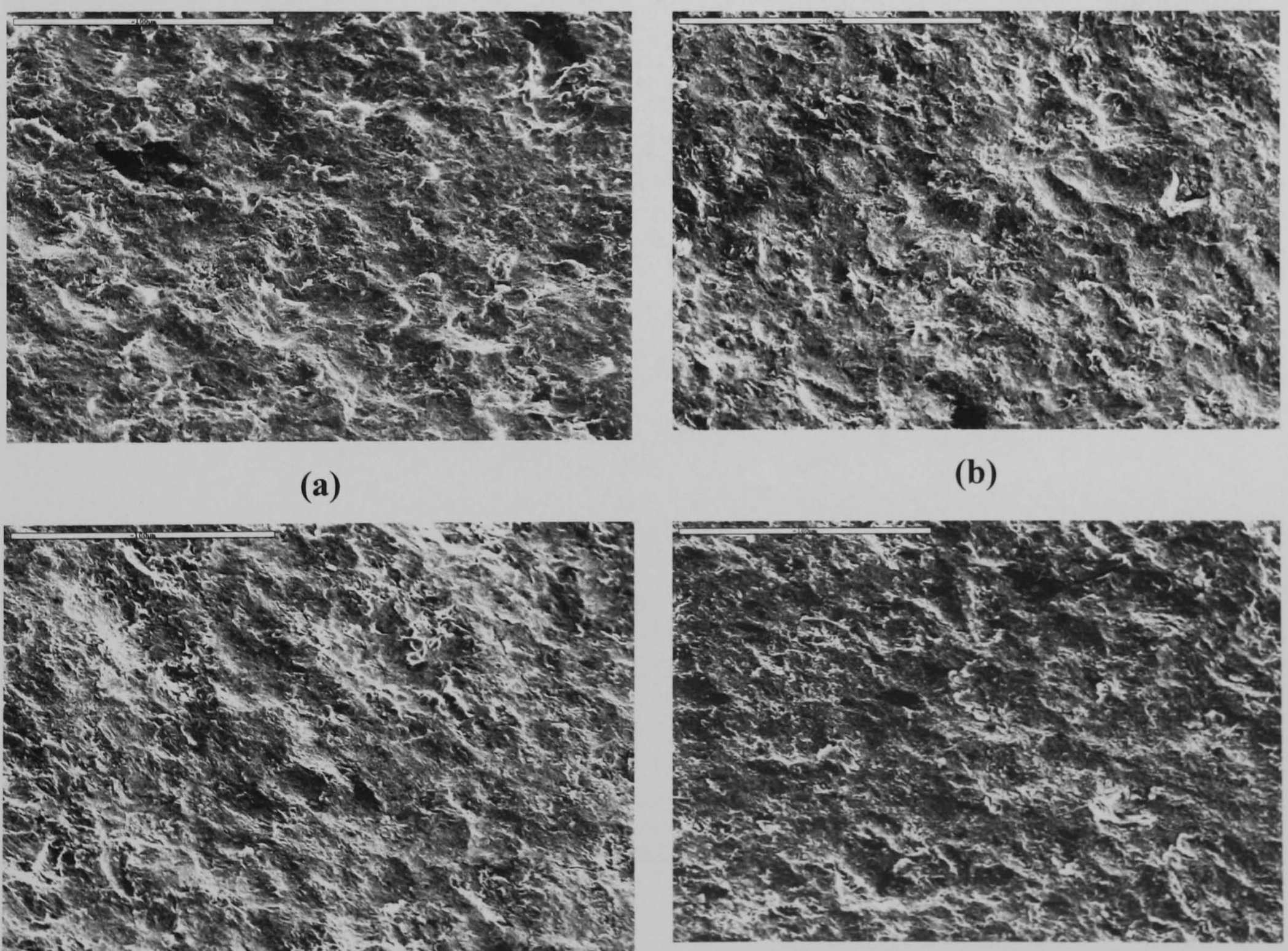

(a) **(b)**

(c) **(d)**

Figure 8.17 SEM images for Zone (I) after tests with inhibitor CRW9 at concentrations of (a) 25ppm, (b) 50ppm, (c) 100ppm and (d) 150ppm

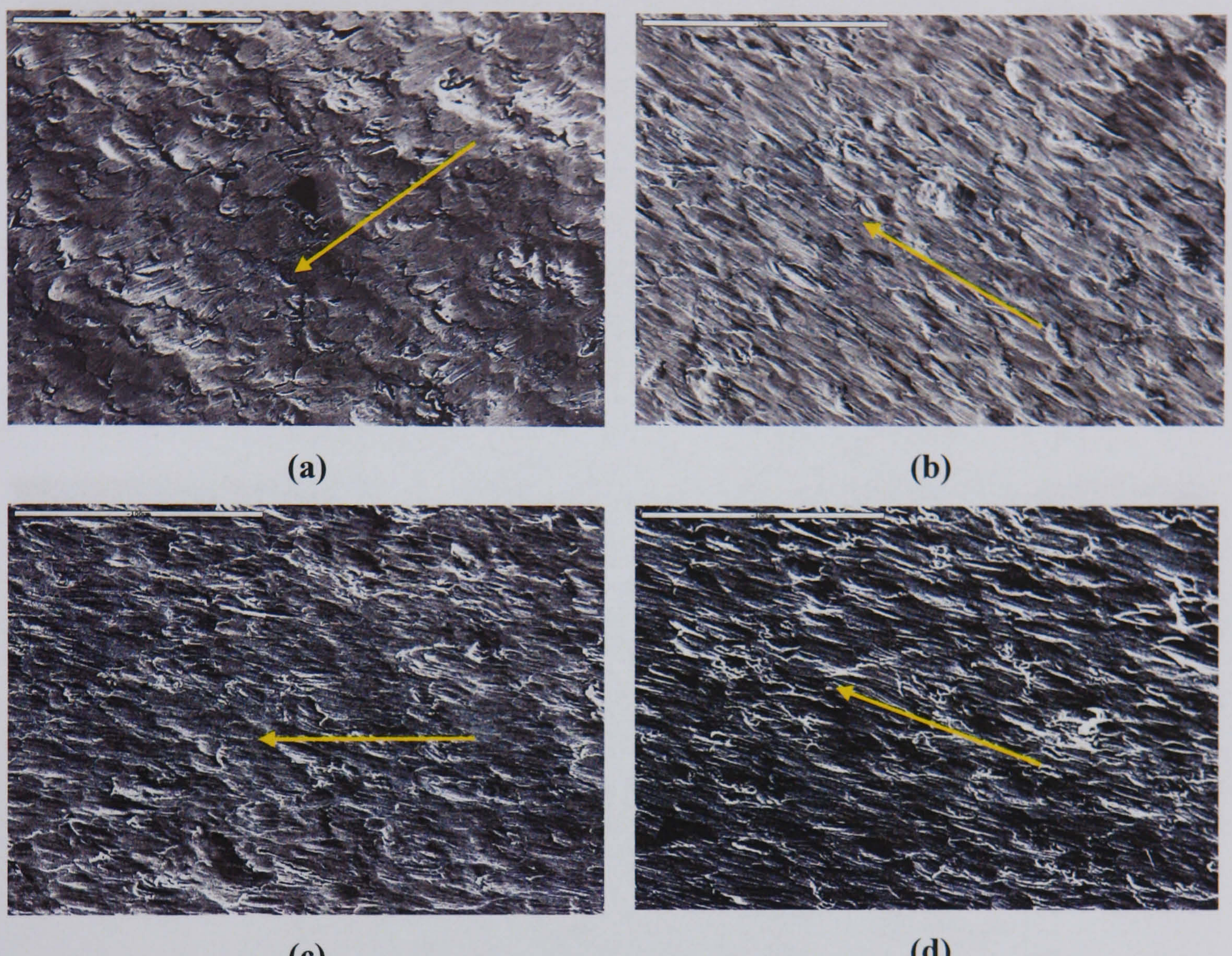

(a) **(b)**

(c) **(d)**

Figure 8.18 SEM images for Zone (II) with inhibitor CRW9 at concentrations of (a) 25ppm, (b) 50ppm, (c) 100ppm and (d) 150ppm

Figure 8.19 (a)-(d) shows the SEM images for Zone (III) with CRW9 at 25ppm, 50ppm, 100ppm and 150ppm concentration respectively. Pitting is less extensive with 50ppm inhibitor concentration than any other concentrations. More areas of the metal surface were chipping out at 25ppm concentration due to the inhibitor concentration is not enough for protective inhibitor film forming. It can be seen that the inhibitor reduces the pitting corrosion under erosion-corrosion condition at 50ppm concentrations.

For inhibitor CRW8, Figure 8.20 shows that at 25ppm concentration, at Zone (III) pitting is more extensive than that of CRW9 at the same concentration. It indicates that for better inhibitor film forming on the metal surface, concentration should be higher for CRW8 than CRW9.

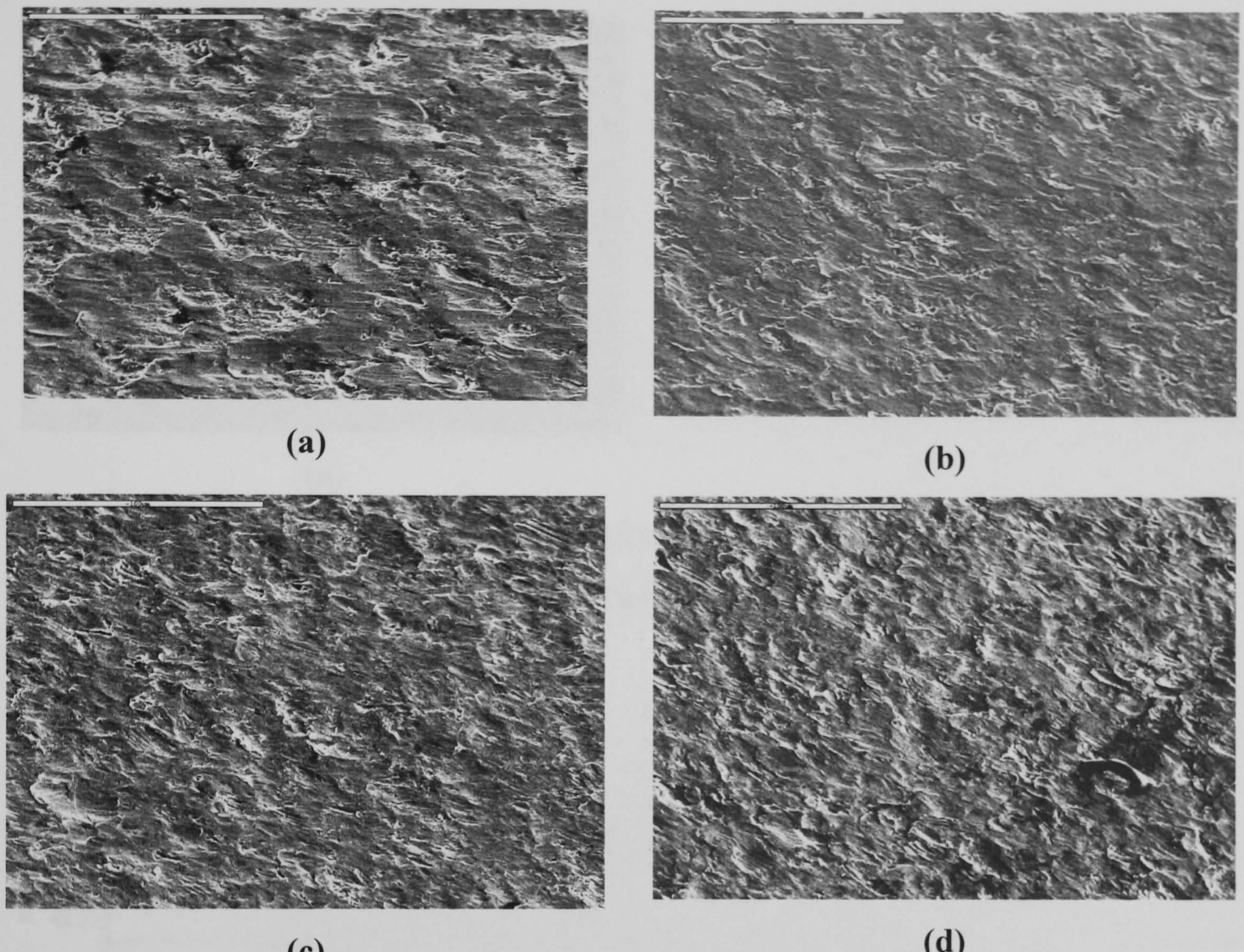

(a) **(b)**

(c) **(d)**

Figure 8.19 SEM images for Zone (III) with inhibitor CRW9 at concentrations of (a) 25ppm, (b) 50ppm, (c) 100ppm and (d) 150ppm

Surface roughness was measured for each sample at Zone (III) after tests with inhibitor CRW8. From the surface roughness result as shown in Figure 8.21, the inhibitor at its optimum concentration has the least surface roughness among other concentrations. The roughness values R_q should be used as the R_q is roughness average value of root mean square, and it is more accurate than average R_a values. It is shown that inhibition leads to smaller roughness factors and hence would lower pressure drop and in turn lower the shear stress at high production rates (Schmitt *et al.*, 1990). This Zone (III) has been used to represent the whole surface because as state above that in this zone, the effect of inhibitor is as the same as other zones and sand also impacts the surface at Zone (III).

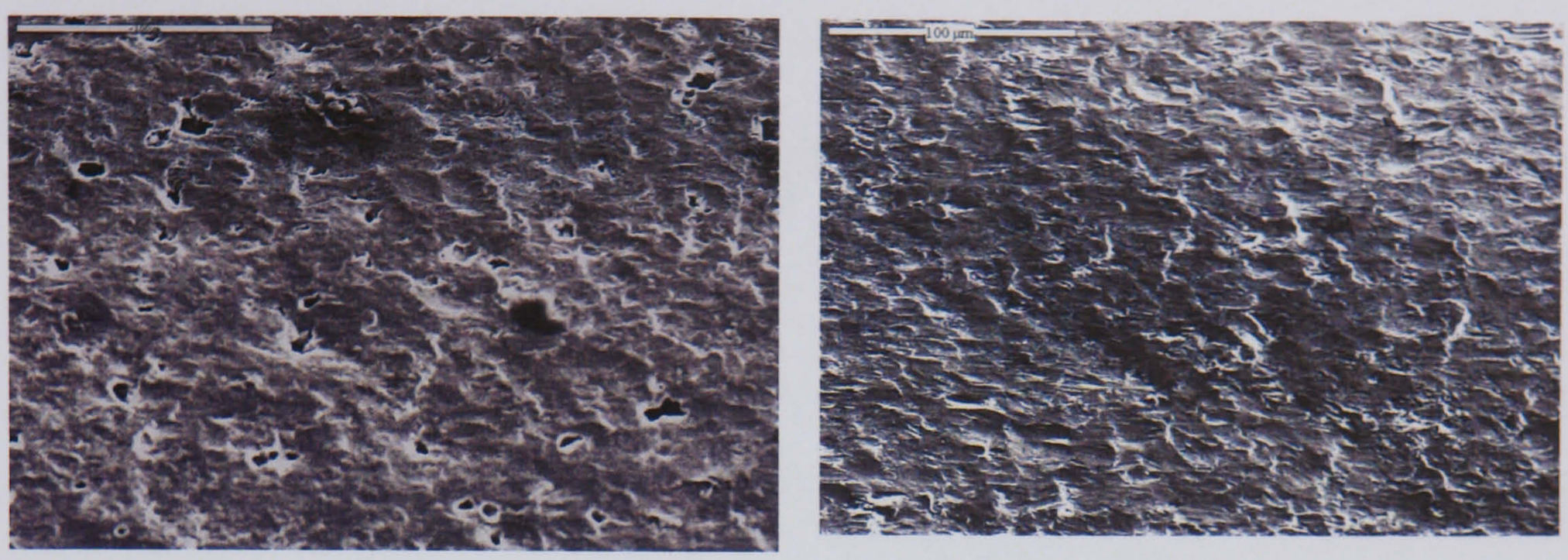

(a) **(b)**

Figure 8.20 SEM images for Zone (III) with inhibitor CRW8 at concentrations of (a) 25ppm and (b) 100ppm

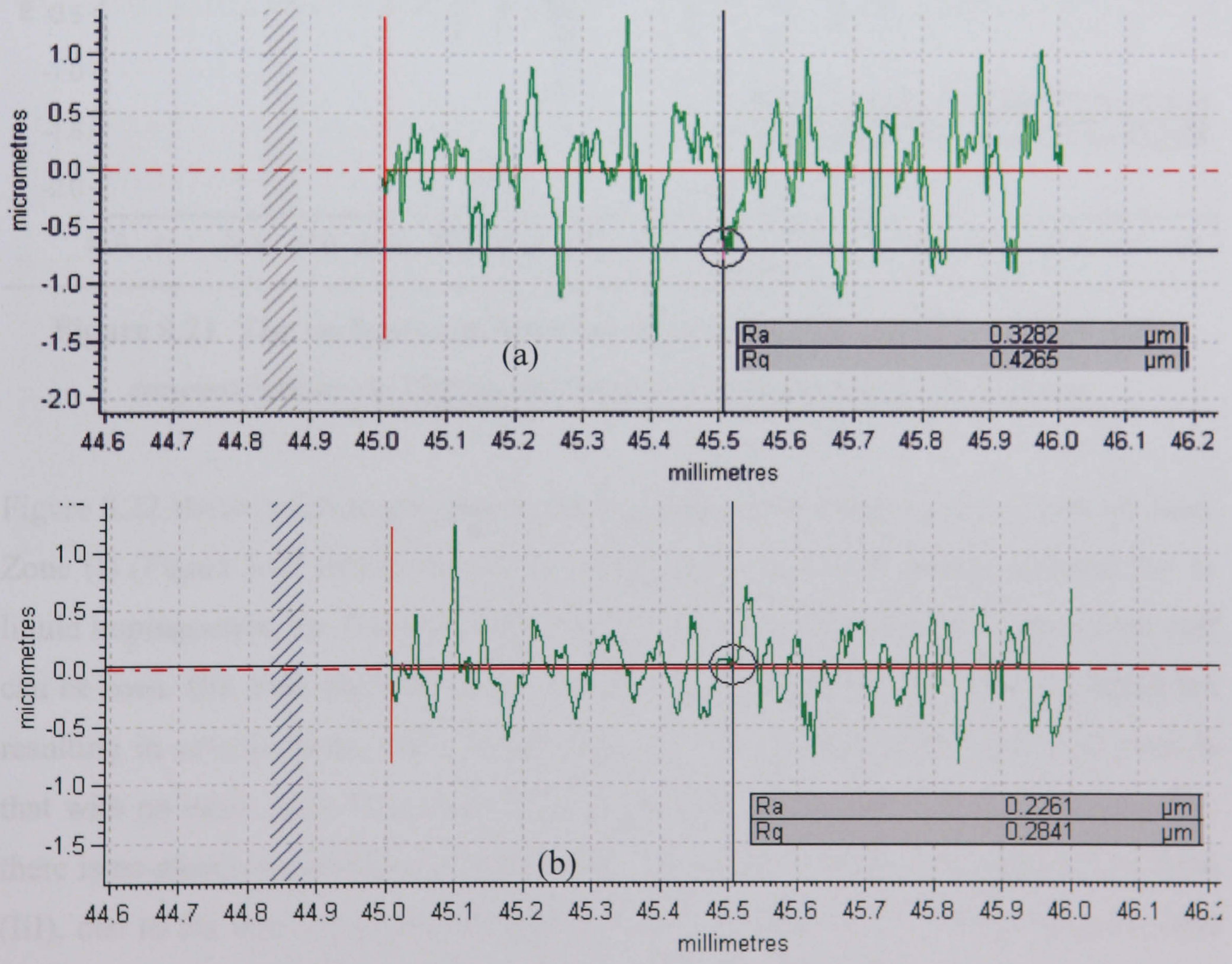

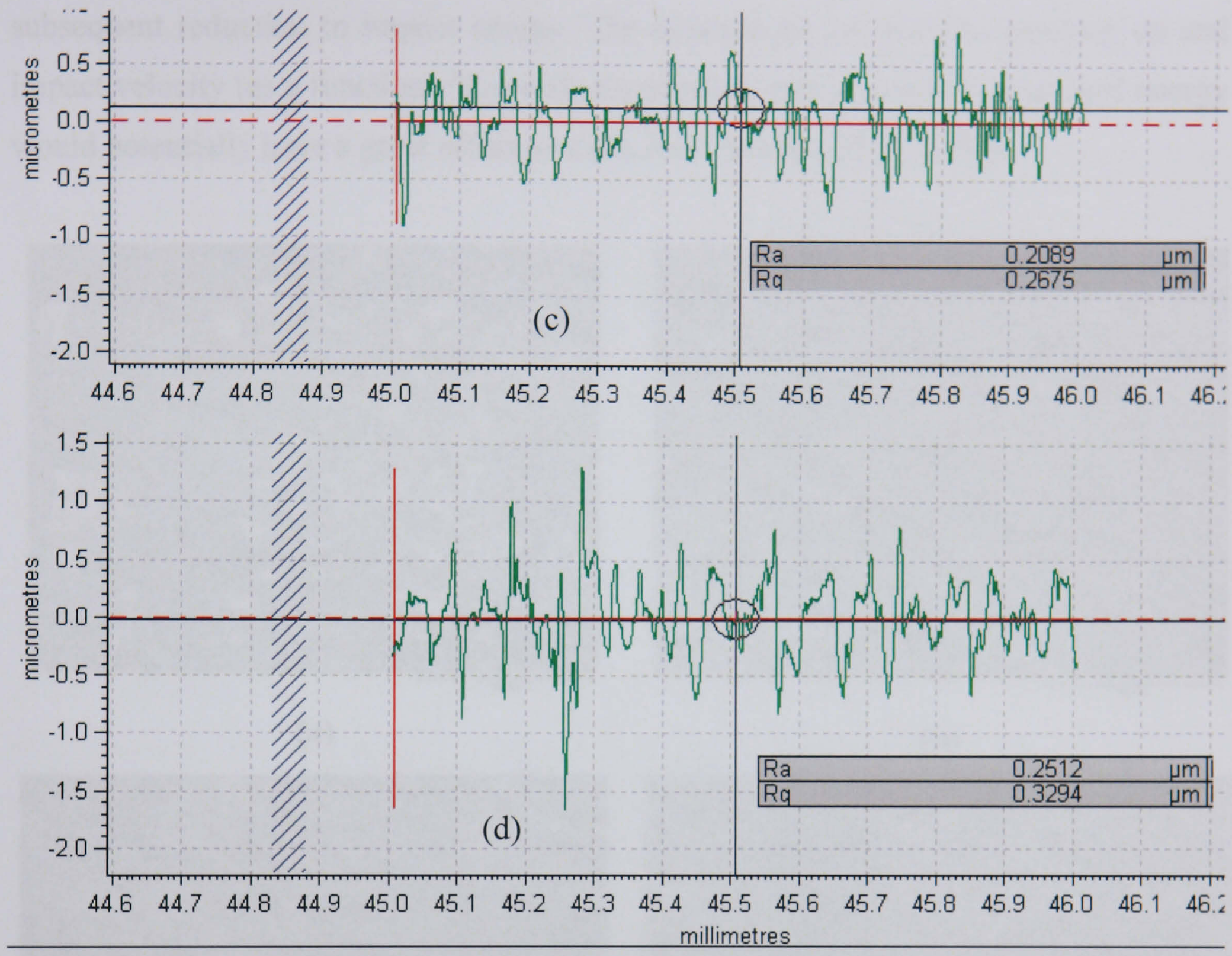

Figure 8.21 The surface roughness for Zone (III) with inhibitor CRW8 with concentrations (a) 25ppm, (b) 50ppm, (c) 100ppm and (d) 150ppm

Figure 8.22 shows microscope images for the blank test at different zones with no sand. Zone (I) (Figure 8.22 (a)) shows severe pitting corrosion and material removal due to liquid impingement, but from the lighter part of the image, the original surface level still can be seen. But with sand, the entire surface could be removed by sand impingement resulting in severe plastic deformation. The obvious different from tests with sand is that with no sand there is no sign of sand ploughing the surface at Zone (II) to (IV); there is no plastic deformation of the material, and Zone (IV) has less pitting than Zone (III), due to the less impingement force in Zone (IV) than at Zone (III), but with sand abrasing the material with low angle at Zone (III) to (IV) like that shown in Figure 3.3 (a), Zone (IV) has more pitting than Zone (III) due to sand abrase the corrosion products before deep pits forms. Inhibitor can reduce the material degradation by forming an inhibitor film with much higher efficiency without sand than with sand. One mechanism of reducing mass loss by inhibitor is through adsorption of inhibitor on sand and

subsequent reduction in impact energy. The dependence on erosion-corrosion on and impact velocity (as a function v^n) is well documented and so a reduction in sand energy would potentially have a great effect on mass loss (Shadley *et al.*, 1998).

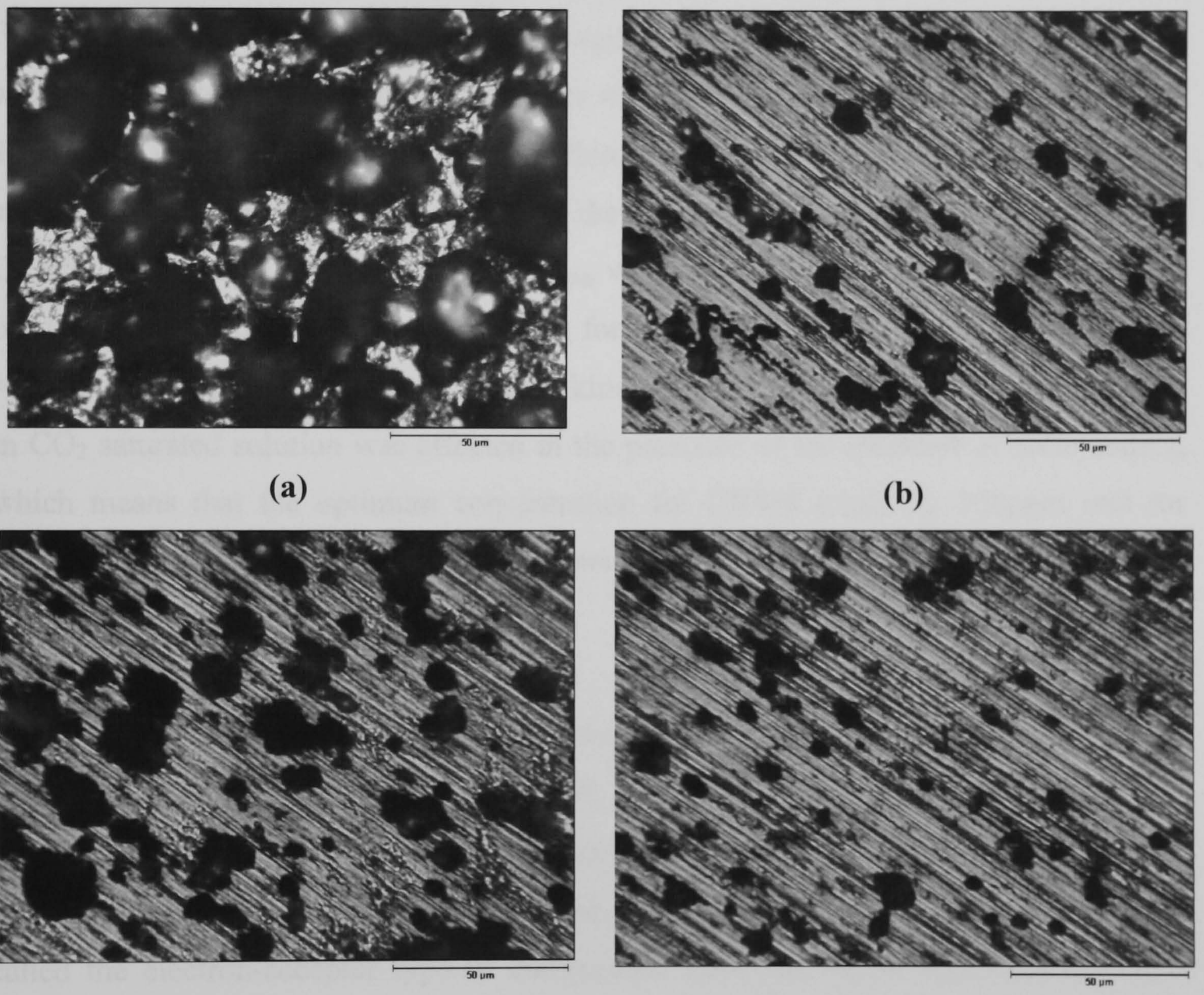

(a) **(b)**

(c) **(d)**

Figure 8.22 Microscope images for sample after blank test with no sand at a) Zone (I), b) Zone (II), c) Zone (III) and d) Zone (IV)

8.2 Electrochemical Tests Results—Corrosion *in-Situ* Condition

To evaluate the corrosion inhibition effect of inhibitors, linear polarisation data can be very useful in determining the corrosion resistance. AC impedance is very informative method to investigate the features of inhibitor film formation, elimination and repair. As the tests have been done under erosion-corrosion conditions, the corrosion rate *in-situ* conditions includes the effect of erosion on corrosion.

8.2.1 Free Corrosion Potential Measurement

Free corrosion potential data obtained at 0, 1 and 2 hours exposure time are shown in Figure 8.23 (a) and (b) for CRW8 and CRW9 under different concentrations at 50°C. For both inhibitors, the free corrosion potential shifts in the noble direction compared with the blank tests. The shift also increases with the increase of inhibitor concentration. This again is an indication that both inhibitors covered the anodic sites of the metal surface and the inhibitors can be called the electron-acceptor type of inhibitor. For CRW8, the results clearly indicate that E_{corr} was shifted to noble direction in the order of 100ppm ≈ 150ppm > 50ppm > 25ppm; for CRW9, in the order of 50ppm >100ppm >150ppm > 25ppm. This suggests that the kinetics of the anodic reaction of carbon steel in CO_2 saturated solution was affected in the presence of the inhibitor of these orders. which means that the optimum concentration for CRW8 might be 100ppm and for CRW9 50ppm under impinging jet, the potential with least concentration is very close to that of blank test.

Figure 8.24 shows the free corrosion potential for single components SA-SK and compared with blank solution and CRW8. For all the single components. the free corrosion potential shift to noble direction comparing with blank tests. This again is an indication that these components covered the anodic site of the metal surface and can be called the electron-acceptor type of component. Then the whole inhibitors can be a mixture of electron-acceptors. However, E_{corr} was shifted to noble direction in the order of SD > SA > SB > SC > SE > CRW8 ≈ SK > SG ≈ SJ > SH ≈ SI ≈ SF > blank. Never the less. as stated before. the free corrosion can be used to ascertain what the controlling processes (either anodic or cathodic) are in corrosion environments but it does not give any information about the corrosion rate of the material.

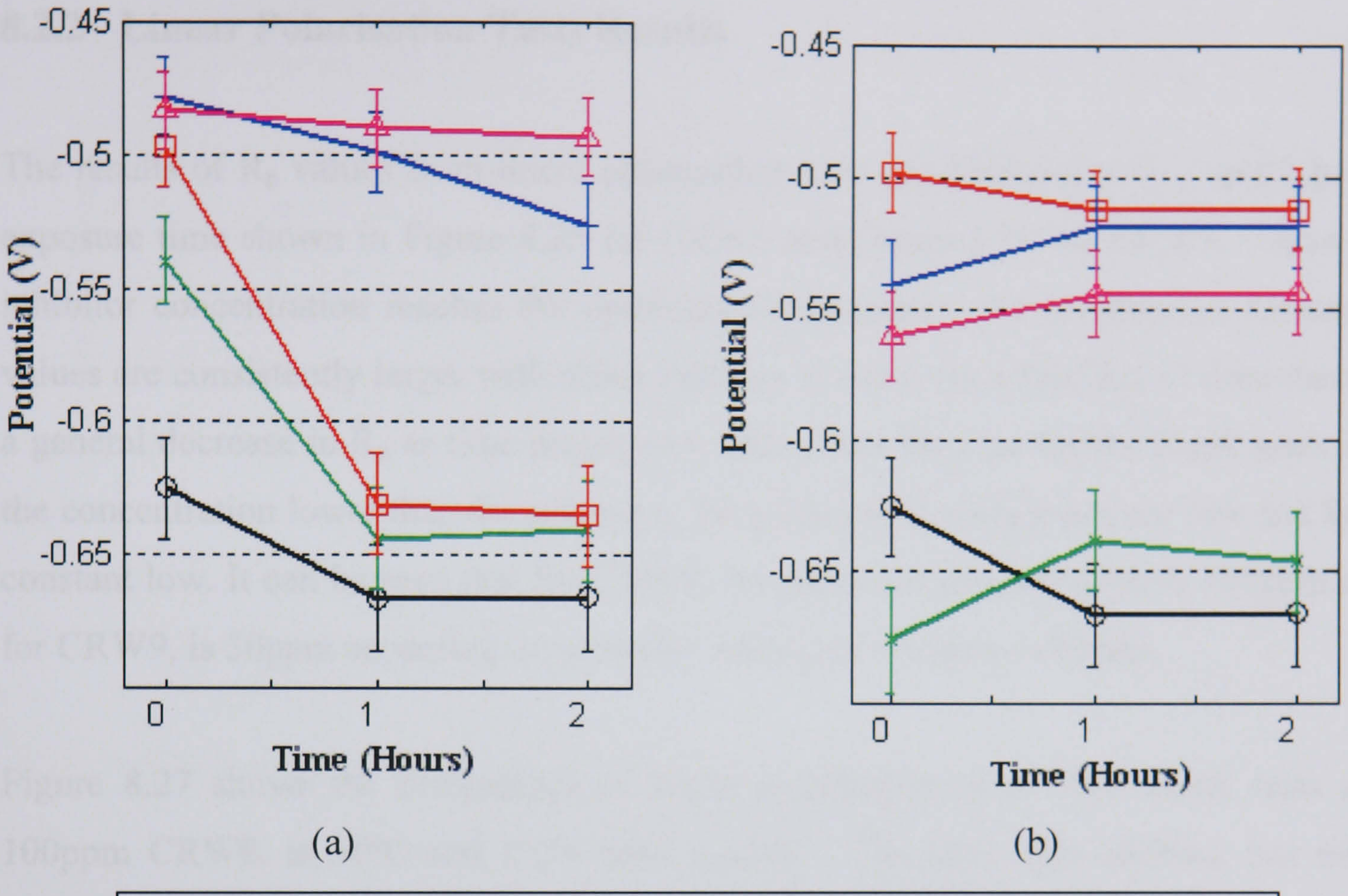

Figure 8.23 Free corrosion potential change of the carbon steel with time for tests with (a) CRW8 and (b) CRW9

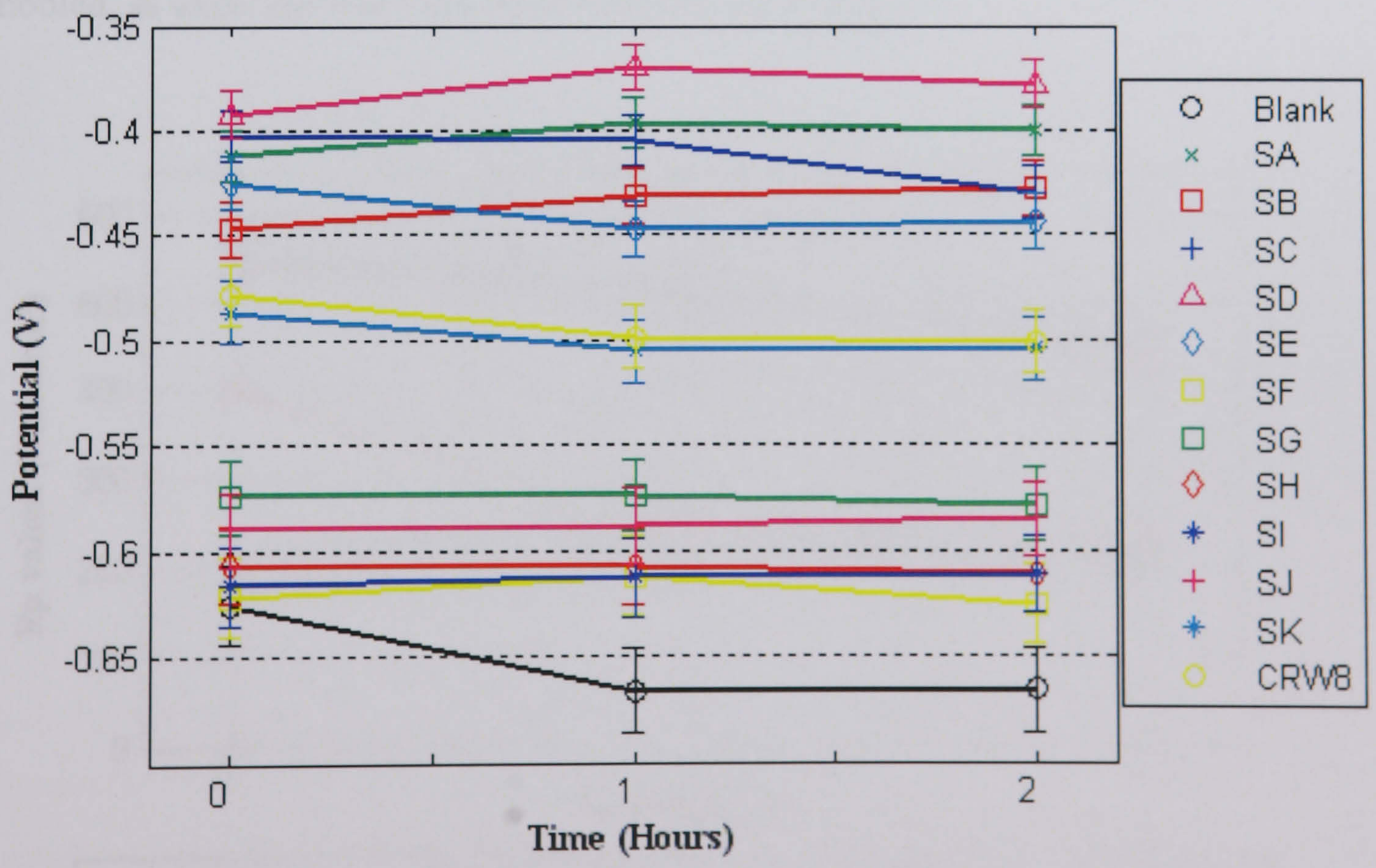

Figure 8.24 Free corrosion potential change of the carton steel with time for tests with the single components SA to SK compared with the blank solution and CRW8

8.2.2 Linear Polarisation Tests Results

The results of R_p values from linear polarisation tests are obtained at 0, 1 and 2 hours exposure time shown in Figure 8.25 for CRW8 and Figure 8.26 for CRW9. Once the inhibitor concentration reaches the optimum concentration, the polarisation resistance values are consistently larger with either inhibitor is used. As a function of time there is a general decrease in R_p as time progresses. This is not the case for the blank tests. For the concentration lower than the optimum, the polarisation resistances are low and keep constant low. It can be seen that for CRW8, the optimum concentration is 100ppm and for CRW9, is 50ppm according to corrosion behaviour *in-situ* conditions.

Figure 8.27 shows the comparison of linear polarisation plots with blank tests and 100ppm CRW8, at 50°C and 0.1% sand loading. The plot with inhibitor has more oscillation than blank one, indicating that inhibitor either acting as an obstacle for the diffusion of the species or causing instability in the transfer of charges at the metal surface. The R_p values are obviously increased as inhibitor is added and E_{corr} is ennobled, as expected when the corrosion rate is reduced.

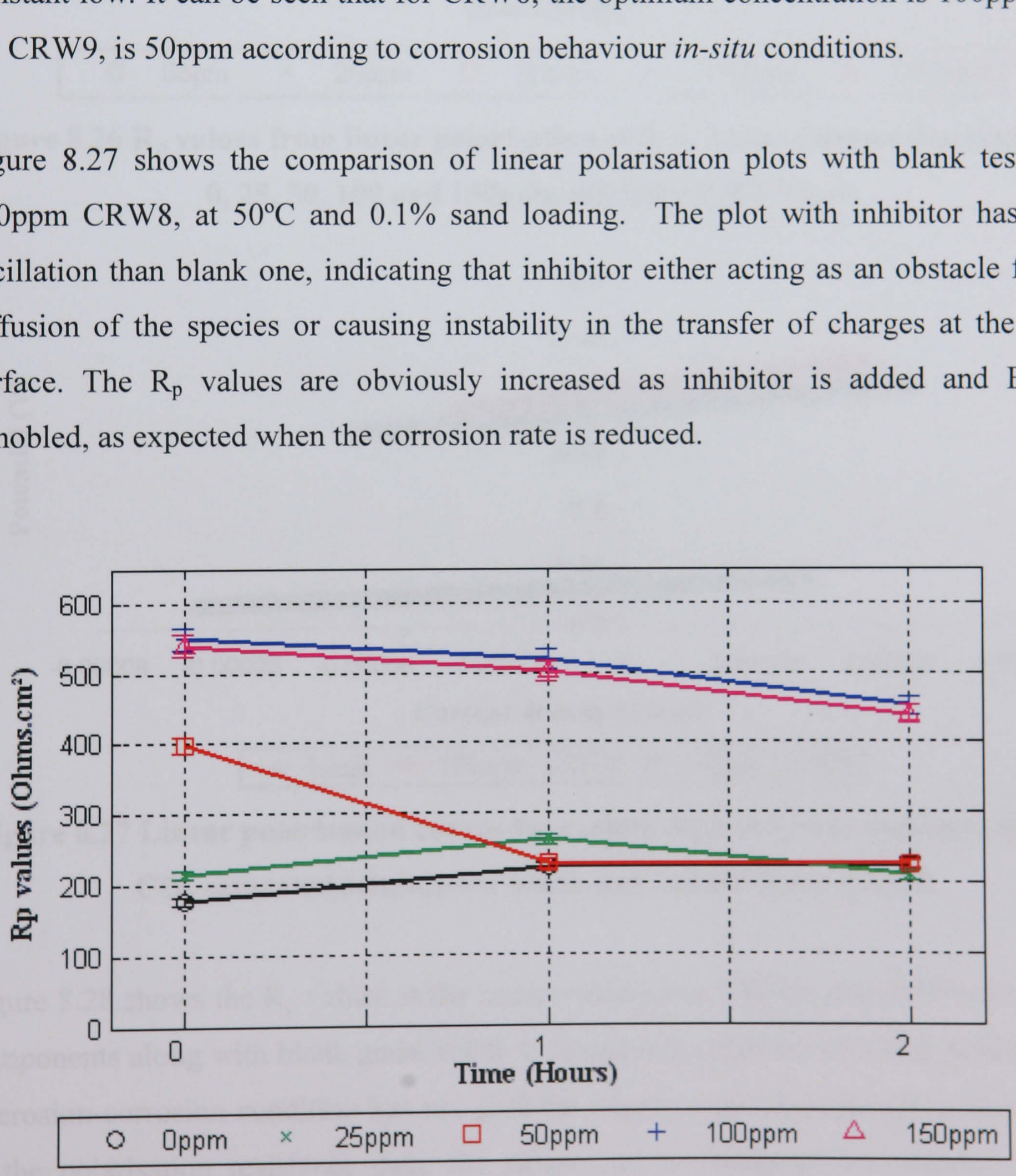

Figure 8.25 Rp values from linear polarisation at 0, 1, 2 hours exposure time with 0, 25, 50, 100 and 150ppm CRW8 tests

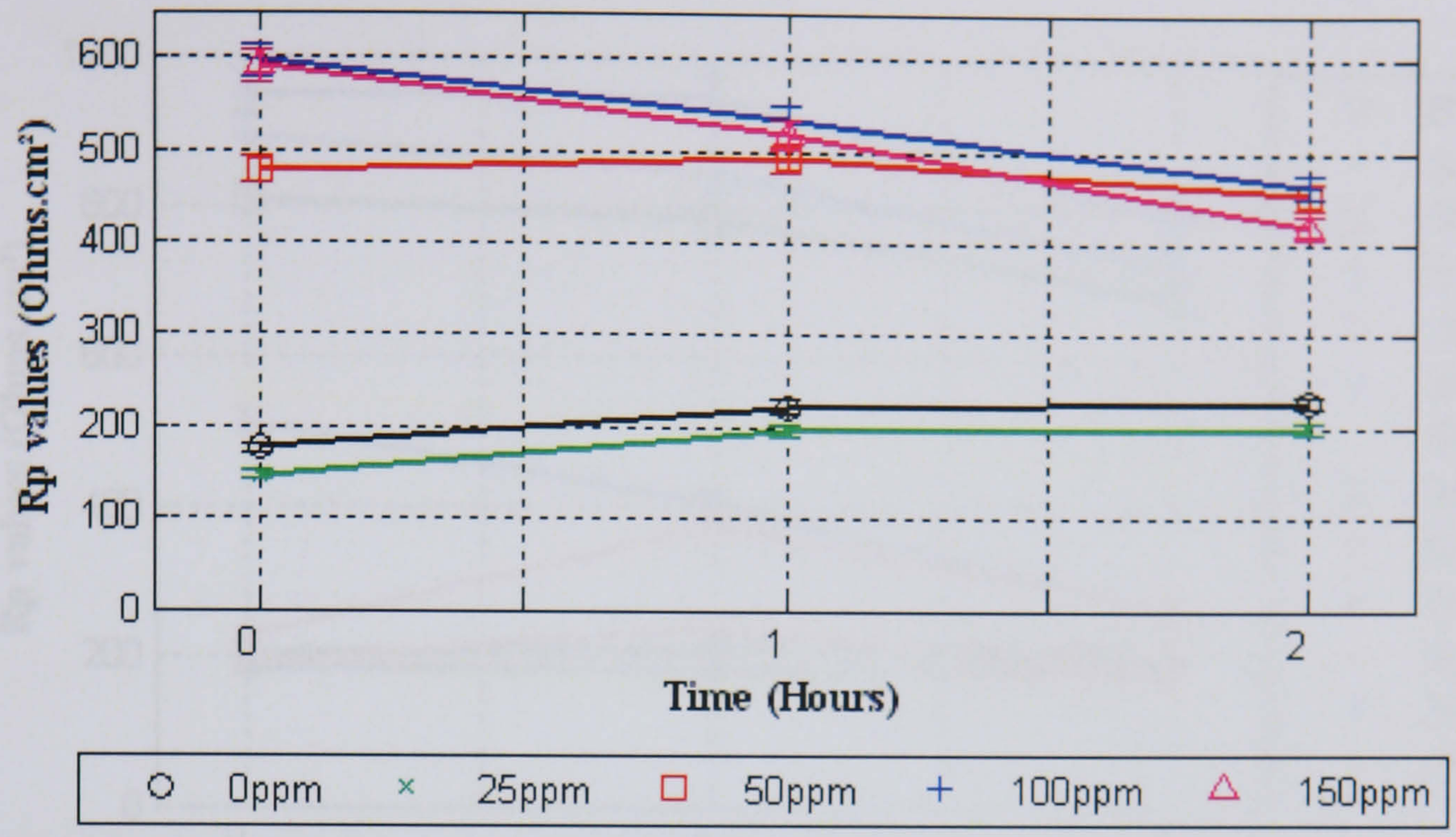

Figure 8.26 R_p values from linear polarisation at 0, 1, 2 hours immersion time with 0, 25, 50, 100 and 150ppm inhibitor CRW9 tests

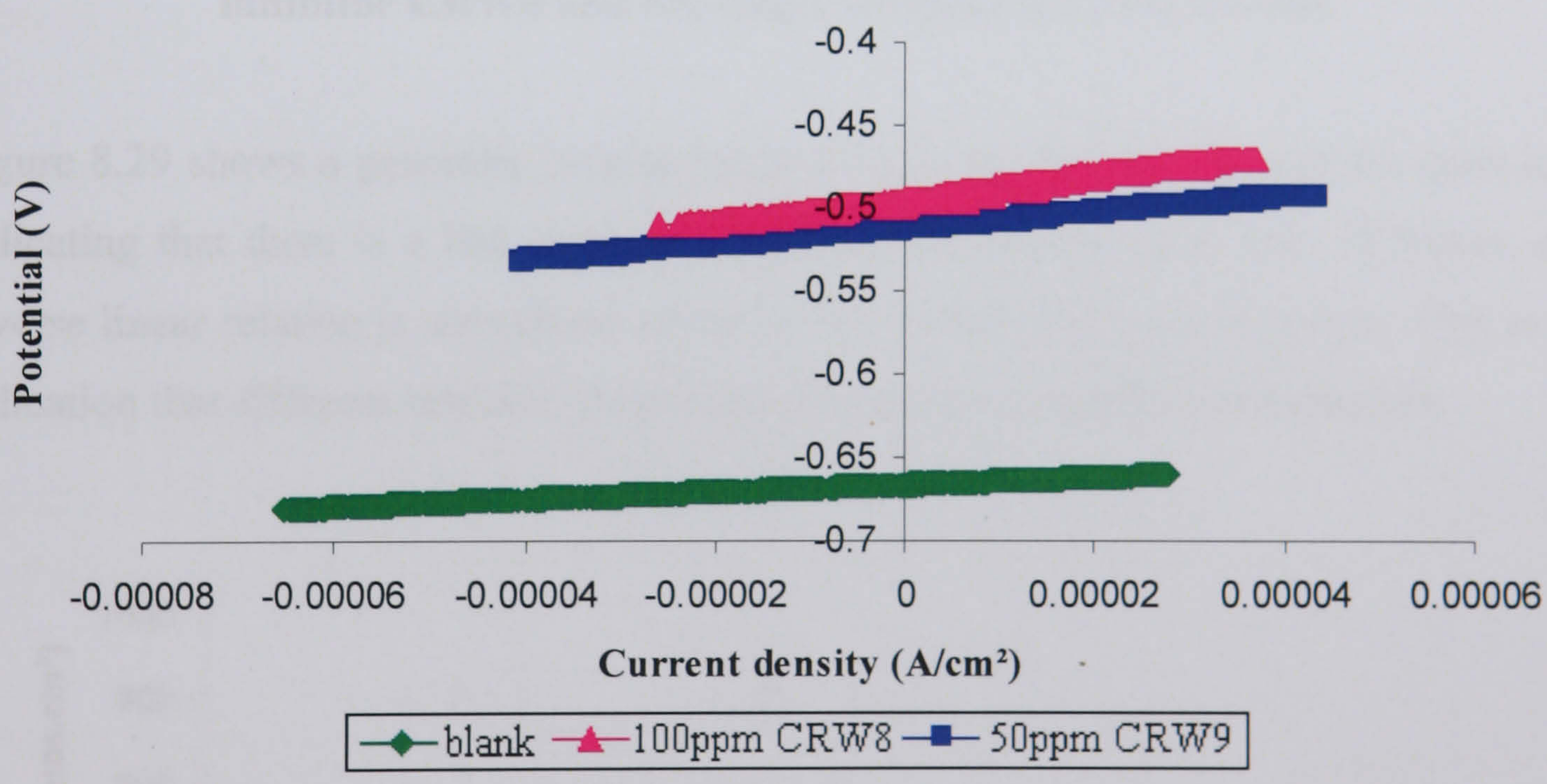

Figure 8.27 Linear polarisation curves for carbon steel at 0 hour exposure time in CO_2 saturated solution for blank test and inhibitor CRW8

Figure 8.28 shows the R_p values at the same condition as CRW8 and CRW9, for single components along with blank and CRW8. It shows that inhibitor with best performance at erosion-corrosion condition has not give the biggest corrosion resistance. According to the polarisation resistance data, the ranking of performance on corrosion *in-situ* conditions for the single components should be as SE > SK > SG > CRW8 > SC > S D > SJ ≈ blank ≈ SI ≈ SF ≈ SA ≈ SB ≈ SH.

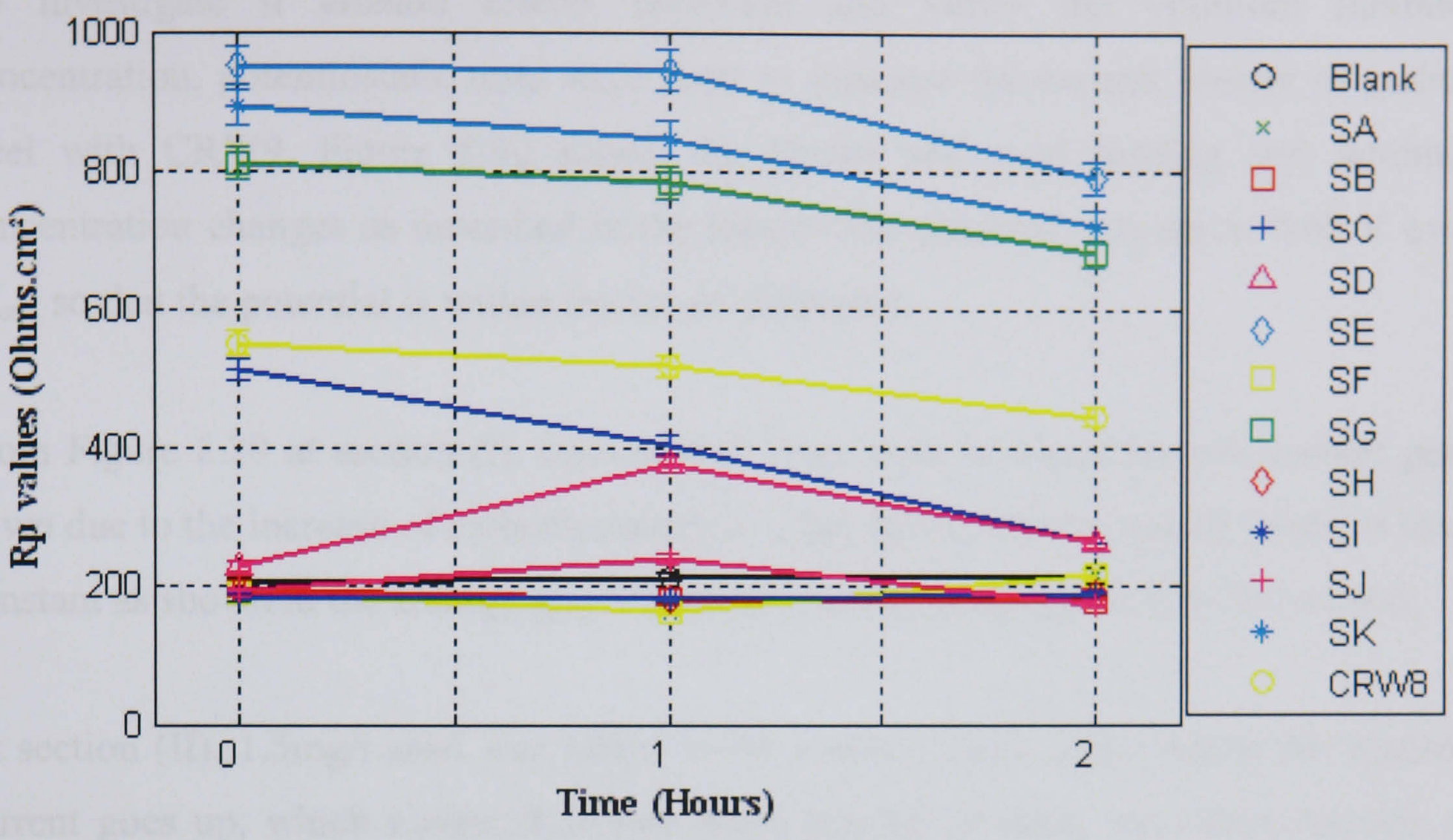

Figure 8.28 R_p values from linear polarisation at 0, 1, 2 hours exposure time with inhibitor CRW8 and the single components from SA-SK

Figure 8.29 shows a generally inverse linear correlation between R_p and the mass loss indicating that there is a link between corrosion and erosion processes. However, the inverse linear relation is not robust, which is like the line show on the graph. This is an indication that different inhibitor component has different inhibition mechanism.

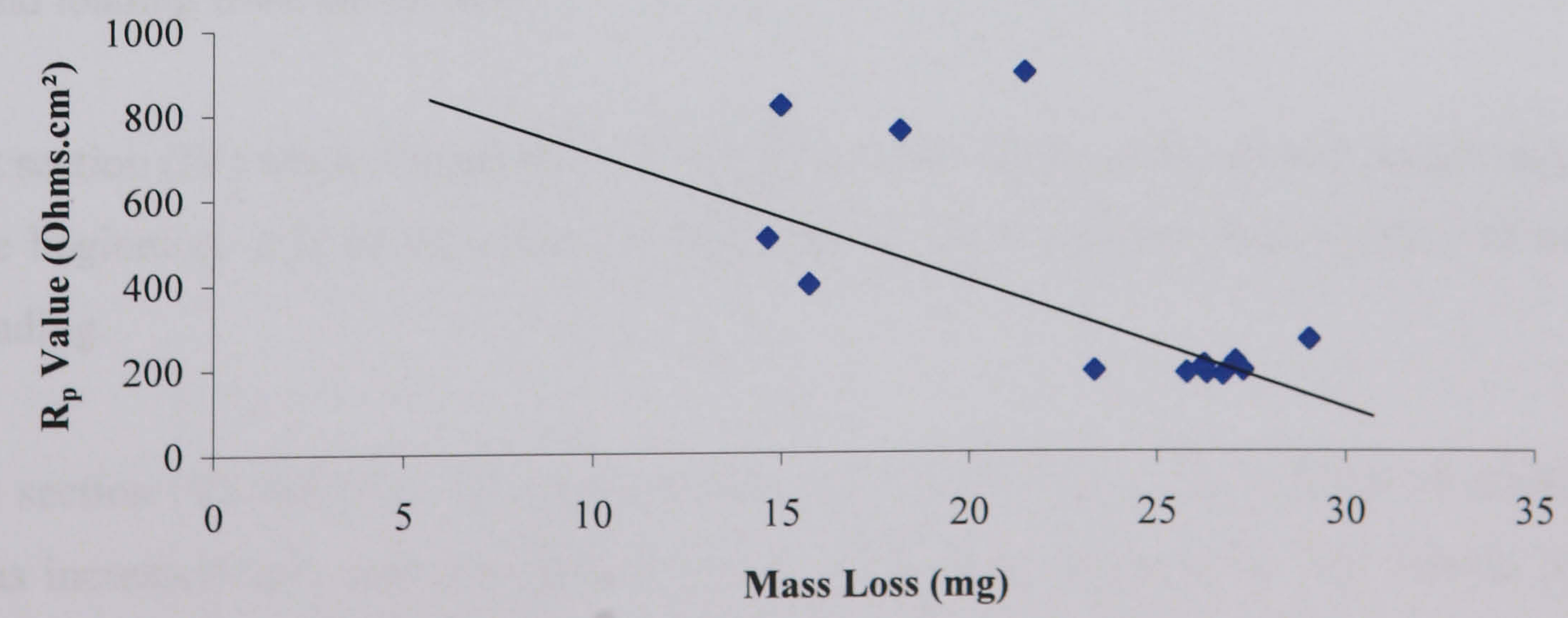

Figure 8.29 R_p values as a function of mass loss from each single component tests, 100ppm inhibitor CRW8 and blank tests

To investigate if erosion affects corrosion and verify the optimum inhibitor concentration, potentiostatic tests were done to measure the current density of carbon steel with CRW9. Figure 8.30 shows the results and sand loading and inhibitor concentration changes as described in the figure. The potential was set to 0.02 V over E_{corr}, so that the potential is within the linear Tafel plot.

From Figure 8.29 at section (I), tests started from static to liquid jet, the current goes down due to the increase of cathodic reaction, after the current becoming stable, it keep constant as shown in the enlarge graph at upper part of the figure from 0-300 second.

At section (II), 1.5mg/l sand was added to the system. Once sand exist in the system, current goes up, which means that even small amount of sand, can cause damage of inhibitor film formed on the metal surface and increase the anodic current of corrosion process.

At section (III), 15mg/l sand was added to the system. The current continuously goes up, which could be due to two reasons. One is that the current increase as time progresses. The other is due to increase of sand loading, erosion enhances corrosion processes. However there is no step of current change at this stage which means that increase sand loading from 1.5 mg/l to 15 mg/l did not really change very much the sand loading from the nozzles.

At section (IV) when 30mg/l sand was added, current keeps going up with small steps at the beginning; it is an indication of sand impact effect increase with increase of solid loading.

At section (V) and (VI), the solid loading was kept constant, but addition of inhibitor was increased upto concentration 150ppm and 200ppm respectively. The current goes up again and then remain constant as time progresses. This is an indication that when the inhibitor concentration exceeds the optimum concentration, more inhibitor will be adsorbed onto the sand surface and reduce the effect of erosion (by sand impacts) enhanced corrosion.

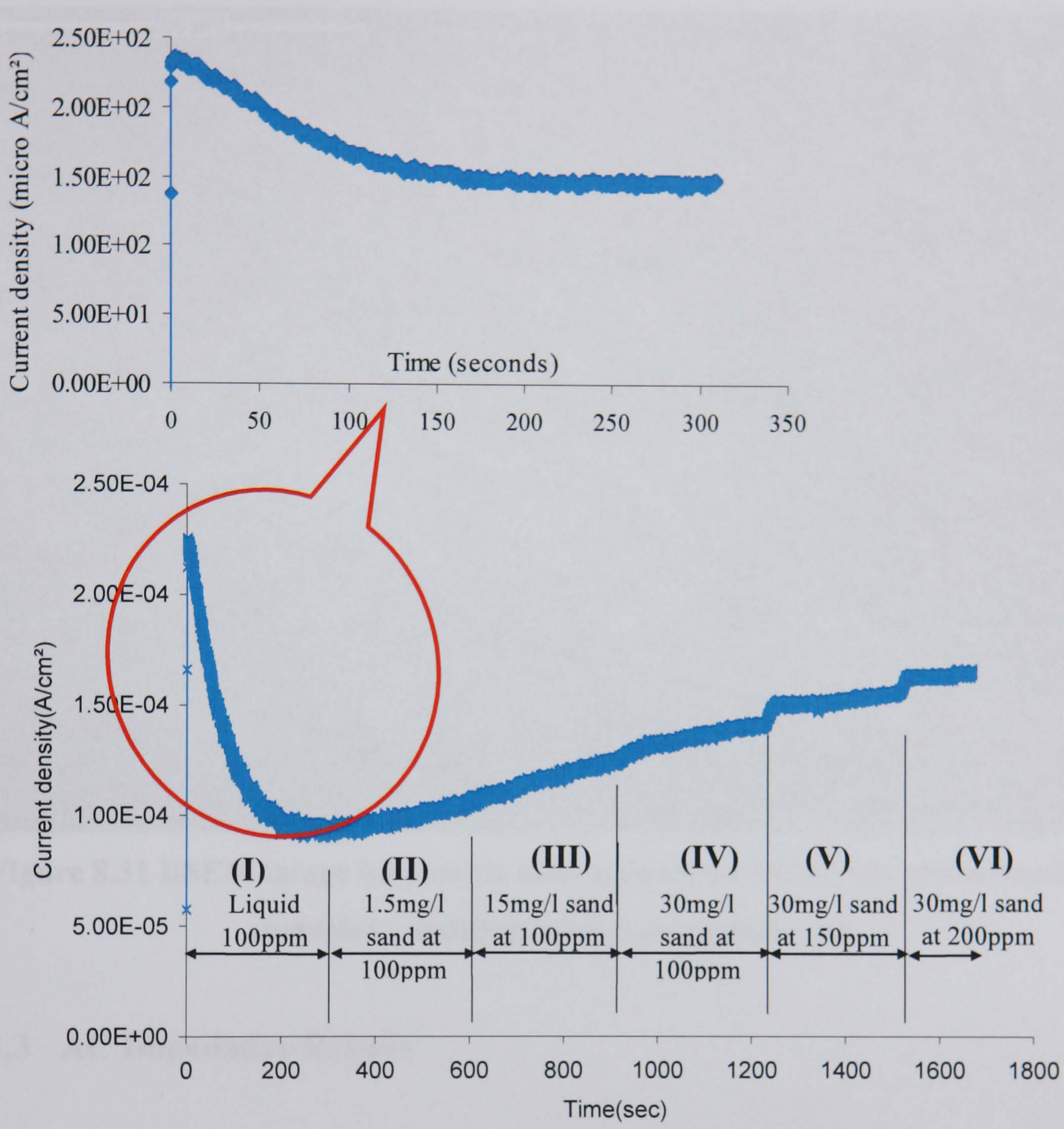

Figure 8.30 Potentiostatic test results of current density measurement of carbon steel in 100ppm CRW9 solution tests (0.02 V over E_{corr})

In order to investigate the corrosion mechanism under erosion-corrosion conditions, SEM was performed with etched sample (using 2ml nital) after blank test under the erosion-corrosion in impinging jet, as shown in Figure 8.31. It shows that pitting still takes place from grain boundary as in static condition shown in chapter 5. The possible signs of grain boundary were pointed with arrows, it can not be seen as clear as in the static conditions. It indicates that the pitting corrosion under the erosion-corrosion conditions also starts from the grain boundary, therefore, the corrosion mechanism under erosion-corrosion is as the same as at static conditions.

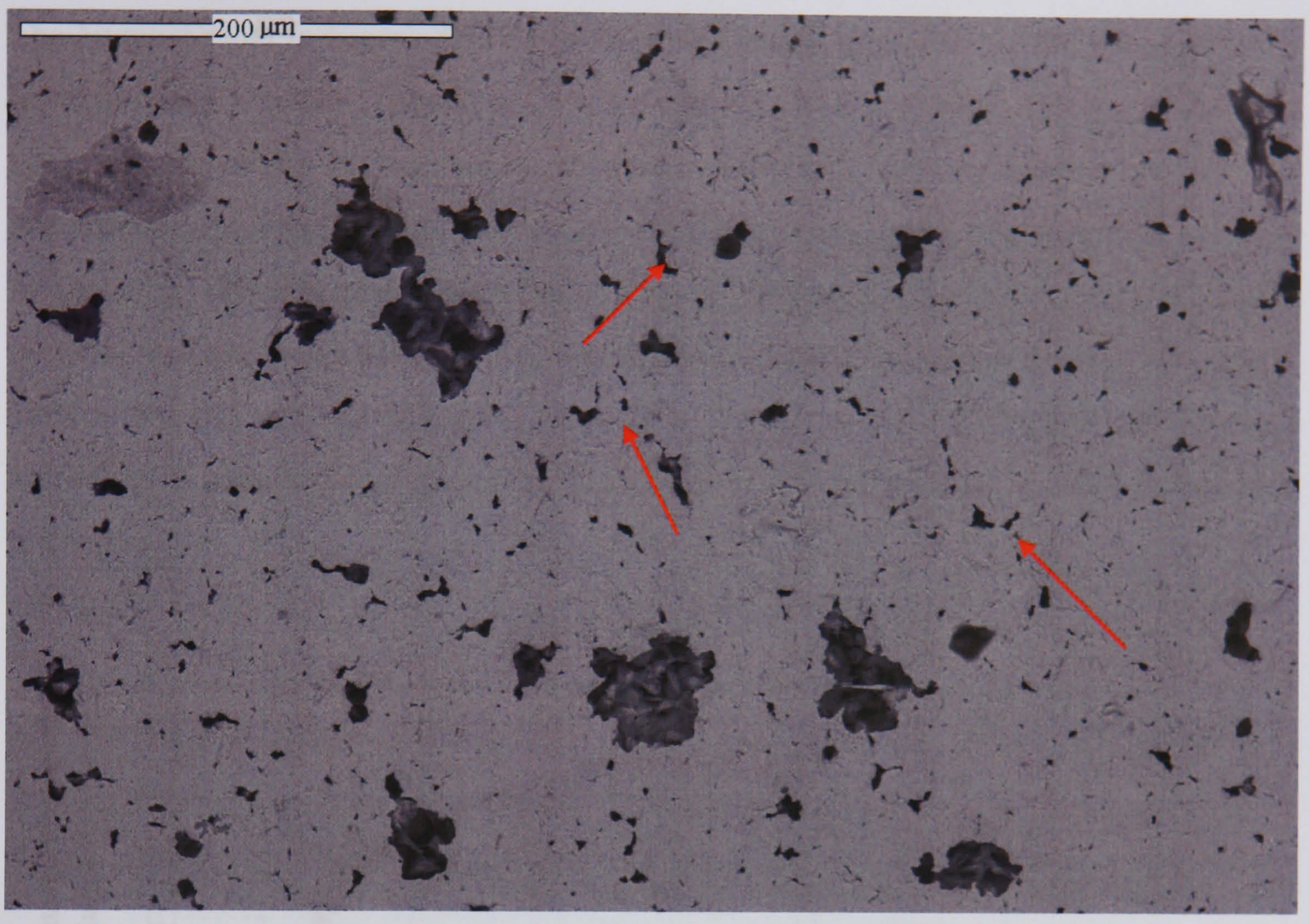

Figure 8.31 BSEM image for sample after etching for blank test under erosion-corrosion condition using impingement rig

8.2.3 AC Impedance Results

In order to understand the inhibition mechanism and to determine the rate of corrosion, AC impedance measurements were carried out with blank test after exposure to the solution for 0, 1 and 2 hours immersion times and with inhibitor CRW8 or CRW9 respectively. The aim is to understand the corrosion inhibition mechanism of the two inhibitors.

8.2.3.1 AC impedance for blank tests

The Nyquist, Bode magnitude and phase plots for the blank tests are shown in Figure 8.32 (a), (b) and (c) respectively to be as a reference for results with inhibitor at various concentrations.

The Nyquist plots in Figure 8.32 (a) exhibit depressed semicircles with both capacitive behaviour and inductive behaviour which is characterized by a portion of the impedance spectrum appearing in the fourth quadrant when the data are plotted as the real impedance component versus the negative of the imaginary component at high and low frequencies. The diameter of semicircle tends to increase a little from 0 hour to 2 hours immersion time, suggesting a small amount of corrosion product formed on the metal surface but did not provide good protection. Induction also associated with a rapid corroding of bare metal as one of the possibility resulting in inductive behaviour stated in chapter 3.

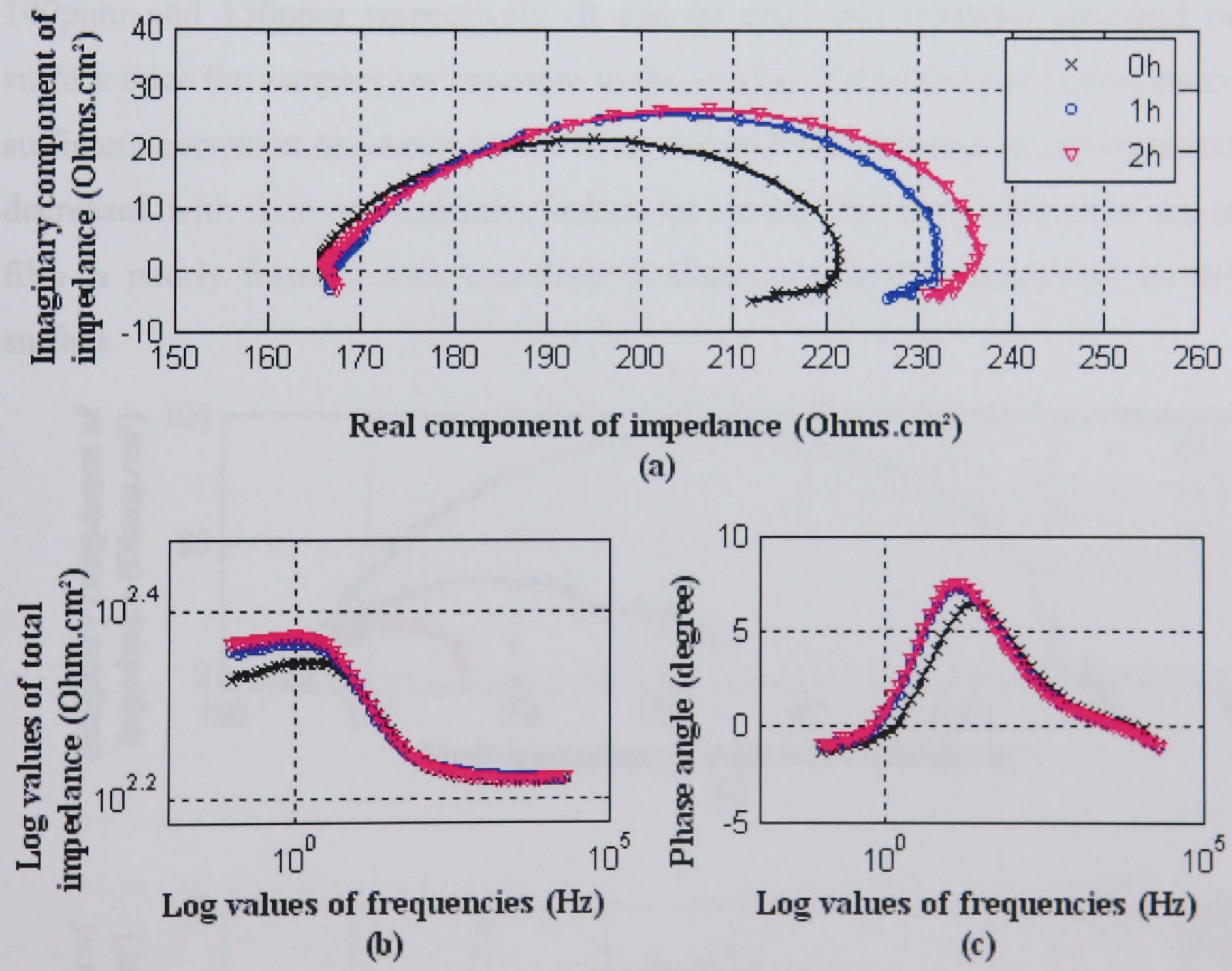

Figure 8.32 Impedance spectra for blank test using impingement rig: (a) Nyquist, (b) Bode magnitude, (c) Bode phase plots

The bode phase plots (Figure 8.32 (c)) show the peak angle is at frequency range 10^1-10^2 Hz. Compared with the static results in Figure 5.10, it could be due to corrosion products taking place at metal/electrolyte interface. The small value of phase angle of maximum phase angle relates to less protection of any film and corrosion taking place.

As Nyquist plots revealed an inductive behaviour, the impedance data can not be fitted with one time constant equivalent circuit as commonly used for blank tests. An equivalent circuit which is different from the conventional one is proposed to use to fit the experimental impedance data as shown in Figure 7.25. The close fitting of the data with the equivalent circuit indicates that this equivalent circuit model can successfully represent the electrochemical processes on the metal/solution interface.

8.2.3.2 Tests with inhibitor CRW8

Figure 8.33 (a) – (d) shows Nyquist plots of the impedance spectra with 25ppm, 50ppm, 100ppm and 150ppm respectively. It can be seen that inhibitor adsorbed onto the surface once the samples are exposure to the system. If the inhibitor concentration is not sufficient corrosion resistance which is related with the diameter of the semicircles will decreased with time and inductive behaviour exists. This is an indication the inhibitor film is poorly formed, with corrosion products competed accumulated on the metal surface.

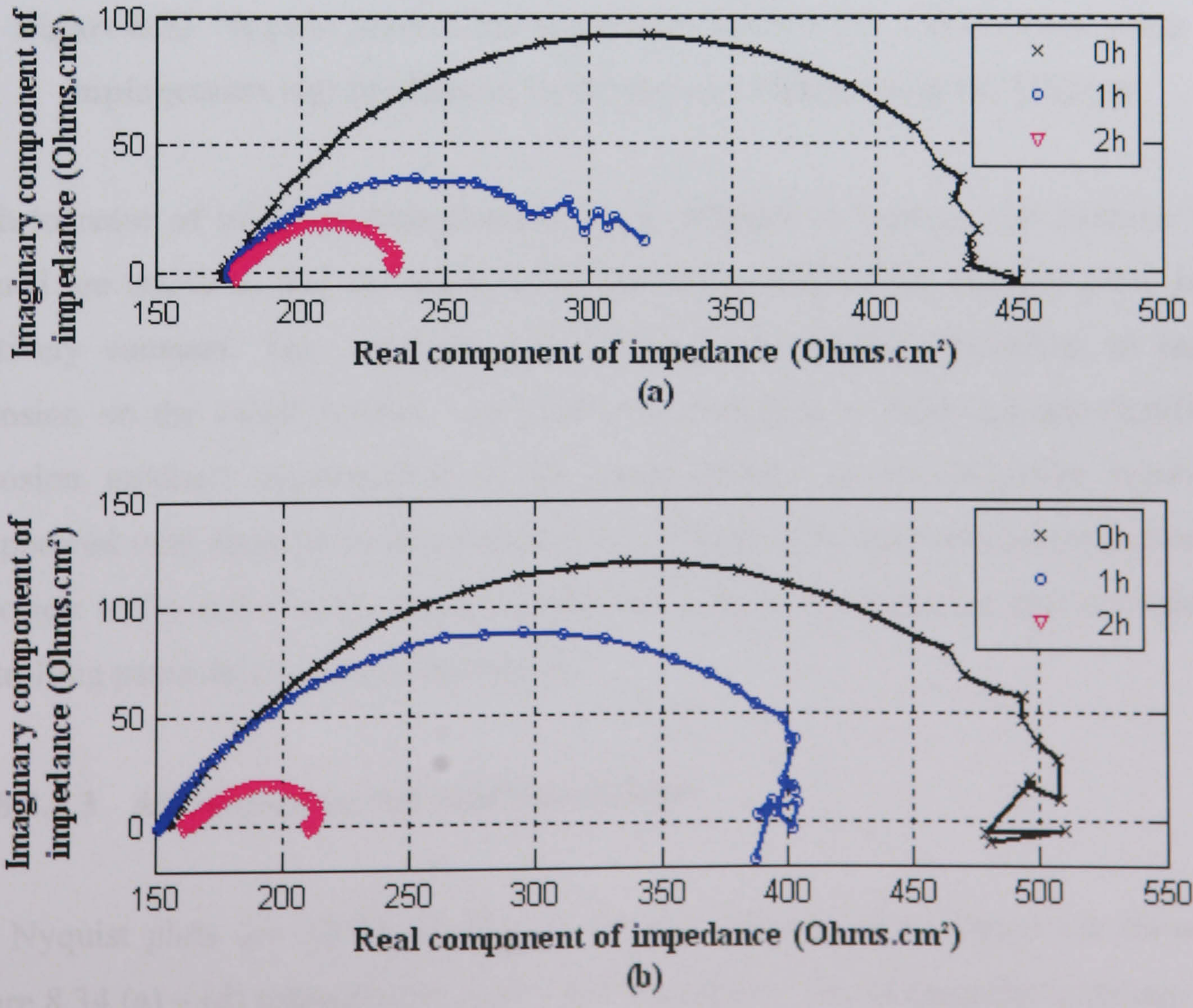

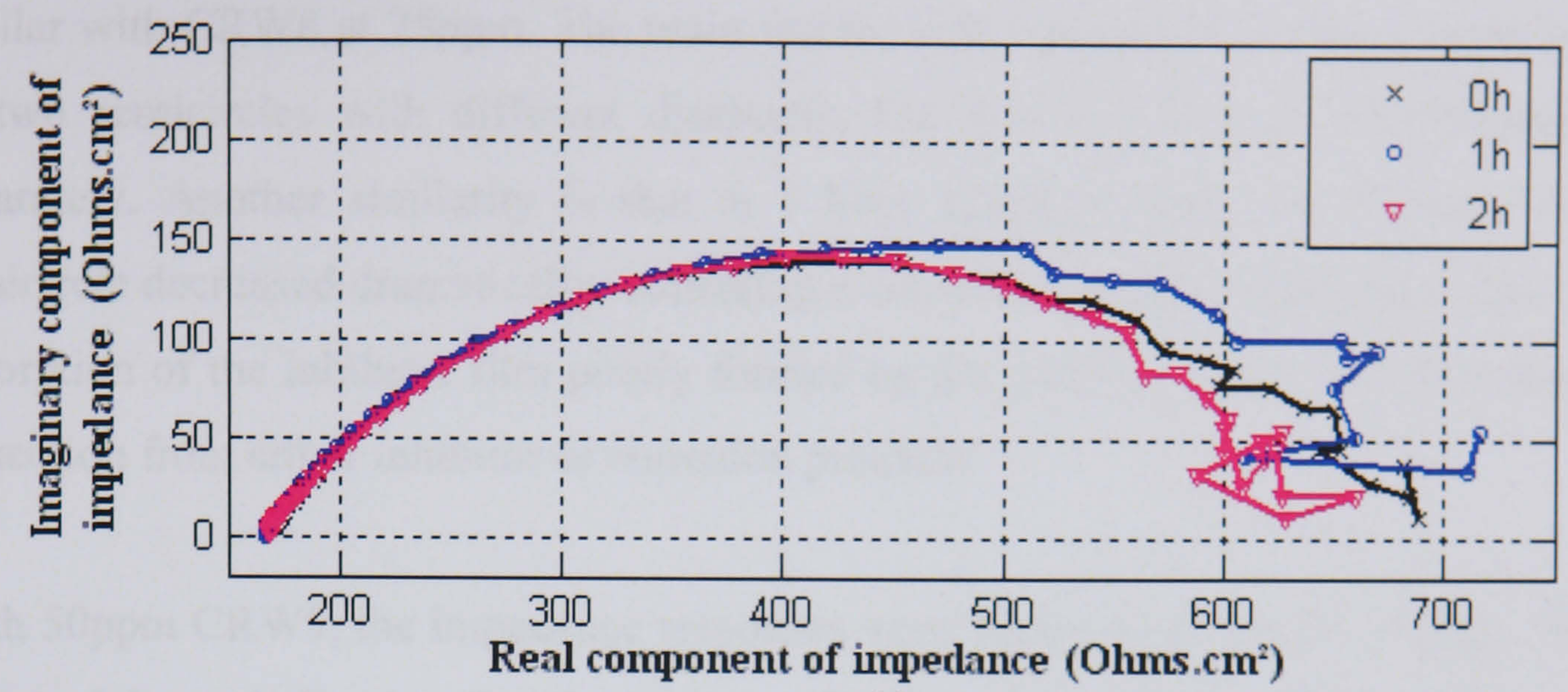

(c)

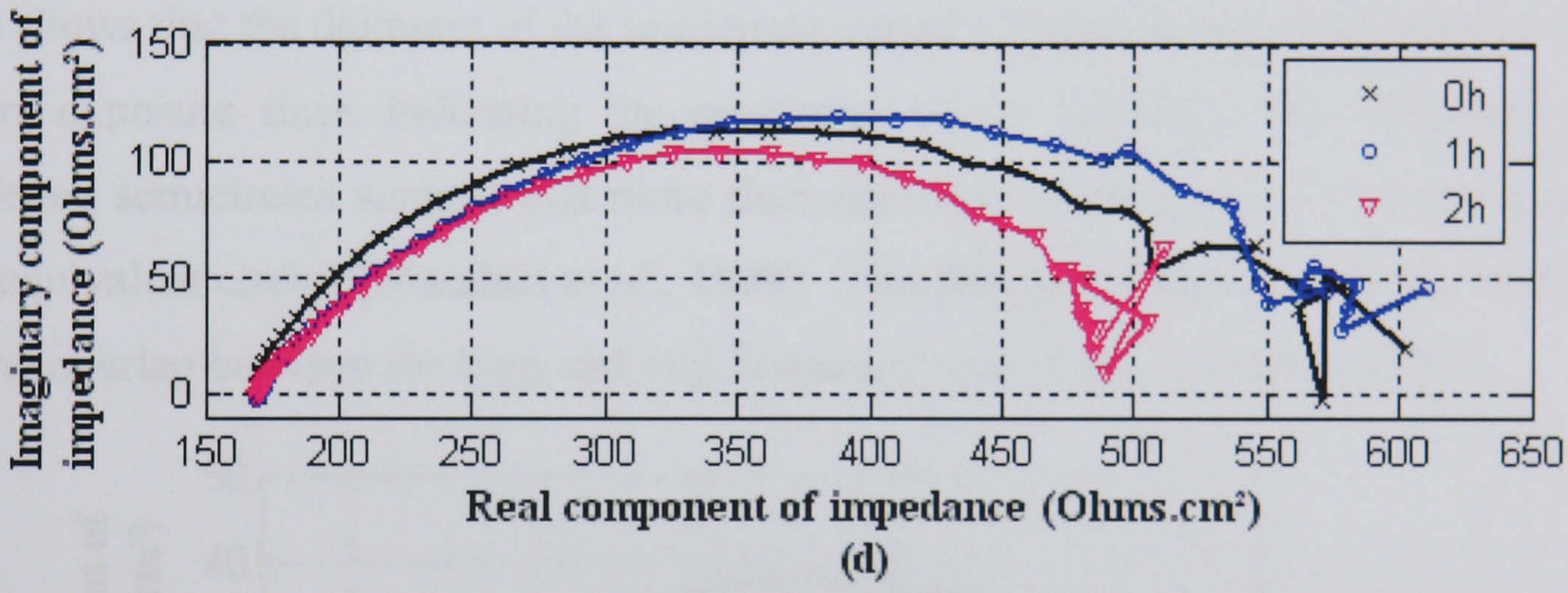

(d)

Figure 8.33 Nyquist plots of the impedance spectra for CRW8 tests using impingement rig: (a) 25ppm, (b)50ppm, (c) 100ppm and (d) 150ppm

With increase of inhibitor concentration up to 100ppm or beyond, the inhibitor film formed are stable in that the diameter of the semicircles of the Nyquist plots keeps relatively constant. This indicates that inhibitor can provide protection to reduce corrosion on the metal surface. The corrosion resistance is high and not significant corrosion products accumulated on the metal surface as the inductive behaviour disappeared with increase concentration up to 100ppm. The optimum concentration for corrosion is the same as for erosion-corrosion. This is an indication that corrosion is controlling parameter in erosion-corrosion.

8.2.3.3 AC impedance for inhibitor CRW9

The Nyquist plots for CRW9 at 25ppm, 50ppm, 100ppm and 150ppm are shown in Figure 8.34 (a) – (d) respectively. With CRW9 at 25ppm shows impedance spectra very

similar with CRW8 at 25ppm. The main feature is the semicircle seems a combination of two semicircles with different diameters, but it is not easy to be distinguished separately. Another similarity is that at 1 hour exposure time, the diameter of the semicircle decreased dramatically, indicating a corrosion process taking place due to the desorption of the inhibitor film poorly formed on the surface. At 2 h exposure time no protection from either inhibitor or corrosion products.

With 50ppm CRW9, the impedance responses were found no noticeable change from 0 hour to 1 hour, indicating that the inhibitor film is relatively stable during this time. It also shows that the diameter of the semicircle varied with exposure time from and 1 to 2 hours exposure time, indicating the protection of the inhibitor film decreased. The flattened semicircles suggest that more than one time constant should be contained in the equivalent circuit (Masalski *et al*., 1999). This flattened behaviour can be attributed to the overlap between the high and mid frequency arcs (Flint and Slade, 1997).

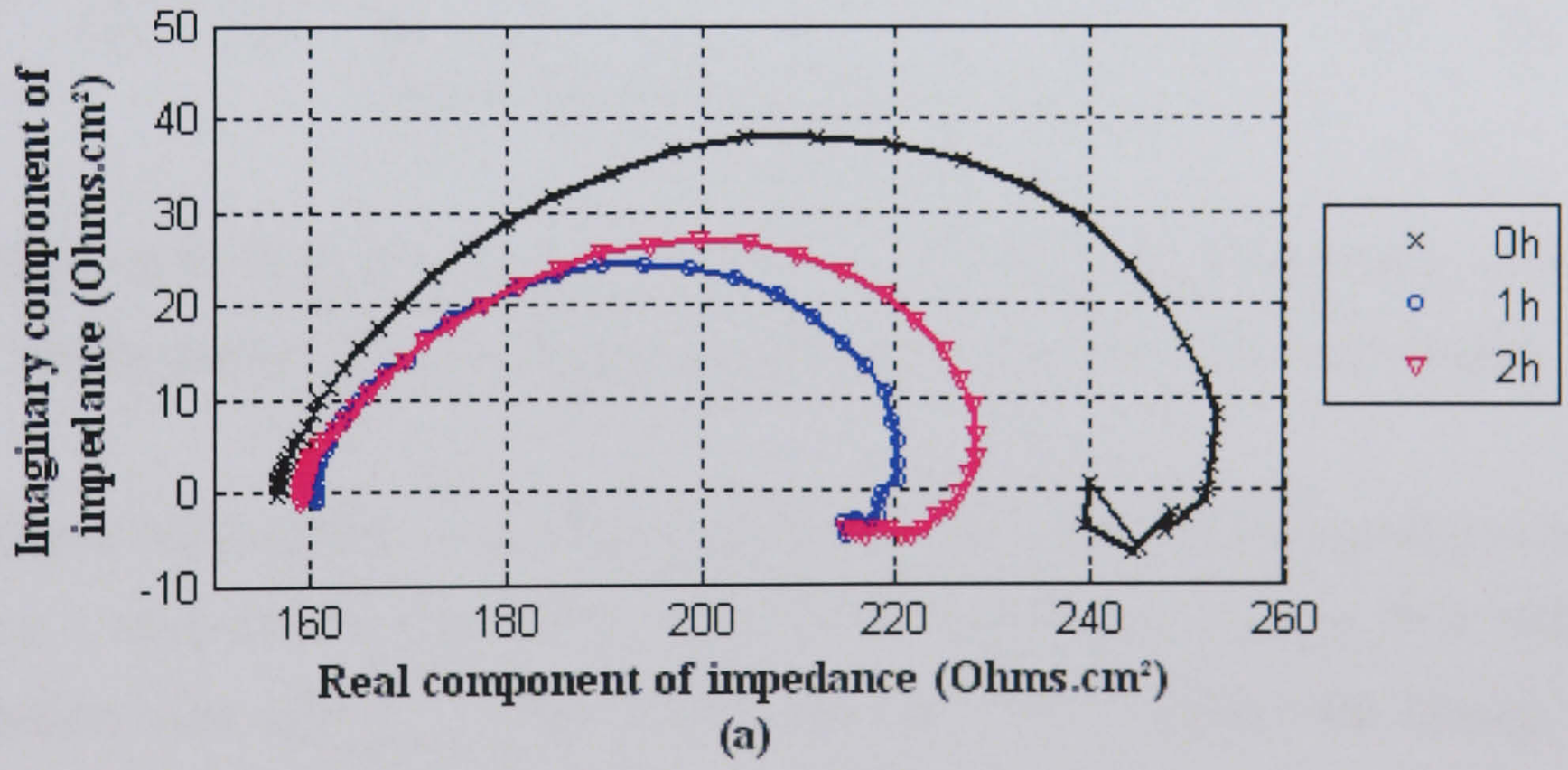

(a)

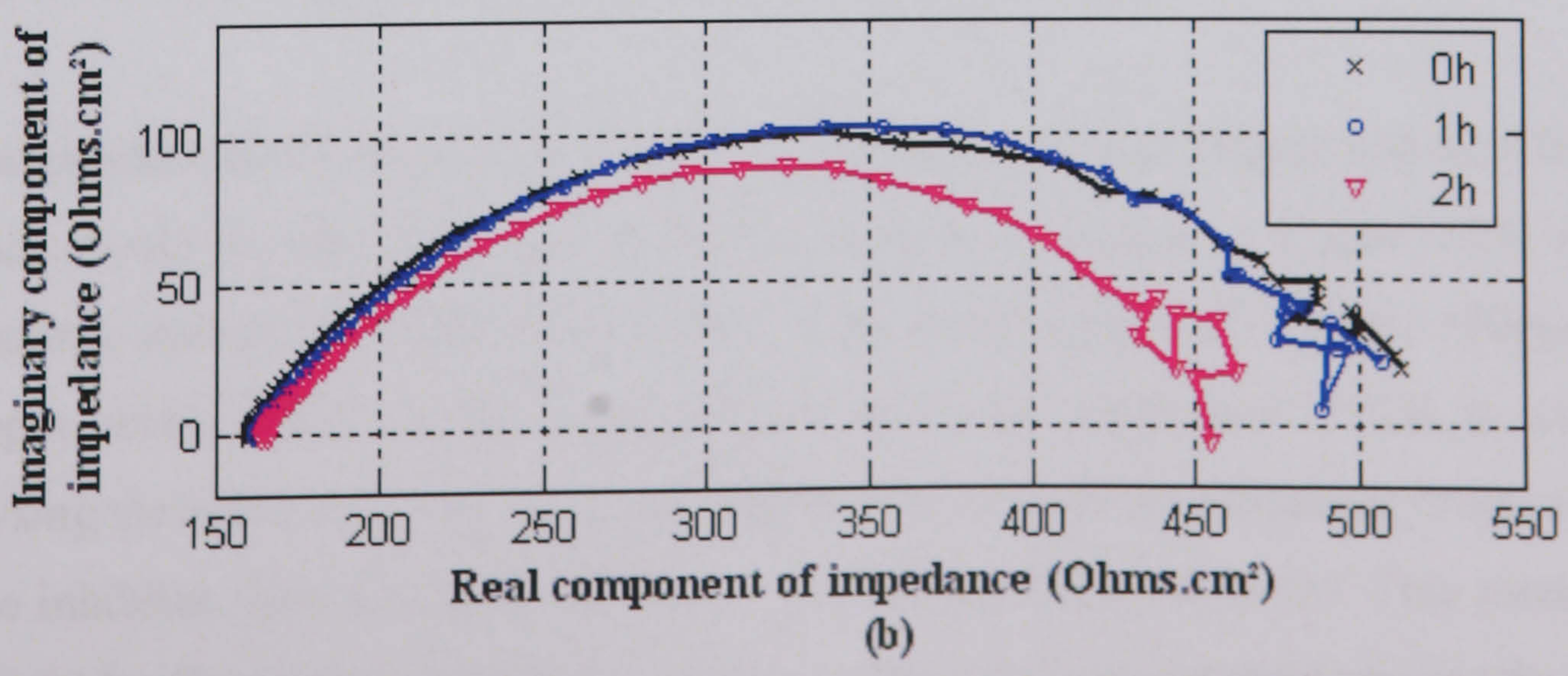

(b)

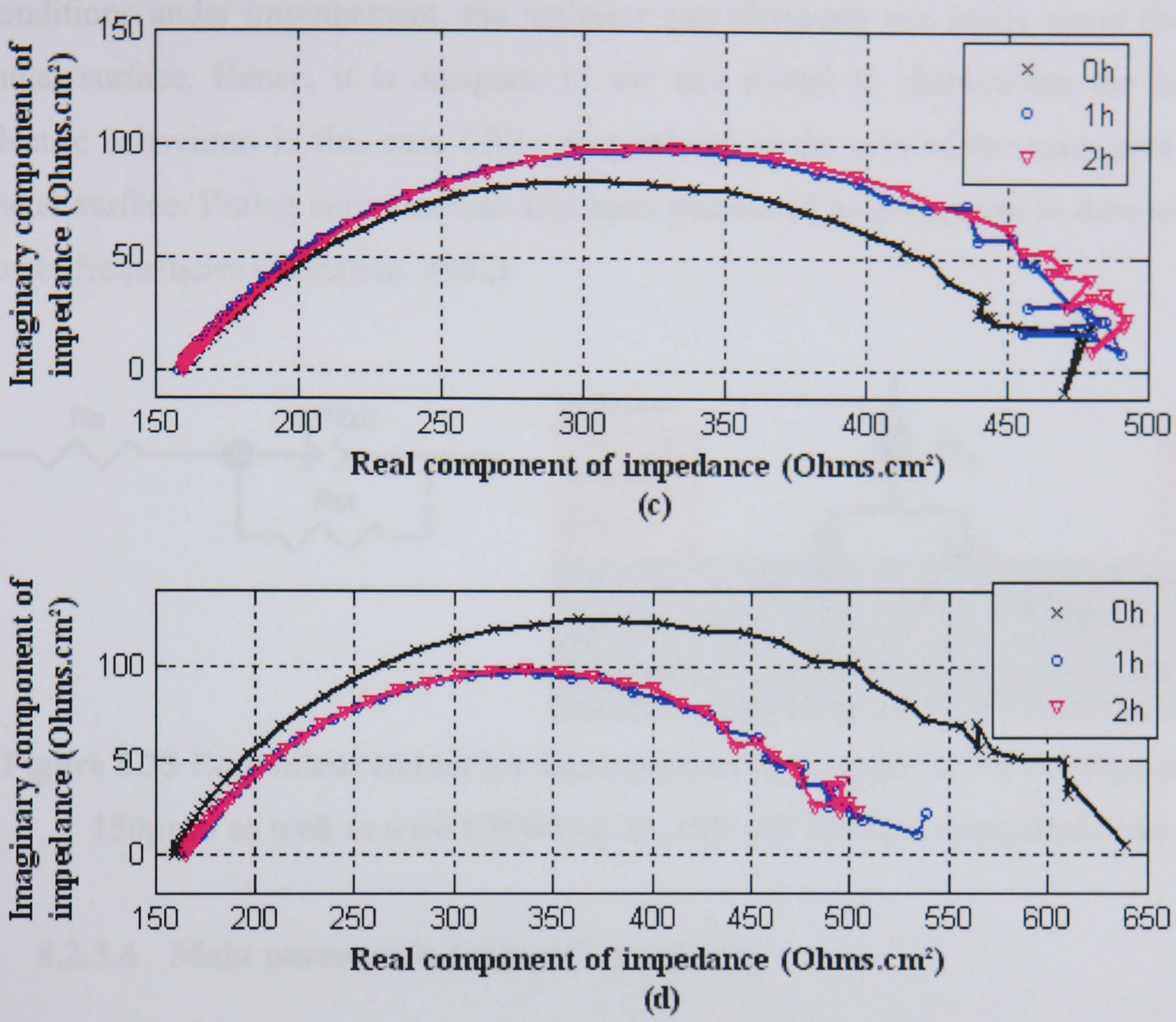

Figure 8.34 Nyquist plots of the impedance spectra for CRW9 tests using impingement rig: (a) 25ppm, (b) 50ppm, (c) 100ppm and (d) 150ppm

For 100ppm the impedance responses were found to be varied with exposure time from 0 hour to 1 hour and no noticeable change from 1 to 2 hours exposure time, indicating the inhibitor film relatively stable during this time. For 150ppm, the change of the spectra with time is almost the same as with 50ppm concentration.

The equivalent circuit used to fit data for CRW8 at 25ppm and 50ppm and for CRW9 at 25ppm would be the same as with blank solution as shown in Figure 7.25. As the impedance spectra are similar for CRW9 with concentration of 50ppm, 100ppm and 150ppm, and CRW8 100ppm and 150ppm, the same equivalent circuit is used for analysing the impedance data as shown Figure 8.35 (a) with its schematic cross-sections of the inhibitor films and metal substrate presented at Figure 8.35 (b). This model was proposed by Zeng *et al*. (2002) for a coating with open pores as state previously. In the

conditions under impingement, the inhibitor was obviously not easily cover the entire metal surface. Hence, it is adequate to use this model to characterize the interface electric behaviour. In this case CPE_{dl} proportional to the area of the open pore on the metal surface. Pitting corrosion has also been postulated as giving rise to data scatter at lower frequencies (Mansfeld, 1992).

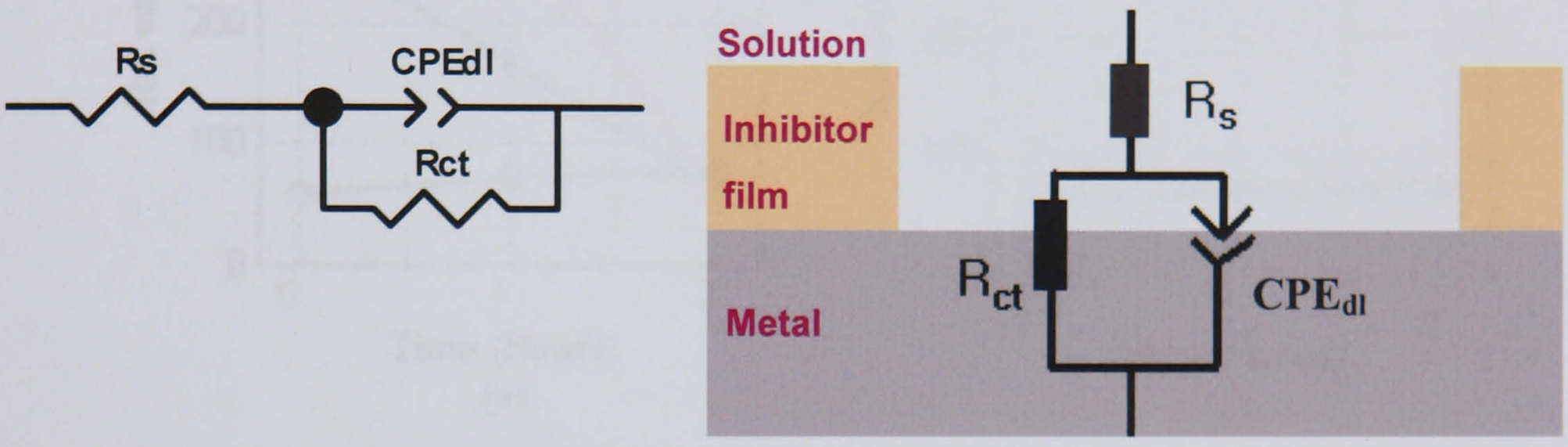

Figure 8.35 Equivalent circuit for impingement tests with CRW8 at 100ppm and 150ppm as well as with CRW9 at 50, 100 and 150ppm concentrations

8.2.3.4 Main parameters from AC impedance

The main parameters, R_{ct} and C_{dl} obtained from AC impedance tests are presented in Figure 8.36 and Figure 8.37 respectively. It can be seen that with CRW8 at 25ppm and 50ppm (Figure 8.36 (a)), the charge transfer resistance R_{ct} decreases with time rapidly due to the inadequate inhibitor molecules until it reach the optimum concentration, 100ppm, it start to decrease slightly with time. While with CRW9 (Figure 8.36 (b)), at 25ppm the inhibitor has no effect with similar R_{ct} value with that with blank tests; From 50ppm to 150ppm, there is no remarkable change of the R_{ct} with increase of inhibitor concentration. This is indication that 50ppm CRW9 is critical concentration for corrosion inhibition. The comparison of the R_{ct} values between 0, 25, 50, 100, 150ppm concentrations proves that the inhibitor plays an important role in hindering the corrosion process.

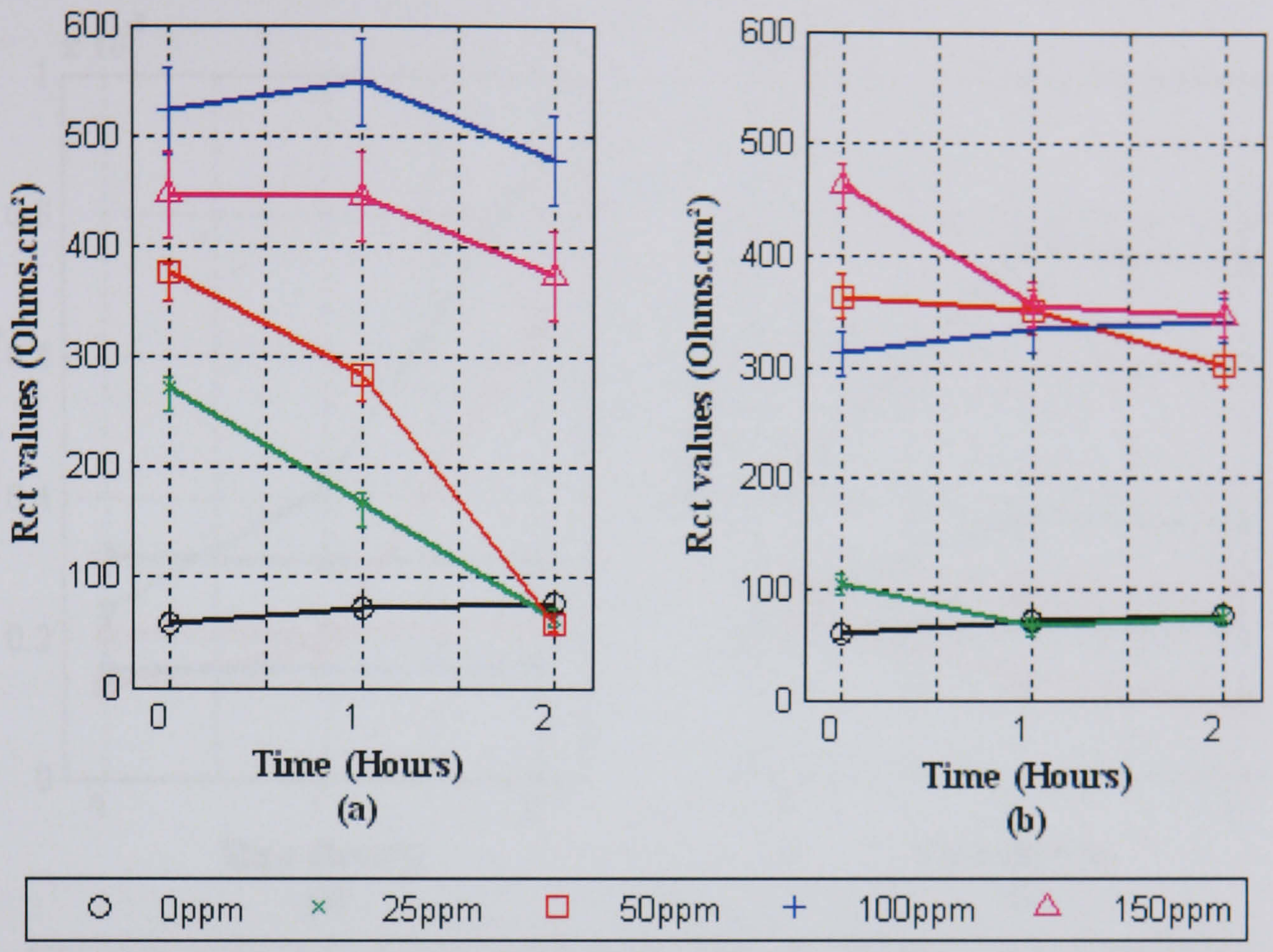

Figure 8.36 R_{ct} values obtained from AC impedance with different concentrations of (a) CRW8 and (b) CRW9

The adsorbed inhibitor layer can affect the basic corrosion reactions in various ways. One way is caused by the geometric blocking effect of adsorbed inhibitive species on the metal surface; In this case, the inhibition comes from the reduction of reaction area on the metal surface; Another way can be due to the electrocatalytic effect of the inhibitor or its reaction products; For this case, the inhibition effects are due to the change in average activation energy barriers of the anodic and cathodic reactions of the corrosion process (Mansfeld *et al*., 1985). From the results of capacitance values, it can be seen that for CRW8, the inhibition most probably comes from the reduction of reaction area on the metal surface. As the optimum concentration is 100ppm, at which the inhibitor has its highest corrosion resistance and lowest capacitance values. However, for CRW9, there is a big difference of the C_{dl} values with and without inhibitors, but it is not very much different with different inhibitor concentrations. It may indicate that CRW9 provide inhibition to the carbon steel mainly due to change the activation energy of anodic reaction on the metal surface.

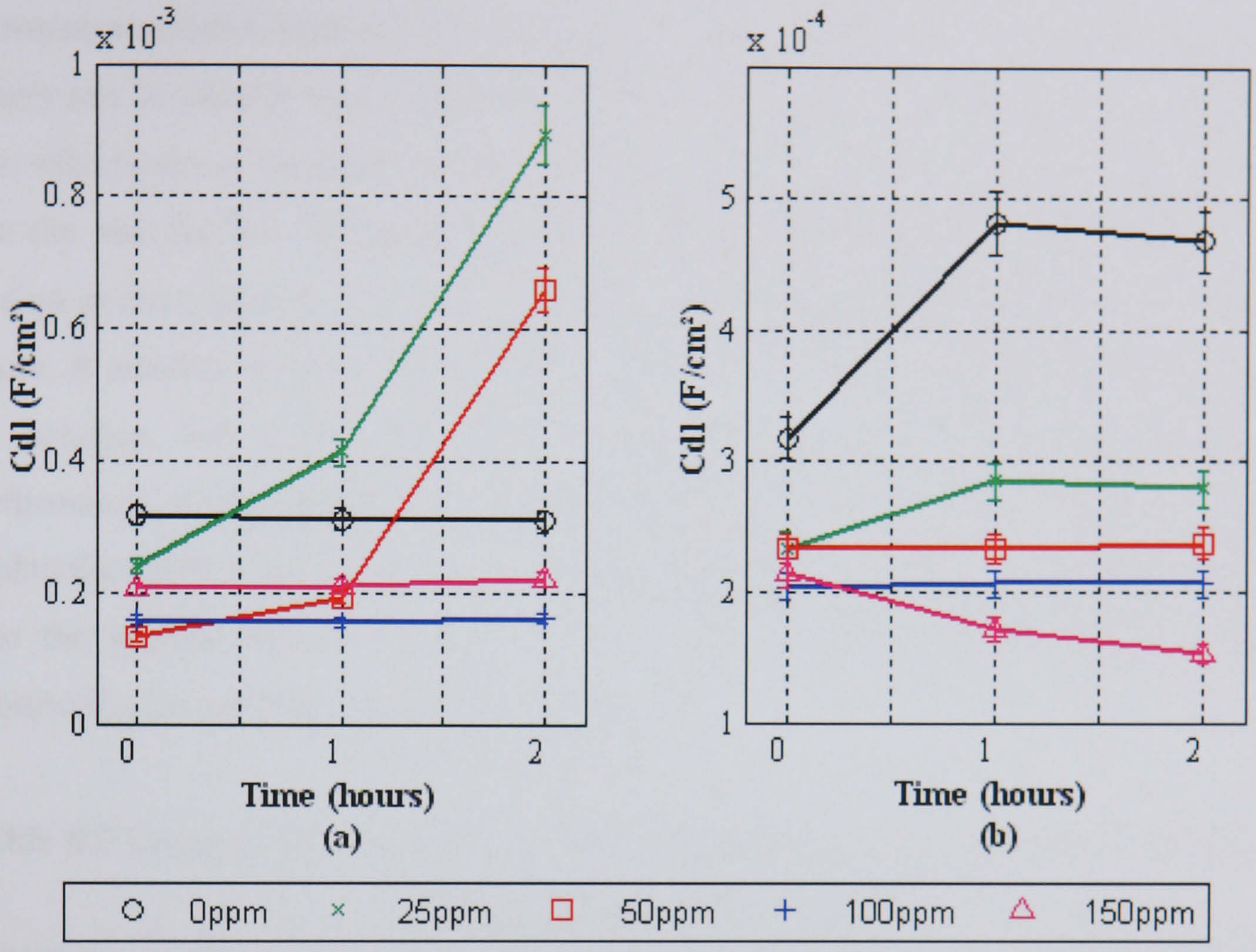

Figure 8.37 C_{dl} values obtained from AC impedance with different concentrations of (a) CRW8 and (b) CRW9

8.2.3.5 AC impedance results for single components

The AC impedance spectra in Nyquist plots obtained for single components SA, SB, …, SK are shown in Figure 8.39 (a) to (k) respectively. The shape and the size of the diameter along with the trend of their changing can give basic information for ranking of the components performance on corrosion *in-situ* conditions. The ranking is shown in Table 8.2 and comparing R_p data. Only rank for SE did not follow the trend as R_p data. Since the fitting data from AC impedance measurements followed the same trend for all the tests with inhibitors stated earlier, R_p data can be used as corrosion resistance to qualitatively analysis the relation between the mass loss, corrosion resistance and free corrosion potential.

The best and the worst performance for overall damage are SK and SD respectively. Except for SE which corrosion resistance is the highest however the erosion-corrosion performance is very average level among the all components, it is observed that the

corrosion resistance reduced and mass loss results increased. It can be assumed that SE is only can be adsorbed onto the metal surface to reduced corrosion, it will not adsorbed onto effectively to the sand surface and can be seen that the corrosion performance is also the best for SK. SD has better performance than many other component, but the erosion performance is very poor. SD is oil soluble component and also very sticky in nature. It actually sticks to the metal surface and surface of the equipment once get into the solution, but could not evenly be adsorbed on the sand which reduces its performance of reduction on erosion. From the results, it can be seen that ethoxylated imidazoline and anhydride/polyamine reaction products have the best ability to adsorb onto the anodic site of the carbon steel surface. E_{corr} can not provide the ranking information on corrosion and erosion-corrosion.

Table 8.2 Comparison of ranking of the resistance from AC impedance and R_p for single components SA to SK

From AC impedance	SK > SG > SE > SC > S D > SH ≈ SB ≈ SF ≈ SA ≈ SJ ≈ SI
From R_p values	SE > SK > SG > SC > S D > SJ ≈ SI ≈ SF ≈ SA ≈ SB ≈ SH

Figure 8.38 shows the correlation of the ranking on mass loss, corrosion resistance and E_{corr} for single components with inhibitor CRW8 as well as blank solution.

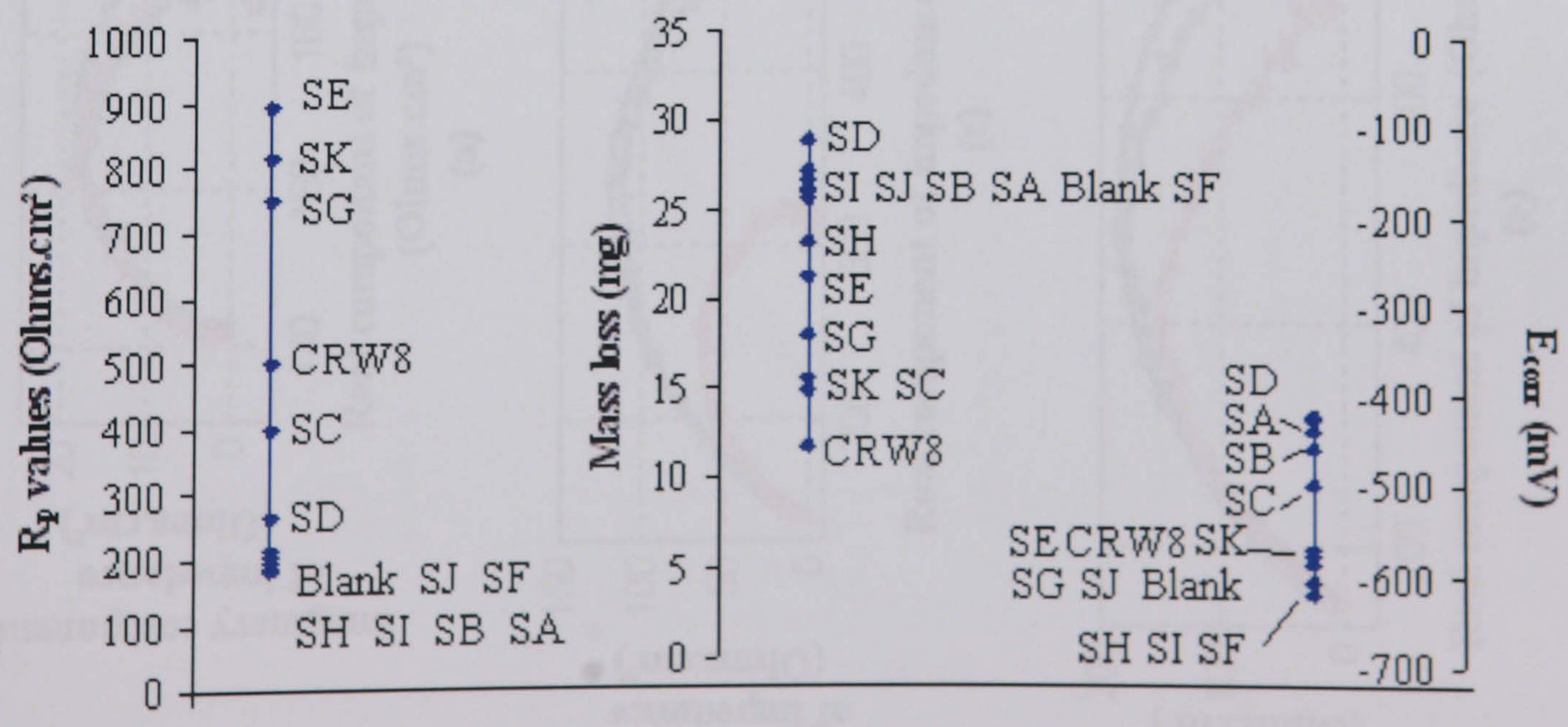

Figure 8.38 Comparison of quantitative ranking of performance for the single components and CRW8, blank solution

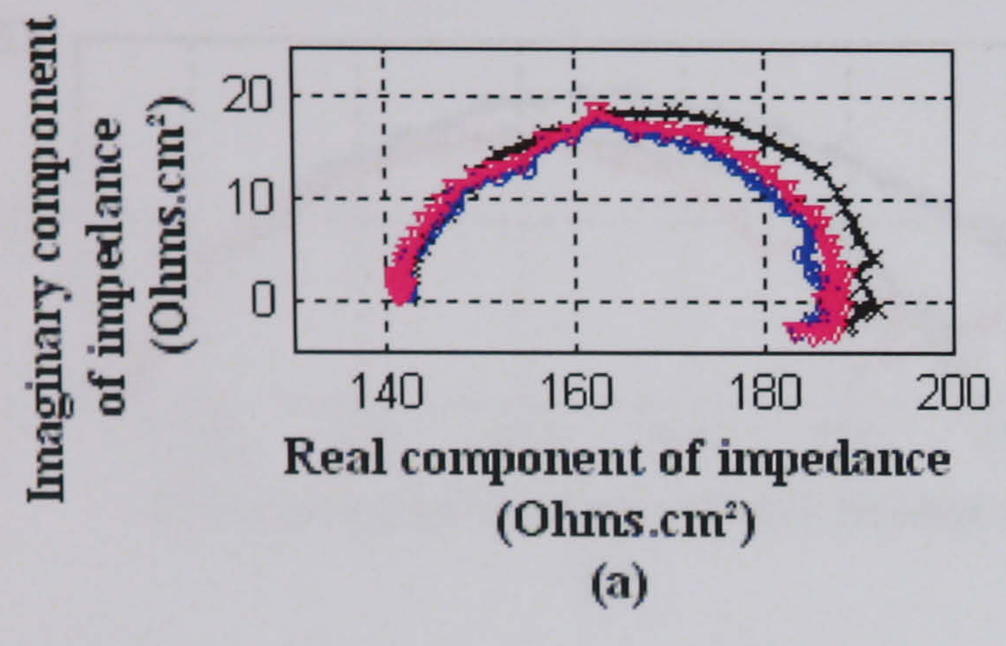
Imaginary component of impedance (Ohms.cm²)
20
10
0
140
160
180
200
Real component of impedance (Ohms.cm²)

(a)

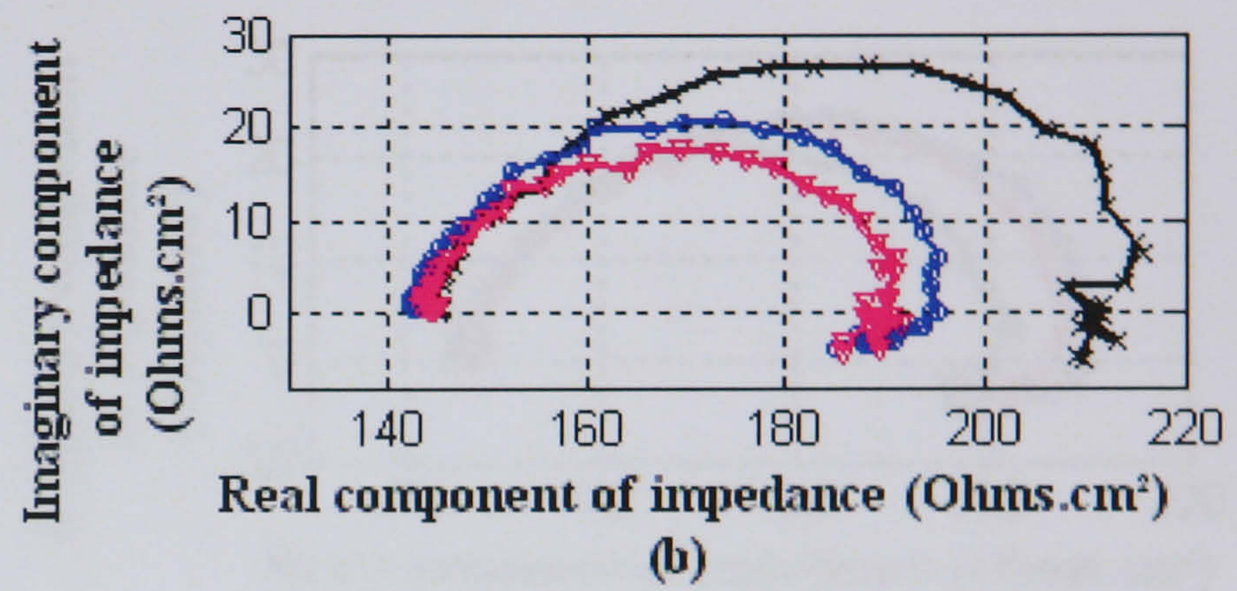
Imaginary component of impedance (Ohms.cm²)
30
20
10
0
140
160
180
200
220
Real component of impedance (Ohms.cm²)

(b)


Imaginary component of impedance (Ohms.cm²)
150
100
50
0
200
300
400
500
600
Real component of impedance (Ohms.cm²)

(c)

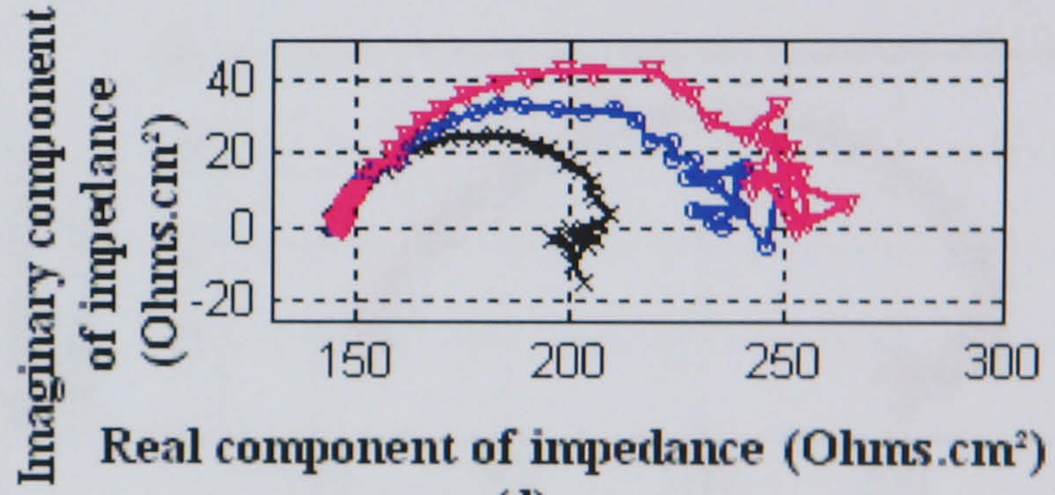
Imaginary component of impedance (Ohms.cm²)
40
20
0
-20
150
200
250
300
Real component of impedance (Ohms.cm²)

(d)

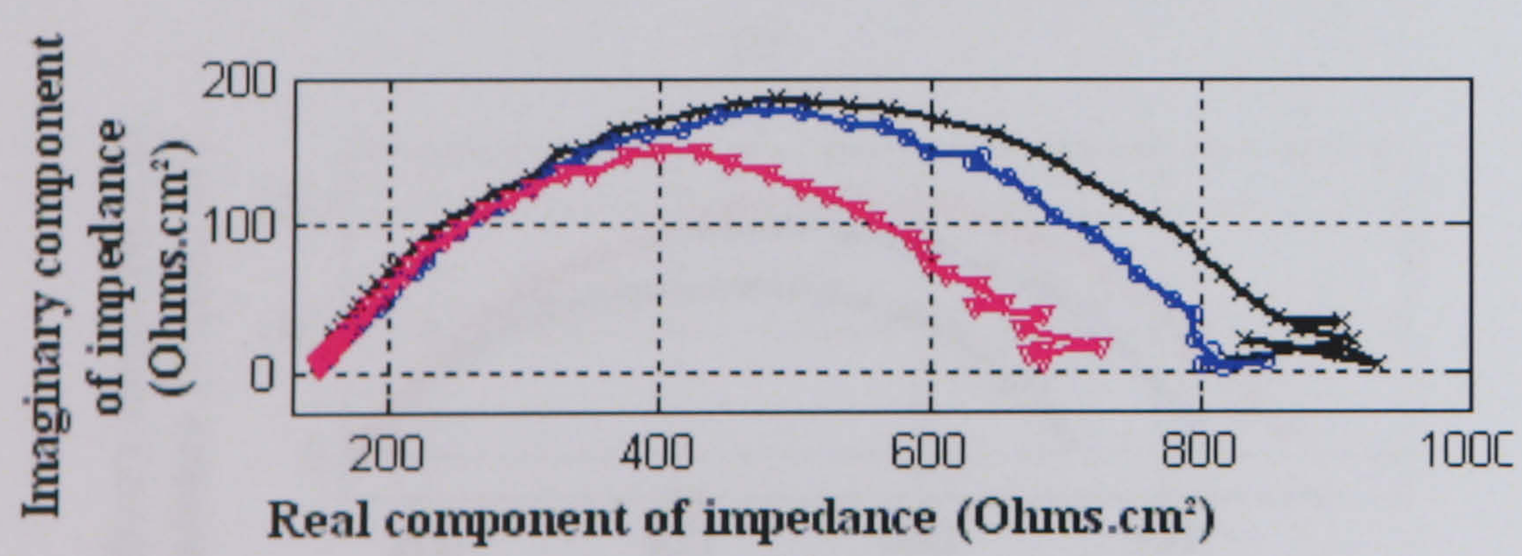
Imaginary component of impedance (Ohms.cm²)
200
100
0
200
400
600
800
1000
Real component of impedance (Ohms.cm²)

(e)

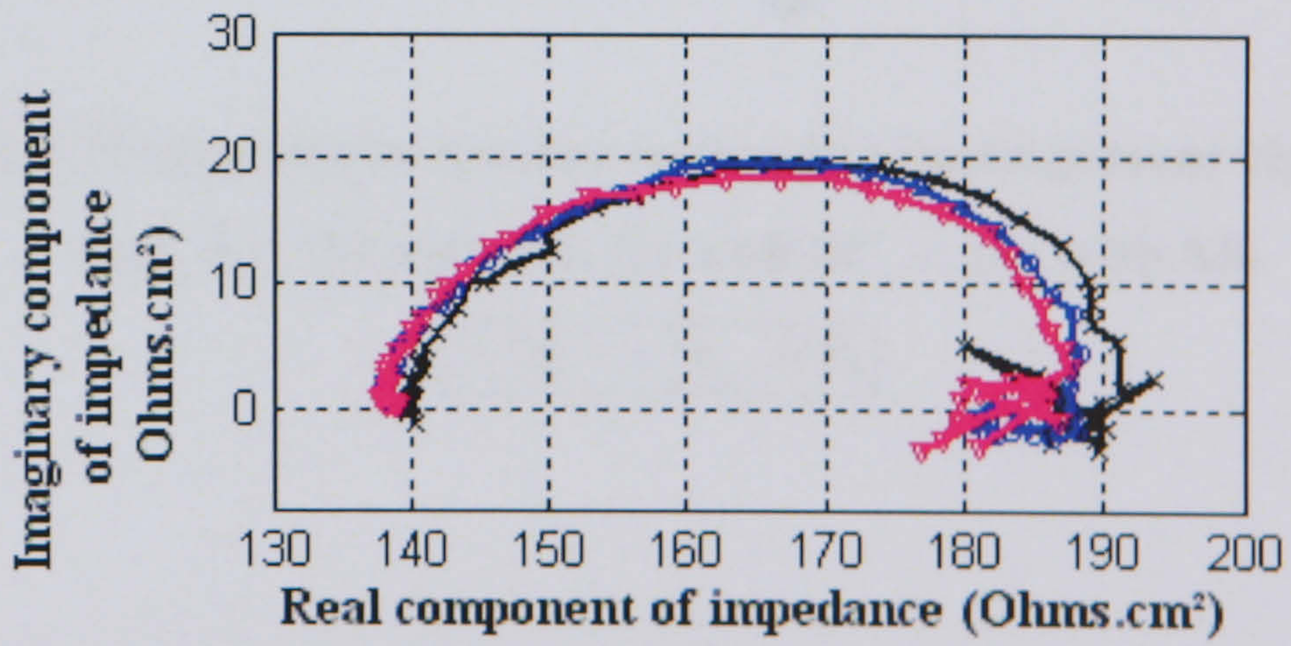
Imaginary component of impedance Ohms.cm²)
30
20
10
0
130
140
150
160
170
180
190
200
Real component of impedance (Ohms.cm²)

(f)

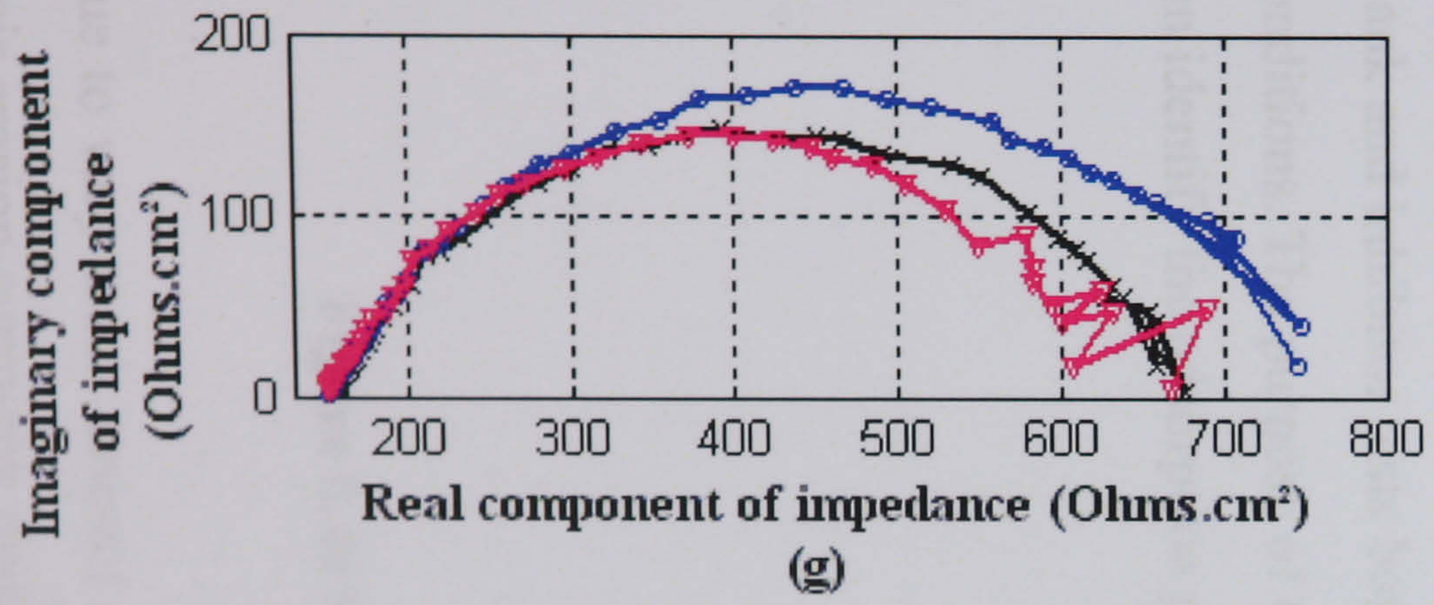

(g)

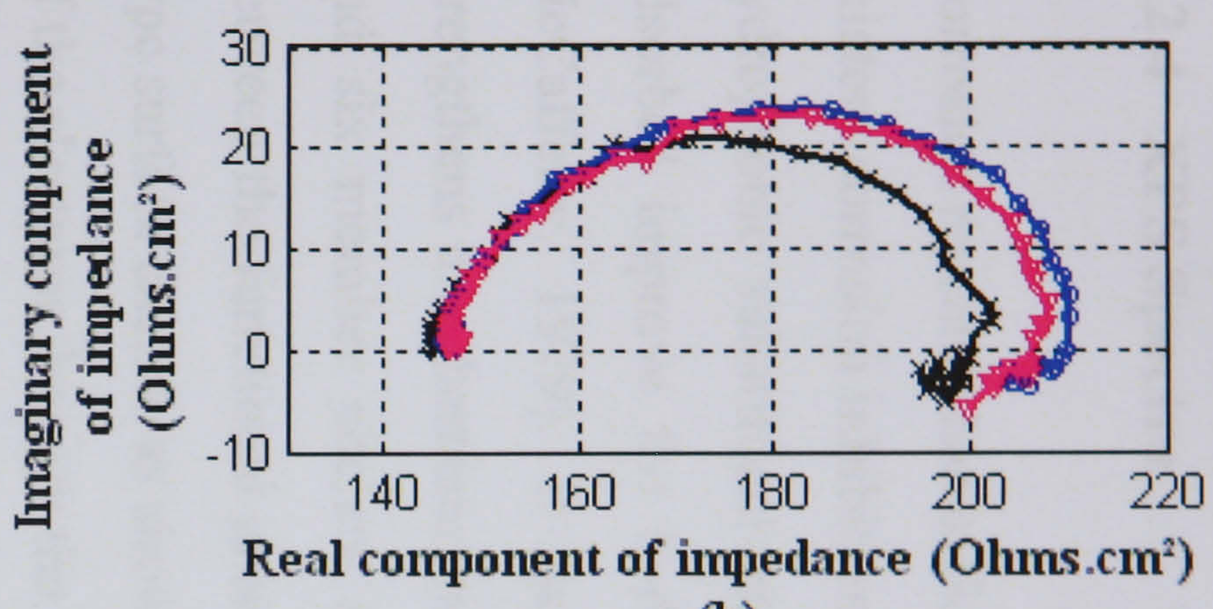

(h)

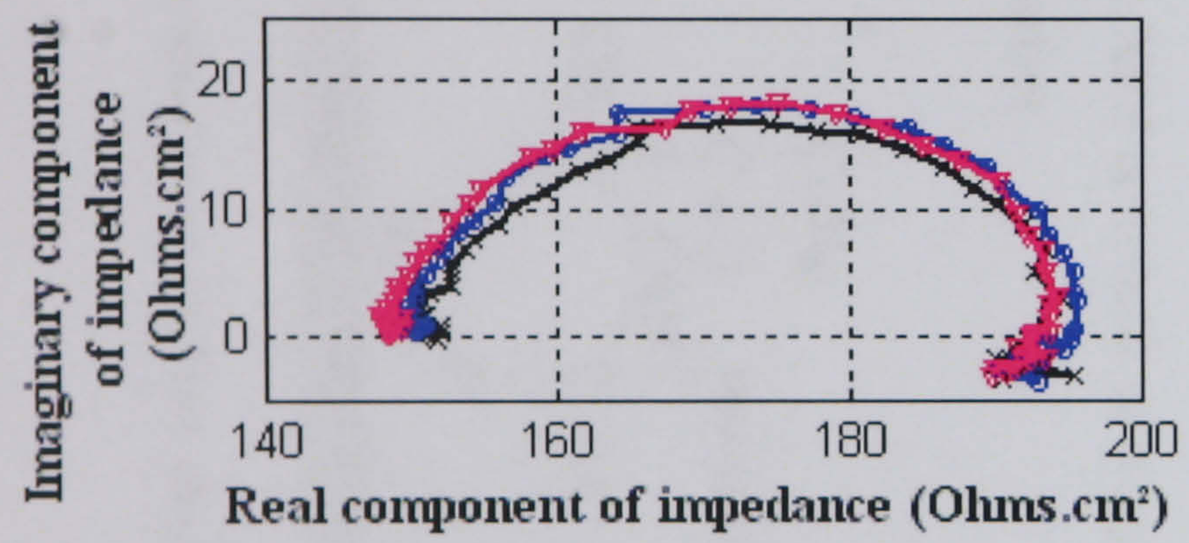

(i)

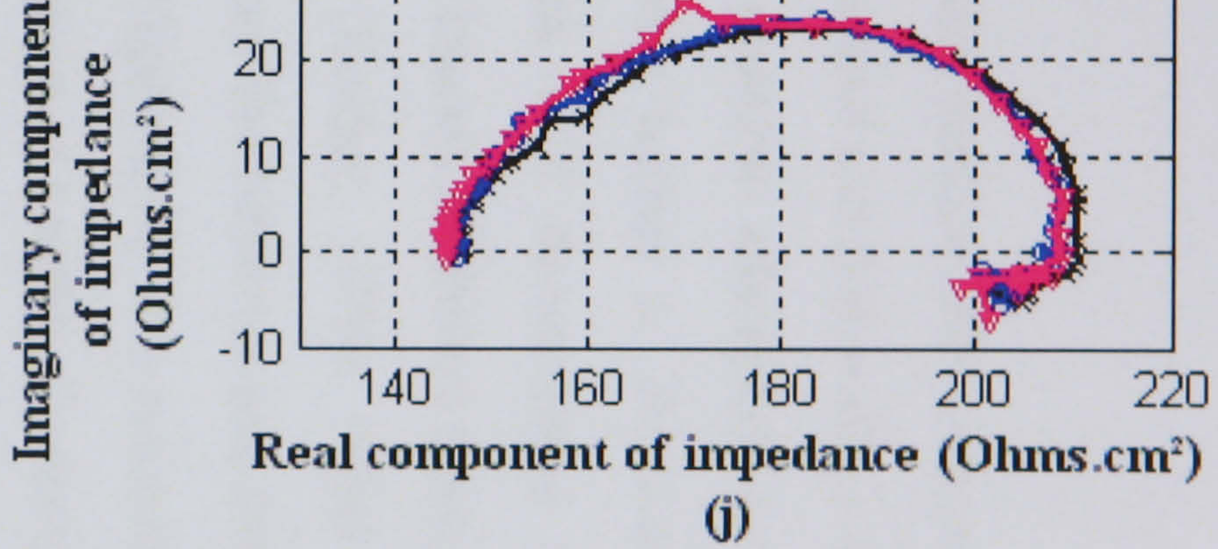

(j)

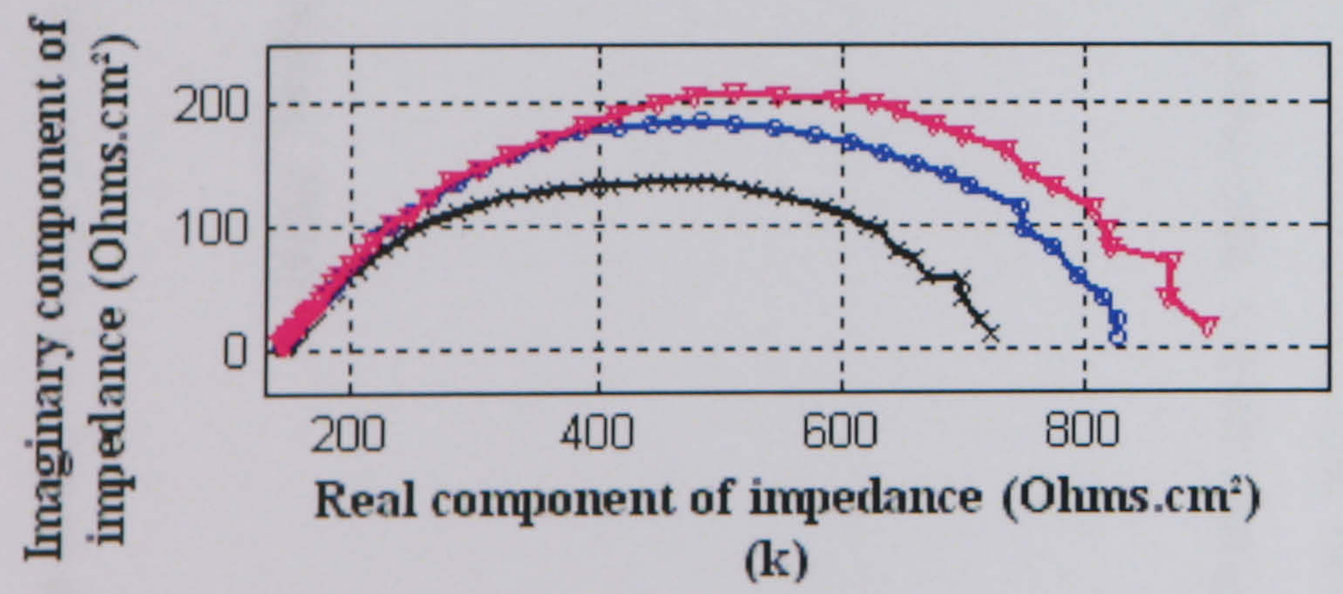

(k)

Figure 8.39 Impedance spectra tests using impingement rig for (a) with SA, (b) with SB, (c) with SC … (k) with SK

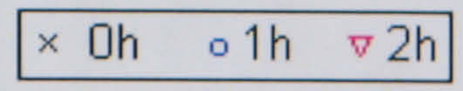

8.2.4 XPS Spectra

Corrosion research has indicated that surface chelation provides enhancement of already existent corrosion inhibition properties and that surface-active chelants possessing large hydrophobic substituent groups promote adsorption onto the steel surface and once adsorbed improve the hydrophobic barrier to electrolyte penetration (Nmai, 2004; McCafferty, 1979). It has been well documented that chelating enhances and strengthens the chemisorption of known inhibitors through the formation of stable five and six member chelate rings (Zecher, 1976). Nmai (2004) showed the bonding between the functional groups from the inhibitor and the cation metal in the sarcosine-type surface chelate as shown in Figure 8.40. It is resonance stabilized by delocalization of the electrons through the formation of a stable six-membered ring.

To identify whether the inhibitor components can be chemisorbed onto the metal surface by forming surface chelate and whether they can form bilayer film with $FeCO_3$ to protect the material from erosion-corrosion, XPS were practiced on samples after blank and inhibitor tests both at static conditions and erosion-corrosion multiphase flow conditions. The purpose of these XPS is to look at N and Fe in particular, which change can identify the adsorption properties.

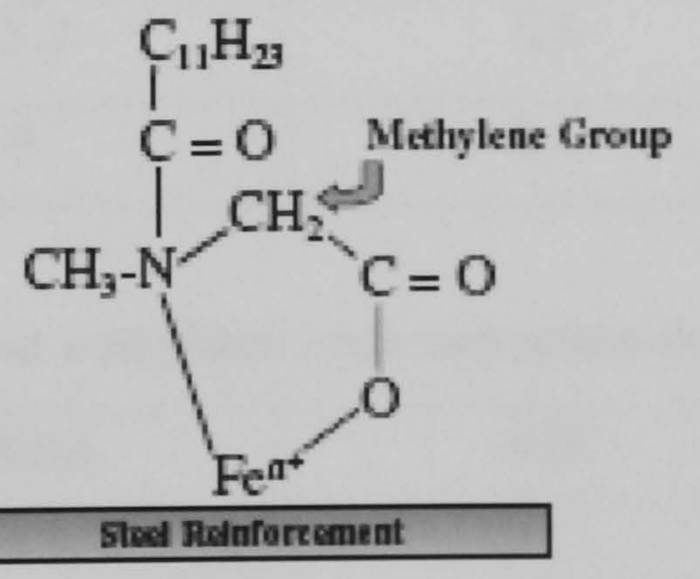

Figure 8.40 Sarcosine-type surface chelate (Nmai, 2004)

Due to very much amount of work involved in data collection and analysis, based on their erosion-corrosion performance, XPS was performed only two single components, namely SD and SK. SD was found as the worst single component while SK the best in

erosion-corrosion condition tests. XPS analysis was also performed on blank sample to make a reference for SD and SK. Quaternary ammonium chloride is the constitutive of the SD and SK consists of SD with ethoxylated imidazolines and anhydride/polyamine reaction products. The specimens were exposed to these conditions for 2 hours. Coupons were stored in vacuum desiccators until XPS analysis.

After a survey scan for blank test and inhibitor components SK and SD, long scans were conducted for iron, oxygen, carbon and nitrogen. The concentrations of these elements are given in Table 8. and Table 8.4 respectively. A reduction of Fe content on the surface for static conditions was noticed when SK and SD were added in the solution. This is because the inhibitor film blocked the iron ions reaction with carbonic acid and thus decreased the corrosion kinetic by forming a barrier on the metallic surface. For erosion-corrosion tests, the Fe content for blank test and with SD and DK tests is very similar. This indicates that under erosion-corrosion conditions, corrosion alone is not dominant factor.

Table 8.3 Static condition concentration comparisons

Element	Blank	SD	DK
O	58.9	38.9	38
C	29.2	52.4	56.2
Fe	11.9	5.0	4.6
N	0	2.6	1.2

Table 8.4 Erosion condition concentration comparison

Element	Blank	SD	SK
O	55.8	47.7	45
C	44.2	43.8	46.7
Fe	7.8	7.9	7.3
N	0	0.6	1.0

Figure 8.41 and Figure 8.42 show the comparison of Fe 2p spectra with blank, SK and SD under static conditions and erosion-corrosion condition respectively. A chemical

bonding of Fe appears at binging energy 719.8 eV for SD and SK for both static and erosion-corrosion conditions while in both cases it was absent for the blank tests. The binding energy indicates the presence of Fe^{3+} (Lasurface, 2006) which means it may form chelate on the metal surface.

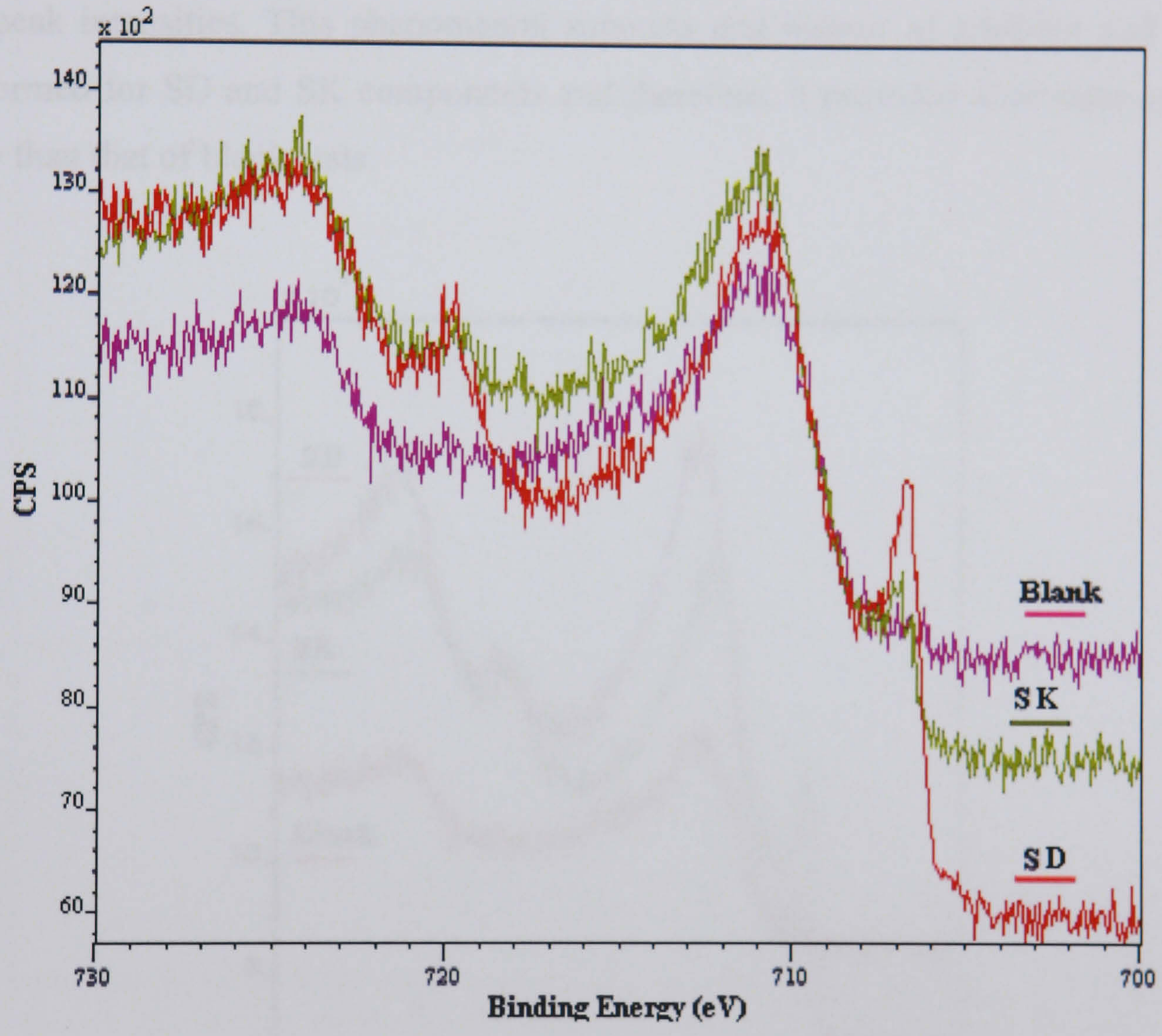

Figure 8.41 XPS spectra of Fe 2p for sample after static tests with blank solution, with single component SK and with single component SD

XPS analysis by Heuer and Stubbins (1998) reveals that the XPS C(1s), Fe(2p) and O(1s) peaks at binding energy 284.9 eV, 710.2 eV and 531.9 eV correspond to pure iron carbonate crystal. Both Figure 8.41 and Figure 8.42 show Fe 2p3/2 peaks at binding energy of 710.6 eV, which represent the formation of on the surface (Briggs and Seah, 1990). The presence of C1s peaks at 288.5 eV for static condition and at 288.2 eV for erosion-corrosion conditions was found and these binding energies clearly indicate the presence of CO_3^{2-} (Lasurface, 2006). Thus it supports the formation of $FeCO_3$ on the surface.

The intensity of the peak for $FeCO_3$ was very close to each other for static tests while it showed clear difference in erosion-corrosion tests. It is assumed that in static tests, the $FeCO_3$ was formed but not being stripped off for with single component or without, and hence showed the similar peak intensities. In contrast, the mechanical effect of sand particles stripped off the $FeCO_3$ for blank surface and thus provided difference in the XPS peak intensities. This phenomenon supports that bilayer of inhibitor and $FeCO_3$ was formed for SD and SK components and therefore, it provided a stronger adhesive ability than that of blank tests.

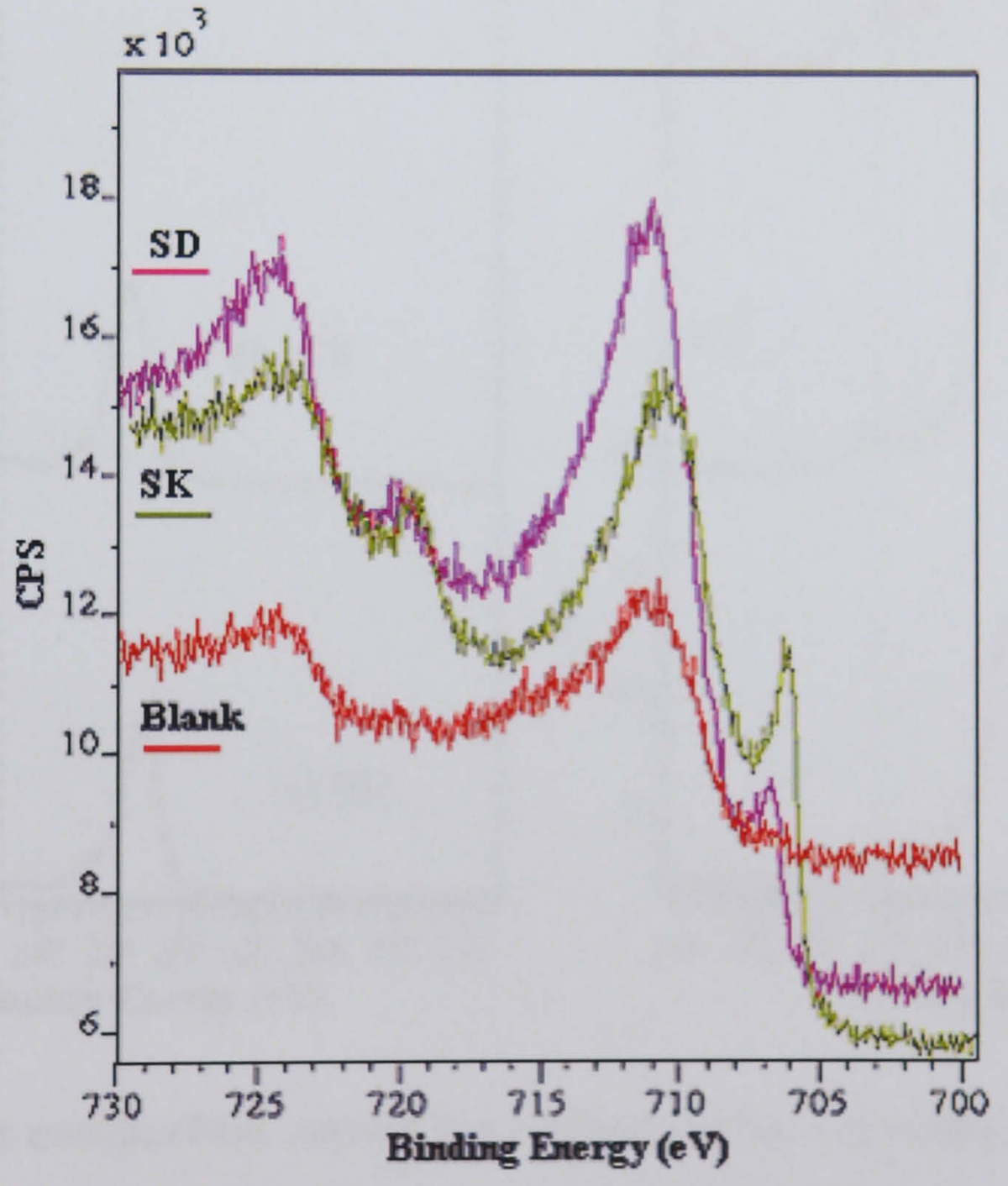

Figure 8.42 XPS spectra of Fe 2p for sample after erosion-corrosion tests with blank solution, with single component SK and with single component SD

In terms of N (1s) peak, detailed XPS N (1s) region long scans are shown both for static and erosion-corrosion conditions in Figure 8.44 and Figure 8.45 for SK and SD tests respectively. N(1s) peak exists for inhibitor tests only but the intensities are very low and do not show much difference between the two inhibitor components. The presence of nitrogen indicates that chelate was formed on the surface by both inhibitor single

components; however, because of small difference in peak intensities, it is not possible to compare their performance based on the N(1s) peaks.

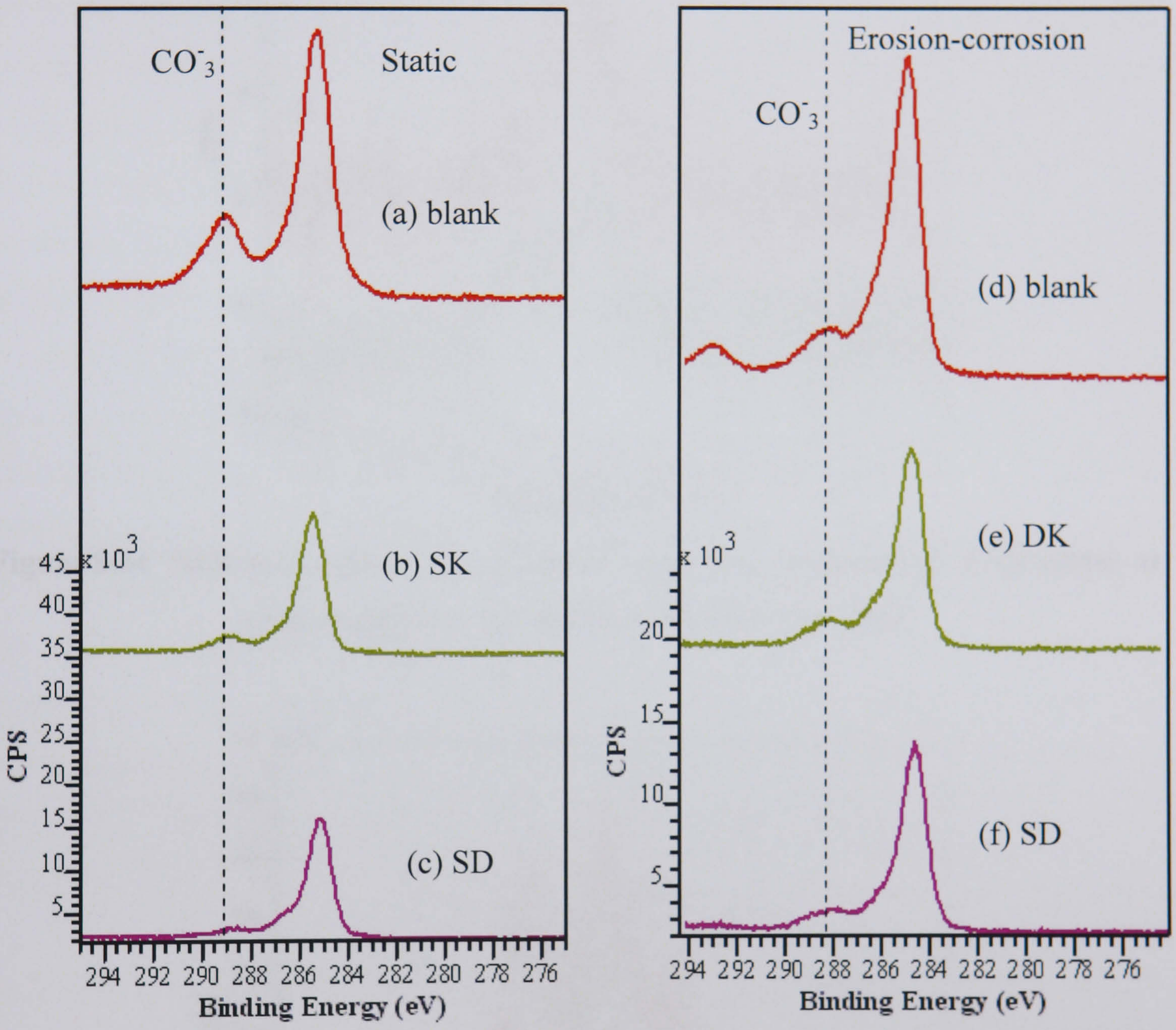

Figure 8.43 The comparison among the carbon peaks: (a) blank, (b) DK and (c) SD for static conditions; (d) blank, (e) SK and (f) SD for erosion-corrosion conditions

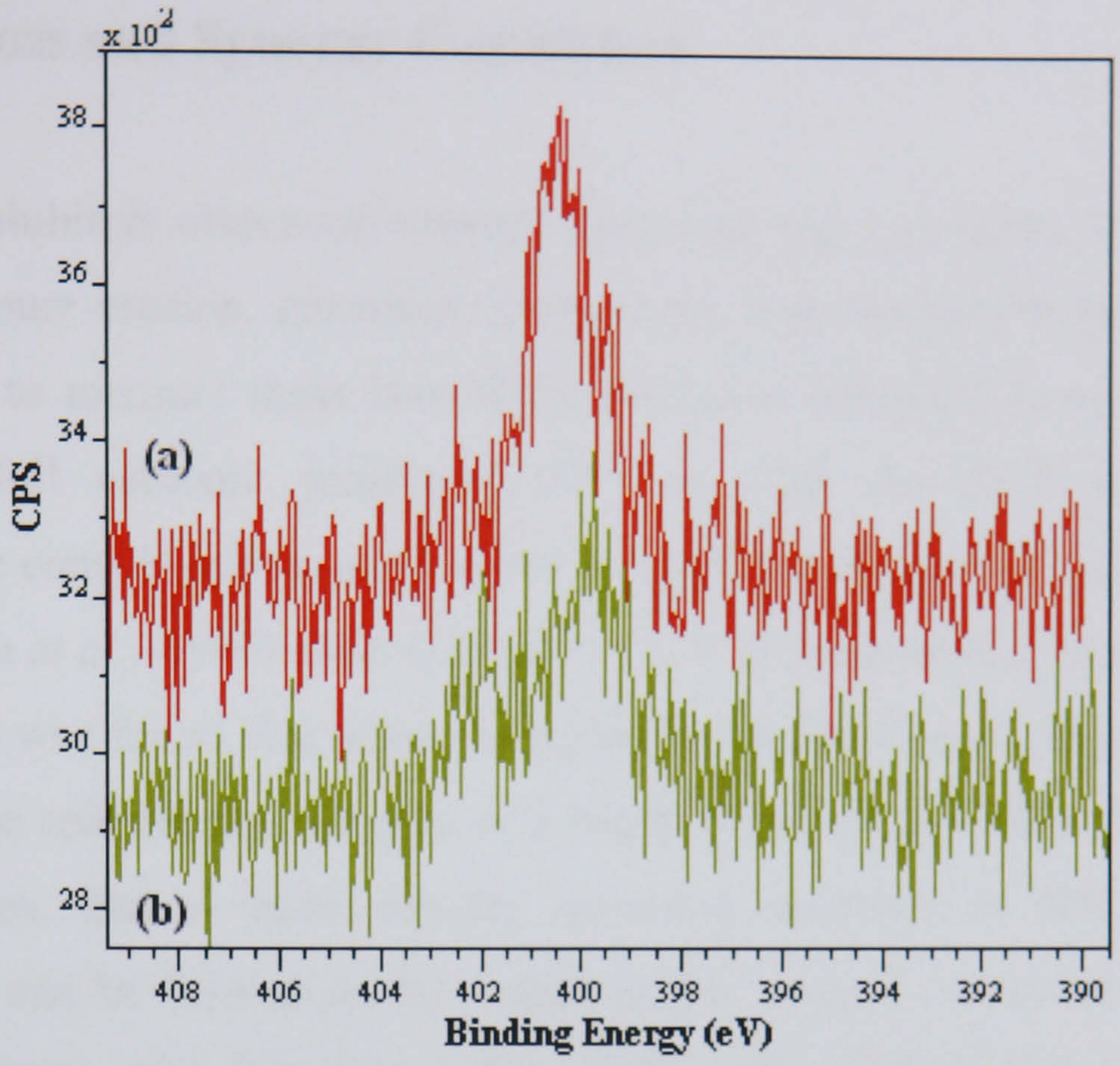

Figure 8.44 XPS N(1s) spectra for specimen with single component of SK under a) static condition, b) erosion-corrosion condition

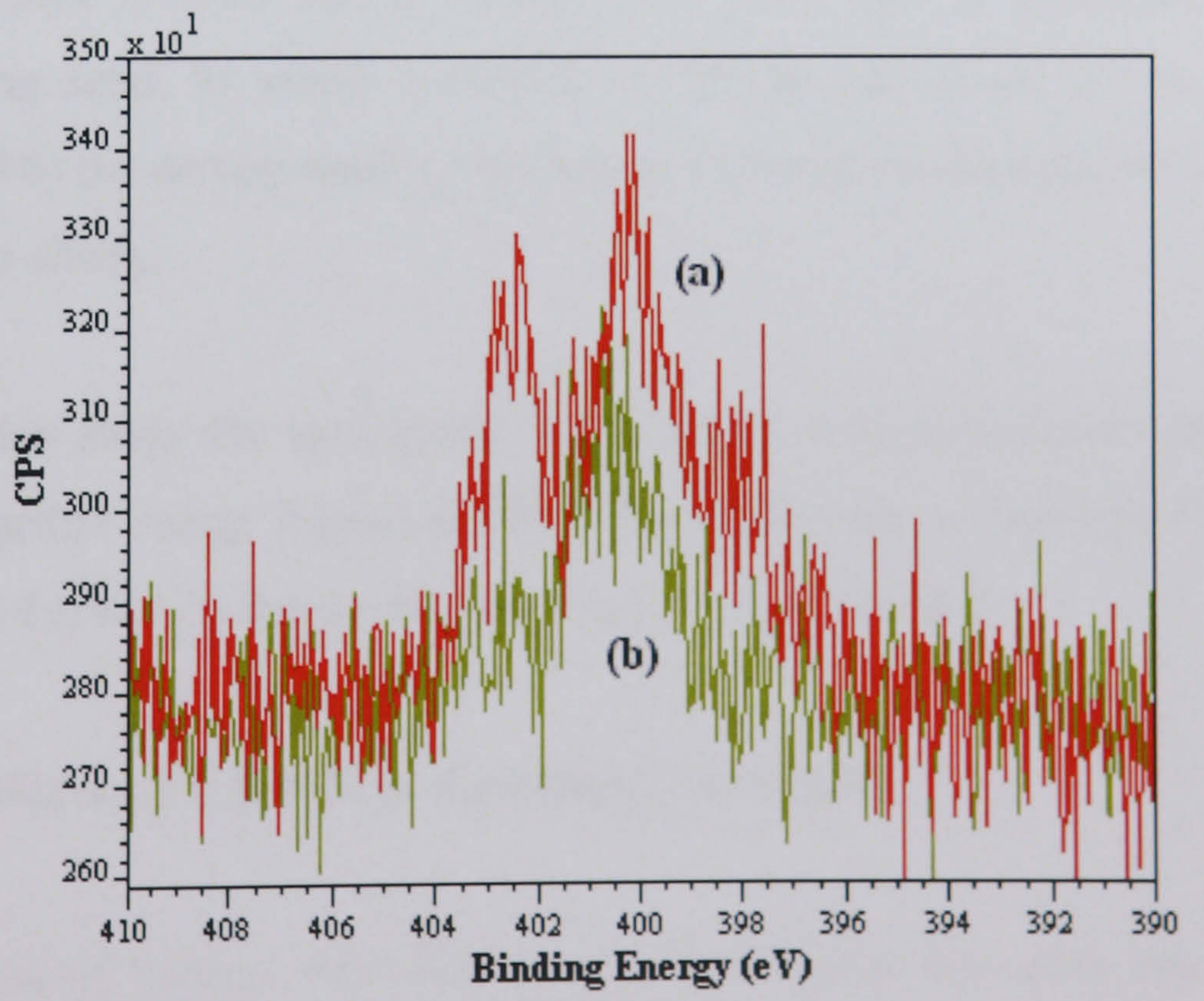

Figure 8.45 XPS N(1s) spectra for specimen with single component of SD under a) static condition, b) erosion-corrosion condition

8.3 Mass Loss and Synergy Calculation

In studies of inhibitors effects on erosion, corrosion and synergism, it is important to determine the pure erosion, corrosion components. One method of assessing the pure erosion rate is to measure mass loss of the specimen subjected to erosion conditions while under full cathodic protection (CP) as done for RCE tests. Based on thermodynamic considerations, polarisation at -0.8V should provide sufficient CP from corrosion. Zhou *et al.* (1996) used -0.95 and -1.0 V to measure the erosion rate with no inhibitor and it was found that when the potential moved to more negative values, the erosion rate was reduced dramatically as a result of iron redeposition of dissolved iron ions or complex. But as under erosion corrosion condition at 50°C, the corrosion products layer can be formed on the metal surface, even it is can be stripped away. With inhibitor tests, with CP applied, the inhibitor film formed will be altered as the electron acceptor kind of inhibitor will gain electron form the metal surface and change the inhibitor properties. Thus wrong erosion rate will be measured. Another method of measuring the pure erosion rate is to determine mass loss in deionized water or top water containing sand, in which corrosion would be minimized. From the results of Zhou *et al.* (1996) for carbon steel the corrosion occurred on the specimen surface in the deionized water slurry.

Therefore for this study the synergistic effect due to erosion and pure erosion rate are determined together using Equation (86). The corrosion component $C + dC_c$ were calculated from Faraday's law as the same method for RCE test.

8.3.1 The Effects of CRW8 on Erosion-Corrosion

The distributions of various contributors to overall mass loss after erosion-corrosion tests with CRW8 at various concentrations under impingement are presented in Figure 8.46. It can be seen that electrochemical corrosion in-*situ* conditions is only small part of the total damage, pure erosion and synergistic effects have more contribution to the material loss than the sum of erosion enhanced corrosion and pure corrosion.

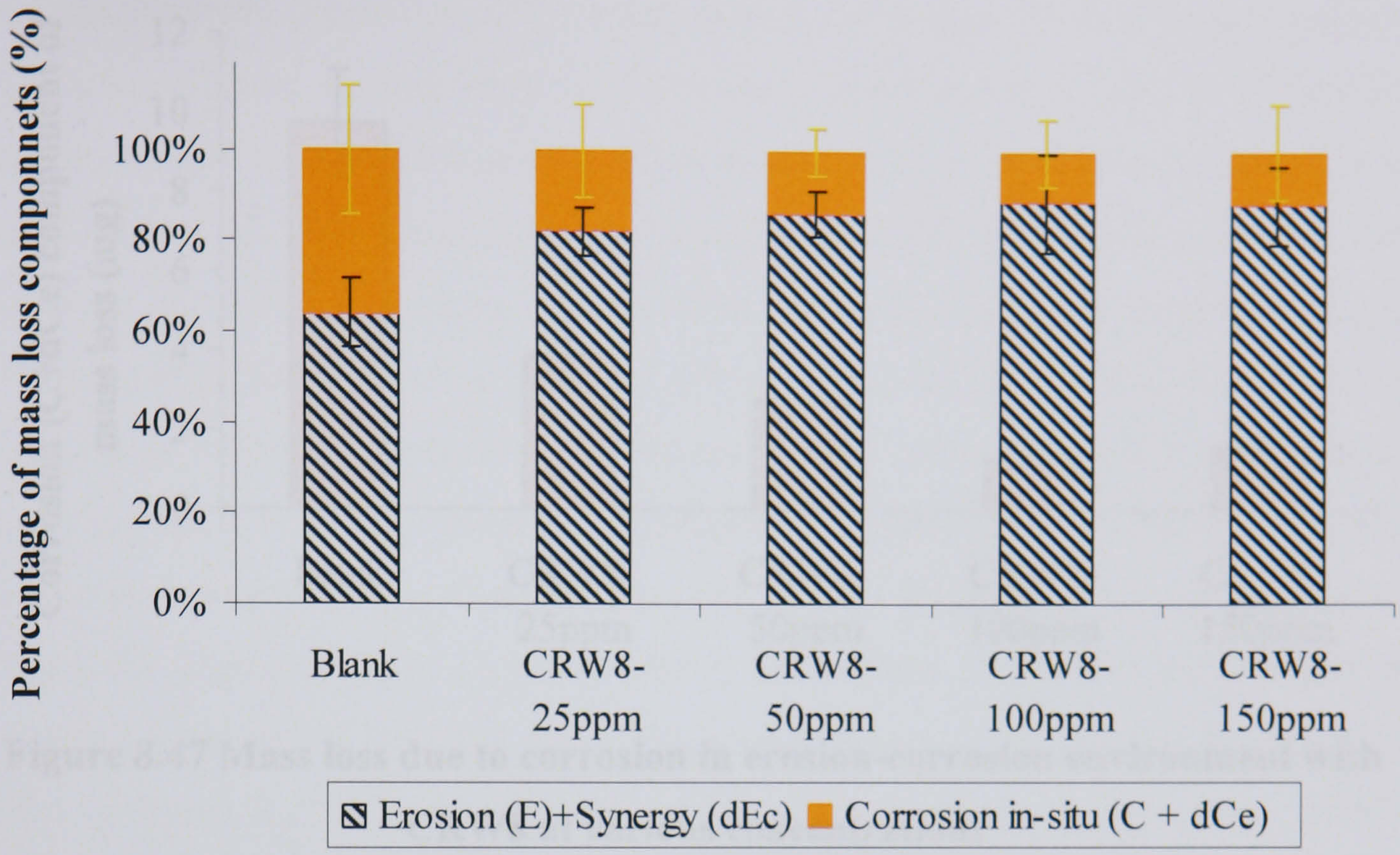

Figure 8.46 Contribution of total mass loss from its components for CRW8 tests at various concentrations

The inhibitor effects on corrosion with various concentrations can be seen from mass loss component of the total damage by corrosion with CRW8 at various concentrations, as shown in Figure 8.47. It can be seen the mass loss due to corrosion decreases from 0ppm to 100ppm, but increased from 150ppm. Namely, 100ppm is an optimum concentration for corrosion under this impingement conditions. This kind of peak-value-phenomenon could be associated with adsorption mode of inhibitor (Durnie *et al*., 2001). When inhibitor concentration is lower than 100ppm, adsorbed inhibitor molecules paralleled to metal surface and decreased the number of surface active sites, which was also the explanation by Jiang *et al*. (2004). The higher the inhibitor concentration is, the more inhibitor molecules adsorbed on the metal surface until the concentration reach to 150ppm. With the increase of inhibitor concentration, inhibitor molecules mutually repulsed more greatly. Then the molecules tended to perpendicularly adsorb onto metal surface due to electrostatic repellent function. In this case, small surface area would be occupied by each inhibitor molecule comparing with paralleled adsorbed one. This peak-value-phenomenon of inhibitor concentration also been verified by Singh (1993).

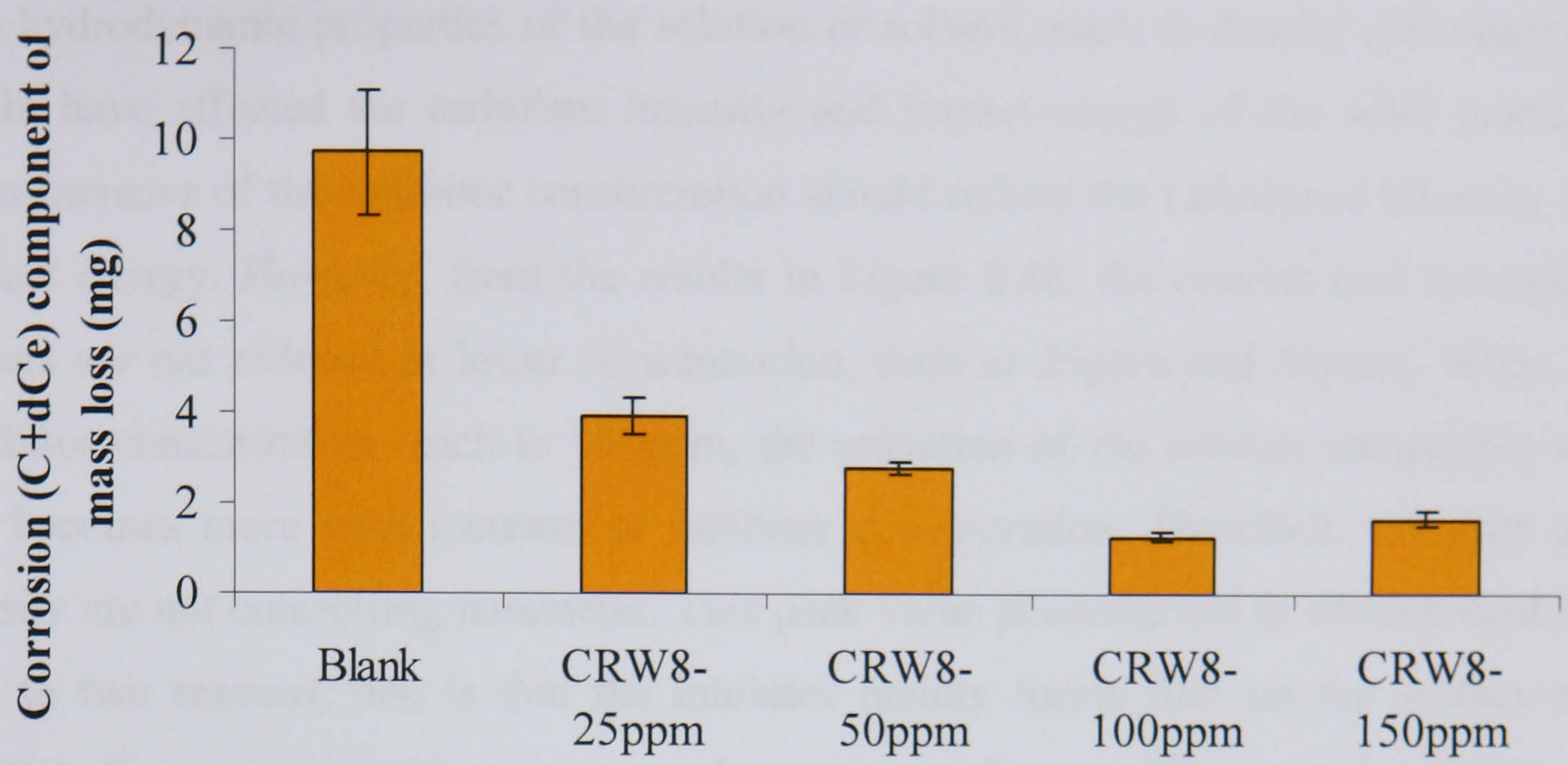

Figure 8.47 Mass loss due to corrosion in erosion-corrosion environment with CRW8 at various concentrations

The inhibitor performance to erosion component of the total mass loss can be seen from the mass loss calculated by Equation (86) and shown in Figure 8.48. The optimum concentration is still at 100ppm, with which the inhibitor has the largest effect to reduce erosion component of the total mass loss. The highest reduction to erosion component with CRW8 is about 40%.

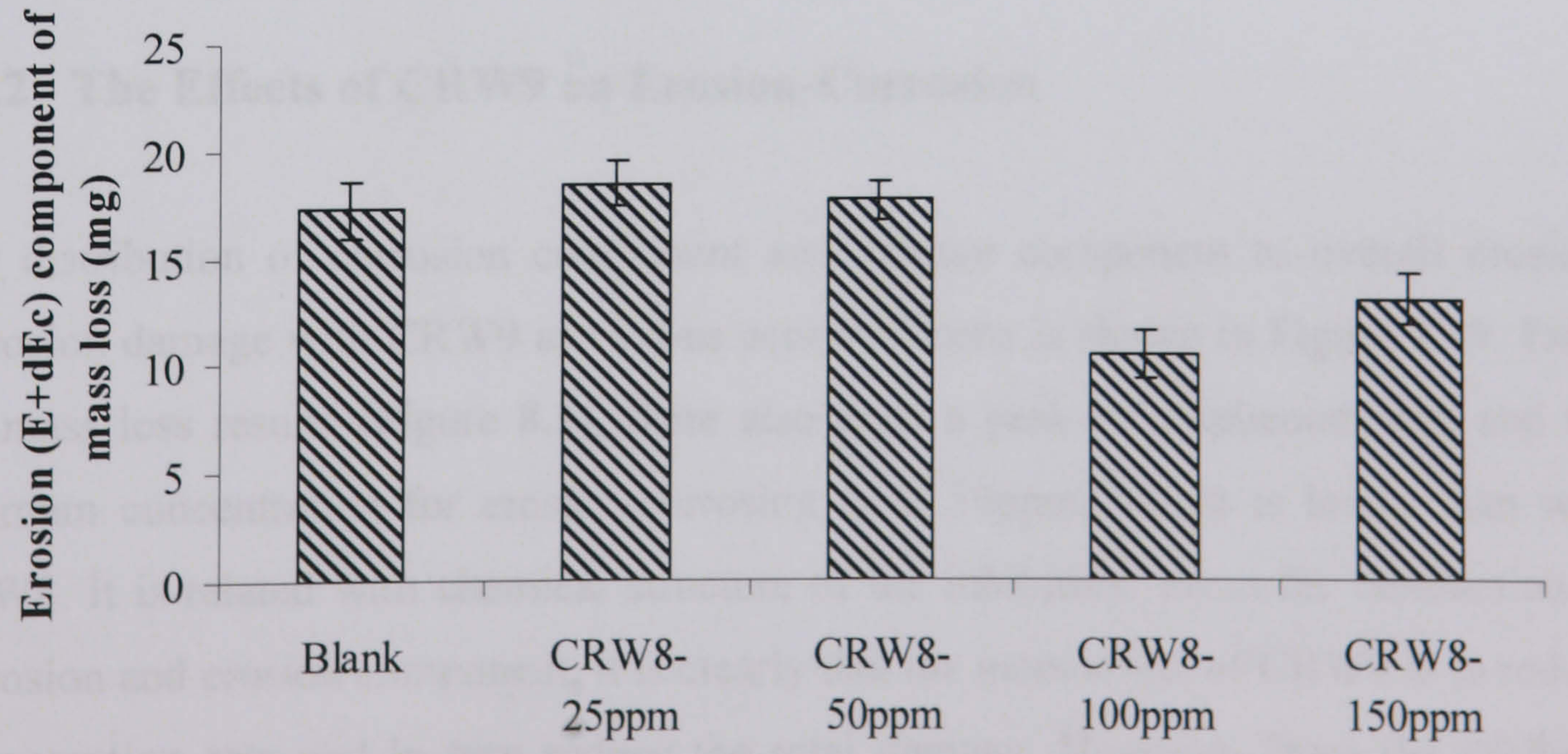

Figure 8.48 Mass loss due to erosion in erosion-corrosion environment with CRW8 at various concentrations

The hydrodynamic properties of the solution or solvent. such as density and viscosity. might have affected the turbulent intensity and impact energy of the solid particles. Thus increase of the inhibitor concentration should reduce the turbulence intensity and impact energy. However, from the results in Figure 8.48, the erosion and synergistic effects are not reduced at lower concentration, such as 25ppm and 50ppm. When the inhibitor concentration reach to 100ppm, the reduction of the erosion component was not becomes more with increase of inhibitor concentration. Therefore, viscosity and density are not controlling parameter. This peak value phenomenon to erosion could be due to two reasons; one is that the inhibitor mainly forms film on the surface and reduces the corrosion rate, in turn reduces the surface roughness and reduces the turbulence intensity of the local flow. The roughness result support the hypothesis as shown in Figure 8.21. The fact that the total erosion-corrosion behaviour was affected significantly by corrosion is in agreement with the work by Zhou *et al*. (1996). Another reason can be due to the at 100ppm, the inhibitor can form a rod like structure as a water soluble inhibitor forming a rod like structure can have drag reduction effects so as to reduce the wall shear stress and protect the metal surface from erosion (Schmitt, 2001). After all, as the inhibitor mainly reduce the corrosion component and as a result reduce erosion component so that mitigate erosion-corrosion damage to the carbon steel. Therefore, corrosion is dominant parameter under erosion-corrosion condition.

8.3.2 The Effects of CRW9 on Erosion-Corrosion

The distribution of corrosion component and erosion component to overall erosion-corrosion damage with CRW9 at various concentrations is shown in Figure 8.49. From the mass loss results (Figure 8.3), there also exist a peak-value-phenomenon and the optimum concentration for erosion-corrosion is at 50ppm, which is lower than with CRW8. It is related with chemical structure of the inhibitors. From the destruction of corrosion and erosion component, it is clearly that the main effect of CRW9 is to reduce the corrosion rate and in turn reduce the total damage. However. from the inhibitor effects to corrosion in Figure 8.50. it shows that with CRW9. the corrosion rate is reduced with increase of inhibitor concentration. When the concentration reaches to

100ppm the concentration will not effect to corrosion rate further. The maximum reduction effect to corrosion is about 82% efficiency at 100ppm.

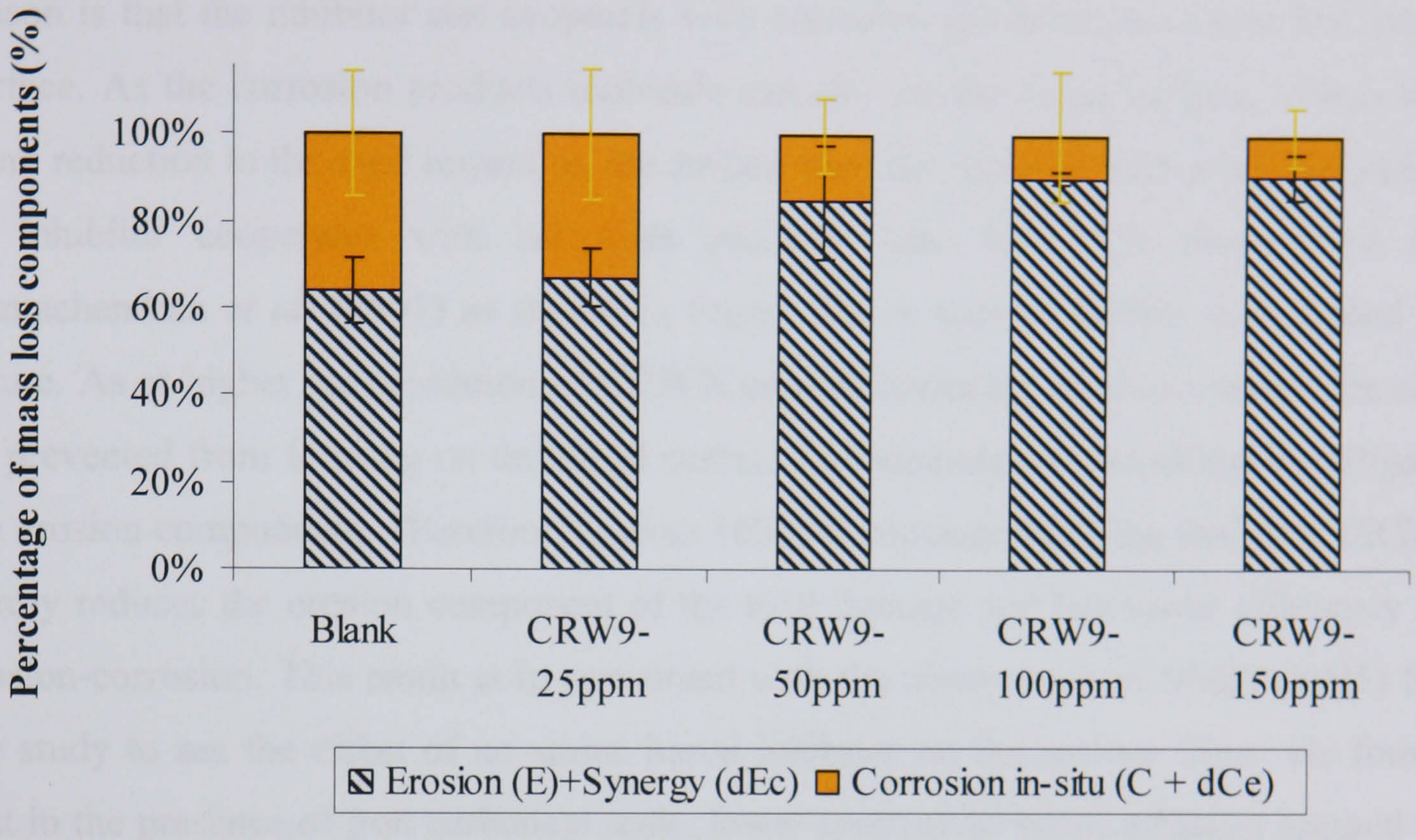

Figure 8.49 Contribution of total mass loss from its components for CRW9 tests at various concentrations

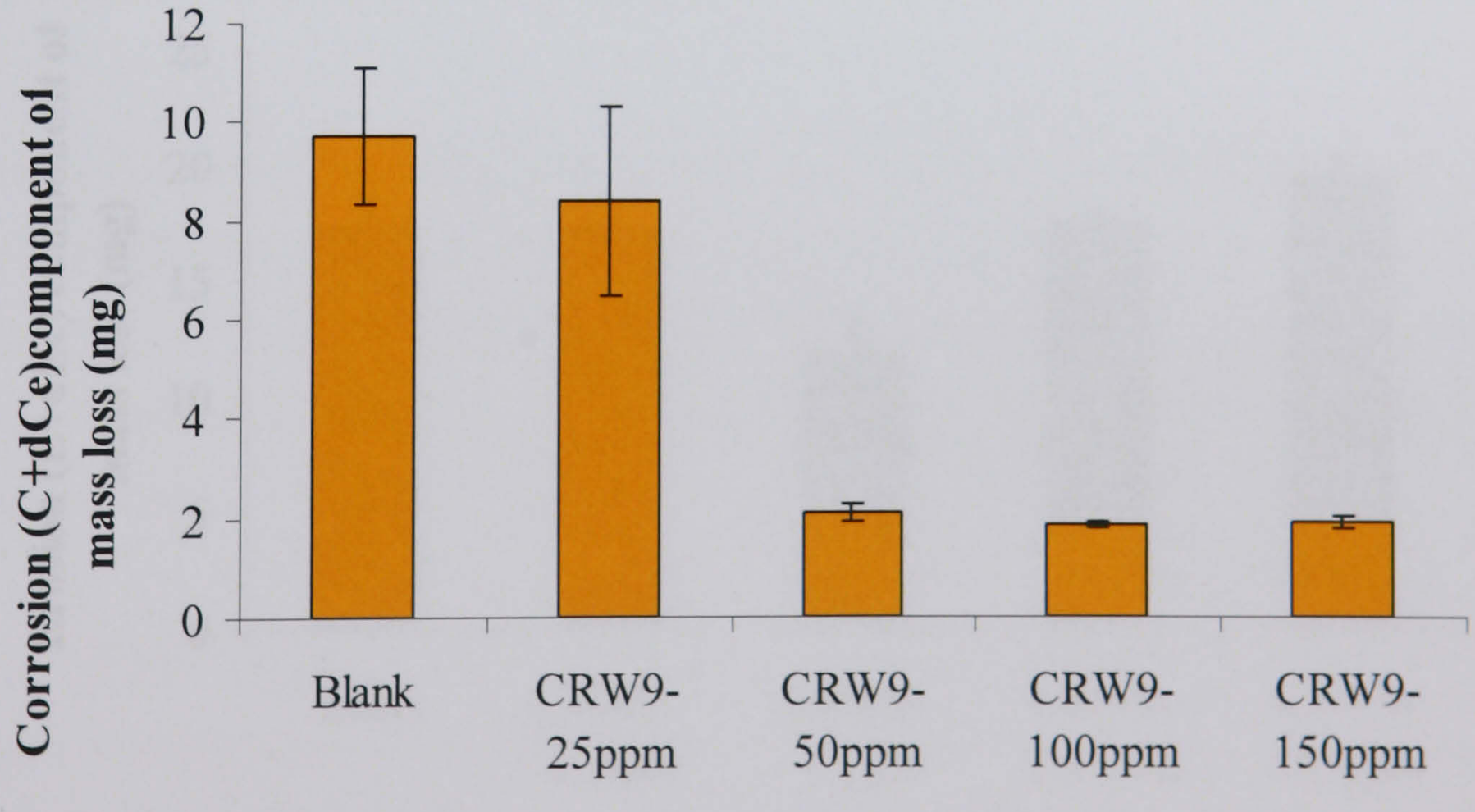

Figure 8.50 Mass loss due to corrosion in erosion-corrosion environment with CRW9 at various concentrations

It is interesting to know that the inhibitor effects to erosion component only happened at 50ppm as shown in Figure 8.51. And the efficiency to erosion component is about 30%.

It can be seen that at concentration lower than 50ppm, corrosion rate is as high as with no inhibitor. Thus the inhibitor has no protection to total damage. The most possible reason is that the inhibitor can cooperate with corrosion products formed on the metal surface. As the corrosion products molecule can stay on the metal surface, it then has more reduction to the sand impact on the surface than the inhibitor film itself. This kind of inhibitor cooperates with corrosion products film has been investigated by Ramachandran *et al.* (2001) as shown in Figure 3.8. It will be further investigated in future. As at higher concentration of CRW9, enough corrosion products molecules can be prevented from forming on the metal surface to cooperate with inhibitor to mitigate the erosion components. Therefore, beyond 100ppm concentration, the inhibitor CRW9 hardly reduces the erosion component of the total damage and has lower efficiency to erosion-corrosion. This result is in agreement with the observation of Malik (1995) for the study to see the effect of an amine based inhibitor on the surface films. He found that in the presence of iron carbonate scale, lower concentrations of inhibitor seemed to work better than the higher concentrations. He also found that in the presence of inhibitor, there was a transformation of the surface structure of iron carbonate.

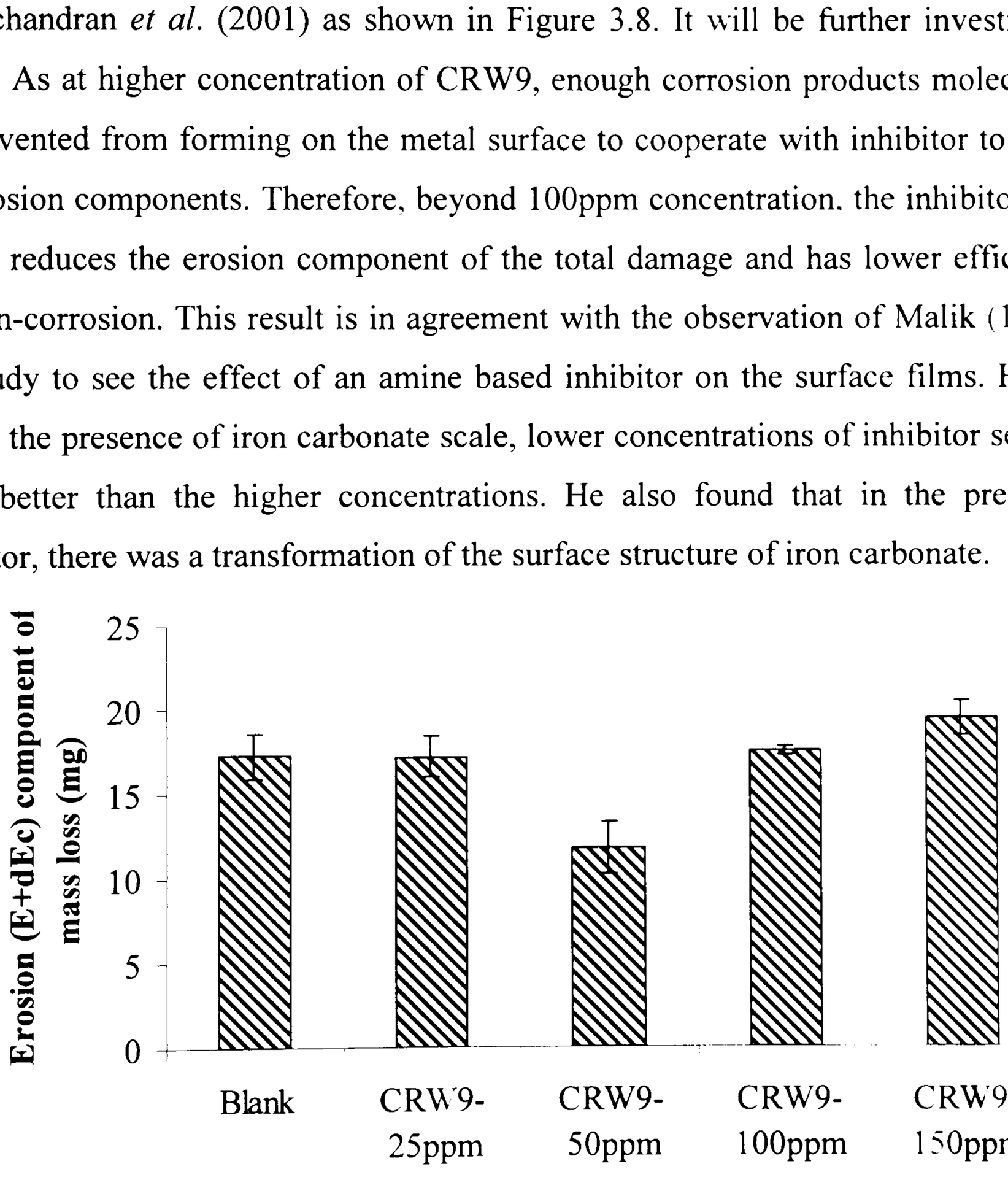

Figure 8.51 Mass loss due to erosion in erosion-corrosion environment with CRW9 at various concentrations

It should be mentioned that corrosion current density can also be measured using anodic polarisation method. The advantage to use anodic polarisation is that it can provide information on the Tafel slopes with or without inhibitor to provide more accurate data

on corrosion in-situ components. However, the corrosion components calculated with Tafel constants β_a and β_c of 0.06 V/decade or 0.12 V/decade make little difference on the percentage of the corrosion mass loss over the total damage. The advantage of using AC impedance and LPR techniques is to enable to continuously monitor the corrosion rate with time which is important for investigating the inhibition mechanisms.

Nesic *et al.* (1995) observed that in the presence of iron carbide as well as iron carbonate scale the performance of an imidazoline-based inhibitor was very poor. They concluded that it was the changes on the steel surface due to the precorrosion, which as responsible for the weaker performance of the inhibitor rather than the scale itself acting as a diffusion barrier for the inhibitor. Therefore, it also important to investigate the inhibitor effects to erosion-corrosion with precorrosion in future.

8.4 Summarising Corrosion and Erosion-Corrosion Results and Discussion Using Impinging Jet

Corrosion component is about 36% of the total damage. Erosion is the predominant under impinging flow condition with sand. Inhibitor reduce the corrosion component by forming film on the metal surface and also inhibition leads to smaller roughness factors and hence would lower pressure drop at higher flowing rates so that increase the production rates.

Both of the two inhibitors tested with SIJ have peak-value phenomena, for CRW8, the optimum concentration is 100ppm and for CRW9, is 50ppm according to corrosion behaviour *in-situ* conditions.

Mixture of the inhibitor components has better performance of mitigation of erosion-corrosion than individual chemicals. Thus the single components mixture of SK has the best resistance to corrosion and erosion-corrosion under multiphase flow of high speed with sand.

CHAPTER 9 CONCLUSIONS AND FUTURE WORK

9.1 General Conclusions

This work has been carried out to investigate the corrosion and erosion-corrosion behaviour of the four commercial organic inhibitors. The mechanism related to the corrosion and erosion-corrosion processes have been identified, analysed and quantified under different conditions and configurations.

Inhibitors can play a role in reducing damage in erosion-corrosion and that effect is by affecting more than corrosion processes. Under both configurations (RCE and SIJ), the erosion-corrosion interaction is the main component of damage, but corrosion is also a controlling parameter. With increasing flow rate and shear stress, erosion damage becomes more dominant.

- In the submerged impinging jet condition, the material degradation is erosion-corrosion more due to sand erosion; in the RCE condition, it is erosion-corrosion more due to the flow induced corrosion. For both configurations, inhibitor reduces corrosion by forming an inhibitor film on the metal surface; and it reduces the erosion by both forming an inhibitor film on the metal surface and adsorption onto the sand surface, which reduce the impact energy of the sand.

- The information of charge transfer resistance from AC impedance tests which could be compared with linear polarisation results provides a very useful way to study performance of inhibitors. Other information such as double layer capacitance can be used to characterize the mechanism of the inhibitor film.

- Extensive protective carbonate films on the metal surface did not form in this work, primarily due to the lower temperature and CO_2 partial pressure. Notwithstanding this the inhibitor still has a significant effect in reducing erosion-corrosion.

9.1.1 Static Conditions

Free corrosion measurements in static conditions show that all the inhibitor used are anodic kind of inhibitors as with addition of inhibitors the E_{corr} shifts in the noble direction. The amount of shift is expressed by the decrease of activity of iron. In obtaining nearly 100% inhibition efficiency for pure corrosion, the reduction of activity of iron with CRW8 and CRW9 reaches to 0.0005 to 0.0002 respectively. CRW9 has the highest corrosion resistance under static conditions. The amount of reduction of the metal activity can be used as criteria to estimate the inhibitor performance under static conditions.

The change of the potential with time not only provides details on the nature of the inhibitors, but also reflects its rate of adsorption on the metal surface. At 20°C, when there is no corrosion product formed on the metal surface, the free corrosion potential is constant in the blank solution, while small fluctuations are observed for inhibitor tests, related to the inhibitor adsorption processes. In the case of CRW9, the potential shifts negative with time, while the corrosion resistance increases.

With addition of inhibitor the linear polarisation curves show increased oscillation with immersion time. The thicker the inhibitor film, the more oscillation occurred on the plot.

Accuracy of linear polarisation measurements in determining corrosion rates is reduced if there is a corrosion product scale or inhibitor film formed on the metal surface. This is because the technique measures the total resistance and does not separate the resistance of the electrochemical corrosion process from the resistance of the corrosion product scale or inhibitor film. Therefore, linear polarisation used in this work can give a semi-quantitative idea and good indication of correct equivalent circuit (EC) selection for analysis of AC impedance data.

The best performances of inhibitors are water soluble CRW8 and CRW9. Both can form a denser barrier on the metal surface, especially for CRW9, the charge transfer

resistance reaches 116000 Ohms.cm² which is comparable with effective coating systems. The addition of the inhibitor reduces the double layer capacitance value to approximately 35 μF/cm². The reduction factors (ψ = 94.2%) for C_{dl} indicate that most of the effect of inhibition depends upon C_{dl} and only a small part depends upon other components of the equivalent circuit like the diffusion element.

Under static conditions, the penetration rate for blank tests is about 50 mpy. A dense film formed on the surface can change the electrochemical kinetics greatly, and can give 99.4% efficiency up to 100 hours immersion time. Oil soluble inhibitors did not give as good efficiency as the water soluble ones. This is due to the inhibitor having poor hydrophobic properties, resulting in unevenly layer of the inhibitor film and more pores.

The impedance spectra show that corrosion system basically has the characteristics that the diameter of the Nyquist semicircle decreases continuously, the peak angle shifting continuously to the lower frequency range.

Under static conditions, the corrosion includes general corrosion and pitting corrosion: pitting if initiated will start from the grain boundaries and extend into the pearlite phase.

9.1.2 RCE Conditions

At 20°C and 1000rpm, all the inhibitors offer a degree of protection when compared with the uninhibited case. CRW8 has the best performance with the inhibitor efficiency of nearly 100%; CGO also provides reasonably good efficiency (80%). The hydrodynamic factor under this condition made the inhibitor reach the metal surface easily for CGO, resulting in higher corrosion resistance than under static condition but not the case for CRO.

At 20°C and 6000rpm, CGO and CRO offer no reduction in mass loss compared to blank solution; CRW9 offers the most reduction in mass loss. It has the potential to be used as an inhibitor under erosion-corrosion conditions. With blank tests, the

penetration rate can be as high as 160 mpy. CRW9 can achieve the reduction of the mass loss of about 80%.

At 20°C and 6000rpm, for CRW9, increase of inhibitor concentration, the inhibition efficiency increased. At the concentration of 50ppm there is a small increase in the mass loss compared to the uninhibited test. As the inhibitor concentration increases to 100ppm and 150ppm the efficiency was improved substantially.

At 1000rpm, for blank tests the mass loss at 50°C is lower than at 20°C. This is likely to be caused by the corrosion products accumulated on the metal surface protecting the carbon steel from erosion-corrosion. At this condition, AC impedance measurements also show that the corrosion resistance reduction during the test duration. Corrosion products can be formed although XRD showed there to be very small amount at 50°C.

At 50°C and 6000rpm, all the inhibitors have some inhibition effect, among which CRO and CRW8 have the best performance. The results show the combination of rotational speed and temperature is the most important factor to affect the inhibitor efficiency. CRW9 has the best performance at higher rotational speed but lower temperature, while CRW8 provides better efficiency compared with others at higher temperature.

Oil soluble inhibitors (CGO and CRO) cannot provide protection with increased shear stress. CRO could not provide protection under any flowing conditions at low temperature. However, CRO can reduce pitting size at higher temperature, even at 6000rpm rotational speed. The pitting size is the smallest among all the tests. CRO performance is better compared to other inhibitors at higher temperature than at lower temperature.

Due to iron dissolution, the cementite from the pearlite is left on the surface, making the surface rough. Surface analysis supports the results from corrosion and erosion-corrosion measurements. Inhibitors can reduce the general corrosion and reduce the surface roughness. When the corrosion products or inhibitor film were stripped by the flow or sand, the area with no film layer covered corroded at a higher rate than the ones

covered by film, pitting corrosion happens. Inhibitor with good efficiency can effectively reduce the pit number and pit size.

Inhibitors with the characteristics of absorption on sand can not only affect the corrosion component by forming a film on the metal surface but also reduce erosion component of the total damage by reducing the sand impact both due to forming a film on the metal surface and absorbed on sand.

With applying CP, corrosion is reduced significantly. The most important aspect is that with applying CP and in addition of inhibitor. the mass loss is lower than with applying CP alone. This indicates that even the inhibitor film is changed after applying CP. it still shows that inhibitor can reduce erosion damage to the metal surface perhaps by reducing the sand impact energy.

To test whether the inhibitor is anodic or cathodic type. static conditions are necessary to avoid the potential agitation due to high speed.

With CRW8, it shows that at 1000rpm and at 20°C the R_p values were extremely large. indicative of the inhibitor forming a film which imparts a large resistance to charge transfer on the metal surface. Also the film appeared to remain intact and no significant lowering of R_p over time occurred. It is postulated that the high and constantly corrosion resistance plays an important role in reducing erosion-corrosion and providing high inhibition efficiency.

Except at 1000rpm and at 20°C for CRW8. in other inhibitor tests. R_p values drop as exposure time progresses. This is an indication that an inhibitor film is formed on the metal surface and the coverage can be reduced by flow and sand impact. Increasing the rotating speed, accelerates the desorption process due to the increased shear stress.

R_{ct} is more accurate than R_p. because R_p value includes the resistance of any film formed on the metal surface and of the metal substrate. while R_{ct} only represents the resistance of the metal/electrolyte or metal/film interface.

The corrosion process under the tested conditions is mainly under charge transfer-control. Tests with inhibitor include both electrochemical kinetic and diffusion processes. Two time constants of $CPE_{film}R_{film}$ and $CPE_{dl}R_{ct}$ can be used to describe the dielectric properties of the inhibitor film and the charge transfer process at the metal substrate when inhibitor offers high efficiency. CRW8 with nearly 100% efficiency also exhibits diffusion behaviour. With inhibition efficiency decreasing, inductive behaviour likely exists. The inductive behaviour can result from the combination of corrosion products and inhibitor molecules on the metal surface as well as their removal from the metal surface. The calculated parameter from AC impedance results can be compared with those for blank tests to get the information about inhibitor film characteristics. The smallest value for capacitance is about 40 μF/cm² with CRW8 at 1000rpm and 20°C. The biggest one with blank tests at 6000rpm and 20°C is about 15 mF/cm².

At 20°C, there is no corrosion product layer formed on the metal surface. The corrosion component (measured as an *in-situ* corrosion rate, C+dCe) is about 25% of the total damage, increase the rotational speed from 1000rpm to 6000rpm the corrosion rate increased about 2%. At 50°C, the corrosion component is 57% to 75% of the total damage, increase rotational speed; the corrosion rate is increased about 20%. At 50°C and 6000rpm rotational speed, corrosion products can not be formed due to the high flow rate with sand.

9.1.3 Impinging Jet Conclusion

In terms of penetration rates (of the order of 1200mpy), tests using impinging jet lie in the severe erosion-corrosion regime. At all concentrations the inhibitors are effective in reducing mass loss over the 2-hour test duration mass loss for carbon steel with inhibitor approaches the mass loss on stainless steel UNSS31603. The highest inhibition efficiency with inhibitor is 56% with 100ppm CRW8.

Both of the two inhibitors tested with SIJ have peak-value phenomena, for CRW8, the optimum concentration is 100ppm and for CRW9, is 50ppm according to corrosion behaviour *in-situ* conditions.

The corrosion component (C+Cde) is about 36% of the total damage for blank tests. With inhibitor tests the proportion is lower than the blank ones. Erosion (E+dEc) is the predominant under impinging flow condition with sand. Inhibitor reduces the corrosion component by forming film on the metal surface and also inhibition leads to smaller roughness factors and hence would lower pressure drop at higher flowing rates so that increase the production rates.

The surface of the specimen can be subdivided into four zones defined by the fluid dynamic influence. In the central zone, both indentation due to the impingement and cutting mode of the slurry flow removed all the material resulted in U shape wear scar at this zone. With addition of inhibitor, the depth of the wear scar can be reduced by about 70% compared to blank tests. Further from centre, in the second zone, sand impinged the surface at lower angle like ploughing for both blank tests and inhibitor tests. There is no apparent difference in the type of mechanical impact damage by visual examination. Pitting can be eliminated by inhibitor in this zone. At the third zone, flow with sand impacts the surface at low angle and sand abrases the material. Inhibitor reduced the surface roughness and also reduced the pits number and pit size as well as pit depth. With optimum inhibitor concentration has biggest effect in these reductions. At the edge zone, the impact by sand reduced as kinetic energy of the flow reduces along the radius direction.

With increasing sand concentration, the depth of wear in centre zone increased. With no sand there is no U shape formed in this zone. Inhibitor adsorbed onto the sand and on the metal surface both give reduction in sand energy would potentially have a great effect on mass loss.

The much higher efficiency of inhibitor with no sand than with sand indicates that not only the sand being an efficient abrasive but also that the inhibitor effectiveness is substantially reduced when sand impacts can breach any protective surface films.

For CRW8, the results indicate that E_{corr} was shifted to noble direction in the order of 100ppm ≈ 150ppm > 50ppm > 25ppm; for CRW9, in the order of 50ppm >100ppm

>150ppm > 25ppm. This suggests that the kinetics of the anodic reaction of carbon steel in CO_2 saturated solution was affected in the presence of the inhibitor of these orders. This is in agreement with the order of polarisation resistance values as well as in agreement with optimum concentration of the inhibitor.

The plot with inhibitor has more oscillation than blank one, indicating that inhibitor either acting as an obstacle for the diffusion of the species or causing instability in the transfer of charges at the metal surface.

The corrosion mechanism under erosion-corrosion is as the same as at static conditions. The optimum concentration for corrosion is the same as for erosion-corrosion. This is an indication that corrosion is controlling parameter in erosion-corrosion.

From AC impedance for blank tests, both capacitive behaviour and inductive behaviour exhibits. The induction also associated with a rapid corroding of bare metal. The equivalent circuit used to fit data for CRW8 at 25ppm and 50ppm and for CRW9 at 25ppm would be the same as with blank solution.

In the conditions under impingement, the inhibitor was obviously not easily cover the entire metal surface. For CRW9 with concentration of 50ppm, 100ppm and 150ppm, and CRW8 100ppm and 150ppm, the equivalent circuit is used for analysing the impedance data were used as the one for a coating with open pore. Double layer capacitance still is proportional to the area of the open pore on the metal surface and can be compared with those obtained with indicative behaviour.

There is a big difference of the C_{dl} values with and without inhibitors, but it is not very much different with different inhibitor concentrations although R_{ct} values are different. Therefore, it provides inhibition to the carbon steel mainly due to change the activation energy of anodic reaction on the metal surface.

Mixture of the inhibitor components has better performance of mitigation of erosion-corrosion than individual chemicals. The single components SA, SI and SJ provide no

protection against erosion-corrosion under these conditions: while SD and SF have even opposite effects, namely increase the mass loss, but SC and SK perform almost as good as the whole inhibitor CRW8 package.

SD has better performance than many other components in corrosion, but the erosion performance is very poor. SD is oil soluble component and also very sticky in nature. It actually sticks to the metal surface and surface of the equipment once get into the solution, but could not evenly be adsorbed on the sand which reduces its performance of reduction on erosion. Therefore, to reduced erosion-corrosion with inhibitor in impingement condition, the absorption of inhibitor on sand is very important.

Mechanical effect of sand particles stripped off the $FeCO_3$ for blank tests. Bilayer of inhibitor and $FeCO_3$ was formed for SD and SK single components, which provide a stronger adhesive ability than that of blank tests.

The difference of XPS spectra with N(1s) indicates the presence of nitrates on the metal surface and the most possible that the single components can be chemisorbed on the metal surface forming chelate.

Both of the two inhibitors tested with SIJ have peak-value phenomena, for CRW8, the optimum concentration is 100ppm and for CRW9, is 50ppm according to both corrosion behaviour *in-situ* conditions and erosion-corrosion results.

9.2 Future Work

Further mechanistic studies for corrosion and erosion-corrosion are to identify the reacting species at the electrode/electrolyte interface and/or the resulting interphase which may comprise both the corrosion product and a protective inhibitor. Polarized grazing angle Fourier transfer infrared spectroscopy (PGA-FTIR) can be used to get insight into the orientation of adsorbed molecules. XPS can be used to detect the chemical information on the inhibitor layer. Those ex-situ surface analyses techniques are more widely used as routine techniques.

However, in-situ techniques are more desirable to reflect accurately the composition at the electrode/electrolyte interface. EXAFS in-situ measurement for chemical composition at the interface can be used to further investigate what is generated at the interface at each stage.

Further single component tests need to be done to see which single component provide the best protection for erosion. It is important to distinguish quantitatively how much inhibitor adsorbed on sand and how much adsorbed on the metal surface. In addition, measure the drag reduction properties of inhibitors and its single component to identify what rod-like organic molecules provide the damping effect on the transfer of hydrodynamic forces.

The presence of corrosion products may reduce the efficiency of corrosion inhibitors, therefore, tests should also carried out on pre-corroded surfaces. The cooperation effects of corrosion inhibitor with corrosion products provide the information for selection of inhibitors under multiphase condition with sand.

The effect of slurry flow on the optimum concentration of inhibitor is an interesting question. Further investigation need to be done relating to optimum concentration of inhibitor with its structure to develop a model to predict optimum concentration under certain conditions.

The hydrodynamic factor had two opposite effects on inhibitor performance. It made the inhibitor reach the metal surface easily and also slurry flow causes the inhibitor to desorption from the metal surface. It is useful to determine which factor is dominant for each inhibitor under different conditions.

For accurate calculation of the weight loss of corrosion component among the total weight loss, Tafel slope values should be attained from experiment for each condition. Diffusion limited current densities are a function of electrolyte stirring rate, therefore, Tafel plot measurements should employ the hydrodynamic conditions (such as Reynolds numbers).

The concentration of sand could be higher or lower than 1000ppm. It is necessary to investigate what amount of sand can start to affect the inhibition mechanism.

REFERENCES

Alberty, R. (1983) Physical Chemistry. John Wiley and Sons

Al-Hassan, S., Mishra, B., Olson, D.L. and Salama, M.M. (1998), Effect of microstructure on corrosion of steels in aqueous solutions containing carbon dioxide, *Corrosion*, 54, no.6, pp.480-491

API RP 14E (1991), API recommended practice for design and installation of offshore production platform piping systems, American petroleum institute, Fifth edition, Washington D.C. October

Armstrong, R.D., Bell, M.F. and Metcalfe, A.A. (1978), Electrochemistry, 6, pp. 98-127, Chemical Society Specialist Periodical Reports, UK

ASTM HANDBOOK (1987), Volume 13 A Corrosion: Fundamentals, Testing, and Protection, 'Corrosion Inhibitors for Oil and Gas Production' Revised by Richard L. Martin, BJ Unichem Chemical Services, pp.878-886

ASTM E407-93 (1993), Standard practice for microetching metals and alloys, ASTM, USA

ASTM STP-1188 (1993), Electrochemical Impedance: Analysis and Interpretation, Scully, J.R., Silverman, D.C. and Kending, M.W. (editors), Philadelphia

ASTM G 106-189 (1999), Standard practice for verification of algorithm and equipment for electrochemical impedance, *Annual Book of ASTM Standards*, Section 3, Vol. 03.02, pp.436-446.

Barton, N.A. (2003), Erosion in elbows in hydrocarbon production systems: Review document, Research report 115, HSE Health & safety executive

Benchaita, M.T., Griffith, P. and Rabinowicz, E. (1983), Erosion of metallic plate by solid particles entrained in a liquid jet, *Journal of Engineering for Industry*, Transactions ASME, v.104, no. 3, pp. 215-222

Bird, R.B., Stewart, W.E. and Lightfoot, E.N. (1976), *Transport Phenomena*, John Wiley and Sons, Singapore

Bisquert, J. (access 2006), http://www.elp.uji.es/juan_home/research/impedance.htm

Bockris, J.O'M. and Drazic, D.M. (1972), *Electro-Chemical Science*, Taylor and Francis, London

Bockris, J.O'M., Drazic, D. and Despic, A.R. (1965). The electrode kinetics of the deposition and dissolution of iron, *Electrochemica Acta*. vol.4, no. 325. pp. 325-361

Bockris J. O'M, Bonciocat N and Gutman F (1974). *An Introduction to Electrochemical Science*, London, Wykeham Pub. Ltd

Boukamp, B.A. (1988/89), *Equivalent Circuit*. University of Twente, The Netherlands

Briggs, D. and Seah, M.P. (1990), *Practical Surface Analysis*. John Wiley & Spms. NY.

Bregman, J.I. (1963), *Corrosion Inhibitors*, Pub. Macmillan Company. New York

Burke, P.A. (1985). Synopsis: Recent progress in the understanding of CO_2 corrosion. *in Advances in CO_2 corrosion*, v.1 (Houston, TX: NACE). pp.3-9

Burstein, G.T. and Sasaki, K. (2001). Detecting electrochemical transients generated by erosion–corrosion, *Electrochemica Acta*. vol.46. issue. 24-25. pp. 3675-3683

Chen, Y, Hong, T., Gopa, M. and Jepson, W.P. (2000). EIS studies of a corrosion inhibitor behaviour under multiphase flow conditions, *Corrosion Science*. 42. pp.979-990

Chin, D.T. and Tsang, C.H. (1978), Mass-transfer to an impinging jet electrode. *Journal of the Electrochemical Society*. v.125, no.9, pp. 1461-1470

Campbell, S. and Jovancicevic, V. (1999), Corrosion inhibitor film formation studies by ART-FTIR, *CORROSION/99*. paper No.484

Cao, C. (1996), On electrochemical techniques for interface inhibitor research. *Corrosion Science*, 38, pp.2073-2082

Cole, K.S and Cole, R.H. (1941). Dispersion and absorption in dielectrics. *Journal of chemical physics*, vol.9, pp.341-351

CorCon (access in 2004). http://www.xs4all.nl/~cdewaard/#CO2

Crolet, J.L. (1994), Which CO_2 corrosion, hence which prediction?, in *Predicting CO_2 Corrosion in the Oil and Gas Industry*. European Federation of Corrosion Publication no. 13 (London, U.K.: Institute of Materials). pp.1-29

Crolet, J.L., Thevenot, N. and Nesic, S. (1998). Role of conductive corrosion products in the protectiveness of corrosion layers. *Corrosion* 54. pp.194-203

Dawson, J.L., Shih, C,C., Geary, D. and Miller, R.G. (1991). Flow effects on erosion-corrosion. *Material Performance*, NACE. v.30, no.4. April. pp.57-60

Dawson, J.L., Shih, C.C., John, D.G. and Eden, D.A. (1987), Electrochemical testing of differential flow induced corrosion using jet impingement rigs, *CORROSION/87*, paper no. 453, San Francisco Cal. USA, pp.9-13

Dawson, J.L., Shih, C.C. and Bartlett, P.K.N. (1993), Models and predictions of CO_2 corrosion and erosion-corrosion under flowing conditions", in "*Progress in The Understanding and Prevention of Corrosion*", v.1, Inst. of Mat. For the Soc. J.M.Costa, A.D.Mercer (eds.), UK, pp.513-530.

Dayalan, E., de Moraes, F.D., Shadley, J.R., Shirazi, S.A. and Ribicki, E.F.(1998), CO_2 corrosion prediction in pipe flow under $FeCO_3$ scale-forming conditions, *CORROSION/98*, NACE, paper No. 98051

De Marco, R., Durnie, W., Jefferson, A., Kinsella, B. and Crawford, A. (2002) Persistence of carbon dioxide corrosion inhibitors, *Corrosion*, vol. 58, pp.354-363

de Waard, C. and Milliams, D.E. (1975), Carbonic Acid Corrosion of Steel, *Corrosion*, v.31, no.5, pp.177-181

de Waard, C., Lotz, U. and Milliams, D.E. (1991), Predictive model for CO_2 corrosion engineering in wet natural gas pipelines, *Corrosion*, 47, pp.976-

Dugstad, A. (1992), The importance of $FeCO_3$ supersaturation of carbon steel, *CORROSION/92*, NACE, USA, paper no. 14

Dugstad, A., Lunde, L. and Videm, K. (1994), Parametric study of CO_2 corrosion of carbon steel", *CORROSION/94*, (Houston, TX:NACE International) paper no. 14

Durnie, W., De Marco, R., Jefferson, A. And Kinsella, B.(1999), Development of a structure-activity relationship for oil field corrosion inhibitors, *Journal of The Electrochemical Society*, v. 146, no.5, pp.1751-1756

Efird, K.D. (1998), http://www.efirdcor.com/Jet_Imp_Test.htm

Efird, K.D., Wright, E.J., Boros, J.A. and Hailey, T.G. (1993), Correlation of steel corrosion in pipe flow with jet impingement and rotating cylinder tests, *Corrosion*, 49, pp.992-1003

Epelboin, I. and Keddam, M. (1972), Kinetics of formation of primary and secondary passivity in sulphuric aqueous media. *Electrochimica Acta*, 17(2), 177-186

Epelboin, I., Keddam, M, Takenouti, H. (1972), Use of impedance measurements for the determination of the instant rate of metal corrosion, *Journal of Applied Electrochemistry*, vol.2. pp. 71-79

Eriksrud, E. and Sontvedt, T. (1983), Effect of flow on CO_2 corrosion rates in real and synthetic formation waters", *CORROSION/83*, Paper no.44, Anaheim Cal., April pp.18-22

Esih, I., Soric, T. and Pavlinic, Z. (1995), Inhibition of mild steel corrosion in CO_2-saturated chloride solutions by acylated polyamine salts, *Proceedings of the 8th European Symposium on Corrosion Inhibitors (8 SEIC)*, Ann, Univ. Ferrara, N.S., Sez. V, N.10

Evans, T.N., Sun, Y., Babaian-Kibala, E., Bennett Jnr, H.R., Martin, J.W. and Alvarez, J. (2004), Studies of inhibition and monitoring of metal loss in gas systems containing solids, *CORROSION/2004*, paper No. 362, (Houston, TX:NACE International)

Farshad, F.F., Garber, J.D. and Polaki V. (2000), Comprehensive model for predicting corrosion rates in gas wells containing CO_2, *SPE Production and Facilities,* v.15, n 3, Auguest, pp. 183-190

Fokin, A.V., Pospelov, M.V., Churshukov, E.S., Maiko, L.P., Sergeikin, A.Ya., Shekhter, Yu.N. and Belova, T.I. (1986), Influence of structure of hydrophobic fragments of oil-soluble corrosion inhibitors on their protective properties, *Institute of physical chemistry, Academy of Sciences of the USSR. Translated from Khimiya i Tekhnologiya Topliv i Masel,* No. 2, pp. 10-11, Februray, 1986

Finnie, I. (1960), Erosion of surfaces by solid particles, *Wear*, 3, pp.87-103

Gabe, D.R. and Walsh, F.C. (1983), The Rotating cylinder electrode: a review of development, *Journal of Applied Electrochemistry*, v.13, no. 1, pp.3-21

Gabrielli, C. (1980), Identification of electrochemical processes by frequency response analysis, *Solartron Instrumentation Group*

Gabrielli, C. and Keddam, M. (1992), Review of applications of impedance and noise analysis to uniform and localized corrosion, *Corrosion* 48 pp.794-811

Gamry Instruments (1997), *EIS primer* [online]. Warminster, PA: Gamry Instruments. http://www.gamry.com/App_Notes/EIS_Primer/EIS_Primer.htm

Giralt, F. and Trass, O. (1976), Mass transfer from crystalline surfaces in a turbulent impinging jet EM DASH2. erosion and diffusional transfer, *Canadian Journal of Chemical Engineering*, V. 54, no. 3, pp. 148-155

Granese, S.L., Rosales, B.M., Oviedo, C. and Zerbino, J.O. (1992), The inhibition action of heterocyclic nitrogen organic compounds on Fe and steel in HCl media, Corrosion Science, vol. 33, pp.1439-1453

Harrop, Don. (2004), Chemical inhibition in demanding environment: Assuring continuing asset integrity through best practice deployment, *Corrosion Management in Upstream Oil& Gas*, Aberdeen

Harrop, D., Webster, S., McMahom, A.J. and Pertridge, G.J. (1993), CO_2 corrosion: a testing problem with a predictive solution", in "*Progress in The Understanding and*

Prevention of Corrosion", v.1. Inst. of Mat. For the Soc. J.M.Costa . A.D.Mercer (eds.). UK, pp.498-503

Hausler, R.H. and Stegmann, D.W. (1988), Studies relating to the predictiveness of corrosion inhibitor evaluations in laboratory and field environments. *European Petroleum Conference, SPE*, Paper No. 18369, SPE, Richardson, TX, pp.317-328

Hawkins, C. (1995) PhD thesis, University of Manchester

Heeg, B., Moros, T. and Klenerman, D. (1998), Persistency of corrosion inhibitor films on c-steel under multiphase flow conditions. Part I: The jet-cylinder arrangement". *Corrosion Science*, vol. 40, no. 8, pp1303-1311

Heitz, E. (1991), Chemo-Mechanical Effects of Flow on Corrosion, *Corrosion Engineering*, v. 47. no.2, pp.135-145

Heuer, J.K. and Stubbins, J.F. (1998), Microstructure analysis of coupons exposed to carbon dioxide corrosion in multiphase flow, *Corrosion* 54, No. 7, pp.566-575

Heuer, J.K. and Stubbins, J.F. (1999), An XPS characterization of $FeCO_3$ films from CO_2 corrosion", *Corrosion Science* 41, pp. 1231-1243

Ikeda, A., Ueda, M. and Mukai, S. (1984), CO_2 behaviour of carbon and Cr steels, in P.H.Hausler and H.P.Codard (Eds.), *Advances in CO_2 Corrosion*, Houston, TX, NACE, v.1, pp.39-51

Jiang, X., Zheng, Y.G., Ke, W. (2005), Effect of flow velocity and entrained sand on inhibition performances of two inhibitors for CO_2 corrosion of N80 steel in 3% NaCl solution, *Corrosion Science*. Article in press.

Johnson, M.L. and Tomson, M.B. (1991), Ferrous carbonate precipitation kinetics and its impact CO_2 corrosion, *CORROSION/91*, NACE, USA, paper 268

Jordan, K. (1998), Erosion in multiphase production of oil and gas, *CORROSION 98*, paper no. 58, NACE International Annual Conference, San Antonio, TX

Jovancicevic, V., Ramachandran, S. and Prince, P.(1999), Inhibition of carbon dioxide corrosion of mild steel by imidazolines and their precursors, *Corrosion*, vol. 55, no. 5, pp.449-455

Juettner, K., Lorenz, W.J., Kendig, M.W. and Mansfeld, F. (1988), Spectroscopy on 3-D inhomogeneous surfaces: corrosion in neutral aerated solutions, Journal of the Electrochemcal Society, vol.135, no. 2, pp. 332-339

Kaminski, M. and Sklarska-Smialowska, Z. (1973), Adsorption of thiophene derivatives on steel in sulphuric acid solutions, *Corrosion Science*, vol. 13, pp.557-565

Kelley, J.A. and Bowman, C.W. (1984), The chemistry of corrosion inhibitors used in oil production, *UK Corrosion*, Nov. 1984, London

Kendig, M.W. and Mansfeld, F. (1983), Corrosion rates from impedance measurements: An improved approach for rapid automatic analysis", *Corrosion* 39, 466-467

Kermani, M.B. and Harrop, D. (1996), The impact of corrosion on the oil and gas industry, *SPE Production Facilities*, v.11, n.3, pp.186-190

Kermani, M.B. and Morshed, A. (2003), Carbon dioxide corrosion in oil and gas production—A compendium, *Corrosion*, 59, No.8, pp.659-683

Kern, D.M. (1984), The hydration of carbon dioxide, in "*CO_2 Corrosion In Oil And Gas Production-Selected Papers, Abstracts And References", Newton, L.E. and Hausler, R.H. (eds), NACE T-1-3*, USA, pp.75-88

Kinsella, B., Tan, Y.J. and Bailey, S. (1998), Electrochemical impedance spectroscopy and surface characterization techniques to study carbon dioxide corrosion product scales, *Corrosion,* 54 (10), pp.835-842

Lahodny-sarc, O. (1994), in A Working Party Report on Corrosion Inhibitors, *European Federation of Corrosion*, The institute of Materials, London, pp.104

Lasurface (access 2006), http://www.lasurface.com/database/index.php

Leibig, M. and Halsey, T. (1993), Double layer impedance as a probe of surface roughness, *Electrochimic Acta*, vol.38, n.14, pp.1985-1988

Levy, A.V. (1981), The solid particle erosion behaviour of steel as a function of microstructure, *Wear*, v.68, pp.269-287

Li, P., Tan, T.C. and Lee, J.Y. (1997), Corrosion protection of mild steel by electroactive polyaniline coatings, *Synthetic Metals*, v.88, pp.237-242

Lindner, P., Bewersdorff, H.B., Heen, R., Sittart, P., Tiel, H., Langowski, J. and Oberthur, R. (1990), Drag-reducing surfactant solutions in laminar and turbulent flow investigated by small-angle neutron scattering and light scattering, *Progress of Colloid Polymer Science*, 81. pp. 107-112

Liu, C., Leyland, A., Bi, Q. and Matthews, A. (2001), Corrosion resistance of multi-layered plasma-assisted physical vapour deposition TiN and CrN coatings. *Surface and Coatings Technology*, v.141, pp.164-173

Lotz, U. (1990), Velocity effects in flow-induced corrosion, *CORROSION/90*, paper no. 27 (Houston, TX:NACE, 1990)

Lotz, U. and Sydberger, (1988), CO_2 corrosion of carbon steel and 13Cr steel in particle-laden fluid, *Corrosion (Houston)*, v 44, n 11, pp,800-809

Lyklema, J.(1991), Electrostatic characterization of solid/liquid interfaces, influence of adsorbates, *Proceedings of the 6th IFP Exploration and Production Research Conference*, Sept. Saint-Raphael, Fr.

Malik, H.P. (1992), The influence of pH and surface films on corrosion inhibitor performance in CO_2 saturated 5% NaCl, *PhD thesis*. The Victoria university of Manchester

Malik, H.P. (1995), Influence of C16 quaternary amine of surface films and polarisation resistance of mild steel in carbon dioxide-saturated 5% sodium chloride, Corrosion 51, no. 4, pp. 321-328

Malka, R., Nesic, S. and Gulino, D.A. (2006), Erosion corrosion and synergistic effects in disturbed liquid-particle flow, *CORROSION/2006*, NACE, paper No. 06594

Mansfeld, F. (1977), in: R. Baboian (Ed.), Electrochemical techniques for corrosion, *National Association of Corrosion Engineers*, Texas, pp.18-26

Mansfeld, F. (1981), Recording and analysis of AC impedance data for corrosion studies. I. Background and methods of analysis, *Corrosion*, vol. 36, no.5, pp.301-307

Mansfeld, F. (1990), Electrochemical impedance spectroscopy (EIS) as a new tool for investigation methods of corrosion protection, *Electrochemical Acta* vol.35, no.10, pp. 1533-1544

Mansfeld, F. (1992), *Second International Symposium on Electrochemical Impedance Spedance Spectroscopy*, July 12-17, in Santa Barbara, CA

Mansfeld, F., Kendig, M.W. and Lorenz, W.J. (1985), Corrosion inhibition in Neutral, aerated media, *Journal of the Electrochemical Society*, vol.132, no.2, pp.290-296

Mansfeld, F., Shih, H., Greene, H. and Tsai, C.H. (1993), Analysis of EIS data for common corrosion processes, Electrochemical impedance: Analysis and Interpretation, *ASTM STP 1188*, Scully, J.R., Silverman, D.C. and Dendig, M.W. Eds. Philadephia, pp. 37-53

Mansfeld, F. and Tsai, C.H. (1991), Determination of coating deterioration with EIS. I. Basic relationships, *Corrosion*, vol. 47, pp.958-963

Martin, R.L. and Braga, T.G. (1987), Corrosion control in enhanced oil recovery wells, *Material Performance*, vol. 27 no. 2, pp.16-22

McLaury, B.S. and Shirazi, S.A. (1999), Generalization of API RP14E for erosion service in multiphase production, *SPE Annual Technical Conference and Exhibition*, v. 2, pp. 423-432

McCafferty, E.(1979), Mechanisms of corrosion control by inhibitors, In: Leidheiser Jr H, editor. *Corrosion Control by Coatings*, Princeton: Science Press, pp. 279-317

Menendez, C.M. and Jovancicevic, V. (1995), Novel approach for assessing inhibitors performance against localized corrosion, CORROSION/03, paper No. 374, NACE International, Houston, TX

Mendoza-Flore, J. and Turgoose, S. (1995), A rotating cylinder electrode study of cathodic kinetics and corrosion rates in CO_2 corrosion, *CORROSION 95*, Paper no. 124, Orlando, Fla.

Mendoza-Flore, J. and Turgoose, S. (2002), Fe_3C influence on the corrosion rate of mild steel in aqueous CO_2 systems under turbulent flow conditions, *Corrosion Science* 44 pp.1223-1246

Mishra, B., Al-Hassan, S., Olson, D.L. and Salama, M.M. (1997), Development of a predictive model for activation-controlled corrosion of steel in solutions containing carbon dioxide, *Corrosion*, 53, pp.852-859

Mok, W.Y., Jenkins, A.E. and Gamble, C.G. (2003), Localised corrosion and inhibitor selection, *Journal of Corrosion Science and Engineering*, at http://www.umist.ac.uk/corrosion/jcse

Murray, J. N., Moran, P.J. and Gileadi, E. (1988), Utilization of the specific pseudocapacitance for determination of the area of corroding steel surfaces, *Corrosion*, 44 (8), pp.533-538

Nesic, S. and Lunde, L. (1994), Carbon dioxide corrosion of carbon steel interface flow, *Corrosion* 50, pp. 717-727

Nesic, S. and Postlethwaite, J. (1991), Hydrodynamics of disturbed flow and erosion-corrosion, part I---single-phase flow study, *The Canadian journal of chemical engineering*, vol. 69, June

Nesic, S., Postlethwaite, J. and Olsen, S. (1995), An electrochemical model for prediction of CO_2 corrosion, *CORROSION/95*, paper no. 131, (Houston, TX:NACE International, 1995)

Neville, A. (1995), An investigation of the corrosion behaviour of engineering materials in marine environments, *PhD Thesis*, University of Glasgow

Neville, A., Hodgkiess, T., Dallas, J.T. (1995), A study of the erosion-corrosion of engineering steels for marine pumping applications, *Wear*, 186-187, pp.497-507

Neville, A., and Morizot, A.P. (2002), Calcareous scales formed by cathodic protection-an assessment of characteristics and kinetics, *Journal of Crystal Growth*, vol. 243, pp.490-502

Nmai, C.K. (2004), Multi-functional organic corrosion inhibitor, *Cement & Concrete Composites*, vol. 26, pp.199-207

Ogundele, G. I. and White, W.E. (1986), Some observations on corrosion of carbon steel in aqueous environments containing carbon dioxide, *Corrosion 42*, no.2, pp.71-78

Olsen, S., Dugstad, T. and Wenn, T.(1995), Flow effects on corrosion inhibitors in topside flowlines, *CORROSION/95* NACE, paper no. 129

Oltra, R., Chapey, B. and Renaud, L. (1995), Abrasion-corrosion studies of passive stainless steels in acidic media: combination of acoustic emission and electrochemical techniques, Wear, vol.186-187, part 2, pp. 533-541

Palacios, C.A. and Shadley, J.R.(1991), Characteristics of corrosion scales on steel in a CO_2-saturated NaCl brine", *Corrosion* 47, no.2, pp. 122-127

Palacios, C.A. and Shadley, J.R.(1993), CO_2 corrosion of N-80 steel at 71°C in a two-phase flow system, Corrosion, 49, no. 8, pp.686-693

Palmer, D.A. and van Eldik, R. (1983), The Chemistry of Metal Carbonate and Carbon Dioxide Complexes, *Chem. Rev.*, v. 83, no. 6, pp.651-727

Papavinasam, S., Revie, R.W., Attard, M., Demoz, A. and Michaelian, K.(2003), Comparison of laboratory methodologies to evaluate corrosion inhibitors for oil and gas pipelines, *Corrosion 59*, no.10, pp.897-912

PaulingFile (access in 2004), http://crystdb.nims.go.jp/

Peterson, G., (access in 2006), The Belousov-Zhabotinsky reaction, *http://online.redwoods.cc.ca.us/instruct/darnold/DEProj/Sp98/Gabe/bzreact.htm*

Plieth, W. (1992), Additives in the electrocrystallization process, *Electrochimica Acta*, vol. 37 pp.2115-2121

Pospelov, M.V. and Fokin, A.V. (1993), in *Reviews on Corrosion Inhibitor Science and Technology*, A.Raman, P.Labine, Eds., NACE, Houston, pp. I-4-1

Poulson, B. (1983), Electrochemical measurements in flowing solutions, *Corrosion Science*, v. 23, no. 1-4, pp.391-430

Poulson, B. (1993), Advances in understanding hydrodynamic effects on corrosion, *Corrosion Science*, vol. 35, No.1-4, pp. 655-665

Ramachandran, S., Campell, S. and Ward, M.B. (2001), Interactions and properties of corrosion inhibitors with by-product layers, *Corrosion*, 57, no. 6, pp.508-515

Ramachandran, S., Ward, M.B., Bartrip, K.A. and Jovancicevic, V.(2002), Inhibition of the effects of erosion corrosion, *CORROSION/2002*, paper no. 2498 (NACE, Houston)

Ramachandran, S., Ahn, Y.S., Bartrip, K.A., Jovancicevic, V. and Bassett, J. (2005). Further advances in the development of erosion corrosion inhibitors. *CORROSION/2005*, paper no. 5292(NACE, Houston)

Rammelt, U. and Reinhard, G. (1987), The influence of surface roughness on the impedance data for iron electrodes in acid solutions. *Corrosion Science*, 27 (4), pp. 373-382

Riggs, O.L. (1981), Theoretical aspects of corrosion inhibitors and inhibition. in *Corrosion Inhibitors*, Nathan, C.C. editor. NACE. Houston, TX, pp. 7-27

Roberge, P. (2004), *Erosion-Corrosion, Corrosion Testing Made Easy*, by NACE international

Roberge, P.R. and Sastri, V.S.(1994). On-line corrosion monitoring with electrochemical impedance spectroscopy. *Corrosion* 50. Oct. pp. 744-754

Salama, M.M. (1998), An alternative to API 14E erosional velocity limits for sand laden fluids, presented at the 1998 Offshore Technnology Conference. Houston, TX. OTC8898

Salama, M.M. and Venkatesh, E.S. (1983). Evaluation of API RP 14E Erosion at velocity limitations for offshore gas wells. paper OTC4485 presented at the 1983 *Annual Offshore Technology Conference*, May 2-5

Sastri, V.S. (1998), *Corrosion Inhibitors- Principles and Applications*

Schaschl, E. (1981). Methods for evaluation and testing of corrosion inhibitors. in *Corrosion Inhibitors*, ed. Nathan, C.C. (Houston, NACE), pp.28

Schmitt, G. (1983). Fundamental aspects of CO_2 corrosion. *CORROSION/83*, paper no. 43 (Houston, TX: NACE, 1983)

Schmitt, G. (1995), Hydrodynamic limitations of corrosion inhibitor performance. Proceeding of the 8th European Symposium on Corrosion Inhibitor. pp.1075-1099

Schmitt, G. (2001). Drag reduction by corrosion inhibitors- A neglected option for mitigation of flow induced localized corrosion. *Material and Corrosion* 52. pp. 329-343

Schmitt, G. (2003). Future challenges for functional Chemicals in oil and gas production. *The Journal of Corrosion Science and Engineering*, vol. 6. paper. C146

Schmitt, G., Gudde, T. and Strobel-Effertz, E. (1996). Fracture mechanical properties of CO_2 corrosion product scales and their relation to localized corrosion. *CORROSION 96*. NACE International. Houston. Texas. Paper No. 96009

Schmitt, G. and Gudde, T. (1995). Local mass transfer coefficients and local wall shear stresses at flow disturbances. *CORROSION 95*. paper no. 102 (Houston, TX: NACE)

Schmitt, G., Labus, B.N., Sun, H. and Stradmann, N. (1995), Synergisms and antagonisms in CO_2 corrosion inhibition, *Proc. 8th Europ. Symp. on Corrosion Inhibitors* (8SEIC). Ann. Univ. Ferrara, N.S, Sez. V, Suppl. N. 10, pp.1113-1123

Schmitt, G. and Rothmann, B. (1977), Studies on the corrosion mechanism of unalloyed steel in oxygen-free carbon dioxide solutions. Part I: Kinetics of the liberation of hydrogen, *Werkstoffe Und Korrosion v.28, 1977, in: L.E.Newton, R.K.Hausler (Eds.) "CO_2 Corrosion In Oil and Gas Production—Selected Papers, Abstracts and References", NACE T-1-3, 1984,* USA, pp. 167-177

Schmitt, G., Simon, T. and Hausler, R. H. (1990), CO_2 erosion corrosion and its inhibition under extreme shear stress, I. development of methodology, *CORROSION/95*, NACE, Las Vegas/Nevada, paper no. 90022

Scott, S.K. (1994), *Oscillations, Waves and Chaos in Chemical Kinetics*, First edition. New York, New York: Oxford University Press

Shadley, J.R., Rybicki, E.F., Shirazi, S.A. and Dayalan, E.(1998), Velocity guidelines for avoiding erosion-corrosion damage in sweet production with sand, *Journal of Energy Resources Technology*, ASME, Vol. 120, pp. 78-83

Shadley, J.R., Shirazi, S.A., Dayalan, E. and Rybicki, E.F. (1998), Prediction of erosion-corrosion penetration rate in carbon dioxide environment with sand, *Corrosion*, vol. 54, no. 12, pp.972-978

Shirazi, S.A., McLaury, B.S., Shadley, J.R. and Rybicki, E.F.(1995), Generalization of the API RP 14E guideline for erosion services, *Journal of Petroleum Technology* (Distinguished author series), pp.693-698

Silva, L.M., Hernandez, J. and Genesca, J.and Duran, R. and Mendoza, J. (2004), Effect of flow on the corrosion mechanism of different API pipeline steels grades in NaCl solutions containing CO_2, *CORROSION/2004*, paper No. 04651, NACE International.

Silverman, D.C (1989), Corrosion rate estimation from pseudo-inductive electrochemical impedance response", *CORROSION/89*.NACE

Singh, I. (1993), Inhibition of steel corrosion by thiourea derivatives, *Corrosion*, vol. 49, n. 6, pp. 473-478

Sinnott, R.K. (1999), *Coulson and Richardson's Chemical Engineering, Volume 6, Third edition, Chemical Engineering Design*, Butterworth/Heinemann

De Souza, V.A. and Neville, A.(2003), Corrosion and erosion damage mechanisms during erosion-corrosion of WC-Co-Cr cermet coatings, *Wear*, vol. 255, pp.146-156

Srhiri, A., Etman, M. and Dabosi, F. (1996), Electro and physicochemical study of corrosion inhibition of carbon steel in 3% NaCl by alkylimidazoles, Electrochimica Acta vol. 41, pp. 429-437

Stachowiak, G.W. and Batchelor, A.W. (2001), *Engineering Tribology Second Edition*, Butterworth Heinemann, U.S.A.

Stack, M.M., Corlett, N., Zhoi, S. (1997), A methodology for the construction of the erosion-corrosion maps in aqueous environments, *Wear*, 215, pp.67-76

Stansbury, E.E. and Buchanan, R.A. (2000), *Fundamentals of Electrochemical Corrosion*, ASM International

Stephen, W. Tait (1994), *An introduction on electrochemical corrosion testing for practicing engineers and scientists*, Pair O Docs Publications

Stern, M. and Geary, A. L. J. (1957), Electrochemical polarisation: I. a theoretical analysis of the shape of polarisation curves, *Journal of the Electrochemical Society*, 104(1), pp.56-63

Tan, Y.J., Bailey, S., and Kinsella, B. (1996), An investigation of the formation and destruction of corrosion inhibitor films using electrochemical impedance spectroscopy (EIS), *Corrosion Science*, vol. 38, No 9, pp1545-1561

Thomas, J.G.N. (1979), *The Mechanism of Corrosion Prevention by Inhibitors*; from L.L.Shreir, *Corrosion control*, Vol. 2, Second edition; Newnes-Butterworths, U.K.

Trabanelli, G. (1989), Fundamental and general aspects of inhibition science, *CORROSION/89* NACE International, paper No. 13

Turgoose, S. and Cottis, R.A. (1993), The impedance response of film covered metals, paper obtained from: J.R.Scully, D.C.Silverman and M.W.Kending (editors), *Electrochemical Impedance: Analysis and Interpretation*, ASTM STP-1188, Philadelphia

Turgoose, S., Cottis, R.A. and Lawson, K. (1992), Modeling of electrode processes and surface chemistry in carbon dioxide containing solutions, in *"Computer Modeling in Corrosion", R.S.Munn (ed.), ASTM STP 1154, American Society for Testing and* Materials, USA, pp.67-81

Videm, K. and Dugstad, A. (1989), Corrosion of carbon steel in an aqueous carbon dioxide environment. Part 2. Film formation, *Material Performance*, vol. 28,pp. 46-50

Videm, K., Kvarekval, J., Perez, T. and Fitzsimons, G. (1996), Surface effects on the electrochemistry of iron and carbon steel electrodes in aqueous CO_2 solutions, *CORROSION/96*, NACE, paper no.1

Vilamizar, W. and Casales, M.(2006), An EIS study of the effect of the pedant group in imidazolines as corrosion inhibitors for carbon steel in CO_2 environments, *Material and Corrosion*, 57, No. 9, pp. 696-704

Waids, NM, (access in 2005), http://octane.nmt.edu/WaterQuality/corrosion/CO2.htm

Walter, G.W. (1986), A review of impedance plot methods used for corrosion performance analysis of painted metals, *Corrosion Science*, 26 (9), pp. 681-703

Wang, D., Li, S, Ying, Y., Wang, M, Xiao, He., and Chen, Z. (1999). Theoretical and experimental studies of structure and inhibition efficiency of imidazoline derivatives. *Corrosion Science*, vol. 41, pp. 1911-1919

Wood, F.W. (1986), Erosion by solid-particle impact: a testing update, *Journal of Testing and Evaluation*, JTEVA, vol.14, no. 1, p.23-27

Wood, R.J.K. (2006), Erosion-corrosion interactions and their effect on marine and offshore materials, *Wear*, vol.261, pp. 1012-1023

Wood, R.J.K. and Speyer, A.J. (2004), Erosion-corrosion of candidate HVOF aluminium-based marine coatings, Wear, vol. 256, pp. 545-556

Wood, R.J.K., Jones, T.F., Ganeshalingam, J. and Miles, N.J. (2004), Comparison of predicted and experimental erosion estimates in slurry ducts, *Wear*, vol. 25, pp. 937-947

Xia, Z., Chou, K.C. and Smialowska, Z.S. (1989), Pitting corrosion of carbon steel in CO_2-containing NaCl brine, *Corrosion*, vol. 45, n. 8, pp.636-642

Yariv, A. and Cross, H. (1979) *Geochemistry of Colloid Systems for Earth Scientists*, New York, Springer-Verlag.

Zecher, D.C. (1976), Corrosion inhibition by surface-active chelants, *Materials performance*, vol. 15, no.4 pp. 33-37

Zhang, A.F., Xing, J.D., Fang, L. and Su, J.Y.(2004), Inter-phase corrosion of chromium white cast irons in dynamic state, *Wear*, vol. 257, pp. 198-204

Zhang, X., Wang, F., He, Y. and Du, Y. (2001), Study of the inhibition mechanism of imidazoline amide on CO_2 corrosion of Armco iron, *Corrosion Science*, 43, pp.1417-1431

Zvauya, R. and Dawson, J.L. (1993), Inhibitor studies in sweet corrosion systems by a quaternary ammonium compound, Journal of Applied Electrochemistry, vol. 24, pp.943-947